UNIVERSITY *of* MISSOURI

RESEARCH REACTOR CENTER

August 24, 2011

U.S. Nuclear Regulatory Commission
Attention: Document Control Desk
Mail Station P1-37
Washington, DC 20555-0001

REFERENCE: Docket 50-186
University of Missouri-Columbia Research Reactor
Amended Facility License R-103

SUBJECT: Written communication as specified by 10 CFR 50.4 regarding an application to amend Amended Facility License R-103 by revising the University of Missouri-Columbia Research Reactor Technical Specification 2.1, "Reactor Core Safety Limit," pursuant to 10 CFR 50.90

The University of Missouri Research Reactor (MURR) is requesting approval from the U.S. Nuclear Regulatory Commission (NRC) to revise Technical Specification (TS) 2.1, "Reactor Core Safety Limit," because of an error that was discovered in the MURR Safety Limit (SL) Analysis while answering a relicensing Request for Additional Information (RAI) question.

The current MURR SL curves were developed in 1973 by the NUS Corporation for the 1974 uprate in power from 5 to 10 MW. These curves establish the maximum allowable reactor power limits, the dependent variable, for safe operation under different combinations of three (3) measureable independent operating parameters – primary coolant flow, reactor inlet water temperature, and primary coolant pressurizer pressure. The limits provide the basis for determining the Limiting Safety System Settings (LSSSs) and operating limits for 5 and 10 MW operation (also known as Mode II and Mode I operation, respectively).

Appendix F of Addendum 4 to the MURR Hazards Summary Report (HSR) (Attachment 1) provided the SL Analysis for Mode I and II operation. This analysis generated two (2) SL curves corresponding to primary coolant pressurizer pressures of 60 and 75 psia. Attachment 2 (*Safety Limit Analysis for the MURR Facility*, NUS Corporation, NUS-TM-EC-9, May 1973) was the base document that was used in preparing Appendix F. Section 6.0 of Addendum 5 to the MURR HSR (Attachment 3) extended the original analysis to include a third SL curve for a pressurizer pressure of 85 psia, i.e. the nominal operating pressure. The power peaking factors used in the determination of the MURR SLs for Mode I and II operation are provided in Section 3.3 of Addendum 3 to the MURR HSR (Attachment 4).

1513 Research Park Drive Columbia, MO 65211 Phone: 573-882-4211 Fax: 573-882-6360 Web: www.murr.missouri.edu

Appendix H of Addendum 4 to the MURR HSR (Attachment 5) provides the bases for determining the LSSSs for Mode I and Mode II operation. The safety analysis for natural convective cooling of the core (Mode III operation) is provided in Section 5.5.3 of the MURR HSR (Attachment 6).

By letter dated January 17, 2011, a report, as required by MURR TS 6.1.h (2), was submitted to the NRC which detailed the error and the subsequent actions after the error was discovered. As stated in the report, the NUS Corporation used the Advanced Test Reactor (ATR) preliminary flow tests, which were performed in 1964 and 1966 by Croft and Waters (Attachments 7 and 8), to show that the flow instability burnout heat flux was 0.6 of the critical heat flux (CHF) predicted by the Bernath CHF Correlation (Attachment 9). This supported using a more conservative value of 0.5 of the Bernath Correlation to develop the MURR Mode I and II SLs. If the local value of heat flux anywhere in a fuel element exceeds 50% of the local CHF value, as predicted by the Bernath Correlation, then flow instability is assumed to have occurred. The error that was discovered was a discrepancy between the "diameter of heated surface," known as the variable D_i, as it is defined by Bernath and a more commonly used "heat diameter" definition inadvertently used by the NUS Corporation when developing the SL curves.

Revised SL tables and curves for Mode I and II operation have been developed applying the correct Bernath D_i definition, however no changes to the current MURR LSSSs are required in order to maintain approximately the same safety margins. Additionally, the safety analysis for Mode III operation is based on the original 5.2 Kg ^{235}U alloy fuel which assumed a combination of power peaking factors that exceed the combined power peaking factors for the current 6.2 Kg ^{235}U aluminide fuel core. Therefore, the analysis in Section 5.5.3 still conservatively envelopes Mode III operation of the MURR and requires no revision.

The revised SLs are based on new power peaking factors (Attachment 10) developed by a team of MURR staff working with staff from Argonne National Laboratory (ANL). As described in the August 31, 2010 submittal to relicensing RAI 4.17 regarding the NUS Corporation developed SLs, the power peaking factors used were extremely conservative because they utilized a combination of unrealistic or impossible peaking factors determined by three (3) different 2D diffusion code models, which was the only code method available in the early 1970's. Since 2006, the MURR has been actively collaborating with the Reduced Enrichment for Research and Test Reactor (RERTR) Program on the conversion from highly-enriched uranium (HEU) to low-enriched uranium (LEU) fuel. During this time, the ANL/MURR team has benchmarked the MURR HEU fuel and reactor core design performance. We now have more accurate peaking factors that were used to determine the new SLs.

With the revised curves, the MURR has a new SL of 14.894 MW for Mode I operation with all three (3) non-power LSSS variables set at their corresponding limits, i.e. primary coolant pressurizer pressure at 75 psia, total core flow rate at 3200 gpm, and reactor inlet water temperature at 155 °F. This provides a 2.39 MW margin between the reactor power LSSS of 12.5 MW and the SL. This is actually slightly higher than the previous NUS Corporation calculated SL of 14.892 MW. For Mode II operation, with the revised SL curves, the MURR has a new SL of 8.763 MW with all three (3) non-power LSSS variables once again set at their corresponding limits, i.e. primary coolant pressurizer pressure at 75 psia, total core

flow rate at 1575 gpm, and reactor inlet water temperature at 155 °F. This provides a 2.51 MW margin between the reactor power LSSS of 6.25 MW and the SL.

Attached are the revised Appendix F (Attachment 11) and Appendix H (Attachment 12) for Addendum 4 to the MURR HSR which supports the change to MURR TS 2.1. The revised Appendix F combines and replaces the current versions of the following three documents:

1. Section 3.3 of Addendum 3 to the MURR HSR (Attachment 4);
2. Appendix F of Addendum 4 to the MURR HSR (Attachment 1); and
3. Section 6.0 of Addendum 5 to the MURR HSR (Attachment 3).

Also attached are the current TS 2.1 (Attachment 13) and the draft TS 2.1 pages (Attachment 14) that will implement the requested change and a document from ANL (Attachment 15), which is referenced in the revised Appendix F, which helped determine the margin to flow instability for any MURR core coolant channel and the outlet saturation temperature.

If there are any questions regarding this application, please contact me at (573) 882-5319 or fruitsj@missouri.edu. I declare under penalty of perjury that the foregoing is true and correct.

Sincerely,

John L. Fruits
Reactor Manager

ENDORSEMENT:
Reviewed and Approved

Ralph A. Butler, P.E.
Director

xc: Mr. Alexander Adams, U.S. NRC
Mr. Craig Basset, U.S. NRC
Reactor Advisory Committee
Reactor Safety Subcommittee
Dr. Robert Duncan, Vice Chancellor for Research

NOTARY PUBLIC NOTARY SEAL STATE OF MISSOURI

MARGEE P. STOUT
My Commission Expires
March 24, 2012
Montgomery County
Commission #08511436

Attachments:

1. MURR Hazards Summary Report, University of Missouri Research Reactor Facility, Addendum 4, Appendix F, *Safety Limit Analysis for the MURR*, October 1973.

2. Vaughan, F.R., "Safety Limit Analysis for the MURR Facility," NUS Corporation, NUS-TM-EC-9, Appendix A, May 1973.

3. MURR Hazards Summary Report, University of Missouri Research Reactor Facility, Addendum 5, Section 6.0, *Addendum to the Safety Limit Analysis for the MURR*, January 1974.

4. MURR Hazards Summary Report, University of Missouri Research Reactor Facility, Addendum 3, Section 3.3, *Evaluation of Power Peaking Factors in the MURR 6.2 Kg Core*, 1972.

5. MURR Hazards Summary Report, University of Missouri Research Reactor Facility, Addendum 4, Appendix H, *Bases for Limiting Safety System Settings for Modes I and II Operation*, October 1973.

6. MURR Hazards Summary Report, University of Missouri Research Reactor Facility, Section 5.5.3, *Analysis of Natural Convective Cooling of the Core*, July 1965.

7. Croft, M.W., "Advanced Test Reactor Burnout Heat Transfer Tests," USAEC Report IDO-24475, Babcock & Wilcox Co., January 1964.

8. Waters, E.D., "Heat Transfer Experiments for the Advanced Test Reactor," USAEC Report BNWL-216, Battelle-Northwest, May 1966.

9. Louis Bernath, "A Theory of Local-Boiling Burnout and Its Application to Existing Data," *Chemical Engineering Progress Symposium*, Series No. 30, Volume 56, pp. 95-116, 1960.

10. MURR Technical Data Report TDR-0125, "Feasibility Analyses for HEU to LEU Conversion of the University of Missouri Research Reactor (MURR)," University of Missouri-Columbia Research Reactor, Columbia Missouri, September 2009.

11. Revised Appendix F, *Safety Limit Analysis for the MURR.*

12. Revised Appendix H, *Bases for Limiting Safety System Settings for Modes I and II Operation.*

13. Current TS 2.1, "Reactor Core Safety Limit" (pages 1 through 6).

14. Revised TS 2.1, "Reactor Core Safety Limit" (pages 1 through 6).

15. Feldman, E.E., "Implementation of the Flow Instability Model for the University of Missouri Reactor (MURR) that is Based on the Bernath Critical Heat Flux Correlation," Conversion Program Nuclear Engineering Division, Argonne National Laboratory, June 2011.

APPENDIX F

SAFETY LIMIT ANALYSIS FOR THE MURR

F. SAFETY LIMIT ANALYSIS FOR THE MURR

F. 1 Introduction

The University of Missouri authorized the NUS Corporation to develop safety limit curves for MURR operation. These curves establish the maximum allowable power limits for safe operation for different combinations of measurable reactor operating variables. The measurable operating variables or process variables used in this study include reactor power, pressurizer pressure, and coolant temperature and flow rate. The safety limits presented herein provide the basis for determining the limiting safety system set points and operating limits required in submission of a Safety Analysis Report pursuant to a license for proposed MURR operation at 10 MW.

For any combination of the process variables, safe reactor operation is achieved by limiting the reactor power to a level which avoids either (1) subcooled boiling burnout (or departure from nucleate boiling) or (2) flow instabilities which can lead to premature burnout. Operation above this power limit can cause unpredictably high fuel and clad temperatures and consequential permanent fuel damage and fission product release to reactor coolant. This condition must be avoided for every core region and for every reactor operating condition.

All data used in the determination of the MURR safety limits were obtained from the MURR Hazards Summary Reports (1,2,3)*, the MURR Design Data report (4), and the MURR hydraulic analysis (5).

---

* Numbers in parenthesis refer to References in Section F.5.

F.2 Conclusions and Results

The results of the MURR safety limit analysis are summarized in Table F.1 and are plotted on Figures F.1 and F.2. The data presented are reactor thermal power limits for a range of measurable coolant conditions at the core inlet and at two pressurizer operating pressures. The criterion used to establish the safety limit on reactor power depends on the combination of the independent process variables. This can be seen by referring to Table F. 1. The underscored table entries are the power limits as established by the criterion of avoiding any bulk boiling of the coolant, whereas the remaining entries reflect the thermal limits established by the subcooled burnout criterion. The safety limit criterion on incipient bulk boiling of the coolant is associated with experimentally observed premature burnout caused by hydraulic instabilities. In the present study, the power limits for coolant flow rates greater than 2800 gpm are always dictated by the burnout criterion, while for flow rates less than 800 gpm the incipient bulk boiling criterion dictates the safe power level.

Table F.2 presents a summary of hot channel factors used in the analysis. The limiting channel (or hot channel) used as the basis for the safety limit analysis has a power level 2.72 times the average and a flow rate of 0.81 times the average. The safety limits given in Table F.1 and Figures F. 1 and F.2 implicitly depend on these power and flow-related factors. Any future changes in these factors will require a corresponding change to the power limit results of this study. Changes to power-related factors can be treated

TABLE F.1

SAFETY LIMITS FOR M U R R OPERATION

Maximum Allowable Core Power Level, MW with Pressurizer at 60 PSIA

I N L E T W A T E R C O N D I T I O N S

Temperature DEG F	Flow Rate, GPM 400.	800.	1200.	1600.	2000.	2400.	2800.	3200.	3600.	4000
120.	3.011	5.870	7.980	9.843	11.574	13.099	14.426	15.450	16.217	16.65
140.	2.650	5.262	7.299	9.035	10.582	11.960	13.155	14.071	14.729	15.07
160.	2.292	4.546	6.675	8.202	9.600	10.822	11.877	12.669	13.228	13.50
180.	1.935	3.834	5.667	7.409	8.612	9.685	10.603	11.267	11.715	11.90
200.	1.583	3.131	4.615	6.009	7.282	8.400	9.301	9.863	10.204	10.26

Maximum Allowable Core Power Level, MW with Pressurizer at 75 PSIA

I N L E T W A T E R C O N D I T I O N S

Temperature DEG F	Flow Rate, GPM 400.	800.	1200.	1600.	2000.	2400.	2800.	3200.	3600.	400(
120.	3.278	6.334	8.647	10.742	12.668	14.435	16.050	17.394	18.532	19.4
140.	2.916	5.798	7.939	9.906	11.667	13.282	14.746	15.967	16.993	17.7
160.	2.556	5.080	7.317	9.067	10.676	12.138	13.458	14.534	15.437	16.1
180.	2.197	4.363	6.474	8.236	9.680	10.988	12.152	13.104	13.892	14.4
200.	1.843	3.656	5.415	7.099	8.686	9.845	10.868	11.689	12.339	12.8

NOTE... Underlined power levels are limited by bulk boiling.

TABLE F.2

SUMMARY OF M U R R HOT CHANNEL FACTORS

On Enthalpy Rise.....		
Power-related Factors		
Nuclear Peaking Factors		
Radial	2.220	
Local (Circumferential)	1.040	
Non-uniform Burnup	1.112	
Axial	1.000	
Engineering Hot Channel Factors on Enthalpy Rise		
Fuel Content Variation	1.030	
Fuel Thickness/Width Variation	1.030	
Overall Product		2.72
Flow-Related Factors		
Core/Loop Flow Fraction	1.000	
Assembly Minimum/Average Flow Fraction	1.000	
Channel Minimum/Average Flow Fraction		
Inlet Variation	1.000	
Width Variation	1.000	
Thickness Variation	1./1.080	
Within Channel Minimum/Average Flow Fraction		
Thickness Variation	1./1.050	
Effective Flow Area	0.3231/0.3505	
Overall Product		0.81
On Heat Flux.....		
Power-Related Factors		
Nuclear Peaking Factors		
Radial	2.220	
Local(Circumferential)	1.040	
Non-uniform Burnup	1.112	
Axial	1.432	
Engineering Hot Channel Factors on Flux		
Fuel Content Variation	1.030	
Fuel Thickness/Width Variation	1.150	
Overall Product		4.35
Energy Fraction Generated in Fuel Plate	0.930	

FIGURE F.1
MURR SAFETY LIMIT CURVES
FOR PRESSURIZER AT 60 PSIA

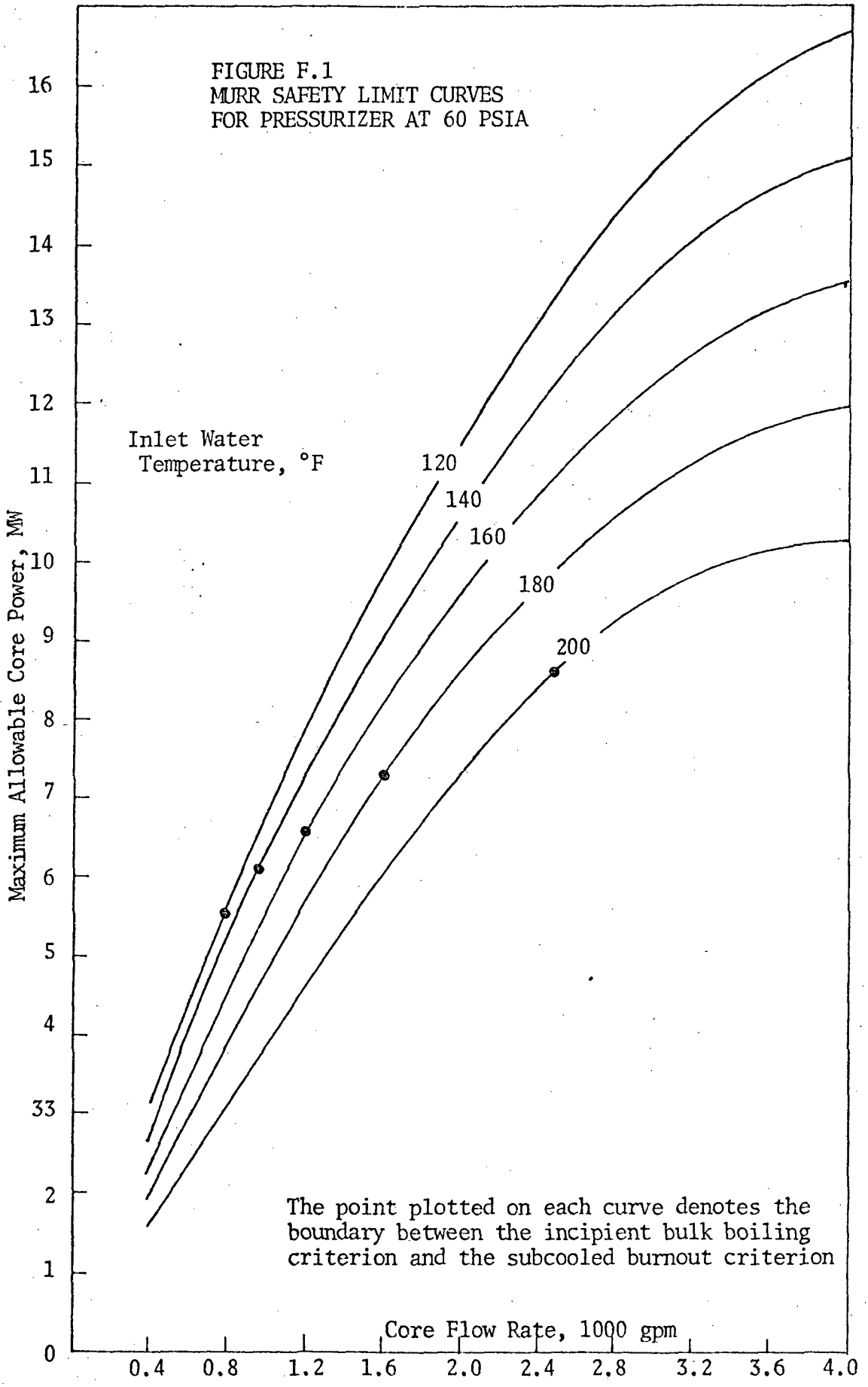
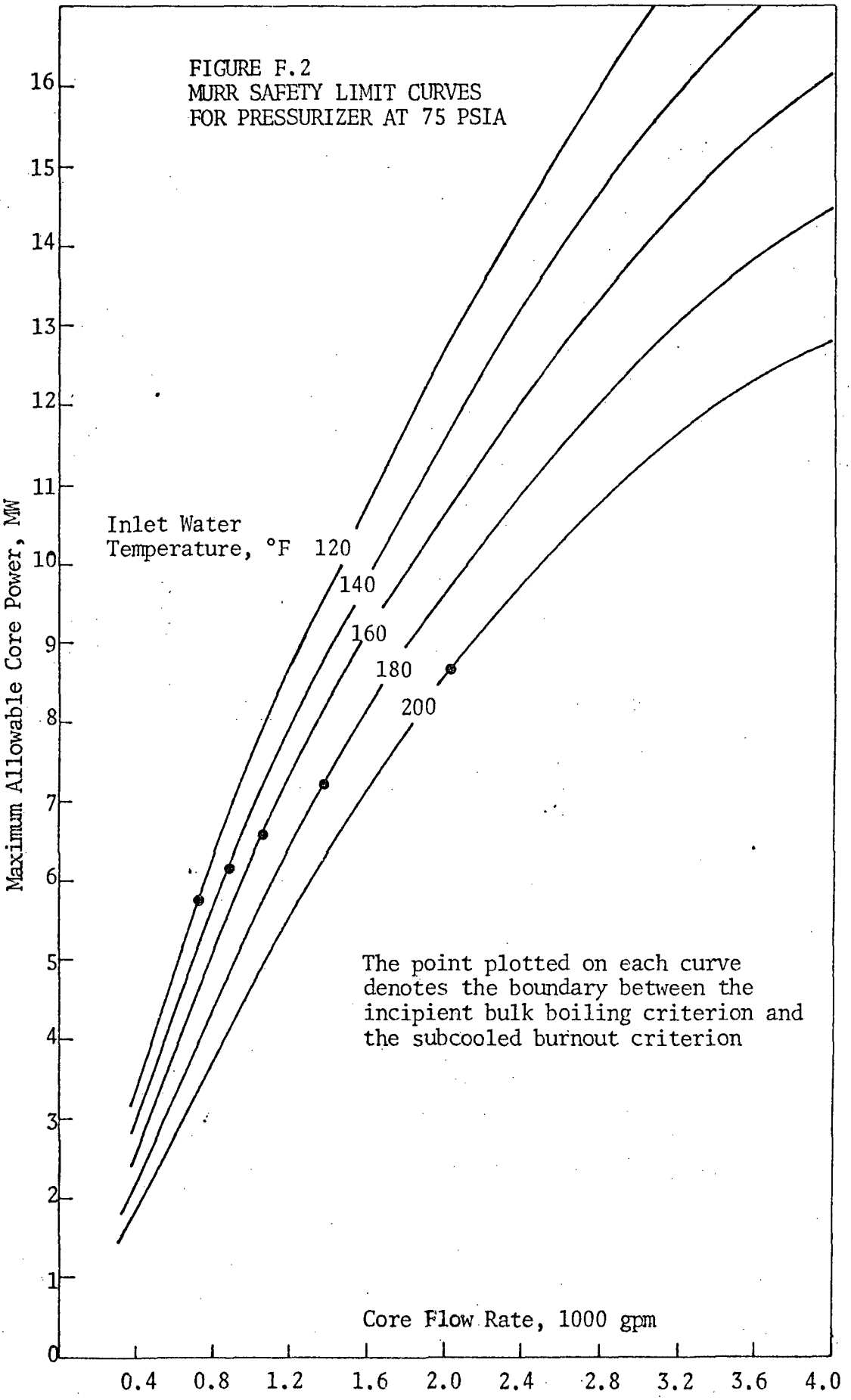


FIGURE F.2
MURR SAFETY LIMIT CURVES
FOR PRESSURIZER AT 75 PSIA



in a straight forward manner; namely, by maintaining the product of the limiting power and the affected power factor equal for both the new and referenced condition. Corresponding changes to flow-related factors are more difficult to accommodate, because of the non-linear dependence of the limiting power on the core flow rate. The effect of this non-linearity is to introduce a proportionately greater change in the limiting power level than the change in the flow-related factor. For small changes in flow (not to exceed 5%), it is possible to estimate the new limiting power from the slope of the power-flow curve (Figure F. 1 or F.2) for the desired operating conditions. Larger changes in the flow-related factors will require a re-evaluation of the safety limits.

F.3 Method of Analysis

The method for evaluating the core power limits for Table F.1 are discussed below. The details for selecting the safety limit criteria, and for using the BOLERO (6) computer program are included.

F.3.1 Safety Limit Criteria

The study objective was to determine core power limits for safe operation at specified combinations of possible core operating conditions. Safe operation here is defined to mean avoiding burnout (or DNB) where excessive fuel or clad temperatures could cause clad failure and thereby release fission

products into the primary coolant. To avoid DNB, the heat flux at each local section in the core is maintained at a value less than the locally-evaluated DNB heat flux. It is also necessary to avoid any core operating conditions (such as hydraulic instability) that could prematurely reduce the DNB heat flux. The following discussion presents the basis for specifying criteria to include both possibilities.

The MURR fuel geometry (near rectangular channels in a closed matrix) and the MURR operating conditions (subcooled water near atmospheric pressure) are outside the normal range of interest for today's commercial reactors. Consequently, only a limited amount of experience is available for establishing safety limit criteria. Fortunately, however, the MURR fuel assembly geometry is similar to the Advanced Test Reactor (ATR) fuel element so that ATR experience (8,9) can be applied to MURR. Since the MURR fuel channel length (~24") is about one-half that of ATR, the use of ATR test results can, in fact, provide conservatism for MURR because investigators (10) have shown higher or equal burnout heat flux levels for shorter channel length. Similarly, the shorter channel lengths are less susceptible to the hydraulic instabilities related to incipient bulk boiling.

Other test reactors (HFIR, ETR) have design and operating conditions that depart further from the MURR conditions, and their test results were not directly useful in developing the MURR safety criteria.

Preliminary ATR testing (8) indicated that both subcooled boiling burnout and bulk boiling burnout can occur for the range of channel thicknesses then under design consideration. Tests were performed at Argonne in 1963 on three channel thicknesses (0.054", 0.072", 0.094"), and it was found that

for the two thinnest channels (0.054", 0.072") the burnouts were due to hydraulic instability (or autocatalytic vapor binding) when the coolant reached saturation at the channel exit. Presumably, the hydraulic instabilities led to subnormal flow conditions and a lower burnout heat flux. Subcooled burnout occurred for the 0.094 inch channel before the coolant reached saturation conditions at channel exit. The subcooled burnout heat flux data obtained in these tests were 0.6 of the burnout heat flux predicted by the Bernath correlation (7):

$$\Phi_{DNB} = h_{bo} \left(T_{bo} - T_{sat} + \Delta T_{sub}\right)$$

where:

$$h_{bo} = 10890. \left(\frac{D_e}{D_e + D_i}\right) + \frac{48}{D_e^{0.6}} \cdot V$$

$$T_{bo} = 1.8\left[57 \ln P - 54 \left(\frac{P}{P + 15}\right) - \frac{V}{4}\right] + 32.$$

T_{sat} = saturation temperature at P, ^{o}F

ΔT_{sub} = bulk water temperature, degrees subcooling, ^{o}F

D_e = wetted hydraulic diameter, ft

D_i = heated hydraulic diameter, ft

V = coolant velocity, fps

P = system pressure, psia

Subsequent full-scale ATR testing (9) at Battelle Northwest with a channel thickness of 0.070" confirmed the earlier test results; namely, that burnout induced by hydraulic instability was the limiting factor for ATR. In addition, it was established that the hydraulic instability condition did not correspond to initiation of local boiling, but to the beginning of bulk boiling at the channel exit in the region where the coolant enthalpy was highest. Test results also indicated that lateral mixing (in the channel) was quite small.

In view of the ATR experience, and in absence of burnout test results for MURR fuel and at MURR operating conditions, the following safety limit criteria were adopted for this study:

> The coolant exit temperature from the hot channel shall be less than the saturation temperature at the core exit pressure
>
> The local heat flux at any point in the core shall be less than 0.5 of the burnout heat flux as given by the Bernath correlation at that point.

The bulk boiling limitation is adopted to exclude occurrence of the in-core hydraulic instabilities related to incipient bulk boiling. The above burnout heat flux limitation is adopted to provide some additional design safety margin by a reduction of the correlated ATR test data by the factor 0.5/0.6 relative to the orginal Bernath correlation. The above criteria are sufficient to preclude the possibility of fuel failure and attendent fission product release due to excessive temperatures.

F.3.2 Calculational Method

The BOLERO program was used to perform the calculations which determine local conditions of enthalpy, heat flux, and DNB heat flux for the core hot channel. Since the Bernath burnout heat flux depends on absolute pressure, it was necessary to calculate the absolute pressure at the core exit for each set of inlet water conditions and core power. Since most BOLERO input is dependent on absolute pressure and on either flow rate or power, a special computer program MURRPGM, was written to generate consistent input for all the cases needed for the study. A description of the MURRPGM program, the basis for BOLERO input, and the treatment of BOLERO results are presented below.

F.3.2.1 MURRPGM Program

The MURRPGM program was developed to calculate the absolute pressure (psia) at the core outlet for every combination of operating conditions in this study. Since the core outlet pressure calculation required the same data as BOLERO, the program was expanded further to generate input cards for the BOLERO program.

The pressure drop from the pressurizer to the core outlet was calculated by correcting individual Δp components as given in reference (5) to new flow, temperature, and core power conditions (see Table F.3). The new Δp

TABLE F.3

REFERENCE PRESSURE DROP DATA*

COMPONENT**	ΔP_o (PSI)	Q_o (GPM)	T_o (F)	FRICTIONAL	IN CORE
1,2,3	3,259	1800	155	yes	no
4	0.2689	1800	155	no	no
5,6,...10	4.08	3600	155	yes	no
11	0.1977	3600	155	yes	no
12	0.8980	3600	155	no	no
13	12.35	3600	165	yes	yes

* Data from Reference (5)

** Component description using notation of reference (5)

1. Across pressurizer surge line to pressurizer outlet
2. Across 5 feet of 8 inch pipe
3. Across 8 inch Y strainer
4. Across 8 inch/12 inch expansion
5. Across 80 feet of 12 inch pipe
6. Across four 12 inch 90 degree elbows
7. Across three 12 inch 45 degree elbows
8. Across one 12 inch butterfly valve(507B)
9. Across one 12 inch swing check valve(502)
10. Across entrance to annular pressure vessel
11. Across 6 feet of annular pressure vessel
12. Across entrance to fuel element plates
13. Across Core ...25.5 inches of fuel element plates..to core exit

components were then totaled and the result was subtracted from the desired pressurizer operating pressure (60 psia or 75 psia) to obtain the absolute pressure at the core outlet.

The method for correcting the reference Δp components depended on the type of pressure drop involved. For non-frictional components, pressure drop is proportional to density and flow,

$$\Delta p = \Delta p_o \left[\frac{\rho(T)}{\rho(T_o)} \right]^{1.0} \left[\frac{Q}{Q_o} \right]^{2.0}$$

where the subscript o denotes the reference conditions as given in Table F.3.

For the frictional loss components, the pressure drop was assumed to be given by the Blasius equation and,

$$\Delta p = \Delta p_o \cdot \left[\frac{\rho(T)}{\rho(T_o)} \right]^{0.8} \left[\frac{Q}{Q_o} \right]^{1.8} \left[\frac{\mu(T)}{\mu(T_o)} \right]^{0.2}$$

If the core pressure drop component was involved, then the temperature T in the above equation was taken as the average core temperature calculated from the core power and flow. Otherwise the value for T was the core inlet water temperature.

MURRPGM also includes:

An iterative scheme to determine the core power level that would cause incipient bulk boiling at the hot channel exit.

Interpolation routines to evaluate intermediate fluid property values from tabulated input values using absolute pressure as the independent variable.

Simple transformations to generate BOLERO input from non-standard BOLERO flow and power units.

F.3.2.2 BOLERO Input

The BOLERO program performs all necessary thermal-hydraulic calculations required to establish the minimum ratio of the local burnout heat flux to the local surface heat flux (DNBR) for a single coolant channel. BOLERO input specifies the single channel dimensions, operating conditions, and the Bernath DNB correlation and its parameters.

The single channel analyzed in BOLERO is a representation of the thermally limiting channel (or hot channel). The channel power is 2.72 times average channel power, and the channel flow rate is 0.81 times average channel flow rate. The basis for these data and for the local heat flux multipliers are given in Table F.2. The normalized axial power distribution used for the channel is given in Figure 1 of TM-WRP-62-10 contained in reference (4). This power distribution occurs at beginning core life when the control rods are partially inserted and represents the most limiting condition during core life due to the high flux level at the channel exit. Channel dimensions are developed from nominal core dimensions such as flow area (0.3505 ft^2), heat transfer surface area (184.28 ft^2) and core length (2.0 ft). The effects of worst-case dimensions are included in the corresponding hot channel factors.

BOLERO input data for the Bernath DNB correlation include a DNB heat flux multiplier (0.5), a heated-to-wetted perimeter ratio (0.924) and a saturation temperature corresponding to the absolute pressure at the core exit (available from the MURRPGM program results) for each core power, pressurizer pressure, and core inlet condition. This approach ensures the correct Bernath DNB heat flux when the minimum DNBR occurs at the channel exit, and produces a conservative result when the minimum DNBR occurs elsewhere in the channel.

F.3.2.3 BOLERO Output

The maximum core power levels summarized in Table F.1 were limited by either the bulk boiling or DNB heat flux criterion. Those values limited by bulk boiling (underscored values in Table F.1) were immediately evident because BOLERO results indicated that

$$DNBR = \frac{\Phi \text{ DNB}}{\Phi \text{ LOCAL}} > 1.0$$

for the initial core power estimate evaluated by the MURRPGM program at the threshold of bulk boiling. No further iterative procedure was required because any core power increase to reach the DNB flux limit would also violate the bulk boiling criterion.

The core power levels limited by the DNB criterion were the result of an iterative procedure. The procedure included the sequential use of the MURRPGM program to calculate the absolute pressure at core exit and the

BOLERO program to calculate the DNBR. The DNB-limited power levels in Table F.1 were determined by terminating the iteration procedure when the DNBR = 1.0000+0.01.

F.4 Discussion of Results

Figures F.1 and F.2 illustrate the effects of core operating conditions on the maximum allowable core power for safe MURR operation. The trends noted here generally represent the behavior of the two design criterion for various core operating conditions.

The variable most strongly affecting safe core operation is core flow rate. The higher the core flow rate, the higher the maximum allowable core power level. The effect is essentially linear at low core flow rates where the bulk boiling criterion is controlling and becomes non-linear as the flow rate is increased into the DNB controlled regions. The non-linearity in the safety limit is more pronounced for higher inlet water temperatures. Two competitive coolant flow related phenomena are responsible for this observed behavior. An increase in the coolant flow rate results in (1) lower absolute pressures at core exit which, in turn, decreases the water saturation temperature and thereby decreases the Bernath burnout heat flux limit; and (2) higher predictions of the Bernath burnout heat flux limit with increasing coolant velocity.

The allowable core power limit is inversely related to the core inlet water temperatures. This is readily understood in terms of a higher permissible core power level for an increased inlet subcooling; that is, the

channel power to achieve incipient bulk boiling or local burnout increases as the inlet subcooling increases (coolant inlet temperature decreases) with all other variables held constant.

The effect of pressurizer pressure is available from a comparison of corresponding curves on Figures F.1 and F.2. Clearly, higher pressurizer pressure results in an increase in the safety limits on core power due to the increase in the coolant saturation temperature and the pronounced absolute pressure dependence of Bernath correlation at low absolute pressure. As already noted, the influence of the coolant flow rate on the channel exit pressure and the dependence of the Bernath correlation on absolute pressure is responsible for the slope change observed in the safety limit curves of Figures F.1 and F.2.

F.5 References

(1) "MURR Hazards Summary Report", University of Missouri Research Reactor Facility. (1965).

(2) "MURR Hazards Summary Report", Addendum 1, University of Missouri Research Facility, (1966).

(3) "MURR Hazards Summary Report", Addendum 3, University of Missouri Research Reactor Facility, (1972).

(4) "MURR Design Data, Volume I" (copy 86) by Internuclear Company (1962).

(5) "Hydraulic Analysis of the MURR Primary Cooling System - 10 MW Operation", 1973.

(6) Schmidt, E.R., Couchman, M.L., and Edwards, D.R. , BOLERO-II, Burnout Limit Evaluation Routine-II, NUS-TM-ENG-119 (Rev.3, modified).

(7) Bernath, L. "A Theory of Local-Boiling Burnout and Its Application to Existing Data", Chem Eng. Progm. Symp. Ser., 56, No. 30, 95-116 (1960).

(8) Croft, M.W., "Advanced Test Reactor Burnout Heat Transfer Tests", USAEC Report IDO-24475, Babcock & Wilcox Co., January 1964.

(9) Waters, E.D., "Heat Transfer Experiments for the Advanced Test Reactor," USAEC Report BNWL-216, Battelle-Northwest, May 1966.

(10) Tong, L.S., Boiling Crisis and Critical Heat Flux, USAEC Office of Information Services (1970) page 26.

ATTACHMENT 2

NUS-TM-EC-9

SAFETY LIMIT ANALYSIS FOR THE MURR FACILITY

By

F. R. Vaughan

Prepared for

University of Missouri

May 1973

NUS CORPORATION
4 Research Place
Rockville, Maryland 20850

Approved by:

D. G. Fitzgerald, Ph.D.
Project Manager

J. N. Sorensen
Manager, Reactor Engineering

TABLE OF CONTENTS

	Page No.
LIST OF FIGURES	ii
LIST OF TABLES	iii
1.0 INTRODUCTION	1
2.0 CONCLUSIONS AND RESULTS	2
3.0 METHOD OF ANALYSIS	8
3.1 Safety Limit Criteria	8
3.2 Calculational Method	11
4.0 DISCUSSION OF RESULTS	16
5.0 REFERENCES	18
APPENDIX A-The MURRPGM Program Listing	A-1
APPENDIX B-BOLERO Program Input Development	B-1

LIST OF FIGURES

Figure No.		Page No.
2.1	MURR Safety Limit Curves for Pressurizer at 60 psia	4
2.2	MURR Safety Limit Curves for Pressurizer at 75 psia	5

LIST OF TABLES

Table No.		Page No.
2.1	Safety Limits for MURR Operation	3
2.2	Summary of MURR Hot Channel Factors	6
3.1	Reference Pressure Drop Data	12

1.0 INTRODUCTION

The University of Missouri authorized the NUS Corporation to develop safety limit curves for MURR operation. These curves establish the maximum allowable power limits for safe operation under different combinations of measurable reactor operating variables. The measurable operating variables or process variables used in this study include reactor power, pressurizer pressure, and coolant temperature and flow rate. The safety limits presented herein provide the basis for determining the limiting safety system set points and operating limits required in submission of a Safety Analysis Report pursuant to a license for proposed MURR operation at 10 MW.

For any combination of the process variables, safe reactor operation is achieved by limiting the reactor power to a level which avoids either (1) subcooled boiling burnout (or departure from nucleate boiling) or (2) flow instabilities which can lead to premature burnout. Operation above this power limit can cause unpredictably high fuel and clad temperatures and consequential permanent fuel damage and fission product release to reactor coolant. This condition must be avoided for every core region and for every reactor operating condition.

All data used in the determination of the MURR safety limits were obtained from the MURR Hazards Summary Reports (1, 2, 3)*, the MURR Design Data report (4), and the revised MURR hydraulic analysis (5).

---

* Numbers in parenthesis refer to References in Section 5.0.

2.0 CONCLUSIONS AND RESULTS

The results of the MURR safety limit analysis are summarized in Table 2.1 and are plotted on Figures 2.1 and 2.2. The data presented are reactor thermal power limits for a range of measurable coolant conditions at the core inlet and at two pressurizer operating pressures. The criterion used to establish the safety limit on reactor power depends on the combination of the independent process variables. This can be seen by referring to Table 2.1. The underscored table entries are the power limits as established by the criterion of avoiding any bulk boiling of the coolant, whereas the remaining entries reflect the thermal limits established by the subcooled burnout criterion. The safety limit criterion on incipient bulk boiling of the coolant is associated with experimentally observed premature burnout caused by hydraulic instabilities. In the present study, the power limits for coolant flow rates greater than 2800 pgm are always dictated by the burnout criterion, while for flow rates less than 800 gpm the incipient bulk boiling criterion dictates the safe power level.

Table 2.2 presents a summary of hot channel factors used in the analysis. The limiting channel (or hot channel) used as the basis for the safety limit analysis has a power level 2.72 times the average and a flow rate of 0.81 times the average. The safety limits given in Table 2.1 and Figures 2.1 and 2.2 implicitly depend on these power and flow-related factors. Any future changes in these factors will require a corresponding change to power limit results of this study. Changes to power-related factors can be treated in a straight forward manner; namely, by maintaining the product of the limiting power and the affected power factor equal for both the new and referenced condition. Corresponding changes to flow-related factors are more difficult to accommodate, because of the non-linear dependence of the limiting power

TABLE 2.1

SAFETY LIMITS FOR M U R R OPERATION

MAXIMUM ALLOWABLE CORE POWER LEVEL,MW WITH PRESSURIZER AT 60 PSIA

	INLET WATER CONDITIONS									
TEMPERATURE	FLOW RATE,GPM									
DEG F	400.	800.	1200.	1600.	2000.	2400.	2800.	3200.	3600.	4000.
120.	3.011	5.870	7.980	9.843	11.574	13.099	14.426	15.450	16.217	16.654
140.	2.650	5.262	7.299	9.035	10.582	11.960	13.155	14.071	14.729	15.075
160.	2.292	4.546	6.675	8.202	9.600	10.822	11.877	12.669	13.228	13.501
180.	1.935	3.834	5.667	7.409	8.612	9.685	10.603	11.267	11.715	11.906
200.	1.583	3.131	4.615	6.009	7.282	8.400	9.301	9.863	10.204	10.267

MAXIMUM ALLOWABLE CORE POWER LEVEL,MW WITH PRESSURIZER AT 75 PSIA

	INLET WATER CONDITIONS									
TEMPERATURE	FLOW RATE,GPM									
DEG F	400.	800.	1200.	1600.	2000.	2400.	2800.	3200.	3600.	4000.
120.	3.278	6.334	8.647	10.742	12.668	14.435	16.050	17.394	18.532	19.438
140.	2.916	5.798	7.939	9.906	11.667	13.282	14.746	15.967	16.993	17.787
160.	2.556	5.080	7.317	9.067	10.676	12.138	13.458	14.534	15.437	16.139
180.	2.197	4.363	6.474	8.236	9.680	10.988	12.152	13.104	13.892	14.467
200.	1.843	3.656	5.415	7.099	8.686	9.845	10.868	11.689	12.339	12.810

NOTE...UNDERLINED POWER LEVELS ARE LIMITED BY BULK BOILING

FIGURE 2.1
MURR SAFETY LIMIT CURVES FOR PRESSURIZER AT 60 PSIA

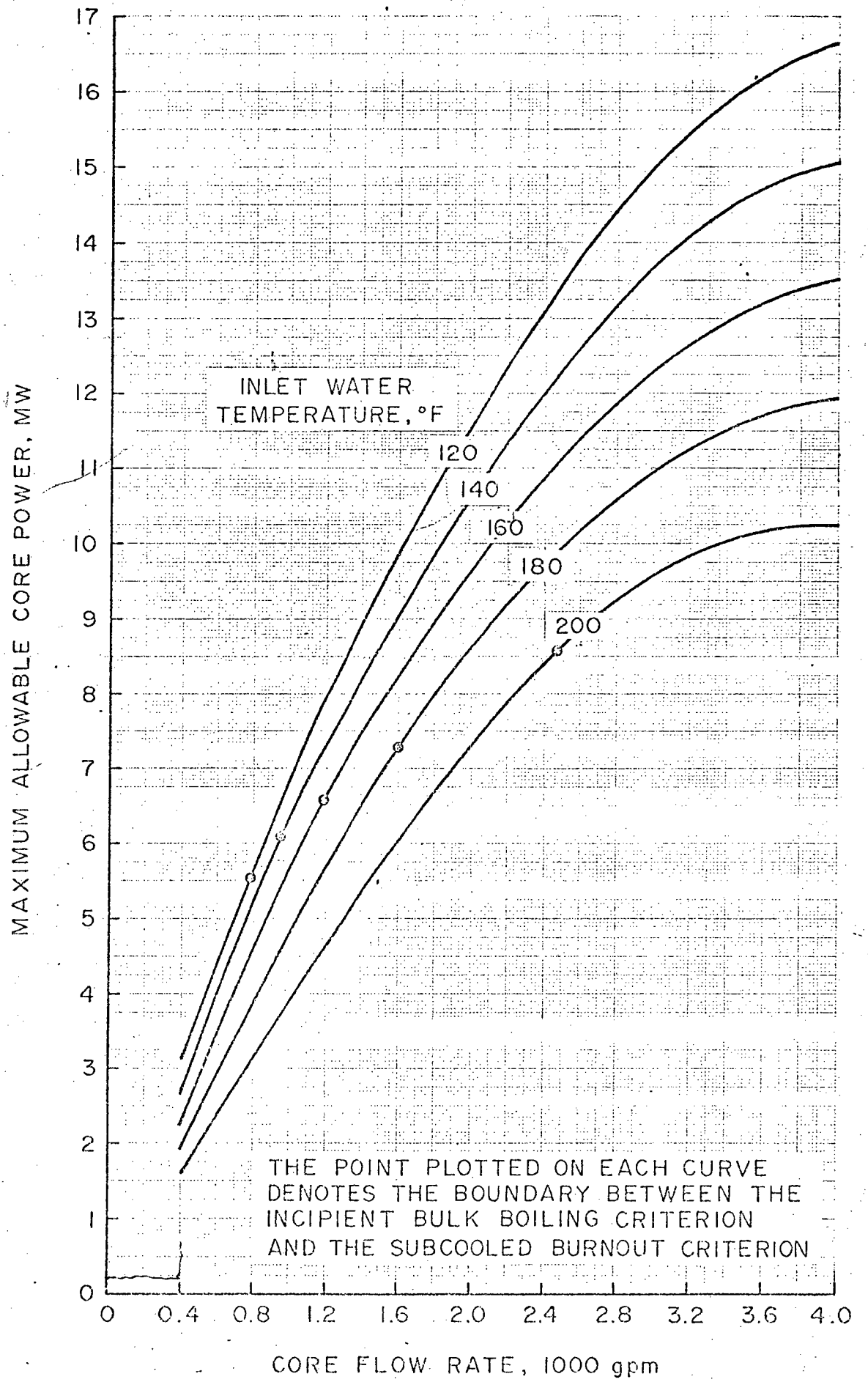


FIGURE 2.2
MURR SAFETY LIMIT CURVES
FOR PRESSURIZER AT 75 PSIA

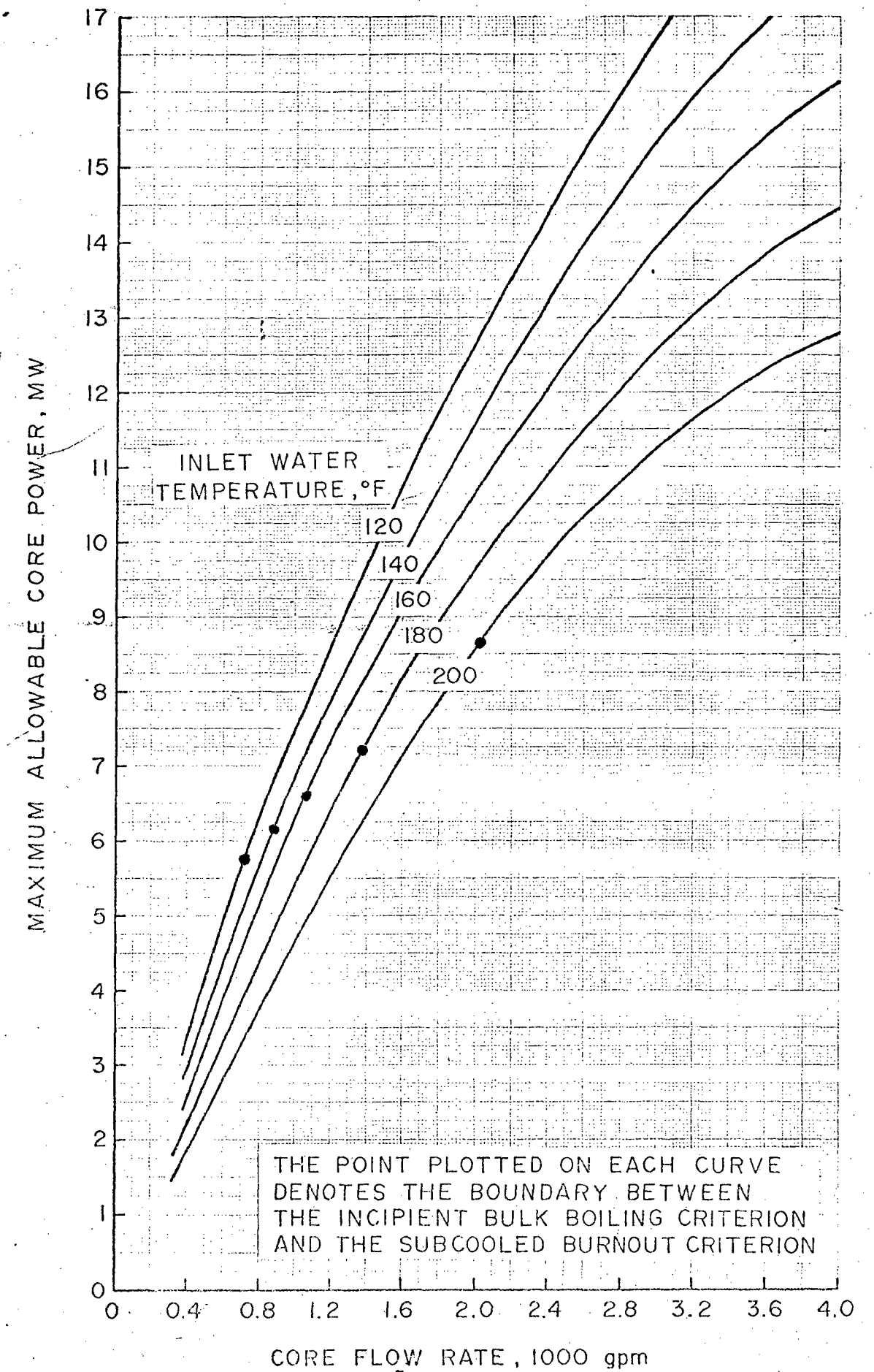


TABLE 2.2

SUMMARY OF M U R R HOT CHANNEL FACTORS

ON ENTHALPY RISE.....

POWER-RELATED FACTORS
- NUCLEAR PEAKING FACTORS
  - RADIAL.....2.220
  - LOCAL(CIRCUMFERENTIAL).....1.040
  - NON-UNIFORM BURNUP.....1.112
  - AXIAL.....1.000
- ENGINEERING HOT CHANNEL FACTORS ON ENTHALPY RISE
  - FUEL CONTENT VARIATION.....1.030
  - FUEL THICKNESS/WIDTH VARIATION.....1.030

OVERALL PRODUCT.....2.72

FLOW-RELATED FACTORS
- CORE/LOOP FLOW FRACTION.....1.000
- ASSEMBLY MINIMUM/AVERAGE FLOW FRACTION.....1.000
- CHANNEL MINIMUM/AVERAGE FLOW FRACTION
  - INLET VARIATION.....1.000
  - WIDTH VARIATION.....1.000
  - THICKNESS VARIATION.....1./1.080 — 0.6
- WITHIN CHANNEL MINIMUM/AVERAGE FLOW FRACTION
  - THICKNESS VARIATI(.....1./1.050
  - EFFECTIVE FLOW AREA.....0.3231/0.3505

OVERALL PRODUCT.....0.81

ON HEAT FLUX.....

POWER-RELATED FACTORS
- NUCLEAR PEAKING FACTORS
  - RADIAL.....2.220
  - LOCAL(CIRCUMFERENTIAL).....1.040
  - NON-UNIFORM BURNUP.....1.112
  - AXIAL.....1.432
- ENGINEERING HOT CHANNEL FACTORS ON FLUX
  - FUEL CONTENT VARIATION.....1.030
  - FUEL THICKNESS/WIDTH VARIATION.....1.150

OVERALL PRODUCT.....4.35

ENERGY FRACTION GENERATED IN FUEL PLATE.....0.930

$2.22 \times 1.432 = 3.179$

on the core flow rate. The effect of this non-linearity is to introduce a proportionately greater change in the limiting power level than the change in the flow-related factor. For small changes in flow (not to exceed 5%), it is possible to estimate the new limiting power from the slope of the power-flow curve (Figure 2.1 or 2.2) for the desired operating conditions. Larger changes in the flow-related factors will require a re-evaluation of the safety limits.

The safety limits presented in Table 2.1 or Figures 2.1 or 2.2 do not include any power adjustments which might account for

- power measurement errors
- flow measurement errors
- required overpower margins.

Such adjustments must be included before specifying actual core operating limits. As an example, take pressurizer pressure and core inlet temperature at the parametric values of 75 psia and 140°F, respectively. With an assumed flow measurement error of 5% and a nominal flow of 3600 gpm, actual flow is about 3400 gpm. At these conditions the maximum, i.e., safety limit power level, is (from Figure 2.2) 16.4 megawatts. The corresponding measured power level, assuming a 5% power measurement error, would be about 15.6 megawatts. With a limiting safety system setting (overpower scram) at 125% of nominal full power the resulting safety margin is 3.1 megawatts. The ratio of safety limit power level to scram setting power level is $15.6/12.5 = 1.25$.

3.0 METHOD OF ANALYSIS

The method for evaluating the core power limits for Table 2.1 are discussed below. The details for selecting the safety limit criteria, and for using the BOLERO (6) computer program are included.

3.1 Safety Limit Criteria

The study objective was to determine core power limits for safe operation at specified combinations of possible core operating conditions. Safe operation here is defined to mean avoiding burnout (or DNB) where excessive fuel or clad temperatures could cause clad failure and thereby release fission products into the primary coolant. To avoid DNB, the heat flux at each local section in the core is maintained at a value less than the locally-evaluated DNB heat flux. It is also necessary to avoid any core operating conditions (such as hydraulic instability) that could prematurely reduce the DNB heat flux. The following discussion presents the basis for specifying criteria to include both possibilities.

The MURR fuel geometry (near rectangular channels in a closed matrix) and the MURR operating conditions (subcooled water near atmospheric pressure) are outside the normal range of interest for today's commercial reactors. Consequently, only a limited amount of experience is available for establishing safety limit criteria. Fortunately, however, the MURR fuel assembly geometry is similar to the Advanced Test Reactor (ATR) fuel element so that ATR experience (8,9) can be applied to MURR. Since the MURR fuel channel length (~24") is about one-half that of ATR, the use of ATR test results can, in fact, provide conservatism for MURR because investigators (10) have shown higher or equal burnout heat flux levels for shorter channel lengths. Similarly, the shorter channel lengths are less susceptible to the hydraulic instabilities related to incipient bulk boiling.

Other test reactors (HFIR, ETR) have design and operating conditions that depart further from the MURR conditions, and their test results were not directly useful in developing the MURR safety criteria.

Preliminary ATR testing (8) indicated that both subcooled boiling burnout and bulk boiling burnout can occur for the range of channel thicknesses then under design consideration. Tests were performed at Argonne in 1963 on three channel thicknesses (0.054", 0.072", 0.094"), and it was found that for the two thinnest channels (0.054", 0.072") the burnouts were due to hydraulic instability (or autocatalytic vapor binding) when the coolant reached saturation at the channel exit. Presumably, the hydraulic instabilities led to subnormal flow conditions and a lower burnout heat flux. Subcooled burnout occurred for the 0.094 inch channel before the coolant reached saturation conditions at channel exit. The subcooled burnout heat flux data obtained in these tests were 0.6 of the burnout heat flux predicted by the Bernath correlation (7):

$$\Phi_{DNB} = h_{bo} (T_{bo} - T_{sat} + \Delta T_{sub})$$

where:

$$h_{bo} = 10890. \left(\frac{D_e}{D_e + D_i}\right) + \frac{48}{D_e^{0.6}} \cdot V$$

$$T_{bo} = 1.8 \left[57 \ln P - 54 \left(\frac{P}{P+15}\right) - \frac{V}{4}\right] + 32.$$

T_{sat} = saturation temperature at P, ^{o}F

ΔT_{sub} = bulk water temperature, degrees subcooling, ^{o}F

D_e = wetted hydraulic diameter, ft

D_i = heated hydraulic diameter, ft

V = coolant velocity, fps

P = system pressure, psia

Subsequent full-scale ATR testing (9) at Battelle Northwest with a channel thickness of 0.070" confirmed the earlier test results; namely, that burnout induced by hydraulic instability was the limiting factor for ATR. In addition, it was established that the hydraulic instability condition did not correspond to initiation of local boiling, but to the beginning of bulk boiling at the channel exit in the region where the coolant enthalpy was highest. Test results also indicated that lateral mixing (in the channel) was quite small.

In view of the ATR experience, and in absence of burnout test results for MURR fuel and at MURR operating conditions, the following safety limit criteria were adopted for this study:

- The coolant exit temperature from the hot channel shall be less than the saturation temperature at the core exit pressure
- The local heat flux at any point in the core shall be less than 0.5 of the burnout heat flux as given by the Bernath correlation at that point.

The bulk boiling limitation is adopted to exclude occurrence of the in-core hydraulic instabilities related to incipient bulk boiling. The above burnout heat flux limitation is adopted to provide some additional design safety margin by a reduction of the correlated ATR test data by the factor 0.5/0.6 relative to the original Bernath correlation. The above criteria are sufficient to preclude the possibility of fuel failure and attendent fission product release due to excessive temperatures.

3.2 Calculational Method

The BOLERO program was used to perform the calculations which determine local conditions of enthalpy, heat flux, and DNB heat flux for the core hot channel. Since the Bernath burnout heat flux depends on absolute pressure, it was necessary to calculate the absolute pressure at the core exit for each set of inlet water conditions and core power. Since most BOLERO input is dependent on absolute pressure and on either flow rate or power, a special computer program MURRPGM, was written to generate consistent input for all the cases needed for the study. A description of the MURRPGM program, the basis for BOLERO input, and the treatment of BOLERO results are presented below.

3.2.1 MURRPGM Program

The MURRPGM program was developed to calculate the absolute pressure (psia) at the core outlet for every combination of operating conditions in this study. Since the core outlet pressure calculation required the same data as BOLERO, the program was expanded further to generate input cards for the BOLERO program. Appendix A contains a listing of MURRPGM.

The pressure drop from the pressurizer to the core outlet was calculated by correcting individual Δp components as given in reference (5) to new flow, temperature, and core power conditions (see Table 3.1). The new Δp components were then totaled and the result was subtracted from the desired pressurizer operating pressure (60 psia or 75 psia) to obtain the absolute pressure at the core outlet.

The method for correcting the reference Δp components depended on the type of pressure drop involved. For non-frictional components, pressure

TABLE 3.1

REFERENCE PRESSURE DROP DATA*

COMPONENT**	ΔP_o (PSI)	Q_o (GPM)	T_o (F)	FRICTIONAL	IN CORE
1,2,3	3.259	1800	155	YES	NO
4	0.2689	1800	155	NO	NO
5,6,...,10	4.08	3600	155	YES	NO
11	0.1977	3600	155	YES	NO
12	0.8980	3600	155	NO	NO
13	12.35	3600	165	YES	YES

* DATA FROM REFERENCE (5)

** COMPONENT DESCRIPTION USING NOTATION OF REFERENCE (5).

1. ACROSS PRESSURIZER SURGE LINE TO PRESSURIZER OUTLET
2. ACROSS 5 FEET OF 8 INCH PIPE
3. ACROSS 8 INCH Y STRAINER
4. ACROSS 8 INCH/12 INCH EXPANSION
5. ACROSS 80 FEET OF 12 INCH PIPE
6. ACROSS FOUR 12 INCH 90 DEGREE ELBOWS
7. ACROSS THREE 12 INCH 45 DEGREE ELBOWS
8. ACROSS ONE 12 INCH BUTTERFLY VALVE(507B)
9. ACROSS ONE 12 INCH SWING CHECK VALVE(502)
10. ACROSS ENTRANCE TO ANNULAR PRESSURE VESSEL
11. ACROSS 6 FEET OF ANNULAR PRESSURE VESSEL
12. ACROSS ENTRANCE TO FUEL ELEMENT PLATES
13. ACROSS CORE...25.5 INCHES OF FUEL ELEMENT PLATES..TO CORE EXIT

$K_{in} = 0.28$

$K_{exit} = 0.386$

drop is proportional to density and flow,

$$\Delta p = \Delta p_o \left[\frac{\rho\,(T)}{\rho\,(T_o)}\right]^{1.0} \left[\frac{Q}{Q_o}\right]^{2.0}$$

where the subscript o denotes the reference conditions as given in Table 3.1.

For the frictional loss components, the pressure drop was assumed to be given by the Blasius equation and,

$$\Delta p = \Delta p_o \cdot \left[\frac{\rho\,(T)}{\rho\,(T_o)}\right]^{0.8} \left[\frac{Q}{Q_o}\right]^{1.8} \left[\frac{\mu\,(T)}{\mu\,(T_o)}\right]^{0.2}$$

If the core pressure drop component was involved, then the temperature T in the above equation was taken as the average core temperature calculated from the core power and flow. Otherwise the value for T was the core inlet water temperature .

MURRPGM also includes:

- An iterative scheme to determine the core power level that would cause incipient bulk boiling at the hot channel exit.
- Interpolation routines to evaluate intermediate fluid property values from tabulated input values using absolute pressure as the independent variable.
- Simple transformations to generate BOLERO input from non-standard BOLERO flow and power units.

3.2.2 BOLERO Input

The BOLERO program performs all necessary thermal-hydraulic calculations required to establish the minimum ratio of the local burnout heat flux to

the local surface heat flux (DNBR) for a single coolant channel. BOLERO input specifies the single channel dimensions, operating conditions, and the Bernath DNB correlation and its parameters. A more detailed discussion is given in Appendix B.

The single channel analyzed in BOLERO is a representation of the thermally limiting channel (or hot channel). The channel power is 2.72 times average channel power, and the channel flow rate is 0.81 times average channel flow rate. The basis for these data and for the local heat flux multipliers are given in Table 2.2. The normalized axial power distribution used for the channel is given in Figure 1 of TM-WRP-62-10 contained in reference (4). This power distribution occurs at beginning core life when the control rods are partially inserted and represents the most limiting condition during core life due to the high flux level at the channel exit. Channel dimensions are developed from nominal core dimensions such as flow area (0.3505 ft^2), heat transfer surface area (184.28 ft^2) and core length 2.0 ft). The effects of worst-case dimensions are included in the corresponding hot channel factors.

BOLERO input data for the Bernath DNB correlation include a DNB heat flux multiplier (0.5), a heated-to-wetted perimeter ratio (0.924) and a saturation temperature corresponding to the absolute pressure at the core exit (available from the MURRPGM program results) for each core power, pressurizer pressure, and core inlet condition. This approach ensures the correct Bernath DNB heat flux when the minimum DNBR occurs at the channel exit, and produces a conservative result when the minimum DNBR occurs elsewhere in the channel.

3.2.3 BOLERO Output

The maximum core power levels summarized in Table 2.1 were limited by either the bulk boiling or DNB heat flux criterion. Those values limited by

bulk boiling (underscored values in Table 2.1) were immediately evident because BOLERO results indicated that

$$\text{DNBR} = \frac{\Phi \text{ DNB}}{\Phi \text{ LOCAL}} > 1.0$$

for the initial core power estimate evaluated by the MURRPGM program at the threshold of bulk boiling. No further iterative procedure was required because any core power increase to reach the DNB flux limit would also violate the bulk boiling criterion.

The core power levels limited by the DNB criterion were the result of an iterative procedure. The procedure included the sequential use of the MURRPGM program to calculate the absolute pressure at core exit and the BOLERO program to calculate the DNBR. The DNB-limited power levels in Table 2.1 were determined by terminating the iteration procedure when the 1.0000 ± 0.01.

$\hat{DNBR} = 1.0000 \pm 0.01$

4.0 DISCUSSION OF RESULTS

Figures 2.1 and 2.2 illustrate the effects of core operating conditions on the maximum allowable core power for safe MURR operation. The trends noted here generally represent the behavior of the two design criterion for various core operating conditions.

The variable most strongly affecting safe core operation is core flow rate. The higher the core flow rate, the higher the maximum allowable core power level. The effect is essentially linear at low core flow rates where the bulk boiling criterion is controlling and becomes non-linear as the flow rate is increased into the DNB controlled regions. The non-linearity in the safety limit is more pronounced for higher inlet water temperatures. Two competitive coolant flow related phenomena are responsible for this observed behavior. An increase in the coolant flow rate results in (1) lower absolute pressures at core exit which, in turn, decreases the water saturation temperature and thereby decreases the Bernath burnout heat flux limit; and (2) higher predictions of the Bernath burnout heat flux limit with increasing coolant velocity.

The allowable core power limit is inversely related to the core inlet water temperatures. This is readily understood in terms of a higher permissible core power level for an increased inlet subcooling; that is, the channel power to achieve incipient bulk boiling or local burnout increases as the inlet subcooling increases (coolant inlet temperature decreases) with all other variables held constant.

The effect of pressurizer pressure is available from a comparison of corresponding curves on Figures 2.1 and 2.2. Clearly, higher pressurizer pressure results

in an increase in the safety limits on core power due to the increase in the coolant saturation temperature and the pronounced absolute pressure dependence of Bernath correlation at low absolute pressure. As already noted, the influence of the coolant flow rate on the channel exit pressure and the dependence of the Bernath correlation on absolute pressure is responsible for the slope change observed in the safety limit curves of Figures 2.1 and 2.2.

5.0 REFERENCES

(1) "MURR Hazards Summary Report", University of Missouri Research Reactor Facility. (1965).

(2) "MURR Hazards Summary Report", Addendum 1, University of Missouri Research Facility, (1966).

(3) "MURR Hazards Summary Report", Addendum 3, University of Missouri Research Reactor Facility, (1972).

(4) "MURR Design Data, Volume I" (copy 86) by Internuclear Company (1962).

(5) "Revised Hydraulic Analysis of the MURR Primary Cooling System - 10 MW Operation", 1973.

(6) Schmidt, E.R., Couchman, M.L., and Edwards, D. R., BOLERO-II, Burnout Limit Evaluation Routine-II, NUS-TM-ENG-119 (Rev. 3, modified).

(7) Bernath, L. "A Theory of Local-Boiling Burnout and Its Application to Existing Data", Chem. Eng. Progm. Symp. Ser., 56, No. 30, 95-116 (1960).

(8) Croft, M.W., "Advanced Test Reactor Burnout Heat Transfer Tests", USAEC Report IDO-24475, Babcock & Wilcox Co., January 1964 :

(9) Waters, E.D., "Heat Transfer Experiments for the Advanced Test Reactor," USAEC Report BNWL-216, Battelle-Northwest, May 1966.

(10) Tong, L.S., Boiling Crisis and Critical Heat Flux, USAEC Office of Information Services (1970) page 26.

APPENDIX A

THE MURRPGM PROGRAM LISTING

```
      PROGRAM MURRPGM(INPUT,OUTPUT,TAPE62)
C
C     M U R R SAFETY LIMIT ANALYSIS
C     PROGRAM TO CALCULATE CORE EXIT PRESSURE(PSIA) FOR GIVEN PRESSURE
C        DROP COMPONENTS SPECIFIED AT REFERENCE FLOW/TEMPERATURE VALUES
C        ...B O L E R O INPUT DATA CARDS ARE ALSO GENERATED BASED ON
C           THESE DATA
C        04/73 N U S CORP  F R VAUGHAN
C
      COMMON /PROPT/SPACE(301),HSAT,TSATT
      DIMENSION TITLE(8)
      DIMENSION DP0(50),Q0(50),RHO0(50),XMU0(50),FACTOR(50)
      DIMENSION TSAT(8),DENS(8),XMU(8),CP(8),H(8)
C               TSAT(I)...SATURATION TEMPERATURE,DEG F
      DATA TSAT
     * / 100.,  120.,  140.,  160.,  180.,  200.,  220.,  240./
C               DENS(I)...SATURATED WATER DENSITY,LB/CU FT
      DATA DENS
     * /61.996,61.728,61.387,61.013,60.569,60.132,59.630,59.102/
C               XMU(I)...VISCOSITY OF SATURATED WATER,LB/FT/HR
      DATA XMU
     * / 1.650, 1.353, 1.137, 0.970, 0.839, 0.738, 0.660, 0.595/
C               CP(I)...SPECIFIC HEAT OF SATURATED WATER,BTU/LB/DEG F
      DATA CP
     * /0.9976,0.9977,0.9988,1.0004,1.0022,1.0047,1.0079,1.0119/
C               H(I)...ENTHALPY OF SATURATED WATER,BTU/LB
      DATA H
     * / 67.97, 87.92,107.89,127.89,147.92,167.99,188.13,208.34/
C
      DATA IPUNCH/1/
C
C     ******************************************************************
C     HOT CHANNEL FACTORS AND OTHER DATA
      FDHE = 1.03*1.03
      FRAN = 2.220*1.040*1.112
C
      AR = 0.3231/0.3505
      FWE = 1./1.08/1.05
C
      FQE = 1.03*1.15
      FQR = 0.07
      DF = 0.5
      PR = 0.924
      FACTER = 1.-1.E-05
C     ******************************************************************
C
      HSFQ = (1.-FQR)*FQE/FDHE
C
  302 CONTINUE
C
C     INPUT...CARD 1...TITLE CARD      BLANK CC01-10 CAUSES PROGRAM STOP
      READ  100,TITLE
      IF(TITLE(1).EQ.10H          ) STOP
      PRINT 100,TITLE
```

```
      PRINT 100
C
C     INPUT...CARDS 2 TO J...FLUID PROPERTY LIBRARY DATA(SEE SUBR PROPCI)
      CALL PROPCDI(X,X,X,X,IPUNCH)
C
C     INPUT...CARD J+1...P0...PRESSURIZER PRESSURE,PSIA
      READ  102,P0
C
C
      N = 0
C
C     INPUT...CARDS J+2 TO K...REFERENCE PRESSURE DROP DATA FROM PRESSURIZER
C             DP00...REFERENCE PRESSURE DROP,PSID
C             Q000...REFERENCE FLOW FOR DP00,GPM
C             T...REFERENCE TEMPERATURE FOR Q00,DP00 VALUES,DEG F
C             FR...FRACTION OF CORE FLOW FOR WHICH Q00 APPLIES,FRACTIONAL
C             FACTOR0...TYPE OF DP00 CORRECTION REQUIRED
C                       0.0 FLOW AND DENSITY CORRECTION
C                       1.0 FRICTION FACTOR AND 0.0 CORRECTION
C                       2.0 FRICTION FACTOR AND 0.0 CORRECTION AT AVG CORE TEMPE
  200 READ 102,DP00,Q00,T,FR,FACTOR0
      IF(DP00.EQ.0.0) GO TO 201
C
      N = N+1
      DP0(N) = DP00
      Q0(N) = Q00
      FACTOR(N) = FACTOR0
      RHO0(N) = YVALUE(T,8,TSAT,DENS)
      XMU0(N) = YVALUE(T,8,TSAT,XMU)
      PRINT 102,DP0(N),Q0(N),T,FR,FACTOR(N),RHO0(N),XMU0(N)
      Q0(N) = Q0(N)/FR
      IF(N.LT.50) GO TO 200
C
C
  201 CALL STARTR(X,X,X,X,IPUNCH)
C     INPUT...CARD K+1...CORE OPERATING CONDITIONS
C             X...DUMMY
C             Q1...CORE INLET FLOW RATE,GPM    0.0 VALUE CAUSES EXIT FROM LOOP
C             T1...CORE INLET WATER TEMPERATURE,DEG F
C             P0...CORE POWER,MW
  300 READ 102,X,Q1,T1,P0
      IF(Q1.EQ.0.0) GO TO 301
      PRINT 121,P0,Q1,T1
      RHO1 = YVALUE(T1,8,TSAT,DENS)
      XMU1 = YVALUE(T1,8,TSAT,XMU)
      HIN = YVALUE(T1,8,TSAT,H)
      CHFL = 60.*0.13368*RHO1*Q1
  401 CONTINUE
      CHPO = P0
      DHAC = 3.412/E06*CHPO/CHFL
      T2 = T1 + DHAC/2.
      RHO2 = YVALUE(T2,8,TSAT,DENS)
      XMU2 = YVALUE(T2,8,TSAT,XMU )
      PRINT 102,X,Q1,T1,RHO1,XMU1,T2,RHO2,XMU2
C
```

```
      C
            P = P0
            PRINT 102,P
            DO 202 J=1,N
115         QR = Q1/Q0(J)
            RHOR = RHO1/RHO0(J)
            IF(FACTOR(J).EQ.2) RHOR = RHO2/RHO0(J)
            XMUR = XMU1/XMU0(J)
            IF(FACTOR(J).EQ.2) XMUR = XMU2/XMU0(J)
120         F1 = QR*QR*RHOR
            F2 = (XMUR/RHOR/QR)**0.2
            DP = DP0(J)*F1
            IF(FACTOR(J).GT.0.0) DP = DP*F2
            P = P - DP
125         PRINT 102,P,DP
          202 CONTINUE
            PRINT 102,P
      C
      C
130         CALL PROPCD(P,X,X,X,2)
      C
            DHMAX = HSAT-HIN
      C
            DHHC = DHAC*FDHE*FRAN/AR/FWE
135         IF(DHHC.LE.DHMAX) GO TO 400
      C
            PRINT 120
            P0 = P0*DHMAX/DHHC
            P0 = P0*FACTER
140         GO TO 401
      C
          400 CONTINUE
            CALL TITLECD(P0,Q1,T1,P0,IPUNCH)
      C
145         CHP0 = CHP0*FDHE*FRAN
            CHFL = CHFL*AR*FWE
            CALL RCONDCD(CHP0,CHFL,HIN,HSFQ,IPUNCH)
      C
            CALL PROPCD(P,X,X,X,IPUNCH)
150   C
            CALL BNTHCD(DF,PR,TSATT,X,IPUNCH)
      C
            CALL ENDCD(X,X,X,X,IPUNCH)
            GO TO 300
155   C
          301 CALL ENDR(X,X,X,X,IPUNCH)
            GO TO 302
      C
          100 FORMAT(8A10)
160       102 FORMAT(8F10.4)
          120 FORMAT(1X,90X,20H***WAS BOILING******)
          121 FORMAT(40H1 PRESSURIZER PRESSURE,PSIA.............F6.1/
             *       40H  FLOW RATE,GPM.....................F6.1/
             *       40H  INLET TEMPERATURE,DEG F...........F6.1/
165          *      )
            END
```

```
      FUNCTION YVALUE(X,N,XA,YA)
C
C     ROUTINE TO LINEARLY INTERPOLATE BETWEEN N PAIRS OF (XA(I),YA(I))
C        DATA IN A DATA TABLE
C     NOTE.....IF X.LT.XA(1),THEN YVALUE = YA(1)
C       .....IF X.GT.XA(N),THEN YVALUE = YA(N)
C     CHECKED OUT , 07/11/72  F R VAUGHAN
C
C
C     INPUT   X...ABSCISSA VALUE FOR WHICH YVALUE IS DESIRED
C             N...NUMBER OF PAIRS OF (XA(I),YA(I) DATA IN DATA TABLE
C             XA...ARRAY OF ABSCISSA VALUES IN DATA TABLE
C             YA...ARRAY OF ORDINATE VALUES IN DATA TABLE
C
      DIMENSION XA(N),YA(N)
C
C
      IF(X.GT.XA(1)) GO TO 100
      J = 1
      GO TO 102
C
  100 IF(X.LT.XA(N)) GO TO 101
      J = N
  102 YVALUE = YA(J)
      RETURN
C
  101 DO 200 J=2,N
      IF(X.LT.XA(J)) GO TO 201
  200 CONTINUE
C
C
      ENTRY YYVALUE
  201 JJ = J-1
      YVALUE = YA(JJ) + (YA(J)-YA(JJ))*(X-XA(JJ))/(XA(J)-XA(JJ))
      RETURN
      END
```

```
      SUBROUTINE BOLEROI(X1,X2,X3,X4,IPUNCH)
C     ROUTINE TO GENERATE AND PUNCH INPUT CARDS FOR B O L E R O PROGRAM
C               IPUNCH...CARD PUNCH OPTION,0... TO SKIP,1... TO PUNCH
C
      COMMON /PROPT/ NTAB,TSAT(50),PSAT(50),VF(50),VG(50),HF(50),HFG(50)
     *              ,HSAT,TSATT
C
C
C
      ENTRY TITLECD
C     ROUTINE TO PUNCH .TITLE. CARD FOR BOLERO
C               P0...CORE POWER LEVEL,MW
C               Q1...CORE FLOW RATE,GPM
C               T1...CORE INLET WATER TEMPERATURE,DEG F
C               P0...PRESSURIZER PRESSURE,PSIA
C
      P0 = X1
      Q1 = X2
      T1 = X3
      P0 = X4
      PRINT 201,P0,Q1,T1,P0
      IF(IPUNCH.EQ.1) WRITE(62,201) P0,Q1,T1,P0
      RETURN
C
      ENTRY RCONDCD
C     ROUTINE TO PUNCH .RCOND. CARD FOR BOLERO
C               CHPO...CORE POWER,MW
C               CHFL...CORE FLOW,LB/HR
C               HIN...CORE INLET ENTHALPY,BTU/LB
C               HSFQ...LOCAL HOT-SPOT FACTOR,DIMENSIONLESS
C
      CHPO = X1
      CHFL = X2
      HIN = X3
      HSFQ = X4
      PRINT 202,CHPO,CHFL,HIN,HSFQ
      IF(IPUNCH.EQ.1) WRITE(62,202) CHPO,CHFL,HIN,HSFQ
      RETURN
C
      ENTRY PROPCDI
C     ROUTINE TO READ IN PROPERTY TABLES FOR .ENTRY. PROPCD
C
      NTAB = 0
C
C     INPUT...CARDS 2 TO J...FLUID PROPERTY LIBRARY DATA
C               TSAT0...SATURATION TEMPERATURE AT PSAT0,DEG F
C               PSAT0...SATURATION PRESSURE AT TSAT0,PSIA
C               VF0...SPECIFIC VOLUME OF LIQUID AT PSAT0,CU FT/LB
C               VG0...SPECIFIC VOLUME OF VAPOR AT PSAT0,CU FT/LB
C               HF0...ENTHALPY OF LIQUID AT PSAT0,BTU/LB
C               HFG0...ENTHALPY OF VAPOR AT PSAT0,BTU/LB
  100 READ 101,TSAT0,PSAT0,VF0,VG0,HF0,HFG0
      IF(TSAT0.EQ.0.0) RETURN
C
      NTAB = NTAB+1
```

```
      TSAT(NTAB) = TSAT0
      PSAT(NTAB) = PSAT0
      VF(NTAB) = VF0
      VG(NTAB) = VG0
60    HF(NTAB) = HF0
      HFG(NTAB) = HFG0
      GO TO 100
C
      ENTRY PROPCD
65    C     ROUTINE TO GENERATE .PROP. CARD FOR BOLERO PROGRAM
C           PSIA...SYSTEM PRESSURE,PSIA
C           X2...
C           X3...
C           X4...
70    C
      PSIA = X1
      HSAT = YVALUE(PSIA,NTAB,PSAT,HF)
      HFGG = YVALUE(PSIA,NTAB,PSAT,HFG)
      DENW = 1./YVALUE(PSIA,NTAB,PSAT,VF)
75    DENR = DENW*YVALUE(PSIA,NTAB,PSAT,VG)
      TSATT = YVALUE(PSIA,NTAB,PSAT,TSAT)
      IF(IPUNCH.EQ.2) RETURN
C
      PRINT 203,PSIA,HSAT,HFGG,DENR,DENW
80    IF(IPUNCH.EQ.1) WRITE(62,203) PSIA,HSAT,HFGG,DENR,DENW
      RETURN
C
      ENTRY BNTHCD
C     ROUTINE TO GENERATE .BNTH. CARD FOR BOLERO
85    C           DF...DESIGN FACTOR FOR BERNATH CORRELATION
C           PR...HEATED/WETTED PERIMETER RATIO
C           TSATT...SATURATION TEMPERATURE FOR SYSTEM PRESSURE,DEG F
C           X4...
C
90    DF = X1
      PR = X2
      TSATT = X3
      PRINT 204,DF,PR,TSATT
      IF(IPUNCH.EQ.1) WRITE(62,204) DF,PR,TSATT
95    RETURN
C
      ENTRY ENDCD
C     ROUTINE TO GENERATE .END. CARD FOR BOLERO
C           X1...
100   C           X2...
C           X3...
C           X4...
C
      PRINT 205
105   IF(IPUNCH.EQ.1) WRITE(62,205)
      RETURN
C
      ENTRY STARTR
      IF(IPUNCH.EQ.1) WRITE(62,110)
110   RETURN
```

```
      C
            ENTRY ENDR
            IF(IPUNCH.EQ.1) WRITE(62,111)
            RETURN
115   C
        101 FORMAT(6E10.4)
        110 FORMAT(1X,3H[[C)
        111 FORMAT(1X,3H[[L)
        201 FORMAT(1X,32HTITLE      M U R R SAFETY STUDY ,F6.3, 3HMW ,F5.0, 4H
120        *GPM ,F4.0, 6HDEG F ,F3.0, 5HPSIA ,2X,
           *    10H  T,Q,    P)
        202 FORMAT(1X,10HRCOND      ,F10.4,F10.1,F10.2,F10.4,20X,
           *    10H  T,Q,    P)
        203 FORMAT(1X,10HPROP       ,F10.1,F10.2,F10.2,F10.2,F10.3,10X,
125        *    10H  T,Q,PR  )
        204 FORMAT(1X,10HBNTH       ,F10.4,F10.4,F10.2,30X,
           *    10H  T,Q,PR  )
        205 FORMAT(1X,04HEND )
            END
```

APPENDIX B

BOLERO Program Input Development

The sample BOLERO input data set given in Table B.1 was used in the MURR Safety Analysis. It is typical of all other cases and is the basis for discussing each BOLERO data card and its included data. The data on the DIMEN card and the AXIAL cards were fixed throughout the Safety Analysis, whereas all remaining cards had variable data and were for convenience, generated by the MURRPGM program. Each BOLERO input card and its data are discussed below:

The TITLE card specifies the heading of all BOLERO output for each data set.

The DIMEN card specifies hot channel (or core in this study) dimensions such as flow area (0.3505 ft^2), hydraulic diameter (0.15573 in.), heat transfer surface area (184.28 ft^2) and core length (2.0 ft). Nominal core dimensions are used since the hot channel factors account for extreme dimensions.

The AXIAL cards specify the normalized axial power distribution from core flow inlet to exit. This power shape corresponds to that occuring at beginning of core life when control rods are half-in, and is most limiting during core life because of the high flux level at core exit.

The RCOND card specifies the core operating conditions in terms of hot channel parameters. The related power and flow factors are given in Table 2.2. The hot channel power is 8.9278 MW (3.278 MW x 2.220 x 1.040 x 1.112 x 1.03 x 1.03)*.

---

* Rounding of computer output prevents an exact check of these numbers.

The hot channel flow is 160988.8 lb/hr (400. gpm x 60. x 0.13368 x 61.728/1.08/1.05 x 0.3231/0.3505) where the water density at 120°F is 61.728 lb/cu. ft. The inlet water enthalpy (at 120°F) is 87.92 BTU/lb . The local hot spot factor is required to reduce the hot channel power used in enthalpy calculations to the power required by heat flux values. Its 1.0383 value is calculated from 0.93 x 1.03 x 1.15/1.03/1.03.

The PROP card specifies the water properties for a given system pressure, which is the value calculated at the core (or channel) exit. This approach ensures the correct Bernath DNB heat flux when the DNB limit occurs at the channel exit, and produces a conservatism result when the DNB limit occurs elsewhere. For the example in Table B.1, where core conditions are 3.278 MW, core flow is 400 gpm, core inlet temperature is 120°F, and pressurizer is 75 psia, the calculated core exit pressure is 74.6 psia. The water properties corresponding to this absolute pressure are:

- saturated enthalpy of 277.18 BTU/lb
- latent heat of vaporization of 904.59 BTU/lb
- steam/water density ratio of 333.73
- water density of 57.071 lb/cu ft.

The BNTN card specifies data for the Bernath DNB heat flux correlation. It contains the Bernath DNB heat flux multiplier (0.5), the heated-to-wetted perimeter ratio (0.924), and the saturation temperature corresponding to an absolute pressure of 74.6 psia (307.22°F).

The END card specifies end of input for a data set, and initiates the BOLERO calculations.

TABLE B.1

SAMPLE B O L E R O INPUT DATA SET

```
TITLE      M U R R SAFETY STUDY  3.278MW   400GPM  120DEG F 75 PSIA      T,Q.
DIMEN      0.3505    0.15573   184.28    2.0
AXIAL 1 48 0.360     0.340     0.350     0.375     0.400     0.435     0.470
AXIAL 2    0.505     0.540     0.580     0.620     0.660     0.700     0.745
AXIAL 3    0.785     0.830     0.875     0.920     0.965     1.015     1.065
AXIAL 4    1.110     1.155     1.200     1.245     1.285     1.325     1.355
AXIAL 5    1.385     1.405     1.425     1.440     1.450     1.450     1.440
AXIAL 6    1.425     1.405     1.375     1.345     1.305     1.260     1.210
AXIAL 7    1.160     1.105     1.055     1.015     1.010     1.070
RCOND        8.9278  160988.8    87.92     1.0383                      T,Q,   F
PROP          74.6     277.18   904.59    333.73    57.071              T,Q,PR
BNTH          .5000     .9240   307.22                                  T,Q,PR
END
```

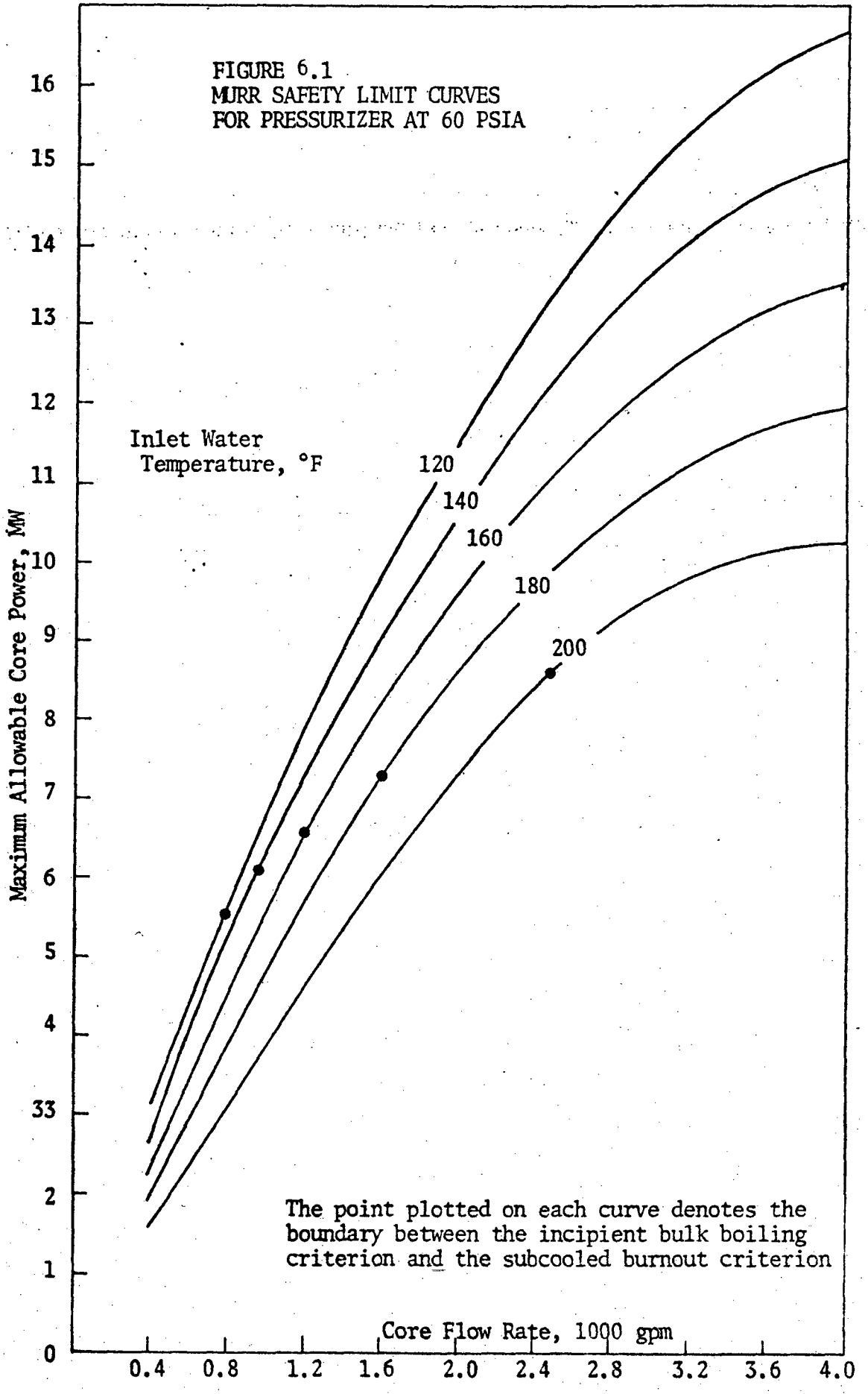
6.0 ADDENDUM TO THE SAFETY LIMIT ANALYSIS FOR THE MURR

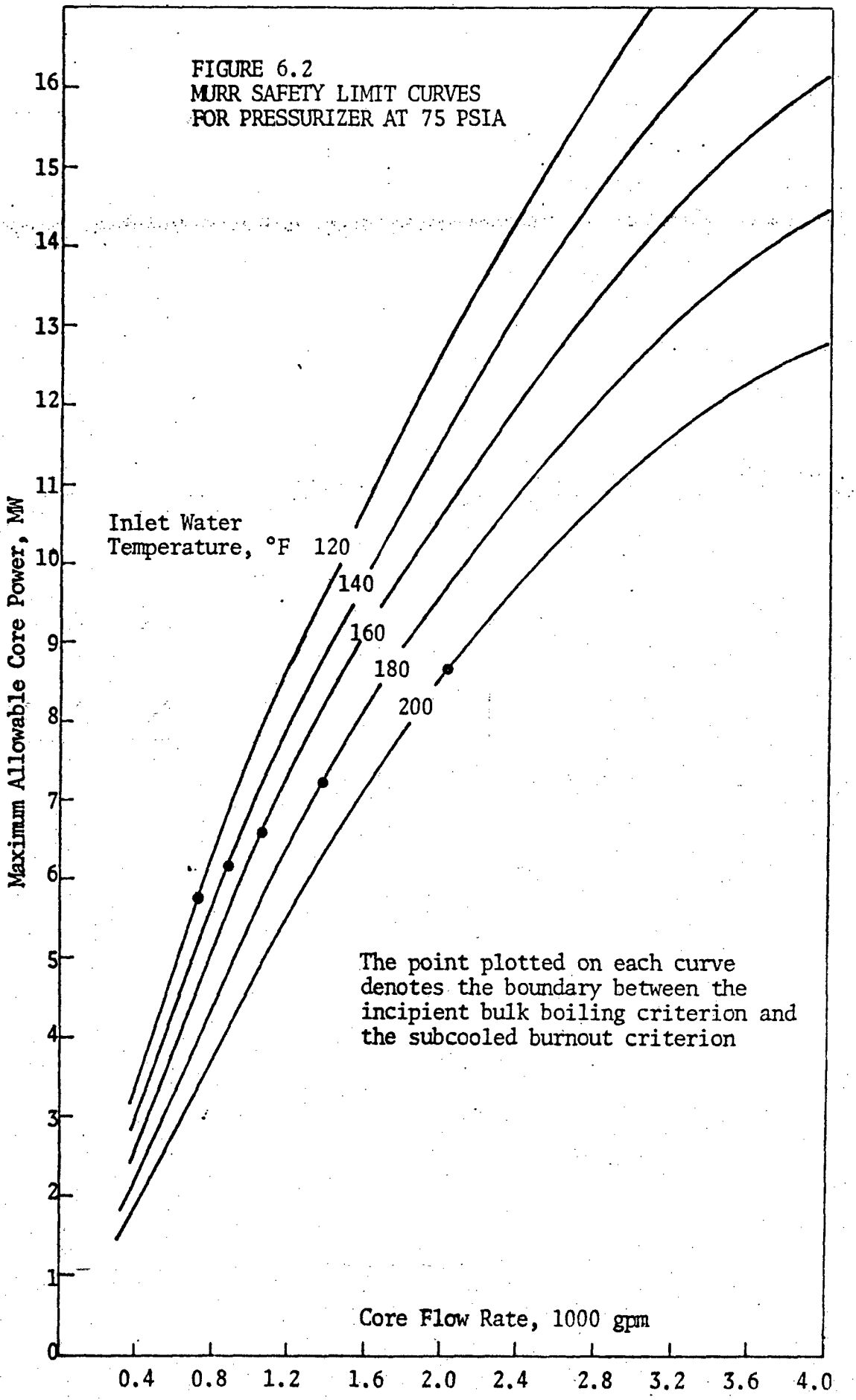
6.1 Introduction

In October 1973 the MURR submitted, as Appendix F of Addendum 4 to the Hazards Summary Report, a safety limit analysis performed by the NUS Corporation on the MURR reactor (1). In response to AEC inquiry, the University of Missouri authorized NUS Corporation to extend that analysis. The results are discussed below.

6.2 Safety Limit Curves

The original work generated two safety limit curves corresponding to pressurizer pressures of 60 and 75 psia. These curves are reproduced here as Figures 6.1 and 6.2, respectively. Additional work, employing techniques identical to the original study, has produced Figure 6.3 which depicts a safety limit curve for a pressurizer pressure of 85 psia, i.e., the nominal operating pressurizer pressure. Table 6.1 presents the numerical results of this work. These three curves together define a four-dimensional safety limit envelope prescribing limiting combinations of values for reactor power, pressurizer pressure, primary coolant inlet temperature and core flow rate. Operation of the MURR within this safety envelope will prohibit fuel meltdown or cladding damage as a result of departure from nucleate boiling (DNB). To evaluate safety limits for pressurizer pressures intermediate to the three cases considered, interpolation will be used. For example, the true values of core flow and inlet temperature in a particular case may be applied to the three curves to obtain a three point relationship between pressurizer pressure and the limiting reactor power. The safety limit on reactor power level will then be fixed by interpolation. For pressurizer pressures below 60 psia extrapolation will be used to determine the safety limits.


FIGURE 6.1
MURR SAFETY LIMIT CURVES
FOR PRESSURIZER AT 60 PSIA
Inlet Water
Temperature, °F
120
140
160
180
200
Maximum Allowable Core Power, MW
16
15
14
13
12
11
10
9
8
7
6
5
4
33
2
1
0
0.4
0.8
1.2
1.6
2.0
2.4
2.8
3.2
3.6
4.0
Core Flow Rate, 1000 gpm
The point plotted on each curve denotes the boundary between the incipient bulk boiling criterion and the subcooled burnout criterion


FIGURE 6.2
MURR SAFETY LIMIT CURVES
FOR PRESSURIZER AT 75 PSIA
Maximum Allowable Core Power, MW
Inlet Water
Temperature, °F
120
140
160
180
200
The point plotted on each curve denotes the boundary between the incipient bulk boiling criterion and the subcooled burnout criterion
Core Flow Rate, 1000 gpm
0
1
2
3
4
5
6
7
8
9
10
11
12
13
14
15
16
0.4
0.8
1.2
1.6
2.0
2.4
2.8
3.2
3.6
4.0

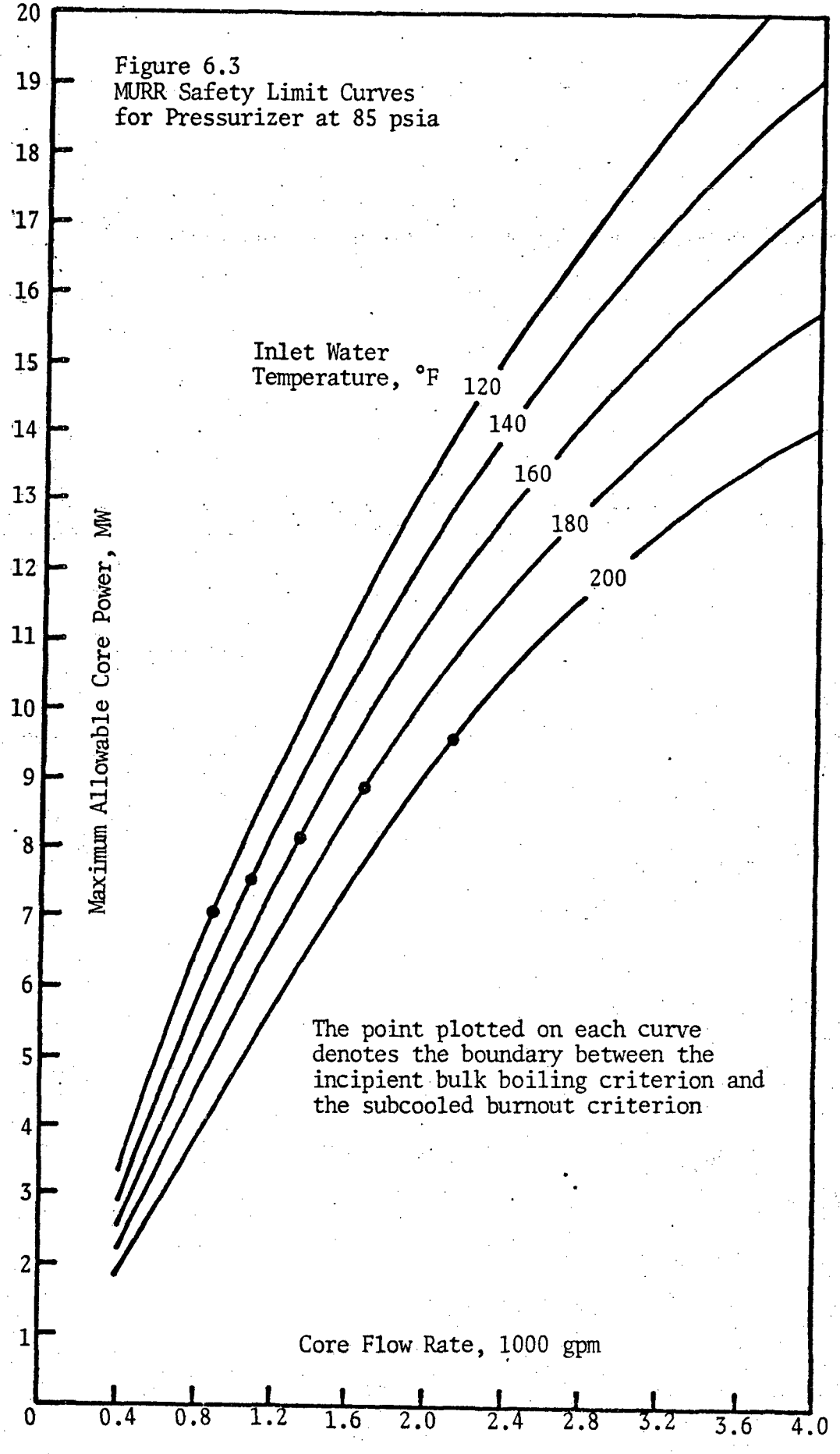

Figure 6.3
MURR Safety Limit Curves
for Pressurizer at 85 psia
Inlet Water
Temperature, °F
120
140
160
180
200
Maximum Allowable Core Power, MW
The point plotted on each curve
denotes the boundary between the
incipient bulk boiling criterion and
the subcooled burnout criterion
Core Flow Rate, 1000 gpm
0
1
2
3
4
5
6
7
8
9
10
11
12
13
14
15
16
17
18
19
20
0.4
0.8
1.2
1.6
2.0
2.4
2.8
3.2
3.6
4.0

TABLE 6.1

SAFETY LIMITS FOR M U R R OPERATION

Maximum Allowable Core Power Level, MW with Pressurizer at 60 PSIA

INLET WATER CONDITIONS

Temperature DEG F	Flow Rate, GPM 400.	800.	1200.	1600.	2000.	2400.	2800.	3200.	3600.	4000.
120.	3.011	5.870	7.980	9.843	11.574	13.099	14.426	15.450	16.217	16.65
140.	2.650	5.262	7.299	9.035	10.582	11.960	13.155	14.071	14.729	15.07
160.	2.292	4.546	6.675	8.202	9.600	10.822	11.877	12.669	13.228	13.50
180.	1.935	3.834	5.667	7.409	8.612	9.685	10.603	11.267	11.715	11.90
200.	1.583	3.131	4.615	6.009	7.282	8.400	9.301	9.863	10.204	10.26

Maximum Allowable Core Power Level, MW with Pressurizer at 75 PSIA

INLET WATER CONDITIONS

Temperature DEG F	Flow Rate, GPM 400.	800.	1200.	1600.	2000.	2400.	2800.	3200.	3600.	4000.
120.	3.278	6.334	8.647	10.742	12.668	14.435	16.050	17.394	18.532	19.43
140.	2.916	5.798	7.939	9.906	11.667	13.282	14.746	15.967	16.993	17.78
160.	2.556	5.080	7.317	9.067	10.676	12.138	13.458	14.534	15.437	16.13
180.	2.197	4.363	6.474	8.236	9.680	10.988	12.152	13.104	13.892	14.46
200.	1.843	3.656	5.415	7.099	8.686	9.845	10.868	11.689	12.339	12.81

Maximum Allowable Core Power Level, MW with Pressurizer at 85 PSIA

INLET WATER CONDITIONS

Temperature DEG F	Flow Rate, GPM 400.	800.	1200.	1600.	2000.	2400.	2800.	3200.	3600.	4000.
120.	3.292	6.584	9.097	11.299	13.336	15.227	16.878	18.356	19.662	20.776
140.	2.930	5.860	8.421	10.452	12.326	14.062	15.568	16.920	18.108	19.102
160.	2.570	5.139	7.709	9.607	11.326	12.908	14.271	15.488	16.549	17.434
180.	2.211	4.421	6.632	8.766	10.319	11.749	12.969	14.051	14.980	15.741
200.	1.856	3.712	5.568	7.424	9.280	10.593	11.673	12.617	13.418	14.069

NOTE . . . Underlined power levels are limited by bulk boiling.

6.3 Calculational Methods

As described in the previous analysis (1) the BOLERO and MURRPGM computer codes were used to model the steady state thermodynamic and hydrodynamic operation of the MURR reactor. The singularity of design makes experimental determination of an exact DNB correlation for every individual research reactor prohibitively expensive. A literature review demonstrates that the Advanced Test Reactor (ATR) closely compares to the MURR in fuel design, although the ATR core is twice as long as that of the MURR. Extensive experimental tests (2,3) were made on mockups of ATR coolant channels to determine the most accurate of the numerous DNB burnout correlations available. It was observed that the limiting conditions for ATR operation were set by subcooled burnout due to hydraulic instabilities in the hot channel. This was found to occur at 60% of the DNB heat flux predicted by the widely used Bernath correlation (4). To provide a reasonable margin between predicted DNB conditions and the MURR safety limits, the safety limit criterion was established that the local heat flux at any point in the core shall be less than 50% of the burnout heat flux given by the Bernath correlation at that point.

A parameter of safety significance for nuclear reactors is the DNB ratio (DNBR) defined as the ratio of the anticipated DNB heat flux to the actual peak reactor core heat flux. Thus, DNB and associated fuel damage will not occur as long as the DNBR is greater than 1.0. For the study in question, safety limits were derived based on a DNBR of 2.0 relative to the Bernath correlation, i.e., conditions were limited to 50% of the predicted burnout heat flux. However, in relation to the experimentally observed burnout at 60% of the Bernath prediction, one can say with assurance that the DNBR for the MURR safety limit curves is not less than 60%/50% or 1.2. Thus, the derived curves allow sufficient margin between the safety limits and actual predicted DNB. The usual conservatism of worst case power peaking and non-uniform fuel loading and appropriate hot channel

factors were used, lending greater assurance that the MURR reactor will not appraoch DNB under the most severe anticipated transient from the proposed 10 MW power level.

The safety limit criteria for Mode I and II operation with core flow rates below 400 gpm has been changed to a fuel plate cladding surface temperature of 366°F. This number is derived from additional calculations made with the PARET code for the Loss of Flow Accident. The input data for these calculations was identical to that used in the analysis summarized on pages D-9 through D-13 of Addendum 4 (1), with the exception of the core pressure. In the previous analysis it was assumed that the core was completely depressurized through the anti-siphon system. In the proposed design of the process control system (Figure A.5 of Add 4) the anti-siphon valves (543A/B) do not open on a loss of flow and thus core depressurization is not credible for this accident.

The latest PARET results for a core pressure of 75 psia (scram set-point) and the worst case loss of flow accident yield a maximum cladding surface temperature of 327°F and a DNB surface temperature of 366°F. The DNB ratio for this maximum surface temperature is 2.84 and thus there is sufficient margin to insure that this accident will not result in core damage.

References

1. "MURR Hazards Summary Report," Addendum 4, Appendix F, University of Missouri Research Reactor Facility, October 1973.
2. Croft, M. W., "Advanced Test Reactor Burnout Heat Transfer Tests," USAEC Report IDO-24475, Babcock & Wilcox Co., January 1964.
3. Waters, E. D., "Heat Transfer Experiments for the Advanced Test Reactor," USAEC Report BNWL-216, Battelle-Northwest, May 1966.
4. Bernath, L., "A Theory of Local-Boiling Burnout and Its Application to Existing Data," Chem. Eng. Progm. Symp Ser., 56, No. 30, 95-116 (1960).

3.3 Evaluation of Power Peaking Factors in the MURR 6.2 Kg Core

Reference: Hazards Summary Report Addendum 1, Section 3.9.

The original MURR design study, as presented in the Hazards Summary Report, presented power peaking values based on a 5.0 kilogram ^{235}U uniformly loaded core. Correction factors derived from one-dimensional calculations were used to extrapolate the power peaking values to various core configurations. During the course of the physics evaluation of the MURR's 6.2 kilogram uranium-aluminide core, a second study was performed which focused directly on the "as constructed" MURR and included the input of observed operating characteristics to date. The results reported (1) are outlined here.

The primary tools employed for reactor physics studies at the MURR are the Exterminator-II two-dimensional multigroup neutron diffusion code and the MURR four-group macroscopic cross-section set. Exterminator II is listed as abstract number 156 with the Argonne National Laboratory Code Center. The code is capable of modeling extremely complex reactor systems in X-Y, R-Z or R-θ geometries. This code calculates the spatial and energy dependent neutron flux, the effective multiplication factor (K_{eff}) and several other reactor parameters of the system modeled. This code has been in use at the MURR for two years and has produced consistently reliable predictions of various reactor physics parameters of the MURR.

The MURR 4-group cross section set was compiled by Internuclear Company and is listed in reference (2). The three epithermal groups were generated by the MUFT-4 (3) program and the thermal group was derived from maxwellian averaged microscopic cross sections as presented in Appendix A of reference (2).

To obtain a conservative estimate for power peaking in a 6.2 Kg MURR core, we may consider an Exterminator R-Z calculation of the flux distribution in a "smeared" core, i.e. one in which the cross sections have been homogenized over the core region. For a clean critical situation with the control blades 12" withdrawn, the hot channel is at the inner fuel plate and the hot spot is 5" below core center line.

Define the axial peaking factor as

$$P_a = \frac{\text{Maximum Power in the Hot Channel}}{\text{Average Power in the Hot Channel}}$$

For a clean uniformly loaded core, this is just the ratio of the peak to average flux in the hot channel. This value is $P_a = 1.432$.

Define the radial peaking factor as

$$P_r = \frac{\text{Average Power in the Hot Channel}}{\text{Average Power in the Core}}$$

Again for the clean critical situation, this is just the ratio of the corresponding thermal fluxes. Exterminator calculates this value to be 2.643. The smeared core actually extends inside the physical location of the inner plate, however. To account for this, the radial flux profile at the axial peak position, as calculated by Exterminator, was examined and a correction factor derived which is just the ratio of the thermal flux at the actual innermost fuel plate location to the thermal flux at the inner edge of the

smeared core. This factor was computed to be 0.84 and when multiplied by 2.643 gives a clean core radial peaking factor P_r of 2.220.

A third factor which must be included is the circumferential peaking factor. The thermal flux tends to peak in the aluminum side plates and the water gap between elements. For the inner fuel plate, this value has been computed to be $P_\theta = 1.04$ from modeling the core in R-θ geometry with no rods. Therefore, the overall power peaking factor for a clean, uniformly loaded, critical 6.2 Kg MURR core is $P_r P_a P_\theta = 2.220 \times 1.432 \times 1.04 = 3.306$.

A fourth factor which must be introduced is a correction for non-uniform loading. In order to use fuel economically and to maintain sufficient excess reactivity to reactivity to recover from unforeseen shutdowns under high xenon conditions, it has proven desirable to mix load old and new fuel elements. The MURR's UAl_x standard elements contain 775 grams ^{235}U each. The worst nonuniform power peaking situation foreseeable is a mixed loading of seven fully depleted elements, i.e. approaching the MURR burnup limit of 99 megawatt-days per element, and one clean 775-gram element.

This configuration was studied in detail at the MURR and values were obtained for nonuniform power peaking factors. Define P_n, the nonuniform power peaking factor, as

$$P_n = \frac{\text{R-}\phi \text{ peak/average power ratio in nonuniform core}}{\text{R-}\theta \text{ peak/average power ratio in corresponding uniformly loaded core}}$$

For the case of seven depleted elements and one clean element it was found that $P_n = 1.112$.

Then for the worst case of a clean critical MURR core in the worst possible nonuniform loading, the power peaking factor is $P_n P_r P_a P_\theta$ = 1.112 x 2.220 x 1.432 x 1.04 = 3.676.

This is considered to be a realistic power peaking factor derived from calculations on the exact expected MURR conditions and should be used for further heat transfer and fluid flow analysis on the MURR reactor under 10 megawatt power with a 6.2 kilogram ^{235}U core.

References

1. Letter of August 5, 1970 from the MURR to AEC Division of Reactor Licensing regarding a request for change in Technical Specifications.
2. "Missouri University Research Reactor Design Data," Volume II, Internuclear Company, Clayton, Missouri, 1962.
3. "MUFT-4, Fast Neutron Spectrum Code for the IBM 704," WAPD-TM-72, Bohl, et. al.

APPENDIX H

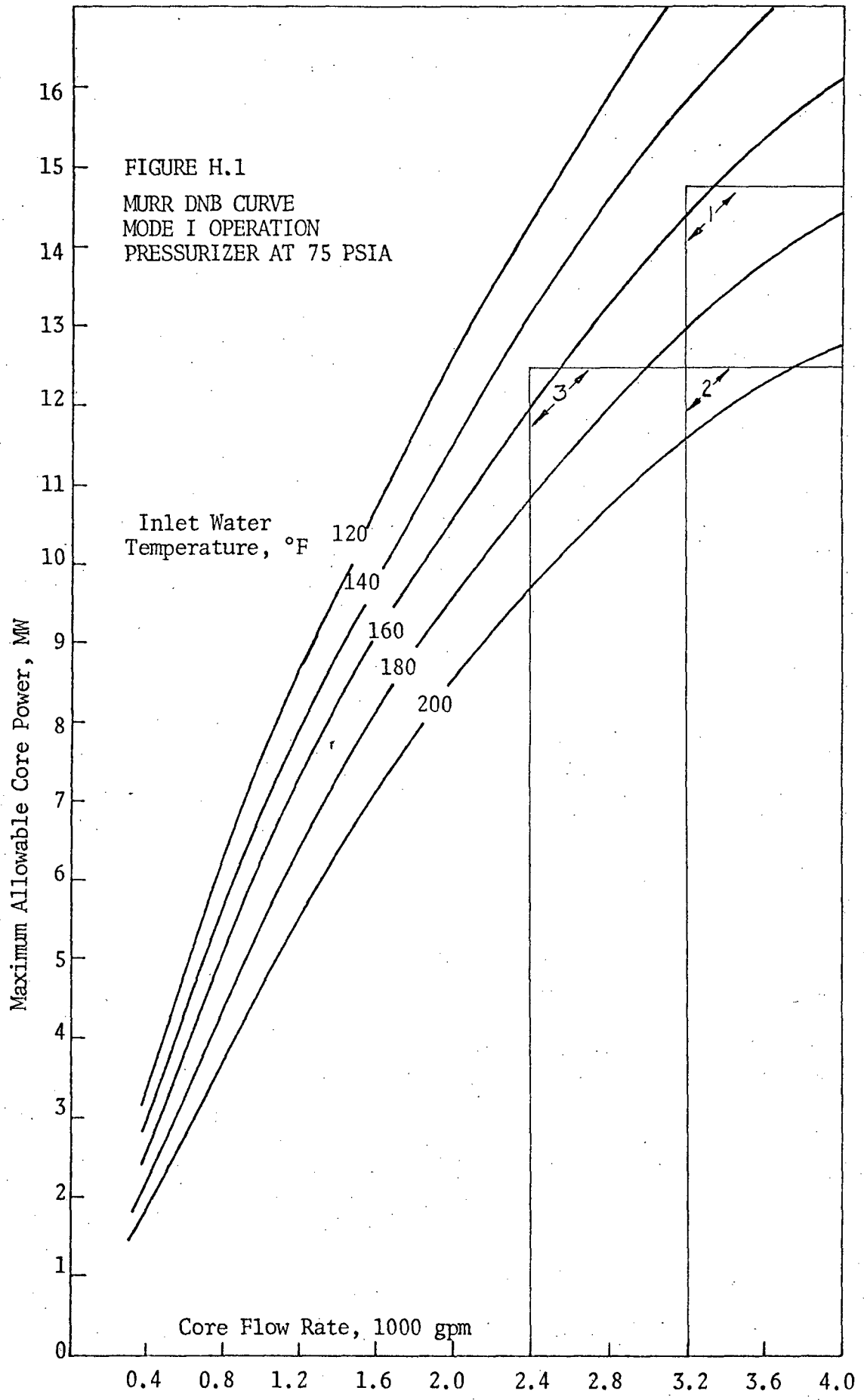
BASES FOR LIMITING SAFETY SYSTEM SETTINGS FOR MODES I AND II OPERATION

H. BASES FOR LIMITING SAFETY SYSTEM SETTINGS FOR MODES I AND II OPERATION

The limiting safety system settings (LSSS) proposed for Modes I and II i.e., 10 MW and 5 MW operation respectively, of the MURR are as follows. For reactor power level the LSSS is 125% of full power for both modes thus the highest powers obtainable before a reactor scram would be 12.5 MW (1.25 X 10 MW) in Mode I and 6.25 MW (1.25 X 5 MW) in Mode II. For both modes, the LSSS on pressure is a minimum of 75 psia in the pressurizer, and the LSSS on primary coolant core inlet temperature is a maximum of 155°F. The LSSS on primary coolant flow for Mode I operation is a minimum of 1625 gpm in either of the parallel coolant loops. The same LSSS of 1625 gpm applies for the single operating loop in Mode II operation. Since 50 gpm of the primary coolant flow is diverted to the cleanup system, the actual core flow rates at the LSSS are 3200 gpm and 1575 gpm in Modes I and II respectively.

Appendix F of this report presents parametric curves for the conditions which would lead to departure from nucleate boiling (DNB) and resulting fuel damage. From that analysis, Figure H.1 depicts the DNB conditions for the LSSS on pressurizer pressure of 75 psia. From this curve one may predict the safety margin for several anticipated transients.

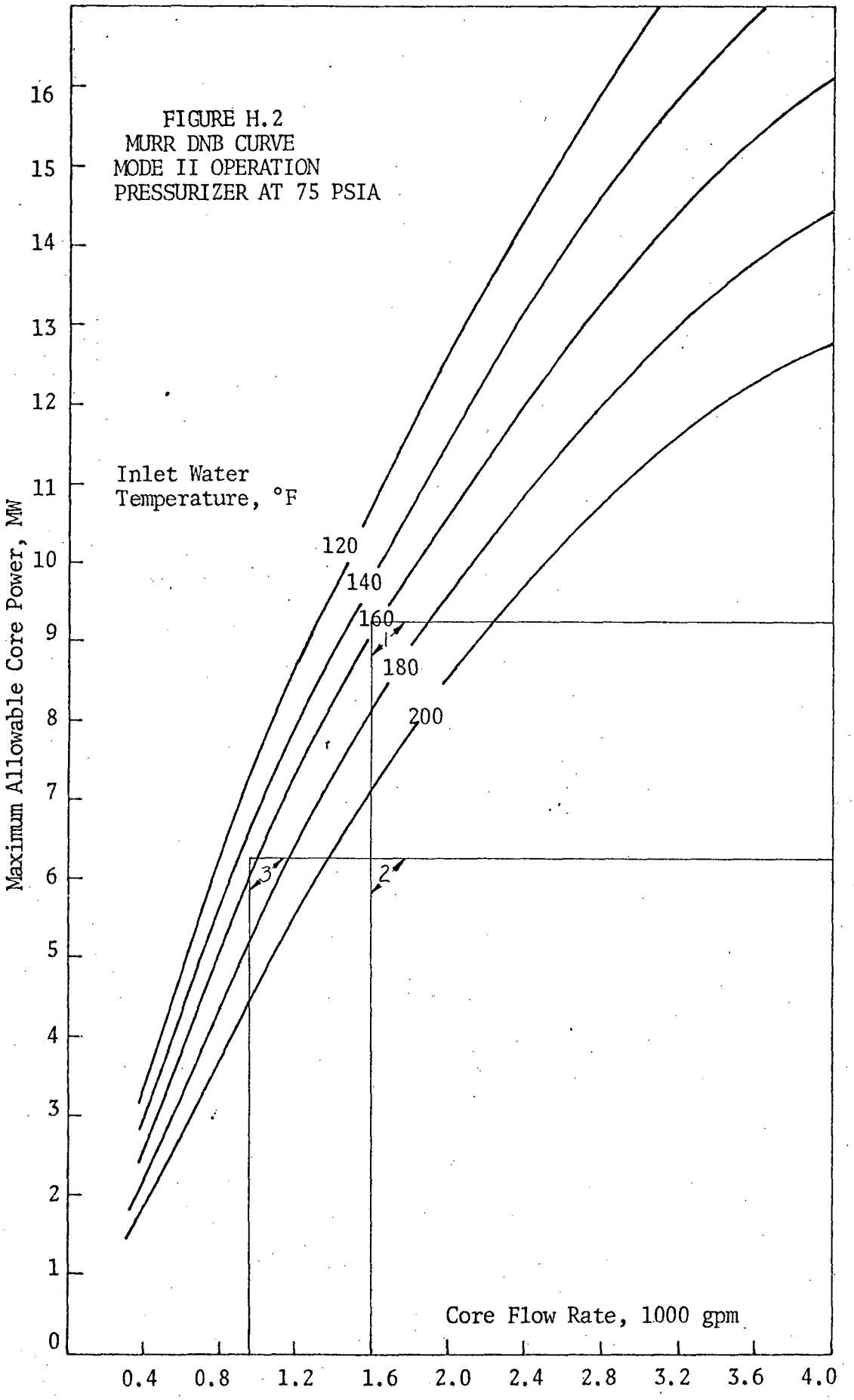
Case one postulates a severe power transient with primary flow and pressure already reduced to their LSSS value in Mode I operation. Figure H.1


FIGURE H.1
MURR DNB CURVE
MODE I OPERATION
PRESSURIZER AT 75 PSIA
Inlet Water Temperature, °F
120
140
160
180
200
1
2
3
Maximum Allowable Core Power, MW
Core Flow Rate, 1000 gpm
0
1
2
3
4
5
6
7
8
9
10
11
12
13
14
15
16
0.4
0.8
1.2
1.6
2.0
2.4
2.8
3.2
3.6
4.0

predicts that the temperature LSSS of 155°F could not be reached until the reactor power has risen to 14.75 MW, or 2.25 MW above the reactor power scram point, thus an ample safety margin exists for safety system reaction time required to prevent reaching the DNB threshold.

Case two postulates steady state Mode I operation of the reactor with flow and pressure again reduced to their LSSS and reactor power at the LSSS of 12.5 MW. Figure H.1 predicts that DNB would not occur until a core inlet temperature of approximately 185°F was obtained. The safety margin is thus 30°F above the LSSS of 155°F on core inlet temperature. Primary coolant temperature increase would be slow, so little or no margin is required for safety system reaction time. Frequent compliance checks and past operating history provide confidence that the primary coolant temperature measurement error is no greater than $\pm$ 5°F. Therefore there is excess safety margin for a temperature transient of this type.

Case three postulates Mode I operation with pressurizer pressure reduced to the LSSS of 75 psia, reactor power and coolant inlet temperature raised to their LSSS of 12.5 MW and 155°F respectively. Figure H.1 predicts that the primary coolant flow rate could be reduced to approximately 2400 gpm before DNB would occur, implying a safety margin of 800 gpm below the LSSS of 3200 gpm on coolant flow through the core. Operating history has shown that the true value of primary coolant flow does not vary from the measured value by more than $\pm$ 50 gpm, thus there is excess margin for safety system reaction time to scram the reactor before DNB occurs. Appendix D provides a detailed analysis of the results of the most severe loss of flow accident for the MURR.


FIGURE H.2
MURR DNB CURVE
MODE II OPERATION
PRESSURIZER AT 75 PSIA
Inlet Water
Temperature, °F
120
140
160
180
200
Maximum Allowable Core Power, MW
Core Flow Rate, 1000 gpm
0
1
2
3
4
5
6
7
8
9
10
11
12
13
14
15
16
0.4
0.8
1.2
1.6
2.0
2.4
2.8
3.2
3.6
4.0

Consideration of the same transients for Mode II (5 MW) operation yields even greater safety margins. Figure H.2 presents the results, for Mode II operation, of the same transients discussed above. Case one predicts DNB at 9.25 MW i.e., 3 MW above the LSSS of 6.25 MW for lMode II. Case two results indicate that the reactor could be operated with a coolant inlet temperature in excess of 200°F for Mode II without reaching DNB. Case three shows DNB occurring only with flow reduced to 1000 gpm or 575 gpm below the LSSS. Thus the safety margin is 36% of the LSSS flow value for Mode II operation as compared to 25% for Mode I.

The LSSS for pressurizer pressure is 75 psia; a margin of 15 psi above the safety limit of 60 psia. Past operating experience has shown the pressurizer pressure sensors to be accurate within $\pm$ 2 psi. Additionally, there are four independent sensors capable of causing a reactor scram in the event of a loss of pressure transient, thus there is sufficient margin to insure that the low pressure safety limit will not be violated.

Therefore the proposed limiting safety system settings on the four important parameters of reactor power, pressurizer pressure, primary coolant flow rate and primary coolant inlet core temperature are easily capable of causing the reactor to scram and preventing the violation of the safety limit envelope.

Figure 5.5 shows the pressure required to suppress boiling at 1 MW with the most adverse fuel loading.

Figure 5.6 presents the effect of the multiplier R, and is used to aid the interpretation of various peaking assumptions.

Figure 5.7 shows the total pressure drop across the core as a function of flow rate.

5.5.3 Analysis of Natural Convective Cooling of the Core

The reactor core will be cooled by natural convection during initial low power operation. To accomplish this a flanged opening is provided in the invert loop. By removing this flange and the reactor vessel head an open path is provided between the pool and the core allowing natural circulation to take place. The object of this analysis is to determine the natural convection flow rate and the corresponding maximum fuel plate temperature for the initial low power operation.

5.5.3.1 Natural Convection Flow Rate

During natural convection operation, the reactor core is cooled by pool water flowing in through the open flange, down through the 12 inch pipe, up through the pressure vessel and core, and out again into the pool. The flow rate is determined by equating the total system pressure loss to the driving head resulting from the heating of the water in the core.

Table 5.4 lists the factors used to determine the quantities F_b and F_θ appearing in equation (1).

TABLE 5.4

Hot Channel & Hot Spot Factors

	F_b	F_θ
Error in power measurement	1.05	1.05
Fuel content variation	1.03	1.03
Meat thickness and variation	1.03	1.15
Coolant channel variation	1.08	1.03
Velocity variation	1.05	1.04
Heat transfer coefficient	-	1.00
	F_b = 1.263	F_θ = 1.332

The heat transfer coefficient used in these calculations is given by

$$h = 0.02 \frac{k}{D} (R_e)^{0.8} (P_r)^{0.4}$$

which was evaluated at the average film temperature by iteration.

5.5.2.5 Results

Figure 5.3 presents the pressure required at the core inlet to suppress boiling at 5 MW and at 10 MW. For 5 MW operation the most adverse nonuniform fuel loading is assumed.

Figure 5.4 shows the effect of the degree of nonuniformity of fuel loading on the pressure required to suppress boiling at 5 MW.

The total pressure loss consists of turbulent friction loss in the piping and pressure vessel, laminar friction loss in the core, and expansion and contraction losses at changes in cross section throughout the loop. For turbulent flow the frictional pressure loss is given by,

$$\Delta p = 2f \frac{L}{D} \frac{w^2}{g\rho A^2} \quad psf \tag{2}$$

where:

f = Fanning friction factor
L = length - ft.
D_e = equivalent diameter - ft.
w = flow rate - lb./sec.
g = 32.2 ft./sec.^{2}
ρ = density of water - lb./ft.^{3}
A = flow area - ft.^{2}

To permit an analytical solution of the equations, the friction factor was evaluated from

$$f = 0.046 \ (Re)^{-0.20} \tag{3}$$

This gives a conservative value for the friction factor for smooth pipe over a range of Reynold's Numbers (Re) from 5000 to 200,000 and was obtained from Bonilla[1*].

In the core the pressure drop was taken as that for laminar flow between broad parallel plates given by [3]

$$\Delta p = \frac{12 \mu w L}{z^2 g\rho A} \quad psf \tag{4}$$

---

*References for Section 5.0 are listed at the end of the section.

where:

μ = water viscosity - lb./ft. sec.

z = plate spacing - ft.

Expansion and contraction losses were determined from

$$\Delta p = \frac{K \ w^2}{A^2 \ 2g\rho} \ \text{psf} \qquad (5)$$

where K is the expansion or contraction loss coefficient based on the area, A. The loss coefficients were taken from Bonilla[2]. From equations (2) through (5) the total pressure loss may be determined as a function of only the flow rate (w) if constant temperatures are assumed. The loss will be of the form

$$\Delta p_L = C_1 \ w^2 + C_2 w^{1.8} + C_3 w \ \text{psf} \qquad (6)$$

$C_1 w^2$ is the term representing the expansion and contraction losses. Table 2.1 lists the value of C_1 associated with each section of the loop. For simplicity the values are based on a single average loop temperature of 100°F, the pool temperature.

TABLE 5.5

Expansion, Contraction & Transition Losses

Location	$C_1 \times 10^3$
Pool to 12" flange	.175
Tee to invert loop	.624
90° Ell to pressure vessel	.220
Entry to pressure vessel	1.020
Core	2.130
Pressure vessel to pool	.625
Total	4.794

The second term in equation (5) is the turbulent flow frictional pressure drop as found from equations (1) and (2). Table 2.2 lists the length of pipe and the value of C_2 for each component, again assuming 100°F water temperature.

TABLE 5.6

Turbulent Flow Frictional Pressure Loss

Component	Length - ft.	$C_2 \times 10^4$
Pressure vessel	8.25	4.22
12" pipe	17.01	2.71
	Total	6.93

The third term in equation (5) is the laminar flow pressure drop in the core as determined from equation (3). At 100° F C_3 has a value of 3.14×10^{-2}.

The natural convection driving head, or pressure gain, is in general

$$\Delta p_g = L(\rho_i - \rho_o) \qquad (7)$$

Assuming a linear variation of temperature in the core, L is the distance between the centerline of the core and top of the pressure vessel. ρ_i and ρ_o are the core inlet and outlet water densities respectively.

Expressing the density difference as a function of coefficient of volumetric expansion and temperature difference, and the temperature difference as a function of heat generation rate, flow rate and specific heat, equation (7) becomes

$$\Delta p_g = \frac{L \rho \beta q}{w C_p} \quad \text{psf} \tag{8}$$

where:

β = coefficient of volumetric expansion - $^{o}F^{-1}$
q = heat generation rate - Btu/sec.
C_p = specific heat - Btu/lb.^{o}F

At an average temperature of 100^{o}F

$$\Delta p_g = .102 \ (q/w) \text{ psf}$$

for

L = 8.08 ft.
β = 2.0149 x 10^{-4} $^{o}F^{-1}$
ρ = 61.99 lb./ft.^{3}
C_p = .997 Btu/lb.^{o}F

Assuming that 93% of the reactor heat is released in the core, the heat generation rate (q), for a reactor power of 150 KW, is 132.2 Btu/sec. The pressure gain for this heat rate is

$$\Delta p_g = 13.4/w \text{ psf}$$

Equating the pressure loss to the pressure gain, the flow rate is found to be 11.96 lb./sec. For this flow rate the Reynold's Number in the core is 993, indicating the validity of the assumption of laminar flow in the core for determining the core pressure loss. The Reynold's Number in the balance of the system exceeds 17,400.

5.5.3.2 Maximum Wall Temperature

Calculation of the maximum core wall temperature is based on the procedures and equations presented in TM-WRP-62-10[4]. The maximum wall temperature (t_w) exceeds the core inlet temperature (t_i) by

$$t_w - t_i = F_b f(z) \overline{\Delta T} + F_\theta P_a \frac{\overline{\Phi}}{h} P_r R_2 R_3 \qquad (9)$$

where:

F_b = bulk temperature factor = 1.263

F_θ = film factor = 1.332

P_r = $\frac{\text{average power density in hot channel}}{\text{average core power density}}$

= 2.263 for reference case of 5 Kg uniform loading.

P_a = $\frac{\text{maximum power density in hot channel}}{\text{average power density in hot channel}}$ = 1.443

$f(z)$ = fraction of heat delivered at design point in hot channel = 1.0

ΔT = average bulk temperature rise = 11.0°F

$\overline{\Phi}$ = average heat flux = 2583 Btu/hr. - ft.^{2}

h = heat transfer coefficient = 218 Btu/hr. - ft.^{2}°F

R_2 = design safety margin in power level = 1.1

R_3 = ratio of power peaking relative to that for a 5 KW uniform loading = 1.425

The values of peaking factors are those appearing in Section 5.5.2. The bulk temperature rise is from the power and flow rate results of the previous section. The average heat flux is for a heat transfer area of 184.3 $ft.^2$ and a core heat generation rate of 132.2 Btu/sec. The core heat transfer coefficient is for laminar or steamline flow in flat channels. For these conditions the Nusselt Number has a constant value of about 8.0 [5]. At a water temperature of 100°F this yields a heat transfer coefficient of 218 Btu/hr. - $ft.^{2-o}F$.

From equation (9) at 150 KW reactor power the temperature difference, $t_w - t_i$, is 130.2°F, which for a pool temperature of 100°F gives 230.2 as the maximum fuel plate surface temperature.

5.5.3.3 Pressure Required to Suppress Local Boiling

Local or nucleate boiling will occur when the maximum wall temperature is greater than the local saturation temperature. The necessary temperature difference to cause boiling may be found from the Jens-Lottes correlation [6]

$$\Delta T_{sat} = \frac{60\ (\phi/10^6)^{1/4}}{e^{p/900}} \quad {}^oF \qquad (10)$$

assuming it to apply at these low pressures. The heat flux ϕ is given by

$$\phi = \bar{\phi}\ P_r P_a R_2 R_3 \qquad (11)$$

Using the values of the factors presented previously, the maximum heat flux is 13,222 Btu/hr.-ft.^{2}-^{o}F. This conservatively neglects the effects of local fuel content and meat thickness, and width variations.

For a pressure (p) of 20 psia, equation (10) gives 19.9^{o}F as the allowable wall superheat. The required local saturation temperature is

$$T_{sat} = t_w - \Delta T_{sat} = 247.1 - 19.9 = 227.2^oF$$

From the steam tables a pressure of 19.72 psia or 5.0 psig is required to suppress local boiling. For a pool temperature of 100^{o}F, 11.7 ft. of water above the top of the fuel plates will give the required pressure. This pool depth is less than that required for shielding.

5.5.3.4 Conclusions

Calculations indicate that a reactor power of 150 KW may be safely attained with natural convection cooling of the core. The maximum fuel surface temperature is 230.2^{o}F and the natural convection flow rate is 11.96 lb./sec. The 17 feet of water required for shielding at low powers is more than sufficient to prevent local boiling in the core.

The core temperature rise of 11.0^{o}F is large compared to the 1-2^{o}F rise which would occur coincidentally in the island. Consequently, no problems should be encountered with respect to the temperature coefficient of reactivity during cooling of both the core and the island by natural convection.

ATTACHMENT 7

ATR-FE-102
Ca-2

Facsimile Price $ 5.60
Microfilm Price $ 2.00

Available from the
Office of Technical Services
Department of Commerce
Washington 25, D. C.

ADVANCED TEST REACTOR BURNOUT HEAT TRANSFER TESTS

January 1964

By
M. W. Croft

Thermal Analysis Section
Engineering Department

AEC Contract No. AT(10-1)-1075
B&W Contract No. 59-3064

Prepared for
EBASCO SERVICES, INC.
and Submitted to
THE UNITED STATES ATOMIC ENERGY COMMISSION
Idaho Operations Office
by
THE BABCOCK & WILCOX COMPANY
Atomic Energy Division
Lynchburg, Virginia

APPROVED BY

M. F. Sankovich, Thermal
Analysis Section Chief

A. H. Lazar, ATR
Project Manager

ACKNOWLEDGMENT

The author is indebted to the many persons who contributed directly to the success of this program. In addition, he wishes to thank the following persons for their outstanding contributions:

Mr. Carl Drummond, Babcock & Wilcox: mechanical design of test specimens.

Dr. Michael Petrick and Dr. Paul Lottes, Reactor Engineering Division, Argonne National Laboratory: review of our results and helpful suggestions during test work.

Messrs. Ed Spleha, T. Anderson, J. Chase, D. Giarrante, and J. Kemp, Argonne National Laboratory: fabrication of test specimens and preparation of test loop for operation and testing.

The Babcock & Wilcox Company
Atomic Energy Division
Report ATR-FE-102

ABSTRACT

The Babcock & Wilcox Company, subcontractor to Ebasco Services, Inc., for the Advanced Test Reactor, is responsible for the nuclear design and development of the ATR. As part of this development, burnout tests were conducted at Argonne National Laboratory to determine the limiting heat flux in a simulated ATR fuel element channel.

Burnout was approached holding all variables constant except one. Power, pressure, flow, and inlet temperature were all varied to approach burnout in different tests. Channel exit pressures were varied from 80 to 250 psia, mass velocities from 5.5×10^6 to 12.5×10^6 lb/hr-ft^2, and inlet temperatures from 120 to 240 F. Maximum heat flux at burnout varied from 0.95×10^6 to 3.88×10^6 Btu/hr-ft^2.

Burnout in the 0.054- and 0.072-inch channels was due to hydraulic instability or autocatalytic vapor binding when the coolant reached saturation at the exit of the channel. Burnout in the 0.094-inch channel occurred at a power level less than that required to produce saturation at the exit in most of the tests. The burnout heat flux in this channel was about 60% of the burnout flux predicted by Bernath's equation.

CONTENTS

		Page
1.	INTRODUCTION	1-1
2.	TEST FACILITY DESCRIPTION	2-1
	2.1. Test Specimen Design	2-1
	2.2. Test Specimen Fabrication and Installation	2-2
	2.3. Test Loop	2-4
3.	TEST PROCEDURE AND DATA	3-1
4.	DISCUSSION OF RESULTS	4-1
	4.1. Loop Checkout Operation	4-1
	4.2. Burnout Results	4-4
5.	CONCLUSIONS	5-1

List of Tables

Table		
3-1.	Test Conditions	3-4
3-2.	0.054-Inch-Channel Data	3-5
3-3.	0.072-Inch-Channel Data	3-6
3-4.	0.094-Inch-Channel Data	3-7
4-1.	0.054-Inch-Channel Calculations	4-10
4-2.	0.072-Inch-Channel Calculations	4-11
4-3.	0.094-Inch-Channel Calculations	4-12

List of Figures

Figure		
1-1.	ATR Fuel Element Cross Section	1-4
2-1.	Burnout Test Specimen Subassembly and Components	2-7
2-2.	Burnout Test Specimen Subassembly (Assembled)	2-9
2-3.	Backup Plates, Flanges, and Terminal Connectors	2-10
2-4.	Burnout Test Specimen With Backup Plates and Flanges	2-11
2-5.	Burnout Test Assembly	2-12
2-6.	Burnout Test Assembly Cross Section	2-13
2-7.	Installed Burnout Test Assembly	2-15
2-8.	Burnout Test Loop Schematic	2-16
2-9.	Pre-Test Integrated Average and Local Channel Thickness (0.072-Inch Channel)	2-17

Figures (Cont'd)

Page

Figure

2-10 After-Test Integrated Average and Local Channel Thickness (0.072-Inch Channel) 2-18
4-1. Burnout Test Results - Temperature Vs X/L (Test 3, 0 054-Inch Channel) 4-13
4-2 Burnout Test Results - Heat Flux Vs X/L (Test 3, 0 054-Inch Channel) 4-14
4-3. Burnout Test Recorder Chart (Test 3, 0 054-Inch Channel) 4-15
4-4. Burnout Test Results - Temperature Vs X/L (Test 1, 0.072-Inch Channel) 4-16
4-5. Burnout Test Results - Heat Flux Vs X/L (Test 1, 0.072-Inch Channel) 4-17
4-6 Burnout Test Recorder Chart (Test 1, 0.072-Inch Channel) 4-18
4-7. Destructive Burnout Results - Test Specimen 4-19
4-8 Burnout Test Results - Temperature Vs X/L (Test 1, 0 094-Inch Channel) 4-20
4-9. Burnout Test Results - Heat Flux Vs X/L (Test 1, 0.094-Inch Channel) 4-21
4-10. Burnout Test Recorder Chart (Test 1, 0.094-Inch Channel) 4-22
4-11 Burnout Test Recorder Chart (Test 10, 0.094-Inch Channel) 4-23

1. INTRODUCTION

Thermal and hydraulic calculations for the Advanced Test Reactor (ATR) indicated that the hot channel in the fuel element could burn out by subcooled film blanketing of the fuel plate surface or by autocatalytic vapor binding of the channel. Proof tests were run at Argonne National Laboratory (ANL) on 4-foot-long by 0.054-, 0.072-, and 0.094-inch-thick test channels. The 1.2-inch-wide channel was heated over the center 1-inch portion of the width with a 1.4 peak-to-average axial chopped cosine heat flux.

The ATR fuel element (Figure 1-1) is an assembly of 19 aluminum-clad curved fuel plates that forms a 45-degree sector of a right circular cylinder. The plates are 49-1/2 inches long and enclose 0.078-inch channels that vary in width from about 1.6 to 3.4 inches. The highly enriched fuel, powdered U_3O_8 in an X-8001 aluminum matrix, is uniformly distributed in the fuel plates over the center 48 inches of length and extends across the plate width to a minimum of 0.050 inch from the side plates on each side.

When burnout testing was initiated, the ATR hot channel operating conditions were as follows:

Reactor rated power, MW	250
Coolant inlet temperature, F	133
Coolant exit temperature, F	325
Maximum fuel plate temperature, F	432
Inlet pressure, psig	300
Exit pressure, psig	208
Average coolant velocity, fps	44
Maximum heat flux, Btu/hr-ft^2	1.92×10^6
Approximate channel L/D ratio	300

In the initial phases of ATR design work, about ten burnout relationships were examined. Many of these correlations were eliminated owing to their development from data obtained at conditions far different

from those in the ATR. Of the original group of correlations, four seemed to offer the most promise, but even these were questionable at ATR conditions. For example, the B&W correlation, based mainly on WAPD data for rectangular channels along with some data from Battelle, seemed to fit the data very well, but most of the data were taken at 2,000 psi. Fewer lower pressure data down to 500 psi were available, but none of the low pressure points were taken in the subcooled range.

The Bettis correlation was attractive since it was made from a large number of rectangular channel experiments and did not depend on subcooling. The correlation, however, was developed for data in the range of 2,000 psi and had no low pressure data to allow for a pressure correction.

The Zenkevitch-Subbotin correlation has been planned for predicting burnout in the High Flux Intensity Reactor (HFIR). A few tests had been made for HFIR conditions, and the correlation seemed to compare satisfactorily. However, the conditions of these tests differed from those for the ATR. The channels tested were only about one third and one fourth of the length of the ATR channels, thus the effect of coolant temperature rise was less pronounced than it is in the ATR.

The Bernath correlation (extended method) was used by Phillips Petroleum Company in the original conceptual design of the ATR. This work indicates that the data were taken by a large number of investigators over a wide range of conditions and for several geometrical arrangements, including round tubes, annular passages, thin strips, and rectangular channels. While different sets of data used in developing the equation covered most of the variables in the ATR no single data point represented all conditions simultaneously. For example, velocity might be in the correct range in some data, but not pressure, pressure might be in the range in other data, but not channel geometry.

When burnout tests, conducted at ORNL for the HFIR were reported, the results were compared with the Bernath correlation The comparison showed that the mean value of the ratio ϕ_{exp}/ϕ_{calc} was only 0.77. The scatter was +0.17 −0.51, and the lowest value of the ratio was 0.49. Due to the wide disagreement, the danger of extrapolating to the ATR conditions was evident. Without tests, the more pessimistic values

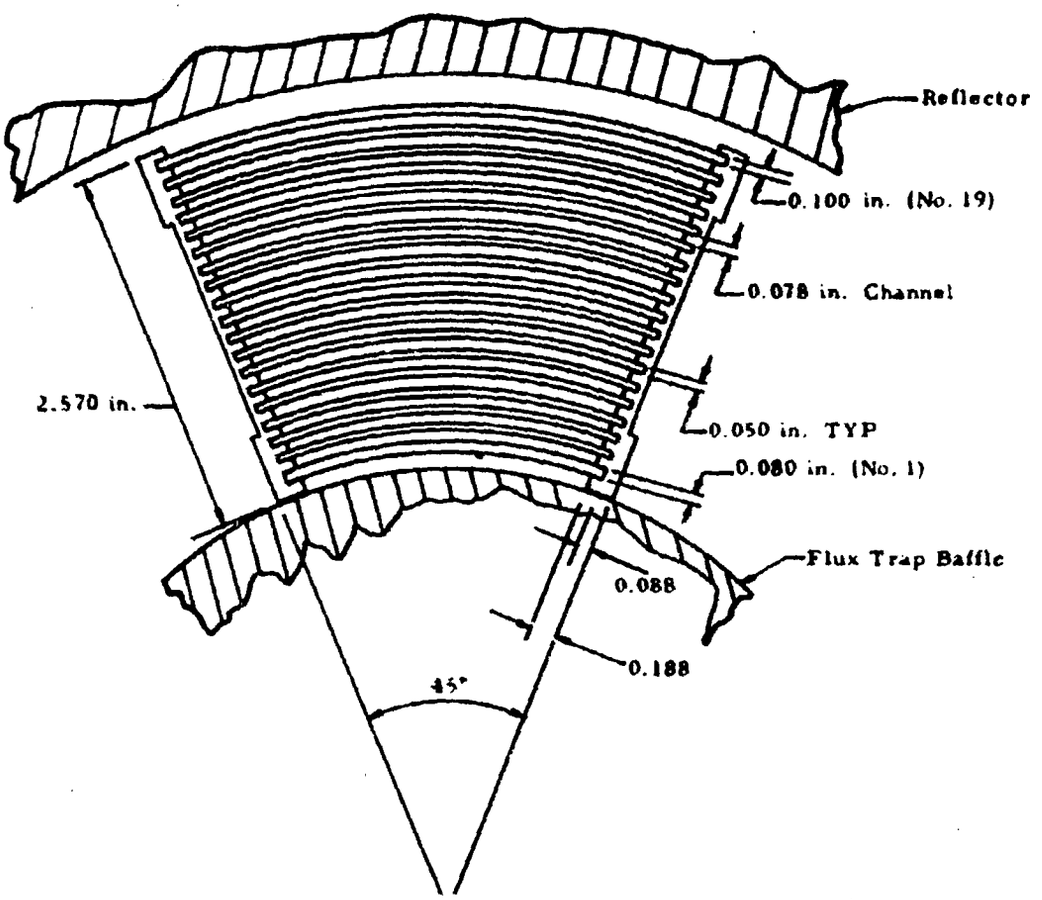
would had to have been used to ensure a safe design. This alone provided justification for burnout tests to verify the predictions and design equations.

Unfortunately, the problem was not one of interpolating between data conditions, but rather of extrapolating beyond the test conditions already used. This was obviously a dangerous approach owing to the completely empirical nature of the burnout correlations. This appears to be partly the reason why there is wide disagreement between many of the correlations when they are examined at ATR conditions.

Futhermore, early analytical results indicated that heat input at the hot channel conditions could be limited by the heat flux that produces subcooled burnout of the fuel plate surface or by autocatalytic vapor binding of the channel when net boiling occurs at the exit. Both of these limits were predicted at about the same power level when 60% of the heat flux calculated by Bernath's equation was used as the limiting criteria. However, the applicability of Bernath's or any other burnout correlation had not been verified at ATR conditions, and it could not be definitely established that burnout would not occur at a power level below that which produces coolant saturation at the exit of the channel.

This report describes the test work performed on simulated fuel element channels at conditions expected in the ATR. The over-all objective of these tests was to obtain burnout data that would either verify the analytical results or define the true limiting conditions directly. To satisfy the latter objective, data were obtained at heat fluxes, coolant flow rates, pressures, and geometries corresponding as closely as possible to those expected in the ATR.

Figure 1-1. ATR Fuel Element Cross Section



2. TEST FACILITY DESCRIPTION

2.1. Test Specimen Design

The test specimens, closely simulating the ATR fuel element channels, were designed to operate under probable core conditions. To obtain data over a wide range of geometry, specimens having three different channel thicknesses (0.054, 0.072, and 0.094 inches) were used in the tests. Full-length, 1.25-inch-wide channels, which were heated over 48 inches of their length, provided a 1.4 axial peak-to-average chopped cosine heat flux distribution. The center 1-inch portion of the channel was resistance heated uniformly across the width with heat generation plates. The specimens were designed for a maximum heat input of 800 kw at 32 volts and a heat flux of 5.7×10^6 Btu/hr-ft^2. Heat flux in the two 0.125-inch sections of the channel on either side of the 1-inch-wide heat generation plates was limited to less than 5% of the flux at the midspan of the channel. Although this design feature prevented premature burnout that is sometimes caused by high heat fluxes at the corner of the channel, it also caused a fairly large portion of the channel to be relatively unheated. Actually, the unheated portions made it possible to qualitatively evaluate lateral coolant mixing within the channel and proved to be a fortunate design feature as described in Section 4.

The high heat fluxes and large L/D requirements, together with the axial chopped cosine flux distribution, reduced heat generation in the corners of the channel, and operational limitations of available test facilities somewhat restricted the test specimen design. Ideally, the test channel should have been fabricated of aluminum to conform with the cladding material for the ATR elements. However, to provide the desired heat flux by resistance heating at a maximum of 32 volts, the heat generation plate resistance must be 1.4×10^{-3} ohms. Since the resistivity of aluminum at operating plate temperatures is about 5.6

microhms-centimeters, the average thickness of an aluminum plate would only be 0 036 inch To produce the 1 4 axial peak-to-average flux by increasing the plate resistance as a function of distance from each end, the plate thickness would have decreased to a minimum of 0 026 inch at the mid-length. Consequently, the anticipated fabrication problems made it necessary to consider other test section materials (stainless steel, A-nickel, brass, and phosphor bronze)

Phosphor bronze was selected, because it was the only material considered in which the combination of electrical resistivity and thermal conductivity did not produce too high operating temperatures or specimen configurations that were impractical to fabricate. However, this material could not be used directly to form the coolant channel since it is subject to corrosion that could affect the burnout results In the final design, flattened A-nickel tubing was used to form the coolant channel, and phosphor bronze plates brazed to the tubing were used as the primary heat generating material Prior to the brazing operation, the plates were machined to a different thickness over short increments of the length to produce the axial cosine flux distribution As shown in Figure 2-1, the plate thickness varies from 0 066 inch at the mid-length to 0 318 inch at each end The dimensions of the A-nickel tubing, which are also shown in Figure 2-1, vary with each specimen size

2.2. Test Specimen Fabrication and Installation

All test sections were fabricated by centering and brazing the machined heat generation plates to the flattened tubing The heat generation plates were copper plated, and specially designed brazing fixture was used to facilitate the brazing operation Tapered copper end fittings were attached to the test section in a second brazing operation, using a braze alloy having a slightly lower melting point than that used in the first brazing operation Figure 2-2 shows a completed subassembly containing pressure taps Flow nozzles, insulating bushings, and machined Mycalex that were used to insulate and support the test assembly are also shown in Figure 2-2

Detailed measurements were made on the subassembly to determine channel dimension Recorder charts showing both integrated average channel thickness and local variation as a function of length were obtained on each assembly, as described in Section 2.3

Backup plates and flanges fabricated from Type 304 stainless steel, and copper terminal connectors containing a tapered hole to accept the tapered copper end fittings are shown in Figure 2-3. A conical 0.010-inch-thick silver shim was placed between the tapered upper end fitting and the terminal connector to ensure good electrical conduction.

After assembly with the terminal connector blocks, seven thermocouples and eleven voltage taps were attached to the heat generation plates by "touch-brazing" at locations shown in Figure 2-1. The Mycalex insulation blocks were placed on the test section and the instrument leads were brought out through holes in the blocks. Sauereisen No. 8 cement was used to fill the irregular void between the insulation blocks and the heat generation plates. Using this cement eliminated the need to step-mill the Mycalex blocks so they would precisely conform to the conductor plate steps. Partial assembly of the test specimen is shown in Figure 2-4.

Owing to assembly expansion characteristics, the backup plates were fabricated of stainless steel and positioned on the test section. The thermocouple and voltage tap leads were brought to the outside through holes in one of the backup plates. Again, Sauereisen No. 8 cement was used to fill the space between the Mycalex blocks and the backup plates to avoid precision machining of these components.

Durabla gaskets provided electrical insulation between the stainless backup plates and the copper terminal connectors. Entrance and exit flow nozzles and insulating bushing were installed. The complete test assembly, ready for installation in the test facility, is shown in Figures 2-5 and 2-6.

The entrance and exit flow nozzles and insulating bushings, backup plates and flanges, copper terminal connectors and conductors, and portions of the Mycalex insulation were re-usable. Several test channels of each size were fabricated as needed to complete the test work.

The test assembly was installed in the ANL 2000-pound burnout test facility. The assembly was connected to the test facility pipe flanges by Durabla wrapped bolts extending through the test assembly side plate flanges, copper terminal connectors, and the pipe flanges. Durabla gaskets electrically insulated the piping system from the copper terminal conductors. Pre-formed 1/2- by 6-inch copper conductors were bolted to the copper terminal connectors of the test assembly and to the existing electrical power supply conductors to complete the electrical circuit for

test section heating. Connection of pressure taps, thermocouple leads, and voltage taps to appropriate measuring and recording instruments completed the installation. Figure 2-7 shows the test assembly installed in the test facility. After pressure testing, the assembly was covered with thermal insulating material.

2.3. Test Loop

A schematic diagram of the test loop is shown in Figure 2-8. Four centrifugal pumps, which were capable of delivering 100 gpm at a developed head of 150 psi, circulated demineralized water through the electrically heated test specimen in a semi-closed loop. The water temperature into the specimen was initially controlled by directing the mixed specimen and bypass flow through air blast coolers downstream from the test specimen. Auxiliary coolers were added later. When the cooling capacity still proved inadequate to remove the heat, a portion of the hot specimen flow was discharged from the loop about 3 feet downstream from the test channel before it mixed with the bypass flow. An equal amount of cold makeup water was added to maintain system pressure.

The power supply used to heat the test specimen supplied a maximum of 30,000 amps of d-c current at a maximum of 52 volts when the four units were connected in series. The specimen design was, however, based on a maximum of 32 volts at 25,000 amps. Specimen and bypass flows were regulated by the bypass valve position and the number of pumps operating.

The channel flow rate was measured with a turbine-type flow meter installed in a 1-inch line upstream from the test channel. Flow rate was indicated on a meter and recorded. The total loop flow, used in combination with channel flow rate to calculate bypass flow, was measured by an orifice meter and indicated on a mercury manometer.

The pressures were measured upstream and downstream of the test assembly and at the taps located about 1 inch inside the specimen entrance and exit shown in Figure 2-1. These pressures were indicated on 0-500 psi Heise gauges. In addition, the test section differential was continuously recorded in most of the runs. In later tests, the specimen exit tap was used in measuring coolant temperature, making it impossible to measure pressure at this location.

Power input was determined from d-c current measurements and voltage drop information. In addition to the over-all voltage drop that

was measured and used in determining heat input, the drop between voltage taps shown in Figure 2-1 was measured to confirm the axial power profile shape. A typical plot of axial peak-to-average power is shown in Section 4 as a function of heated length.

The temperatures on the outer surface of the phosphor bronze heat generation plates were measured with chromel-constantan thermocouples spot welded at approximately 4-inch intervals from the mid-length to the exit of the channel (Figure 2-1). Four of these seven thermocouples were connected to burnout detectors and were not available for measuring surface temperatures. One thermocouple, usually the second from the end, was connected to the Sanborn recorder in order to continuously record surface temperature variation. The other two were monitored as a check on the recorded surface temperature.

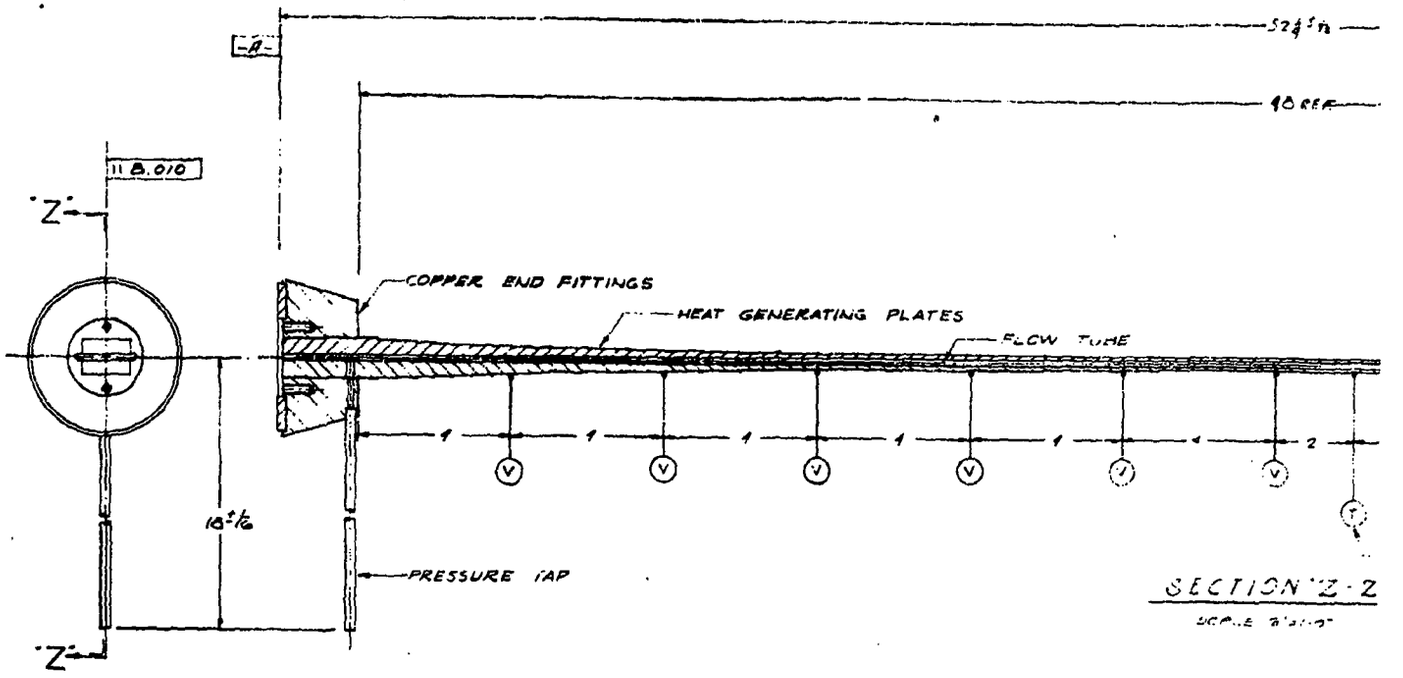
The coolant temperatures were measured at the inlet to the test channel, at a point several inches downstream from the exit, and at the mid-width portion of the channel near the exit. The exit iron-constantan thermocouple was installed in the 1-inch pipe that connected the test channel and bypass portion of the loop. It was located several inches from the exit of the test channel to allow for coolant mixing prior to the temperature measurement. Thus, mixed-mean temperatures could be determined and more accurate heat balances made. Inlet and outlet temperatures were determined from potentiometer readings, and the coolant outlet temperature was recorded in some of the tests.

The thermocouple used to measure the temperature at the midspan of the channel was installed through the exit pressure tap shown in Figure 2-1. This shielded chromel-alumel thermocouple was installed with care to ensure that it was insulated from the heater section and that the tip of the shield was at the channel mid-thickness. At the end of the tests on each specimen, the thermocouple was calibrated and its location in the channel was rechecked. Potentiometer readings were taken periodically and the thermocouple emf was continuously recorded in most tests.

As previously mentioned, all test channels were measured before they were installed in the test loop and after the tests were completed. Figure 2-9 shows local variation and integrated average channel thickness as a function of length as recorded during measurement of an 0.074-inch-nominal channel prior to installation in the loop. Three

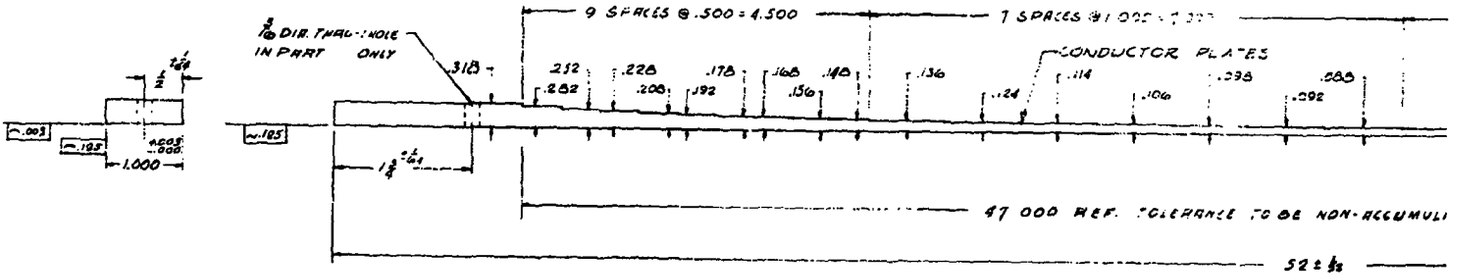
different measurements were obtained: one at the mid-width of the channel and two approximately 0.25 inch from each edge. Channel inside width was measured at each end, and outside width was measured at 6-inch intervals along the length.

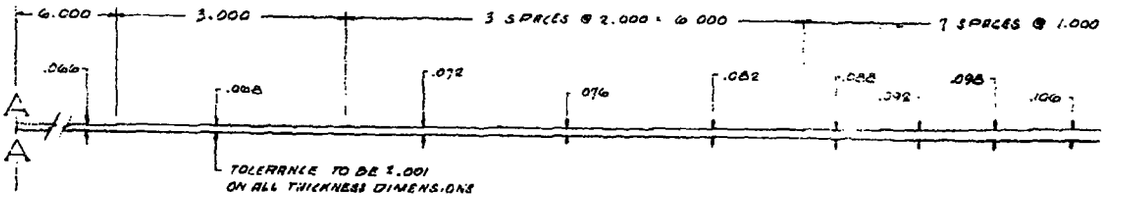
Pressure drop information obtained during the test indicated that the channel had expanded. Post-test measurements of the channel confirmed this finding. The post-test dimensions on the 0.074-inch-nominal channel including the integrated average channel thickness are shown in Figure 2-10. Typically, the post-test integrated average thickness was about 5 mils larger, and local variations were larger and more frequent than in the pre-test measurement. However, this change did not affect the limiting power level as was demonstrated several times by repeating the initial test results in the final test on the specimen.



SECTION "Z-Z"

SCALE 3/4"=1"





PART NO	A
	.038
	.056
	.070
	.074
	.090
	.094

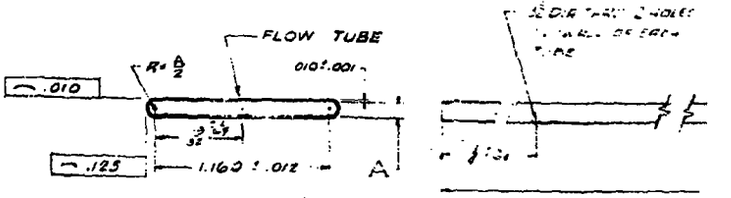
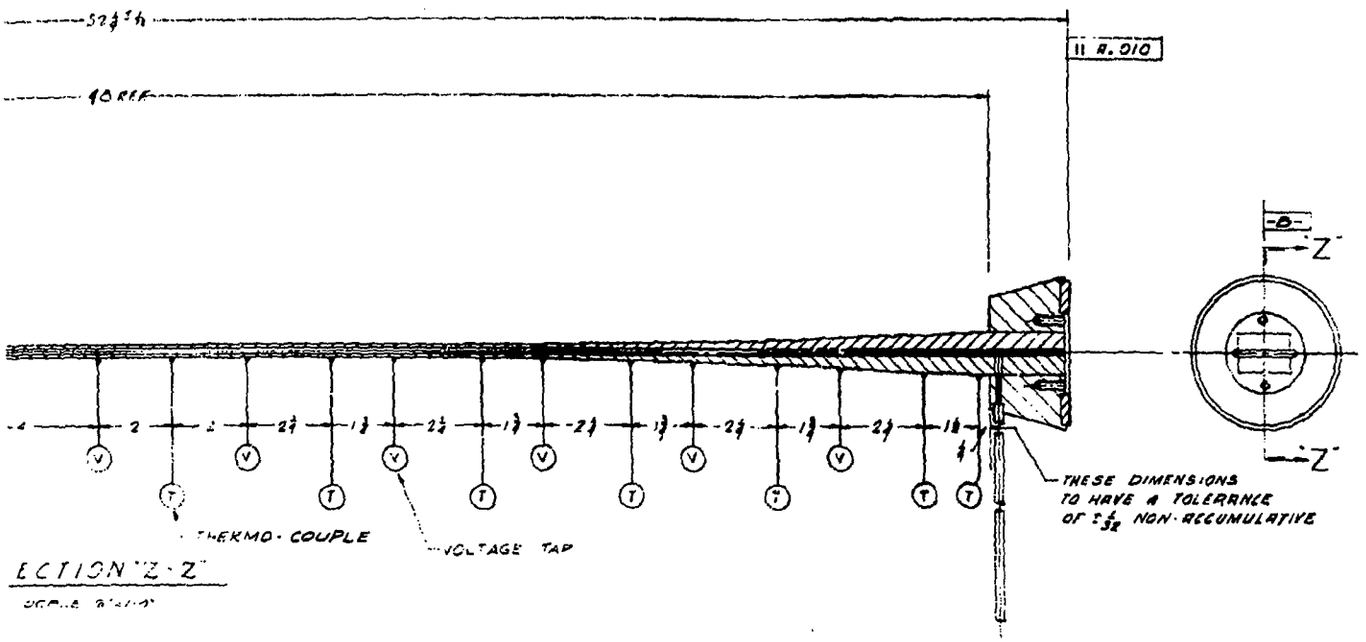


Figure 2-1. Burnout Test Specimen Sub-Assembly and Components (Dwg SKC-3460-F)



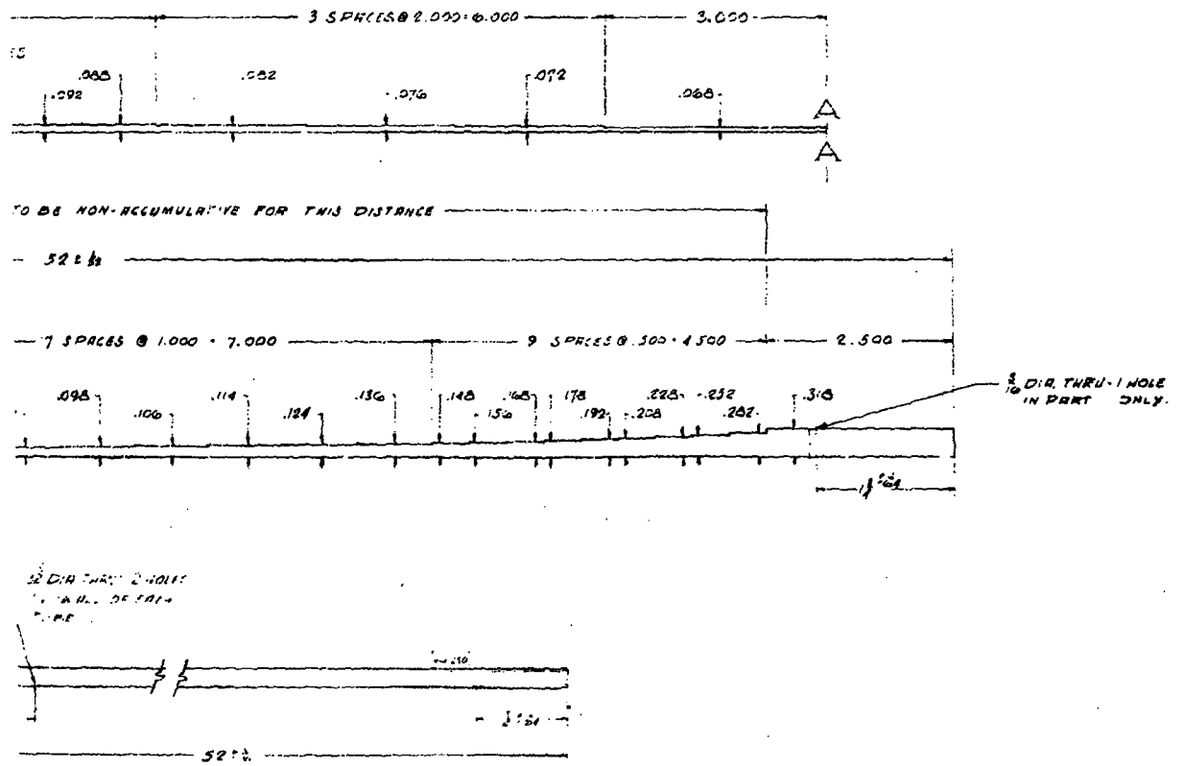


Figure 2-2. Burnout Test Specimen Subassembly (Assembled)

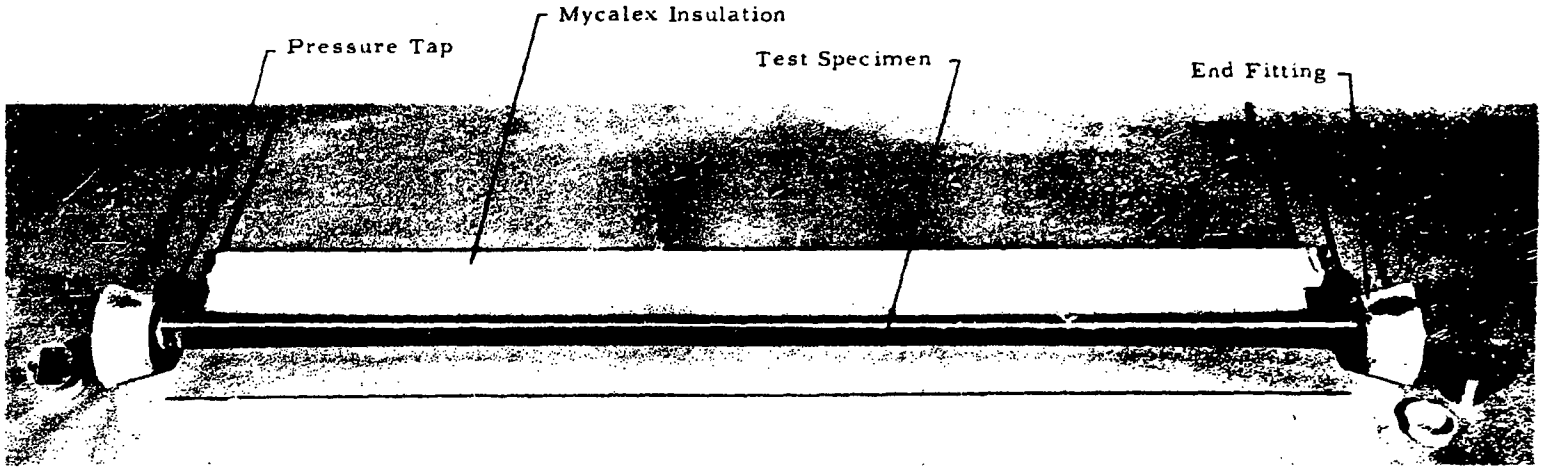


Figure 2-3. Backup Plates, Flanges, and Terminal Connectors

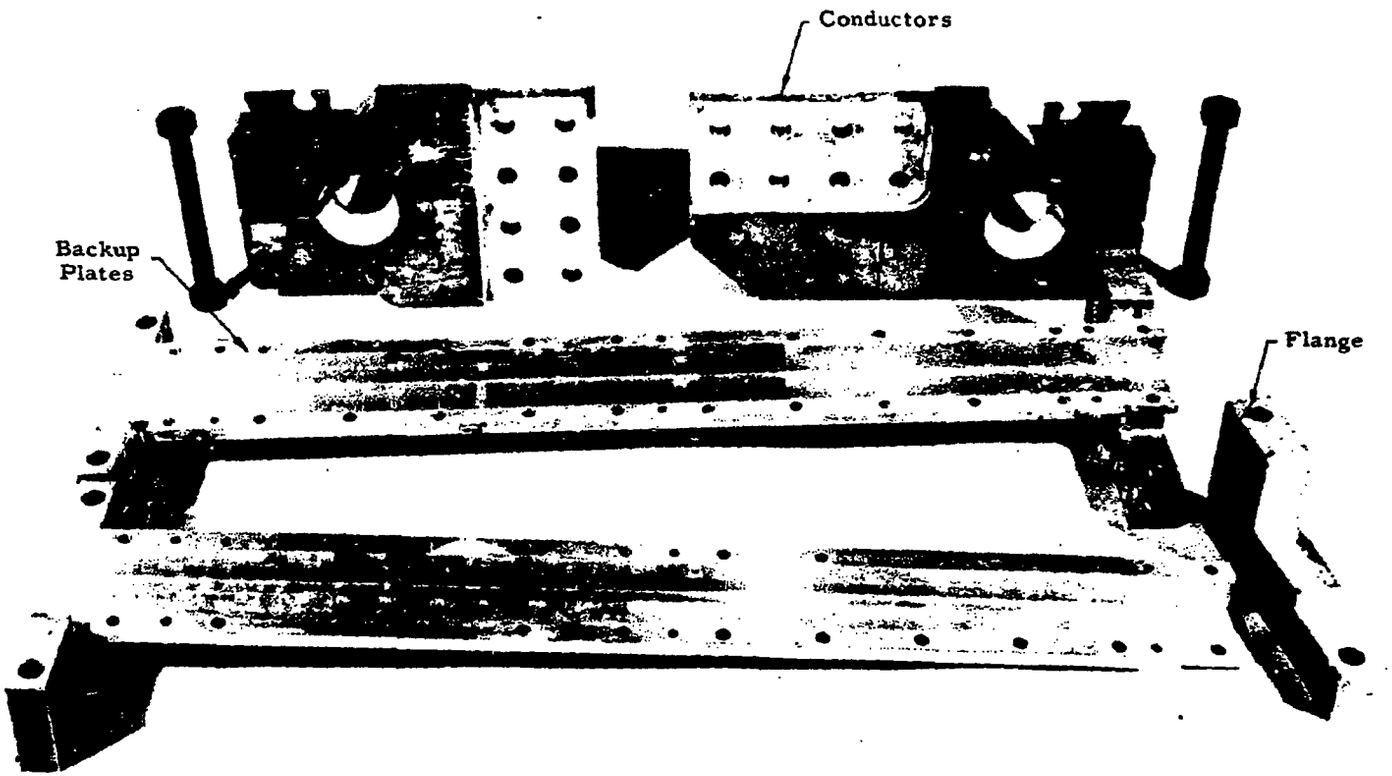


Figure 2-4. Burnout Test Specimen With Backup Plates and Flanges

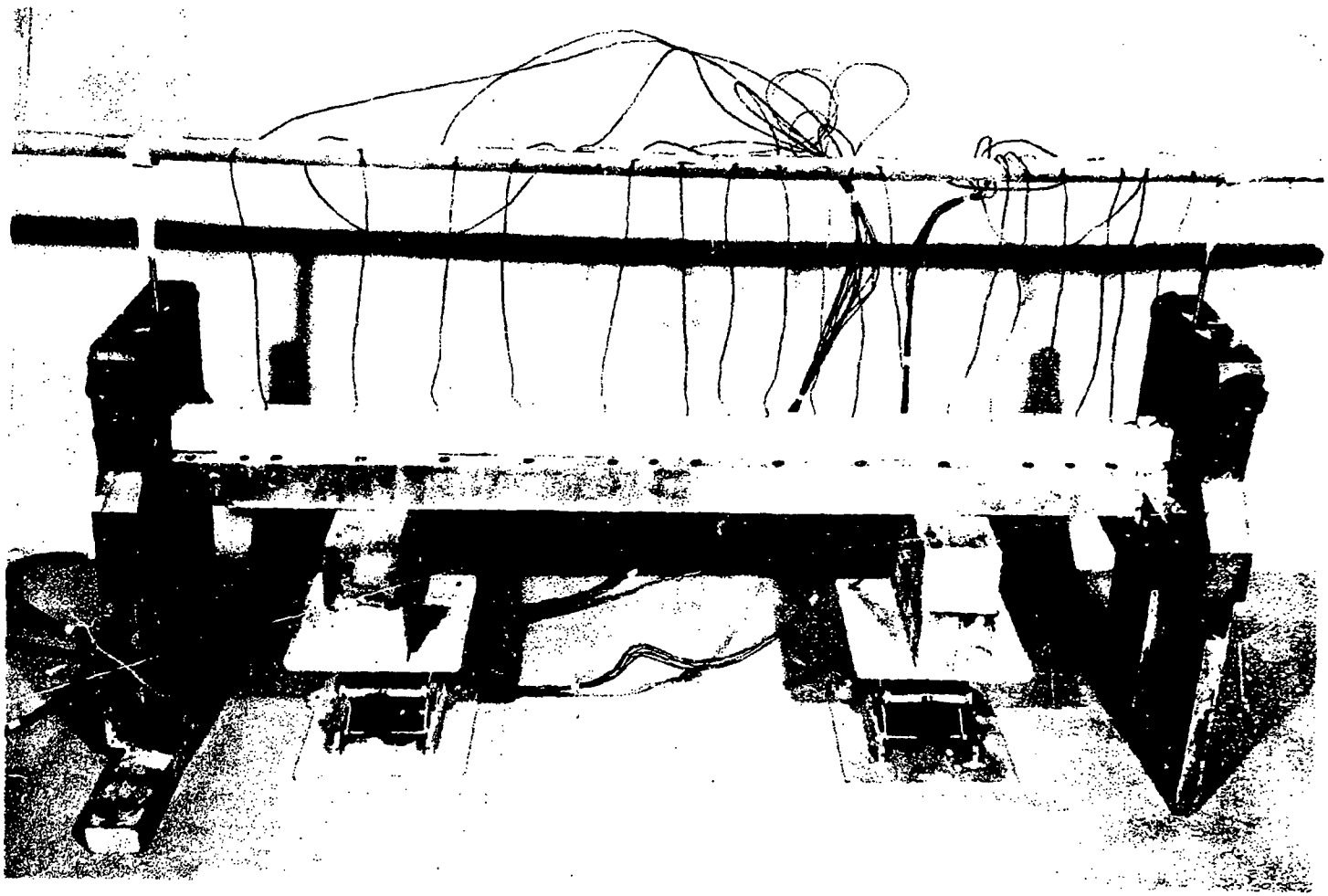
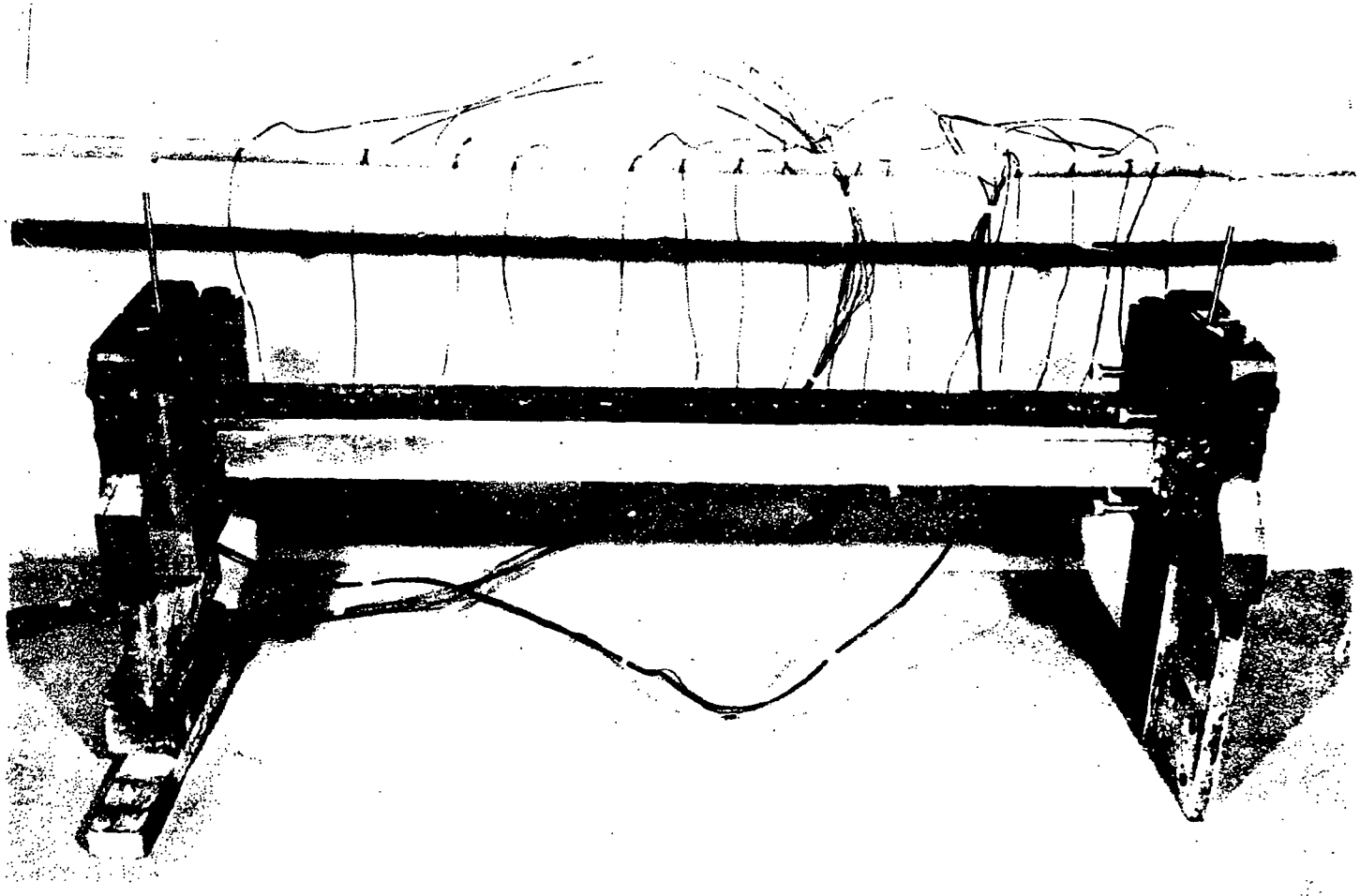
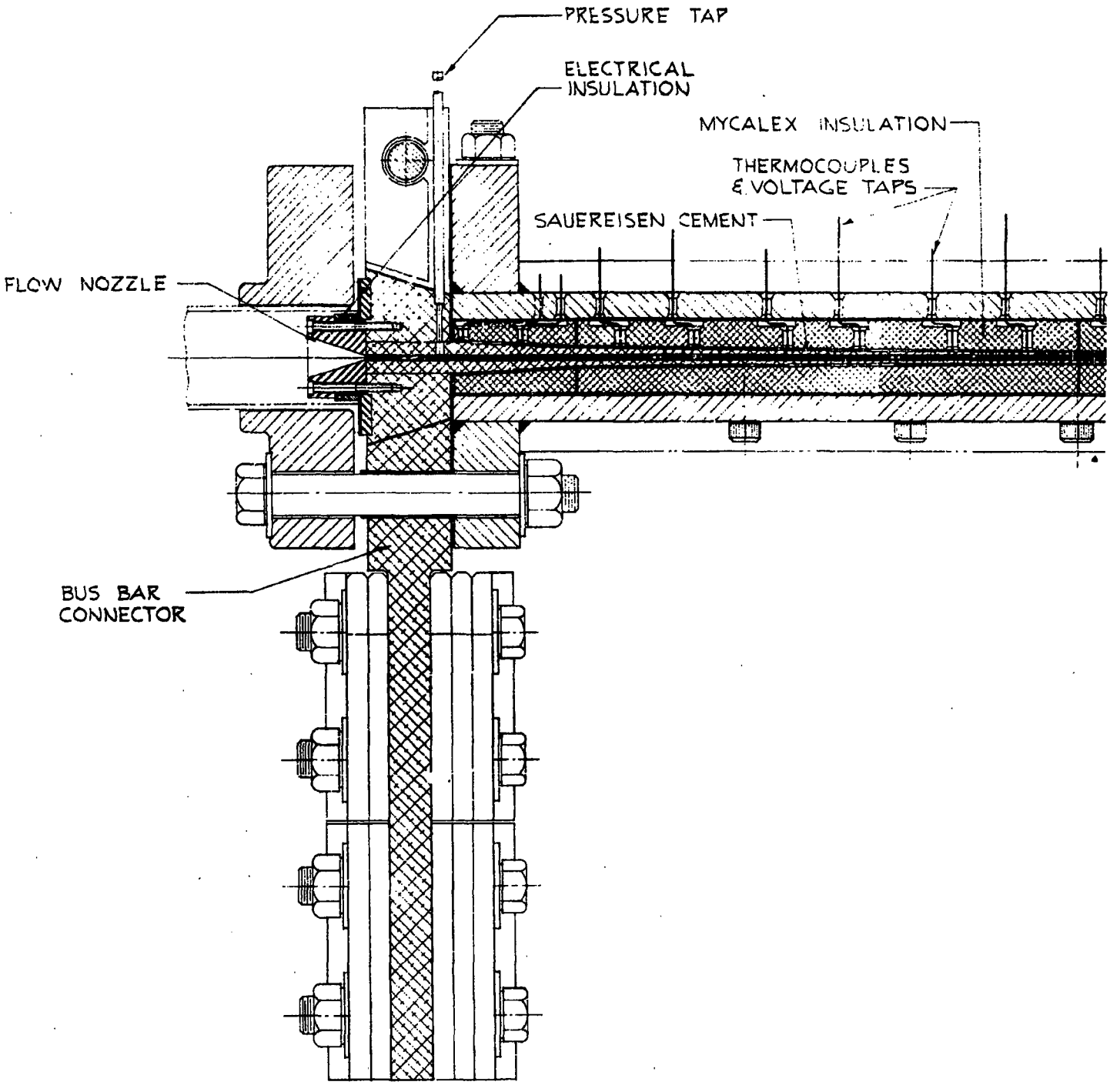
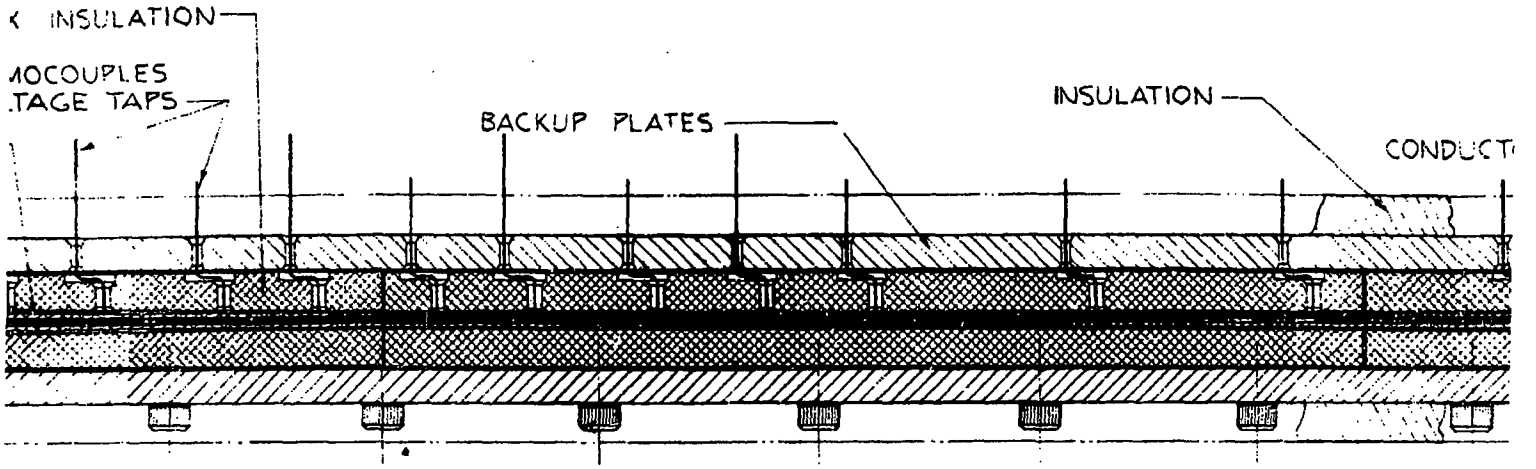
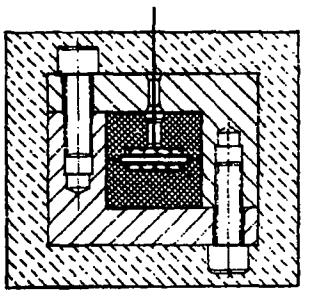


Figure 2-5. Burnout Test Assembly

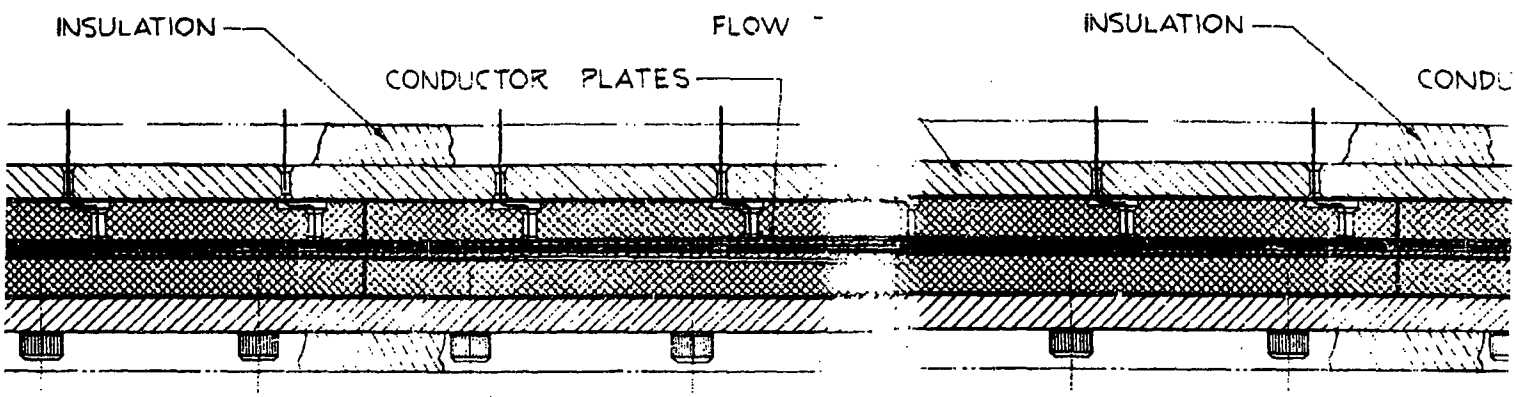


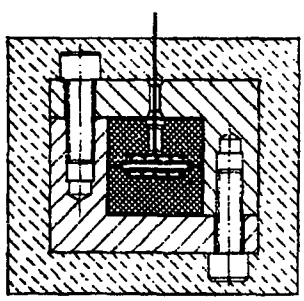

PRESSURE TAP
ELECTRICAL INSULATION
MYCALEX INSULATION
THERMOCOUPLES & VOLTAGE TAPS
SAUEREISEN CEMENT
FLOW NOZZLE
BUS BAR CONNECTOR


INSULATION
MOCOUPLES
TAGE TAPS
BACKUP PLATES
INSULATION
CONDUCT



Figur





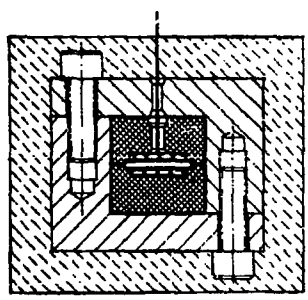


Figure 2-6. Burnout Test Assembly
Cross Section
(Dwg SKC-3459-F)

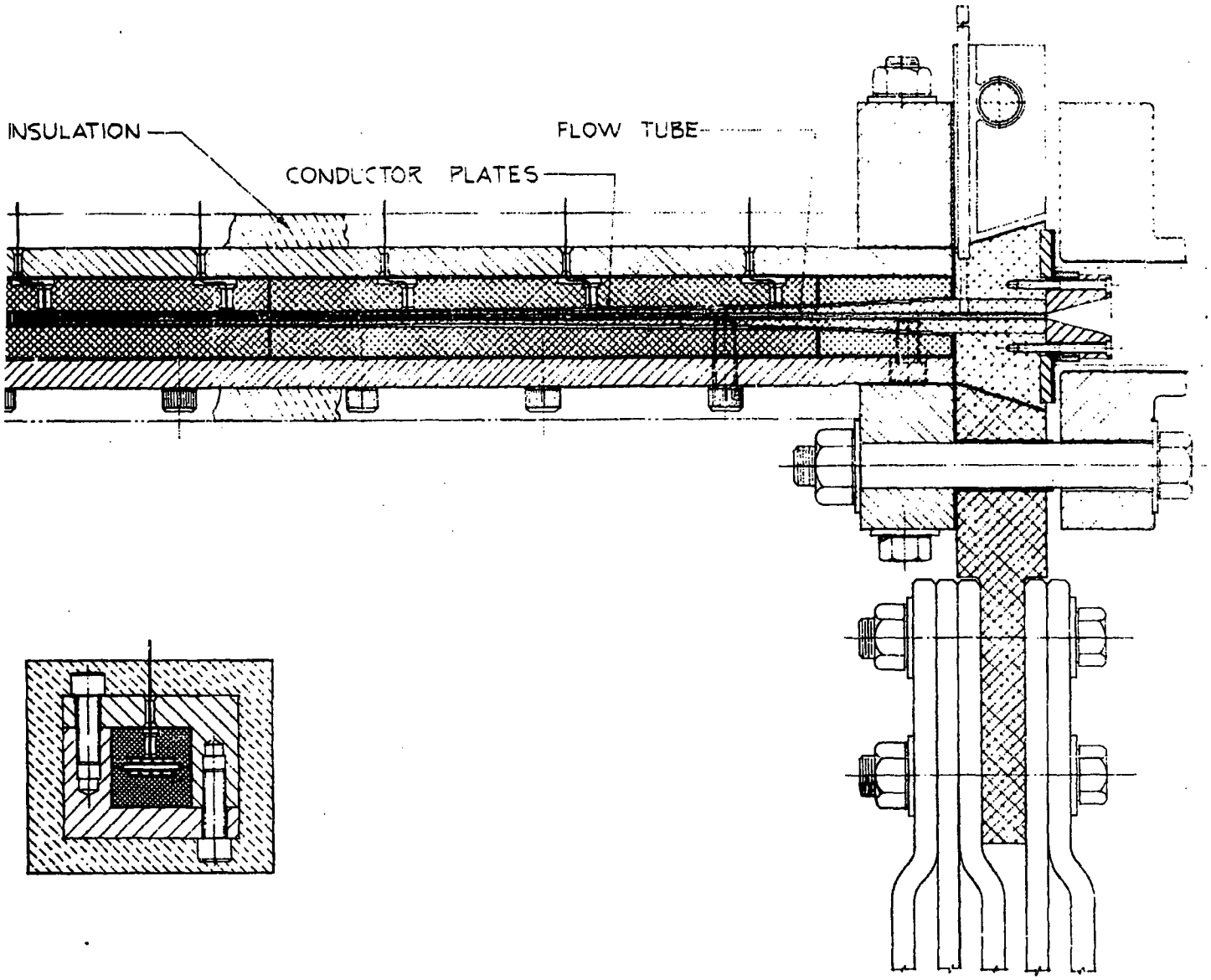


Figure 2-7. Installed Burnout Test Assembly



Figure 2-8. Burnout Test Loop Schematic

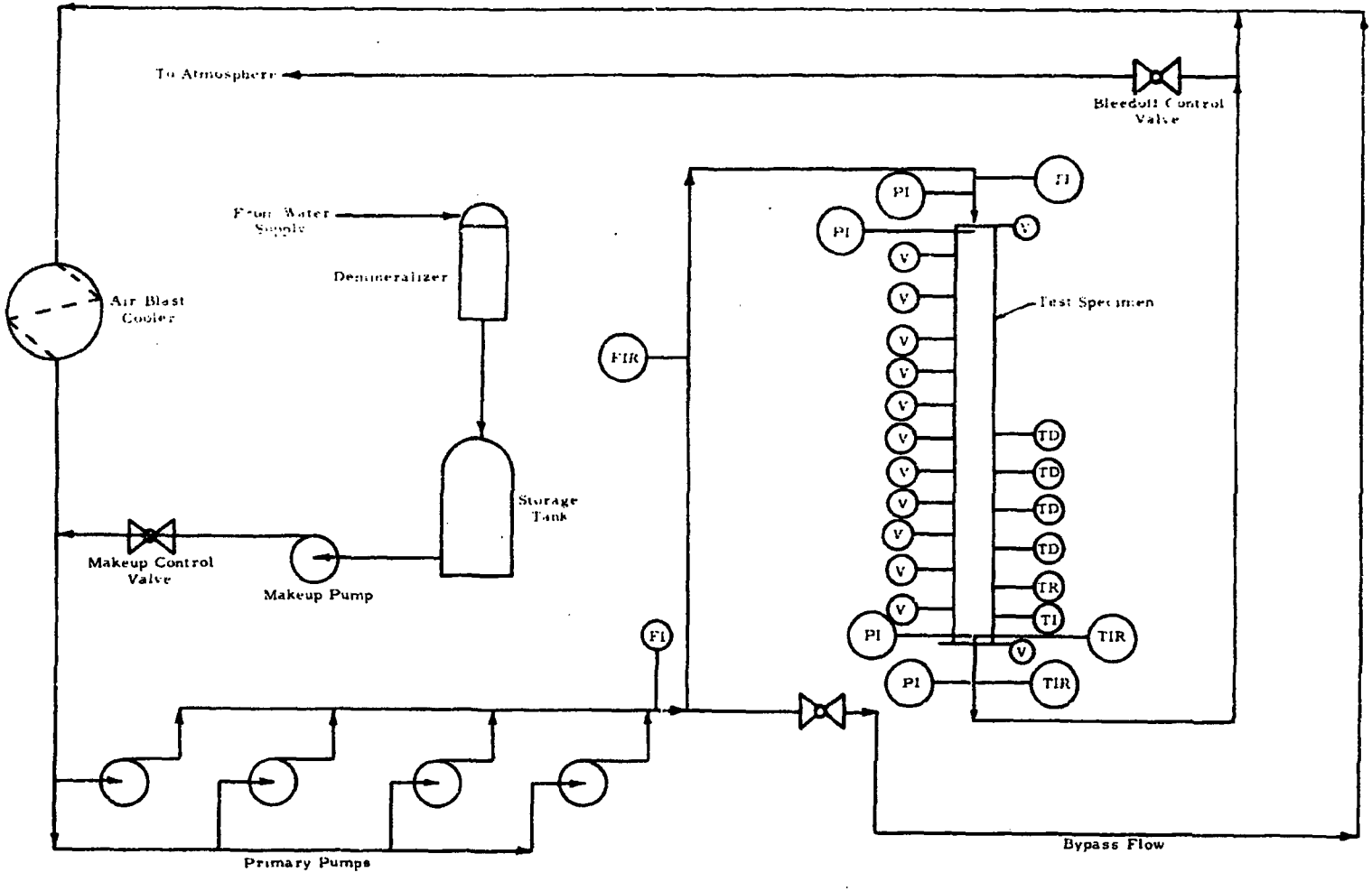


Figure 2-9. Pre-Test Integrated Average and Local Channel Thickness (0.072-Inch Channel)

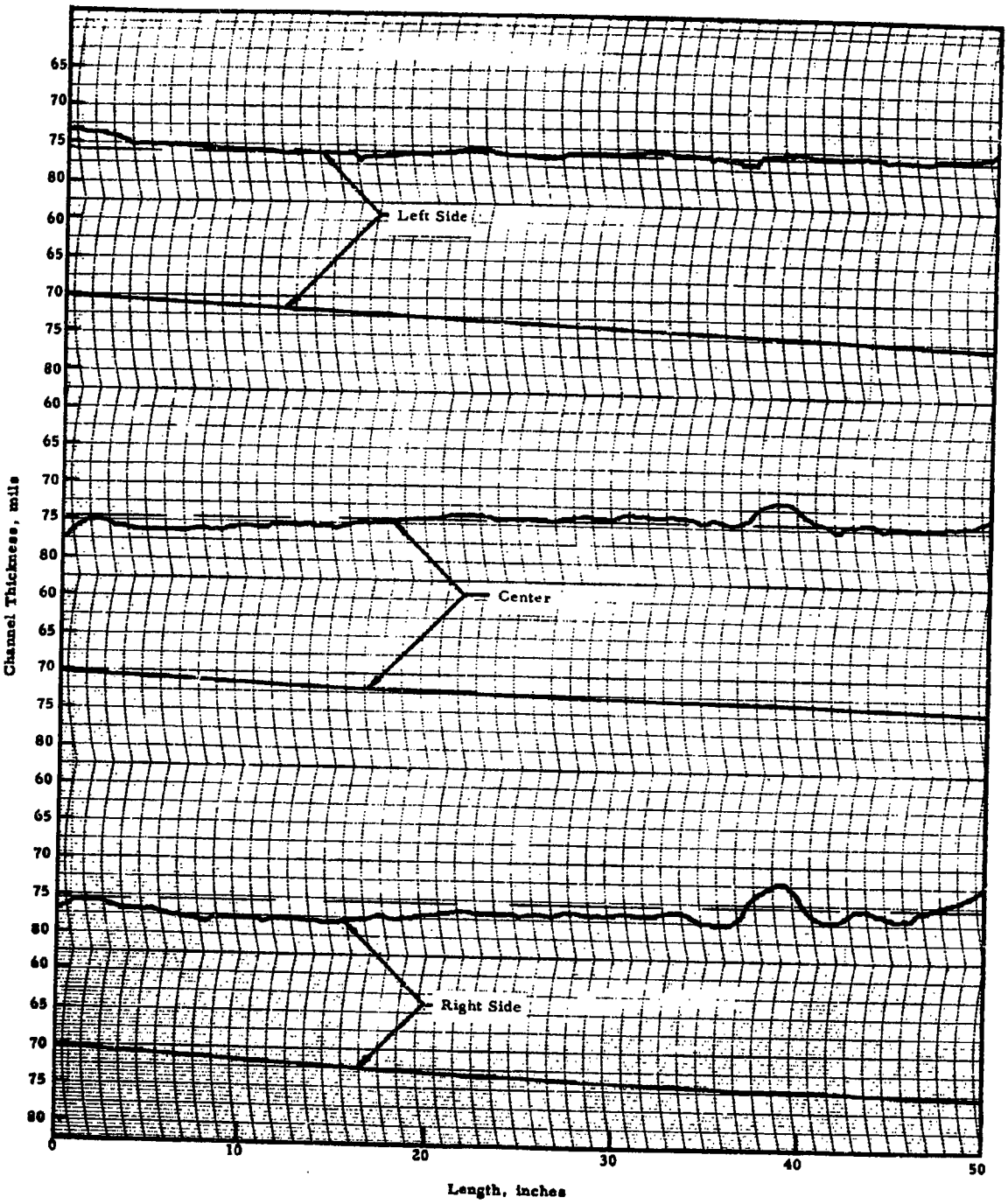
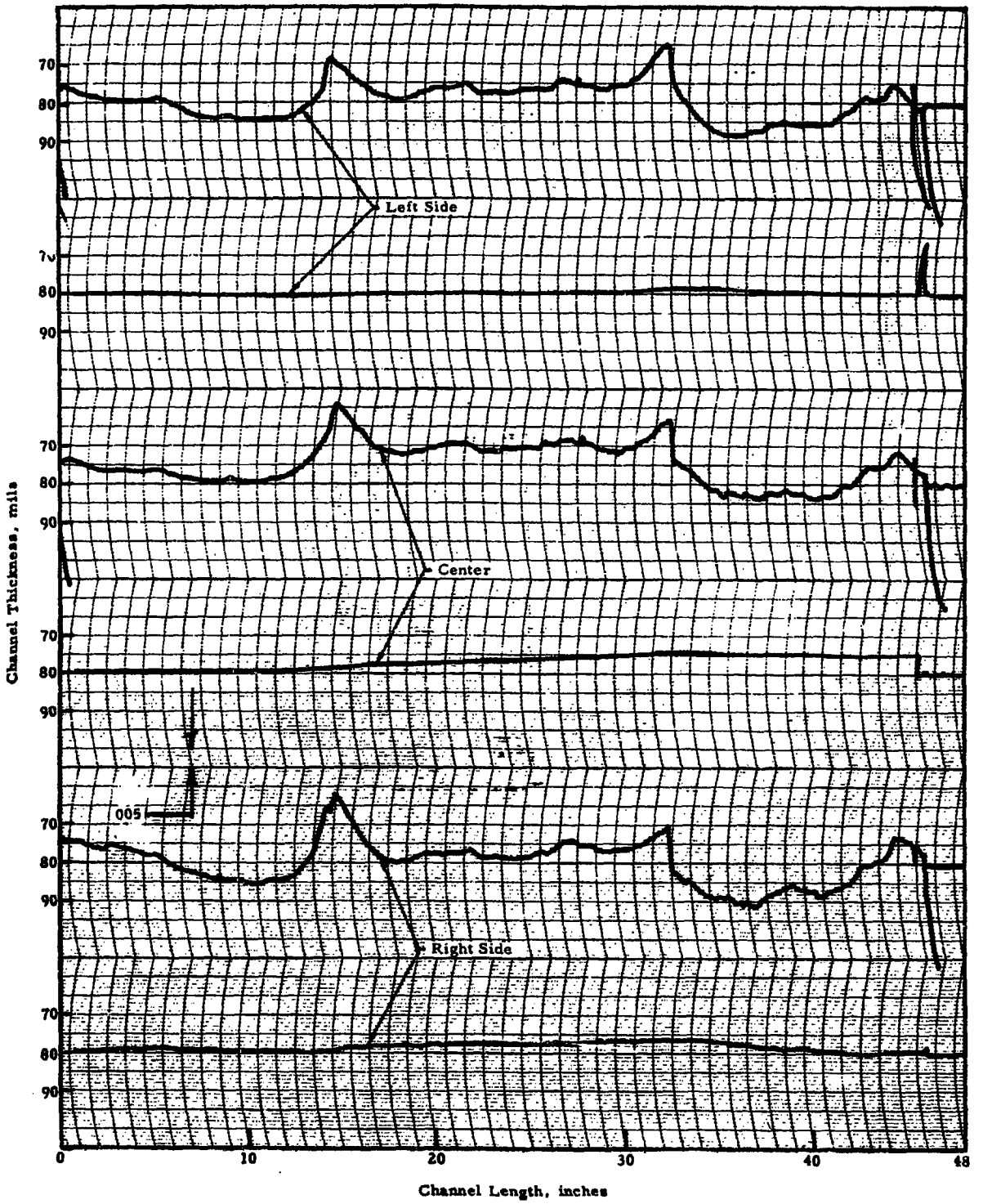


Figure 2-10. After-Test Integrated Average and Local Channel Thickness (0.072-Inch Channel)



3. TEST PROCEDURE AND DATA

A minimum of three basic tests were performed on each of the 0.054-, 0.072-, and 0.094-inch specimens. Each test was repeated at least once to demonstrate reproducibility. A heat balance in each test and burnout power in both tests that agreed within 5% was required. If these criteria were not met, testing was discontinued until the source of the discrepancy had been determined and corrected. In addition to the nine basic tests and the nine tests to show reproducibility, several auxiliary runs were made to verify the conclusions drawn from the original results. The test conditions for the nine basic tests are presented in Table 3-1.

Burnout was approached holding all variables constant except one. Power, pressure, flow, and inlet temperature were all treated as variables in different tests. For example, power was varied in the first test on each specimen while all other variables were held constant. The power input that produced burnout in this test was then reduced by a factor of 1.4 and held constant at this value in all subsequent tests. The coolant inlet temperature was held at 133 ± 10 F in all tests except those in which this variable was intentionally changed. Correspondingly, flow was regulated to produce the velocities shown in Table 3-1, and exit pressure was held at 225 ± 5 psia. Bypass flow, approximately equal to ten times the flow through the test section, was maintained through an unheated leg of the loop in parallel with the test assembly to simulate the effect of parallel channel flow. In a few auxiliary tests, this flow was eliminated to determine if the simulation of parallel channels affected the burnout power.

The first basic test on each different sized specimen was run to determine the steady state burnout power at ATR operating conditions. Flow was adjusted to produce the velocity in the test section (see Table 3-1). System pressure was regulated to maintain 225 psia at the exit

of the channel. Power was gradually increased in increments of approximately 5 kw until departure from nucleate boiling or burnout occurred. At burnout, when the test specimen surface temperature increased rapidly, power cutoff was initiated by thermocouple activated burnout detectors.

The second basic test was run to provide data on burnout at reduced pressure. The outlet pressure and flow rate initially set in the first test were re-established. The input power to the section corresponded to 71.4% of the previously determined burnout power. While power and flow rate were held constant, the specimen exit pressure was reduced gradually until burnout was reached. The pressure was reduced continuously at a rate of 1 psi/min, or less, as burnout conditions were approached.

The third test, conducted to evaluate the effect of reduced flow in the ATR, began with parameters identical to those initially fixed in the second test. All of these parameters were held constant except flow, which was reduced until power was cut off by rapidly increasing surface temperatures. Flow was reduced gradually at about 0.2 gpm as burnout conditions were approached.

Data were taken at several different times during a test to obtain heat balance information, and the variables were monitored closely as predicted burnout conditions were reached. Also, several parameters were continuously recorded. The values of these recorded variables at burnout conditions and the changes that occurred in the last few seconds prior to burnout were clearly shown on high-speed recorder tracings. Typical charts are shown in Section 4.

Data were obtained to indicate loop and test channel flow rate (F_m), input power and its distribution, coolant temperature (T_{in}) and pressure (P_{in}) at the inlet to the specimen and just downstream of the exit (T_{out} and P_{out}). The coolant temperature was also measured just upstream from the exit at the midspan of the channel (T_{mp}). All reliable data, including information obtained for some of the heat balances, are shown in Tables 3-2 through 3-4 with the exception of bypass flow and power distribution. Bypass flow was maintained at approximately ten times the test specimen flow but had no detectable affect on burnout power levels. Axial power distribution could be represented by a 1.4 peak-to-average chopped cosine curve in all test data presented. Consequently, these values are not shown in the data compilation.

Since coolant flow and specimen pressure fluctuated considerably at burnout, the precise value of these variables could not be determined. The last points tabulated for each test, burnout minus 5 seconds (BO-5S) for example, were obtained from the recorder tracings just before flow rate, pressure differentials, and wall temperatures began to change drastically. The calculated heat flux (ϕ_{max}) at the channel mid-length and the calculated flow from the heat balances (F_{calc}) are also tabulated.

Table 3-1. Test Conditions

Channel thickness, in.	Inlet velocity, fps	Flow rate $\times 10^6$, lb/hr-ft^2	Flow rate, gpm	Estimated burnout power, kw	Exit pressure, psig
0.054	34.2	7.57	6.9	266	212
0.054	34.2	7.57	6.9	190	--
0.054	--	--	--	190	212
0.072	41.0	9.08	11.2	430	212
0.072	41.0	9.08	11.2	307	--
0.072	--	--	--	307	212
0.094	47.5	10.52	17.2	660	212
0.094	47.5	10.52	17.2	471	--
0.094	--	--	--	471	212

Table 3-2. 0.054-Inch-Channel Data

Test	T_{in}, F	T_{out}, F	T_{mp}, F	P_{in}, psia	P_{out}, psia	Input power, kw	$\phi_{max} \times 10^{-6}$, Btu/hr-ft^2	F_m, lb/hr	F_{calc}, lb/hr
1 HB 1	139	339.6	354.3	279	225	203	1.46	3365	3425
HB 2	130.3	340.6	356	283	228	212	1.52	3365	3390
BO-5S	130	373	389	281	226	246	1.78	3365	3385
2 HB 2	127.3	351.6	365.5	285	229	231	1.65	3565	3460
BO-5S	131	374	389	282	227	251	1.80	3565	3450
3 HB 1	122	290.7	309.3	160	106	179	1.28	3665	3600
BO-5S	131	299	316	139	85	179	1.28	3665	3600
4 HB 1	126	299	310	157	103	180	1.29	3610	3520
BO-5S	126	308	315.6	139	85	181	1.29	3610	3360
5 HB 1	129.3	304	326.5	280	226	181	1.30	3665	3500
HB 2	125	359	375	254	226	181	1.30	2670	2600
BO-5S	131	373.5	388.3	252	227	181	1.30	2475	2495
6 HB 1	130	245	256	345	217	183	1.32	5690	5420
HB 2	132	317	335	355	227	296	2.12	5640	5410
BO-5S	131	373.5	389	361	233	390	2.79	5590	5390
7 BO-5S	239	384	389	264	227	132	0.95	3120	3000
8 HB 1	127	340	354	269	229	193	1.38	3220	3050
BO-5S	132	377	391	267	227	224	1.60	3190	3055

Table 3-3. 0.072-Inch-Channel Data

	Test	T_{in}, F	T_{out}, F	T_{mp}, F	P_{in}, psia	P_{out}, psia	Input power, kw	$\phi_{max} \times 10^{-6}$, Btu/hr-ft^2	F_m, lb/hr	F_{calc}, lb/hr
1	HB 1	118	240	253.5	300	225	202	1.45	5680	5640
	HB 2	129	295	315.0	301	225	275.5	1.97	5680	5615
	HB 3	128	323	346.5	300	224	332.0	2.38	5735	5740
	HB 4	128	334	360.0	301	225	350.0	2.51	5680	5720
	HB 5	128	355	384.0	305	227	390.0	2.79	5735	5770
	BO-2S	128	357	386.0	305	227	396.0	2.84	5735	5770
2	HB 1	124	345	372.5	303	225	382.5	2.74	5755	5820
	BO-2S	128	357	386.0	305	227	398.0	2.88	5730	5770
3	HB 1	135	306	327	299	226	285.0	2.04	5735	5630
	HB 2	132	300	319	190	115	285.0	2.04	5880	5735
	BO-5S	133	297	319	161	86	287.0	2.06	5930	5920
4	HB 1	126.3	293.7	315	215	140	285	2.04	5830	5760
	HB 2	129	292.3	314	173	95	287	2.06	5980	5950
	BO-5S	131	295	317	162	83.5	287	2.06	5930	5918
5	HB 1	119.6	290.3	312	295	224	287	2.06	5735	5700
	HB 2	114.3	319.3	345	276	229	287	2.06	4745	4725
	HB 3	135	348.5	375	271	226	285	2.04	4545	4480
	BO-3S	136	358	392	268	227	286	2.05	4350	4320
6	HB 1	125	329	355	275	225	287	2.06	4745	4745
	HB 2	125	345	371	269	227	285	2.04	4350	4350
	BO-3S	125	358	390	269	227	286	2.05	4100	4120
7	HB 1	119	288	310	356	225	391	2.80	7810	7840
	HB 2	129	348	378	357	225	496	3.55	7710	7610
	HB 3	132	353	384	355	223	501	3.59	7680	7600
	BO-2S	132	359	392	360	227	509	3.64	7660	7515
8	HB 1	132	347.5	375	353	227	490	3.51	7760	7640
	HB 2	130.5	351	382	353	227	501	3.59	7710	7630
	HB 3	131.5	355	386	353	227	509	3.64	7710	7640
	BO-2S	131.5	358	392	352	225	511	3.65	7660	7570
9	HB 1	126.3	295	315.3	319	252	274.5	1.97	5540	5510
	HB 2	131	324.5	348.3	322	252	325.0	2.33	5680	5660
	HB 3	129	356	385	323	252	383.0	2.74	5630	5660
	BO-2S	132	365	400	325	252	392.0	2.81	5660	5640
10	HB 1	124.5	349	377	323	252	379	2.71	5730	5670
	BO-2S	132.5	368	404	323	252	398	2.85	5680	5660
11	HB 1	105	327	351.5	299	227	378	2.70	5810	5750
	BO-2S	101	356	393	300	227	437	3.13	5730	5760
12	BO-3S	230	375	396	298	227	251	1.80	5680	5720

Table 3-4. 0.094-Inch-Channel Data

	Test	T_{in}, F	T_{out}, F	T_{mp}, F	P_{in}, psia	P_{out}, psia	Input power, kw	$\phi_{max} \times 10^{-6}$, Btu/hr-ft^2	F_m, lb/hr	F_{calc}, lb/hr
1	HB 1	126	247	259	324	227	302.5	--	8400	8500
	HB 2	128	332	354	325	229	508	--	8500	8400
	BO-2S	130	352	380	323	227	541	3.88	8200	8180
2	HB 1	132	282	295.5	205	101	388	2.78	8610	8760
	BO-1M	132	285	299.0	--	87	388	2.78	8610	8590
	BO-5S	132	303	317	186	82	388	2.78	7580	7660
3	HB 1	129.6	290.7	305.5	209	115	387	2.77	8220	8130
	BO-1S	129	300	318	189	95	387	2.77	7725	7650
4	HB 1	131.5	284	296.3	201	95	387	2.77	8615	8590
	BO-1S	131	299	317.8	189	83	387	2.77	7720	7800
5	HB 1	130.7	346	381.5	287	214	388	2.78	6070	6040
	BO-1S	130	356	--	294	227	388	2.78	5860	5760
6	HB 1	132	314	--	335	230	388	2.78	7425	7200
	HB 2	131.3	329.6	--	315	226	388	2.78	6710	6590
	HB 3	128.3	334	--	311	227	388	2.78	6165	6355
	BO-5S	124	349	--	279	227	388	2.78	5545	5750
7	HB 1	133	289	315	343	228	387	2.77	8370	8400
	HB 2	124	318	350	304	230	387	2.77	6730	6730
	HB 3	123.5	338	374	295	230	387	2.77	6140	6070
	BO-5S	123	341	384	290	230	387	2.77	5940	5985
8	HB 1	137	340	374	~292	~227	388	2.78	6380	6430
	BO-1S	137	344	386	292	227	388	2.78	6240	6130
9	BO-1S	132	294	320	220	110	388	2.78	8120	8100
10	HB 1	136	292	317	215	105	388	2.78	8370	8410
	BO-4S	136	297	~324	205	97	388	2.78	8120	8150

4. DISCUSSION OF RESULTS

4.1. Loop Checkout Operation

Tests were conducted on three 0.054-inch channels and two 0.072- and 0.094-inch specimens. Two of the 0.054-inch channels and one 0.072-inch specimen were used in loop checkout operation. The investigations conducted to determine the source of data discrepancies and the changes made to improve loop performance during checkout runs contributed to the interpretation of the burnout results and are described in this section.

The initial loop checkout operation conducted with an 0.054-inch specimen revealed that the test channels were expanding during operation; that there was inadequate cooling capacity in the loop; and that the Potter flow meter was indicating unrealistic flow variations, probably due to "power pickup" or electronic noise. The heat balance did not check, but destructive burnout occurred before sufficient information had been obtained to define the source of the discrepancies. It is possible that the calculated flow, approximately 30% higher than the measured flow rate, was wrong owing to erroneous power input or coolant temperature information. Also, the flow rate could have been higher than was indicated by the measurements.

Burnout occurred at an indicated power input of 194 kw. Measured bulk coolant temperature and pressure at the exit were 310 F and 210 psig, respectively, corresponding to 76 F subcooling. Burnout occurred 35 inches from the inlet, or at a predicted burnout location (X/L) of 0.73.

Later investigation confirmed that the indicated flow variations were due to instrument characteristics and that significant flow variations were not really occurring. The 360-cycle pickup causing these variations was eliminated by placing a coil of magnetic wire, designed to pick up a voltage of equal magnitude but opposite phase, near the

Potter meter coil. While this modification made it possible to read the recorded flow rate more accurately, neither this improvement nor recalibration of the instrument significantly affected the heat balance.

Results from continued loop checkout operation with a new 0.054-inch specimen installed in the loop indicated that measured exit coolant temperatures were probably low. This hypothesis was supported by the fact that the connecting piping between the specimen and the bypass loop was only about 7 inches long. Since the thermocouple that was used to measure the exit coolant temperature was located about mid-length of this pipe, it was near the cold bypass flow. This proximity could probably cause an erroneous low exit temperature indication. Rerouting this connecting length so that the thermocouple was approximately 2 feet from the point where this pipe connected to the bypass loop significantly improved the heat balance and confirmed the suspected error.

After installation of additional cooling equipment proved inadequate, loop cooling-capacity problems were solved by bleeding off and discharging up to 75% of the hot test section flow. An equal amount of cool makeup water was provided downstream of the test section. The discharge flow was set manually to maintain the test section inlet temperature, and the makeup flow was adjusted to maintain system pressure.

At this stage of testing, coolant flow and temperature measuring instrumentation had been checked and adequate control on all loop parameters had been provided. The test section expansion, though not eliminated, had been minimized by a change in assembly procedures. Flow calculated from the heat balance, though consistently lower than the measured flow, was within the 5% limits established as acceptable in most cases.

Two situations, possibly due to faulty information, were still unexplained. In the first, data on the 0.054-inch specimen indicated an axial heat flux shape of 0.5 minimum-to-average and 1.25 maximum-to-average. While the specimen design could have caused this distribution rather than the corresponding values of 0.28 and 1.4 that were desired, power measuring instrumentation were suspected. A check confirmed that one of the voltmeters was providing erroneous information.

Tests on an 0.072-inch specimen that had been installed in the loop along with a new voltmeter showed that the design flux shape was obtained and that the heat balance improved.

In both tests on the 0.054- and 0.072-inch channels, the coolant temperature measured downstream from the exit was still 20 to 40 F subcooled at burnout, and the burnout power was only 85 to 95% of that required to produce coolant saturation at the exit of the channel. When perfect mixing of the coolant or uniform coolant temperature across the width of the channels was assumed, the burnout power corresponded closely to the power calculated for initiation of local boiling. This information, together with the 10 to 20% decrease in flow occurring suddenly in the last 5 to 10 seconds before burnout, suggested that autocatalytic vapor binding could be occurring due to local boiling. In other words, it appeared that frictional resistance increased significantly when local boiling began. As a result, the flow decreased in the constant pressure drop system and further increased the local boiling length and frictional resistance. In turn, the flow decreased further until burnout occurred. While this phenomenon had been predicted when net boiling was reached, autocatalytic flow reduction as a result of local boiling was unexpected, and the results were subject to considerable skepticism.

Since all instrumentation had been checked and the heat balances confirmed the accuracy of the measurements, it was doubtful that these results were caused by instrumentation error. The only assumption made in evaluating the results was that perfect coolant mixing occurred across the width of the channel. It was realized that this assumption could be invalid since only 80% of the channel cross-sectional area was heated (ignoring the small amount of heat generated on either side of the heat generation plates).

To check this assumption, a thermocouple was installed in the pressure tap near the exit of the channel so that the coolant temperature could be measured at the channel mid-width. If imperfect coolant mixing was occurring, this temperature at the mid-width would be higher than the mixed-mean temperature just downstream from the exit. In addition, auxiliary tests were scheduled to indicate whether local boiling or net boiling over some portion of the channel width was causing the observed flow reduction and subsequent burnout. The results confirmed that imperfect mixing occurred.

4. 2. Burnout Results

Calculations were performed using the data in Tables 3-2 through 3-4 and a standard computer code. Input data and calculated results are summarized in Tables 4-1 through 4-3. Input data were pre-test average channel dimensions, inlet pressure, coolant flow rate, power, and power distribution. The results from these calculations provided information on the predicted burnout location, the heat flux at this location, theoretical specimen pressure differential, and fluid and surface temperature as a function of channel length. An iteration was also made to determine the minimum ratio of calculated-to-measured power to either burnout based on 60% of Bernath's equation or bulk boiling, whichever occurred first.

Since channel dimensions varied with length and changed some during testing, the pressure drop calculated by the computer did not always agree with the differential measured. Consequently, the exit pressure, which is one of the important parameters in boiling was not correct in the first calculation (Calc 1). In addition, the temperature rise and coolant temperature calculations were incorrectly based on a perfect mixing model.

A second calculation (Calc 2) was made to correct these deficiencies. Input pressure was adjusted so that the calculated pressure at the channel exit would correspond to that measured. A coolant temperature rise multiplier ($F_{\Delta t}$) was also used so that the coolant temperature calculated at the exit would correspond to the temperature measured at the mid-width of the channel. This multiplier, which reflects the effect of only partial lateral mixing of the coolant within the channel, was determined from the equation:

$$F_{\Delta t} = (T_{mp} - T_{in})/(T_{out} - T_{in})$$

The product of this multiplier and the average temperature rise based on perfect mixing is believed to represent the true temperature rise in a track located at the mid-width of the channel. The multiplier and the adjustment to the inlet pressure are shown in Tables 4-1 through 4-3.

Typical results from tests on the 0.054- and 0.072-inch channels are shown in Figures 4-1 through 4-6. Two test specimens run to destruction are shown in Figure 4-7. Figures 4-1 and 4-4 show the

temperatures as a function of channel length at burnout conditions. The two coolant temperatures shown by solid lines are temperatures that would have existed if coolant mixing had been perfect and no thermal gradients had existed across the channel width, and temperature that would have existed if no coolant mixing occurred. In other words, the exit temperature shown in the first case corresponds to the mixed-mean value measured downstream from the specimen. In the second case, all heat input was assumed to be transferred to the coolant in the cross-sectional area of the channel bounded only by the heat generation plates. The temperatures shown by the dashed lines represent some mixing of coolant within the channel and appear to be characteristic of the temperatures in a track located at the mid-width of the channel. This line shows that the temperature just reached saturation conditions at the exit, corresponding to those measured at this mid-width location. The surface temperatures were calculated using the coolant temperatures shown in the dashed line and either the modified Colburn equation with a 1.25 safety factor or the Jens and Lottes equation. Figures 4-2 and 4-5 show the predicted burnout flux when using 60% of the flux calculated from Bernath's equation, the heat flux calculated using a 1.4 maximum to average chopped-cosine axial flux distribution and the power distribution obtained from measured values. The burnout flux was calculated using the coolant temperatures represented by the dashed lines in Figures 4-1 and 4-4.

The recorder charts obtained at burnout conditions in these tests are reproduced in Figures 4-3 and 4-6. These charts show the coolant flow rate, temperature at the mid-width of the channel near the exit, the test section pressure differential, and the specimen outside surface temperature about 6 inches from the exit. In the test on the 0.054-inch channel, the mixed-mean coolant temperature was recorded rather than the channel mid-width temperature. The variation in these quantities that developed in the last few seconds before power cutoff may also be observed.

The test results shown in Figures 4-1 through 4-3 were obtained in a test on an 0.054-inch channel at reduced pressures (Test 3, Table 4-1). Power was set at 179 kw corresponding to a maximum heat flux of 1.28×10^6 Btu/hr-ft^2. Flow was established at 7.2 gpm corresponding

to a velocity of 35 fps, and inlet pressure was reduced gradually from 300 psig. When exit pressure had been reduced to 73 psig, approximately 15 seconds before power cutoff, flow began to decrease gradually. Flow decreased to 6.9 gpm 1 second before burnout; exit pressure was 70 psig; the mixed-mean coolant temperature measured downstream from the exit was 299 F; and the temperature measured at the channel mid-width was at saturation conditions or 316 F. Within the next 0.8 second, flow decreased 29% to 4.9 gpm without further reduction in pressure and then increased to 8.6 gpm in the next 0.4 second. After power cutoff, pressure decreased again to 6.0 gpm before recovering to the pre-burnout level. Even though approximately a 10-to-1 bypass flow was maintained, test section pressure differentials varied simultaneously with the change in flow rate, as shown in Figure 4-3.

The test results shown in Figures 4-4 through 4-6 (Test 1, Table 4-2) were obtained in a test on an 0.072-inch-nominal channel, and burnout was approached by increasing power. Flow was set at 15.5 gpm, which produced a velocity of 54 fps in the 0.076-inch channel. System pressure was established so that the test section exit pressure was 212 psig. Power input, which had been raised in increments of about 5 kw, was increased to 505 kw about 2 minutes before burnout. Approximately 1 minute later, a power increase to 509 kw was initiated. Twelve seconds after completing this change, the flow decreased sharply, and the increasing outside surface temperature activated the burnout detectors. Before the last power increase the coolant mixed-mean temperature downstream from the exit was 356 F, and the coolant was 388 F or 4 F subcooled at the channel midspan near the exit. The midspan temperature peaked at about 395 F during the flow reduction from 16.0 to 10.0 gpm.

The transient behavior described above and shown in Figures 4-3 and 4-6 is typical of the results obtained in all tests including those on the 0.094-inch channel. In all tests, including the two in which power input was continued until the specimen melted, steady state conditions were re-established only once. In the one case, flow recovered from the initial dip and stabilized for about 3 seconds before flow variations reoccurred and initiated power cutoff.

As may be observed in both Figures 4-1 and 4-4, the coolant temperature measured at the channel midspan just reached saturation conditions, even though pressures in the two tests were different by more than 100 psi. This situation occurred in every test on these smaller channels, including one test that was run at 230 F inlet temperature; therefore, heat flux required to produce saturation was only half that existing in the test described previously.

Apparently, heat flux is not the governing criteria in this case. As indicated by initial calculations, autocatalytic vapor binding occurs when coolant saturation is reached at the exit of the channel. However, burnout in the one test on the small channel that was continued to destruction occurred at the predicted burnout location. It is believed that bulk boiling at the exit reduced flow due to the increasing resistance offered by two phase flow, which in turn, increased the boiling length and further reduced flow. The process continued until the lower velocity and higher coolant temperature, together with the heat flux existing at the normal burnout location, produced burnout.

While coolant saturation is apparently necessary at the exit of the channel to produce autocatalytic vapor binding, the flow reduction or instability can occur when a portion of the coolant in the channel cross-sectional area is still subcooled. In other words, bulk boiling across the entire channel width is not required to initiate the flow reductions. For example, in the tests on the 0.054- and 0.072-inch channels described, autocatalytic vapor binding occurred at a power level equal to 91 and 87%, respectively, to heat all of the coolant flowing to saturation. In general, the limiting power level ranged between 90 and 96% of the saturation power level in the 0.054-inch channels and 85 to 92% in the 0.072-inch channels.

Obviously, these results indicate that perfect coolant mixing could not have occurred across the channel width. On the other hand, if no mixing had occurred, 80 to 82% of the coolant that was flowing in the heated perimeter portion of the channel would have received the heat and reached saturation, while the coolant on either side of the heat generation plates remained at inlet temperature. Although design calculations indicated that some heat would be generated in the tube on either side of these plates (5% maximum), the results still indicate that some lateral coolant mixing did occur.

Since burnout was initiated by autocatalytic vapor binding, the heat flux itself is of little significance. However, for comparative purposes, the heat flux that caused the flow reductions and subsequent burnout was 25 and 51%, respectively, of the burnout flux calculated by Bernath's equation. In general, the ratio of the limiting heat flux at the predicted burnout location and the burnout flux calculated by Bernath's equation varied from 0.22 to 0.46 in the 0.054-inch channel and from 0.36 to 0.54 in the 0.072-inch channel.

Figures 4-8 through 4-10 (Test 1, Table 4-3) show results obtained in a test on the 0.094-inch channel. In this test, power was increased while all other variables were held constant. Figure 4-8 shows that the coolant temperature did not reach saturation at the exit even at the channel midspan. Burnout occurred while the coolant at the channel midspan was still subcooled in all tests on the 0.094-inch channel except those in which pressure was treated as the variable and reduced to approach burnout. In this test, the midspan temperature was 380 or 12 F subcooled and the mixed-mean coolant temperature measured downstream from the exit was 352 or 40 F subcooled. The subcooling ranged between 10 to 15 F in all these tests except at low pressure. In most of the tests at reduced pressures, coolant saturation was reached at the channel midspan before power cutoff occurred.

Figure 4-9 shows that the actual heat flux curve and the line representing 60% of the burnout heat flux calculated by Bernath's equation are essentially tangent at an X/L (ratio of distance from inlet to total channel length) of 0.7. The heat flux in all tests on this specimen ranged between 57 and 60% of the flux predicted by Bernath's equation regardless of whether coolant saturation was reached or not. Again, however, the temperatures represented by the dashed line in Figure 4-7, corresponding to the channel midspan values, was used in Bernath's equation. If mixed-mean coolant temperatures are substituted into Bernath's equation, the predicted burnout flux increases so that the actual flux in the tests is only 54 to 56% of the value obtained from the equation.

Figure 4-10 shows the recorder chart obtained in this test. (Note that the flow reduction pattern in this subcooled burnout test is similar to the pattern obtained when cooled saturation occurred.) The flow

recovered immediately after burnout to a value slightly above that of the pre-burnout level. While not observed in tests on the smaller channels, this recovery characteristic was evident in most tests on the 0.094-inch channel. The effect is more pronounced in Figure 4-11 (Test 10, Table 4-3), which is included to show the flow reduction pattern obtained at higher recorder speeds. Furthermore, the flow recovered to the higher value even though specimen pressure differential decreased slightly. This recovery together with the fact that flow rate decreased suddenly while the fluid was still subcooled indicates that local boiling might initiate an autocatalytic effect in these larger channels; however, this could be a typical characteristic that occurs at all burnout conditions rather than only at local boiling conditions.

Table 4-1. 0.054-Inch-Channel Calculations

Test	T_{in}, F	T_{out}, F	P_{in}, psia	P_{out}, psia	Predicted burnout location, X/L	Actual ϕ at predicted burnout location $\times 10^{-6}$, Btu/hr-ft^2	$\phi_{max} \times 10^{-6}$, Btu/hr-ft^2	F_{calc}, lb/hr	F_{op}	$F_{\Delta t}$	$\frac{\phi_{BO\ (Bernath)}}{\phi_{BO\ (Actual)}}$[a]
Test 1											
Calc 1	129	372.8	231	198.7	--	--	1.76	3385	1.000	1.000	--
	129	380.4	281	198.6	--	--	1.82	3385	1.033	1.000	--
Calc 2	129	388.2	308	225.6	0.70	1.50	1.76	3385	1.000	1.066	3.33
	129	391.2	308	225.6	0.70	1.52	1.78	3385	1.012	1.066	3.26
Test 2											
Calc 1	130	373.8	282	196.5	--	--	1.80	3450	1.000	1.000	--
	130	379.5	282	196.5	--	--	1.84	3450	1.024	1.000	--
Calc 2	130	388	312	226.4	0.70	1.53	1.80	3450	1.000	1.061	3.35
	130	391.5	312	226.4	0.75	1.41	1.82	3450	1.014	1.061	3.24
Test 3											
Calc 1	130	298.5	139	46.3	--	--	1.28	3600	1.000	1.000	--
	130	280	139	46.3	--	--	1.14	3600	0.889	1.000	--
Calc 2	130	316.3	178	85.3	0.75	0.99	1.28	3600	1.000	1.108	4.05
Test 4											
Calc 1	125	307.5	139	58.3	--	--	1.29	3350	1.000	1.000	--
	125	292	139	58.2	--	--	1.18	3350	0.914	1.000	--
Calc 2	125	317.3	166	85.3	0.75	1.00	1.29	3350	1.000	1.055	3.72
Test 5											
Calc 1	130	373.8	252	206.5	--	--	1.30	2495	1.000	1.000	--
	130	383.6	252	206.4	--	--	1.35	2495	1.042	1.000	--
Calc 2	130	387.6	272	226.4	0.70	1.11	1.30	2495	1.000	1.059	3.42
	130	391.5	272	226.4	0.70	1.13	1.32	2495	1.016	1.059	3.31
Test 6											
Calc 1	130	372.8	361	159	--	--	2.79	5390	1.000	1.000	--
	130	362.3	361	159.3	--	--	2.67	5390	0.955	1.000	--
Calc 2	130	387.6	435	232.8	0.75	2.16	2.79	5390	1.000	1.064	3.37
	130	393.9	435	232.7	0.75	2.22	2.86	5390	1.026	1.064	3.18
Test 7											
Calc 1	238	384	264	200	--	--	0.95	3000	1.000	1.000	--
	238	381	264	199.8	--	--	0.93	3000	0.979	1.000	--
Calc 2	238	389	291	226.7	0.65	0.87	0.95	3000	1.000	1.036	4.75
	238	391.6	291	226.7	0.65	0.88	0.96	3000	1.019	1.036	4.60
Test 8											
Calc 1	131	377	267	199.5	--	--	1.60	3055	1.000	1.000	--
	131	380.8	267	199.5	0.75	1.26	1.63	3055	1.017	1.000	3.15
Calc 2	131	390.4	294	226.4	0.70	1.37	1.60	3055	1.000	1.058	3.30

[a] BO = burnout.

Table 4-2. 0.072-Inch-Channel Calculations

Test	T_{in}, F	T_{out}, F	P_{in}, psia	P_{out}, psia	Predicted burnout location, X/L	Actual ϕ at predicted burnout location $\times 10^{-6}$, Btu/hr-ft^2	$\phi_{max} \times 10^{-6}$, Btu/hr-ft^2	F_{calc}, lb/hr	F_{cp}	$F_{\Delta t}$	$\frac{\phi_{BO\ (Bernath)}}{\phi_{BO\ (Actual)}}$[a]
Test 1											
Calc 1	127	363.8	305	226.9	--	--	2.84	5620	1.000	1.000	--
	127	391.7	305	226.9	0.75	2.47	3.19	5620	1.124	1.000	1.73
Calc 2	128	386.0	305	226.9	0.75	2.19	2.84	5620	1.000	1.123	1.95
Test 3											
Calc 1	133	297	166	79.5	--	--	2.06	5935	1.000	1.000	--
	133	311	166	79.5	--	--	2.24	5935	1.014	1.000	--
Calc 2	133	318.1	172.5	86	--	--	2.06	5935	1.000	1.135	2.20
	132.6	316.3	172.5	86	0.75	1.53	1.98	5935	0.990	1.135	2.40
Test 4											
Calc 1	130	294.5	162	75.6	--	--	2.06	5918	1.000	1.000	--
	130	308.1	162	76.0	--	--	2.23	5918	1.084	1.000	--
Calc 2	130	316.1	170	84.0	0.70	1.75	2.06	5918	1.000	1.134	2.33
Test 5											
Calc 1	135	357.7	268	221.5	--	--	2.05	4320	1.000	1.000	--
	135	389.6	268	221.5	--	--	2.36	4320	1.150	1.000	--
Calc 2	135	391.4	273.5	227	0.70	1.75	2.05	4320	1.000	1.158	2.13
Test 6											
Calc 1	124	357.7	262	219.5	--	--	2.05	4120	1.000	1.000	--
	124	388.9	262	219.5	--	--	2.33	4120	1.139	1.000	--
Calc 2	124	391.2	269.5	227.0	0.70	1.75	2.05	4120	1.000	1.150	2.08
Test 7											
Calc 1	131	358.7	357	220	--	--	3.64	7515	1.000	1.000	--
	131	389.0	357	219.6	--	--	4.15	7515	1.139	1.000	--
Calc 2	131	391.3	364	226.6	0.75	2.82	3.64	7515	1.000	1.150	1.96
Test 9											
Calc 1	131	364.8	323	244.7	--	--	2.81	5640	1.000	1.000	--
	131	398.3	323	244.5	--	--	3.24	5640	1.151	1.000	--
Calc 2	131	398.2	330.3	251.8	0.75	2.17	2.81	5640	1.000	1.150	2.03
	131	400.8	330.3	251.8	0.75	2.20	2.84	5640	1.010	1.150	1.98
Test 10											
Calc 1	131	368.8	323	245	--	--	2.85	5620	1.000	1.000	--
	131	398.4	323	244.9	--	--	3.23	5620	1.131	1.000	--
Calc 2	131	402.2	330	251.8	--	--	2.85	5620	1.000	1.148	1.95
Test 11											
Calc 1	100	355.7	299	216.6	--	--	3.13	5760	1.000	1.000	--
	100	387.7	299	216.5	--	--	3.54	5760	1.131	1.000	--
Calc 2	100	391.1	309.4	226.9	0.75	2.42	3.13	5760	1.000	1.145	1.87
Test 12											
Calc 1	229.3	374.8	302	221.7	--	--	1.80	5720	1.000	1.000	--
	229.3	389.7	302	221.6	--	--	1.99	5720	1.106	1.000	--
Calc 2	229.3	398.0	307.3	226.8	--	--	1.80	5720	1.000	1.165	--
	229.3	391.7	307.3	226.9	0.70	1.47	1.73	5720	0.961	1.165	2.82

[a] BO = burnout.

Table 4-3. 0.094-Inch-Channel Calculations

Test	T_{in}, F	T_{out}, F	P_{in}, psia	P_{out}, psia	Predicted burnout location, X/L	Actual ϕ at predicted burnout location $\times 10^{-6}$, Btu/hr-ft^2	$\phi_{max} \times 10^{-6}$, Btu/hr-ft^2	F_{calc}, lb/hr	F_{op}	$F_{\Delta t}$	$\frac{\phi_{BO\ (Bernath)}}{\phi_{BO\ (Actual)}}$[a]
Test 1											
Calc 1	129	352	323	229	0.70	3.31	3.88	8180	1.000	1.000	1.83
	129	362.3	323	228.8	0.70	3.47	3.91	8180	1.049	1.000	1.68
Calc 2	129	378.6	321	226.7	0.70	3.31	3.88	8180	1.000	1.126	1.63
	129	376	321	226.7	0.70	3.27	3.83	8180	0.989	1.126	1.68
Test 2											
Calc 1	131	303.5	178	96	--	--	2.78	7620	1.000	1.000	--
	131	314.5	178	96.1	--	--	2.96	7620	1.065	1.000	--
Calc 2	131	316.2	164	82.1	0.75	2.15	2.78	7620	1.000	1.075	1.59
	131	312.2	164	82.1	0.75	2.10	2.72	7620	0.978	1.075	1.68
Test 3											
Calc 1	128	299.5	189	106.4	--	--	2.77	7650	1.000	1.000	--
	128	319.4	189	106.4	--	--	3.10	7650	1.119	1.000	--
Calc 2	128	318.3	178	95.4	0.75	2.15	2.77	7650	1.000	1.112	1.76
	128	323.3	178	95.4	0.75	2.20	2.84	7650	1.027	1.112	1.66
Test 4											
Calc 1	130	300.5	189	105.5	--	--	2.77	7690	1.000	1.000	--
	130	319.6	189	105.5	--	--	3.09	7690	1.115	1.000	--
Calc 2	130	308.4	166	82.5	0.75	2.15	2.77	7690	1.000	1.047	1.71
	130	310.6	166	82.5	0.75	2.17	2.81	7690	1.013	1.047	1.66
Test 5											
Calc 1	129	355.7	294	246.6	0.65	2.55	2.78	5760	1.000	1.000	1.92
	129	373.0	294	246.6	0.65	2.75	3.00	5760	1.080	1.000	1.69
Test 6											
Calc 1	123	348.7	279	231	--	--	2.78	5750	1.000	1.000	--
	123	366.7	279	231	--	--	3.01	5750	1.083	1.000	--
Test 7											
Calc 1	122.5	340.6	290	238.8	--	--	2.77	5985	1.000	1.000	--
	122.5	364.9	290	238.8	--	--	3.09	5985	1.115	1.000	--
Test 8											
Calc 1	136	343.7	292	235.7	--	--	2.78	6290	1.000	1.000	--
	136	371	292	235.7	--	--	3.16	6290	1.136	1.000	--
Test 9											
Calc 1	132	293.5	213	119.7	--	--	2.78	8150	1.000	1.000	--
	132	326.7	213	119.6	--	--	3.37	8150	1.210	1.000	--
Test 10											
Calc 1	135	296.5	222	128.8	--	--	2.78	8150	1.000	1.000	--
	135	331.7	222	128.8	--	--	3.40	8150	1.224	1.000	--

[a] BO = burnout.

Figure 4-1. Burnout Test Results - Temperature Vs X/L
(Test 3, 0.054-Inch Channel)

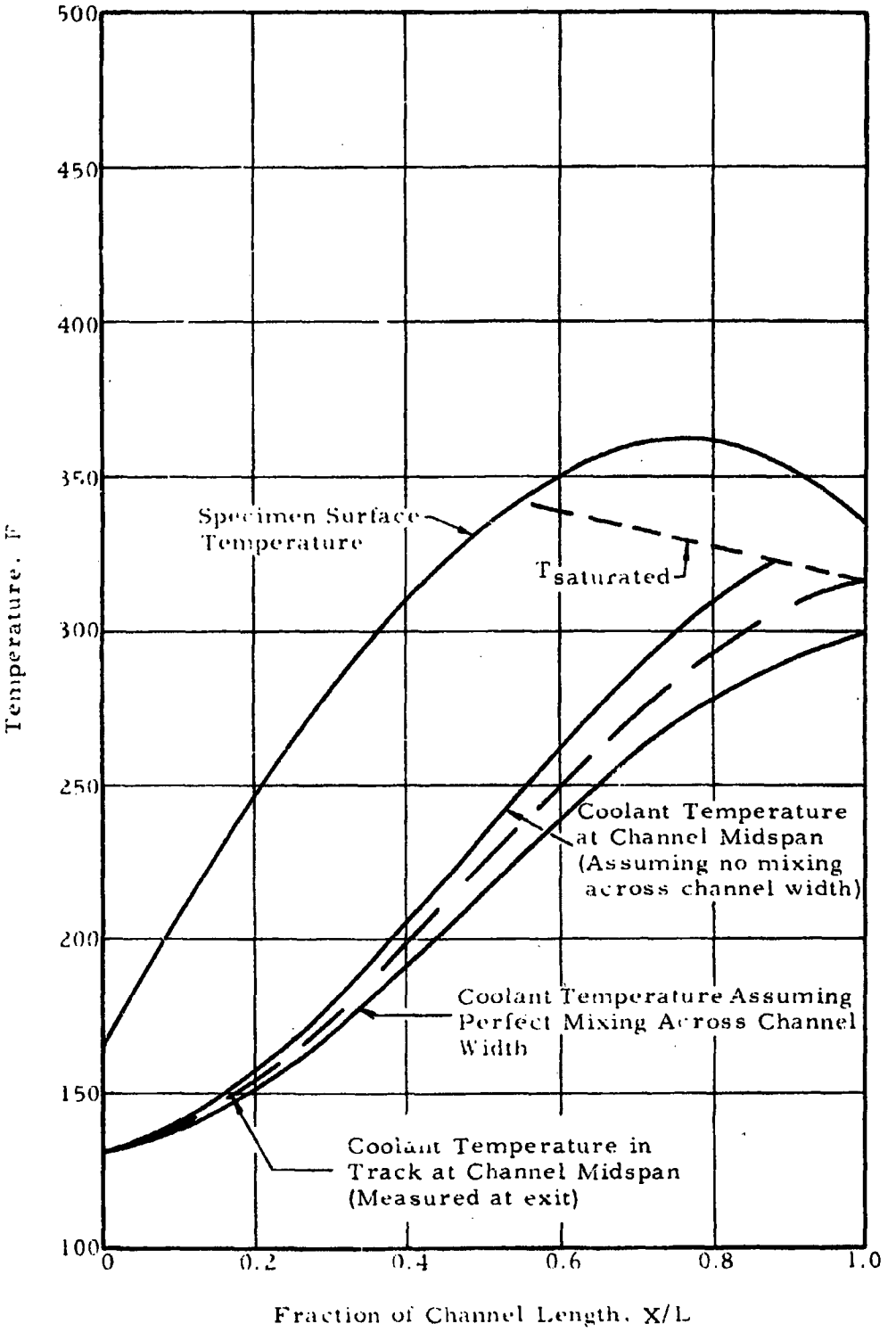


Figure 4-2. Burnout Test Results - Heat Flux Vs X/L
(Test 3, 0.054-Inch Channel)

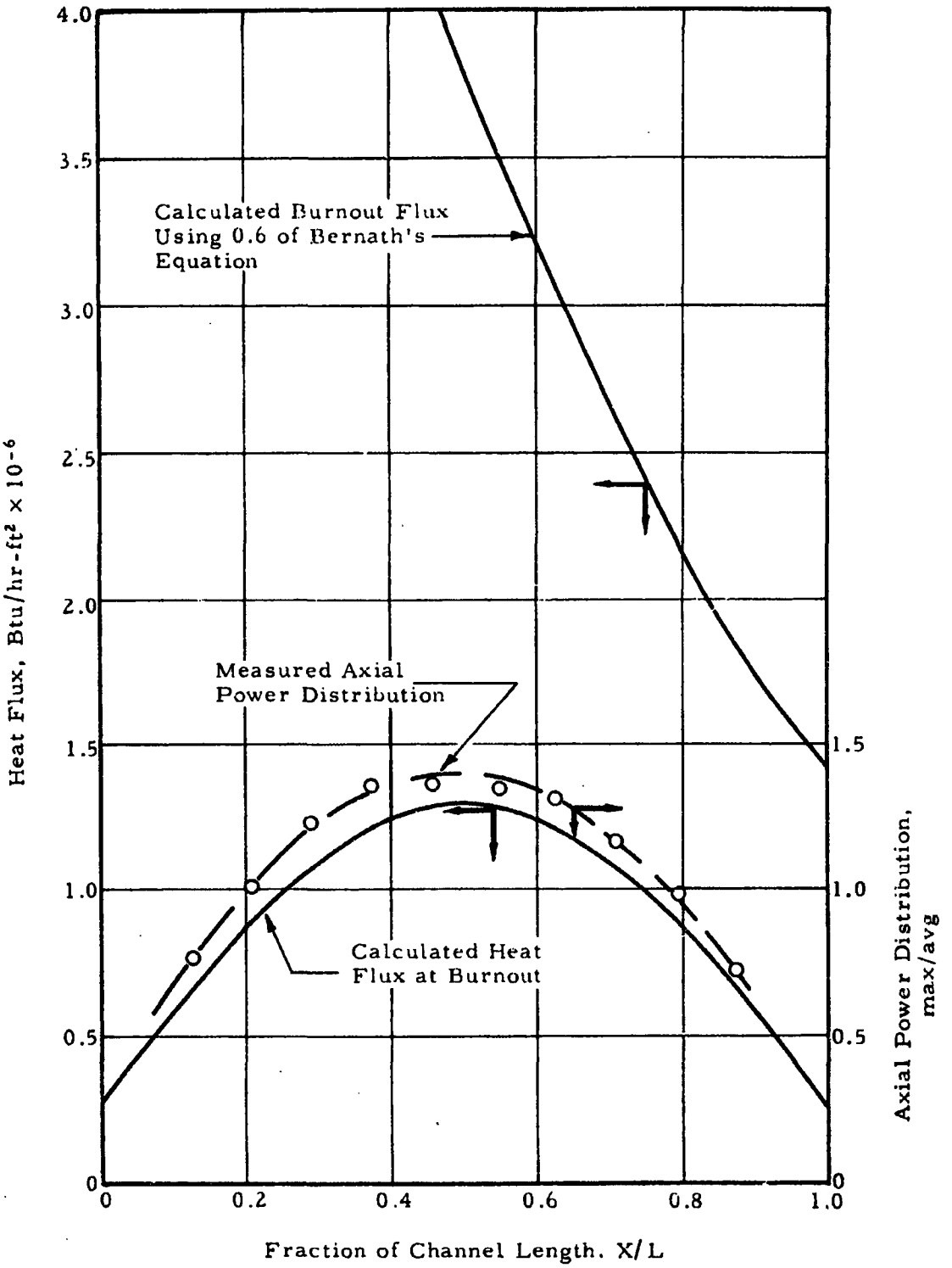
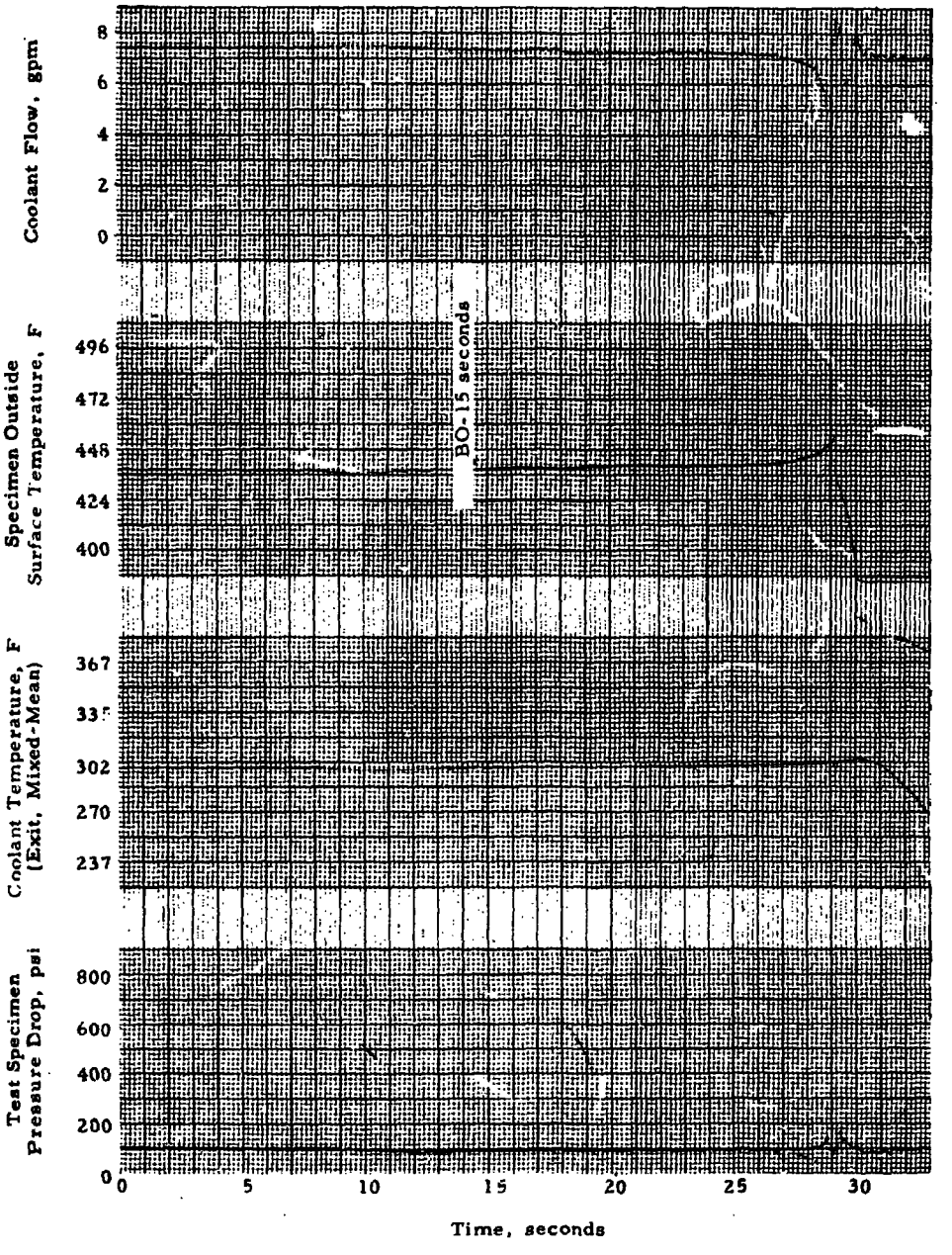


Figure 4-3. Burnout Test Recorder Chart (Test 3, 0.054-Inch Channel)



max/avg

Figure 4-4. Burnout Test Results - Temperature Vs X/L
(Test 1, 0.072-Inch Channel)

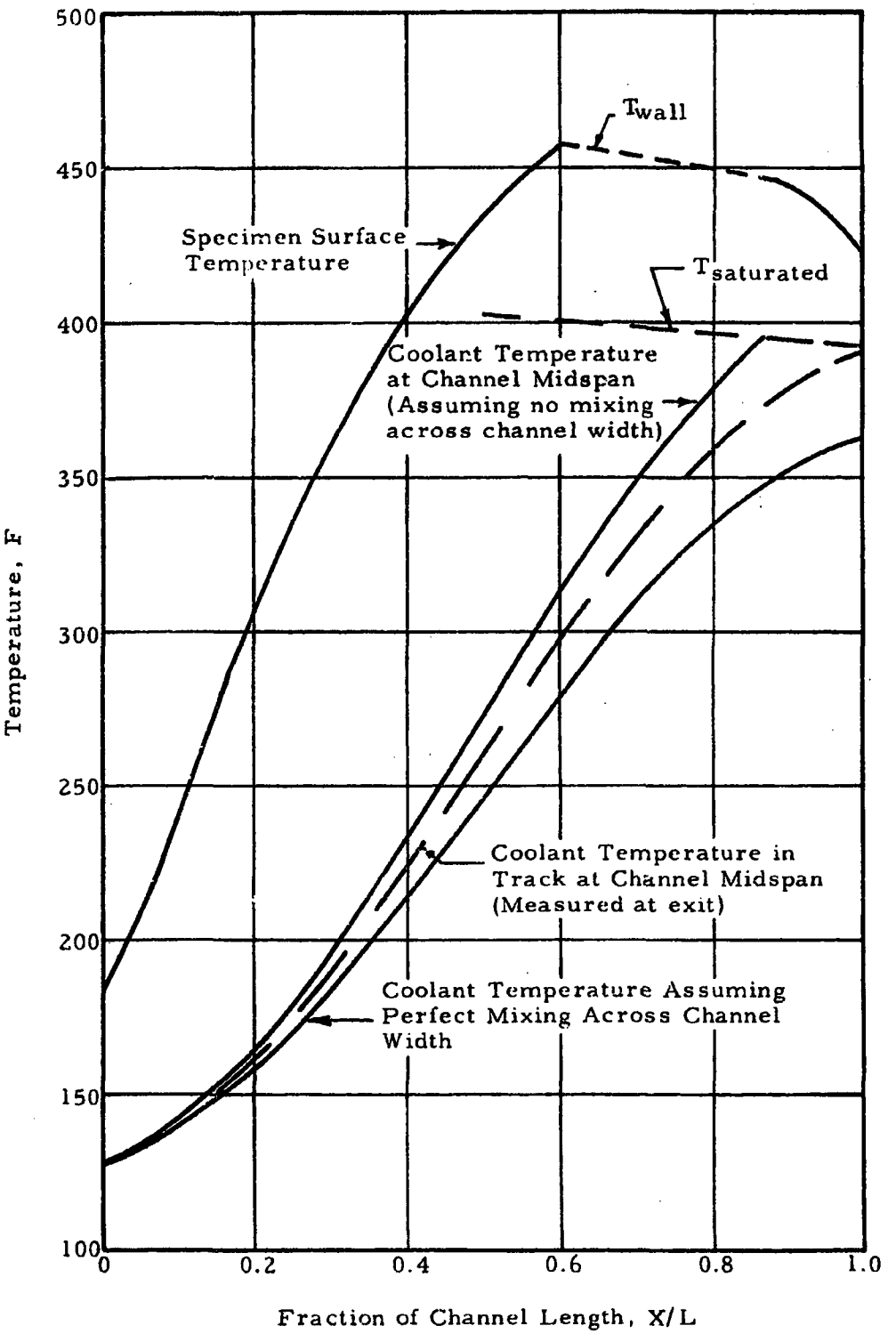


Figure 4-5. Burnout Test Results - Heat Flux Vs X/L
(Test 1, 0.072-Inch Channel)

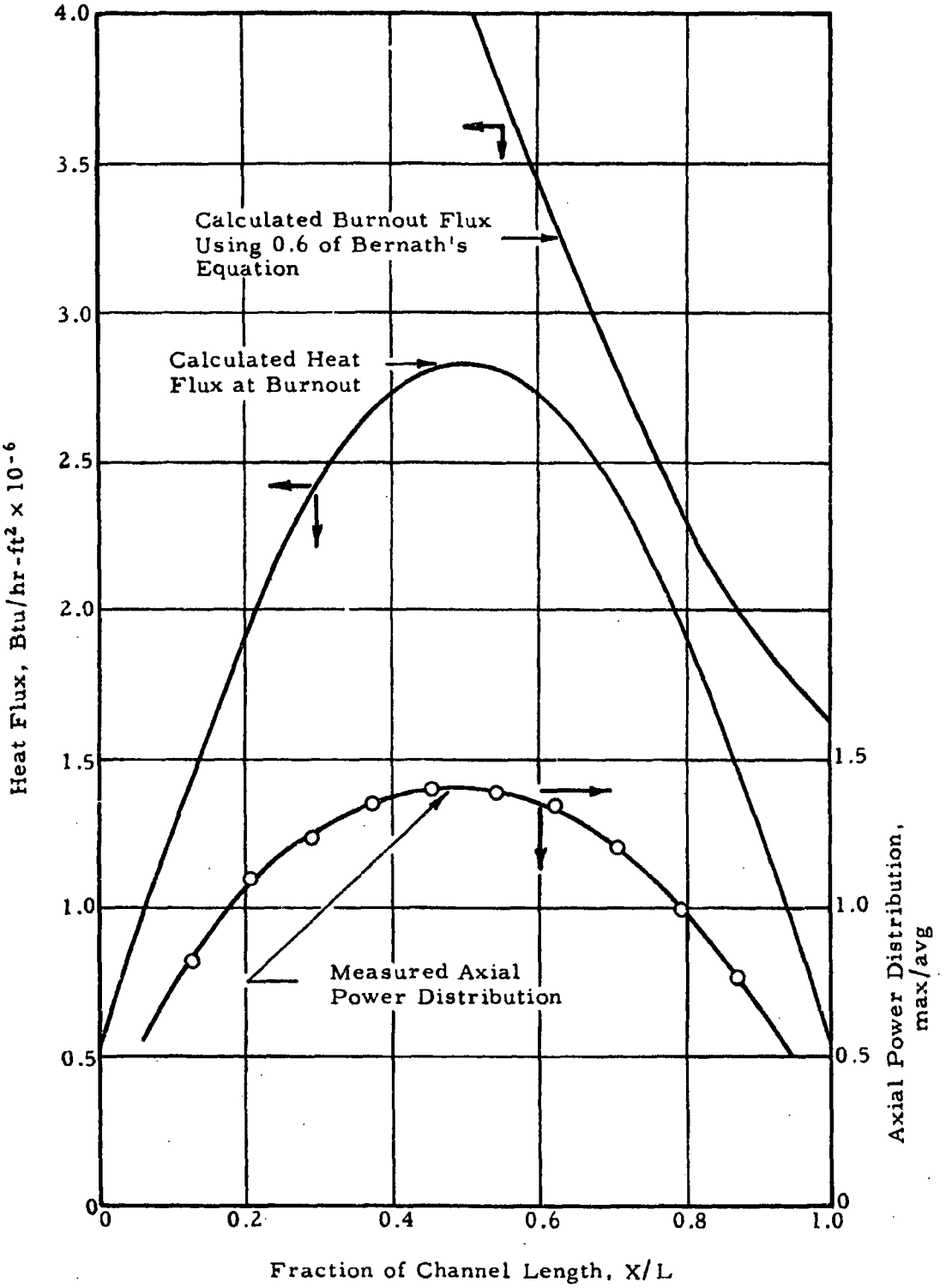


Figure 4-6. Burnout Test Recorder Chart
(Test 1, 0.072-Inch Channel)

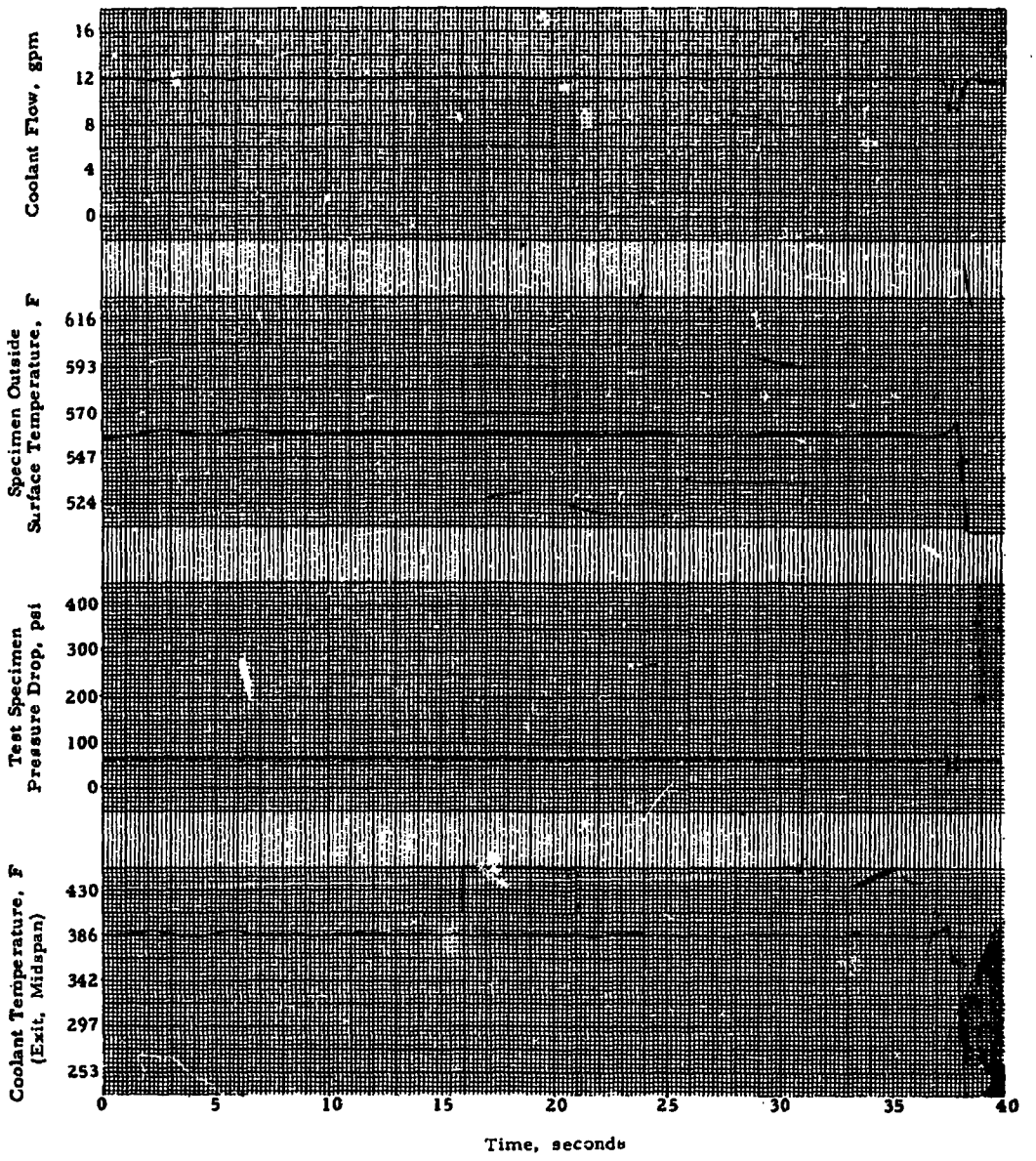
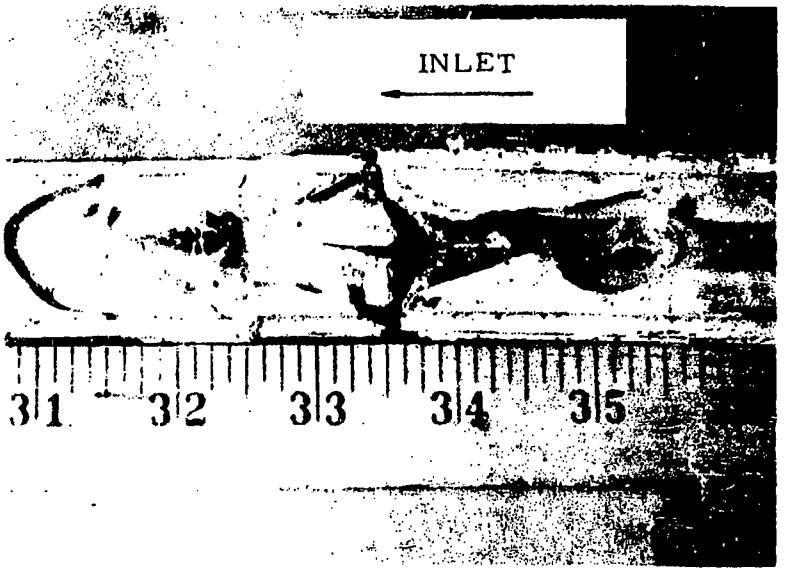
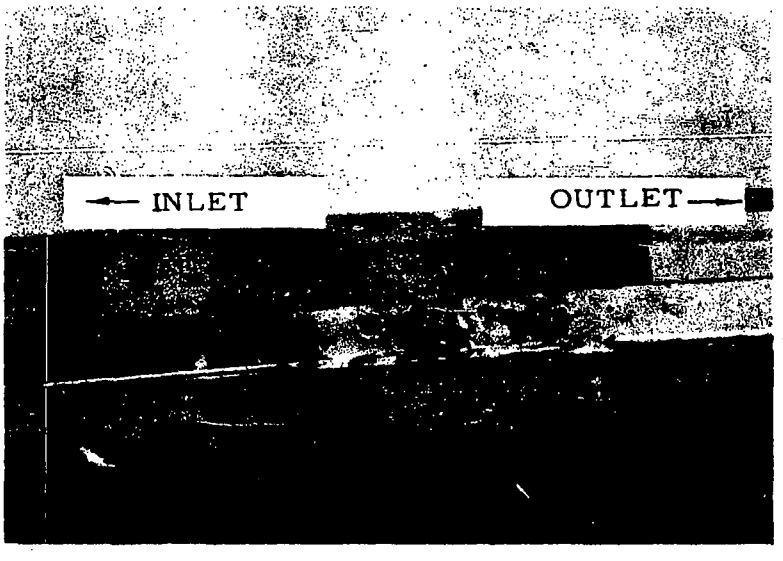


Figure 4-7. Destructive Burnout Results - Test Specimen



0.094-Inch Channel



0.054-Inch Channel

Figure 4-8. Burnout Test Results - Temperature Vs X/L (Test 1, 0.094-Inch Channel)

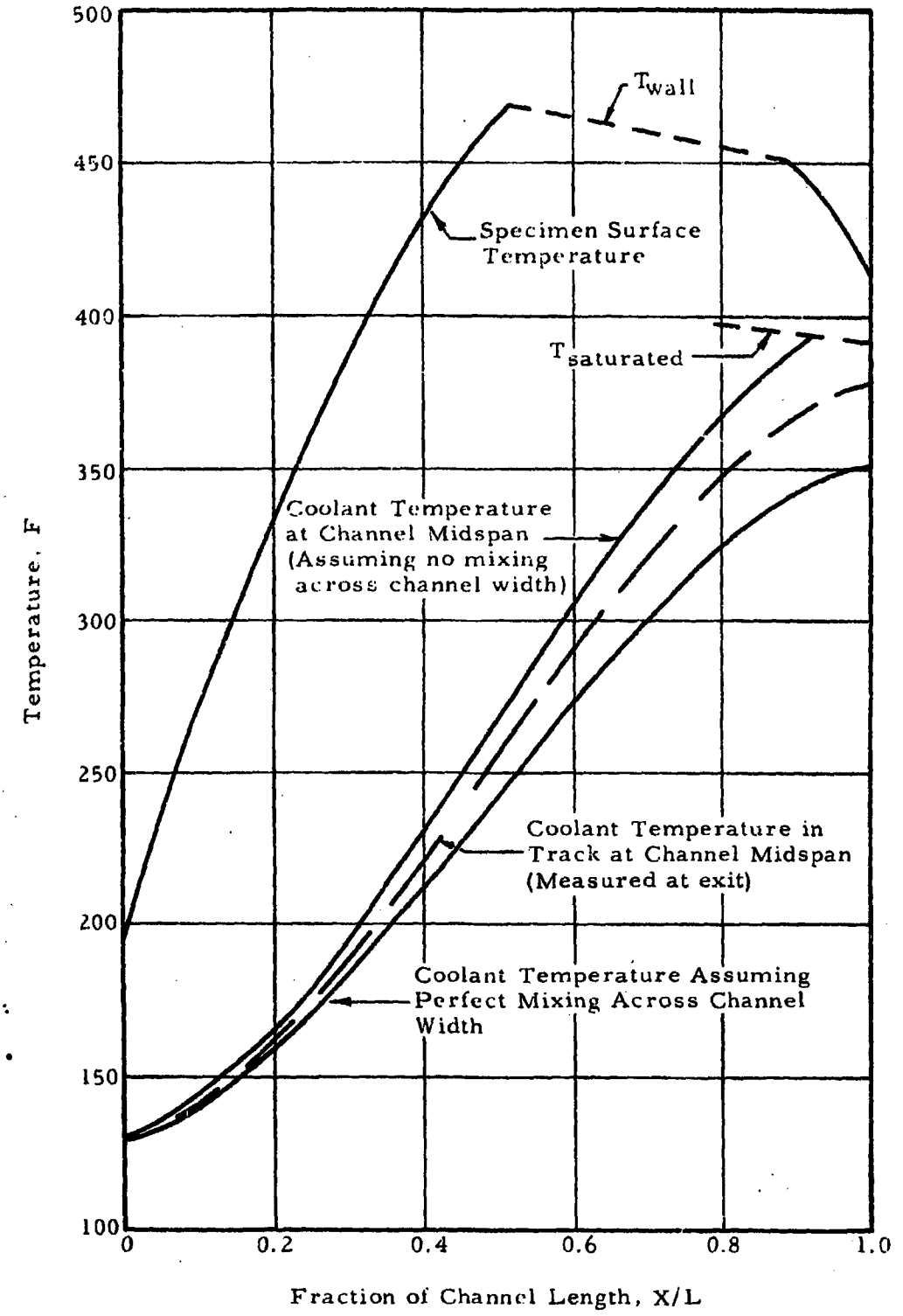


Figure 4-9. Burnout Test Results - Heat Flux Vs X/L
(Test 1, 0.094-Inch Channel)

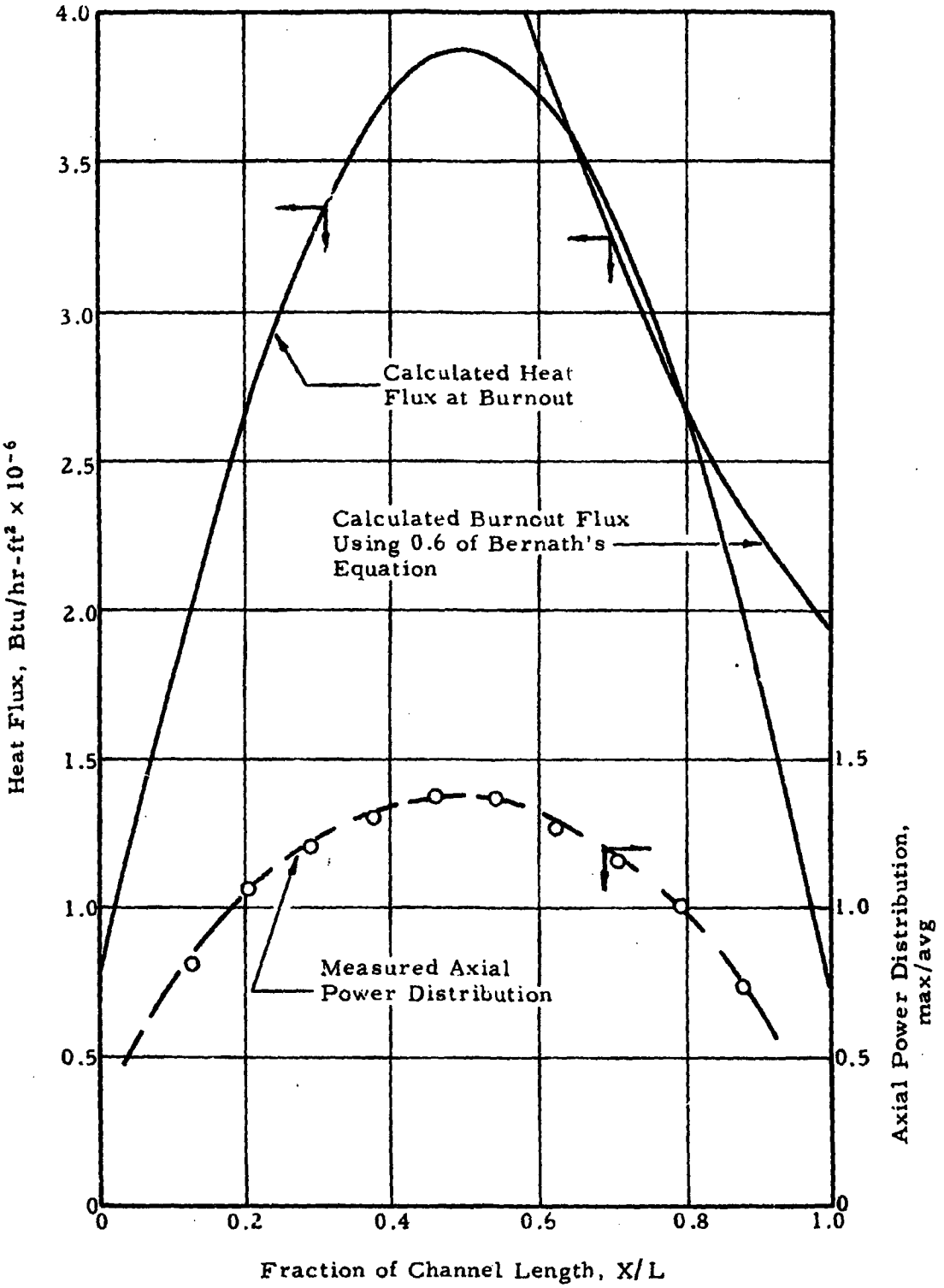


Figure 4-10. Burnout Test Recorder Chart
(Test 1, 0.094-Inch Channel)

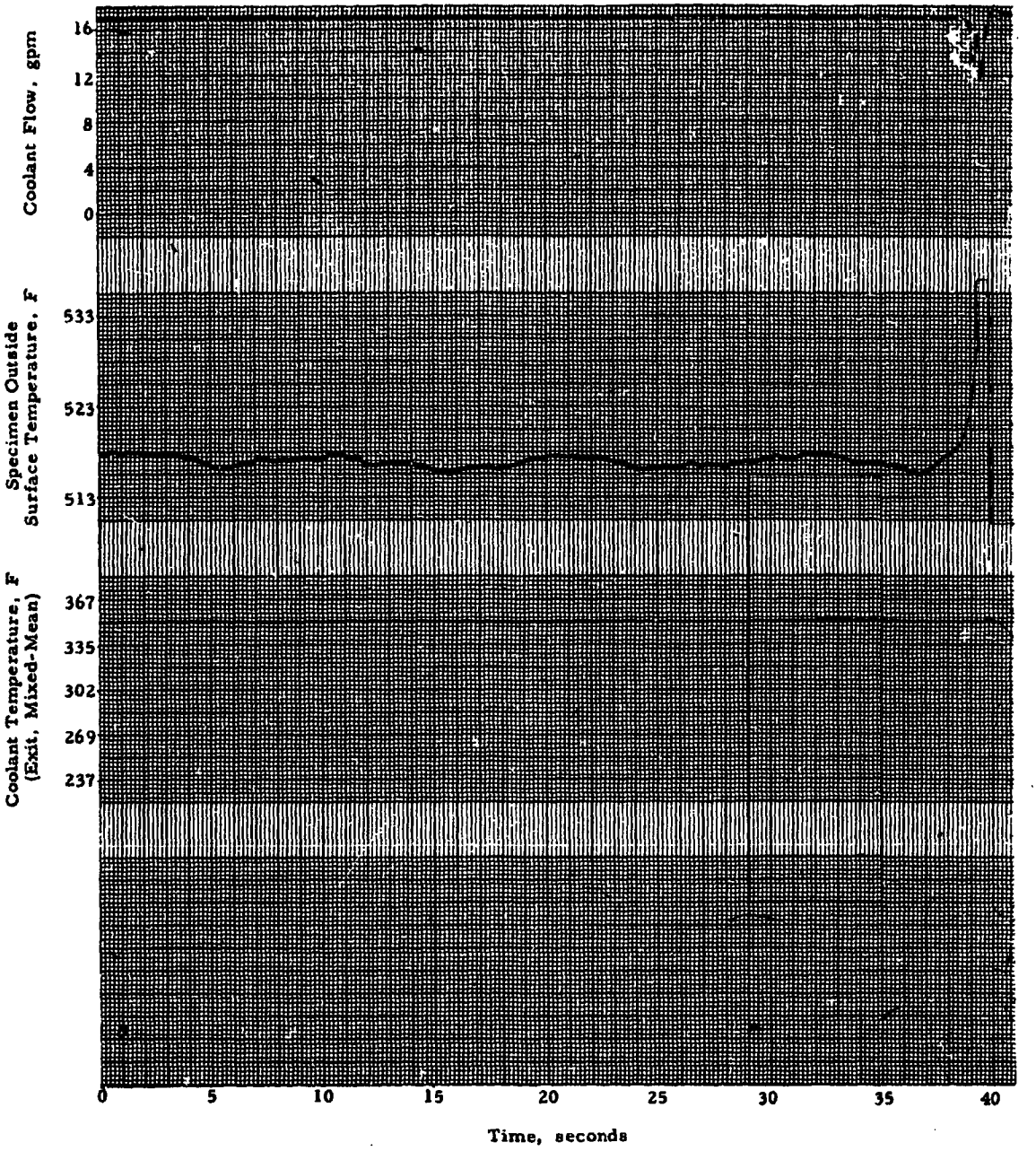
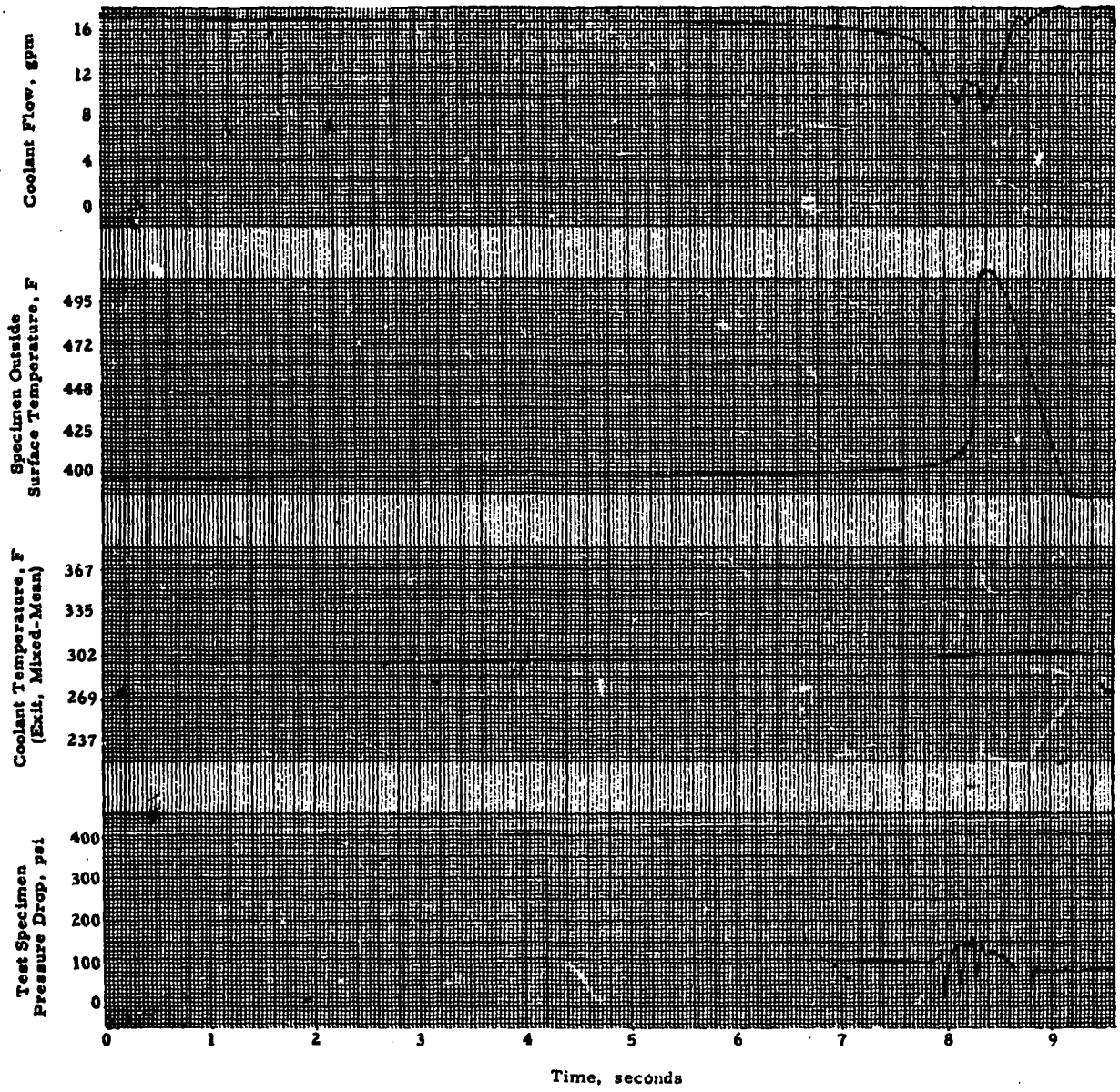


Figure 4-11. Burnout Test Recorder Chart
(Test 10, 0.094-Inch Channel)



5. CONCLUSIONS

Data on both the 0.054- and 0.072-inch-nominal channels indicated that burnout was initiated by autocatalytic vapor binding or flow instability when coolant saturation was reached at the exit of the channel. This was the limiting criteria in all tests ranging in pressures from 80 to 250 psia, mass velocities from 5.5×10^6 to 12.5×10^6 lb/hr-ft^2, and maximum heat flux from 0.95×10^6 to 2.83×10^6 Btu/hr-ft^2. While burnout was preceded by a large flow reduction, the burnout location in the two specimens run to destruction was about two thirds of the channel length from the inlet as predicted by Bernath's equation.

The data also indicated that imperfect coolant mixing occurred and that bulk boiling across the entire channel width was not required to initiate the flow reductions. Burnout in the 0.094-inch channel was limited to about 60% of the value predicted by Bernath's equation either by bulk boiling at the exit in the pressure reduction tests or by subcooled burnout in the normal and reduced flow tests. The subcooled burnout may have been initiated prematurely by autocatalytic vapor binding due to local boiling.

ATTACHMENT 8

BNWL-216
UC-80, Reactor Technology
(TID-4500)
FIRST UNRESTRICTED DISTRIBUTION MADE JUN 1 '66

HEAT TRANSFER EXPERIMENTS FOR THE ADVANCED TEST REACTOR

CFSTI PRICES

H.C. $ 4.00; MN .75

By

E. D. Waters

Thermal Hydraulics Unit
Reactor and Materials Technology Department

May, 1966

RELEASED FOR ANNOUNCEMENT

IN NUCLEAR SCIENCE ABSTRACTS

PACIFIC NORTHWEST LABORATORY
RICHLAND, WASHINGTON

LEGAL NOTICE

This report was prepared as an account of Government sponsored work. Neither the United States, nor the Commission, nor any person acting on behalf of the Commission:

A. Makes any warranty or representation, expressed or implied, with respect to the accuracy, completeness, or usefulness of the information contained in this report, or that the use of any information, apparatus, method, or process disclosed in this report may not infringe privately owned rights; or

B. Assumes any liabilities with respect to the use of, or for damages resulting from the use of any information, apparatus, method, or process disclosed in this report.

As used in the above, "person acting on behalf of the Commission" includes any employee or contractor of the Commission, or employee of such contractor, to the extent that such employee or contractor of the Commission, or employee of such contractor prepares, disseminates, or provides access to, any information pursuant to his employment or contract with the Commission, or his employment with such contractor.

TABLE OF CONTENTS

		Page
1.0	INTRODUCTION	1
2.0	SUMMARY AND CONCLUSIONS	2
3.0	SIMPLIFIED ATR CHANNEL CHARACTERISTICS	4
	3.1 Heat Transfer Analysis	4
	Case I	6
	Case II	7
	Case III	8
	3.2 Hydraulics	10
4.0	EXPERIMENTAL EQUIPMENT AND PROCEDURE	13
	4.1 Test Section	13
	4.2 Loop Description	20
	4.3 Loop Hydraulics	22
	4.4 Test Procedures	23
5.0	TEST RESULTS AND DISCUSSION	24
	5.1 Uniform Lateral Heat Flux Test Section	24
	5.2 Nonuniform Lateral Heat Flux Test Section	26
	5.3 Characteristics of Hydraulic Demand Curve Minima	28
	5.3.1 Uniform Lateral Flux Test Section	28
	5.3.2 Nonuniform Lateral Flux Test Section	31
	5.3.3 Local Boiling Effects	34
	5.3.4 Comparison of Data with Burnout Correlations	36
	5.4 Lateral Coolant Temperature Variation	37
	5.5 Axial Flux Distribution	40
	5.6 Channel Dimensions and Test Section Status	40

Table of Contents (continued)

Page

6.0 APPLICATION OF TEST DATA TO PREDICTION OF HYDRAULIC INSTABILITY LIMITS FOR ATR 44

6.1 Required Information 45

6.2 Calculation Procedure - High Power Levels 45

6.3 Calculation Procedure - Low Power Levels 46

6.4 Example of Procedure as Applied to Present Test Data 46

6.5 Example of Procedure as Applied to B&W Data 48

7.0 LIMITATIONS OF INSTABILITY PREDICTIONS 49

8.0 TEST SECTION PARAMETERS AND CONVERSION FACTORS 51

8.1 Uniform Lateral Flux Test Section 51

8.2 Nonuniform Lateral Flux Test Section 53

Acknowledgement 55

Appendix A-1 - Analysis of Lateral Heat Flux Distribution 56

Appendix B-1 - Data for Uniform Lateral Flux 59

Appendix B-2 - Data for Nonuniform Lateral Flux Test Section 69

Figures

HEAT TRANSFER EXPERIMENTS FOR THE ADVANCED TEST REACTOR

By

E. D. Waters

1.0 INTRODUCTION

The Advanced Test Reactor (ATR) is a water-cooled high-power-density test reactor being constructed at the Idaho National Reactor Testing Station. Phillips Petroleum Company will be responsible to the Atomic Energy Commission for the operation of the reactor.

In the course of their hazards analysis for establishing operating limits and for satisfying AEC licensing procedures, Phillips Petroleum found it desirable to have boiling burnout heat flux data which would be directly applicable to coolant conditions of the ATR. Existing data for rectangular channels were principally for high pressures, and the use of existing burnout correlations required the extrapolation beyond the original test conditions. The empirical nature and the obvious disagreement of some of the burnout correlations indicated that extrapolation to new conditions would be unsatisfactory.

An agreement was established between Phillips Petroleum Company and Hanford Laboratories* whereby the latter would perform heat transfer tests

---

*On January 4, 1965, Hanford Laboratories (with General Electric as operating contractor) became Pacific Northwest Laboratory (with Battelle Memorial Institute as operating contractor).

with electrically heated models of ATR fuel element channels at conditions expected in the reactor. The principal objectives of these tests were to obtain data which defined the allowable heat fluxes for ATR coolant passages and to determine whether localized film boiling or hydraulic instability would be the cause of the limiting heat flux conditions. The results of these laboratory tests are reported here.

2.0 SUMMARY AND CONCLUSIONS

Heat transfer experiments were conducted with electrically heated test sections which were full scale models of a typical coolant channel of the Advanced Test Reactor (ATR). The test section coolant channel was 2.03 in. wide by 0.070 in. thick by 49.5 in. long. A steady state heat conduction analysis of an ATR fuel channel was used to determine the proper size and shape of the resistance heater bars to produce heat flux distribution typical of the reactor fuel elements. A chopped cosine axial heat flux pattern was used in both test sections, and in one test section a lateral flux peaking factor of 1.36 peak/average was also used.

A hydraulic analysis was made for the ATR core with many parallel flow channels (Section 3.2). The analysis showed that if the hydraulic demand (pressure drop vs. flow) curves for any coolant channel exhibited minima (near boiling) which were greater than the constant core pressure drop, then flow instability would occur in that channel and lead to boiling burnout conditions. Experiments were then performed to verify this analysis.

Experiments were first conducted to determine hydraulic demand (ΔP vs. flow) curves at constant power input rates to the coolant. Coolant

velocities from about 1.5 to 5 ft/sec and 25 to 55 ft/sec were used to simulate reactor shutdown conditions and normal reactor operating conditions, respectively. The pressure drop along the test section was recorded as the flow rate was decreased in small steps by a control valve while power input was held constant. Flow reductions were continued until the channel pressure drop reached a minimum and increased appreciably due to boiling and two-phase flow conditions. Typical data are shown in Figures 24 and 25.

The experimental apparatus was then arranged to simulate reactor operation with a constant head supplied to the test section. The power input was then increased slowly until flow instability occurred and initiated film boiling conditions. The transient conditions during flow instability were recorded on high speed recorders.

The test results show that hydraulic instability, not boiling burnout, will be the limiting factor for the ATR. With enforced stable flow, boiling burnout conditions were not encountered in any of the experiments even though bulk boiling was allowed and even though peak heat fluxes up to 4.0 million Btu/hr-sq ft were reached.

From the test results, it was concluded that lateral coolant mixing is quite small. Coolant temperature differences of at least 25°F existed within the uniform lateral heat flux test section and coolant temperature differences as high as 100°F were measured within the nonuniform lateral flux test section at the discharge end.

The data further show that the minima in the hydraulic demand curves - the flow instability condition for ATR - do not correspond with initiation

of local boiling, but rather correspond with beginning of bulk boiling in the high coolant enthalpy region of the flow channel.

With a knowledge of the test section lateral heat flux pattern, the data were used to develop a means of calculating the flow instability conditions for a coolant channel. The calculational procedure was compared with hydraulic instability data from independent tests and found to compare well (see Section 6.0).

The prediction of instability conditions depends on a knowledge of the perimetrical heat flux pattern for a coolant channel and on a knowledge of the flow rate through the channel at the available head. An inaccuracy in either of these parameters will affect the accuracy of the predictions.

The uniform lateral flux test section was destroyed by a power surge (heat flux about 10^7 Btu/hr-sq ft) because of a power supply control malfunction. The nonuniform lateral flux test section sustained no damage during the experiments, even during the three flow instability burnout transients at peak heat fluxes of 3.5 million Btu/hr-sq ft.

3.0 SIMPLIFIED ATR CHANNEL CHARACTERISTICS

3.1 Heat Transfer Analysis

The ATR is designed for plate-type fuel elements. Each fuel element is an assembly of aluminum-clad curved plates which form a 45-degree sector of a right circular cylinder, as shown in Figure 1. The radii of curvation of the plates ranges from about 2-1/2 to 5-1/2 in. The plates are 49-1/2 in. long and enclose water channels that vary in width from about 1-1/2 to 3-3/4 in. The nominal water channel thickness is 0.078-in. Enriched U_3O_8 powder in an aluminum matrix is the "meat" of each fuel plate. It extends along the center

48 in. of length and extends across the plate width to a minimum of 0.050-in. from the support plates on each side of the fuel assembly. The reactor flux distribution will result in a chopped cosine axial heat generation distribution in the meat with a peak-to-average ratio of 1.4 to 1.

It is quite impractical to simulate a complete ATR fuel element assembly for heat transfer tests using electrical resistance heating. Therefore, one coolant channel between two fuel plates was selected as a typical "unit cell" of the fuel assembly. Test section design was further simplified by assuming that the fuel plates were flat rather than curved. The resultant simplified typical ATR coolant passage would be as shown in Figure 2.

In this figure, each fuel plate is shown as only 1/2 of its total thickness. Hence, each external fuel plate surface of the unit cell in Figure 2 would represent an adiabatic surface in a fuel element assembly.

A heat flow analysis was made to determine the peripheral heat flux and temperature distribution for a unit-cell coolant passage. Some investigators have shown that equal heat flux around the periphery of a rectangular coolant passage of high aspect ratio (i.e., large width-to-thickness ratio) will result in preferential burnout at the corners or edges of the coolant passage.(1) Other investigators indicate that an edge heat flux of 20 percent of the center heat

---

(1) S. Levy, R. A. Fuller, R. O. Niemi. "Heat Transfer to Water in Thin Rectangular Channels," ASME Journal of Heat Transfer, pp 129-143, May, 1959.

flux does not allow preferential corner burnout.[2] Since the threshold of preferential corner burnout heat flux is not known, it is important to match the heat flux distribution of the experimental test section with that of the ATR coolant passage as closely as possible.

The details of the heat flow analysis, the liquid film heat transfer coefficients, and the material thermal properties are presented in Appendix A-1, while the principal results of the analysis are presented below.

Case I -- Uniform heat generation in the fuel; noninsulated support plate.

The simplest case is when the neutron flux produces a uniform volumetric heat generation in all parts of the fuel plate meat. Some nuclear (gamma) heating also occurs in the aluminum cladding and the 0.187-in. thick support plates. The gamma heating was assumed to be 5 percent of the total reactor power. Using reactor core parameters supplied by Phillips personnel, the unit volume heating rate in the aluminum support plates and cladding was calculated to be 1.32 percent of the unit volume heat generation rate in the fuel meat.

The liquid film heat transfer coefficient will be lower in the corners and along the edges of a coolant passage as discussed in Appendix A-1. Using an average heat transfer coefficient along the edges equal to about 4/10 of that in the center region of the fuel plate surface and assuming good contact between the fuel cladding and the support plates (i.e., h = 10,000 Btu/hr-sq ft-°F), the steady

---

(2) Discussion of Levy's paper by Green and LeTourneau. ASME Journal of Heat Transfer, p 141, May, 1959.

state lateral heat conduction pattern of the unit cell was calculated. A typical heat flux pattern is shown in Figure 3.

From the calculations, it was found that the relative temperatures of the coolant between the fuel plates and the coolant which is exterior to the side support plates greatly affected the edge heat flux. For example, when the fuel plate coolant is 180°F above the support plate coolant, heat will be removed from the fuel plate coolant at the channel edges at a rate of -36 percent of the fuel plate center heat flux. However, if the two coolant streams are at equal temperatures, the edge heat flux to the fuel plate coolant will be about +21 percent of the fuel plate center heat flux.

Figure 4 shows the edge heat flux as a function of the relative temperatures of the coolant streams. Since the total heat input to the ATR support plate coolant streams is relatively low, a large temperature difference will exist over much of the fuel length. Negative heat fluxes at the chennel edge will be common in the ATR.

Case II -- Uniform heat generation in the fuel with insulated spacer.

At certain locations along each fuel assembly, the fuel support plates are made thicker to serve as bumpers or spacers between adjacent fuel assemblies. The heat flux patterns for the coolant channel at spacer locations were analyzed as Case II. This was the same as Case I, except that it was made for a 0.223-in. thick support plate and all heat generated in the support plate was transferred to the fuel plate coolant channel rather than partially to the coolant flow between adjacent support plates. This condition represents a

region where a spacer fits tightly against the support plate of the adjacent fuel assembly.

The heat flux distribution for Case II is shown in Figure 5. The edge heat flux becomes 44 percent of the center channel heat flux. This is considerably higher than the edge heat flux for regions away from spacers. Since the threshold heat flux for edge burnout is not known, it might be desirable to reduce the edge heat flux at spacer locations. This could be done easily by providing longitudinal slots in the spacers. A small amount of coolant flow through a spacer would reduce the main coolant channel edge heat flux appreciably.

Case III -- Variable heat generation across fuel-plate width.

Figure 2 would be representative of a unit-cell fuel and coolant channel of the inner regions of a fuel assembly. However, the coolant channel between fuel plates 18 and 19 (and fuel plates 1 and 2) would have a thicker fuel plate on one side (No. 1 or No. 19). Also, flux distortion in the ATR can cause the volumetric heat generation in the meat to vary across the width of the fuel plates as well as from one plate to another. The greatest distortion will occur near the outer radius of a fuel assembly. Physics calculations performed by Phillips personnel have resulted in a power distribution across a coolant channel as shown in Figure 6, where the two different curves are for fuel plates 18 and 19 as sides of the coolant passage.

For the heat flux pattern analysis of Case III, the unit cell shown in Figure 2 was modified to account for the thicker cladding of fuel plate 19 (0.040-in. cladding for plate 19 vs. 0.015-in. cladding

for plate 18). The width of the coolant channel was increased to 3.78 in. Then, the heat generation rate was varied from node to node in the fuel meat region of the calculational grid to make a stepped approximation to the power distribution curves of Figure 6. The volumetric heat generation rate for the aluminum was set at 0.495 percent of the unit volume heating in the meat at the left edge of plate 19. (When the peak heat flux on plate 19 is about 2.25×10^6 Btu/hr-sq ft, the gamma heating rates of Cases I and III are equal.) The heat transfer coefficients for Case III were the same as those used in Cases I and II. The support plate thickness was 0.187-in. and heat flow was allowed to the support plate coolant stream.

The results of the analysis for Case III are shown in Figure 7. It was found that the heat flux pattern at the surface of the fuel plate does not differ appreciably from the heat generation pattern in the fuel meat except for distances from the channel edge less than 10 percent of the coolant channel width. These differences near the channel edge result from heat conduction through the side support plates. One must note that if there was poor contact and a large thermal resistance between the fuel plate and the side support plate, then the rapid drop off in heat flux shown in Figure 7 near the edge of the channel would not occur, and the heat flux pattern would be essentially the same as the heat generation pattern.

The edge heat fluxes for the Case III unit cell were all negative denoting that heat was transferred from the fuel plate coolant stream to the support plate coolant stream through the channel edge. The edge heat fluxes were about -10 percent of the peak heat flux for fuel plate 19.

The results of the above analyses were used in the design of the electrically heated test sections to assure a suitable heat flux distribution around the periphery of the coolant channel.

3.2 Hydraulics

Each individual coolant passage or unit cell of the ATR core originates in the upper plenum and terminates in the lower plenum of the reactor vessel (i.e., flow vertically down). With this parallel flow arrangement, any change in the hydraulic resistance of one or even a few of the 800 coolant channels of the reactor would have negligible effect on the total reactor flow or upon the plenum-to-plenum pressure drop. Thus, any individual coolant channel operates at a constant pressure drop, i.e., a pressure drop which is unaffected by any changes such as boiling within the channel. The hydraulic supply and demand curves of such a system can be represented as Figure 8-a.

The "supply" curve represents the plenum-to-plenum pressure drop supplied to the coolant channel by the reactor pumps and associated piping at a given flow rate. The "demand" curve represents the pressure drop required (demanded) by the coolant channel to force a given flow rate through the channel. The intersection of the supply and demand curves shows the operating point for that combined supply-demand system.

The system represented in Figure 8-a can be referred to as a "soft" system, meaning that a change in hydraulic resistance produces a large change in the coolant channel flow rate. In contrast, a "stiff"

hydraulic system would be represented by Figure 8-b, wherein it is seen that a given change in hydraulic resistance (demand) causes less change in the flow rate than for the soft system. The difference between the soft and the stiff systems is due to the different supply curve characteristics.

Figures 8-a and 8-b apply for single-phase coolant (adiabatic or nonboiling) flow passages. But the difference between soft and stiff systems is even more important for flow passages in which boiling occurs. This is illustrated in Figures 8-c and 8-d. In these figures, the dashed curves represent hydraulic demand curves (ΔP vs. flow rate) which will be obtained if the power input P to the coolant is held constant while the flow rate through the test section is decreased in small steps. Such curves are obtained experimentally by using a very stiff supply curve; this is achieved by using a high head pump and throttling upstream of the test section. The points labeled FB then correspond to film boiling (burnout) conditions as approached by flow reduction at constant power. Curves like these have been determined at Battelle-Northwest for several different test section geometries and coolant conditions in years past.

For the soft system, point I corresponds to a point of flow instability which would result in a self-induced flow reduction to point BBO (beyond burnout). The same power input with a stiff system would result in stable operation (point S) at a flow rate much greater than that at which burnout would occur.

From figures such as these, it is apparent that a soft system would result in flow instability and "apparent burnout" at a power level, P_2, which is less than that, P_4, which results in stable film boiling burnout with a stiff hydraulic system. It follows that determination of limiting heat fluxes or limiting channel power inputs for the ATR should be done with a soft system to duplicate ATR conditions of constant pressure drop across the reactor core.

If flow rate vs. test section pressure drop data are obtained with a stiff hydraulic system for a series of different power inputs, as represented by curves P_1, P_2, P_3, and P_4 of Figure 8, it should be possible to predict the apparent burnout (flow instability) power level for the same test section with known soft system hydraulic characteristics. This approach was used in the present experiments.

Hydraulic-demand curve data were obtained using a stiff hydraulic supply and the data used to predict the flow instability burnout conditions for a soft system. The predictions were then verified by operation with a soft system.

The following hydraulic conditions were specified as typical to ATR during normal operation:

Plenum-to-plenum ΔP	100 psi or 60 psi
Inlet temperature	130°F
Inlet plenum pressures	300 psig or 350 psig

With these fluid conditions and the unit cell coolant passage shown in Figure 2, the mass velocities in the coolant channel can be calculated to be about 9.7×10^6 and 7.4×10^6 lb/hr-sq ft for the

100-psi and 60-psi ΔP cases, respectively. These flow rates correspond to bulk velocities of about 44 and 34 ft/sec, respectively. These flow rates were used in a standard Nusselt relation for calculation of the bulk heat transfer coefficients used in the heat transfer calculations discussed previously.

4.0 EXPERIMENTAL EQUIPMENT AND PROCEDURE

4.1 Test Section

The test sections were designed to simulate as nearly as practical the heat flow and fluid flow characteristics of the ATR unit cell coolant passage described previously and shown in Figure 2. The uniform lateral heat flux pattern and the nonuniform lateral flux pattern were both simulated with 0.070-in. thick coolant passage test sections.

In simulating an ATR unit cell, there are three important operational characteristics which the test section must provide:

1) Proper internal dimensions and shape

2) Proper longitudinal heat flux distribution

3) Proper lateral heat flux distribution.

To meet these requirements, the test sections consisted essentially of a stainless steel coolant duct with 70-30 Cu-Ni heater bars bonded to each of the wide sides of the duct. This is shown in Figure 9.

The test section components were assembled by first vacuum brazing a 2.5-in. wide rectangular Cu-Ni bar to a 0.010-in. thick stainless steel sheet. The Cu-Ni was then machined to the proper width and profile. Two such prefabricated channel sides were then welded

together, with small U-channels formed from 0.010-in. stainless steel serving as intermediate pieces to form the channel edges. The intricate welds were made on each tip of each U-channel along the full length of the test section. It was considered desirable to use these U-channels as the coolant passage edges because this would simulate the reentrant corners which exist in the ATR fuel assemblies when fuel plates are rolled into the side support plates.

The desired longitudinal heat flux distribution was attained by varying the thickness of the Cu-Ni heater bars along their length. The longitudinal profile of the heater bars was cut on a planer using a hydraulically controlled Tru-Trace curve follower attachment and a carefully made model as the Tru-Trace pattern. The profile was a smooth curve and not a stepped profile. The calculations for the determination of the Cu-Ni heater bar thickness included the effects of the stainless steel coolant duct on resistance heating rates at various axial positions. The axial heat flux profile was measured during the tests; the results will be discussed in Section 5.5.

The method of analysis and the resultant lateral heat flux distribution for the ATR unit cell are discussed in Section 3.1. It was attempted to make the lateral heat flux distribution of the test sections correspond to that of the unit cell. This was done by selection of the height of the U-channel edges, and selection of the transverse distance from the inside edge of the coolant channel to the outer edge of the Cu-Ni heater bar. The resultant lateral profile for the uniform test section is shown in Figure 9 and the

table which accompanies the figure. As shown in the table, one side of the test section was made 5 to 7 percent thicker than the other. This was done to make a preferential burnout location; the majority of the surface thermocouples were on the thicker side. The lateral heat flux distribution in the test sections could not be measured, but calculated lateral distributions are shown in Figure 10 for the case of the uniform lateral heat flux test section. The relative heat flux from the edges of the test section coolant channel varied somewhat with axial position because of the combination of constant width edge strip and varying thickness Cu-Ni heater bar. The values for edge heat flux at various axial positions are as follows:

	Edge Heat Flux Relative to Channel Midwidth Flux
0 inches from end	3.1%
6 inches from end	5.7%
10 inches from end	8.1%
24 inches from end	11.8%

One will notice slightly different heat flux patterns on and near the edges of the coolant channel for the test section and for the ATR unit cell. (Compare Figures 3 and 10.) In particular, the heat flux on the edges of the test section seems too high. However, these different heat flux patterns were dictated by the differences in the thermal conductivity and the geometry external to the coolant channel.

The basis of the test section design was that the ratio of the coolant enthalpy rise in the edge region to the enthalpy rise in the

central region of the flow channel be the same for the test section and the unit cell. An overall height of 0.050-in. was selected for the U-channel edge pieces and the setback of the Cu-Ni heaters from the coolant channel edge (0.064-in.) was calculated to result in the proper enthalpy rise ratio. The enthalpy ratios are listed below for the unit cell and the test section and compared with the ratio for a coolant channel which has a uniform heat flux around the entire periphery.

Configuration	Ratio, $\frac{\Delta h \text{ in edge region}}{\Delta h \text{ in central region}}$	
	0.070-in. wide region	0.140-in. wide region
ATR Unit Cell	0.48	0.69
0.070-in. Channel Uniform Test Section		
at 24 in. from end	0.46	0.74
at 10 in. from end	0.36	0.70
at 6 in. from end	0.31	0.67
at 0 in. from end	0.24	0.64
Uniform Peripheral Heat Flux	1.84	1.40

Although the enthalpy rise ratio for the present test section varies slightly along the length, the average value would be quite close to that for the unit cell.

It was concluded that even though the edge heat flux of the present test section was higher than might be desired, premature edge burnouts would not occur when the fluid enthalpy in the edge region was of the proper magnitude. If edge heat fluxes of this relative magnitude are sufficient to cause edge burnout, then burnout would

surely occur at locations of support plate bumpers. The analysis presented in Section 3.1, Case II, showed that edge heat flux at bumper locations would be about 43 percent of the channel average heat flux.

The enthalpy rise ratio for a uniform peripheral flux is very large, as shown in the above tabulation, and reaches a value of about 2.8 if one considers a 0.035-in. wide region. High values of local enthalpy probably caused the edge burnouts at low heat fluxes reported by Levy, et al.(3) for a test section with uniform peripheral heat flux.

One test section of the 0.070-in. thickness was used to simulate the situation of nonuniform heat generation across the fuel width. For this case, the heat generation distribution for the fuel element was specified by Phillips Petroleum Company as shown in Figure 6. Thermal analysis of opposing nonuniform fuel plates resulted in the lateral heat flux distribution shown in Figure 7.

Since the test section coolant channel was only 2.0 in. wide, whereas the fuel element coolant channel involving fuel plates 18 and 19 was specified as 3.78 in. wide, the entire lateral heat flux pattern was not simulated with the nonuniform test section. Instead, only the portions of the heat flux distribution curves across about 50 percent of the channel width were to be approximated with the test section.

The test section was machined with a lateral taper as shown in Figure 11. The taper angle varied with axial position on the test

(3) Levy, et al., op.cit.

section in order that the lateral flux distribution be the same along the entire test section length. Small secondary cuts on the left-hand edge of the Cu-Ni heater bar provided the flattening in the heat flux profile which was desired to match the lateral flux profile of the nonuniform unit cell. The calculated lateral heat flux profile for the nonuniform test section is shown in Figure 12 and is seen to match the desired profile (Figure 7) quite closely. Edge heat fluxes for the nonuniform test section were a maximum about 15 percent of the peak heat flux at any channel cross section.

The test section coolant channel terminated at each end by sudden transition to a 2-in. diameter plenum. In these plenums, pressure and temperature measurements were made of the inlet or outlet coolant conditions. In addition, test section pressure taps were provided in the rectangular coolant channel at a distance of 1/4-in. from either end. The plenums were made of copper and were silver soldered to the test section proper. Copper tubing attached to the plenums was used to conduct the electric current to the test section. These details are shown in Figure 13.

During final assembly of each test section, the heater assembly was carefully positioned within a support box assembly. This assembly was designed to prevent expansion (of the thickness) of the coolant channel from internal hydrostatic pressure, but at the same time, to allow axial movement of the heater backup plates on roller bearings and prevent axial buckling due to thermal expansion. Figures 14 and 15 show some of the details of this support box assembly.

Since the rectangular channel alone would be unable to support even small internal pressures without expanding, the support box provided the principal control of channel thickness. Careful measurement of each component within the support box allowed selection of fine shims necessary to produce the desired 0.070-in. thickness. Channel thickness was measured along the full length of the test section using a variable reluctance gauging device prior to installation of the test section in the test loop.

Results of these measurements will be presented in Section 5.6. In general, it was found that the test section dimensions were quite stable through the constant-power experiments.

The temperature of the outer surface of the Cu-Ni heater bars of the test sections was monitored during the experiments by thermocouples inserted through holes in the backup plates and support box assembly. The thermocouples were each held against the heater bars by a coiled spring fitted around the thermocouple sheath. The springs provided a pressure force of two to three pounds on each thermocouple. Preliminary tests were conducted to compare the temperature response of these thermocouples with thermocouples whose sheath was welded to the heater surface. It was found that a pressure contact sheathed thermocouple would respond to a temperature transient as well or better than a welded contact sheathed thermocouple if the sheath tip is coated with silver solder and then ground flat to give a good contact surface.

The location of the surface thermocouples is shown in Figure 15. Not all of these thermocouple locations were monitored at all times.

The sheaths of the heater surface thermocouples were used as special voltage taps during the constant power experiments. Determination of the voltage drop for various lengths along the test section allowed determination of the power distribution as plotted in Figure 17.

Special thermocouples were positioned at the downstream end of the coolant channel to measure the coolant temperature variation across the width of the channel. One thermocouple was held at the center of the channel. A second thermocouple was at 0.70 in. from the center and a third thermocouple was opposite from center at 0.90 in. The thermocouples (0.060-in. OD sheathed type) extended into the channel 1/4 in. and were parallel to the coolant path. The thermocouple holder is shown in Figure 16. Indexing pins allowed accurate positioning of the thermocouples.

4.2 Loop Description

A schematic diagram of the low-pressure heat-transfer apparatus at Hanford is shown in Figure 18 as it was arranged for the ATR tests. Deaerated, deionized water was recirculated through the loop by a 14-stage centrifugal pump. A steam-water preheater and a water-cooled after-cooler allowed temperature regulation of the recirculating water.

Pressures were measured in the 2-in. diameter plenums upstream and downstream of the test section as well as at pressure taps just inside of the rectangular channel, as discussed previously. These pressures were read on Heise precision gages. The test section

differential pressure was measured on a gauge and also recorded continuously as the output from a differential pressure transducer. The pressure in the inlet or outlet plenum was used as a reference for control of the system pressure. System pressure regulation was achieved by a continuous injection-and-bleed system using a small centrifugal pump for injecting water into the loop.

Power was supplied to the test section from the 50-volt, 22,000-ampere dc generators. Power input was determined from current and voltage drop measurements. This power input was compared with calculated coolant enthalpy rise using temperature-flow data whenever practical as a check on the temperatures, flow rate, and voltage-current measurements. Heat balances generally fell within ±3 percent after corrections for heat losses determined by isothermal runs.

Loop and test section flow rates were measured by turbine-type flowmeters. Test section flow rate was continuously monitored on a strip chart recorder while loop flow rate was read periodically from an indicator.

The coolant temperatures and test section temperatures were read on various indicating or strip chart recording instruments. The strip chart instruments were used primarily for the test section surface temperatures which were used as burnout monitors. In addition, many of the temperatures (also test section flow rate, pressure drop, voltage drop, and electrical current) were read out periodically on the ADA (Automatic Data Acquisition) equipment of the laboratory. Basically, this equipment functions as signal voltage-to-frequency

conversion, pulse count for fixed time interval, and conversion of count to digital output as typewriter printout and/or punched paper tape for computer processing. This equipment eliminates much of the need for hand recording of data during operation.

4.3 Loop Hydraulics

The characteristics of a soft hydraulic supply curve for the test section were discussed in Section 3.2. To achieve such a supply curve, one needs either (1) a near-constant head pump with little pressure drop in piping external to the test section, or (2) a very large flow in parallel with the test section. The latter arrangement was used in the present tests while simulating ATR constant pressure-drop conditions.

The bypass loop, as shown in Figure 18, was designed to handle a flow rate of about 200 gpm while the test section flow was 20 gpm. This bypass arrangement, when considered with the pump and valves characteristics, results in the test section supply curves shown in Figure 19. Curves A and B depend, of course, on the amount of throttling which is done by the bypass valve and the upstream and downstream throttling valves. But, once these valves are set, the test section supply curve is then fixed.

Curves A and B of Figure 19 were determined experimentally prior to installation of the test section by insertion of a valve and connecting piping in place of the test section. Closing this valve in small steps simulated a change in test section resistance and allowed the data points on Curves A and B to be obtained. While the

test section supply curves obtained in the experiments are not perfectly flat (i.e., not constant head as those in Figures 8-a and 8-c), it can be shown that the slight change in pressure drop with test section flow would have negligible effect on the flow instability results.

4.4 Test Procedures

The heat transfer experiments with each test section were divided into two different types (1) constant-power experiments, and (2) constant-head experiments.

The constant-power experiments were run with the bypass valve completely closed. This provided a stiff hydraulic system typified in Figures 8-b and 8-d. Flow was established through the test section at a relatively high rate. The inlet temperature was then established and controlled at 130°F and the test section outlet pressure was controlled at the appropriate value, depending on the combination of inlet pressure and normal ΔP which was used as the basis of the run. The test section power input was then established. The experimental runs then consisted of recording steady-state data of flow rates, pressures, and temperatures as the flow rate was reduced in small steps by closing the upstream throttle valve of Figure 18. The flow decrease increments were continued until a definite minimum point had been obtained in the flow rate vs. test section ΔP (demand) curve. Flow was then increased to restore original conditions and a new run was made.

The constant-head experiments were made with the bypass valve open and the bypass flow rate about 10 times the test section flow rate. This provided a soft hydraulic system. After establishing the loop coolant temperature at 130°F, the bypass valve was adjusted to establish the desired test section pressure drop. Final adjustments were then made to control the test section outlet pressure at the desired value. Electrical power was then applied to the test section. The run consisted of increasing the power input in small steps and recording the steady-state data after each power step. Test section surface temperatures, pressure drop, and flow rate were recorded continuously. The power steps were continued until flow instability burnout indications were obtained from the test section flow rate and surface temperatures. The power input was then reduced rapidly and new conditions were established for the next run.

5.0 TEST RESULTS AND DISCUSSION

5.1 Uniform Lateral Heat Flux Test Section

The first tests were conducted with the uniform lateral flux test section. The test results are tabulated as Appendix B-1. The principal characteristics of the data are shown in Figures 20 through 23. A discussion of the data follows.

Data were obtained first at low flow rates and low power inputs which approximate steady state conditions following a reactor shutdown. Hydraulic demand curves were determined at three different outlet plenum pressures - 25 psig, 150 psig, and 350 psig - using the procedure of Section 4.1. The results of these experiments are shown

in Figures 20, 21, and 22. In all cases, the point of minimum pressure drop was very sharp and distinct. The pressure drop increased rapidly with flow rate reductions beyond the minimum of the curve.

Figures 21 and 22, with the higher outlet pressures of 150 and 350 psig, show a noticeable and appreciable deviation of the ΔP data from a straight line isothermal curve as the flow rate is reduced toward that flow which corresponds to the curve minimum. This deviation can be attributed to the decreasing fluid density within the test section at reduced flow rates and correspondingly higher outlet temperatures. For example, the differential pressure measured from plenum to plenum is calculated to increase by about 0.10 psi as the outlet temperature increases from 130°F to saturation temperature (436°F) at 350 psig. Since this change in ΔP due to density effects would occur in the reactor as well as in the test section, no adjustment of data for this effect was made. For a plenum pressure of 25 psig, the density change is less and the ΔP change should be maximum of only about 0.03 psi.

Hydraulic demand curves were then determined with a stiff hydraulic system at higher flow rates and power input rates typical of reactor operation. These data are shown as the 472-kw and 702-kw curves of Figure 23. Again, the pressure drop increased rapidly with flow rate reductions beyond the minima of the curves, although at the higher power level the point of minimum pressure drop was not very distinct. This will be discussed later. During neither of these runs were any indications found of temperature or flow rate instability or film boiling conditions.

The final run series with the uniform lateral flux test section was a constant-head hydraulic instability run. The original plan was to hold a ΔP of 100 psi and increase power input until instability occurred, as outlined in Section 4.1. However, a dc breaker failure occurred on one motor-generator set at a power level of 725 kw. It was then decided to hold the power level constant and decrease the ΔP in small steps until instability occurred. A rapid power reduction prevented damage to the test section after instability occurred. The resultant data are plotted as the 725-kw curve on Figure 23.

All data obtained with the uniform lateral flux test section support the hypothesis of Section 3.2 that operation with a constant head system will result in hydraulic instability when the minimum of the hydraulic demand curve falls above the constant (or near constant) head supply curve. Then the important thing to investigate is the characteristics of demand curve minima. These characteristics will be discussed in Section 5.3 following presentation of the data for the nonuniform lateral flux test section.

5.2 Nonuniform Lateral Heat Flux Test Section

The test results for the nonuniform lateral flux test section are tabulated as Appendix B-2 and the data are plotted mainly in Figures 24 and 25.

Data were first obtained at low flow rates and low power levels. One hydraulic demand curve was obtained at 26 psig and one at 350 psig outlet plenum pressure. The number of runs at low flow conditions was intentionally limited to avoid risk of test section damage before obtaining data at high power levels.

The low power data are shown on Figure 24. Again, the point of minimum pressure drop is very sharp and distinct. The effect of variable density is apparent, especially for the curve for 350 psig back pressure.

Hydraulic demand curves were then obtained with a stiff supply system at high power input rates. These data are shown on Figure 25. They were all obtained with an outlet plenum pressure of 240 psig. The curves show a distinct minimum for the low power case, but the minima are rounded for the higher power levels. No indications of temperature or flow rate instabilities or film boiling conditions were found during any of these runs even though the peak local heat flux was about 4.0×10^6 Btu/hr-sq ft at the highest power level.

The final series with the nonuniform lateral flux test section were constant-head instability runs and were conducted according to the procedure of Section 4.1. Transient recordings of the power, flow rate, pressures and temperatures were made for each run - a typical recording is shown as Figure 26. This recording was made on a six-channel Offner recorder. The pen synchronization was not adjusted carefully and may be off by 1/2 sec. This recording was not intended to show precise sequence of events, but was used principally to detect the initiation of instability conditions.

The flow rate, power input, and pressure drop across the test section before instability occurred are presented on Figure 27 for the nonuniform test section, as well as for the one instability run with the uniform lateral flux test section. This figure shows very

definitely that the nonuniform lateral heat flux test section requires considerably higher flow rates (and pressure drops) to prevent instability at a given power level than the uniform flux test section. The data show that hydraulic instability will occur before film boiling conditions are initiated at the pressure drops currently of interest in the ATR, even with nonuniform lateral heat flux conditions.

One instability experiment was conducted to determine the effect of inlet water temperature on allowable power level. Runs 335 and 342 in Table B-2 show this comparison. It was found that the power level at instability was directly proportional to the bulk enthalpy rise for the same flow rate. Thus, the effect of inlet water temperature changes on allowable power levels can be calculated directly.

5.3 Characteristics of Hydraulic Demand Curve Minima

As discussed in Section 3.2, hydraulic instability with a nearly constant head system is associated with the intersection (or lack of intersection) of the supply curve with a minimum in the hydraulic demand curve. It naturally follows that prediction of instability conditions depends on a knowledge of the characteristics of the demand curve minima.

A specific characteristic would be exhibited if the minima correspond to bulk boiling at the coolant channel outlet.

5.3.1 Uniform Lateral Flux Test Section

Table 5.3.1 presents data and calculations concerning the hydraulic demand curve minima for the uniform lateral heat flux test section. The flow rates at the curve minima were first

TABLE 5.3.1

CHARACTERISTICS OF DEMAND CURVE MINIMA - UNIFORM TEST SECTION

	Approximate Run Number										Line No.
	141	149	156	166	173	180	191	204	215	222 g*	1
Outlet Pressure psig	25	24.5	24.5	150	150	350	350	240	241	240	2
Saturation Temperature °F	267	266	266	366	366	436	436	402	403	402	3
Power Input kw	14.4	20.5	27.0	36.2	51.4	37.5	68.3	472	702	725	4
Flow at Demand Curve Minima gpm	0.77	1.14	1.48	1.13	1.61	0.87	1.61	12.2	17.9	18.7	5
Flow Calculated for Bulk Saturation gpm	0.71	1.01	1.35	1.04	1.48	0.82	1.51	11.6	17.1	17.6	6
$\frac{\text{Measured}}{\text{Calculated}}$ Ratio	1.09	1.13	1.10	1.09	1.09	1.06	1.07	1.05	1.05	1.06	7
Calculated Hot Region Δh Ratio (see Section 8.1)	← 1.054 →										8
Calculated Hot Stripe Δh Ratio	← 1.08 →										9
Bulk Outlet Temperature °F	267	270	267	349	349	424	431	395	395	387	10
Hot Region Temperature °F	269	269	269	353	361	427	427	399	399	390	11

*Hydraulic Instability Run

A THEORY OF LOCAL-BOILING BURNOUT AND ITS APPLICATION TO EXISTING DATA

Louis Bernath

A theory of local-boiling burnout is presented based on an analogy between the microconvective processes in local boiling and the conventional approach to turbulent diffusion processes. This theory describes, in a plausible manner, the physical significance of the mathematical relationships evolved in an empirical method of prediction of the burnout heat flux for water with local boiling over a wide range of experimental conditions. The prediction method is generalized to liquids other than water. Available data are assembled and discussed, and the results of the prediction method are compared with experimental values.

THE BURNOUT PROCESS

During local boiling, heat is transferred from the heated surface through the boiling film (*9*) into the subcooled bulk coolant. The boiling film is characterized by vigorous mixing of the two phases; the vapor in the form of bubbles leaves the surface and flows counter to discrete streams of subcooled liquid that partially quench the bubbles (while flowing toward the surface) and impinge on the surface in the wakes of the departing bubbles. The thickness of this boiling film is a function of the physical properties of the coolant, the heat flux, and the velocity and subcooling of the coolant and determines the wall superheat, or excess of temperature of the surface above the saturation temperature of the coolant. Westwater (*52*) has found that at heat fluxes up to approximately 80% of the maximum (burnout), the frequency of bubble evolution (per unit area) and the mean bubble diameter are both very nearly constant at atmospheric pressure. With heat fluxes approaching the maximum, both bubble frequency and diameter increase rapidly, resulting in the formation of patches of vapor on the surface. At the maximum heat flux, bubbles and vapor patches coalesce on the surface to form discontinuous vapor films which migrate over the surface, departing as clusters of bubbles or large single bubbles, after which new patches of vapor rapidly form. Burnout occurs when a large vapor patch adheres to a region of the surface; the heat generated in that region cannot be completely conducted away through the vapor film and through the metal and so is stored in the metal, raising its temperature rapidly. If the surface temperature corresponding to the resumption of steady state heat flow exceeds the melting point of the surface metal, the heated member fails structurally and it is said to have "burned out."

In local boiling two counteracting processes combine to determine the relationship between surface and bulk coolant temperatures and the heat flux—viz., the process of vapor generation at the surface (controlled by the kinetics of heterogeneous-phase formation) and the process of bubble quenching and turbulent mixing (controlled by the thermal and momentum diffusion properties of the coolant). At the burnout condition, however, only the quenching-mixing process pertains since the surface is essentially isolated from the coolant by the vapor barrier. Thus, only the forces acting from the liquid phase to disrupt the continuity of the vapor layer on the surface require definition in order to describe the burnout condition, which occurs only when the quenching-mixing process can no longer penetrate to the heated surface.

E. I. du Pont de Nemours and Company, Inc., Wilmington, Delaware.

CURRENT THEORIES UNDERLYING METHODS OF PREDICTION OF BURNOUT HEAT FLUX

Quantitative studies of bubble histories during local boiling were made by Kreith, Summerfield, and Gunther (*1*). These pioneer workers showed that less than 5% of the heat transferred from a surface is carried as latent heat in the vapor bubbles; the primary path of heat transport is via the heating of the streams of coolant that impinge directly on the surface. They described the agitated appearance of the coolant near the heated surface as *microconvective mixing*, or turbulence.

All theories of the burnout mechanism underlying the existing methods of correlation are based on this turbulent-mixing process in local boiling and on the sequence of events described above in the onset of the burnout phenomenon. Chang's theory (*2*) is based upon the postulation of wave motion in the heated film and has been applied to nonboiling, as well as nucleate and film boiling heat transfer. The wave motion introduces turbulence into the heated film; "the heat flow can be considered, similar to that of convection, as an equivalent conduction process through the gross boundary film and the absorp-

tion of heat by bubbles has negligible effect on the temperature distribution across this film." The driving force utilized by Chang for all modes of heat transfer, including that at the burnout point, is the difference between the surface and bulk coolant temperatures.

Zuber's theory (3) is an attempt to derive, via purely theoretical considerations, a description of the transition boiling regime, which is bounded by the peak nucleate and minimum film boiling heat fluxes. The equations derived by Zuber correspond very closely to those by Kutateladze (4) and Borishanski (5), both of which were derived semiempirically on the assumption that as the peak nucleate boiling heat flux is approached, the two phases—vapor and liquid—coexist in a relatively well-defined manner. The theory of Rohsenow (6) is based on an analysis of bubble frequencies and population on the surface at the point of coalescense of the bubbles, i.e., when the heated surface is completely covered by vapor; it applies only to pool-boiling phenonema. This theory has been adjusted by Griffith (7) to incorporate the influence of thermal gradients at the heated surface, utilizing postulated bubble lifetimes and bubble growth velocities. Ellion's theory (8) is an extension of the Colburn forced-convection analysis. It incorporates the measured maximum radii of bubbles as well as the measured bubble growth velocities in computing Reynolds and Nusselt numbers to determine the burnout film heat transfer coefficient. Ellion makes use of the over-all driving force to obtain the burnout heat flux.

TURBULENT MIXING THEORY OF LOCAL-BOILING BURNOUT

The theory presented here is based on the following concept: at the heat flux corresponding to the incipient burnout condition* the coolant adjacent to the heated surface is highly turbulent and, despite the presence of bubbles and clusters of bubbles, the two phases are so well mixed that the coolant in this region may be considered homogeneous. Therefore, the transport of heat normal to the heated surface may be viewed as a conduction process, in which the conductance of the turbulent, two-phase layer adjacent to the surface is given by the ratio $(k_{eff}/\Delta X)$ of the effective thermal conductivity and the thickness of the layer, while the driving force is taken as the difference in temperature between the heated surface and the bulk coolant. This relationship may be written in the form conventionally used for heat-conduction problems:

$$(Q/A)_{BO} = (k_{eff}/\Delta X)_{BO} (T_w - T_b)_{BO} \qquad (1)$$

Since neither k_{eff} nor ΔX can be readily measured or computed, the conductance of the boiling layer at incipient burnout can be written as a film coefficient, as is customary in describing convective heat transfer. Thus

$$(Q/A)_{BO} = h_{BO} (T_w - T_b)_{BO} \qquad (2)$$

in which h_{BO} corresponds to the maximum or limiting film coefficient the magnitude of which cannot be exceeded in the local boiling regime of heat transfer. Equation (2) coincides both with the expression obtained empirically in an earlier study (10) of burnout and with that determined by Ellion (8) in an experimental study of burnout phenomena.

It is interesting and perhaps surprising to note that although local boiling heat transfer cannot readily be correlated by means of a film coefficient, the upper boundary of the local boiling regime, viz. the peak or burnout heat flux, is readily predicted by such a coefficient. Furthermore, this limiting coefficient closely resembles the convective film coefficient since it is found to be independent of both heat flux and temperature driving force.

Considerations of bubble dynamics and turbulent mixing in the boiling region provide a physical explanation for the existence of a limiting film coefficient. Recalling the observations of Westwater cited earlier, with increasing heat flux approaching the burnout condition, both the diameter and the frequency of evolution of bubbles from the heated surface increase rapidly. Increasing frequency of bubble evolution should increase the intensity of agitation in the boiling film tending to increase the film coefficient, whereas increasing the diameter of the bubbles should increase the thickness of the boiling film and hinder the influx of coolant to the surface tending to diminish the film coefficient. These two counteracting influences cause the film coefficient to tend to a maximum value, an orderly reduction of which cannot occur (into the region of transition boiling) since beyond the peak heat flux, the bubbles (of relatively large diameter) coalesce at the heated surface to form a continuous, adherent blanket of vapor.

Justification for the use of the over-all temperature driving force arises not only from the analogy between the turbulent mixing burnout process and convective heat transfer, but also from the fact that in all regimes of heat transfer, excepting local boiling, the over-all driving force is required. In the local boiling regime, the studies reported by Begell and Bernath (9) reveal that neither the wall superheat, $T_w - T_{sat}$, nor the subcooling, $T_{sat} - T_b$, is adequate to describe accurately the heat transfer process, but that a complex combination of the two is required.

The analogy between the turbulent-mixing burnout process and convective (nonboiling) heat transfer leads to the expectation that the limiting film coefficient, h_{BO}, is a function of fluid properties, coolant velocity, and hydraulic diameter. Since the physical properties of water vary considerably with pressure, one would expect h_{BO} to vary with pressure. As is shown in a later sec-

*Just prior to the adherence to the surface of the coalescing clusters of bubbles and patches of vapor.

tion, the fluid properties (that are required to permit generalization of the burnout prediction method to coolants other than water) combine in such a way that the resultant group is a rather weak function of pressure over a very wide range (0 to 2,000 lb./sq. in.). It must be acknowledged, however, that the possibility exists that a part of the pressure dependence of h_{BO} may have been incorporated into the driving-force term through the lack of reliable wall-temperature data at high pressures. (See section on Correlation of Burnout Data, Original Method.) Although this possibility exists, the accuracy of prediction of local-boiling burnout with coolants other than water illustrates that the pressure-dependence of the fluid properties is adequately described. However, until accurate experimental values of wall temperatures at burnout for water at high pressures become available, this possibility cannot be rigorously denied.

Since significant heat fluxes are observed when there is no imposed coolant velocity, it is to be expected that "natural" velocities exist in the coolant as a consequence of the departure of bubbles from the heated surface (as was found in the data analyzed by Begell and Bernath) and hence, that h_{BO} may be composed of several terms reflecting the additive effect of free stream velocity on the "natural" bubble velocities. Indeed, h_{BO} is found to be composed of two terms only one of which contains the free stream velocity. The term containing the free stream velocity represents the shearing action of the coolant stream, which thins the boiling film and enhances the penetration of coolant to the surface. In this term, therefore, it is to be expected that the hydraulic diameter will be found in the denominator since a decrease in the hydraulic diameter corresponds to an increase in the steepness of the velocity gradient at the boundary.

If, as has been postulated above, the other term describes the dynamic behavior of the bubbles, it should be expected that the hydraulic diameter will be found in the numerator, since in large coolant passages bubble trajectories will be unhindered by the presence of the unheated boundary, whereas a "blocking" effect on bubble motion is to be expected for narrow channels. Logic also compells the consideration that the relative size of the surface being heated be reflected by this term in h_{BO}; the nominal hydraulic diameter of a coolant channel heated from one surface is identical with that of a channel with both boundaries heated. However, bubbles leaving two surfaces facing each other will encounter hindrance of motion and quenching when the coolant channel is narrow. This is an extension of the "blocking" effect mentioned above. Consequently, it is to be expected that the term in h_{BO} that describes the natural behavior of the bubbles should contain an expression of the ratio of the hydraulic-to-heated diameters. This is exactly the form obtained in the correlation of burnout data.

CORRELATION OF DATA AND PREDICTION OF BURNOUT HEAT FLUX

SELECTION OF DATA FOR CORRELATION

Published data of the heat flux at burnout with local boiling were examined for internal consistency and reproducibility. The data of investigators experimenting in the same range of the variables were compared with each other to establish the reliability of experimental techniques. Where possible, the procedure of the experimenters was analyzed and their analysis of errors was reviewed. This selection of data was employed to permit only the most carefully obtained data to determine the constants of the correlating equations.

In general even the most careful experimental technique yielded data containing some scatter; however, the degree of scatter of the data varied considerably from data source to data source. Reasons for wide scatter in the data include

1. "premature" burnouts due to the
   (*a*) use of a burnout detector, generally unreliable
   (*b*) use of very thin-walled heaters to permit attainment of high heat fluxes with low current input
   (*c*) use of a.c. heating with thin-walled heaters
   (*d*) too rapid an increase of power applied to the heater
   (*e*) attainment of flow instability in the apparatus (if not in test section) without proper recognition of the phenomenon
2. high experimental burnout heat fluxes due to the
   (*a*) vibration of the heater (causes shedding of vapor patches from the heater surface)
   (*b*) attainment of bulk boiling with sufficient net steam to cause acceleration of the coolant stream
   (*c*) experimental arrangement in which the combination of massive power leads and short test sections introduces large heat-conduction errors
3. in the case of flat-strip heaters,
   (*a*) the edges of thin strips are more effective in dissipating heat than the faces
   (*b*) heaters with clamped edges can leak coolant to the back (insulated) face resulting in "high" heat fluxes, or the insulator (mastic or adhesive) can ooze over the edges of the heater strip causing hot spots and "premature" or low burnout heat fluxes

CORRELATION OF BURNOUT DATA

Original Method (10)

Only data on the burnout of heater elements in water were reported in the literature prior to 1954. A number of correlations of the data for specific geometric configurations had been presented, but there existed no theory to explain the burnout process. In addition, the correla-

tions available then were based on the parameters coolant velocity, subcooling, and in some cases the system pressure. In general they were of such mathematical form that the heat flux at burnout decreased to zero if either the coolant velocity or subcooling went to zero, in direct contradiction to the known facts.

The method of correlating burnout data adopted here was based on the parameters coolant velocity, temperature, and pressure and the geometrical variables of hydraulic and heated diameters of the test sections. It was assumed that the driving force for heat transfer at the peak nucleate heat flux is the over-all temperature difference between the heater surface and bulk coolant. This assumption was based on the following observations: (1) the over-all ΔT correlates nonboiling heat transfer data, (2) the over-all ΔT correlates film boiling data, (3) the wall superheat and subcooling are both required to describe local boiling heat transfer, and (4) experimental evidence reveals smooth transitions between the various modes of heat transfer. Thus data were required from experiments in which heater surface temperatures had been measured together with the other variables. Only the data of McAdams (*11*) and of Columbia University (*12*) were suitable from this standpoint. The Columbia data are preferred because the use of aluminum as the heater material permits the attainment of high heat fluxes with very modest temperature drop through the heater wall (3° to 5°C.); the corresponding temperature drop through a stainless steel heater wall of the same thickness would be 40° to 60°C. Since most experimenters used materials of relatively low thermal conductivity, only the Columbia data can be relied upon for accurate measurements of surface temperature.

Accordingly, values of h_{BO} [see Equation (2)] were evaluated from the Columbia data. When these values of h_{BO} were plotted against coolant velocity, the data of each geometric configuration were found to lie on a straight line of the form $h_{BO} = A + BV$; the intercept, A, and the slope, B, were found to be functions of the hydraulic and heated diameters of the annulus test sections. McAdams's data yielded a similar equation. By cross-plotting of values of A and B against D_e/D_i and D_e, respectively, the following expression was found to fit the data closely:

$$h_{BO} = 5{,}710\,(D_e/D_i)^{0.6} + 48\,V/D_e^{\,0.6} \qquad (3)$$

Equations (2) and (3) were then applied to the calculation of the surface temperature at burnout for the data from U.C.L.A. (*13*) and A.N.L. (*14*). Thus

$$T_{w_{BO}} = T_b + (Q/A)_{BO}/h_{BO} \qquad (2a)$$

These values of $T_{w_{BO}}$ were required to extend the range of the correlation to pressures beyond the ~100 lb./sq. in. abs. limit of the Columbia and McAdams data. Although burnout experiments had been performed at pressures up to 3,000 lb./sq. in. abs., wall-temperature measurements were not reported. By plotting the values of $T_{w_{BO}}$ from the Columbia data together with those derived from the U.C.L.A. and A.N.L. data against pressure, the following expression was derived:

$$T_{w_{BO}} = 57 \ln P - 54\left(\frac{P}{P+15}\right) - \frac{V}{4} \qquad (4)$$

in which the last term represents a small correction found necessary to account for the thinning of the boiling film under the influence of free-stream velocity. Since the correlation was developed primarily for use at the Savannah River Plant (and the quatrefoil geometry employed there), the correction term found to fit the Columbia data most accurately was of the form $V/4\left(\frac{D_e}{D_i}\right)^{0.6}$. Since nearly all burnout experiments reported in the literature (particularly at high coolant pressure) were performed with tubular heaters cooled internally (for these data the diameter ratio in the denominator becomes unity), the form of this correction term could be verified only by the data from which it was developed, e.g., Columbia and McAdams. However, the fact that the data of Gunther were well fitted by the correlation—despite the assumption of the applicability of a model that involves cylindricizing the experimental geometry—tended to confirm the form of the correction term.

The method of burnout prediction represented by Equations (2), (3), and (4) was then tested by comparing the heat fluxes predicted for additional* experimental data, for example, Gunther (*15*), Purdue (*16*), and Columbia (*17*) small-scale test data. The accuracy of prediction was found satisfactory; i.e., on the average, the experimental burnout heat flux was predicted within ±15%.

Extended Method

In spite of the success of the original method of burnout prediction, a number of features of the expressions were less than satisfying. These were (1) the first term of the h_{BO} equation yields unreasonably high values for small values of D_i or large values of D_e (pool-boiling configurations), and (2) the correction term of the $T_{w_{BO}}$ equation can assume large magnitudes for small values of D_e or large values of D_i (very narrow annuli). These limitations were recognized, but in the absence of reliable data in the regions of equipment geometry cited above, a more general form of the equations could not be given. The prediction method was, therefore, limited to forced-flow conditions in rather confined geometries.

As additional pool-boiling burnout data became available (e.g., the data of Averin, Mirshak, and Bendler), the shape of the relationship between h_{BO} and hydraulic

*Data that had not been used in the formulation of the prediction method.

h in P.C.U./hr-ft² °C P.C.U. = pound centigrade unit Btu = 9/5 · P.C.U.

diameter became clarified. These new data showed that with increasing D_e, h_{BO} increases and approaches an asymptotic value in the limit. Equation (3) has been modified to reflect the extended range of the geometric variables; thus, h_{BO} is now given by

$$h_{BO} = 10{,}890\left(\frac{D_e}{D_e + D_i}\right) + (\text{slope})\,V \qquad (5)$$

Figure 1 presents a comparison of the first term (intercept) of Equation (5) with its earlier counterpart from Equation (3). Close agreement between the two forms is apparent over the range of data employed in the original correlation. The shape of the curve also conforms to the relationship between h_{BO} and D_e established by the recent data. In extension of the range of the prediction method, one less arbitrary constant is used in evaluating h_{BO} than was required in the original method. This is clearly desirable in that greater simplicity of the formula and hence ease of its application results.

In the establishment of the value for the constant of the first term of Equation (5), only Columbia University data (forced-flow in the large-scale apparatus) were used. This procedure is justified on the basis that only these data are known intimately to the writer to have been taken under steady state conditions resulting in destruction of the heater tube in each experiment. For this

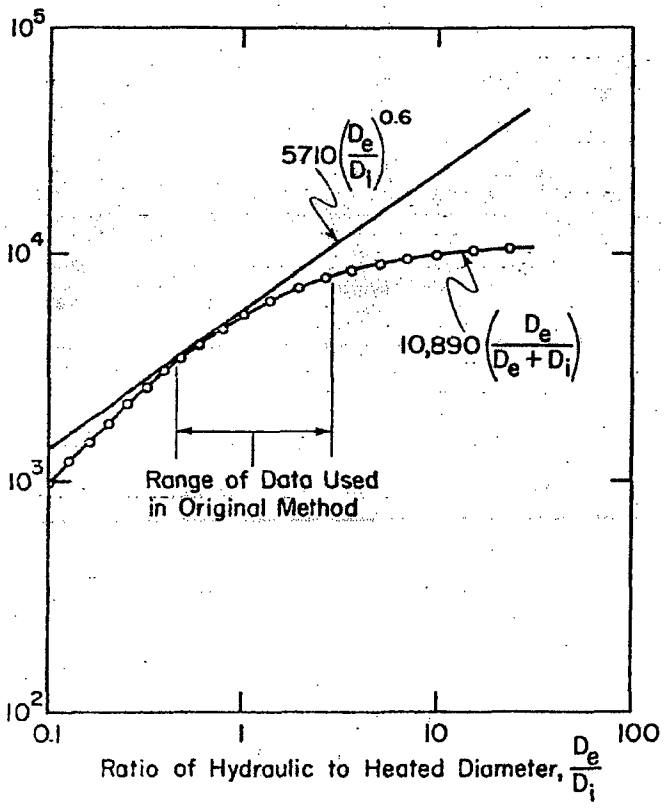


Fig. 1. Comparison of the first terms of h_{BO} formulas.

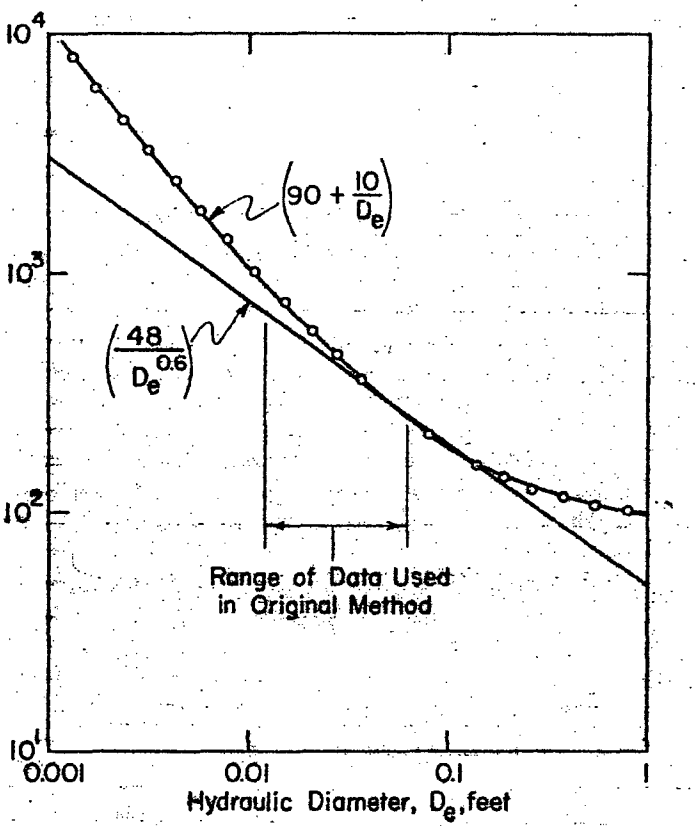


Fig. 2. Comparison of the slopes of h_{BO} formulas.

reason only Columbia University data were used to obtain the constant 10,890 p.c.u./(hr.) (sq. ft.) (°C.) in Equation (5). It represents the arithmetic average of the data of fourteen runs. For tubes cooled internally ($D_e = D_i$), the first term of Equation (5) takes the value 5,445 p.c.u./(hr.) (sq. ft.) (°C.); the value for tubes was 5,710 p.c.u./(hr.) (sq. ft.) (°C.) in the original method [Equation (3)].

The "slope," in the velocity-dependent term of Equation (4), is given by $48/D_e^{0.6}$ for values of $D_e \leq 0.1$ ft. and by $(90 + 10/D_e)$ for $D_e \geq 0.1$ ft. Figure 2 presents a comparison of these "slopes" as a function of hydraulic diameter. It is apparent that over most of the range of the data used in the original correlation, the "slopes" are very nearly the same. However, recent data [e.g., Kezios (*18*)] obtained with forced-flow of coolant in equipment of large hydraulic diameter show that the influence of velocity on the burnout heat flux decreases with increasing D_e. Therefore, it is recommended that the "slope" for small values of D_e be taken as given in Equation (3), whereas for values of $D_e \geq 0.1$ ft. the asymptotic expression $(90 + 10/D_e)$ should be used.

The sheath temperature at burnout, $T_{w_{BO}}$, as given in Equation (4), is retained in the extended method. This equation is almost identical with the former expression (*10*) for $T_{w_{BO}}$ and differs only in the form of the last

term. This simplification prevents the correction term from assuming disproportionate magnitude for configurations of large heated diameter and small hydraulic diameter. Use of Equation (4) rather than the original formula (*10*) for $T_{w_{BO}}$ introduces negligible scatter into the predicted heat fluxes.

Table 1 presents a comparison of the original and extended methods of burnout prediction. The practice here, as in all the literature on the subject, is to evaluate the fit of a formula to the data by taking the arithmetic average of the ratios of predicted to observed burnout heat flux for a series of experiments. It is apparent that satisfactory agreement between prediction and experiment is provided by both prediction methods. Only two sets of data show significant change, McAdams and JPL (Gunther), and in both of these the extended prediction method is more conservative than the original.

TABLE 1. COMPARISON OF PREDICTION METHODS WITH DATA

Source of data	Experimental configuration	No. of tests	Ratio of predicted to measured burnout heat flux	
			Original method	Extended method
Col. Univ. (*12*)	Annuli	14	1.009	1.013
McAdams (*11*)	Annulus	6	1.173	1.009
UCLA (*13*)	Tube	42	1.09	1.094
ANL (*14*)	Tube	15	0.98	0.951
Purdue (*16*)	Tube	24	0.98	0.968
JPL (*15*)	Strip in duct	35	1.04	0.906
Aerojet (*40*)	Annulus	4	...	0.982
Lukomskii (*42*)	Tube	22	...	0.966
KAPL (*41*)	Ribbons	7	...	1.080
WAPD (*39*)	Duct	17	...	1.016
Col. Univ. (*43*)	Tube and annuli	12	...	0.840*

*See discussion, p. 102

Additional data in the forced flow regime have confirmed the validity of the extended prediction method. The fit of predicted to observed burnout heat fluxes is essentially the same for both formulas.

Table 2 presents a comparison of the extended method of burnout prediction with recent data of burnouts in pool boiling and in forced-convection systems with large hydraulic diameter. The agreement between predicted and experimental burnout heat fluxes appears as satisfactory for pool boiling as for confined, forced-flow systems.

TABLE 2. COMPARISON OF EXTENDED PREDICTION METHOD WITH NEW DATA

Source of data	Experimental configuration	No. of tests	Ratio of predicted to measured burnout heat flux
Col. Univ. (*25*)	Vertical tubes	2	0.982
Averin (*23*)	Horizontal tubes	12	1.016
Bendler (*33*)	Vertical tubes*	17	0.999
ANL-5822 (*18*)	Horizontal rod*	31	0.901
SRL (*32*)	Vertical tubes	8	1.054

*These tests conducted with forced flow of coolant.

Figure 3 is a distribution plot based on 240 experimental burnouts—72 in open and 168 in confined geometry—illustrating the fit between the predicted and observed burnout heat fluxes.

Based on the comparisons of Tables 1 and 2 and the distribution plot of Figure 3, it is recommended that the extended prediction method [Equations (2), (4), and (5)] be applied to the calculation of burnout heat fluxes in the local boiling regime.

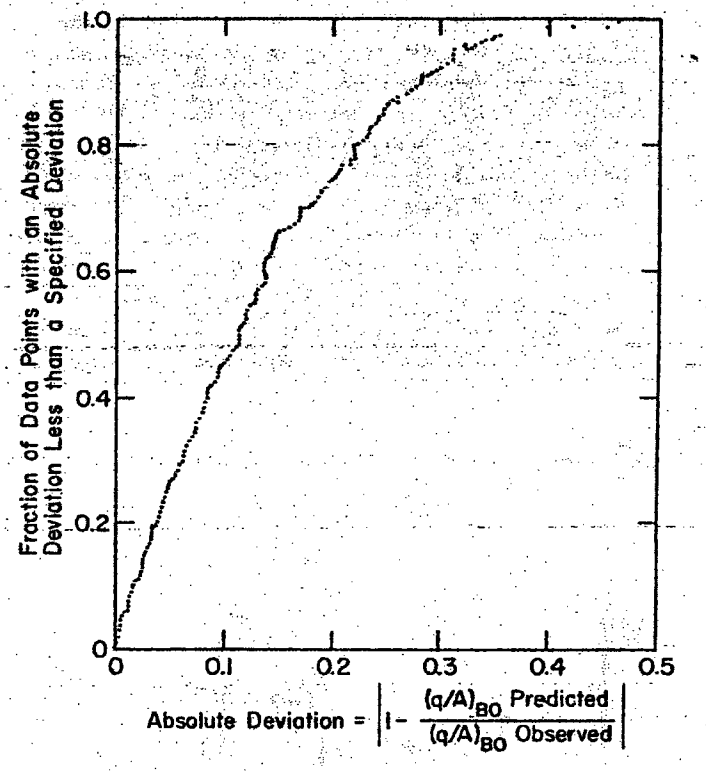


Fig. 3. Distribution plot as a goodness-of-fit test of prediction method (water data).

Generalization (to Other Fluids) of the Extended Method

Generalization of the method of burnout prediction to fluids other than water requires that both the wall superheat at burnout, $T_{w_{BO}} - T_{sat}$, and the limiting film coefficient, h_{BO}, be predicted for the experimental fluid. These quantities must be determined by the physical properties (thermal and thermodynamic) of the fluid. Furthermore, a fundamental requirement of the generalized method is that the environmental variables (coolant velocity and subcooling, and equipment geometry) influence the burnout heat flux in other fluids exactly as they do in water.

The wall superheat at burnout has been generalized by applying the principles of the law of corresponding states. Equation (4) was employed to compute values of wall superheat at burnout

$$T_{w_{BO}} - T_{sat} = 57 \ln P - 54\left(\frac{P}{P+15}\right) - \frac{V}{4} - T_{sat} \quad (4a)$$

for water at discrete pressure levels. At each of these same pressure levels the reduced saturation temperature for water was evaluated from $T_R = T_{sat}$ (°K.)/T_{crit} (°K.). Then a graph was plotted of $T_{w_{BO}} - T_{sat} + \frac{V}{4}$ vs. T_R. This graph (Figure 4), although constructed for water, is applicable to all liquids; it is based upon the assumption that a universal relationship exists between the maximum wall superheat (that can be sustained by any liquid) and the corresponding reduced temperature. Thus, it is tacitly assumed that the wall superheat at burnout reflects primarily the thermodynamic properties of the liquid and that the forces of adsorption (attraction) between the liquid and the surface of the heater are of secondary importance. This interesting side light will be mentioned further in a subsequent section on Pool Boiling Data.)

In the generalization of the limiting film coefficient, h_{BO}, the penetration theory of the mechanism of mass and heat transfer between two phases is applied to the local boiling process in order to establish the effects of the physical properties of the coolant on h_{BO}. The penetration theory, proposed by Danckwerts (*19*), assumes that the interface between the phases is continuously replaced by eddies and that unsteady state molecular transfer into the eddies controls the rate of transfer. It is assumed here that the penetration theory describes reasonably well the turbulent mixing that occurs at the incipient burnout condition.

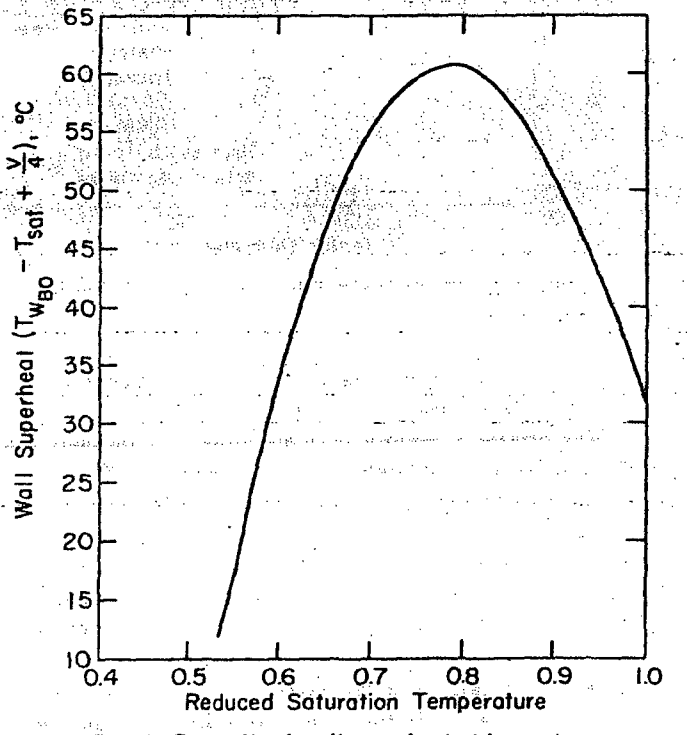


Fig. 4. Generalized wall superheat at burnout.

Following the development of Toor and Marchello (*20*), the heat transfer coefficient, h, is found to depend on the thermal conductivity, k, and the thermal, α, and momentum, ν, diffusivities of the coolant. It follows from the penetration theory that an increase in either k or α should cause the coefficient to increase, while an increase in ν should cause it to decrease. Also, the larger that the ratio of thermal to momentum diffusivity is for a coolant, the smaller should be the relative influence of the scrubbing action of free stream velocity. Therefore, the burnout heat transfer coefficient, h_{BO}, can be written as

$$h_{BO} \sim k\alpha^{0.5}/\mu^{0.4} \quad (6)$$

in which the exponents correspond to those of the Toor and Marchello treatment. Thus, Equation (5) in generalized form is

$$h_{BO} = 10{,}890\left[\frac{D_e}{D_e + D_i}\right]\left[\frac{k_I}{k_{II}}\right]\left[\frac{\alpha_I}{\alpha_{II}}\right]^{0.5}\left[\frac{\nu_{II}}{\nu_I}\right]^{0.4} + (\text{slope})\left[\frac{P_{cI}}{P_{cII}}\right]V \quad (7)$$

in which the subscripts I and II refer to the experimental coolant and water, respectively.* The ratio of critical pressures incorporated into the velocity-dependent term of h_{BO} was evaluated from burnout data for ammonia at 500 lb./ sq. in. abs.

Thus, the method of burnout prediction for fluids other than water consists of

1. Evaluating the reduced saturation temperature for the test coolant from the pressure at which the experiment is conducted.
2. Reading the value of $\left(T_{w_{BO}} - T_{sat} + \frac{V}{4}\right)$ from Figure 4.
3. Tabulating values of k, α, and ν for the test liquid at the saturation temperature of the test and for water at a temperature corresponding to T_R† evaluated in step (1) above.

*The numerical value of the group, $k\alpha^{0.5}/\nu^{0.4}$ evaluated for water, varies less than ±30% from the mean over the range of pressures from 0 to 2,000 lb./sq. in. abs.

†It should be clear that the saturation temperatures at which the physical properties of the experimental coolant and of water are evaluated are usually different. It is the *reduced* saturation temperatures that are identical.

4. Evaluating h_{BO} from Equation (7).
5. Computing the burnout heat flux from

$$\left(\frac{Q}{A}\right)_{BO} = h_{BO}\left[\left(T_{w_{BO}} - T_{sat} + \frac{V}{4}\right) - \frac{V}{4} + \Delta T_{sub}\right] \quad (8)$$

in which ΔT_{sub} is the subcooling of the experimental coolant.

Pool-boiling burnout data provide a test of the validity of the first term of Equation (7), whereas both terms are required in forced-convection experiments. The introduction of the physical properties of coolants into the prediction method [Equation (7)] creates the need for accurate data over wide ranges of temperature (particularly, thermal conductivity); unfortunately, there is a paucity of these data.

As a consequence of the numerous assumptions employed, the development presented above cannot be justified on any other basis than its ability to predict burnout heat fluxes with local boiling, determined under varied experimental conditions, for many liquids. The burnout heat fluxes predicted by that method are compared with the available data in Tables 3, 4, and 5. Table 3 presents the pool-boiling data for a number of coolants, Tables 4 and 5 present forced-flow data for ammonia and diphenyl, respectively. In all three tables of data the agreement between prediction and experiment is reassuringly satisfactory. It is noteworthy that the agreement for ammonia, for which fairly accurate physical property data are available, is as good as for water, whereas the somewhat poorer agreement for diphenyl may be attributed, in part at least, to the lack of accurate data for its physical properties.

DISCUSSION OF LOCAL-BOILING BURNOUT DATA

ATMOSPHERIC POOL BOILING OF WATER

Effect of Diameter of Heater

Nucleate boiling has been studied extensively in pools of saturated water at atmospheric pressure. Heat fluxes at burnout (critical heat flux) have been widely measured for electrically heated horizontal cylinders. Figure 5 summarizes graphically the effect of the diameter of the heater on the burnout heat flux. This graph shows that the burnout heat flux increases rapidly with increasing heater diameter initially and then gradually approaches an asymptotic value. (These data are also presented in Table 6.) The effect of diameter on burnout heat flux, for horizontal heaters, was noted by McAdams, et al (*21*), but with the limited range of data then available, it was assumed that the asymptotic value of 211,000 p.c.u./(hr.) (sq. ft.) was attained at diameters larger than 0.020 in. Figure 5 shows that for most metals the asymptotic value of burnout heat flux is approximately 265,000 p.c.u./(hr.) (sq. ft.) and that it is attained at diameters larger than 0.060 in.

The investigations of van Stralen, et al. (*22*), in pool-boiling heat transfer have demonstrated that there exists an interdependence of heater diameter (for wires), bubble size, and burnout heat flux. Van Stralen, working with a platinum heater of 0.008-in. diameter, found that a decrease of the system pressure (hence, an increase in bubble size) resulted in a decrease in the peak heat flux, and at 10 cm. Hg pressure the first bubble that formed resulted in burnout. He also found that with fixed system pressure, a refinement of bubble size (accomplished by small additions of volatile organic liquids to the water) resulted in raising the peak heat flux to more

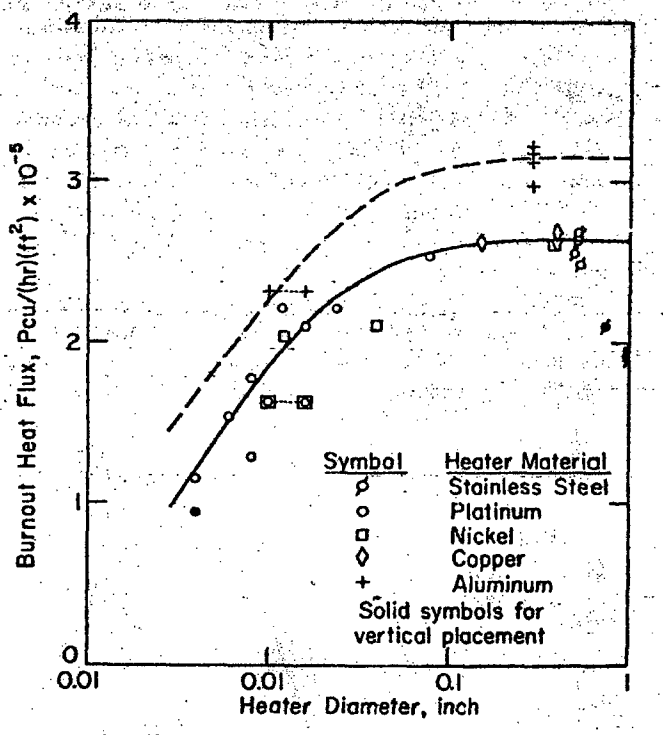


Fig. 5. Effect of heater diameter on burnout heat flux.

than twice its original value and to the "asymptotic" value for large heater diameters.

Van Stralen's results indicate quite convincingly that the mechanism that determines the peak heat flux attainable with wires is the following: when the diameter of the heater is of the same order of magnitude as the mean diameter of the bubbles formed on the surface, the number of "coincident" bubbles—those generated within a period less than the mean lifetime of bubbles on the surface—required to form a coherent vapor film is relatively small. And the larger the diameter of the heater, the larger is the number of coincident bubbles required to blanket the surface and consequently the

TABLE 3. COMPARISON OF GENERALIZED PREDICTION METHOD WITH POOL-BOILING DATA

Source of data	Coolant	Pressure, lb./sq. in. abs.	Subcooling, °C.	Dimensions of heater	Burnout heat flux P.c.u./hr.-sq. ft. × 10^{-3} Measured	Predicted
Westwater (52)	Methanol	14.7	0	¾ in. O.D. tube	63.8–77.1	66.9
McAdams (24)	Methanol	14.7	0	tubes	67.6	66.9
Noel (44)	Ammonia	500	5.6	⅛ in. × 0.004 in. strip	450	502 (335)*
			33.4		535	725 (484)
			55.5		668	902 (601)
Ellion (8)	Deaerated carbon tetrachloride	14.7	24.5	⅛ in. × 0.0043 in. strip	65.7	100
			47.0		109.5	135
			52.4		131	143.5
			83.2		174	191
			83.2		183	191
			88.6		228	200
			89.8		229	201
			91.4		229.5	204
			92.7		230	205

*These values include a factor (from Figure 5) which accounts for heater thickness.

higher is the heat flux at burnout. With large heater diameters, the peak heat flux is reached when the number of coincident bubbles per unit area corresponding to a coherent vapor film is attained; thus, the extent of the surface is no longer of importance.

The uniqueness of the asymptotic peak heat flux is clearly indicated by the wide variety of metals, surface finishes, and heater sizes that all result in the same value of burnout heat flux. As a consequence one must conclude that the burnout heat flux, under these experimental conditions, is a function only of the physical and thermal properties of the coolant.

TABLE 4. COMPARISON OF GENERALIZED PREDICTION METHOD WITH AMMONIA DATA (44)

Pressure: 500 lb./sq. in. abs. $d_o = d_i = 0.232$ in.

Coolant velocity, ft./sec.	Subcooling, °F.	Measured $(Q/A)_{BO}$, B.t.u./sq. in.-sec.	Predicted $(Q/A)_{BO}$, B.t.u./sq. in.-sec.	Ratio of predicted to measured $(Q/A)_{BO}$	Δ*, p.c.u./hr.-sq. ft.
89.9	10	3.97	3.87	0.975	29,000
60	10	2.25	3.28	1.459	297,000
30.2	10	2.10	2.28	1.082	52,000
30.2	10	2.40	2.28	0.948	35,000
3.2	10	1.63	1.05	0.645	167,000
82.1	60	5.80	6.20[5]	1.070	117,000
60	60	4.88	5.19	1.063	89,000
60	60	5.10	5.19	1.018	26,000
30.6	60	3.42	3.48	1.018	17,000
156.2	100	14.00	11.51	0.822	692,000
138.8	100	11.70	10.95	0.936	209,000
137.5	100	12.16	10.92	0.900	345,000
120	100	10.39	10.21	0.984	50,000
120	100	10.77	10.21	0.949	156,000
87.7	100	8.60	8.54	0.992	17,000
84.5	100	9.21	8.35	0.906	239,000
61.6	100	7.12	6.84	0.960	78,000
60.6	100	6.82	6.76	0.992	17,000
45.3	100	5.55	5.61	1.011	17,000
32.0	100	4.60	4.53	0.985	20,000
30.9	100	4.75	4.44	0.934	86,000
15.1	100	3.47	3.04	0.875	120,000
10.3	100	3.21	2.59	0.806	172,000
				Average = 0.971	132,000
					$\bar{\Delta}$ = 51,000 (15 tests)
					$\bar{\Delta}$ = 285,000 (8 tests)

*Δ = absolute difference between predicted and measured burnout heat fluxes. 1 B.t.u./sq. in.-sec. ≡ 518,400 B.t.u./sq. ft.-hr. ≡ 288,000 p.c.u./hr.-sq. ft.

Effect of Heater Material

The behavior of aluminum alone among all the metals investigated remains to be clarified. The data of both Averin (23) and Castles (24) show that aluminum surfaces require higher heat fluxes at burnout than do the other metals, all other experimental conditions being equal. Averin's measurements of the critical Δt show that aluminum tolerates a higher wall superheat (32.5°C.) than do the other metals (~26.5°C.) for atmospheric pool-boiling conditions. An interesting sidelight of Averin's measurements appears when values of h_{BO} are evaluated from $(Q/A)_{BO} \div \Delta t_{crit}$; as summarized in Table 6, h_{BO} is very nearly a constant for all of Averin's experiments, and the value found experimentally can readily be predicted by Equation (5). The constancy of Averin's values of h_{BO} creates considerable confidence in the accuracy of his measurements. Several experiments in subcooled pool boiling (to be discussed later) performed at Columbia University (25), utilizing aluminum, yielded data confirming Averin's findings.

Thus, one must conclude that under pool-boiling conditions aluminum requires a higher Δt_{crit} than do other metals. A plausible explanation of this fact may be found by considering the energy required to drive off water molecules from the hydrated oxides of metals. The energy with which water molecules are bound to hydrated metal oxides may be determined qualitatively by the emulsion stability of oil in water emulsions utilizing a metal oxide as the stabilizer. The experiments of Mukerjee and Srivastava (26) and King and Mukerjee (27) are summarized in the following table:

TABLE 5. COMPARISON OF GENERALIZED PREDICTION METHOD WITH DIPHENYL DATA[40]

$d_e = 0.272"$ (0.263" to 0.276") ; $d_i = 0.960"$

Test No.	Pressure psia	Velocity ft/sec	Subcooling °F.	Burnout Heat Flux Btu/hr-ft² ×10⁻³ Measured	Predicted	Ratio: Predicted/Measured	Δ Btu/hr-ft²
5	210	10.5	153	555	361	0.650	194,000
6	324	10.3	214	598	451	0.724	97,000
7	426	5.4	250	385	396	1.027	11,000
9	250	15.1	181	711	511	0.718	246,000
10	292	15.9	268	859	696	0.811	163,000
11	395	10.3	294	671	600	0.894	71,000
12	399	15.7	328	890	843	0.947	47,000
13	299	10.3	208	495	441	0.892	54,000
15	265	5.1	198	451	288	0.638	163,000
16	393	15.6	233	642	638	0.994	4,000
17	265	4.8	131	339	217	0.640	122,000
18	339	10.2	149	345	351	1.017	6,000
19	293	5.1	129	261	226	0.867	35,000
20	395	5.3	249	401	358	0.890	43,000
21	302	10.8	115	324	409	1.065	25,000
22	259	10.4	81	279	259	0.932	19,000
23	198	10.1	200	556	419	0.752	137,000
24	197	15.3	131	568	422	0.744	146,000
25	203	17.3	89	340	372	1.095	32,000
26	228	5.1	77	227	170	0.749	57,000
27	283	5.3	104	260	203	0.780	57,000
28	380	16.4	156	485	488	1.006	3,000
29	273	5.2	164	277	264	0.952	13,000
TEST 29 CONCLUDES EARLY TEST SERIES.					AVERAGE:	0.865	67,000
42	57	.21	0	117	138	1.179	21,000
43	23	1.35	20	109	63	0.575	46,000
44	51	5.1	0	123	92.5	0.752	30,000
45	266	10.0	28	146	194	1.048	8,000
46	32	4.8	0	152	83.4	0.549	69,000
47	59	9.5	29	193	158	1.096	11,000
48	34	14.2	13	280	181	0.646	99,000
49	65	14.4	28	198	224	1.130	26,000
50	100	5.0	8	145	104	0.715	41,000
51	93	7.6	15	84	157	1.869	73,000
52	165	14.4	0	96	179	1.860	53,000
53	199	14.8	32	138	230	1.729	97,000
54	45	1.0	10	74	60	0.812	14,000
55	100	1.0	0	141	595	0.422	81,000
56	265	1.05	138	188	157	0.834	31,000
57	397	1.04	99	140	125	0.891	15,000
58	226	5.0	22	137	116	0.850	21,000
59	309	1.99	129	195	169	0.867	26,000
60	321	0.95	159	176	164	0.930	12,000
61	312	0.95	51	113	91	0.805	22,000
62	326	0.47	75	136	107	0.785	29,000
63	314	1.99	83	153	133	0.871	20,000
64	215	1.52	0	93	61	0.655	32,000
65	363	1.0	20	100	74	0.744	26,000
66	356	1.9	72	146	123	0.841	23,000
					AVERAGE:	0.937	38,000

TABLE 6. EFFECT OF HEATER DIAMETER ON BURNOUT HEAT-FLUX ATMOSPHERIC POOL BOILING—HORIZONTAL HEATERS—H_2O

Heater Material	Investigator	Heater Diameter-in.	Burnout Heat Flux Btu/hr-ft² ×10⁻³ (a)	(b)	Critical Δt-°C.
Stainless Steel	Averin[23]	0.594	249	257	26.1
"	"	0.590	266	257	27.0
"	"	0.590	269	257	26.8
"	"	0.590	265	257	27.0
"	"	0.515	256	259	24.0
Nickel	"	6.398	262	266	28.4
Copper	"	0.405	262	266	26.3
"	"	0.407	268	266	26.7
"	"	0.156	262	280	26.4
Aluminum	"	0.292	312	333	32.5
"	"	0.292	320	333	33.0
"	"	0.292	317	333	33.0
"	"	0.292	297	333	32.0
Platinum	Kazakova[53]	0.006	154		—
"	"	0.012	205		—
Nichrome	"	0.077	254		—
Platinum	van Stralen[22]	0.008	130		33
"	Rinaldo[54]	0.004	117		—
"	"	0.0081	178		—
"	"	0.016	211		—
"	"	0.0239	222		—
"	Day[21]	0.0117	222		—
Nickel	Farber & Scorah[39]	0.040	211		—
"	Castles[24]	0.010–0.016	163		—
Platinum	"	0.010–0.016	163		—
Aluminum	"	0.010–0.016	232		—
(Vertical Platinum)	Moscicki & Bedder[20]	0.004	99.5		30.2

(a) Measured value
(b) Predicted value

TABLE 7. STABILITY OF EMULSIONS UTILIZING METAL OXIDES AS STABILIZERS

Metal	Relative stability
Al (precipitated at 100°C. and boiled 4 hr.)	183.45
Al (precipitated at 100°C.)	67.3
Al (precipitated at 18°C.)	12.6
Ni	57.3
Fe	52.0
Cr	56.25
Cu	16–20

These results show that boiled hydrated aluminum oxide is severalfold more effective in adsorption of water molecules than are the other metal oxides investigated. Until data become available to permit alternate explanations of the difference in the behavior of aluminum and the other metals, the explanation presented above is accepted as being reasonably accurate.

*Effect of Surface Roughness**

Corty and Foust (28) and other investigators have established the fact that the roughness of heater surfaces affects the relationship between heat flux and tempera-

*Roughness is here considered to be microscale, i.e. smaller than the diameters of bubbles, and hence does not cause an increase in the effective heat transfer area.

ture difference in local boiling. Only the researches of Farber and Scorah (*29*) and Averin are available to estimate this effect on peak heat flux. Averin's data show no connection between roughness and peak heat flux although his nucleate boiling data confirm the findings of Corty and others. Farber and Scorah, however, claim to have detected an effect of roughness. As a consequence of these facts, that (1) these workers used a small heater diameter (which introduces that variable, as discussed above) and (2) Averin's measurements have been found to be very accurate, one must conclude that the relative microroughness of the heater surface does not influence the burnout heat flux.

Effect of Heater Orientation

The entire discussion above has been based on data obtained with heaters placed horizontally. A few experiments have been conducted with vertical placement of the heated element. A comparison of these data with those discussed above reveals that a vertical surface in pool boiling burns out at a heat flux that is approximately three quarters of the value obtained with horizontal surfaces.

Mosciki and Broder (*30*) were the first to report that a "horizontal wire does not give up heat uniformly"; they referred to the flow of vapor from the underside of a horizontal cylinder, which causes bubbles to be liberated preferentially from the upper portion. "So, experiments were conducted with the wire mounted vertically and a stirrer placed half-way along the wire to maintain uniform liquid temperature." They obtained a value of burnout heat flux, approximately 20% less than that found by Rinaldo (*31*) with very nearly the same heater diameter (~ 0.004 in.). This data point is shown in Figure 5.

More recent data, obtained by Mirshak* (*32*), have been compared with the data of Averin; a value of 0.77 is obtained as the ratio of vertical-to-horizontal burnout heat flux.

The data of Bendler (*33*) (to be discussed below), upon interpolation of the results to obtain values corresponding to atmospheric pool boiling, when compared with the asymptotic value of burnout heat flux of Figure 5, yield 0.76 as the ratio of vertical-to-horizontal burnout heat flux.

It is reasonable to expect that a vertically placed heater would burnout at a lower heat flux than one placed horizontally, all other experimental conditions being the same. The boiling film, described by Begell and Bernath (*9*), surrounding a horizontal cylinder is nonuniform (according to Mosciki and Broder), being much thinner on the bottom than on top. With vertical heater placement, the boiling film is uniform in thickness around the surface of the heater at any given elevation. It varies, however, from the bottom of the heater, where it is thin, to an elevation beyond which its effective thickness is constant. This brings forth the observation, to be discussed more fully later, that short vertical heaters, where the boiling film has not been able to attain its equilibrium thickness, should burn out at higher heat fluxes than are obtained with long heaters.

Observations of horizontally placed heaters operating nearly at peak heat flux have revealed that although the upper surface is fully blanketed by vapor (and hence in the transition boiling regime), the lower surface continues to liberate heat via local boiling. Clearly, operation of this sort is impossible with vertical heater placement. It is reasonable, therefore, to postulate that the higher burnout heat flux with horizontal heaters stems from the convection currents that are induced by the liberation of bubbles from the top of the heater. These currents reduce the lifetime of bubbles on the underside by thinning the boiling film. In order to form a stable vapor film on the underside of the heater, a higher heat flux is required. One might argue that, although in pool boiling, a horizontal heater possesses some of the heat transfer properties of a surface cooled by forced convection.

SUBCOOLED POOL BOILING OF WATER AT SEVERAL PRESSURES

Systematic measurements of burnout heat flux for vertical heaters in pool boiling were made at Columbia University in Task IX, a fundamental investigation of boiling conducted under A.E.C. sponsorship. Details of this study are to be reported by A. J. Bendler. Table 7 presents the data assembled to date.

Effect of Heater Length—Vertical Placement

Figure 6 depicts graphically the effect of heater length on the burnout heat flux for vertical heaters boiling in water at a pressure of 93 lb./ sq. in. abs. and a subcooling of 97°C. The data clearly show that heater lengths shorter than 8 in. require higher heat fluxes to burn out, while the burnout heat flux is essentially constant for longer heaters. Successively shorter heaters burn out at heat fluxes approaching the asymptotic value for horizontal cylinders. The ratio of the burnout heat flux for long heaters to that for horizontal cylinders, as computed by use of the extended prediction method described earlier, is found to be 0.76. This result tends to confirm the universality of this ratio; it is identical, within the limits of the highest experimental accuracy, with the value obtained from boiling experiments in saturated pools at atmospheric pressure.

Effect of Heater-Wall Thickness

Nickel heaters 0.50 in. diameter and 0.005 in. in wall thickness were utilized to study local-boiling heat trans-

*These data were obtained with 12 in.-long stainless steel heaters in a large pool. The data at large subcoolings are unfortunately quite variable since the pool was not kept at constant temperature; close to saturation, however, the data appear quite reproducible.

fer from vertical heaters. Burnout heat fluxes measured with these heaters were found to be significantly lower than those obtained with solid nickel heaters. The data of a brief investigation of this effect are summarized in Table 7 and Figure 7.

This study revealed (1) that the curve of burnout heat flux vs. heater-wall thickness, for similar experimental conditions, bears a remarkable resemblance to the curve of burnout heat flux vs. heater diameter for saturated pool boiling (Figure 5) and (2) that the ratio of burnout heat fluxes for thin- (say, 0.005 in.) and thick-wall, vertical heaters at a pressure of 93 lb./sq. in. abs. and with subcooling is approximately the same as the ratio

TABLE 7. POOL BOILING DATA FOR VERTICAL HEATER PLACEMENT

L, Inches	d_o, in.	d_i, in.	T_b, °F	P, Psia	Burnout Heat Flux, Btu/hr-ft² × 10⁻⁶ (a)	Burnout Heat Flux, Btu/hr-ft² × 10⁻⁶ (b)	Ratio: Predicted/Measured	ΔP_{ave}, psi	Source of Data
16	3.638	0.175	64.7	93	1.154	1.189	1.049	15	Bendler-Thesis II*
12	"	"	"	"	1.156	1.169	1.013	13	
6	"	"	65.5	"	1.192	1.180	(0.989)	(12)	Col. Univ.[33]
12	"	"	23.4	"	1.471	1.498	1.018	27	
12	"	"	152.3	"	0.533	0.489	0.915	45	
12	"	"	195.2	"	0.899	0.889	0.944	50	
12	"	"	104.9	248	1.268	1.250	1.034	42	
12	"	"	65.0	252	0.718	0.701	0.976	19	
12	"	"	106.1	"	0.552	0.575	1.044	23	
12	"	"	23.6	"	1.629	1.654	1.027	27	
12	"	"	144.3	242	0.977	0.910	0.932	17	
12	"	"	66.0	2448	1.566	1.571	1.003	5	
12	"	"	23.7	2476	1.597	1.709	1.073	132	
12	"	"	65.6	4.4	0.490	0.503	0.570	12	
12	"	"	14.6	4.3	0.482	0.507	1.051	25	
12	"	"	30.0	4.4	0.523	0.532	1.016	9	
8	"	"	63.1	93	1.179	1.181	1.004	4	
12	"	"	40.8	2725	0.879	0.895	1.025	21	
4	"	"	63.6	93.1	1.24	1.178	(0.977)	(96)	
2	"	"	64.1	93	1.257	1.173	(0.935)	(14)	
12	"	"	53.4	4.6	0.207	0.209	1.002	1	
12	"	"	62.4	12.8	1.173	1.173	1.000	0	
12	3.670	0.254	64.5	93.9	1.132	1.182	1.043	50	
12	3.701	0.252	64.5	93.1	1.206	1.190	0.989	14	
48 H	~7	0.173	63.0	93.2	1.589	1.586	0.998	43	Horizontal Heaters
48 H	~7	0.458	68.1	27.2	0.292	0.939	1.050	45	
6	4.0	2.0	90	147	0.296	0.296	0.958	10	Col. Univ.[25]
6	4.92	1.04	50	147	0.540	0.544	1.009	4	Thesis II**
12	2.25	0.75	98	147	0.228	0.229	1.005	1	SKL***[32]
12	"	"	95	"	0.259	0.253	0.976	1	
12	"	"	99	"	0.222	0.221	0.995	1	
12	2.10	1.0	90	"	0.192	0.219	1.138	27	
12	"	"	99	"	0.206	0.219	1.061	13	
12	"	"	95	"	0.220	0.250	1.138	20	
9	2.25	1.75	90	"	0.240	0.250	0.965	10	

(a) Measured Burnout Heat Flux.
(b) Predicted Burnout Heat Flux, using a vertical-to-horizontal factor of 0.765 for all vertical test results.

* Nickel heaters & coolant velocity of 0.4 ft/sec for all tests.
** Aluminum heaters — Used 32.5°C for wall superheat, per Averin (see Table II).
*** Stainless steel tubing used for heaters.

of burnout heat fluxes for the corresponding heater diameter ratio (0.010 in. and large diameter heaters with horizontal placement) in atmospheric pool boiling, about 0.70.

The comparison of the performance of heaters of small diameter and thin wall-thickness presented is a logical extension of the results of van Stralen, discussed earlier, which illustrate that with heaters of small thermal capacity, the size of the bubbles generated at the surface, or actually the thickness of the boiling film, greatly influences the heat flux at burnout. The fact that the 93 lb./ sq. in. abs. data were obtained with subcooled water should not appreciably influence the validity of the preceding comment since both thick- and thin-walled tubes

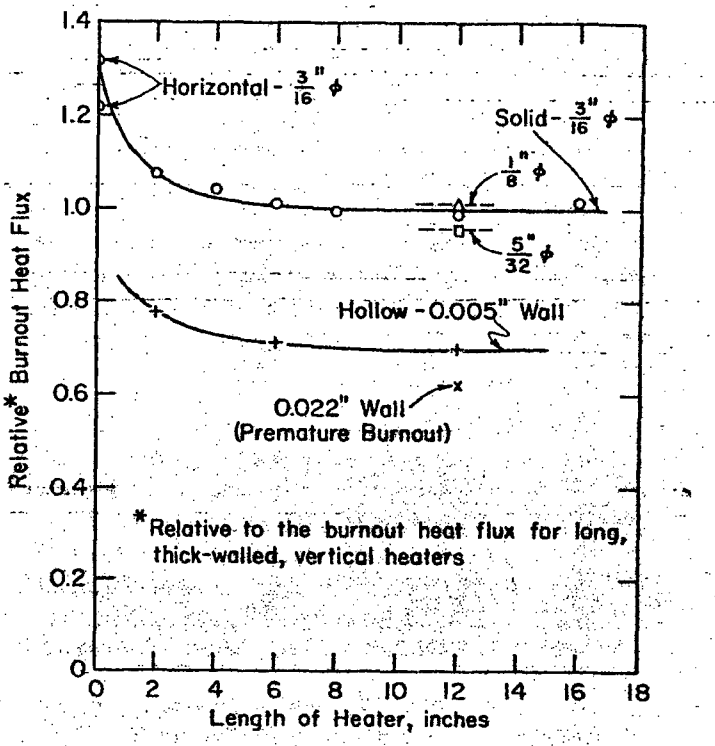


Fig. 6. Effect of vertical heater length on burnout heat flux in pool boiling.

were tested under identical conditions. Furthermore, following the boiling film concept of Begell and Bernath, the effect of subcooling alone on the boiling film thickness (hence, on the maximum bubble size) is slight under pool-boiling conditions.

The introduction here of the influence of boiling-film thickness on the results obtained in burnout experiments permits clarification of effects of the experimental variables on the burnout heat fluxes measured. The comments that follow are of particular importance in the planning of experiments, to be performed on a small scale, to simulate the burnout behavior of much larger equipment, e.g., reactor fuel elements. On the assumption that coolant conditions (pressure, subcooling, and velocity or pressure-drop per unit length of flow path) are accurately simulated, the heater should be made long enough to permit attainment of the equilibrium boiling-film thickness. Also, the thermal capacity of the heater should be selected to prevent a small vapor patch, corresponding to less than equilibrium boiling-film thickness, from causing premature burnout. Continuing with this reasoning, a heater thickness that is too small in pool boiling may be adequate in experiments with forced flow, in which the equilibrium thickness of the boiling film is appreciably less. The data of McAdams et al. (*11*), to be discussed later, illustrate and tend to confirm the last statement; these data show that a tube-wall thickness of 0.012 in.,

although adequate at velocities of 12 and 4 ft./sec., was not thick enough at a velocity of 1 ft./sec. to prevent premature burnouts, even though the burnout heat flux at low velocity is lower than that at high velocity.

The effects of the thicknesses of the boiling film and of the heater wall are quantitatively combined in the Biot modulus; $N_B = hR/k$ for solid cylinders and $N_B = hX/k$ for tubes, where X is the wall thickness. Since the thickness of the boiling film is inversely proportional to the heat transfer coefficient, the Biot modulus is essentially the ratio of wall thickness to boiling film thickness. The data for platinum, presented in Figure 5, permit the evaluation of the minimum value of the Biot modulus that is representative of "thick" heater burnout data. For pool boiling, h_{BO} is very nearly 10,000, k for platinum is 42, and X_{min} is approximately 0.060/12 (all in consistent units); thus, N_B (minimum for platinum) is about 1.2. This analysis implies that the minimum value of the Biot modulus that results in unaffected values of burnout heat flux is a function of the heater material. Unfortunately the range of heater-wall thicknesses required to test this hypothesis has not been adequately covered in burnout experiments for materials having thermal conductivities significantly different from platinum, e.g. stainless steel ($k \approx 9$) and aluminum ($k \approx 120$) or copper ($k \approx 220$). It is suggested that pool-boiling experiments of the type necessary to test this concept should be fruitful and rewarding.

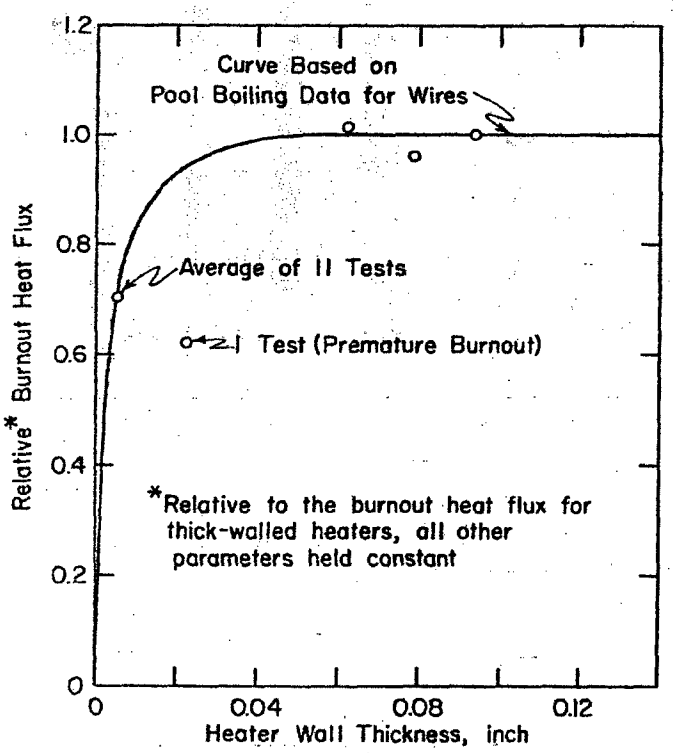


Fig. 7. Effect of heater wall thickness on burnout heat flux in pool boiling.

Comparison of Experimental and Predicted Burnout Heat Fluxes

The data of Bendler (*33*) (for "long," "thick" heaters) are assembled in Table 7 and presented graphically in Figure 8. The ranges of the experimental parameters are listed below.

Pressure, lb./sq. in. abs.	4.2 – 248
Bulk temperature, °F.	58 – 302
Subcooling, °F.	7 – 318
Velocity, ft./sec.	0.06 – 0.67*
Burnout heat flux, B.t.u./(hr.)(sq. ft.) (°F. × 10^{-6})	0.335 – 3.20

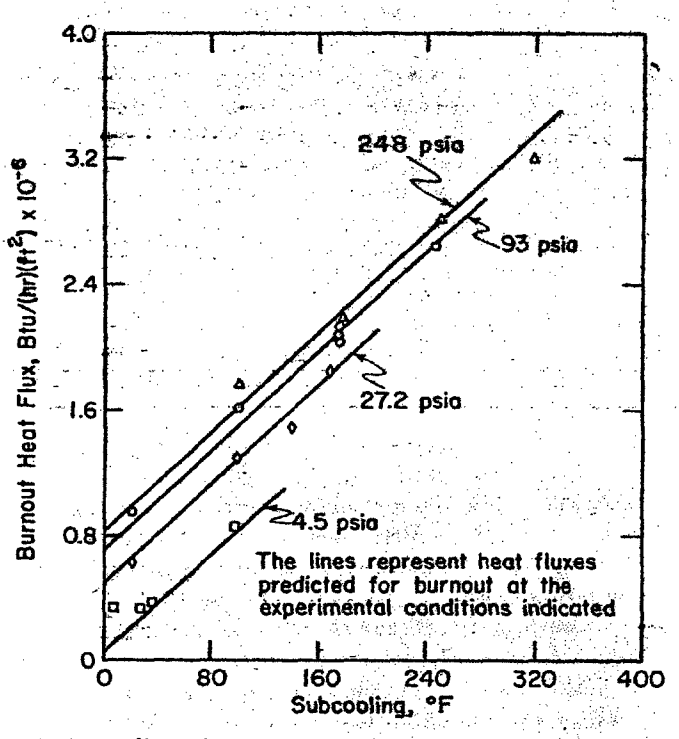


Fig. 8. Effect of pressure and subcooling on pool-boiling burnout heat flux.

The results are plotted as the points in Figure 8. The lines drawn through the data points in Figure 8 are predicted values computed by the extended prediction method (see above), modified to the extent that the coefficient of the first term of Equation (5) was taken as (0.76) (10,890) to reflect the vertical placement of the heaters. Both Figure 8 and Table 7 show a consistent and close agreement between experimental and predicted heat fluxes. These data and those of Averin represent

*The entire range of velocity, although encompassing an order of magnitude, lies well within the values of the bubble-induced convection currents for pool-boiling experiments. No significant effect of velocity, in this range, on burnout heat flux could be established.

the best—most accurately reproducible—measurements of burnout heat flux available in the literature.

Methods of Comparing Data and Predicted Values

The high precision of these data permits resolution of this important question: what is the best, hence most accurate, way to determine how well a prediction method fits the data? The usual method of comparison has been to take the ratio of the predicted value to the experimental value without regard to the absolute magnitude of the values themselves. Implicit in this method is the assumption that the probable error involved in a measurement is proportional to the magnitude of the quantity measured. There is no a priori reason for this assumption. The data above have been grouped into intervals of heat flux, 0 to 1, 1 to 2, and 2 to 3 millions of B.t.u./(hr.) (sq. ft.). The difference between measured and predicted values of burnout heat flux were tabulated according to these intervals. Average values of the differences are shown below.

Interval of burnout heat flux, B.t.u./(hr.) (sq. ft.)	Average difference, B.t.u./(hr.) (sq. ft.)
0 to 1×10^6	85,500
1 to 2×10^6	76,800
2 to 3×10^6	51,000
All data taken as one group	72,000

The percentage difference, as obtained by the ratio method of comparison, varies from 72,000/500,000 = 14% to 72,000/2,500,000 = 3% although the difference is constant. Thus, these data show that the difference method of comparison is a more valid measure of the fit than is the ratio method.

Approximately 200 values of burnout heat flux from at least one dozen different sources were grouped as above. The differences within the individual groups were subjected to the F test for determining the statistical probability that they all belonged to the same population. The results of these computations show clearly that the differences between the measured and predicted heat fluxes were independent of the magnitude of heat flux to a high degree of statistical significance (greater than 95% probability).

As a consequence of the foregoing discussion, it would appear that an accurate way of determining the goodness-of-fit of a prediction method is by comparing differences between the measured and predicted values over a wide range of magnitude of the measured quantity. Small differences in each of the groups indicate a good fit. Furthermore, once a prediction method has been found to fit a large body of data accurately, it can be used to test the accuracy of new data. On this basis, it was possible to state unequivocally that the data of Chirkin and Iukin (*34*) was unsuitable for inclusion with the other data assembled in this work. This conclusion is bolstered by the conspicuous absence of mention of these data in the Russian papers presented recently in Geneva.

Subcooled and Forced Flow, Pool Boiling

Until 1958 there were no burnout data available in this category. However, Kezios and Lo (*18*) published their results and Leppert and coworkers (*35*) obtained two burnouts during their study. Both investigations utilized horizontal heaters of small diameter in large rectangular ducts with upflow of coolant covering a range of velocities.

These data are presented in Table 8 together with values of burnout heat flux predicted by the extended method discussed earlier. The over-all agreement is satisfactory although several data points are 25% higher than predicted (380,000 to 500,000 p.c.u./(hr.) (sq. ft.). These differences are significantly larger than the average of all others (118,500 p.c.u./(hr.) (sq. ft.). The

TABLE 8. FORCED FLOW, POOL BOILING WITH HORIZONTAL HEATERS

DATA OF KEZIOS & LO[18]: $d_o = 13"$; $d_i = 0.125"$ (SOLID ROD)

Test No.	T_b °C.	P psia	V ft/sec	Burnout Heat Flux Btu/hr-ft² ×10⁶ Measured	Predicted	Ratio: Predicted/Measured	Δ Btu/hr-ft² ×10⁻³
1	43.4	17.3	1	1.060	0.988	0.932	72
2	42.8	18.1	2	1.129	1.032	0.914	97
3	43.2	19.2	2	1.129	1.032	0.914	97
4	43.8	21.0	3	1.184	1.076	0.908	108
5	44.8	23.6	4	1.229	1.129	0.919	100
6	34.1	24.9	5	1.445	1.306	0.904	139
7	53.3	29.25	6.8	1.580	1.183	0.758	397
8	16.6	17.75	1	1.440	1.299	0.907	131
9	13.9	18.9	2	1.531	1.346	0.879	185
10	13.6	20.7	3	1.578	1.404	0.890	174
11	17.2	23.45	4	1.628	1.430	0.879	198
12	20.6	26.4	5	1.730	1.473	0.851	257
13	11.1	30.3	6.8	2.082	1.676	0.805	406
14	60.7	17.4	1	0.991	0.991	1.000	0
15	62.0	18.7	2	0.886	0.809	0.913	77
16	60.1	20.3	3	0.968	0.878	0.907	90
17	63.4	23.0	4	1.058	0.969	0.836	179
18	64.1	26.3	5	1.137	0.995	0.857	162
19	63.0	29.6	6.8	1.250	1.065	0.852	185
20	81.6	17.7	1	0.4695	0.571	1.217	101
21	81.8	18.6	2	0.554	0.537	1.059	93
22	78.5	20.25	3	0.644	0.674	1.046	30
23	79.7	22.75	4	0.747	0.726	0.972	21
24	81.2	25.9	5	0.891	0.776	0.871	115
25	78.9	29.6	6.8	1.033	0.824	0.836	149
26	29.4	19.75	1	1.020	1.140	1.117	110
27	29.4	20.6	3	1.525	1.227	0.804	298
28	29.4	24.7	5	1.828	1.376	0.753	452
29	29.4	28.8	2	1.329	1.194	0.898	133
30	29.4	29.4	4	1.621	1.298	0.801	323
31	28.9	30.2	6.8	1.969	1.463	0.744	506
					AVERAGE:	0.901	172

$\bar{\Delta}$ = 112.5 (FOR 25 TESTS)

DATA OF LEPPERT, ET AL.[35]: $d_o = 1.89"$; $d_i = 0.110"$ (0.011" WALL THICKNESS)

1	77.2	16.75	0.5	0.505-0.650	0.590	0.984	9 (FOR AVERAGE)
2	96.2	16.75	0.9	0.853-0.284	0.371	1.38	103 (" ")

{TEST #2 IS APPARENTLY A "PREMATURE" BURNOUT, SINCE THE BURNOUT HEAT FLUX FOR SATURATED WATER IS GREATER THAN THESE MEASURED VALUES, VIZ. 0.289×10^6 Btu/hr-ft²

average difference between measured and predicted burnout heat fluxes for these data is threefold greater than the average difference noted for Bendler's data. This last statement is not an indictment; it is simply fact and may, in part at least, be attributed to the use of an alternating-current power supply, with its attendant uncertainties. Perhaps unnoticed vibrations occurred in the limber (L/D of 80) heaters. The influence of vibration on the burnout heat flux will be discussed at length in a later section.

POOL BOILING—COOLANTS OTHER THAN WATER

These data, summarized in Table 3, were all obtained with horizontal heaters. It is interesting to note that the effect of the thermal capacity of the heater on burnout heat flux is clearly indicated, as it was with water as coolant.

An oft-quoted source of data of this type, namely the work of Cichelli and Bonilla (*36*), is not included in Table 3. The primary reason for this stems from the nature of the experimental apparatus employed; it is difficult to establish the meaning of hydraulic and heated diameters for such equipment. The assumptions required to define these parameters would cast doubt on the validity of the comparison of experimental and predicted burnout heat fluxes.

FORCED FLOW IN CONFINED GEOMETRY—WATER COOLANT

Among the groups of data to be discussed in this section are many that were used to establish and test the original prediction method. These data are grouped, according to the source, in Table 9.

Columbia University—Task IV Data

These data were obtained from large-scale experiments in which aluminum heater tubes, cooled externally by water flowing in annuli, were employed. Details of the experimental setup have been presented in recent publications (*37*). The heat transfer data obtained in this investigation are unique in the literature; the large power source employed permitted use of aluminum heaters, with which very accurate wall temperature data at quite high heat fluxes could be gathered.

Table 9-1 presents the data together with values of burnout heat flux predicted from the extended method. It should be noted that these data are typical of closely controlled experiments; i.e., the maximum difference between predicted and measured burnout heat flux is approximately twice the average value. Also, these data further illustrate the point discussed under Methods of Comparing Data; run 16 has the widest percentage difference, but the actual difference lies near the mean for the distribution.

It was noted earlier that the pool-boiling burnout data for aluminum revealed that it could sustain a higher wall superheat than any of the other metals. A similar effect cannot be detected in the results of the forced-flow tests reviewed above. It may be that under conditions of a thin, intensively turbulent, boiling film the oxide layer on aluminum is hydrated to a different (less effective) degree. It is well known that aluminum oxide forms a number of distinctly different hydrated compounds with water within a rather narrow temperature range (100° to 200°C). Whatever the reason for the change in behavior of aluminum, the forced flow results for all metals investigated confirm that the heater-wall temperature at burnout is given by the single expression, Equation (4).

McAdams's Data (11)

These data are presented in Table 9-2; they were obtained with thin-walled, stainless steel tubes, cooled by water flowing in an annulus, as noted on page 110. Comparison of the predicted and measured heat fluxes shows that the first three runs are not at all representative of this group of data. The differences for these runs are threefold (or more) larger than the average of those for the higher velocity experiments. One may conclude then that, under the conditions of these experiments (low velocity) as in pool boiling (see Figure 7), a wall thickness of 0.012 in. is insufficient to prevent premature burnout. The agreement between measured and predicted heat fluxes at burnout is excellent for the six runs at the higher velocities.

U.C.L.A. Data (13) Table II of ANL-4627

These data are presented in Table 9-3; they were obtained with stainless steel tubes cooled internally by water. Analysis of these data shows that the differences between predicted and measured burnout heat fluxes lie in two distinct classes, almost as though the two groups of experiments had been performed in separate laboratories or had been conducted by different operating personnel. The table below illustrates this comment.

U.C.L.A. BURNOUT DATA

Data group	Coolant pressure, lb./sq. in. abs.	Difference,* p.c.u./(hr.) (sq. ft.)	Number of experiments
1	2,000	232,000	21
1a	2,000	31,000	10
1b	2,000	416,000	11
2	1,000	196,000	8
2a	1,000	29,000	3
2b	1,000	297,000	5
3	500	289,000	13
All	500, 1,000 and 2,000	243,000	42

* Difference between predicted and experimental burnout heat flux—see Table 9-3.

Although this analysis casts doubt on the validity of some of these data, they constitute so large a contribution to the knowledge of burnout behavior at high pressures that all points have been accepted in this study.

A.N.L. Data (38)

These data represent the few experiments that attained burnout conditions in the local-boiling region in a massive study of burnout with bulk boiling. The data, for internally cooled tubes, are presented in Table 9-4. The

tabulated differences (between predicted and measured heat fluxes) show that, except for the three replicate runs at 1,000 lb./sq. in. abs., very good agreement is obtained for essentially saturated coolant conditions; even including these three runs does not cause the average

TABLE 9. COMPARISON OF PREDICTION METHOD WITH DATA—FORCED FLOW "CONFINED" GEOMETRY

Part 1 – Col. Univ. – Task IV[12] – Aluminum Heaters (d_i = 1.08 in.)

Test No.	T_b °C	P psia	V ft/sec	d_e inch	Burnout Heat Flux Btu/hr-ft² ×10⁻⁶ Measured	Predicted	Ratio: Predicted/Measured	A ft-hr-°F²/Btu ×10³
13	95.4	29.2	11.3	0.49	0.371	0.415	1.19	44
14	95.6	29.0	8.6	"	0.347	0.417	1.202	70
15	93.2	32.9	17.4	"	0.735	0.724	0.985	11
16	89.4	28.1	6.5	"	0.201	0.293	1.458	92
17	89.9	28.2	11.6	0.500	0.460	0.445	0.996	2
18	90.1	31.0	17.5	"	0.734	0.593	0.809	14
19	28.2	28.1	17.5	0.250	0.759	0.648	0.855	11
20	88.1	29.3	11.6	"	0.578	0.461	0.800	19
23	105.5	57.0	29.4	0.500	0.535	0.624	1.065	89
25	93.5	32.9	23.4	"	0.695	0.724	1.071	49
34	122	68.7	10.5	"	0.570	0.494	0.865	76
48	104	63.7	5.9	"	0.485	0.468	1.016	33
50	99	62.1	11.7	"	0.590	0.565	0.991	5
88	110.2	44.5	21.6	0.580	0.865	0.778	0.899	17
						Average:	1.018	42

Part 2 – McAdams'[18] – Stainless Steel Heaters (d_i = 0.25" & 0.012" wall)

1	136.6	60	1	0.520	0.296	0.406	1.484	132
2	122.4	60	1	"	0.362	0.530	1.465	* 158
3	93.6	60	1	"	0.1974	0.735	1.332	261
4	117.2	60	4	"	0.573	0.608	1.041	35
5	119.7	90	4	"	0.584	0.650	1.116	66
6	133.3	60	12	"	0.650	0.590	0.908	60
7	117.1	60	12	"	0.713	0.800	1.085	27
8	93.4	60	12	"	0.418	1.015	0.991	33
9	64.2	30	12	"	1.050	0.990	0.961	40
						Average:	1.009	65.5 (6 tests)

* The first three runs appear to be "premature" burnouts (see text).

Part 3 – UCLA[13] – Stainless Steel Heaters ($d_i = d_e$ = 0.226")

651	330	2000	6.7	0.422	0.443	0.695	179
654	311.5	"	6.3	0.616	0.525	0.548	31
657	317	"	6.4	0.578	0.540	0.735	88
661-B	308	"	25.1	1.198	1.200	1.036	42
669	319	"	25.8	1.044	1.028	0.983	16
670	326.5	"	26.5	0.8995	0.910	1.023	21
671	332	"	27.2	0.790	0.802	1.016	12
674	263	"	22.5	1.621	1.903	1.174	282
675	259	"	23.9	1.528	1.518	1.197	196
678	244.5	"	21.9	1.643	2.190	1.332	447
680	260	"	22.0	1.571	1.930	1.229	359
682	270	"	22.6	1.460	1.788	1.207	328
683	256	"	21.9	1.611	1.996	1.239	385
684	331	"	54.1	1.329	1.210	0.911	119
685	335	"	54.0	1.267	1.220	0.966	49
686	332	"	58.7	1.199	1.177	1.032	32
687	317	"	31.0	1.516	1.599	1.021	33
688	318.5	"	47.0	1.678	1.708	1.019	30
689	291	"	42.0	1.859	2.127	1.148	273
690	282	"	44.5	1.977	2.900	1.466	923
691	265	"	44.5	2.100	2.975	1.420	825
692	221	500	20.6	1.390	1.196	0.860	194
695	282	"	20.6	1.511	1.180	0.780	831
696	262	1000	44.0	1.521	1.877	1.234	376
697	272	"	45.0	1.222	1.665	1.346	425
699	254.5	"	21.6	1.183	1.360	1.098	119
700	278.5	"	22.6	0.984	0.962	0.978	22
703	216.5	500	40.4	1.530	1.944	1.297	444
704	238.5	"	42.0	1.482	1.572	1.330	390
705	225	"	42.4	1.072	1.499	1.397	427
707	223.5	"	40.7	1.332	1.643	1.234	311
708	231	"	40.5	1.249	1.562	1.256	378
709	226	"	42.0	1.135	1.500	1.322	367
710	245	"	20.6	1.307	1.120	0.865	177
711	269	"	20.5	1.394	1.223	0.878	171
712	212	"	20.3	1.458	1.530	0.994	159
713	231	"	20.8	1.284	1.090	0.835	209
715	228.5	1000	22.4	1.133	1.111	0.980	22
716	252.5	"	21.6	1.411	1.348	0.969	43
1032	269	"	45.0	1.190	1.442	1.266	302
1033	271	"	45.1	1.411	1.677	1.188	266
1035	233.5	500	21.0	1.268	1.607	0.799	261
					Average:	1.094	243

Δh_{fg} of Tests	Pressure	$\bar{\Delta}$
21	2000	232
10	"	31
11	"	416
7	1000	196
13	"	29
5	"	297
13	500	289

TABLE 9 (Continued)

Part 4 – ANL[14] – Nickel Heaters ($d_i = d_e$)

Test No.	T_b °C	P psia	d_e in.	V ft/sec	Burnout Heat Flux Btu/hr-ft² ×10⁻⁶ Measured	Predicted	Ratio: Predicted/Measured	A ft-hr-°F²/Btu ×10⁻³
1,2,3	225	1000	0.180	15.0	1.069	0.736	0.690	333
4,5,6,7	335	2000	"	21.5	0.639	0.724	1.135	87
8,9,10	335	"	0.306	6.7	0.4526	0.344	0.765	106
11	241	600	0.180	21.2	1.200	1.199	0.992	21
12	241	"	"	21.9	1.194	1.192	0.998	2
13	255	625	"	33.1	1.200	1.257	1.048	57
14	253.5	620	"	32.8	1.200	1.234	1.029	34
15	255	625	"	41	1.467	1.601	1.100	144
						Average:	0.951	128

Part 5 – Purdue[16] – Stainless Steel Heaters ($d_i = d_e$ = 0.143")

7[*]	260.5	2065	0.143	11.4	1.478	1.337	0.928	121
9	302	2195	"	8.1	1.141	1.031	0.899	130
10	293.5	2075	"	21.5	1.750	1.668	0.953	82
11	281	2045	"	31.7	2.235	2.242	1.005	7
12	285	2015	"	42.0	2.295	2.446	1.285	631
13	336	2165	"	11.5	0.666	0.627	0.930	79
14	337	2125	"	20	0.825	0.746	0.930	59
15	320	2105	"	30.1	1.052	1.149	1.071	97
16	336	2155	"	37.2	1.362	1.148	0.911	214
22	341	2223	"	38.2	1.661	1.126	1.060	65
23	341	2235	"	29.8	0.824	0.991	1.100	87
24	338	2185	"	20.2	0.697	0.754	1.081	57
46	248	600	"	5.7	0.484	0.575	0.652	309
1123A[*]	296.3	2000	"	23.4	1.750	1.670	0.955	80
1124	291.8	"	"	12.2	1.141	1.184	1.020	23
1124A	291.3	"	"	34.2	2.234	2.220	1.039	86
1026	328.8	"	"	12.4	0.669	0.659	0.928	1
1028	332	"	"	39.9	1.960	1.249	0.918	111
1029	253	"	"	21.4	2.296	2.457	1.072	171
1046	296	"	"	19.0	1.578	1.250	0.793	328
1030	237	1000	"	11.5	1.870	1.334	0.714	536
1031	228	"	"	16.0	1.982	1.777	0.896	205
1053	252	"	"	25.4	2.340	1.978	0.872	462
1042	291	3400	"	30.8	2.038	2.732	1.342	700
						Average:	0.968	195

$\bar{\Delta}$ = 73 (15 tests)
$\bar{\Delta}$ = 397 (9 tests)

* Tests 7 thru 46 taken from ANL-4603; remainder are from ANL-4627.

Part 6 – WAPD[39] – Stainless Steel Heated Duct (d_i = 0.697"; d_e = 0.777")

150-15	292.4	2000	0.777	17.5	0.685	0.956	0.875	79
151-8	321.4	"	"	20.2	0.722	0.704	0.976	18
152-6	321.1	"	"	22.4	0.746	0.778	0.962	28
154-9	324.9	"	"	23.6	0.944	0.900	0.954	44
160-11	326.3	"	"	18.4	0.729	0.659	0.894	99
160-19	323.0	"	"	21.8	0.855	0.792	0.934	57
161-5	316.1	"	"	24.8	0.917	0.897	0.969	50
161-9	308.6	"	"	27.5	0.965	1.218	1.263	253
161-13	309.1	"	"	34.7	1.623	1.815	1.214	232
157-1	320.2	"	"	15.8	0.744	0.661	0.889	143
157-15	313.6	"	"	15.2	0.729	0.721	0.902	98
162-10	299.7	"	"	12.8	0.821	0.911	1.126	110
162-18	292.5	"	"	21.0	1.001	1.232	1.230	231
165-6	299.7	"	"	24.4	1.121	1.405	1.261	294
164-6	316.1	"	"	4.85	0.480	0.510	0.799	170
165-6	302.5	"	"	15.8	0.996	0.992	0.996	124
165-9	281.1	"	"	19.7	1.104	1.278	1.160	174
						Average:	1.016	129

$\bar{\Delta}$ = 58 (8 tests)
$\bar{\Delta}$ = 193 (9 tests)

Part 7 – JPL (Gunther)[15] – Stainless Steel Strip in Duct (d_i = 0.0795"; d_e = 0.230")

1	92.8	14.2	0.23	5	0.418	0.493	1.180	75
4	72.2	15.6	"	12.3	0.735	0.721	1.977	56
5	60.0	14.4	"	"	1.110	0.913	0.822	197
6	60.0	14.65	"	"	1.023	0.934	0.901	99
7	48.4	14.15	"	"	1.460	1.095	0.750	365
8	51.0	14.65	"	"	1.390	1.239	0.720	337
9	15	"	"	"	2.12	1.930	0.915	610
10	22.6	14.65	"	"	2.48	1.399	0.522	1,210
11	22.8	60	"	"	3.08	2.32	0.759	960
12	22.3	60	"	"	3.08	2.315	0.752	760
13	22.9	114	"	"	3.46	2.76	0.798	700
14	20	113	"	"	3.46	2.74	0.792	720
15	27.8	114	"	40	5.76	5.355	0.930	400
16	26.1	30.8	"	"	1.53	1.160	1.219	330
17	72.2	28.6	"	"	1.93	2.170	1.125	240
18	57.2	28.1	"	"	2.74	2.58	0.942	160
19	42.9	28.2	"	"	3.37	2.965	0.880	405
20	35.6	28.4	"	"	3.85	3.21	0.834	740
21	21.1	29	"	"	5.43	3.89	0.759	1,240
22	27.2	21	"	"	5.82	4.87	0.830	1,010
23	23.2	114	"	"	6.35	5.37	0.846	910
24	30	"	"	12.3	3.22	2.74	0.851	480
25	36.6	"	"	"	3.60	2.74	0.764	260
26	34.4	113	"	"	3.22	2.675	0.830	515
27	33.3	114	"	"	3.09	2.70	0.880	300
28	27.4	29	"	"	2.56	1.809	0.707	757
29	31.6	14.45	"	5.0	1.40	1.00	0.715	400

TABLE 9 (Continued)

Test No.	T_b °C.	P psia	d_e in.	V ft/sec	Burnout Heat Flux, Btu/hr-ft² × 10⁻⁶ Measured	Predicted	Ratio: Predicted/Measured	Δ Btu/hr-ft² ×10⁻⁵
Part 7 (Cont'd.)								
30	312	114	0.238	5.0	2.04	1.985	0.974	75
31	333	56	"	"	1.92	1.629	0.846	91
32	333	28.2	"	4.8	1.61	1.573	0.977	337
33	4%	15.1	"	5.0	1.11	0.864	0.778	246
34	59	14.65	"	"	0.959	0.696	0.730	26
36	97.9	"	"	12.3	0.234	0.503	2.146 (!)	269
37	714	14.65	"	"	0.576	0.657	1.140	81
38	289	114	"	"	3.26	3.025	0.946	178
						Average:	0.906	446
Part 8 - Aerojet[40] - Stainless Steel Heater (d_i=0.460)								
1	152.8	254	0.272	11.6	1.140	0.982	0.861	157
2	142.1	258	"	22.7	1.489	1.710	1.149	221
4	209.7	311	"	19.9	0.916	0.816	0.890	130
5	254.3	493	"	5.8	0.428	0.459	1.071	11
						Average:	0.982	125
Part 9 - KAPL[41] - Twisted Ribbons of "A" Nickel								
				7 ribbons in 0.512-inch hexagonal channel				
				Coil ribbon cross-section — 3.5/8 inch pitch				
1	332	2000		9.5	0.529	0.520	0.974	19
2	"	"		16	0.667	0.570	0.855	97
3	"	"		25	0.722	0.810	1.122	88
4	"	"		33	0.916	1.129	1.242	229
5	324	"		5	0.428	0.490	1.147	62
6	"	"		14.5	0.916	0.944	1.030	28
9	"	"		30	0.944	1.207	1.279	263
						Average:	1.080	114
Part 10 - Lukomskii[42] - Stainless Steel Strips in Tube Wall								
1	119.7	28.5	0.410	0.250	5.9	0.358	0.344	1.118	36
2	122.8	31.3	"	"	"	0.320	0.355	1.110	35
3	138.2	42.7	"	"	"	0.334	0.394	1.178	60
4	149.5	66.3	"	"	"	0.390	0.453	1.163	63
5	151	71.1	"	"	"	0.410	0.456	1.112	46
6	153.2	42.7	"	"	"	0.439	0.394	0.897	45
7	180	142.2	"	"	"	0.593	0.532	0.902	1
8	214	284.6	"	"	"	0.652	0.576	0.823	76
9	211	320	"	"	"	0.672	0.577	0.791	95
10	224	342.6	"	"	"	0.664	0.581	0.895	83
11	214	298.2	"	"	"	0.643	0.576	0.831	117
12	250	569	"	"	"	0.679	0.579	0.853	100
13	264	711	"	"	"	0.643	0.570	0.835	113
14	275	853	"	"	"	0.715	0.558	0.780	167
15	326	1763	"	"	"	0.605	0.461	0.762	144
16	342	2133	"	"	"	0.453	0.420	0.928	53
17	349	2289	"	"	"	0.448	0.399	0.912	89
18	358	2503	"	"	"	0.448	0.374	0.787	114
19	360	2716	"	"	"	0.353	0.352	0.998	1
20	364	2830	"	"	"	0.357	0.343	0.960	14
21	368	3000	"	"	"	0.246	0.328	1.335	82
22	368	"	"	"	"	0.277	0.328	1.184	57
						Average:	0.946	71
Part 11 - Col. Univ.[43] - Stainless Steel Tubes (0.035" wall thickness)								
1	1145	550	3.436	2.125	6.5	0.959	0.914	0.959	40
3	228	"	"	"	3.5	0.725	0.677	0.935	98
4	241	"	0.995	"	14.2	0.769	0.591	0.705	222
5	220	305	2.055	2.055	22.	0.6205	0.559	0.949	32
6	222.5	315	3.636	2.125	0.99	0.784	0.585	0.720	220
8	204.2	300	2.055	2.055	24.7	1.007	0.955	0.849	152
9	222	700	"	"	15.0	0.7605	0.725	0.953	36
10	221.6	530	"	"	25.0	0.732	0.623	0.850	109
11	225.5	"	0.775	2.125	15.6	0.527	0.494	0.934	93
12	183.7	650	"	"	11.1	1.020	0.739	0.685	395
13	230.9	"	"	"	9.04	0.5269	0.449	0.835	87
15	224.2	645	3.436	"	3.52	0.835	0.668	0.800	167
						Average:	0.840*	134

* See Discussion of "Vibration" in text.

difference to become so large as was found for the U.C.L.A. data.

Purdue University Data (16)

These data, presented in Table 9-5, were gathered from two sources as noted in the table and represent only the local-boiling burnout experiments, conducted with internally cooled tubes. Here again it is observed that the differences (between predicted and measured heat fluxes) lie in two groups; fifteen experiments are fitted with an average difference of 73,000 p.c.u./(hr.) (sq. ft.) and nine with an average of 397,000 p.c.u./(hr.) (sq. ft.), which is more than five times larger than the smaller difference. Thus, one might conclude that nine of these experiments are not typical of burnout experiments under the conditions stated.

Recent W.A.P.D. Data (39)

These data, presented in Table 9-6, were obtained from recent* burnout experiments conducted in narrow rectangular channels, cooled internally. In these data one again finds a threefold change in the average differences between the predicted and measured heat fluxes for two groups of experiments. However, the average difference for all the data as a single group indicate that these experiments were as well controlled as the best of the other sources (same as the A.N.L. data). It would appear, therefore, that the precision attainable in low-pressure experiments cannot be demonstrated at the higher pressures.

Data of Gunther (15)

These data, presented in Table 9-7, were obtained with a very thin (0.004-in.) stainless steel heater in a rectangular duct. Although the results of this investigation were extremely useful in demonstrating the effects of coolant pressure, velocity, and subcooling upon the burnout heat flux, the combination of extreme thinness of heater and of strip geometry† appears to have caused very wide scatter in these data. The average difference between the predicted and measured burnout heat fluxes is so much larger [446,000 p.c.u./(hr.) (sq. ft.)] than those of the Columbia University and McAdams' data [62,000 and 43,500 p.c.u./(hr.) (sq. ft.), respectively] for the same range of experimental variables that one must conclude that these data cannot lend quantitative confirmation to the validity of the prediction method presented here.

Aerojet Data (40)

These few data were obtained in calibration experiments for the diphenyl burnout studies. The test section consisted of a heated stainless steel tube, 0.020-in. wall thickness, with an "inert" rod inserted concentrically to form an annular passage for the coolant. (All other data obtained with annuli had the heated tube cooled externally.) They are presented in Table 9-8 and are included here for the reason that the measurements were made within a pressure range (250 to 500 lb./sq. in. abs.) that is rarely investigated. The experiments appear to have been well controlled and the agreement between

*These experiments were performed with a new power source permitting attainment of higher heat fluxes than were possible earlier.

†A thin strip should liberate heat nonuniformly, with the edges and corners having significantly higher heat flux than the strip face.

predicted and measured values of burnout heat flux is very satisfactory. Thus the prediction method appears to fit both internally and externally cooled heaters, with the coolant flowing in an annulus, with satisfactory accuracy.

K.A.P.L. (41) "Twisted Ribbon" Data

Seven burnout measurements have been reported for twisted ribbon assemblies. These tests were conducted at a pressure of 2,000 lb./sq. in. abs. with subcooled water flowing through a vertical bundle of seven electrically heated twisted ribbons. The data are presented in Table 9-9 together with predicted values of the heat flux at burnout. Agreement between experiment and prediction is very satisfactory, and five of the seven tests appear to have been under close control.

These data are valuable additions to the mass of burnout information available primarily for the unique geometry employed. They tend to confirm the adequacy of the geometric variables employed in the prediction method.

Lukomskii (42) Data

These data cover a very wide range of coolant pressures with saturated water at essentially constant velocity (5.9 ft./sec.). The test section geometry is unique in that unconnected, heated strips of stainless steel were "dovetailed" into a tube of magnesium chloride; the coolant flowed upward inside the tube. Although alternating-current electricity was used in heating the strips, these data are sufficiently accurate to demonstrate good agreement between experimental and predicted burnout heat fluxes, as summarized in Table 9-10. These data are useful since they tend to confirm both the effect of geometric variables and that of coolant pressure on the burnout heat flux.

Columbia University (43) Task X Data

These data, presented in Table 9-11, are being obtained in a large medium-pressure (to 750 lb./sq. in. abs.) apparatus that utilizes 70-in.-long heater tubes of stainless steel. These tubes are 2⅛ in. O.D. and have 0.035-in. wall thickness; they comprise the largest test sections used to study burnout reported in the open literature. Although the differences between predicted and experimental burnout heat fluxes are in the same range as other high-pressure data, the predicted value is consistently lower than that measured. The reason currently proposed to explain this fact is that these test sections almost invariably undergo severe vibration as the boiling intensity increases. The effect of vibration on the burnout heat flux is to be discussed in detail later, but briefly the mechanical vibrations of the heater surface tend to dislodge semistable bubbles or clusters of bubbles. Thus, it is more difficult for stable film boiling to be initiated on a vibrating heater and the onset of burnout is retarded.

FORCED FLOW IN "CONFINED GEOMETRY"—OTHER COOLANTS

Burnout Data with Ammonia as Coolant

To date, two groups of local-boiling burnout experiments have been reported in the unclassified literature. The Bartz-Noel (*44*) experiments were conducted at a pressure of 500 lb./sq. in. abs.; 0.250-in. O.D. stainless steel tubes (0.009-in. wall thickness) formed the test sections which were cooled internally. These data are unique in that coolant velocities up to 160 ft./sec. were investigated.

Table 4 presents both the experimental results and those predicted by the generalized method (page 103). The over-all agreement between data and prediction is excellent, but as was noted in the results for water at high pressure, the differences between predicted and experimental burnout heat fluxes fall into two groups, 15 runs with an average difference of 51,000 and 8 runs with an average of 285,000 p.c.u-/(hr.) (sq. ft.), although the percentage differences are small throughout.

The second investigation of ammonia burnout phenomena [Reaction Motors, Inc. (*45*)] covers a wider range of the experimental variables (except for velocity) than did the Bartz-Noel study. These data, however, are less well controlled, apparently as a consequence of the very short test section, the method of thermocouple installation, and the method of data reduction and analysis. Thus, owing to the large scatter in these data, the agreement between predicted and measured burnout heat fluxes, although satisfactory, can be considered as only qualitative.

The physical properties of ammonia used in this analysis were taken from the Smithsonian Physical Tables (1954). Figure 9 is a working graph constructed to simplify the computations of the generalized prediction method. The physical properties of water were taken from the thesis of E. J. Wellman, Purdue University (1950).

Burnout Data with Diphenyl as Coolant (40)

These data were obtained in a two-part investigation of the burnout behavior of local-boiling diphenyl in tubes cooled internally via an annular coolant passage. The data were collected in two campaigns of experiments and are analyzed separately and as a group in Table 5. The later results show better precision, the average differences (between predicted and measured burnout heat fluxes) being 21,000 and 41,000 p.c.u./(hr.) (sq. ft.) respectively for the two groups of tests. The average difference for all tests grouped together is 30,500 p.c.u./(hr.) (sq. ft.), which is excellent agreement between prediction and experiment and is about the same as differ-

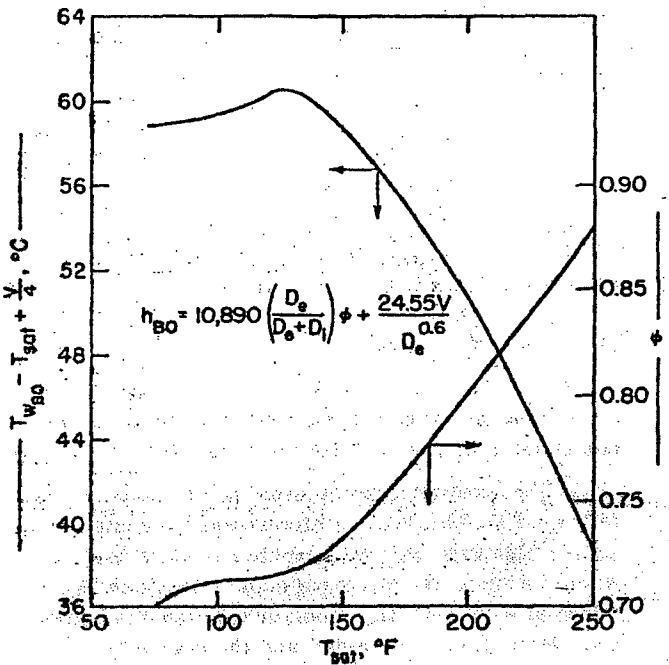


Fig. 9. Working graph for predicting burnout heat flux for ammonia.

ences obtained for the best water data. The percentage of differences, however, show that the prediction method is about 10% conservative. It is this percentage difference that prompted the earlier remark about the accuracy of the physical properties of diphenyl, as currently available.

The data for the physical properties of diphenyl were taken from the reference document, with a curve for the thermal conductivity drawn parallel to that for a polyphenyl mixture (see Figure 15 of reference *40*). The thermal conductivities used in this analysis are given by $k = 0.08125 - 2.64 \times 10^{-5}\,(t - 450)$, where t is the saturation temperature of diphenyl in degrees Fahrenheit and k is in British thermal units per hour per degree Fahrenheit per foot. Figure 10 presents a working graph to simplify the computations of the prediction method.

LIMITATIONS OF THE PREDICTION METHOD

LOCAL BOILING

Effect of Wetting of Surface by Coolant

Averin has shown that the boiling characteristics of a heater are changed markedly when the coolant does not wet the heated surface. His work indicates that nucleate boiling does not occur and that the heat transfer coefficient decreases with increasing temperature driving force for nonwetted systems. The investigations of Bonilla, et al. (*46*), and Katz and co-workers (*47*), with liquid metals also reveal anomalous boiling behavior of heaters with partially or incompletely wetted surfaces. Although the effect of wetting angle on boiling phenomena has been discussed by many authors and attempts have been made to relate the magnitude of the surface tension of a system to its nucleate-boiling behavior, conclusive evidence of a relation between the two has not been demonstrated.

The prediction method presented in this work appears not to depend upon the surface tension or wetting phenomena *as long as nucleate boiling can occur* in the system. The few experiments, conducted to determine the burnout heat fluxes for surfaces boiled for short and long times, have indicated a slight effect even though the nucleate boiling characteristics (relationship between Q/A and Δt) appear to change considerably. It would seem, therefore, that wetting effects—like surface roughness effects—do not influence the onset of burnout.

Effect of Transient Conditions

All analysis and discussion in the sections preceding this one have dealt with steady state phenomena. It is appropriate to raise the question: how short may the period of a transient heat transfer process become before steady state analyses are no longer valid? The investigations of Rosenthal and Miller (*48*) at Oak Ridge National Laboratory, of McLean and co-workers (*49*) at the Naval Research Laboratory, and of Bendler and co-workers (*50*) at Columbia University in atmospheric pools indicate that transient boiling processes, including burnout phenomena, are indistinguishable from the steady

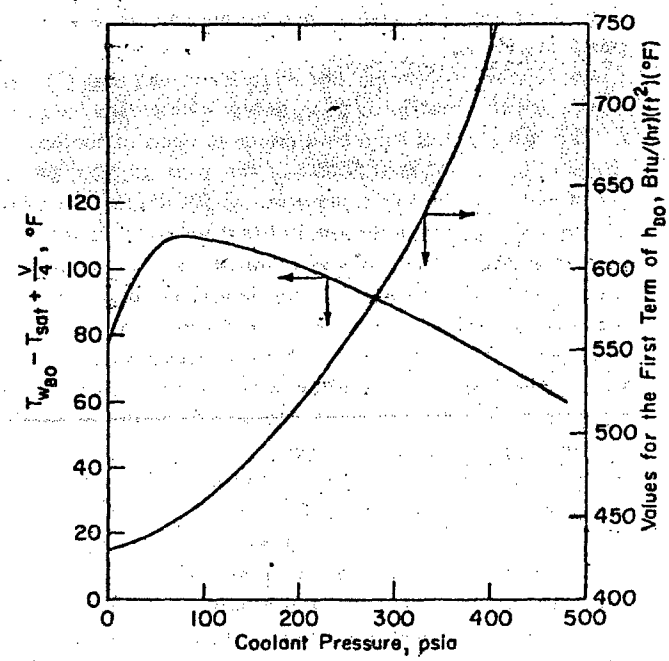


Fig. 10. Working graph for predicting burnout heat flux for diphenyl.

state for periods in excess of about 15 msec. Since these tests were performed with test sections of low thermal capacity (see section on Heater-Wall Thickness), it may be assumed that steady state analyses are valid to periods as short as 5 msec. for massive elements.

It is proposed here that periods in excess of ten times the mean lifetime of surface bubbles should be long enough to permit steady state phenomena to become established at the heated surface. Measurements of bubble lifetimes have been made by Ellion and Gunther and coworkers at the California Institute of Technology. These measurements, based on boiling experiments at pressures close to atmospheric, show that bubble lifetimes are of the order of 1 to 2 msec. for water. Heat flux and subcooling both affect the magnitude of the lifetimes of bubbles as follows: increasing heat flux at constant subcooling decreases the lifetime of bubbles, whereas increasing coolant bulk temperature *increases* the lifetime; neither of these effects, however, changes the bubble lifetime by more than a factor of 2 for very wide changes in the independent variable.

Effect of Heater Vibration

As pointed out earlier, boiling and burnout experiments at Columbia University have demonstrated that vigorous boiling can cause vibration of the heaters. Vibration has been observed throughout a wide range of coolant conditions and with solid and hollow heaters of widely differing length-to-diameter ratios. The appearance of nucleate boiling without vibration is one of random bubble generation and release, whereas with vibration the bubble population appears, grows, and disappears in distinctly periodic pulses.

Preliminary measurements have indicated that (1) the frequency of vibration is low, below 100 cycles/sec., (2) the initiation of vibration depends upon exceeding a threshold value of heat flux—of the order of 500,000 p.c.u./(hr.) (sq. ft.) at a pressure of 500 lb./sq. in. abs., (3) subcooling, pressure and coolant velocity appear to influence the severity of the vibration, and (4) under some conditions vibration of the heater occurs over a range of heat fluxes which is reproducible and without apparent hysteresis effects. Chang reports on a vibration phenomenon, encountered with organic coolants, that appears to be initiated when a threshold value of heater-surface temperature is exceeded.

As noted earlier, vibration of the heater retards the onset of burnout since coalescence of bubbles into a stable vapor film is more difficult. Measurements of the burnout heat flux for similar heaters with and without vibration indicate that the extent to which burnout is retarded decreases with increasing system pressure. The table below summarizes some of the data collected on the effect of heater vibration on the burnout heat flux.

Coolant pressure, lb./sq. in. abs.	Heater dimensions, in.	Ratio of $(Q/A)_{BO}$ with vibration to $(Q/A)_{BO}$ without vibration
4.4	3/16 O.D. solid × 12	1.07 to 1.80
27.2	3/16 O.D. solid × 12	1.06 to 1.35
93	3/16 O.D. solid × 12	1.05 to 1.07
248	3/16 O.D. solid × 12	1.04
93	3/16 O.D. solid × 2	1.02 to 1.07
500	2.125 O.D. × 2.055 I.D. × 70	1.05 to 1.39
650–720	2.125 O.D. × 2.055 I.D. × 70	1.05 to 1.20

The "Cut-off" Velocity

The mathematical form of Equation (4) has been criticized from the point of view that with very high coolant velocities it is possible for the value of $T_{w_{BO}}$ to fall below the saturation temperature of the coolant and to fall to zero. This was interpreted as meaning that at such a high velocity the predicted burnout heat flux would be zero. An alternate explanation can be formulated: at extremely high coolant velocity the initiation of nucleate boiling is retarded and the region over which the forced-convection regime of heat transfer pertains is extended far beyond "normal" bounds. Furthermore, if the coolant velocity were high enough, nucleate boiling need never be attained and burnout phenomena could occur only in the *bulk-boiling regime*. These concepts are illustrated by the curves of Figure 11.

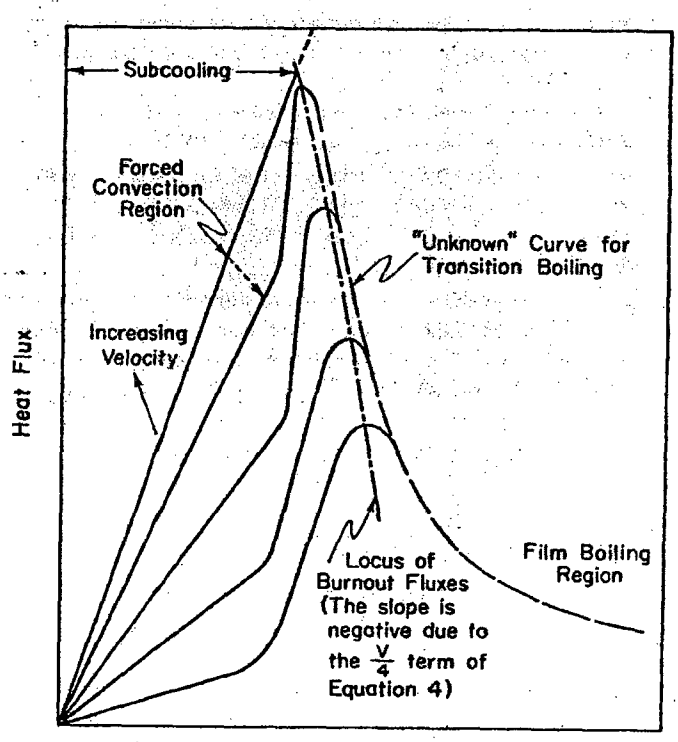


Fig. 11. Effect of velocity on burnout heat flux (pressure and subcooling constant).

With a coolant pressure assumed of 30 lb./ sq. in. abs. for which the wall superheat at zero velocity is 36.5°C., the "cut-off" is 4 × 36.5 = 146 ft./sec. As estimated by the method of McAdams, et al., (*11*), for an annulus of ½-in. hydraulic diameter, the wall superheat required to *initiate* local boiling, even if the subcooling were zero, at a velocity of 146 ft./sec., is about 46°C. Thus McAdams's method predicts that, even at zero subcooling, boiling cannot be initiated. To estimate the heat flux to initiate nucleate boiling under these conditions, the method of Begell and Bernath is employed, as follows:

$$\Delta T_{sat_{initiation}} = 46°C \text{ (by McAdams)} =$$

$$30 - \frac{V}{3.26} + \frac{(Q/A - 1.8 \times 10^5)}{3 \times 10^4}$$

thus,

$$(Q/A)_{initiation} = 1.8 \times 10^5 + (3 \times 10^4)\left(46 - 30 + \frac{V}{3.26}\right) =$$

$$2 \times 10^6 \text{ p.c.u./(hr.) (sq. ft.)}$$

Even if the wall superheat to initiate boiling were 36.5°C, the heat flux required would be 1.72×10^6 p.c.u./(hr.) (sq. ft.).

These calculated estimates indicate that local-boiling burnout will not occur at very high velocities primarily because the forced-convection mechanism is adequate to transfer the heat. These estimates tend to be confirmed by the data for ammonia (see section on Burnout Data with Ammonia) which demonstrate the adequacy of Equation (4) at least to coolant velocities of 160 ft./sec. Thus, it may be assumed that the "cut-off" velocity has no significance in local boiling but may represent the transition from the forced-convection regime of heat transfer to the burnout condition with *bulk boiling*.

BULK BOILING

The prediction method presented has been demonstrated to be valid for local boiling. Since a smooth transition in burnout heat flux from local to bulk boiling must occur, one would expect the prediction method to be fairly accurate over a region of the bulk-boiling regime. Preliminary calculations performed for burnout conditions at high pressures reveal that the method is valid when the inlet coolant velocity exceeds about 10 ft./sec. and the effluent vapor void fraction is less than 0.10. These conditions represent a very small region of the bulk-boiling regime, as seen from the following table.

Coolant pressure, lb./sq. in. abs.	Steam quality corresponding to a void fraction of 0.10, %
2,000	1.6
1,000	0.7
600	0.3

These considerations can be extrapolated to the region in local boiling of low pressures and low subcoolings. Gunther, et al., have shown that at low pressures and low subcoolings the lifetimes of bubbles both on the surface and in the stream become appreciable. Therefore, one would expect that under these conditions an appreciable bubble void fraction could be attained in narrow coolant passages at high heat fluxes. Void fractions in subcooled streams have been measured at the Argonne National Laboratory at pressures up to 600 lb./ sq. in. abs. Visual observations during experiments performed at the Savannah River Laboratory (*51*) at conditions cited above reveal that large void fractions are indeed possible. It is to be expected, therefore, that experiments in this range (below 50 lb./sq. in. abs., below 20°C. subcooling, and below hydraulic diameters of 0.30 in.) should behave very much like bulk-boiling experiments at low pressures and low steam qualities. In this range of experimental variables, two-phase flow phenomena complicate the process of heat transfer burnout. Hence, it is to be expected that the agreement between measured and predicted burnout heat fluxes would not be so close in this region as in the ranges where vapor void fractions are negligible.

NOTATION

A = intercept term of h_{BO} equation; also, surface area, sq. ft.
a = thickness of undulating layer, according to Chang (*2*)
B = slope of velocity-dependent term of h_{BO}
C_p = heat capacity of coolant, p.c.u./(lb.) (°C.)
D_e (d_e) = hydraulic diameter of coolant passage, ft. (in.)
D_l (d_l) = diameter of heated surface (heated perimeter divided by π), ft. (in.)
h = film coefficient of heat transfer, p.c.u./(hr.) (sq. ft.) (°C.)
k = thermal conductivity (coolant or metal), p.c.u./(hr.) (ft.) (°C.)
L = heated length, ft.
ln = Naperian logarithm
N_B = Biot modulus
P = pressure, lb./sq. in. abs.
Q/A = heat flux, p.c.u./(hr.) (sq. ft.)
R = radius of heated rod, ft.
T = temperature, °C.
ΔT = temperature difference, °C.
V = coolant velocity, ft./sec.
X = heater wall thickness, ft.
x = distance, ft.
α = thermal diffusivity (molecular), sq. ft./hr.
ν = momentum diffusivity (molecular), sq. ft./hr.
ε = eddy diffusivity, sq. ft./hr.
δ = boundary layer thickness, ft.

ρ = coolant density, lb./cu. ft.
Δ = difference between predicted and measured burnout heat fluxes

SUBSCRIPTS

BO = burnout condition
b = bulk coolant
c, crit. = critical (in thermodynamic sense)
R = reduced (in thermodynamic sense)
Sat = saturated condition
Sub = subcooling
w = heated surface or wall

ACKNOWLEDGMENT

The author acknowledges his indebtedness to Dale F. Babcock and J. S. Neill of the du Pont Company and to William Begell, A. J. Bemiller, and R. P. Stein of Columbia University for their constant encouragement and constructive criticism. The information contained in this paper was developed or compiled during the course of work under Contract AT (07-2)-1 with the Atomic Energy Commission, whose permission to publish is gratefully acknowledged.

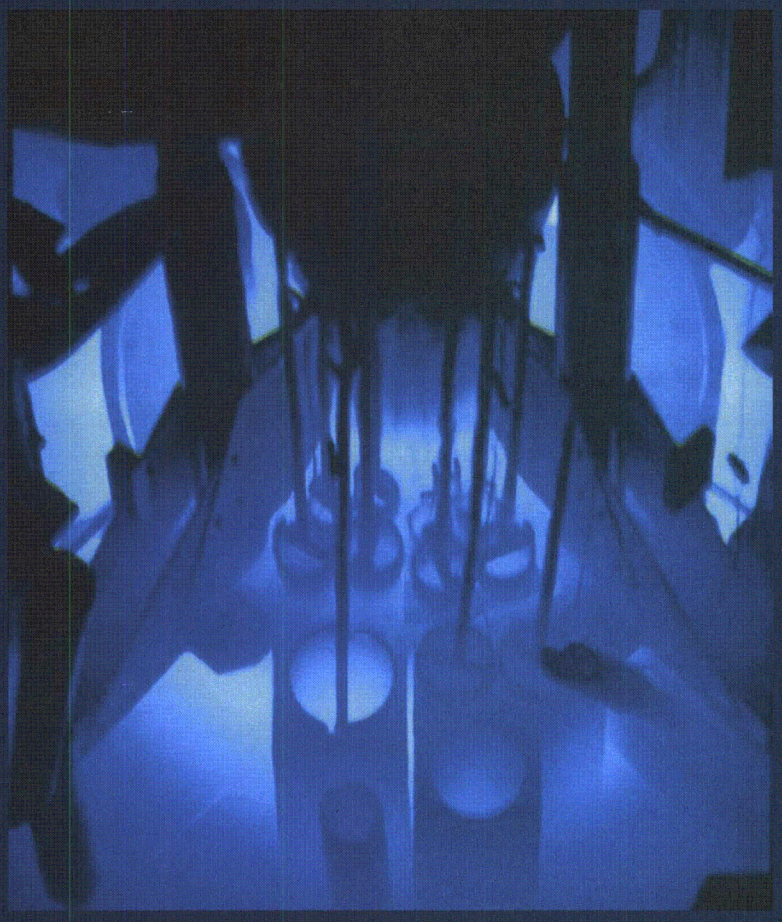
LITERATURE CITED

1a. Gunther, F. C., and W. Kreith, JPL Prog. Rept. No. 4-120, Cal. Inst. Technol., Pasadena (March 1950).
b. Kreith, F., and M. Summerfield, *Trans. Am. Soc. Mech. Engrs.*, 71, 805 (1949).
2a. Chang, Y. P., *ibid.*, 79, 1501 (October, 1957).
b. Chang, Y. P., *A.E.C.U.*-3551 (1956).
3. Zuber, Novak, and Myron Tribus, Rept. 58-5, Univ. Cal., Los Angeles, (January, 1958).
4. Kutateladze, S. S., *Izv. Akad. Nauk SSSR, Otd. Tekh. Nauk*, No. 4, p. 529 (1951).
5. Borishanskii, V. M., *Zhum. Tekh. Fiz.*, 25, 252 (1956).
6. Rohsenow, Warren, and Peter Griffith, *Chem. Eng. Progr. Symposium Series*, No. 18, 52, 47 (1956).
7. Griffith, Peter, A.S.M.E. Paper No. 57-HT-21, State Univ. Penn., Joint A.S.M.E.-A.I.Ch.E. Heat Transfer Conference, (August, 1957).
8. Ellion, M. E., *JPL Memo. No. 20-88*, Cal. Inst. Technol., Pasadena (March, 1954).
9. Begell, William, and Louis Bernath, *Chem. Eng. Progr. Symposium Ser.* No. 29, 55, 3-9 (1959).
10. Bernath, Louis, *Chem. Eng. Progr. Symposium Ser.* No. 18, 52, 1 (1956).
11. McAdams, W. H., et al., *Ind. Eng. Chem.*, 41, 1945 (1949).
12. "Columbia University Data Books," Vol. 1 through 6 (January, 1956).
13. Jens, W. H., and P. A. Lottes, *ANL-4627*, p. 45 (May, 1951).
14. Jameson, A. S., and P. A. Lottes, *Burnout Newsletter No. 1*, B.N.L. Log No. C-8498, Argonne Natl. Lab., Lemont, Ill. (December, 1954).
15. Gunther, F. C., *Trans. Am. Soc. Mech. Engrs.*, 73, 115 (1951).
16a. McGill, H. L., and W. L. Sibbitt, *ANL-4603*, 31 (February, 1951).
b. Reference 13, p. 46.
17. *Burnout Newsletter No. 3*, Brookhaven Nat'l. Lab., Upton, N. Y. (February, 1955).
18. Kezios, S. P., and R. K. Lo, *ANL-5822* (January, 1958).
19. Danckwerts, P. V., *A.I.Ch.E. Journal*, 1, 456 (1955).
20. Toor, H. L., and J. M. Marchello, *A.I.Ch.E. Journal*, 4, No. 1, 97 (March, 1958).
21. McAdams, W. H., et al., *Chem. Eng. Progr.* 44, 639 (1948).
22. Van Stralen, S. J. D., *Chem. Eng. Sci.*, 5, 290 (1956).
23. Averin, E. K., *Izv. Akad. Nauk, SSSR*, Otdel. Tekh. Nauk, No. 3, 116 (1954); also Transl. RJ-305, Assoc. Tech. Services, East Orange, N.J.
24. Castles, J. T., S. M. thesis, Mass. Inst. Technol. (1940); W. H. McAdams, "Heat Transmission," p. 368, McGraw-Hill, New York (1954).
25. Columbia University Repts., A.E.C. subcontract (1954).
26. Mukerjee and Srivastava, *Kolloid Zeitschrift*, 147, Heft 3, June (1956).
27. King and Mukerjee, *J. Soc. Chem. (India)*, 57, 431 (1938).
28. Corty, Claude, and A. S. Foust, *Chem. Eng. Progr. Symposium Ser.*, No. 17, 51, 1 (1955).
29. Farber, E. A., and R. L. Scorah, *Trans. Am. Soc. Mech. Engrs.*, 70, *369 (1948)*.
30. Mosciki, I., and J. Broder, *Rocznik Chem.*, 6, 319 (1926).
31. Reference 21 (above).
32. Mirshak, S., *DP-262*, December (1957).
33. Bendler, A. J., *Columbia University Task IX Reports*, A.E.C. Contract (1957, 1958, 1959).
34. Chirkin, V. S., and V. P. Iukin, *Zhur. Tekh. Fiziki*, 26, No. 7, 1542 (1956).
35. Leppert, G., C. P. Costello, and B. M. Hoglund, Paper No. 57-A-81, *Am. Soc. Mech. Engrs.*, (December, 1957).
36. Cichelli, M. T., and C. F. Bonilla, *Trans. A.I.Ch.E.*, 41, No. 6, 755 (December, 1945).
37. Stein, R. P., and William Begell, *A.I.Ch.E. Journal*, 4, No. 2, 127 (1958).
38. See reference 14 (above).
39. Troy, M., *WAPD-TH-340* (July, 1957).
40. *Rept. No. IDO-28007*, Aerojet-General Corp. (February, 1958).
41. Schultz, W. R., Jr., *NDA-35* (February, 1957).
42. Lukomskii, S. M., Transl., I. G. Trans. R-3, U.K.A.E.A. (1955).
43. *Columbia University Task X Reports*, edited by William Begell (1957, 1958, 1959).
44. Bartz, D. R., *JPL Memo. No. 20-137*, Cal. Inst. Technol., Pasadena, (December, 1956).
45. Dimmock, T. H., *Rept. RMI-124-S1*, Reaction Motors, Inc. (June, 1957).
46. Bonilla, C. F., et al., Reactor Heat Transfer Conference (A.E.C.), New York (November, 1956).
47. Katz, D. L., et al., *Chem. Eng. Progr. Symposium Ser.*, No. 17, 51, 41 (1955).
48. Rosenthal, M. W., and R. L. Miller, *ORNL-2294* (May, 1957).
49. McLean, E. A., et al., Reactor Heat Transfer Conference (A.E.C.), New York (1956).
50. Bendler, A. J., et al., *AECU-3623* (February, 1958).
51. Savannah River Laboratory Rept. (DP-355) to be issued.
52. Westwater, J. W. and A. S. Perkins, *A.I.Ch.E. Journal*, 2, No. 4, 479 (December, 1956).
53. Kazakova, E. A., *AEC-tr-3405*, Chapter on Boiling in Pools (1958).

ATTACHMENT 10

TDR-0125

Feasibility Analyses for HEU to LEU Fuel Conversion of the University of Missouri Research Reactor



University of Missouri Research Reactor

February - 2011

MURR
Technical Data Report

TDR No.: 0125 **Revision No.:** 0

Title: Feasibility Analyses for HEU to LEU Fuel Conversion of the University of Missouri Research Reactor

Originator(s) Signature	Date	Approval(s) Signature	Date
	2-9-11		
	2-9-11		
	4/6/11		
		External Distribution Approval	Date
		N/A	N/A

*	Distribution
	L. Foyto
	C. McKibben
	D. Kutikkad
	J. Fruits
	C. Herbold
	N. Peters
*	R. Butler

Abstract:

This report contains the results of reactor design, performance, and steady-state safety analyses for conversion of the University of Missouri Research Reactor (MURR) from the use of highly-enriched uranium (HEU) fuel to the use of low-enriched uranium (LEU) fuel. The analyses were performed by staff members of the Global Threat Reduction Initiative (GTRI) Reactor Conversion Program at the Argonne National Laboratory (ANL) and the MURR Facility. The core conversion to LEU will be performed with financial support of the US government. This project was approved in early 2006 and this report was completed on September 30, 2009.

The objectives of this work was to show that it is feasible, under a set of manufacturing assumptions, to design a MURR LEU fuel element that could safely replace the current MURR HEU fuel element and maintain performance while requiring minimal, if any changes, to the control blades and control blade drive mechanisms as well as the instrumentation and control system.

The report stated that it is possible to convert MURR to LEU fuel with the following four qualifiers:

1. Complete qualification of the U-10Mo Monolithic Fuel;
2. Demonstrate the hydrodynamic stability of 38-mil thick fuel plates;
3. Demonstrate that fuel plates can be fabricated with 10-mil cladding; and
4. With approval of analysis, have the NRC order MURR to convert at 12 MW.

* – Abstract Only

MURR
Technical Data Report

TDR No.: 0125 **Revision No.:** 0

Rev.	Summary of Change	Approval	Date
0	Original Issue	N/A	N/A

List of Effective Pages

Page	Rev.	Page	Rev.	Page	Rev.	Page	Rev.	Page	Rev.	Page	Rev.	Page	Rev.
1	0	14	0	27	0	40	0	53	0	A1.12	0	B2.1	
2	0	15	0	28	0	41	0	54	0	A1.13	0	B2.2	
3	0	16	0	29	0	42	0	A1.1	0	A1.14	0	B2.3	
4	0	17	0	30	0	43	0	A1.2	0	A1.15	0	B2.4	
5	0	18	0	31	0	44	0	A1.3	0	A1.16	0	B2.5	
6	0	19	0	32	0	45	0	A1.4	0	A1.17	0	B2.6	
7	0	20	0	33	0	46	0	A1.5	0	A1.18	0	B2.7	
8	0	21	0	34	0	47	0	A1.6	0	B1.1	0	B2.8	
9	0	22	0	35	0	48	0	A1.7	0	B1.2	0	B2.9	
10	0	23	0	36	0	49	0	A1.8	0	B1.3			
11	0	24	0	37	0	50	0	A1.9	0	B1.4			
12	0	25	0	38	0	51	0	A1.10	0	B1.5			
13	0	26	0	39	0	52	0	A1.11	0	B1.6			

FEASIBILITY ANALYSES FOR HEU TO LEU FUEL CONVERSION OF THE UNIVERSITY of MISSOURI RESEARCH REACTOR (MURR)

University of Missouri-Columbia Research Reactor
1513 Research Park Drive
Columbia, Missouri 65211

September 30th, 2009

CONTRIBUTORS

Co-ordination of Report

J.C. McKibben MURR*
J.G. Stevens GTRI Reactor Conversion Program
Argonne National Laboratory (ANL)**

Section	Description	Contributor	Affiliation
	Summary		
1	**Introduction**	J.C. McKibben	MURR
2	**General Description of Facility**	L. Foyto	MURR
		J.C. McKibben	MURR
3	**Neutronic Analyses**	K. Kutikkad	MURR
		J.C. McKibben	MURR
		B. Dionne	ANL
		J.G. Stevens	ANL
		J.A. Stillman	ANL
4	**Thermal-Hydraulic Analyses**	E.E. Feldman	ANL
		J.C. McKibben	MURR
5	**Conclusions and Recommendations**	J.C. McKibben	MURR

*University of Missouri-Columbia Research Reactor
1513 Research Park Drive
Columbia, Missouri 65211

**GTRI Reactor Conversion Program[§]
Argonne National Laboratory
Argonne, IL USA 60439

[§]Work supported by the U.S. Department of Energy
National Nuclear Security Administration
Under Contract No. DE-AC02-06CH11357

CONTRIBUTORS i

TABLE OF CONTENTS ii

LIST OF FIGURES iv

LIST OF TABLES vi

SUMMARY vii

TABLE OF CONTENTS

Section	Title	Page
1.	**INTRODUCTION**	1
2.	**GENERAL DESCRIPTION OF FACILITY, REACTOR & FUEL**	1
2.1	Facility Description	1
2.2	Facility History	2
2.3	Basic Reactor Description	3
2.4	Current Fuel Design and Operating Cycle	4
2.5	Facility References	5
3.	**NEUTRONIC ANALYSES**	6
3.1	Description of Neutronics Codes and Methodologies	7
3.2	Scoping Studies for LEU Element Design	8
3.3	Development of the Detailed Neutronic Models	13
3.3.1	Computational Model Credibility – Comparisons with 1971 HEU Core Measurements	13
3.3.2	Description of Changes to HEU Core Models (1971 to 2008 Core Configuration)	14
3.3.3	Development of HEU and LEU Fuel Cycle Models	16
3.3.4	Computational Model Credibility – Comparisons with Estimated Critical Positions	20
3.3.5	Selection of HEU and LEU Reference Cores	22
3.4	Comparison of HEU and LEU Fuel Element Performance and Safety Margins	23
3.4.1	Fuel Cycle Performance	23
3.4.2	Shutdown Margins	24
3.4.3	Experimental Performance – Fluxes and Reaction Rates at Irradiation Locations	24
3.4.4	Power Distributions for Steady State Safety Margin Evaluation	32
3.5	Neutronic References	38

4. STEADY-STATE THERMAL-HYDRAULIC ANALYSES 40

4.1 Background and Introduction 40
4.2 Replication of the Original HEU Safety Analysis 41
4.3 Methods of Predicting the Power Margin to Flow Instability 41
4.4 Hot Channel Factors 42
4.4.1 Hot Channel Factors—Power Distribution Uncertainty 43
4.4.2 Hot Channel Factors—Fuel Plate Loading Uncertainty 44
4.4.3 Hot Channel Factors—Flow Distribution Uncertainty 45
4.4.4 Hot Channel Factors—Channel Thickness Uncertainty 45
4.4.5 Hot Channel Factors—Uncertainties (i.e., Measurement Error) in Reactor Measured Quantities 46
4.5 PLTEMP/ANL Computer Code 46
4.6 Analysis 47
4.6.1 Core Configurations and Operating Conditions 47
4.6.2 Core Pressure Drops 48
4.6.3 Hot Channel Factor Application 48
4.6.4 Power Distribution Along the Arc Length (or Width) of the Fuel Plates ... 50
4.6.5 Fraction of Power Produced in the Reactor Core 50
4.7 Results 51
4.8 Thermal-Hydraulic Discussion and Conclusions 52
4.9 Thermal-Hydraulic References 52

5. FEASIBILITY STUDY CONCLUSIONS AND RECOMMENDATIONS ... 54

APPENDIX A-1: HEAT FLUX DISTRIBUTIONS FOR MURR CORES ... A-1.1

APPENDIX B-1: REPLICATION OF MURR 1974 10 MW UPGRADE SAFETY ANALYSES B.1.1

APPENDIX B-2: PREDICTIONS OF THE FLOW INSTABILITY MEASURMENTS MADE WITH ELECTICALLY HEATED CHANNELS FOR THE ADVANCED TEST REACTOR B-2.1

LIST OF FIGURES

Fig. No.	Title	Page
2.1	University Research Park—University of Missouri-Columbia	2
2.2	MURR Core	2
2.3	Reactor Core Assembly—2D View	3
2.4	Reactor Core Assembly—3D View	3
2.5	Reactor Core Assembly—Plan View	4
2.6	MURR Fuel Element—Pictorial View	5
3.1	Cross Section of MCNP Models of MURR	6
3.2	The Multiple Neutronic Codes Applied to Model the MURR Fuel Cycle	8
3.3	HEU Core Design Peaking Factors	11
3.4	LEU Core Design Power Density Peaking Factors	12
3.5	LEU Core Design Heat Flux Peaking Factors	12
3.6	Weekly Core k-effective for MURR HEU Fuel Cycle Simulation	17
3.7	MURR Fresh Core Reactivity vs. Burnup	18
3.8	Weekly Core k-effective for MURR LEU Fuel Cycle Simulation	19
3.9	Weekly Core k-effective for MURR HEU and LEU Fuel Cycle Simulations	19
3.10	ECP Deviation from Critical vs. Blade History	22
3.11	Critical Withdrawal vs. Blade History	22
3.12	Comparison of LEU and HEU Beam Tube E Outbound Current at Day 0	29
3.13	Comparison of LEU and HEU Beam Tube E Outbound Current at Day 2	29
3.14	Comparisons of LEU 10 MW to HEU 10 MW at Day 0	30
3.15	Comparisons of LEU 12 MW to HEU 10 MW at Day 0	30
3.16	Comparisons of LEU 10 MW to HEU 10 MW at Day 2	31
3.17	Comparisons of LEU 12 MW to HEU 10 MW at Day 2	31
3.18	Normalized Radial Power Factor Shapes	32
3.19	Heat Flux in Each Axial Segment of Each Plate— Case 7B: LEU Week 79 Day 0 with Empty Flux Trap	35
3.20	Axial Average Heat Flux in Each Plate of Each Element— Case 7B: LEU Week 79 Day 0 with Empty Flux Trap	36
3.21	Azimuthal Peaking Factor for Each Plate of Each Element— Case 7B: LEU Week 79 Day 0 with Empty Flux Trap	36
3.22	Hot Stripe Heat Flux for Each Plate of Each Element— Case 7B: LEU Week 79 Day 0 with Empty Flux Trap	37
4.1	Arrangement of the Eight MURR Elements	40
4.2	Thicknesses of Outer Channels	40
4.3	Change in Radial Power Distribution of Element 5	43
4.4	Element Arrangement with Element 5 Shifted Inward 15 mils and Elements 4 & 6 Shifted Outward 15 mils (Shifted Case)	44
4.5	Reactor Power Predicted to Initiate Channel Flow Instability in the HEU Core	51
4.6	Reactor Power Predicted to Initiate Channel Flow Instability in the LEU Core	51
A-1.1	Case 1A: 10 MW HEU Fresh Day 0 with Flux Trap Samples	A-1.3
A-1.2	Case 2A: 10 MW HEU Fresh Day 2 with Flux Trap Samples	A-1.4
A-1.3	Case 3A: 10 MW HEU Week 58 Day 0 with Flux Trap Samples	A-1.5
A-1.4	Case 4A: 10 MW HEU Week 58 Day 2 with Flux Trap Samples	A-1.6
A-1.5	Case 1B: 10 MW HEU Fresh Day 0 with Empty Flux Trap	A-1.7
A-1.6	Case 2B: 10 MW HEU Fresh Day 2 with Empty Flux Trap	A-1.8
A-1.7	Case 3B: 10 MW HEU Week 58 Day 0 with Empty Flux Trap	A-1.9
A-1.8	Case 4B: 10 MW HEU Week 58 Day 2 with Empty Flux Trap	A-1.10

A-1.9 Case 5A: 12 MW LEU Fresh Day 0 with Flux Trap Samples A-1.11
A-1.10 Case 6A: 12 MW LEU Fresh Day 2 with Flux Trap Samples A-1.12
A-1.11 Case 7A: 12 MW LEU Week 79 Day 0 with Flux Trap Samples A-1.13
A-1.12 Case 8A: 12 MW LEU Week 79 Day 2 with Flux Trap Samples A-1.14
A-1.13 Case 5B: 12 MW LEU Fresh Day 0 with Empty Flux Trap A-1.15
A-1.14 Case 6B: 12 MW LEU Fresh Day 2 with Empty Flux Trap A-1.16
A-1.15 Case 7B: 12 MW LEU Week 79 Day 0 with Empty Flux Trap A-1.17
A-1.16 Case 8B: 12 MW LEU Week 79 Day 2 with Empty Flux Trap A-1.18
B-1.1 Maximum Allowed Core Power Based on Original Analysis Methods B-1.5
B-2.1 Illustration of Excursion-Flow (Ledinegg) Instability B-2.3
B-2.2 Lateral Heat Flux Distribution in Non-Uniform Waters Test Section B-2.5

LIST OF TABLES

Tab. No.	Title	Page
3-1	UAl_X and U10Mo Fuel Comparison	10
3-2	Summary of MURR Fuel Element Specifications—Current and Proposed	11
3-3	Critical State Evaluations for 1971 All Fresh HEU Core	14
3-4	Comparison of DIF3D and MCNP k-effectives for Fresh 1971 Core	14
3-5	Graphite Reflector and Flux Trap Loading Worths—2008 HEU core	16
3-6	Graphite Reflector and Flux Trap Loading Worths—2008 LEU core	16
3-7	Comparison of DIF3D and MCNP Core k-effective for HEU and LEU Cores	20
3-8	Summary of Critical States Evaluated for Partially Burned Cores	21
3-9	Current and Proposed MURR Fuel Operating Characteristics	23
3-10	Summary of Blade Worth and Shutdown Margin Evaluations	24
3-11	Comparison of Day 0 LEU Fluxes and Reaction Rates to HEU	27
3-12	Comparison of Day 2 LEU Fluxes and Reaction Rates to HEU	28
3-13	Summary of Power Distribution Evaluations	34
3-14	Summary of Key Hot Stripe Heat Fluxes Evaluated	37
4-1	Hot Channel Factor Components for Enthalpy Rise	49
4-2	Flow Instability Power	52
A-1.1	Summary of Power Distribution Evaluations	A-1.2
A-1.2	Summary of Key Hot Stripe Heat Fluxes Evaluated	A-1.2
B-1.1	Replication of Table 4-14 of Reference [4-2] "Summary of MURR Hot Channel Factors"	B-1.6
B-2.1	PLEMP/ANL Predictions for Croft Tests with 0.054-inch Channel Thickness	B-2.6
B-2.2	PLEMP/ANL Predictions for Croft Tests with 0.072-inch Channel Thickness	B-2.6
B-2.3	PLEMP/ANL Predictions for Croft Tests with 0.094-inch Channel Thickness	B-2.6
B-2.4	PLEMP/ANL Predictions for Waters Tests with Uniform Lateral Heat Flux	B-2.7
B-2.5	PLEMP/ANL Predictions for Waters Tests with Non-Uniform Lateral Heat Flux	B-2.7
B-2.6	Range of Parameters of Whittle and Forgan Tests	B-2.8

SUMMARY

This report contains the results of reactor design, performance, and steady state safety analyses for conversion of the University of Missouri Research Reactor (MURR) from the use of highly-enriched uranium (HEU) fuel to the use of low-enriched uranium (LEU) fuel. The analyses were performed by staff members of the Global Threat Reduction Initiative (GTRI) Reactor Conversion Program at the Argonne National Laboratory (ANL) and the MURR Facility. The core conversion to LEU will be performed with financial support of the US government. This project was approved in early 2006.

The objectives of this work was to show that it is feasible, under a set of manufacturing assumptions, to design a MURR LEU fuel element that could safely replace the current MURR HEU fuel element and maintain performance while requiring minimal, if any changes, to the control blades and control blade drive mechanisms as well as the instrumentation and control system.

Documents that were reviewed by ANL as bases for the design and safety evaluations were the MURR design drawings and historic analyses of the facility. All of the information and data needed to construct the reactor models and perform the analyses were provided by MURR. The methods and codes that were utilized have been qualified by extensive conversion analysis experience and international benchmark.

The current HEU fuel element has 24 plates 50 mil thick (0.050 inches) with fuel meat being 20 mil thick in each plate and consists of aluminide fuel containing uranium with a ^{235}U enrichment of 93% clad with Al-6061 aluminum. The cladding thickness of the HEU plates is 15 mil.

The proposed LEU fuel elements have the same overall design and exterior dimensions as the current HEU fuel elements as well as the same number of fuel plates. However, the proposed LEU fuel element has fuel meat thicknesses varying from 9 mil to 18 mil thick and consists of U10Mo monolithic foils containing uranium with a ^{235}U enrichment of 19.75% clad with Al-6061. The cladding thickness of LEU plates 3-23 is 10 mil for an overall thickness of 38 mil. Plate 2 has 13 mil clad and 38 mil overall thickness. The two exterior plates are 49 mil thick with Plate 1 (the inner plate) having 20 mil clad and Plate 24 (the outer plate) having 16 mil clad. The LEU U10Mo monolithic fuel is not yet qualified as driver fuel in research reactors, but is under intense development under the auspices of the GTRI Fuel Development and Fuel Fabrication Capability programs.

To design the proposed MURR LEU element, analyses were performed to ensure that acceptable shutdown and safety margins as well as experimental performance were maintained. Experimental performance evaluations showed that a power up-rate to 12 MW is needed to maintain fluxes and reaction rates at the mission critical irradiation locations. Consequently, all safety margins were evaluated at the uprated power of 12 MW.

Overall, the report shows that the objectives of this study were realized and that it is feasible to convert the MURR reactor and safely operate at 12 MW with the proposed LEU fuel elements if they can be manufactured according to the specifications described in the report.

Note that two key design points have still not been fully confirmed:

- It is not yet clear whether the 10 mil clad thickness will prove too difficult or expensive to fabricate.
- Furthermore, experiments and analyses to prove the hydrodynamic stability of the thin 38 mil fuel plates must still be performed.

Should a thicker clad be required and/or a stiffer plate, then the inherent penalty of displacing moderating water will need to be addressed to prove technical feasibility of an alternate fuel design.

1. INTRODUCTION

This paper describes the analyses performed to study the feasibility of converting the facility's current highly-enriched uranium (HEU) fuel to low-enriched uranium (LEU) fuel. Because of its compact core design (33 liters), which requires a much higher loading density of ^{235}U, the University of Missouri Research Reactor (MURR) could not perform its mission with any previously qualified LEU fuel products. In 1986, a BOLD VENTURE 3-D model, benchmarked against the only MURR destructively analyzed fuel element, was used to demonstrate that a silicide LEU core loaded to density of 7.2 gU/cm^3, and with no fission product inventory, would result in a k-effective of less than 1.0 [1-1]. However, in 2006 with the prospect of the GTRI fuel development program validating the performance of monolithic UMo foil fuels, MURR started actively collaborating with the Reduced Enrichment for Research and Test Reactors (RERTR) Program, and four other U.S. high-performance research reactors that use HEU fuel, to find a suitable LEU fuel replacement.

[1-1] Letter Request to USNRC, Application for Unique Purpose Exemption from Conversion from HEU Fuel, Facility License No. R-103, University of Missouri Research Reactor, September 1986; and supplemented by Letter Response to USNRC Request for Additional Information Supporting the Unique Purpose Exemption Request, February 1987.

2. GENERAL DESCRIPTION OF FACILITY, REACTOR & FUEL

2.1 Facility Description

The Missouri University Research Reactor (MURR) is a multi-disciplinary research and education facility providing a broad range of analytical and irradiation services to the research community and the commercial sector. The facility is situated on a 7.5-acre (3.0-hectare) lot in the central portion of the University Research Park, an 84-acre (34.0-hectare) tract of land approximately one mile (1.6 km) southwest of the Missouri University main campus. The campus is located in the southern portion of Columbia, the county seat and largest city in Boone County, Missouri.

Scientific programs include research in archaeometry, epidemiology, health physics, human and animal nutrition, nuclear medicine, radiation effects, radioisotope studies, radiotherapy, and nuclear engineering; and research techniques including neutron activation analysis, neutron scattering, and neutron interferometry. MURR staff generates and nurtures extensive collaborations with outside researchers. Research groups are made up of both MURR staff and researchers from the University of Missouri System's four main campuses. The breadth and quality of the research programs and the available facilities and equipment are comparable to those found in the U.S. National Laboratories.

The MURR has six types of experimental facilities designed to support these services and research programs: the Center Test Hole (Flux Trap); the Pneumatic Tube System; the Graphite Reflector Region; the Bulk Pool Area; the (six) Beamports; and the Thermal Column. The first four types provide areas for the placement of sample holders or carriers in different regions of the reactor core assembly for the purposes of material irradiation. Some of the material irradiation services include transmutation doping of silicon, isotope production for the development of radiopharmaceuticals and other life-science research, and neutron activation analysis. The six beamports channel neutron radiation from the reactor core to experimental equipment which is used primarily to determine the structure of solids and liquids through neutron scattering. The graphite thermal column is designed for the purpose of performing neutron radiographs and large sample irradiations.

The MURR also participated in a U.S. Department of Energy (DOE) program to provide the availability of university reactor facilities to non-reactor-owning colleges and universities until this program ended in 2008. The MURR also provides support to institutions with reactors, but which operate at power levels too low to adequately perform required experiments. Reactor sharing projects included work in fields such as anthropology, archaeology, animal science, crystallography, analytical epidemiology-nutrition, geology, materials science, physics, nuclear analysis development, and biochemistry.

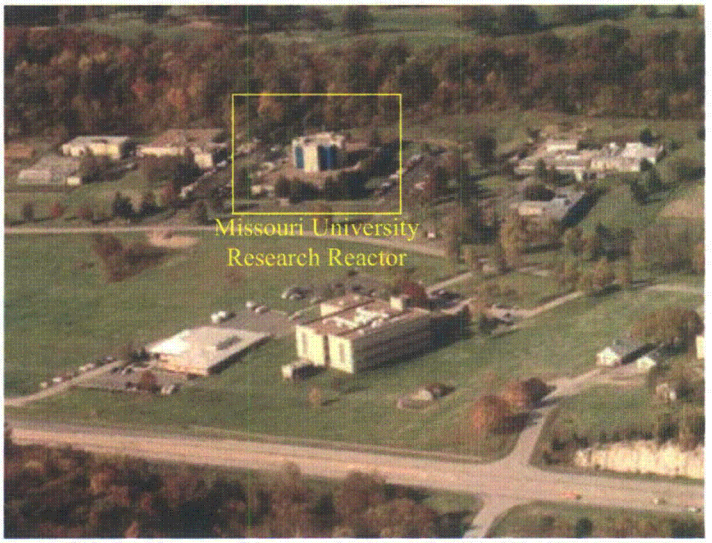


Figure 2.1
University Research Park – University of Missouri-Columbia

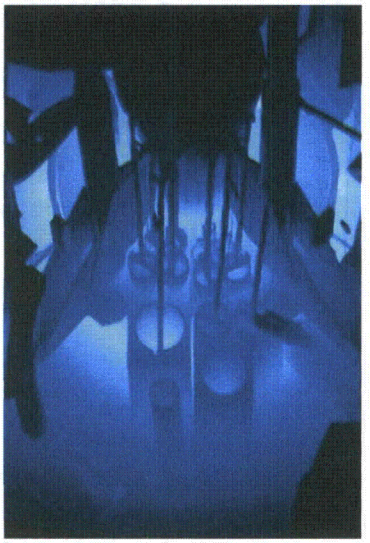


Figure 2.2
MURR Core

2.2 Facility History

The MURR first achieved criticality on October 13, 1966. The reactor was originally designed for 10 MW operation, but was initially licensed to operate at only 5 MW until reactor utilization and operating experience were sufficient to justify full power operation. In 1974, additional cooling equipment was added and the process instrumentation and safety systems were modified as required to facilitate operation of the reactor at the full design power of 10 MW.

In 1986, the University of Missouri requested that a determination be made by the U.S. Nuclear Regulatory Commission (NRC) that the MURR has a *Unique Purpose*, as defined by 10 CFR 50.2, and is therefore exempt from the conversion from HEU to LEU fuel [2-1]. The MURR has a compact core design (33 liters) that cannot perform its intended function with any currently-qualified LEU uranium densities. A BOLD VENTURE 3D model, benchmarked against the only MURR destructively analyzed fuel element, was used to demonstrate that a new silicide LEU core loaded to density of 7.2 g U/cm^3 and with no fission product inventory would result in a k-effective of less than 1.0 [2-1].

Since achieving initial criticality, the reactor has operated safely for over 296,000 full power hours in support of the primary mission of providing the maximum flux, or current, of neutrons to the maximum number of users without endangering the health and safety of facility workers and the general public. In August 2006, the MURR submitted a re-licensing application to the U.S. Nuclear Regulatory Commission for a twenty-year renewal to the facility's operating license, R-103.

2.3 Basic Reactor Description

The MURR is a pressurized, reflected (beryllium and graphite), heterogeneous, open pool-type, which is light-water moderated and cooled. The reactor is designed and licensed to operate at a maximum thermal power level of 10 MW with forced cooling, or up to 50 kW in the natural convection mode.

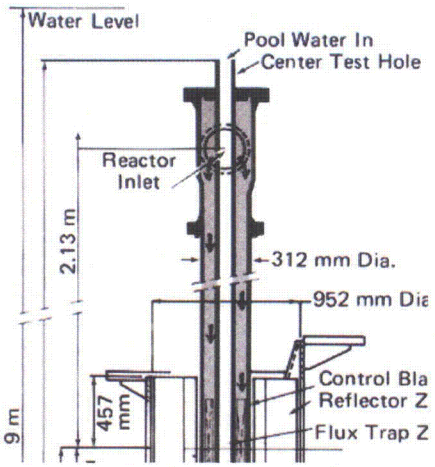


Figure 2.3
Reactor Core Assembly – 2D View

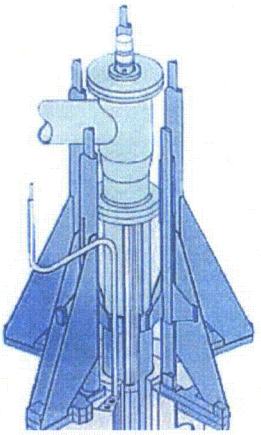


Figure 2.4
Reactor Core Assembly – 3D View

The reactor core assembly is located eccentrically within a cylindrically-shaped, aluminum-lined pool, approximately 10 feet (3.0 m) in diameter and 30 feet (9.1 m) deep. The reactor core consists of four major regions: central test hole (flux trap), fuel, control blade, and reflector. Two and three-dimensional views of the reactor core assembly are shown in Figures 2.1 and 2.2, respectively. A plan view is shown in Figure 2.3.

The flux trap is located inside the inner pressure vessel and therefore surrounded by the fuel elements. It is cooled by pool water circulating from top to bottom and can contain aluminum holder tubes containing the samples to be irradiated. The flux trap is typically loaded with a sample holder made of three aluminum tubes. Each tube is typically filled with a variety of sample containers used for isotope production.

The fuel region has a fixed geometry consisting of eight (8) fuel elements having identical physical dimensions placed vertically around an annulus between two cylindrical aluminum reactor pressure vessels. Each fuel assembly is comprised of 24 circumferential plates. The HEU plates contain uranium enriched to approximately 93% in the isotope ^{235}U as the fuel material.

The control blade region is an annular gap between the outer pressure vessel and the inner reflector annulus, so that no penetration of the pressure vessels is required. Five (5) control blades operate vertically within this gap:- four (4) Boral and one (1) stainless steel.-, The blades control reactor reactivity by varying neutron reflection.

The reflector region consists of two concentric right circular annuluses surrounding the control blade region. The inner reflector annulus is a 2.71 inch (6.9 cm) thick solid sleeve of beryllium metal. The outer reflector annulus consists of vertical elements of graphite canned in aluminum, having a total thickness of 8.89 inches (22.6 cm).

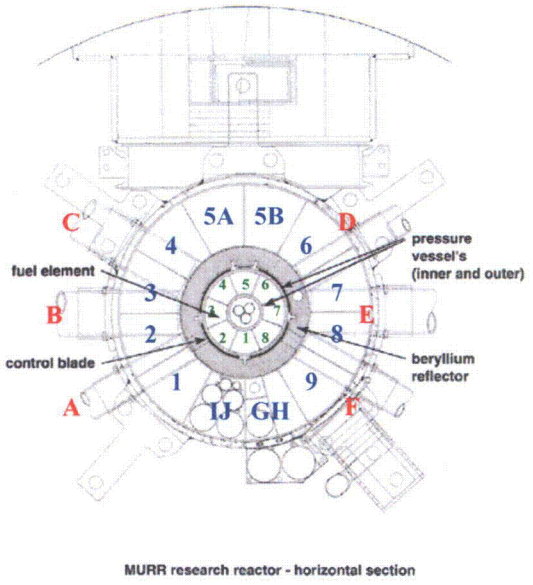


Figure 2.5
Reactor Core Assembly - Plan View

Graphite Reflector Elements (12):	Fuel Elements (8):
1	1
2	2
3	3
4	4
5A	5
5B	6
6	7
7	8
8	
9	**Beamports (6):**
GH	A
IJ	B
	C
	D
	E
	F

2.4 Current Fuel Design and Operating Cycle

The fuel material at the time of initial startup was a uranium-aluminum alloy with each fuel element loaded to a maximum of 650 grams of ^{235}U. This type of fuel system had performed very reliably in the Materials Test Reactor (MTR) and the Engineering Test Reactor (ETR) at the Idaho National Engineering Laboratory (INEL), as well as in other reactors throughout the world. However, in order to reduce the fuel cycle cost and the amount of ^{235}U needed per MWd of energy produced at the MURR, a conversion was performed in 1971 to switch to a uranium-aluminide dispersion UAl_x fuel material with a maximum loading of 775 grams of ^{235}U per element. The UAl_x dispersion fuel system was developed at INEL for the high flux, high power Advanced Test Reactor (ATR) and subsequently used at the MTR and ETR prior to its use at the MURR [2-2, 2-3].

A drawing of the MURR fuel element is shown in Figure 2.6. The fuel elements have an overall length of 32.5 inches (82.55 cm). Each element is longitudinally-symmetrical with 24 fuel bearing plates. The fuel

plates are segments of concentric circles 50 mil thick separated by a coolant channel gap of 80 mil. The fuel meat in each plate is 20 mil thick with 15 mil of aluminum cladding on each side. Additional fuel element specifications can be found in Table 3-2.

The MURR operates continuously with the exception of a weekly scheduled shutdown. Over the past 32 years of operation, the MURR has averaged approximately 6.3 days/week at full power. The weekly shutdown provides an opportunity to access samples in the center test hole, to perform surveillance tests and maintenance, and to replace all eight fuel elements in the core. Replacing the fuel elements provides a xenon free core for restart and the chance to remix or shuffle which elements will be used in the core. The active fuel cycle typically consists of 32 fuel elements; corresponding to sixteen pairs of elements. A core loading will always consist of four different pairs of elements, with the two elements of each pair loaded opposite of each other in the core. The compact core volume limits excess reactivity and causes the control blades to be fully withdrawn when the HEU core, with equilibrium xenon, achieves approximately 670 MWd. This results in an HEU fuel element reaching a maximum burn-up of 150 MWd, which in turn corresponds to a hot spot burn-up of less than 1.8E+21 fissions/cc. This ensures that the Technical Specification limit of 2.3E+21 fissions/cc for the UAl_x dispersion fuel is not approached or exceeded. Cores are usually loaded such that the average power history of a fuel element is approximately 75 MWd. Typically a fuel element will be used in 18 to 20 different core loadings before being retired from the fuel cycle. A core with fuel elements approaching the burn-up limit will also include a corresponding number of elements with very low power history. This maximizes the number of MWd obtainable per fuel element. This same approach is also planned for the LEU fuel cycle.

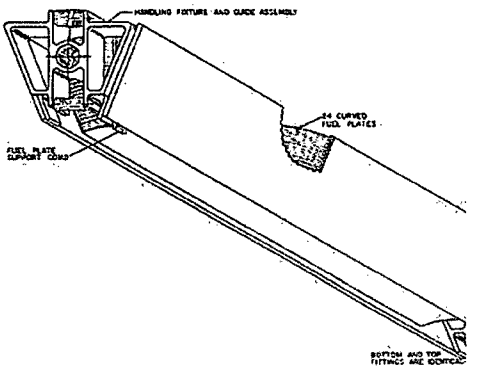


Figure 2.6
MURR Fuel Element – Pictorial View

2.5 Facility References

[2-1] Letter Request to USNRC, Application for Unique Purpose Exemption from Conversion from HEU Fuel, Facility License No. R-103, University of Missouri Research Reactor, September 1986; and supplemented by Letter Response to USNRC Request for Additional Information Supporting the Unique Purpose Exemption Request, February 1987.

[2-2] Gibson, G.W., Graber, M.J., and Francis, W.C., Annual Progress Report on Fuel Element Development for FY-1963, IDO-16934, 1963.

[2-3] Graber, M.J., et al., Performance Evaluation of Core II and III Advanced Test Reactor Fuel Elements, ANCR-1027, Aerojet Nuclear Company, 1971.

3. NEUTRONIC ANALYSES

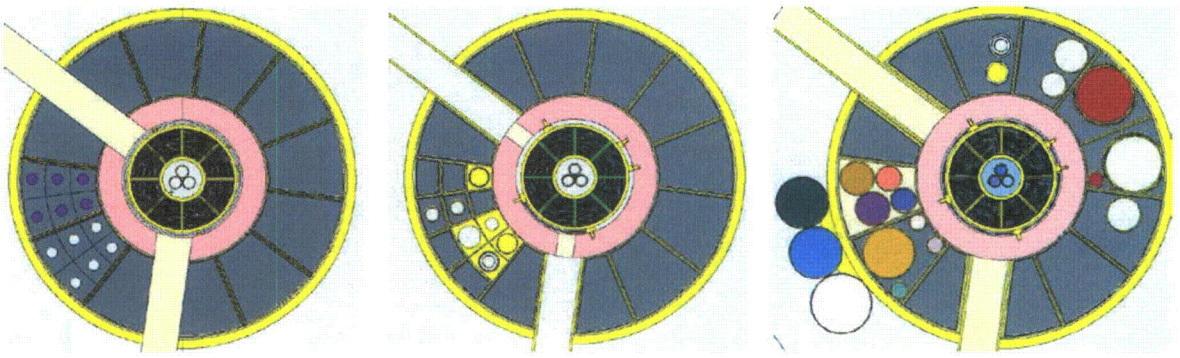
A joint study between MURR and the GTRI Reactor Conversion Program at ANL was conducted to determine a suitable LEU fuel element design and to perform the preliminary analyses necessary to establish the shutdown and safety margins remain acceptable for the converted reactor. The collaboration continues in order to finalize the LEU assembly design and perform complete safety analyses for the converted core.

Depletion calculations are very important for MURR conversion feasibility analysis since the reactor has operated with a weekly operations and fuel cycle for more than twenty years with high reliability and high utilization . The medical isotope production and many other experimental capabilities at MURR are optimized for this weekly cycle. Realistic experimental flux and reaction rate performance must be evaluated for typical weekly cycles rather than for an all fresh core. The fuel shuffling schedule of an LEU element that could efficiently and effectively match or exceed the performance of the typical HEU fuel shuffling scheme must be defined in order for the conversion to LEU fuel be declared feasible.

The LEU fuel element design was performed in four phases:

1. Performed scoping studies on simplified model (see Figure 3.1) to determine initial LEU fuel element design.
2. Developed a more detailed model (see Figure 3.1) and established the credibility of the model by comparing prediction with all HEU fresh core measurements from 1971.
3. Refined the model to represent the current (2008) reactor configuration (see Figure 3.1), developed the HEU and LEU fuel shuffling schemes, developed a representative experimental load, and reinforced credibility by comparing model prediction to corresponding measured critical positions.
4. Defined reference cores and use high fidelity models to evaluate fuel cycle performance, shutdown margins, experimental performance and power distributions for the thermal-hydraulic steady state safety margins calculation.

Figure 3.1 illustrates the types of detail added to the MCNP model as the study moved from scoping model, through the 1971 Reactor with fresh core, to the 2008 Reactor.



Scoping model 1971 Reactor 2008 Reactor

Figure 3.1 – Cross Section of MCNP Models of MURR

Before discussing the analyses, it is useful to review the codes and methodologies used and developed to allow for tractable yet highly detailed neutronic/depletion calculations.

3.1 Description of Neutronics Codes and Methodologies

To perform the neutronics calculation of a compact core such as MURR, it is preferable to use a transport theory code to capture the rapidly changing spectra across the various regions. Therefore, the MCNP [3-1, 3-2] continuous energy Monte Carlo code was used for all detailed calculations of core k-effective, control blade position, as well as detailed power distributions and experimental fluxes/reaction rates.

REBUS-PC [3-3] was used for the MURR depletion calculations.

Although depletion calculations using MCNP for flux and cross section evaluation at each statepoint can be performed using the REBUS-MCNP [3-4, 3-5, 3-6] computer code, the hundreds of statepoints required to model the complex fuel cycle of MURR -- a process repeated during fuel element optimization -- made REBUS-MCNP intractable for the full fuel cycle simulation in a reasonable time frame. It was therefore necessary to develop a less time-consuming diffusion model to perform the depletion calculation. The REBUS-DIF3D [3-7, 3-8] code was chosen for this portion of the feasibility study. Note that REBUS-MCNP models were still developed for the MURR reactor in order to benchmark the REBUS-DIF3D models. The WIMS-ANL [3-9, 3-10] lattice physics code was used to generate a burnup dependent, 69 group lumped fission product to model the fission products not explicitly modeled in the MURR MCNP models [3-11].

A detailed Theta-R-Z diffusion model was developed with the DIF3D finite difference multigroup diffusion code. WIMS-ANL was used to generate burnup dependent cross section libraries for all the materials of the REBUS-DIF3D model. Considerable customization of the cross-section generation process was required to prepare a robust set of 10 group cross sections. The details of the DIF3D and WIMS-ANL models were developed iteratively to assure fidelity of the resulting diffusion calculations with MCNP and experiments [3-12]. Note that, as discussed later, comparisons between DIF3D and MCNP were performed for both the fresh and depleted cores.

Since REBUS-DIF3D depletion was only used to model the weekly operation for HEU and LEU while MCNP was used for all neutronics calculations, it was necessary to develop a methodology to update the MCNP models with the detailed three dimensional, burnup dependent material compositions (i.e., atom densities of all the depleting isotopes modeled) obtained from REBUS-DIF3D. Figure 3-2 illustrates the methodology developed to use all these codes in a consistent manner.

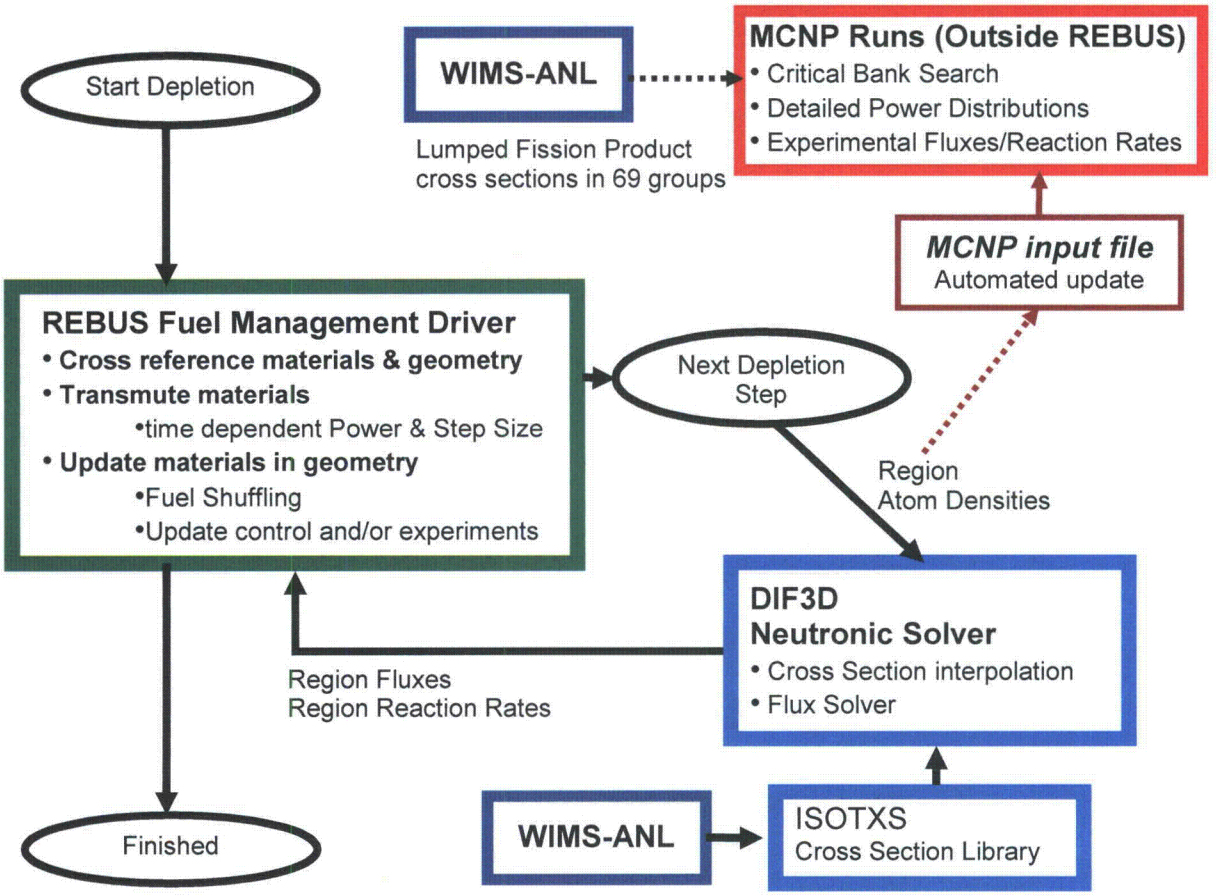


Figure 3.2 – The Multiple Neutronic Codes Applied to Model the MURR Fuel Cycle

3.2 Scoping Studies for LEU Element Design

The initial scoping work of MURR's fuel conversion feasibility study included defining the fuel requirements, describing the HEU core, and defining experimental facility performance indicators. Some of the potential concerns in performing a conversion include (1) matching the performance capabilities of the current 775-gram ^{235}U fuel element, (2) not increasing the fuel storage requirements, (3) having sufficient excess reactivity in order to decrease the loading in fuel plates with high peaking factors, and (4) maintaining or enhancing neutron flux in the center test hole (flux trap), graphite reflector, and beamport regions.

To better appreciate the differences between the HEU and LEU fuel designs, the HEU design will be briefly described. The HEU fuel design of 50mil thick plates with 15 mil thick cladding is based on the initial tests for the ATR performed in the 1960's and early 1970's for improving the original MTR alloy fuel design to the current UAl_x dispersion fuel. With dispersion fuel fabrication methodology, there is more variation in the cladding thickness due to the number of times the plate must be rolled. There is also the concern of stray fuel particles being pressed into the cladding. Consequently, the cladding thickness

is nominally 15 mil to ensure that the required minimal cladding thickness of 10 mil is achieved and that no stray fuel particles are within 8 mil of the cladding surface.

The first technical task performed was a comparison of core excess reactivity between the MURR's current UAl_x dispersion HEU fuel and U10Mo and U7Mo monolithic LEU fuels. Using the transport code MCNP and the scoping model shown in Figure 3.1, broad scoping studies were performed for an all fresh core. The first comparison consisted of replacing the 20 mil thick UAl_x HEU fuel meat with the two different U-Mo LEU fuels. No other physical changes were made to the core – the same fuel plate and coolant channel dimensions were maintained. Although this resulted in lower k-effectives even with the ^{235}U loading more than doubling, the k-effectives were still high enough to ensure sufficient excess reactivity with the core operating at 10 MW. However, the LEU cores would require a greater number of fuel elements in the fuel cycle, thus exceeding our fuel storage capacity.

To further explore the possibilities of an LEU core design that could match or exceed current performance capabilities, the MURR asked the GTRI Fuel Development Program to answer a number of key questions on the following fuel design/manufacturing limitations: peak burn-up, minimum thickness of the fuel meat and cladding, minimum thickness of the curved plate to ensure sufficient rigidness, and the magnitude of engineering peaking factors due to reducing the thickness of the fuel meat. The best information available from U.S. High-Performance research reactor Working Group (USHPWG) collaboration during 2006-2009 is:

- What is the peak fuel burn-up limit? ***~7E+21 fissions/cc***
- How thin can acceptable U10Mo foils be fabricated? ***5 mil (0.127 mm)***
- What is the minimum acceptable cladding thickness? ***10 mil (0.254 mm)***
- How thin can sufficiently rigid curved fuel plates be fabricated? ***38 mil (0.965 mm)***
- Magnitude of engineering peaking factors for thin U10Mo foils? ***≤ UAl_x HEU factors***
- What is the minimum cladding blister temperature? ***850-900 °F (454-482 °C)***

Note that two of these points have still not been fully confirmed:

- It is not yet clear whether the 10 mil clad thickness will prove too difficult or expensive to fabricate.
- Furthermore, experiments and analyses to prove the hydrodynamic stability of the thin 38 mil fuel plates must still be performed.

Should a thicker clad and/or a stiffer plate be required, then the inherent penalty of displacing moderating water will need to be addressed to prove technical feasibility of an alternate fuel design.

Despite the uncertainty surrounding the cladding thickness, the design work continued based on information indicating that a 10 mil clad should be feasible. The next step was therefore to increase the water-to-metal ratio by decreasing either the plate cladding or fuel meat thickness, or both, while increasing the width of the coolant channel gap. First, the standard 15 mil thick aluminum cladding was decreased to 12 mil, while the coolant channel gap was increased from 80 to 86 mil. Next, a 10 mil cladding thickness was modeled with a 90 mil coolant channel gap. For the U10Mo core, with a lower ^{235}U density than the U7Mo, the MCNP results indicated sufficient excess reactivity that could achieve even more MWd per fuel element than the current design; assuming that fuel element performance can handle the higher burnup values. Finally, using the current 15 mil thick cladding, the fuel meat thickness was decreased to 18 mil and then to 16 mil, while increasing the coolant channel gap to 0.0821 and 84.2 mil, respectively. The MCNP analyses indicated that equivalent or slightly higher k-effective values were obtained using less ^{235}U than with standard 15 mil thick aluminum cladding on the proposed LEU core. The cores modeled confirmed the need to increase the water-to-metal ratio in order to gain reactivity [3-14].

Reducing the number of fuel plates in order to increase the water-to-metal ratio was also analyzed to compare the results from reducing the cladding and fuel meat thicknesses. Table 3-1 combines some of the better results of both reducing the thickness of the cladding and fuel meat and reducing the number of fuel plates. Only the results from the U10Mo studies are listed in Table 3-1 since U10Mo has exhibited the least amount of swelling as a function of fuel burnup during irradiation testing, making it the preferred choice from an operational perspective. Reduction in the number of fuel plates seems to provide comparable positive results until the increase in average heat flux is factored in, which results from the corresponding reduction in heat transfer surface area. For a high-performance research reactor such as the MURR, the hot stripe heat flux is the power/flux limiting factor. Therefore, reducing the number of fuel plates is not currently being considered as a preferred way to increase the water-to-metal ratio in order to gain reactivity. Additionally, uniformly loaded LEU results in much higher heat flux peaking factors and would also significantly reduce the maximum power limit and neutron flux. Therefore, the proposed fuel element design reduces the fuel foil thickness of the three highest power density plates.

Table 3-1 UAl_x and U10Mo Fuel Comparison

No. Plates	Fuel Meat (inches)	Clad (inches)	Plate (inches)	Channel (inches)	Core (Kg)	K_{eff}	Flux Trap[3] Therm Ratio	Flux Trap[3] Fast Ratio
24[1]	**0.020**	**0.015**	**0.050**	**0.080**	**6.20**	**1.086**	**1.000**	**1.000**
24	0.020	0.012	0.044	0.086	13.0	1.076	0.885	0.951
24	0.018	0.012	0.042	0.088	11.7	1.079	0.889	0.955
24	0.020	0.010	0.040	0.090	13.0	1.086	0.867	0.921
24	0.018	0.010	0.038	0.093	11.7	1.090	0.874	0.937
24[2]	**0.009 to 0.018**	**0.010 to 0.020**	**0.038 to 0.049**	**0.0916**	**11.3**	**1.079**	**0.884**	**0.916**
23	0.020	0.012	0.044	0.092	12.5	1.082	0.885	0.949
22	0.025	0.012	0.049	0.093	14.9	1.082	0.875	0.951
22	0.022	0.012	0.046	0.097	13.1	1.084	0.876	0.950
22	0.018	0.012	0.042	0.101	10.7	1.086	0.880	0.935
21	0.022	0.012	0.046	0.104	12.5	1.087	0.878	0.931
20	0.022	0.012	0.046	0.112	11.9	1.094	0.876	0.927

[1]Current core using Al_x HEU fuel element.
[2] LEU core using initial design for proposed U10Mo fuel element.
[3]Flux in proposed LEU core divided by the flux in current HEU core with both cores operating at 10 MW. This overestimates for cores with less than 24 plates because of the total plate surface area reduction, which will reduce the maximum safe power level.

The initial LEU scoping studies that led to the current proposed LEU core design were performed in 2006 and 2007 and summarized in papers presented at RERTR International meetings [3-13, 3-14]. Table 3-2 compares the proposed LEU fuel element design with the current HEU fuel element.. Note that the initial design for the proposed LEU fuel element was changed from a 91.6 mil channel spacing shown in Table 3-1 to the 92 mil shown in Table 3-2. This change was made to ensure that the model and analyses applied a channel gap more consistent with expected manufacturing tolerances.

Table 3-2 Summary of MURR Fuel Element Specifications – Current and Proposed

Description	Current HEU Fuel	Proposed LEU Fuel
Fuel		
Material	UAl_x (mostly UAL_3)	U10Mo
Enrichment	93% ^{235}U	19.75% ^{235}U
Thickness Plate 1	20 mil (0.508mm)	9 mil (0.229 mm)
Plate 2	20 mil (0.508mm)	12 mil (0.305 mm)
Plates 3-23	20 mil (0.508mm)	18 mil (0.457 mm)
Plate 24	20 mil (0.508mm)	17 mil (0.432 mm)
Cladding		
Material	Aluminum	
Thickness Plate 1	15 mil (0.381mm)	20 mil (0.508 mm)
Plate 2	15 mil (0.381mm)	13 mil (0.330 mm)
Plates 3-23	15 mil (0.381mm)	10 mil (0.254 mm)
Plate 24	15 mil (0.381mm)	16 mil (0.406 mm)
Fuel Element		
Number of Fuel Plates	24	
Overall Fuel Element Length	32.5 inches (82.550 cm)	
Overall Fuel Plate Length	25.5 inches (64.770 cm)	
Overall Active Fuel Length	24.0 inches (60.960 cm)	
Fuel Plate Thickness 1 &24	50 mil (1.270mm)	49 mil (1.245mm)
Fuel Plate Thickness 2-23	50 mil (1.270mm)	38 mil (0.965mm)
Distance Between Plates (Coolant Channel)	80 mil (2.032mm)	92 mil (2.337mm)
Maximum ^{235}U Loading	775 grams	1439 grams
Fuel Density	1.53 grams/cm^3	3.03 grams/cm^3
Weight	~ 6 Kg	~ 11 Kg

To better understand the proposed LEU fuel design, three figures are provided which compare power density and heat flux peaking between the HEU and LEU fuel. In Figures 3.3, 3.4 and 3.5, the control blades are half out (13-inch withdrawn position), which is approximately the critical position of a cold clean fresh core.

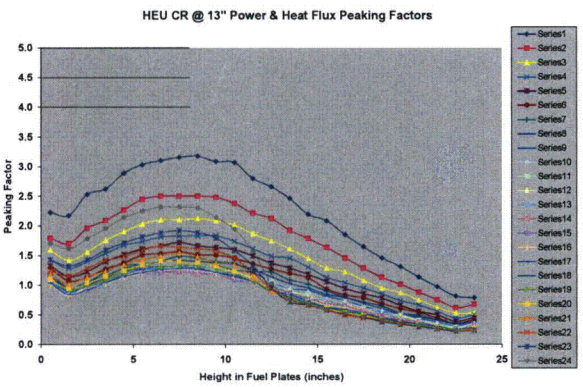


Figure 3.3 – HEU Core Design Peaking Factors

Figure 3.3 illustrates the power density and heat flux peaking factors for the HEU core consisting of eight fresh fuel elements. The peaking factors are graphed for each fuel plate, with plate number-1 adjacent to the inner reactor pressure vessel and plate number-24 adjacent to the outer pressure vessel. The graph points correspond to the mid-point of each one inch vertical segment of the 24 inch long fuel meat, starting at 0.5 inches from the bottom to 23.5 inches at the top. The peaking factor is the average power density in that fuel volume divided by the average for the total fuel meat volume of that fuel element.

Figure 3.4 provides the graphs for the proposed LEU fuel element power density peaking factors. In comparing Figures 3.3 and 3.4, plate number 1 has the highest power density in both cases, while the power peaking factor is about 1.5 times higher in the LEU fuel element than the HEU element. Plate number 2 has the next highest power peaking factor in both the LEU and HEU fuels. The high peak fuel burn-up limit for LEU fuel means that the high power peaking factors can be managed without needing to decrease the ^{235}U density to avoid limiting fuel element lifetime. However, to avoid the highest hot stripe heat flux peaking from limiting the safe operating power level, the thickness of the fuel meat in plates number 1, 2 and 24 was reduced to lower their hot stripe heat flux. Using this approach, the proposed core design consists of fuel meat thicknesses that vary by a factor of two.

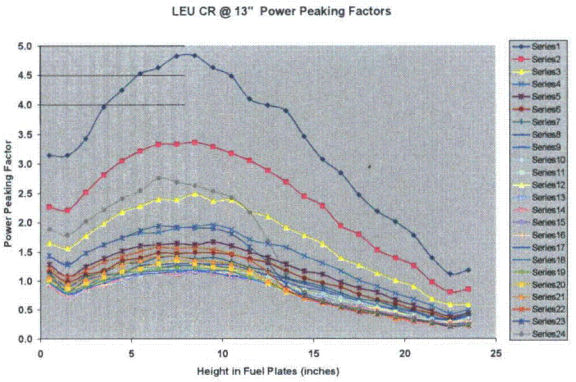


Figure 3.4 – LEU Core Design
Power Density Peaking Factors

Figure 3.5 depicts the heat flux peaking factors for the proposed LEU fuel element. Plate number 1 and 24 are 49 mil thick for the following two reasons: (1) the cladding on these plates are susceptible to being scratched, dented or bumped during fuel handling, and (2) the plates are located between coolant channels with different widths, thus potentially creating a differential pressure across the fuel plate. Plate number 1 has the thinnest fuel meat of 9 mil. Plate number 2 fuel meat thickness is 12 mil with a corresponding cladding thickness of 13 mil. Plate number 24 has a fuel meat thickness of 17 mil. All other plates are 38 mil thick and have a fuel meat thickness of 18 mil with corresponding 10 mil thick cladding.

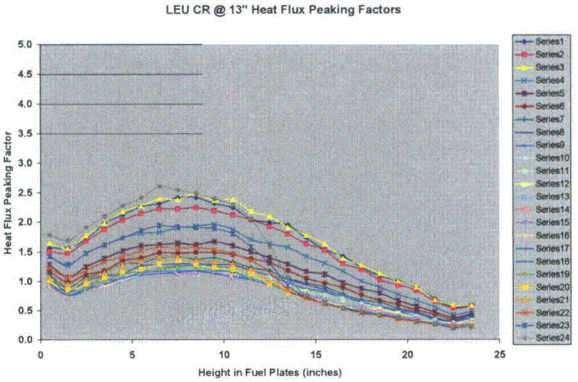


Figure 3.5 – LEU Core Design
Heat Flux Peaking Factors

The possible fabrication techniques for the new U10Mo monolithic fuel plates should require less rolling. Additionally, the monolithic "foil fuel meat" should also substantially reduce or eliminate the chance of fuel particles being pressed into the cladding, thus allowing the 10 mil nominal cladding thickness. However, the fabrication methodologies must be further developed and tested before the thinnest allowable nominal cladding thickness can be confirmed. Flow validation tests also need to be performed to ensure that the 38 mil thick plates have sufficient stability and rigidness to fully withstand the hydraulic forces imposed by a primary coolant flow velocity of 25 ft/sec (7.6 m/sec). Plate stability may also vary depending on the relative thicknesses of the fuel meat and cladding, because their contribution to stiffness can differ. These values need to be determined to complete the optimum core design.

The LEU core fuel meat thicknesses have been reduced such that the maximum heat flux peaking factors are less than those of the current HEU core. This change was made because a power uprate will be necessary to maintain current experimental performance and capabilities (see the Flux Trap Ratios in Table 3-1). The goal is to obtain peaking factors that will allow a power uprate from 10 MW to 12 MW.

Note that confirmation of this result is needed from a more detailed model including a typical mixed core loading. Therefore, more detailed computational models were developed.

3.3 Development of the Detailed Neutronics Models

The MCNP scoping model used to design the candidate LEU element was enhanced to provide details of power distributions and experimental fluxes. The enhanced MCNP model illustrated in Figure 3.1 was benchmarked against a 1971 core with all fresh fuel and many reported critical states.

Furthermore, depletion capability was developed with both REBUS-MCNP and REBUS-DIF3D. Since modeling the complex MURR fuel shuffling sequence requires the evaluation of hundreds of statepoints, iterative design and analysis of the fuel cycle with REBUS-MCNP is intractable. Thus, a REBUS-DIF3D model was developed and benchmarked to MCNP and measurements. Afterwards, the MCNP models were updated to include the depleted materials from REBUS-DIF3D to allow evaluations of measured critical states and to demonstrate the overall accuracy of the fuel cycle simulations.

3.3.1 Computational Model Credibility – Comparisons with 1971 HEU Fresh Core Measurements

The MCNP scoping model was refined to match the 1971 MURR Reactor– this corresponds to the core configuration during the initial critical and physics tests performed on the first MURR aluminide 775 g U-235 HEU core, which is still the current fuel element design. Since around 1980, MURR has not been able to have a full core of unirradiated fuel element to perform any clean critical. The startup campaign of the 1971 all fresh core provided an experimental basis for model benchmarking. The benchmarking effort proved that a high level of detail is needed in the models to accurately predict the compact, high flux MURR reactor.

Note that these changes were made to the model to improve agreement with a report by Julian [3-15]. Many details of the improvements were described in RERTR International Meeting papers in 2007 and 2008 [3-12, 3-14, 3-16]. The MCNP changes were to geometry and material compositions per development of a design basis spreadsheet. It proved important to treat the explicit geometry of the reflectors and control blades well.

This core configuration was also used as a basis to develop the adequate level of approximations in DIF3D and developed the WIMS-ANL methodology. WIMS-ANL and DIF3D model changes were methodological, in addition to the geometry and material updates. Proper generation of cross-sections in WIMS-ANL and appropriate geometric discritization in the DIF3D model were both key to fidelity.

Table 3-3 summarizes the critical states calculated by MCNP for the all fresh HEU core. The RMS deviation from critical for the five cases is -0.584% ± 0.075% Δk/k. While the bias for the 1971 HEU Fresh core remains fairly large, there were details of materials no completely specified in the 1971 data. The compact nature of the MURR core, with both graphite and beryllium reflectors and complex experimental channels is difficult to model. Notably, the best prediction was for Case 1 with all control blades banked. All cases to establish feasibility are for banked control blade positions, which is the mode for normal MURR operations. Furthermore, the small standard deviation of the reactivity bias despite the skewed blade patterns indicates that comparisons of HEU and LEU burnup performance should be sound.

Table 3-4 shows the close agreement achieved for DIF3D vs. MCNP for a variety of core states. The LEU cases applied the fuel element design identified in Table 3-2. For the HEU cases, MCNP predicted a sample holder worth of 0.344% Δk/k, while DIF3D predicted 0.394% Δk/k. . The measured worth of the

sample holder of the HEU MURR core is 0.36% Δk/k. For the LEU case, MCNP predicted a sample holder worth of 0.302% Δk/k, while DIF3D predicted 0.351% Δk/k.

Table 3-3 Critical State Evaluations for 1971 All Fresh HEU Core

Case[1]	Blade Position (inches withdrawn)					Flux Trap State	MCNP		
	A	B	C	D	Regulating Blade		k_{eff}	σ (pcm)	Deviation from Critical[3] (%Δk/k)
1	11.93	11.92	11.92	11.92	26.00	Empty	0.99520	12	-0.482
2	11.93	11.92	11.92	12.63	6.00	Empty	0.99485	11	-0.518
3	11.93	11.92	11.92	10.50	11.24	3 Tubes[2]	0.99377	11	-0.627
3A	11.93	11.92	11.92	10.91	6.00	3 Tubes	0.99378	11	-0.626
3B	11.93	11.92	11.92	10.21	26.00	3 Tubes	0.99357	12	-0.647

[1] Julian report Case Number for startup physics testing of HEU UAl_x core
[2] 3 empty tubes in flux trap indicates sample holder in place, but filled with pool water
[3] Deviation from critical is (k-1)/k

Table 3-4 Comparison of DIF3D and MCNP k-effectives for Fresh 1971 Core

Core	Case	MCNP (k_{eff})	DIF3D (k_{eff})	Deviation (DIF3D vs.MCNP) (%Δk/k)
HEU	No sample holder ARO (blades out)	1.10209 (±11 pcm)	1.10298	+0.073%
LEU	No sample holder ARO (blades out)	1.10003 (±11 pcm)	1.09646	-0.296%
HEU	Empty sample holder ARO (blades out)	1.10629 (±11 pcm)	1.10779	+0.123%
LEU	Empty sample holder ARO (blades out)	1.10370 (±11 pcm)	1.10070	-0.247%
HEU	Empty sample holder blades at measured critical[1]	0.99313 (±11 pcm)	0.99512	+0.201%
LEU	Empty sample holder blades at measured critical[1]	1.00891 (±11 pcm)	1.00598	-0.289%

[1] The control blades are modeled at the recorded heights from a 1971 critical measurements.

3.3.2 Description of Changes to HEU Core Models (1971 to 2008 Core Configuration)

The irradiation positions and typical sample loadings in the graphite reflector and flux trap have changed since the tests performed in 1971. In order to properly model the current reflector and flux trap configurations for the feasibility study, it was necessary to modify the MCNP and DIF3D models.

The key changes between the 1971 and 2008 Reactor configurations were:

- Different control blades are in use, with slight changes in dimension and significant change in composition.

- Most graphite reflector blocks have been replaced, and the associated experimental positions have been markedly changed. One of the most significant features of the current graphite reflector is the presence of large Cd-lined irradiation positions in the L and N wedges, adjacent to fuel element position 5.
- The beryllium reflector no longer has voids at the entrance of Beam Ports A and E.

To compare HEU and LEU performance relative to the current mission of the facility, typical sample loadings were modeled for reflector and flux trap positions.

The reflector irradiation positions and flux trap contents are explicitly modeled in MCNP, but the Theta-R-Z geometry of the DIF3D model does not allow an exact representation of the reflector and flux trap components. Instead, modeling approximations were tested to determine the most effective way of representing the irradiation positions and samples in the DIF3D model.

A series of MCNP cases were prepared to transition the graphite reflector and flux trap contents from the 1971 to current (2008) conditions. The base case had all fresh fuel, empty holder tubes in the flux trap, the control blades at 23" withdrawn, and the regulating blade positioned at the core midplane. The model was sequentially altered to explicitly represent each wedge with its corresponding irradiation positions and typical sample loading. The final step was to model a typical sample loading in the central flux trap.

In the same way, the DIF3D model was transitioned to the current conditions, but with an amount of natural boron smeared into the wedge or flux trap sample holder that matched the reactivity worth calculated by the MCNP cases. The only deviation from this approach was for the 11-wedge, which is a helium filled aluminum can with water-filled irradiation positions. In this case, the water fraction was decreased in the DIF3D representation of the 11-wedge to match the reactivity worth.

Tables 3-5 and 3-6 presents the sequence of cases used to transition the MCNP and DIF3D core models loaded with HEU and LEU fuel, respectively. Both the individual and cumulative worths of each alteration in the sequence are presented. It was known from reactivity change measurements at MURR when these wedges were installed that the cumulative negative reactivity worth of the Cd-lined irradiation positions in the L and N wedges is ~0.75% $\Delta k/k$. It can be seen in Table 3-5 that the 2008 MCNP core model predicts this reactivity worth very well, which reinforces the credibility of the model. It can be seen that the net cumulative effect of all reflector and flux trap alterations to reach current core conditions was 0.985% $\Delta k/k$ for the HEU core, and 0.890% $\Delta k/k$ for the LEU core. With the harder spectrum in the LEU core, it was expected that the total reactivity worth of the samples would be slightly smaller than with HEU fuel. The DIF3D model boron loading or water fraction in the graphite wedges and sample cans was adjusted empirically to match the individual worth of each alteration in the MCNP model within 0.010% $\Delta k/k$.

Table 3-5 Graphite Reflector and Flux Trap Loading Worths – 2008 HEU core

	MCNP HEU			DIF3D/REBUS HEU				
	k-eff	Worth (% Δk/k) Ind.	Cum.	k-eff	*Diff. Rel. to MCNP*	Worth (% Δk/k) Ind.	Cum.	ppm B or water fraction decrease
Base Case[1]	1.09529			1.09803	*0.23%*			
L & N Wedges	1.08637	-0.750%	-0.750%	1.08908	*0.23%*	-0.749%	-0.749%	1280
10 wedge (Yellow-Green)	1.08449	-0.160%	-0.909%	1.08711	*0.22%*	-0.166%	-0.915%	168
11 wedge[2] (Blue, Red, and Hanging wedges)	1.08429	-0.017%	-0.926%	1.08698	*0.23%*	-0.011%	-0.925%	8%
3 Wedge	1.08353	-0.065%	-0.991%	1.08621	*0.23%*	-0.065%	-0.991%	61
4 Wedge	1.08335	-0.015%	-1.006%	1.08600	*0.23%*	-0.018%	-1.009%	30
6 Wedge	1.08299	-0.031%	-1.037%	1.08565	*0.23%*	-0.029%	-1.038%	40
Flux Trap Loaded with Typical Samples	1.08360	0.052%	-0.985%	1.08631	*0.23%*	0.056%	-0.982%	82

[1] All fresh HEU fuel. Blades at 23" withdrawn; reg. blade at core midplane. Empty holder in flux trap. Graphite wedges have no samples or irradiation positions.
[2] This position is a helium-filled aluminum can with water-filled irradiation positions.
In order to model the effect of the water displacement and samples, the water fraction in the DIF3D model was adjusted.
MCNP runs of 60M histories had σ 11 pcm

Table 3-6 Graphite Reflector and Flux Trap Loading Worths – 2008 LEU core

	MCNP LEU			DIF3D/REBUS LEU				
	k-eff	Worth (% Δk/k) Ind.	Cum.	k-eff	*Diff. Rel. to MCNP*	Worth (% Δk/k) Ind.	Cum.	ppm B or water fraction decrease
Base Case[1]	1.08704			1.08724	0.02%			
L & N Wedges	1.07928	-0.661%	-0.661%	1.07947	0.02%	-0.662%	-0.662%	1178
10 wedge (Yellow-Green)	1.07748	-0.155%	-0.816%	1.07767	0.02%	-0.155%	-0.817%	165
11 wedge[2] (Blue, Red, and Hanging wedges)	1.07751	0.003%	-0.814%	1.07767	0.01%	0.000%	-0.817%	0%
3 Wedge	1.07697	-0.047%	-0.860%	1.07723	0.02%	-0.038%	-0.855%	36
4 Wedge	1.07643	-0.047%	-0.907%	1.07674	0.03%	-0.042%	-0.897%	80
6 Wedge	1.07630	-0.011%	-0.918%	1.07658	0.02%	-0.014%	-0.911%	20
Flux Trap Loaded with Typical Samples	1.07662	0.028%	-0.890%	1.07688	0.02%	0.027%	-0.884%	80

[1] All fresh LEU fuel. Blades at 23" withdrawn; reg. blade at core midplane. Empty holder in flux trap. Graphite wedges have no samples or irradiation positions.
[2] This position is a helium-filled aluminum can with water-filled irradiation positions.
In order to model the effect of the water displacement and samples, the water fraction in the DIF3D model was adjusted.
MCNP runs of 60M histories had σ 11 pcm

3.3.3 Development of HEU and LEU Fuel Cycle Models

To compare the performance of the proposed LEU design to typical HEU operation, models were developed for the 2008 reactor configuration with typical experimental loadings. To properly model the current HEU core fuel utilization, shutdown margin and experimental performance, it was necessary to develop a computational shuffling that would accurately model the actual complex cycle used at MURR.

It was also necessary to develop a similar shuffling scheme for the LEU in order to recalculate those parameters and demonstrate that the proposed LEU fuel element described in Section 3.2 is an acceptable fuel design.

Starting with 26 fresh elements, nine pre-cycle cores were modeled totalling 1794 MWd of operating time to produce twelve pairs of fuel elements with appropriate power histories ranging from 0 to 139 MWd. Using these, an 82-week simulation of reactor operations with HEU fuel was modeled with the REBUS-DIF3D code. Each week, the simulated reactor loading follows typical loading pattern practices for the MURR. Fresh fuel elements are loaded in the X1 and X5 positions about every 4 to 5 weeks, and fuel elements are discharged from the X4 and X8 positions at the same rate, with a target burnup of 150 MWd. The simulation was conducted for the reactor with current typical reflector and flux trap sample loadings. Additionally, the control blades were fixed at 23" withdrawn, which is the typical blade position at the end of weekly operations, while the regulating blade was positioned at the core midplane (13.375" withdrawn).

Figure 3.6 shows the core k-effective values at four points during each week of the simulation: day 0 (BOC; xenon free conditions), day 1, day 2 (equilibrium xenon), and 6.3 days (EOC). The average weekly reactivity swing is 3.8% Δk/k. The weekly average EOC core k-effective predicted by the simulation is sub-critical, with k-effective=0.994. However, it should be noted that the DIF3D model bias compared to 1971 critical experiments is -0.49% Δk/k (see Table 3-4) and the simulation was performed with the blades fixed at 23" withdrawn. The estimated critical positions at BOC and EOC for a number of these cores have been calculated by MCNP and found to be within range of typical values.

Figure 3.6 illustrates results for both transition cycles and pseudo-equilibrium cycles. During the transition cycles, two or more of the elements started their depletion in one or more of the pre-cycle cores. Every element of the pseudo-equilibrium cycles was depleted in cores with explicit shuffling. While the k-effective curve is very similar in both phases of the simulation, the pseudo-equilibrium cycles provide the best basis for comparison to current HEU and proposed LEU operations -- particularly for isotopic distributions within the elements.

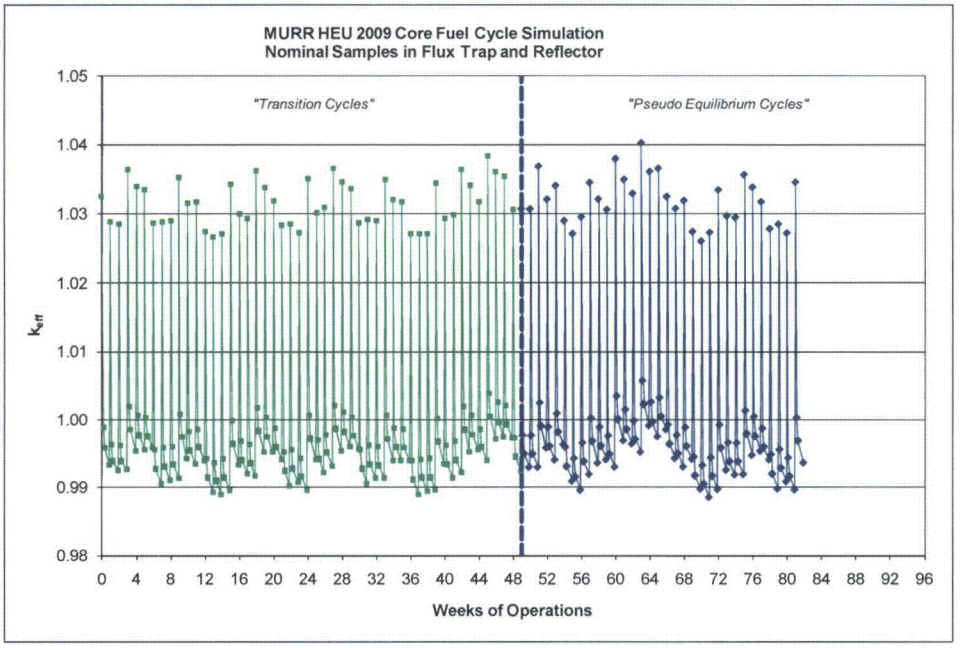


Figure 3.6 – Weekly Core k-effective for MURR HEU Fuel Cycle Simulation

The average EOC core burnup for the HEU fuel cycle simulation is 640 MWd. Figure 3.7 shows the results of a straight rundown of HEU and LEU cores, each beginning with all fresh fuel elements. Taking the HEU core reactivity at 640 MWd core burnup as a target, the corresponding EOC burnup for an LEU core is 928 MWd. For the purpose of this feasibility study, an LEU fuel cycle simulation with an average EOC burnup of 890 MWd was developed and analyzed.

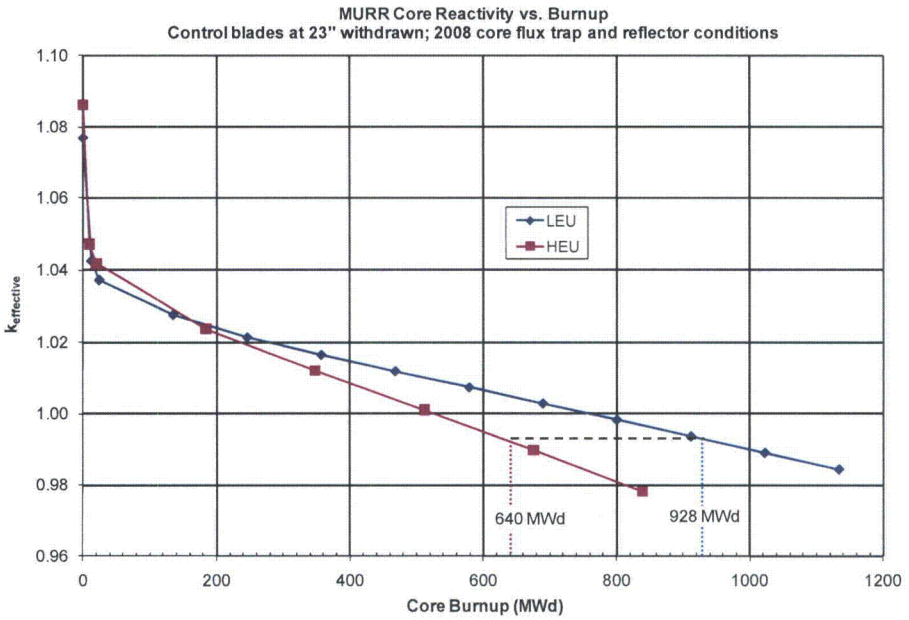


Figure 3.7 – MURR Fresh Core Reactivity vs. Burnup

For the LEU, starting with 26 fresh elements nine pre-cycle cores were modeled totalling 2,421 MWd of operating time to produce twelve pairs of fuel elements with appropriate power histories ranging from 0 to 190 MWd. Using these, a 93-week simulation of reactor operations with LEU fuel was modeled with the REBUS-DIF3D code. Fresh fuel elements are loaded about every 5 weeks in this simulation, and the discharge burnup of the LEU elements is about 208 MWd.

Figure 3.8 shows the weekly LEU core k-effective values during the simulation. The average weekly reactivity swing is 3.5% $\Delta k/k$, and the weekly average EOC core k-effective=0.997.

Figure 3.9 illustrates the comparison of HEU and LEU fuel cycle simulations at 10MW and 12 MW, respectively. It is clear that the k-effectives of the LEU fuel cycle at 12 MW are bounded by the high and low extremes of k-effective for the HEU fuel cycle at 10 MW. The slightly lower reactivity for LEU at the beginning of the week could be advantageous for experiments, since the control blades would be less inserted. Predictions of experimental fluxes for HEU and LEU are compared in Section. 3.4.3.

Table 3-9 provides a comparison of operating characteristics of the current HEU fuel with the proposed LEU fuel for the following parameters: maximum burn-up, core MWd with the control blades full out, frequency of core refuelings, and number of fuel elements in the fuel cycle. The proposed LEU design appears suitable for the weekly fuel cycle at MURR, provided that the element can be fabricated and is demonstrated to be hydrodynamically stable.

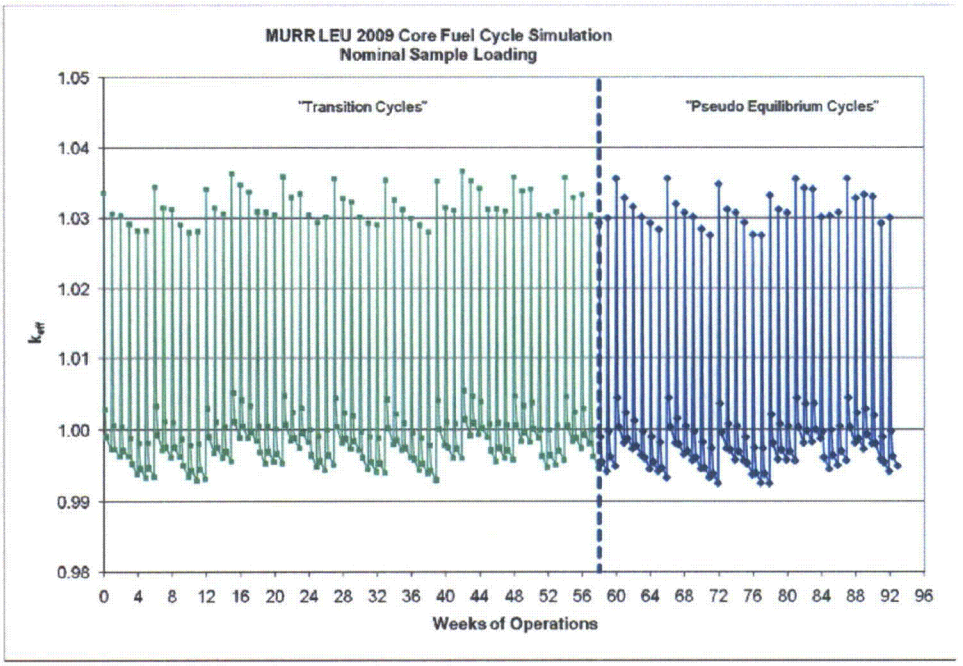


Figure 3.8 – Weekly Core k-effective for MURR LEU Fuel Cycle Simulation

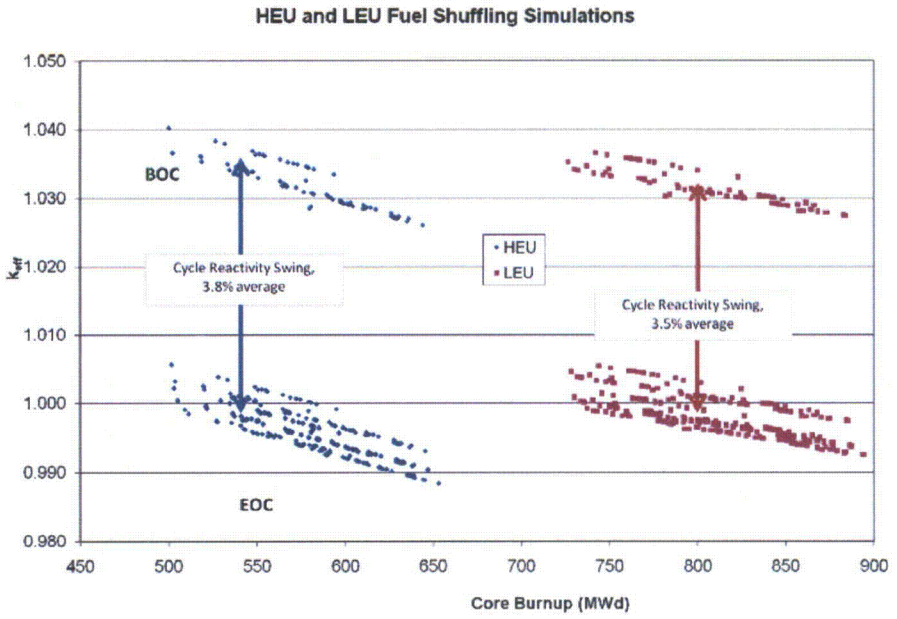


Figure 3.9 – Weekly Core k-effective for MURR HEU and LEU Fuel Cycle Simulations

3.3.4 Computational Model Credibility – Comparisons with Estimated Critical Positions

No all fresh core has been available since 1980, so no measurements for an all fresh core are available for the 2008 reactor configuration. In order to further demonstrate the credibility of the MCNP 2008 core configuration model and the depletion methodology, a series of measured HEU beginning-of-week core critical states were evaluated.

Table 3-7 provides a comparison of core k-effective calculated by MCNP and DIF3D for fresh and depleted cores. The results show very close agreement between the two codes for predicting the core k-effective, increasing confidence in the DIF3D diffusion theory model which is the basis for determining the depleted core compositions and demonstrating that the composition data were correctly transferred from one model to the other. Furthermore, the good agreement between MCNP and DIF3D for mixed cores shows that the values of boron loading used to approximate the worth of reflector wedges remain valid with burnup.

Table 3-7 Comparison of DIF3D and MCNP Core k-effective for HEU and LEU Cores

Case	Fuel	Condition		Control blade position (inches withdrawn)	Regulating blade position (inches withdrawn)	MCNP k_{eff}	MCNP σ (pcm)	DIF3D k_{eff}	Difference (Δk/k)
1A	HEU	All Fresh	Day 0	23	10[1]	1.08326	12	1.08630	0.26%
2A	HEU	All Fresh	Day 2	23	15[1]	1.03923	22	1.04162	0.22%
3A	HEU	Week 58	Day 0	17	10	0.99359	21	0.99293	-0.07%
4A	HEU	Week 58	Day 2	23	15[1]	0.99617	20	0.99668	0.05%
5A	LEU	All Fresh	Day 0	23	10[1]	1.07654	11	1.07689	0.03%
6A	LEU	All Fresh	Day 2	23	15[1]	1.03736	20	1.03706	-0.03%
7A	LEU	Week 79	Day 0	17	10	0.99943	20	0.99880	-0.06%
8A	LEU	Week 79	Day 2	23	15[1]	0.99872	20	0.99805	-0.07%

A series of 15 Estimated Critical Position (ECP) calculations were performed to determine whether the overall depletion scheme provides a good estimate of reactor performance. Each case was a measured critical state at hot conditions. Small differences between the nominal water temperatures and measured temperatures were corrected by applying the reactivity coefficients of HEU operations at MURR. The cores analyzed covered a broad range of fuel loadings (e.g., two fresh elements in the core, or none), a variety of flux trap loading states (including an empty flux trap), and notably, a broad range of control blade history states.

Burned material compositions for each element of the critical states were read from the results of the REBUS-DIF3D fuel cycle simulations. The full set of results for the pseudo-equilibrium cycles were searched to find the closest element average burnup match at a beginning-of-week step. The REBUS-DIF3D materials were tracked as 12 axial regions of each individual plate. That data was mapped to the 24 axial region MCNP model. The transfer of data to update the MCNP input for each case was automated.

Table 3-8 summarizes the cases evaluated, including the deviation of MCNP5 k-effective from 1.0. It is clear that many cases had excellent agreement, but also clear that some cases had a large deviation from

critical. The deviations were compared to element burnup, flux trap state, blade insertion, and prior history of the control blades. The only trend discovered was the control blade history.

MURR control blades are shuffled in a multi-year scheme analogous to fuel shuffling. Only the blade tip regions are expected to deplete since the equilibrium xenon builds up in the first 25of the cycle, allowing blades to be moved from the 17 inches withdrawn typical at the beginning of the week to 23 inches withdrawn after the Xe builds in. However, the Boral material is known to deplete in the region near the tip, which is in a position of high importance.

Figure 3.10 illustrates the clear trend of MCNP deviation from critical vs. the prior history of the control blades. Figure 3.11 shows the trend of control blade withdrawal vs. blade history, which is consistent with Boral depletion in the blade.

The MURR feasibility case is based on fresh control blades in the MCNP model. Seven of the 15 ECP cases had little prior use of the control blades: 271-378 average calendar days of prior use. The RMS bias for those seven cases was 0.226% Δk/k. The trendlines of Figure 3.10 indicate that the deviation for fresh blades should be even better.

Table 3-8 Summary of Critical States Evaluated for Partially Burned Cores

Date	Fuel Element Burnup (MWd)					Flux Trap Reactivity[1] (%Δk/k)	Ave Prior MWd for Control Blades	Critical Bank Height[2] (inches withdrawn)	MCNP5 Deviation from Critical[3] (%Δk/k)
	X1/X5	X1/X6	X3/X7	X4/X8	Sum				
04/23/05	32	92	73	95	584	0.478	271	17.97	-0.263
05/02/05	38	140	44	73	590	0.474	280	18.02	-0.228
05/09/05	0	117	63	115	590	0.427	287	17.63	-0.260
05/16/05	17	137	52	82	576	0.432	294	17.93	-0.270
05/30/05	9	139	21	124	586	0.474	308	18.06	-0.144
07/11/05	29	136	40	84	578	0.464	350	17.98	-0.257
06/16/00	54	72	41	143	620	0.346	1040	17.22	-1.028
08/07/00	16	98	68	117	598	0.384	1092	17.02	-1.086
11/15/00	0	139	56	108	606	0.359	1192	16.72	-1.065
12/17/01	22	124	69	91	612	0.348	1709	16.64	-1.317
12/31/01	14	131	72	87	608	0.340	1723	16.66	-1.285
04/22/02	0	118	64	114	592	0.418	1835	16.00	-1.697
08/08/05	0	143	38	115	592	0	378	18.52	-0.087
09/04/00	24	90	50	141	610	0	1120	17.81	-0.080
02/04/02	11	136	61	96	608	0	1758	17.03	-0.594

[1] The flux trap reactivity indicates the worth of the flux trap contents relative to an empty flux trap
[2] Critical bank heights reported here are corrected for small differences between the nominal water temperatures modeled and those measured at the critical state
[3] MCNP deviation from critical is (k-1)/k, corrected for the difference between flux trap worth of the critical state and flux trap worth modeled with the nominal sample loading (for cases with nonzero flux trap worth)

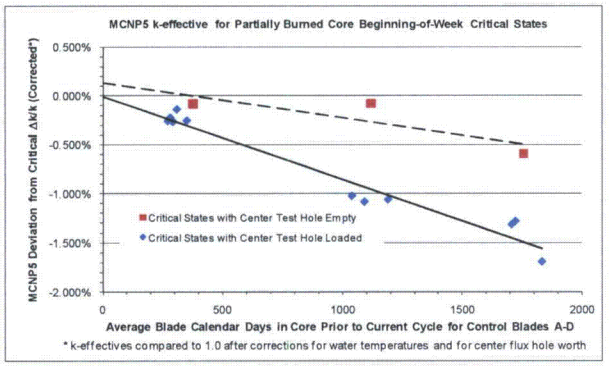


Figure 3.10
ECP Deviation from Critical vs. Blade History

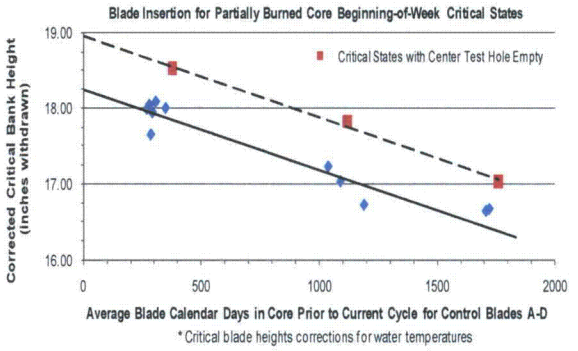


Figure 3.11
Critical Withdrawal vs. Blade History

3.3.5 Selection of HEU and LEU Reference Cores

In order to perform a comparison between HEU and LEU fuel, it is necessary to define reference cores that could be compared in order to establish feasibility of all major parameters: fuel cycle performance, shutdown margin, thermal-hydraulic steady state safety margins, and experimental performance. It was decided that these reference cores should be close to limiting in order to provide additional confidence that the safety margin calculations treat the potentially different limiting power shapes from the HEU and LEU fuel element.

Core configurations with potentially high power peaking were identified from the fuel cycle simulation to be analyzed for thermal-hydraulic behavior and confirm compliance of the proposed LEU fuel element design with operating limits (e.g., flow instability). The fuel cycle simulations provided a collection of more than 325 HEU core states (4 state points per week x 82 weeks), and nearly 375 LEU core states (4 state points per week x 93 weeks).

Each of these state points from the REBUS-DIF3D model was examined and sorted to rank the cases with the highest peak heat flux in the core. As expected, it was found that the highest heat flux always occurs in cases where a fresh element is loaded next to an element that is near its discharge burnup. Other criteria were also used to filter the cases down to a small collection of "worst case" scenarios. For example, as described in section 3.3.3, the fuel cycle simulations were initiated with 26 all fresh HEU or LEU fuel elements, so a number of "transition cycles" existed in the simulations before a regular sequence of loading patterns that fit the typical weekly operations of MURR was established. Therefore, only cores after the transition cycles were considered for detailed thermal-hydraulics analysis.

Based on the selection criteria, the core conditions in week 58 (out of 82) of the HEU fuel cycle simulation and in week 79 (out of 93) of the LEU fuel cycle simulation were chosen for more detailed evaluation. Depleted fuel material compositions were extracted from the REBUS-DIF3D results for each plate and axial depletion zone in the model; this consisted of 2,304 fuel compositions (8 elements x 24 plates x 12 axial zones) for each of the HEU and LEU cores. This data was utilized as material composition data for a detailed MCNP model for calculating power distributions that could be used for the thermal-hydraulics calculations, the calculation of estimated critical positions, and the evaluation of performance parameters such as the neutron flux in irradiation positions.

3.4 Comparison of HEU and LEU Fuel Element Performance and Safety Margins

3.4.1 Fuel Cycle Performance

Considering the average MURR utilization factor of 90%, one year of operation corresponds to 3,285 MWd. Consequently, the 150 MWd average discharge burnup of the HEU elements corresponds to insertion of 21.9 elements/year. The LEU fuel cycle developed in Section 3.3.3 results in an average discharge burnup of 208 MWd. Using the same total annual MWd as the current HEU 10 MW fuel cycle, the number of LEU fuel elements used in a typical year would be 15.8. However, scoping studies showed that a power increase is required to maintain experimental performance. LEU operation at 12 MW would match HEU experimental performance, or provide small gains. At 12 MW, the proposed LEU fuel cycle would require insertion of 18.9 elements/year. This corresponds to a 14% decrease in annual fuel element consumption. Table 3-9 summarizes the fuel operating characteristics of the HEU and proposed LEU fuel cycle.

Table 3-9 Current and Proposed MURR Fuel Operating Characteristics

Parameter	Current HEU Fuel	Proposed LEU Fuel
Maximum burn-up:	150 MWd/element (1,200 MWd/core) limited by insufficient excess reactivity – this achieves less than 1.8E+21fissions/cc burn-up, compared to the Technical Specification limit of 2.3E+21fissions/cc for UAl_x fuel	208 MWd/element (1,664 MWd/core) limited by insufficient excess reactivity – this achieves less than 4E+21 fissions/cc burn-up
Core MWd (control blades full out):	~670 MWd core with equilibrium xenon activity (56% of 1,200 MWd)	~890 MWd core with equilibrium xenon activity (53% of 1,664 MWd)
Refuelings:	Weekly – replace all eight fuel elements; fuel elements are used in 18 to 20 core loadings to achieve 145 to 150 MWd burn-up at 10 MW (~24% burn-up)	Weekly – replace all eight fuel elements; fuel elements are used in ~ 22 core loadings to achieve ~208 MWd burn-up at 12 MW (~18% burn-up)
Fuel Cycle:	22 elements used per year at 10MW; 32 fuel elements in active fuel cycle	19 elements used per year; at 12MW; 32 fuel elements in active fuel cycle

The ability to fabricate plates with 10 mil clad must still be demonstrated. The hydrodynamic stability of 38 mil plates must also be demonstrated. The GTRI Fuel Fabrication Capability and Fuel Development programs are addressing both concerns. The modeling capability created to establish feasibility of the current proposed design can be applied in the future to develop a contingency LEU design with thicker plates, and to compare the current and contingency designs with regard to fuel utilization, safety margins, and experimental performance.

With the aforementioned caveat, this analysis shows that, on the basis of number of fuel elements consumed per year, the conversion of MURR using the proposed LEU fuel element and cycle is feasible. Shutdown margin, experimental performance and thermal-hydraulic safety margins are demonstrated in other sections.

3.4.2 Shutdown Margins

Table 3-10 shows the excess reactivity and shutdown margins for fresh and mixed core states of both HEU and LEU. The mixed core states do not represent the most reactive states possible within the fuel cycle, but the cores are representative of typical operation. The reactivity of all mixed core states is bounded by an all fresh core. The total bank worth is significantly reduced for the LEU core.

Each core analyzed meets the Technical Specification shutdown margin requirement of at least 2% Δk/k with the most reactive blade and the regulating blade fully withdrawn. The all fresh LEU core is close to the limit, however. Furthermore, the calculations were performed for fresh Boral meat in every control blade. The ECP comparisons discussed in Section 3.3.4 indicate that control blade depletion is significant in MURR due to the combination of high fluxes and relatively long blade use. The control blade design and/or the technical specification for control blade burnup history as a function of core excess reactivity should be studied during full safety analyses.

Table 3-10 Summary of Blade Worth and Shutdown Margin Evaluations

Control System Worth Calculations	HEU (2008 Reflector)		LEU	
Simulated Core:	Fresh	Week58 Day 0	Fresh	Week 79 Day 0
Hot[1] Excess Reactivity (% Δk/k)	8.5	4.0	7.8	3.8
Cold[2] Excess Reactivity (% Δk/k)	8.6	4.1	7.9	4.0
Cold Reactivity with All Blades In[3] (% Δk/k)	-11.6	-17.2	-8.4	-13.0
Total Bank Worth at Cold Conditions[4] (% Δk/k)	-20.2	-21.3	-16.3	-17.0
Cold Minimum Shutdown Margin[5] (% Δk/k)	- 4.3	- 9.7	- 2.6	- 7.1

1 Hot conditions are for 10 MW operation with HEU, 12 MW operation with LEU
2 Cold conditions are isothermal after forced convection pumps are running (increased pressure in coolant channels increases moderator density relative to stagnant state).
3 All Blades In is defined as Boral control blades A-D fully inserted, but steel Regulating Blade parked at 10" withdrawn
4 Total Worth of Blades A-d with the regulating rod fixed at 10" withdrawn
5 Minimum Shutdown Margin case is Most Reactive Blade and Regulating Blade fully withdrawn, others fully inserted

All cases had no Xe or I; no Sm for fresh cores, Sm per prior depletion history for mixed cores
k-effectives from MCNP calculations had σ <12 pcm, so reactivities reported have σ <0.02% Δk/k

Further studies are needed to evaluate the impact of control blade depletion and the various options available to address shutdown margin for an all fresh LEU transition core (Cd-wire for fresh LEU to reduce excess reactivity, use of all fresh blades for an all fresh core, redesign of the control blades, etc.). This analysis shows, however, that on the basis of calculated shutdown margins, the conversion of MURR using the proposed LEU fuel element is feasible. Fuel cycle performance, experimental performance and thermal-hydraulic safety margins are demonstrated in other sections.

3.4.3 Experimental Performance – Fluxes and Reaction Rates at Irradiation Locations

The conversion of the MURR from HEU to LEU fuel will affect experimental fluxes. The effects were examined by calculating flux and reaction rate predictions in a number of important experimental locations for several core states.

Based on current and projected MURR utilization, the following three experimental locations were selected for comparing the effect of an HEU to LEU fuel conversion. The tally runs were performed with 600M histories, resulting in the RMS relative error noted in the tables of results.

- Center Test Hole (Flux Trap) Irradiation Positions:
  One of MURR's primary missions is to produce high specific activity isotopes for various applications including medical use. While the majority of isotopes are produced through thermal neutron reactions, a few require fast neutron threshold reactions. The current unperturbed peak thermal flux in the flux trap region is 6E+14 n/cm2-s, whereas the peak fast flux (> 1.0 MeV) is 6E+13 n/cm2-s.

  Detailed 2 group and 69 group tallies in MCNP were used to compare HEU and LEU values of:
  - Flux in Flux Trap (FT) tube B, 18-21" above bottom of holder, where a sulfur bearing sample can was modeled for P33 production;
  - Flux and S32(n,p)P32 reaction rate in FT tube B, 13-15" above bottom of holder, where a sulfur bearing sample can was modeled for P32 production via the fast threshold reaction;
  - Flux and reaction rates of Ir191(n,γ) and Ir193(n,γ) in FT tube C, 17-20" above bottom of holder, where Ir wires were explicitly modeled in an aluminum holder;
  - Flux in FT tube B, 6-8" above bottom of holder, where a BaCO sample was modeled for Cs production.

- Graphite Reflector Region Irradiation Positions:
  The graphite reflector region has a number of sample positions that are used to irradiate various sample materials. The average measured value of thermal flux can vary from approximately 1E+13 n/cm2-s to 1E+14 n/cm2-s.

  Detailed 2 group and 69 group tallies in MCNP were used to compare HEU and LEU values of:
  - Flux in the bottom three inches of the Wedge 3 Row 1 Pneumatic Tube (Ptube);
  - Flux and Si30(n, γ) reaction rate in the Green 5 location, where a 5" silicon sample was modeled.

- Beamports:
  There are four (4) radial and two (2) radial-tangential beamports. The measured thermal and epithermal beams emerging from the beam tubes are approximately 9.0E+9 n/cm2-s and 2.7E+8 n/cm2-s, respectively.

  Detailed tallies in MCNP were used to compare HEU and LEU values of:
  - The 47 group outbound current at a plane bisecting beam tube E at the radius of the inner wall of the reflector tank (i.e., beyond the outer edge of the graphite reflector). Outbound current was defined as current in a direction within the outbound half-space.

The 69 group tallies were made for the energy group structure of the WIMS-ANL libraries to allow. The 47 group spectrum of the Beam Tube E currents was specified by a key experimentalist.

The fluxes and reaction rates were calculated for reference cores described in Section 3.3.5. The cores were Week 58 of the HEU simulation and Week 79 of the LEU simulation. Both the beginning-of-week core at Day 0 (i.e., no Xe, lower control blades) and the same core depleted to Day 2 (equilibrium Xe, higher control blades) were examined.

All tallies were normalized by post-process to allow different power levels to be compared. While the LEU depletions were performed at 12MW, it would be possible to define an LEU fuel cycle for 10MW

operation. Since the fresh and most depleted elements would not have significantly different burnup for a 10MW LEU fuel cycle, we assume that the overall power sharing and associated flux profile would not be significantly different.

Table 3-11 summarizes the ratio of LEU fluxes and reaction rates at 10 MW and 12MW to HEU at 10 MW for the critical state at the beginning of the week, labeled Day 0. Table 3-12 presents the same comparisons after equilibrium Xe, at Day 2 of the key week.

Figures 3.12 and 3.13 illustrates the ratio of LEU 47 group outbound currents in Beam Tube E at 10 MW and 12MW to HEU at 10 MW for Day 0 and Day 2. Figures 3.14 - 3.17 show the 69 group comparison of fluxes and reaction rates.

It is clear from the tables and figures that the flux and reaction rate losses would exceed 10% if the power level of 10MW is maintained for LEU operation. Fortunately, an uprate to 12 MW would provide modest benefit for all of the fluxes and reaction rates tallied. This analysis also justifies a more in depth look into the thermal safety margins of the LEU core at 12 MW.

On the basis of experimental performance, the conversion of MURR using the proposed LEU fuel element is feasible at 12 MW. Fuel cycle performance, shutdown margins, and thermal-hydraulic safety margins are demonstrated in other sections.

Table 3-11 Comparison of Day 0 LEU Fluxes and Reaction Rates to HEU

Metric	Neutron Energy Range					
	<= 1 eV		> 1 eV		Sum	
LEU 10MW Week 79 Day 0, Critical Bank 17.020" withdrawn, Reg Blade 10" withdrawn						
Flux[1] in FT Tube B[2] 18-21"	86%	± 0.1%	91%	± 0.1%	88%	± 0.1%
S32(n,p) Reactions[3] in FT Tube B 13-15"	na	na	95%	± 0.2%	95%	± 0.2%
Flux in FT Tube B 13-15"	88%	± 0.1%	94%	± 0.1%	91%	± 0.1%
Ir191(n,g) Reactions in FT Tube C 17-20"	87%	± 0.3%	93%	± 1.5%	87%	± 0.3%
Ir193(n,g) Reactions in FT Tube C 17-20"	87%	± 0.3%	93%	± 2.0%	88%	± 0.5%
Flux in Ir Wires of FT Tube C 17-20"	87%	± 0.3%	92%	± 0.4%	90%	± 0.3%
Flux in FT Tube B 6-8"	89%	± 0.1%	94%	± 0.1%	91%	± 0.1%
Flux in Wedge 3 Row 1 P-Tube Bottom 3 inches	85%	± 0.1%	91%	± 0.2%	87%	± 0.1%
Si30(n,g) Reactions in Green 5 Position	87%	± 0.0%	91%	± 1.4%	88%	± 0.2%
Flux in Green 5 Sample Position	87%	± 0.0%	91%	± 0.1%	88%	± 0.0%
LEU 12MW Week 79 Day 0, Critical Bank 17.020" withdrawn, Reg Blade 10" withdrawn						
Flux[1] in FT Tube B[2] 18-21"	103%	± 0.1%	110%	± 0.1%	106%	± 0.1%
S32(n,p) Reactions[3] in FT Tube B 13-15"	na	na	114%	± 0.3%	114%	± 0.3%
Flux in FT Tube B 13-15"	105%	± 0.1%	113%	± 0.1%	109%	± 0.1%
Ir191(n,g) Reactions in FT Tube C 17-20"	104%	± 0.4%	111%	± 1.8%	105%	± 0.4%
Ir193(n,g) Reactions in FT Tube C 17-20"	104%	± 0.4%	112%	± 2.4%	106%	± 0.7%
Flux in Ir Wires of FT Tube C 17-20"	104%	± 0.4%	111%	± 0.5%	108%	± 0.3%
Flux in FT Tube B 6-8"	107%	± 0.1%	113%	± 0.1%	110%	± 0.1%
Flux in Wedge 3 Row 1 P-Tube Bottom 3 inches	102%	± 0.1%	109%	± 0.2%	104%	± 0.1%
Si30(n,g) Reactions in Green 5 Position	105%	± 0.1%	110%	± 1.7%	105%	± 0.2%
Flux in Green 5 Sample Position	105%	± 0.0%	109%	± 0.1%	106%	± 0.0%

[1] Fluxes were compared as n/s/cm^2
[2] Axial positions noted as inches above bottom of flux trap sample holder
[3] Reaction rates were compared as Reactions/s

HEU 10 MW Week 58 Day 0, Critical Bank 17.809" withdrawn, Reg Blade 10" withdrawn

Table 3-12 Comparison of Day 2 LEU Fluxes and Reaction Rates to HEU

Metric	Neutron Energy Range					
	<= 1 eV		> 1 eV		Sum	
LEU 10MW Week 79 Day 2, Critical Bank 23.481" withdrawn, Reg Blade 15" withdrawn						
Flux[1] in FT Tube B[2] 18-21"	87%	± 0.1%	93%	± 0.1%	89%	± 0.1%
S32(n,p) Reactions[3] in FT Tube B 13-15"	na	na	95%	± 0.3%	95%	± 0.3%
Flux in FT Tube B 13-15"	87%	± 0.1%	93%	± 0.1%	90%	± 0.1%
Ir191(n,g) Reactions in FT Tube C 17-20"	87%	± 0.3%	93%	± 1.5%	87%	± 0.3%
Ir193(n,g) Reactions in FT Tube C 17-20"	87%	± 0.3%	88%	± 1.9%	87%	± 0.5%
Flux in Ir Wires of FT Tube C 17-20"	87%	± 0.3%	92%	± 0.4%	90%	± 0.3%
Flux in FT Tube B 6-8"	88%	± 0.1%	93%	± 0.1%	90%	± 0.1%
Flux in Wedge 3 Row 1 P-Tube Bottom 3 inches	86%	± 0.1%	91%	± 0.2%	88%	± 0.1%
Si30(n,g) Reactions in Green 5 Position	88%	± 0.0%	90%	± 1.4%	88%	± 0.1%
Flux in Green 5 Sample Position	88%	± 0.0%	91%	± 0.1%	89%	± 0.0%
LEU 12MW Week 79 Day 2, Critical Bank 23.481" withdrawn, Reg Blade 15" withdrawn						
Flux[1] in FT Tube B[2] 18-21"	104%	± 0.1%	111%	± 0.1%	107%	± 0.1%
S32(n,p) Reactions[3] in FT Tube B 13-15"	na	na	113%	± 0.3%	113%	± 0.3%
Flux in FT Tube B 13-15"	104%	± 0.1%	112%	± 0.1%	108%	± 0.1%
Ir191(n,g) Reactions in FT Tube C 17-20"	104%	± 0.4%	112%	± 1.8%	105%	± 0.4%
Ir193(n,g) Reactions in FT Tube C 17-20"	104%	± 0.4%	106%	± 2.3%	105%	± 0.7%
Flux in Ir Wires of FT Tube C 17-20"	105%	± 0.4%	110%	± 0.5%	108%	± 0.3%
Flux in FT Tube B 6-8"	105%	± 0.1%	111%	± 0.1%	108%	± 0.1%
Flux in Wedge 3 Row 1 P-Tube Bottom 3 inches	104%	± 0.1%	110%	± 0.2%	106%	± 0.1%
Si30(n,g) Reactions in Green 5 Position	105%	± 0.0%	108%	± 1.7%	105%	± 0.2%
Flux in Green 5 Sample Position	105%	± 0.0%	109%	± 0.1%	106%	± 0.0%

[1] Fluxes were compared as n/s/cm^2
[2] Axial positions noted as inches above bottom of flux trap sample holder
[3] Reaction rates were compared as Reactions/s

HEU 10 MW Week 58 Day 2, Critical Bank 24.031" withdrawn, Reg Blade 15" withdrawn

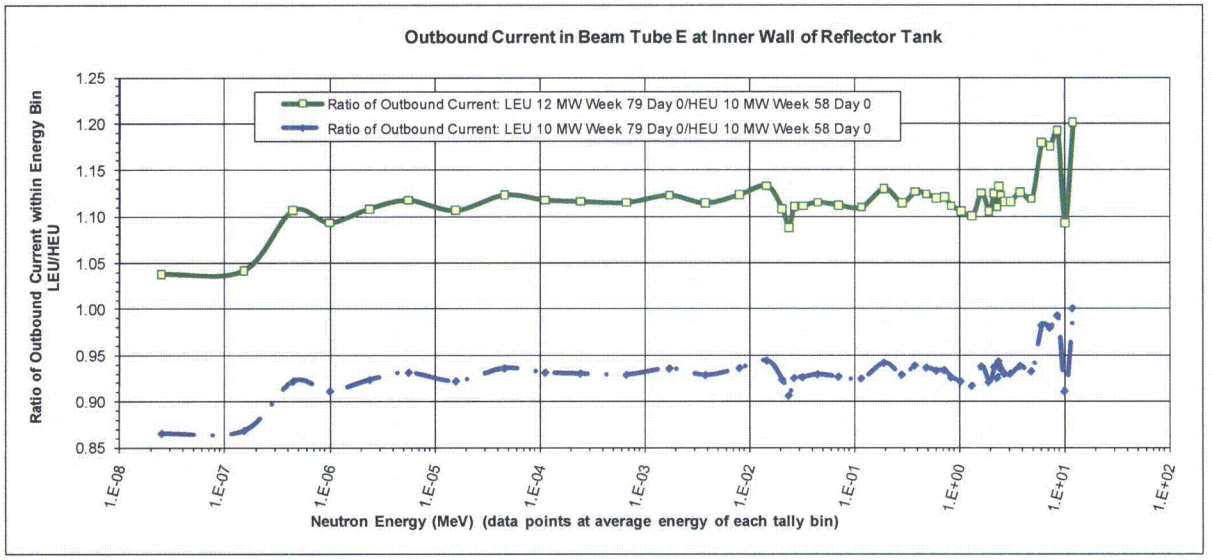


Figure 3.12 – Comparison of LEU and HEU Beam Tube E Outbound Current at Day 0

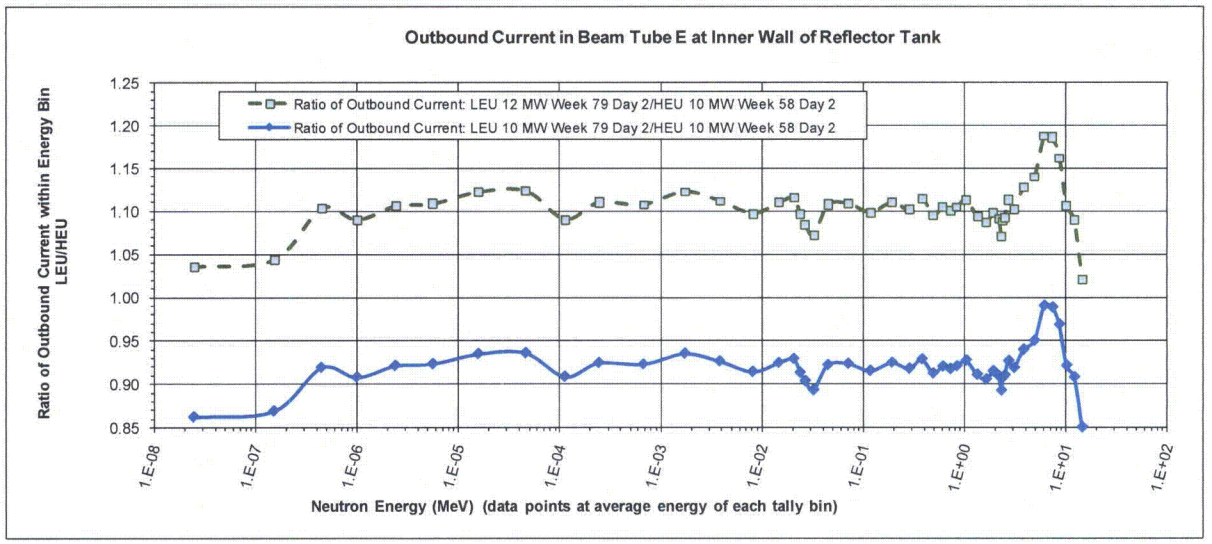


Figure 3.13 – Comparison of LEU and HEU Beam Tube E Outbound Current at Day 2

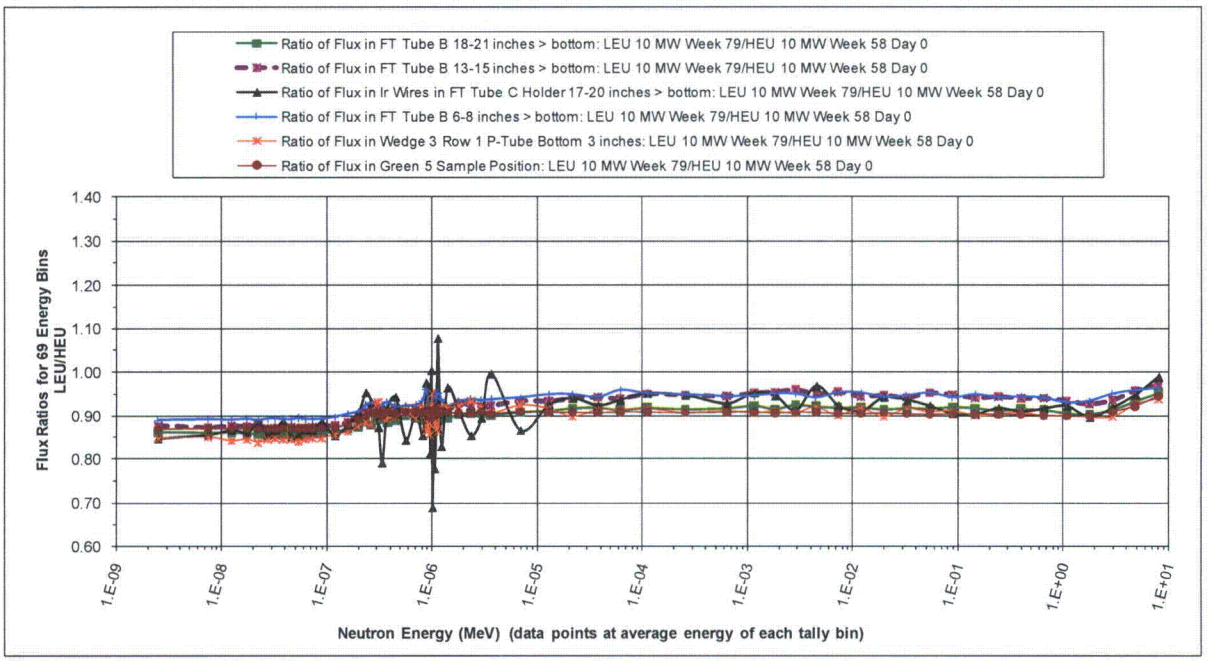


Figure 3.14 – Comparisons of LEU 10MW to HEU 10MW at Day 0

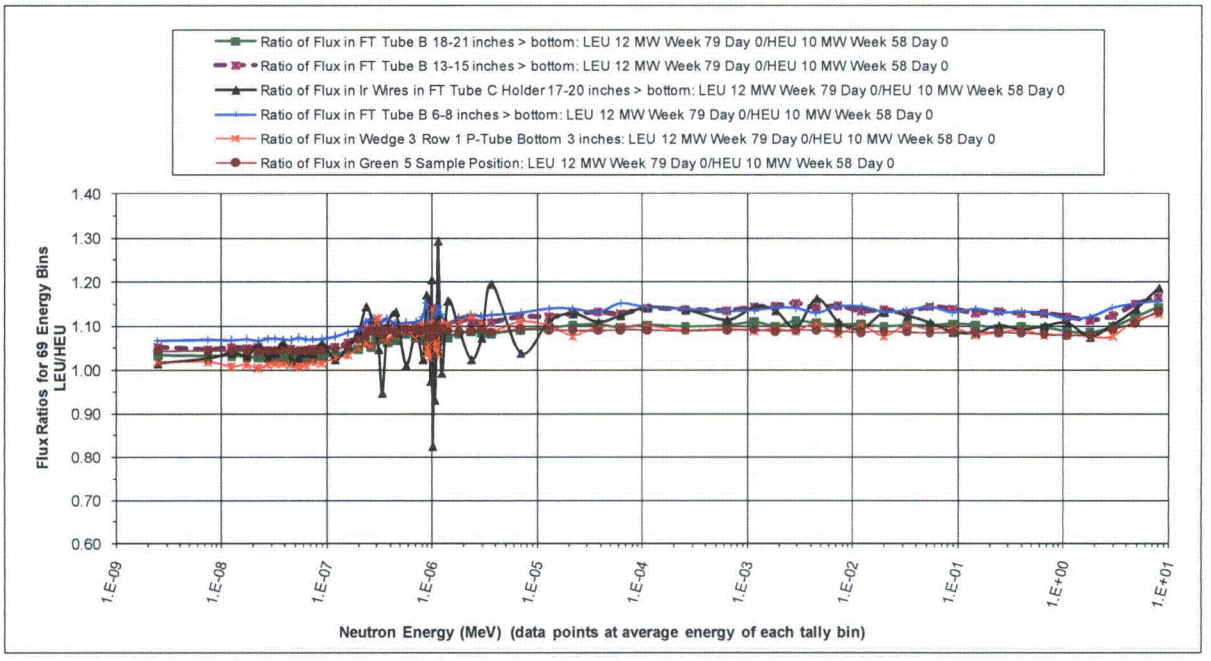


Figure 3.15 – Comparisons of LEU 12MW to HEU 10MW at Day 0

3.4.4 Power Distributions for Steady State Safety Margin Evaluation

Power distributions were calculated with MCNP by tallying the fission power (f7 tally) within 24 radial (i.e., plate-by-plate), 24 axial, and 9 azimuthal segments of the fuel plate meat in the entire core of eight elements (i.e., 216 equal volume segments within each plate; 5,184 segments per element). Power distributions were calculated for a variety of critical banked control blade configurations of various cores in order to identify the highest peaking factors that might limit margin to flow instability. The MCNP tallies were normalized by a post-processor to facilitate studies of different core power levels and different levels of tally detail. It should be noted that credit for power deposition outside the fuel is not modeled here, but is taken into account in the thermal-hydraulic safety margin calculation.

Figure 3.18 illustrates the radial (plate by plate) shapes of power (W), heat generation (W/cc), and heat flux (W/cm^2) for one reference core of the proposed LEU design. Heat flux from the meat is the appropriate quantity to compare among segments tallied in order to predict heat transfer to the coolant, since the tally volumes of uniform angular span within concentric curved plates are of increasing size from inner plate 1 to outer plate 24, and since LEU fuel meat thickness is different in different plates. Power within a segment of an outboard plate is always higher than power within the equivalent segment of an inboard plate. Since the volume of coolant being heated increases at the same rate as the volume of fuel in which power is tallied, the higher power in outboard plates does not imply a more challenging case for thermal margin. Heat generation rate is higher for thin foils than for thick foils (for two plates producing the same total power), but the volume of coolant being heated is directly proportional to the fuel surface area rather than the fuel thickness.

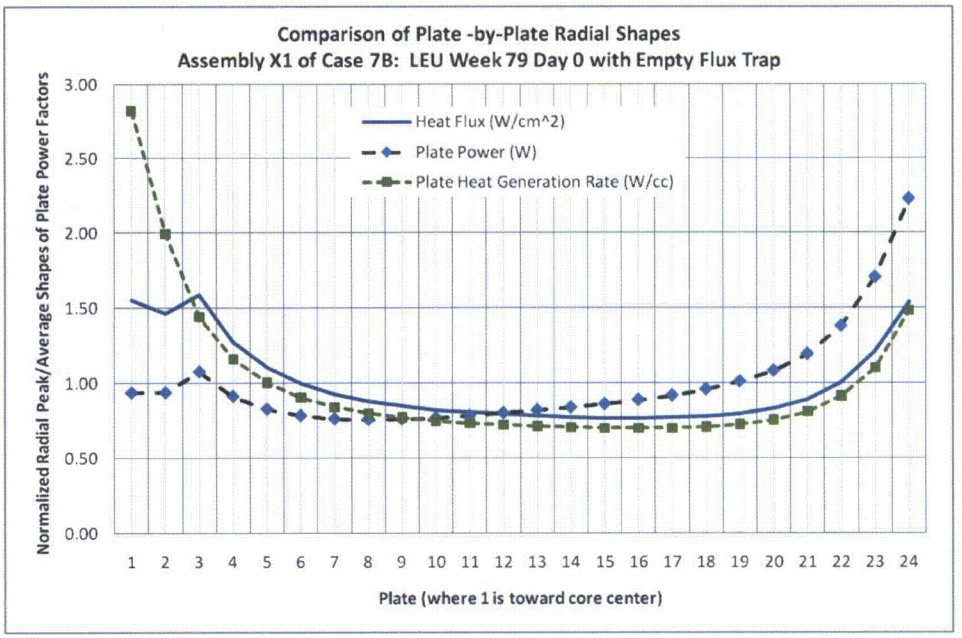


Figure 3.18 – Normalized Radial Power Factor Shapes

Power peaking is dependent upon the mix of burnup states among the elements in the core, upon critical control blade positions, and upon the experiment/sample loadings, particularly in the flux trap.

The mix of burnup states of the elements within the core largely determines the power sharing between elements. A core with both fresh elements and elements that will be discharged at the end of the cycle is expected to have the highest element peaking factor since the fresh elements must produce more power

than they would in an all fresh core. However, the critical control blade position is higher in the mixed core than in an all fresh core.

The critical control blade position is important to power distributions in two ways. First, a lower blade suppresses power in the outer plate(s) (since the MURR control blades are radially adjacent to the outer fuel plates) and therefore increases power in the inner plates. The radial shift effect is important for margin to flow instability since it results in a change in cooling channel temperature rise. But, the lower blade also increases axial peaking, particularly in the outer plates. The change in axial peaking is not important for margin to flow instability. This change is important to critical heat flux since the local axial clad temperature is proportional to the local heat flux. It appears that the safety limits will be only limited by flow instability, but critical heat flux analysis will be included in the detail safety analysis to verify this.

As equilibrium xenon builds up during operation the control blades are withdrawn to compensate for the negative reactivity of the xenon. The change in control blade position shifts the power, as discussed above. The xenon may also alter the power shape directly since it builds up in the regions of highest power. The balance of outward power shift due to blade motion and inherent power flattening by local xenon buildup should be explicitly evaluated.

The experiment/sample loading is also important to power distributions in two ways. First, the displacement of water in the flux trap region from inserting samples results in a reactivity insertion due to a positive void coefficient. Therefore, loading of samples in the flux trap leads to an increase in core reactivity, and thus lower critical blade position. The displacement of moderator from the flux trap or an absorption in the samples could have a direct effect on the power in the interior plates. But the lower control blades would tend to push power inboard. Sample loading in the graphite reflector positions also has a small effect on core reactivity, and thus on the critical control blade position. The balance of the effects must be explicitly evaluated.

After considering the various contributors to power peaking discussed above, power distributions were calculated for the 16 cases that enveloped the distinct combinations of effects. All fresh cores were compared to cores in which fresh elements were combined with elements to be discharged at the end of that weekly cycle (week 58 for the HEU simulation, week 79 for the LEU simulation). Initial startup of the weekly cycle with no xenon was compared to the equilibrium xenon state at 2 days of operation. A typical flux trap loading was compared to an empty flux trap. Thus 8 cases were considered for both HEU and the proposed LEU design. The atom densities of the fuel compositions for each core state were read from REBUS-DIF3D depletion results to automatically update an MCNP input file. An automated search was then performed with MCNP to find the critical banked blade position for the core (i.e., blades moved until MCNP predicted a k-effective of 1.0). The detailed power distributions were then tallied by an MCNP run. Finally, a post-processor was applied to read the mctal file and produce normalized edits suitable for analysis (and to facilitate an automated linkage to the PLTEMP/ANL thermal hydraulics code discussed in Section 4.5). The 16 cases are summarized in Table 3-13.

Figure 3.19 illustrates the axial heat flux shapes for each plate in each element for Case 7B (LEU Week 79 Day 0 Empty Flux Trap). Each of the eight plots has the same axis scale (0-200 W/cm^2). The impact of both element burnup and control blades is evident. The fresh elements in positions X1 and X5 have the highest heat fluxes, while the most depleted elements in positions X4 and X8 have the lowest heat fluxes. The outer plate heat fluxes are significantly skewed toward the bottom of the core, below the critical blade positions.

The margin to flow instability is primarily dependent upon total heat transferred to a coolant channel rather than the axial shape of the heat flux. Figure 3.20 illustrates the axial average heat flux for each

plate of each element of Case 7B. It is clear that the peaking of the outer plates evident in Figure 3.19 is not dominant for margin for flow instability, since the presence of the control blade suppressed the total power produced by the outer plate. The peak axial average heat fluxes for Case 7B are in plates 1 and 3 of element X1. Plate 1 generally has a high heat flux due to the moderator of the flux trap region -- particularly for the case with no flux trap samples loaded. But the proposed LEU design has a thinner fuel foil (9 mil thick) in plate 1 to reduce the peaking. The foil in plate 2 is 12 mil thick. Plate 3 is the first plate with an 18 mil fuel foil, which explains why the plate 3 heat flux is slightly higher than the plate 1 heat flux. The relative radial shape of the heat flux in the figure illustrates the important effect of moderation and fissile material self-shielding. The inner and outer plates have a much higher heat flux (i.e., fission rate) due to their proximity to the heavily-moderated flux trap (plate 1) and reflectors (plate 24). The interior plates have a lower heat flux due to both less moderation from the coolant channels and the self shielding effect of outboard plates consuming thermal neutrons.

The effects of moderation and self-shielding are also important in the azimuthal direction of the MURR elements since there is an unfueled region of the plates adjacent to the side plates. Thus, the fuel near the side plates is in a region with more moderator and less self-shielding than the azimuthal interior region. The MCNP fission power tallies were performed for 9 azimuthal stripes of equal angular span within the fuelled region of the plates. Figure 3.21 illustrates the azimuthal peaking factor for each plate of each element for Case 7B. The effect is small (~5%) for the outboard plates since there is significant moderator and little self-shielding, but clearly pronounced for the interior plates (15-23%). Fortunately, the average heat flux in the interior plates is lower than in the outboard plates, so the largest azimuthal peaking factors do not correspond to a "hot stripe" for the entire element.

Table 3-13 – Summary of Power Distribution Evaluations

Core State that may bound power peaking					Element Burnup (MWd) at Beginning of Week				Inches withdrawn		
Fuel	Case	Burnup State	Time (Days)	Flux Trap	X1 X5	X2 X6	X3 X7	X4 X8	Blades A-D	Reg Blade	MCNP k-eff
HEU	1A	Fresh	0	Samples	0	0	0	0	12.911	10	0.99983
	2A	Fresh	2	Samples	0	0	0	0	16.782	15	1.00017
	3A	Week 58	0	Samples	0	81	65	142	17.809	10	1.00044
	4A	Week 58	2	Samples	0	81	65	142	24.031	15	1.0002
	1B	Fresh	0	Empty	0	0	0	0	13.295	10	0.99974
	2B	Fresh	2	Empty	0	0	0	0	17.367	15	0.99985
	3B	Week 58	0	Empty	0	81	65	142	18.380	10	0.99969
	4B	Week 58	2	Empty	0	81	65	142	26.000	15	1.00029
LEU	5A	Fresh	0	Samples	0	0	0	0	12.267	10	1.00037
	6A	Fresh	2	Samples	0	0	0	0	16.165	15	0.99998
	7A	Week 79	0	Samples	0	116	97	199	17.020	10	1.00011
	8A	Week 79	2	Samples	0	116	97	199	23.481	15	1.00027
	5B	Fresh	0	Empty	0	0	0	0	12.647	10	0.99995
	6B	Fresh	2	Empty	0	0	0	0	16.826	15	1.00021
	7B	**Week 79**	**0**	**Empty**	**0**	**116**	**97**	**199**	**17.632**	**10**	**1.00015**
	8B	Week 79	2	Empty	0	116	97	199	25.116	15	1.00049

Samples indicates a typical loading of samples in all three flux trap tubes
Empty indicates neither samples nor tubes in the flux trap (i.e., "empty island" configuration)
HEU elements discharged at 150 MWd (at 10 MW operation)
LEU elements discharged at 208 MWd (at 12 MW operation)
Full blade withdrawal is 26 inches
MCNP power tally runs were made with 60M histories for σ on k-effective of ~ 12 pcm
Criticality searches were perfomed with 15M histories, σ ~ 22 pcm. Searches to 1.00000 ± 15 pcm

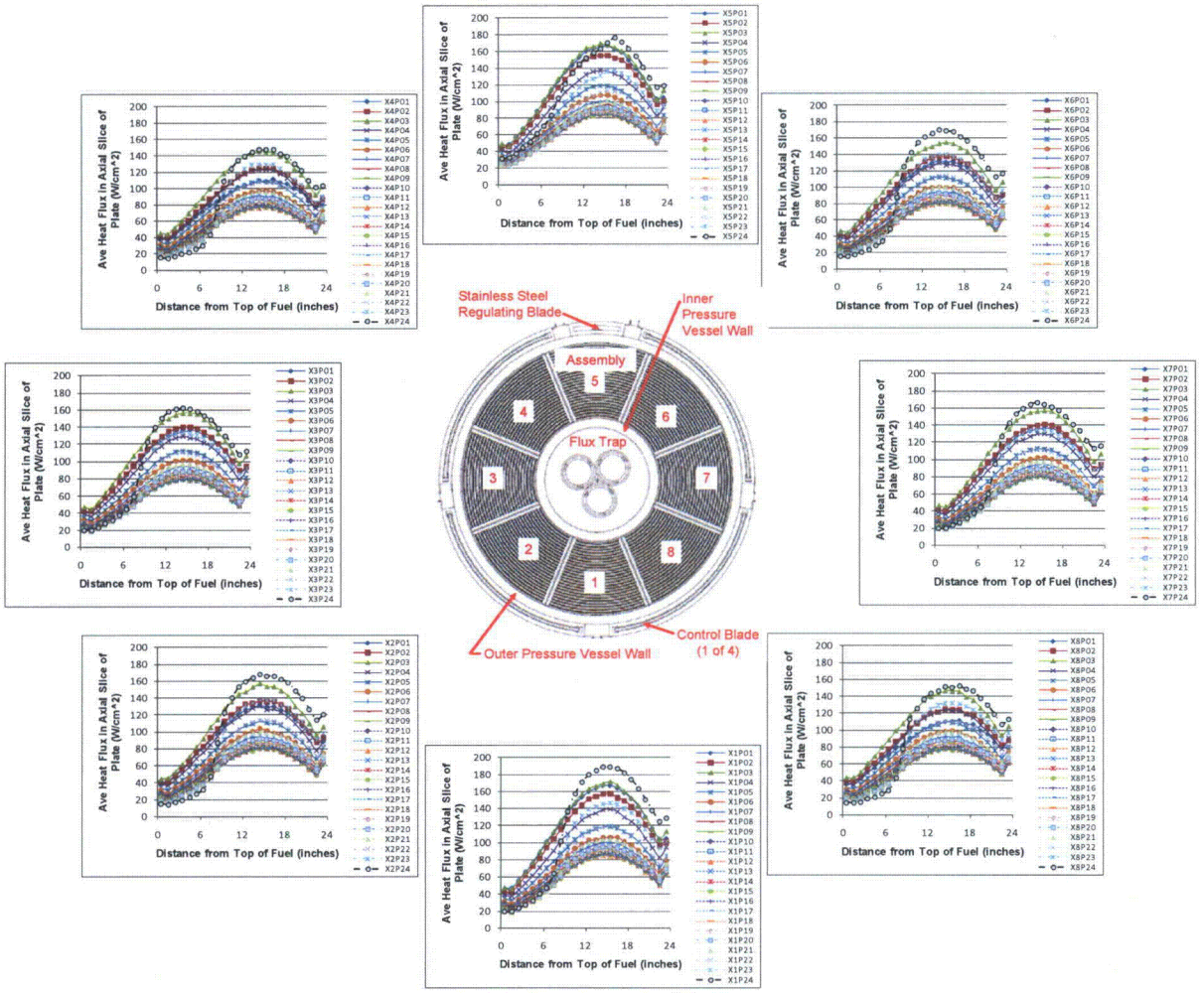


Figure 3.19 – Heat Flux in Each Axial Segment of Each Plate
Case 7B: LEU Week 79 Day 0 with Empty Flux Trap

Figure 3.22 illustrates the "hot stripe heat flux" for each plate of each element for Case 7B. The hot stripe heat fluxes were tallied explicitly, but can be thought of as the multiplication of plate average heat flux * the plate azimuthal peaking factor. The hot stripe heat flux is an effective factor of merit to compare probable effects of the core power distributions on margin to flow instability.

Table 3-14 summarizes the hot stripe heat fluxes in the key plates of the fresh fuel elements for each of the 16 cases for which power distributions were evaluated. Appendix A-1 presents detailed power shapes (per Figures 3.20-3.22) for each of the 16 cases. Examination of those results indicated that the plates with highest hot stripe heat flux were 1, 3, 23, and 24 for the various reference core states modeled. Furthermore, Cases 3B, 4B, 7B, and 8B had the highest overall factors. Cases 3B and 7B are for cores without xenon, so the lower critical control blade position leads to high inboard heat flux. Cases 4B and 8B are for the equilibrium xenon state of the same core, so the higher critical control blade position allows the power to shift toward the outboard plates. Thermal hydraulic analyses were performed for those four cases (using full power distribution detail, not just the summary of Table 3-14), as described in Chapter 4.

This analysis provides the core configurations and power distributions to be used for steady state safety margin calculations. Fuel cycle performance, shutdown margins, and thermal-hydraulic safety margins are demonstrated in other sections.

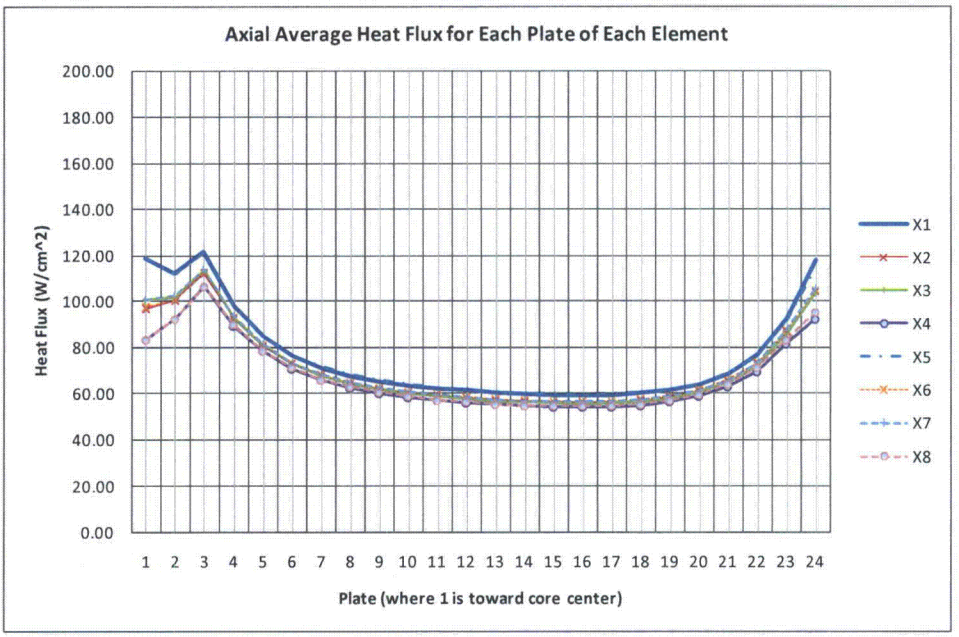


Figure 3.20 – Axial Average Heat Flux in Each Plate of Each Element
Case 7B: LEU Week 79 Day 0 with Empty Flux Trap

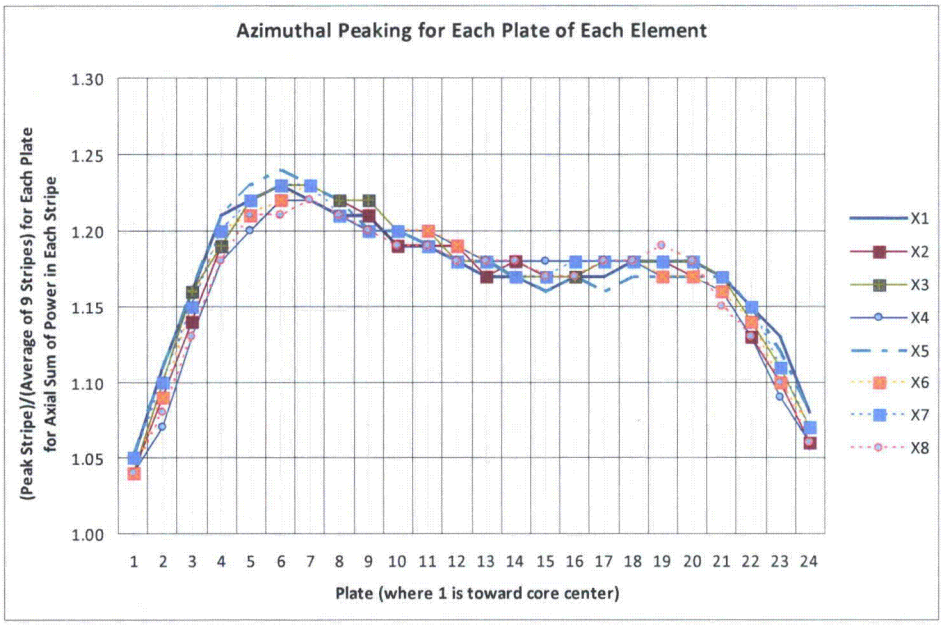


Figure 3.21 – Azimuthal Peaking Factor for Each Plate of Each Element
Case 7B: LEU Week 79 Day 0 with Empty Flux Trap

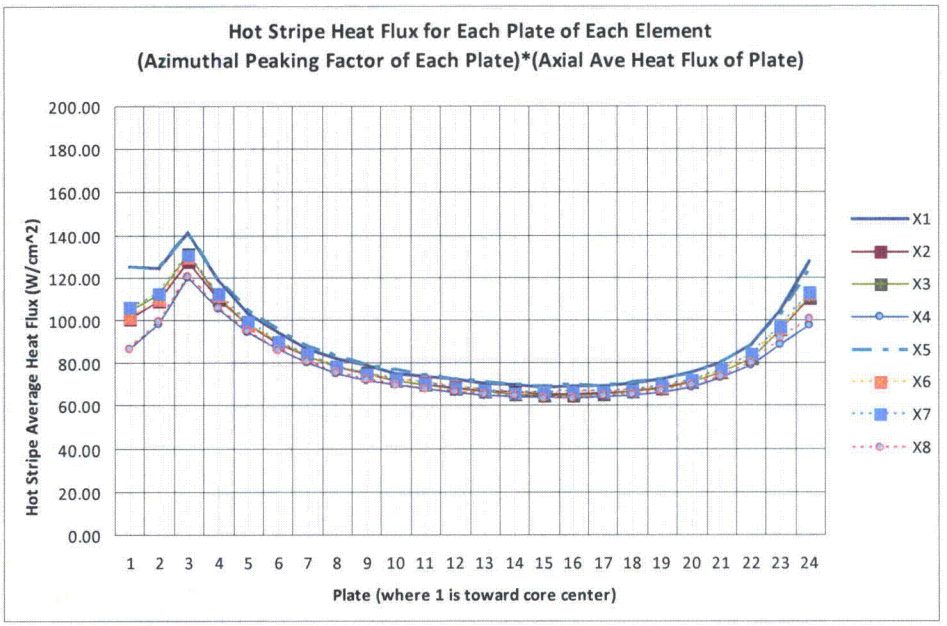


Figure 3.22 – Hot Stripe Heat Flux for Each Plate of Each Element
Case 7B: LEU Week 79 Day 0 with Empty Flux Trap

Table 3-14 – Summary of Key Hot Stripe Heat Fluxes Evaluated

Core State that may bound power peaking					Hot Stripe Heat Flux (W/cm^2) Fresh Element in Position X1				Hot Stripe Heat Flux (W/cm^2) Fresh Element in Position X5			
Fuel	Case	Burnup State	Day	Flux Trap	Plate 1	Plate 3	Plate 23	Plate 24	Plate 1	Plate 3	Plate 23	Plate 24
HEU	1A	Fresh	0	Samples	126.7	91.4	67.3	76.8	128.8	94.0	69.4	80.4
	2A	Fresh	2	Samples	121.6	89.3	74.4	87.3	123.4	89.4	74.8	86.6
10MW	3A	Week 58	0	Samples	131.7	96.6	82.6	96.6	132.3	97.6	79.3	91.8
	4A	Week 58	2	Samples	126.3	92.6	90.4	107.4	125.6	92.6	82.8	97.8
	1B	Fresh	0	Empty	133.2	94.5	66.7	77.2	133.8	96.2	70.0	80.2
	2B	Fresh	2	Empty	127.0	91.3	74.5	87.9	129.3	92.1	74.3	87.1
	3B	**Week 58**	**0**	**Empty**	**138.6**	**99.3**	**83.0**	**97.6**	**138.9**	**99.7**	**78.9**	**92.2**
	4B	**Week 58**	**2**	**Empty**	**132.9**	**94.8**	**90.8**	**109.6**	**132.1**	**93.2**	**82.8**	**97.9**
LEU	5A	Fresh	0	Samples	116.3	134.4	84.9	100.0	119.4	136.6	90.1	107.0
12MW	6A	Fresh	2	Samples	112.2	129.5	94.6	116.0	113.4	130.4	95.8	117.2
	7A	Week 79	0	Samples	119.0	137.6	103.3	126.6	118.4	137.7	101.3	122.3
	8A	Week 79	2	Samples	114.1	130.4	113.8	142.6	113.3	130.1	105.5	131.1
	5B	Fresh	0	Empty	124.0	139.0	85.0	100.8	125.3	140.9	90.8	108.0
	6B	Fresh	2	Empty	119.1	132.4	95.8	118.0	119.6	133.1	96.4	118.2
	7B	**Week 79**	**0**	**Empty**	**124.9**	**141.0**	**104.7**	**127.6**	**125.1**	**140.8**	**102.0**	**123.2**
	8B	**Week 79**	**2**	**Empty**	**120.3**	**133.9**	**114.3**	**145.4**	**119.4**	**132.8**	**105.7**	**131.3**

Samples indicates a typical loading of samples in all three flux trap tubes
Empty indicates neither samples nor tubes in the flux trap (i.e., "empty island" configuration)

Note that HEU operates at 10 MW, while 12 MW is proposed for LEU operation. Thus a 20% increase in LEU heat flux would be expected if the element was not altered (in design and underlying physics).

3.5 Neutronic References

[3-1] Breismeister, J. F., ed., "MCNP - A General Monte Carlo N-Particle Transport Code, Version 4C," LA-13709-M. Los Alamos National Laboratory, 2000.

[3-2] X-5 Monte Carlo Team, "MCNP - A General Monte Carlo N-Particle Transport Code, Version 5," LA-CP-03-0245. Los Alamos National Laboratory, 2003.

[3-3] Olson, A.P., "A Users Guide for the REBUS-PC Code, Version 1.4," ANL/RERTR/TM32, Argonne National Laboratory, 2001.

[3-4] Stevens, J.G., "The REBUS-MCNP Linkage," ANL/RERTR/TM-08-04, Argonne National Laboratory, 2008.

[3-5] Hanan N.A., et al., "A Monte Carlo Burnup Code Linking MCNP and REBUS", Proc. 1998 International Meeting on Reduced Enrichment for Research and Test Reactors, São Paulo, Brazil, Oct. 18-23, 1998.

[3-6] Hanan, N.A., et al., "Comparisons of Diffusion Theory and Monte Carlo Burnup", Proc. 2002 International Meeting on Reduced Enrichment for Research and Test Reactors, San Carlos de Bariloche, Argentina, Nov. 3-8, 2002.

[3-7] Toppel, B. J., "A User's Guide for the REBUS-3 Fuel Cycle Analysis Capability," ANL-83-2, Argonne National Laboratory, 1983.

[3-8] Derstine, K. L., "DIF3D, A Code to Solve One-, Two-, and Three-Dimensional Finite-Difference Diffusion Theory Problems," ANL-83-64, Argonne National Laboratory, 1983.

[3-9] Woodruff, W.L. and Leopando, L.S., "Upgrades to the WIMS-ANL Code," Proc. 1998 International Meeting on Reduced Enrichment for Research and Test Reactors, São Paulo, Brazil, Oct. 18-23, 1998.

[3-10] J.R. Deen et al., "WIMS-ANL User Manual, Rev. 5," ANL/TD/TM99-07, Argonne National Laboratory, 2003.

[3-11] Hanan, N.A., et al., "The Use of WIMS-ANL Lumped Fission Product Cross Sections for Burned Core Analysis with the MCNP Monte Carlo Code," Proc. 1998 International Meeting on Reduced Enrichment for Research and Test Reactors, São Paulo, Brazil, Oct. 18-23, 1998.

[3-12] Dionne, B., Stillman, J, and Stevens, J., "Applicability of WIMS-ANL to Generate Cross Sections for Very High Density UMo Fuel in Proposed LEU Fuel Assembly," Proc. 2008 International Meeting on Reduced Enrichment for Research and Test Reactors, Washington, D.C., Oct. 5-9, 2008.

[3-13] McKibben, J.C., Kutikkad, D., and Foyto, L.P., "Current Status of the Missouri University Research Reactor HEU to LEU Conversion Feasibility Study," Proc. 2006 International Meeting on Reduced Enrichment for Research and Test Reactors, Cape Town, Republic of South Africa, Oct. 29-Nov. 2, 2006.

[3-14] McKibben, J.C., Kutikkad, D., and Foyto, L.P., "Current Status of the Missouri University Research Reactor HEU to LEU Conversion Feasibility Study," Proc. 2007 International Meeting on Reduced Enrichment for Research and Test Reactors, Prague, Czech Republic, Sep. 23-27, 2007.

[3-15] Julian, C., "Low power testing," MURR internal report, 1971.

[3-16] McKibben, J.C., Kutikkad, D., and Foyto, L.P., "Progress Made on the University of Missouri Research Reactor HEU to LEU Fuel Conversion Feasibility Study," Proc. 2008 International Meeting on Reduced Enrichment for Research and Test Reactors, Washington, D.C., Oct. 5-9, 2008.

4. STEADY-STATE THERMAL-HYDRAULIC ANALYSIS

4.1 Background and Introduction

The eight wedged-shaped fuel elements of the highly enriched uranium (HEU) core are of identical design and are arranged in a circle, as shown in Figure 4.1. Each element has 24 curved fuel plates that are parallel to the inner and outer circular boundaries of the annular reactor vessel. In the HEU core all of the plates are 50 mils (1 mil = 0.001 inch) thick. The 24 fuel plates of each element are parallel to each other and separated by 23 coolant channels, each 80±8 mils thick. Figure 4.2 illustrates how the element rides on a series of rollers, which in the HEU design provides a 110±28-mil thick first channel (located at the smallest radius) and a 90±28-mil thick last coolant channel; these channels are noted as D1 and D25, respectively, in Figure 4.2. Thirteen mils of the 28-mil tolerance for the outermost channels are due to an element manufacturing tolerance on the distance from an outer plate surface to the outer envelope of the two nearest rollers, which is dimension C in Figure 4.2. The other 15 mils are due to a 30-mil total clearance,, which is needed to enable the element to be inserted and removed from the reactor vessel (the difference of dimensions A and B in Figure 4.2). It is assumed that nominally the 30-mil clearance is shared equally by the first and last coolant channels, thereby providing a ±15-mil tolerance for each.

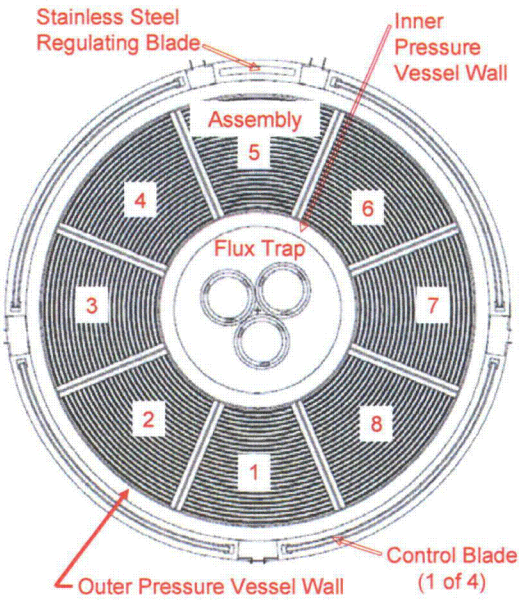


Figure 4.1 – Arrangement of the Eight MURR Elements

The eight wedge-shaped fuel elements of the proposed MURR low-enriched uranium (LEU) core are also of identical design and are arranged in a circle. In the proposed LEU design, the first and the last fuel plate of each element is 49-mils thick. All of the other 22 fuel plates in each element are 38-mils thick. The 24 fuel plates of each element are parallel to each other and separated by 23 coolant channels, each 92±8 mils thick. In the LEU element both outer channels are 95±28 mils thick. The basis of the 28-mil tolerance is the same as in the HEU core with 13-mils for plate-to-roller envelope tolerance and 15-mils for element clearances.

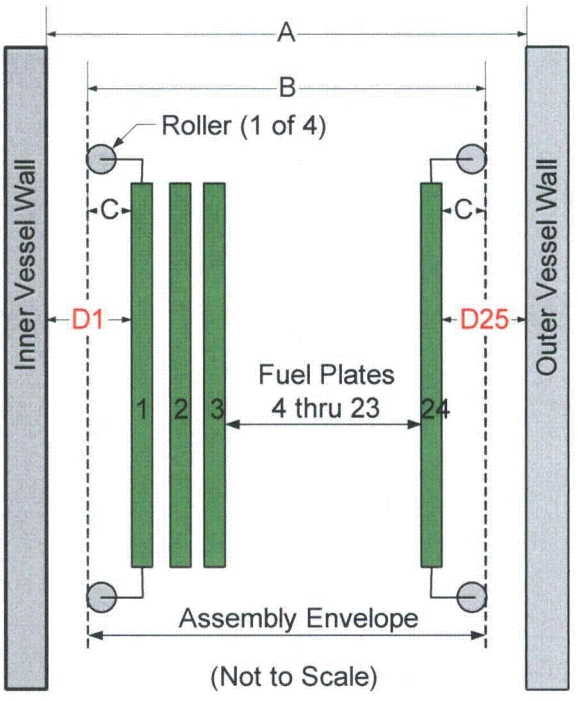


Figure 4.2
Thicknesses of Outer Channels

In section 4.2, a key part of the original HEU thermal analysis[4-1],[4-2] is replicated. (The details are provided in Appendix B-1.) This was done to demonstrate a sound understanding of the original thermal-hydraulic safety analysis that was approved

by the NRC for the HEU core. The key thermal-hydraulic safety criterion in the original analysis is that flow instability be avoided. This safety consideration is equally important for the LEU core. Section 4.3 goes on to explain that a correlation by Whittle and Forgan[4-3] predicts flow instability very accurately in research reactors of the MURR design. Detailed comparisons of analytical predictions with experimental measurements of flow instability are provided in Appendix B-2. Section 4.4 addresses the use of hot channel factors in the analysis to include the effects of design tolerances and calculational uncertainties. Section 4.5 provides a brief description of the PLTEMP/ANL code[4-4] which was essential in performing many of the numerous calculations needed to do the thermal-hydraulic analysis. Sections 4.6 describes how the important analytical elements described in Sections 4.3 through 4.5 are applied to the HEU and LEU cores of the MURR reactor. Section 4.7 provides analytical results in both graphical and tabular form. Section 4.8 tells how these results can be interpreted to clearly demonstrate that the proposed LEU core design is acceptable from a thermal-hydraulic perspective.

4.2 Replication of the Original HEU Safety Analysis

An important first step in developing analytical models to predict the thermal performance of an LEU replacement core for the MURR reactor is to demonstrate an understanding of the analytical basis for the safety limits prescribed for the existing HEU core. Therefore, in Appendix B-1 the original thermal-hydraulic analysis performed for the HEU core[4-1],[4-2] is described and replicated. In the original analysis the power at which flow instability occurs was predicted for 150 combinations of pressure at the reactor pressurizer, core inlet coolant temperature, and reactor core flow rate. Forty cases, which span the entire range of operating conditions represented by the full set of 150 cases, were evaluated in this study. The original results are closely replicated for these 40 cases, as shown in Figure B-1.1 of Appendix B-1.

4.3. Methods of Predicting the Power Margin to Flow Instability

The predicted margin to flow instability was the criterion used in qualifying the original HEU core.[4-1],[4-2] In the original HEU safety analysis it was assumed that flow instability would not occur in a coolant channel if bulk boiling at the channel exit was avoided or each local value of heat flux was less than half of the corresponding value of critical heat flux as predicted by the Bernath correlation[4-5]. This two-part criterion is based on measured data reported by Croft[4-6] in 1964 for electrically-heated channels that were designed to simulate Advance Test Reactor (ATR) channels. Reference [4-6] proposed the same criterion, except that it recommended using 60% of the Bernath critical heat flux but the more restrictive 50% value was used to be more conservative. Reference [4-6] postulated that burnout occurred by a process referred to as "hydraulic instability or autocatalytic vapor binding" which was seen as a form of critical heat flux (CHF) that occurred prematurely. Croft found that a model based on 60% of the Bernath CHF prediction fitted some of the experimental data and that burnout occurred in other cases when the exit bulk coolant temperature reached the saturation temperature.

In addition to Croft,[4-6] Waters[4-7] also used tests in electrically heated channels to measure the onset of fuel burnout caused by flow instability in the Advanced Test Reactor (ATR). The ATR fuel elements are thermal-hydraulically similar to those in the MURR reactor. Because, as shown in Appendix B-2, the Whittle and Forgan correlation[4-3] with a value of η of 32.5 accurately predicts flow instability in the Croft and the Waters experiments, it is used in the current analysis.

The Whittle and Forgan criterion is:

$$\frac{T_{allowed} - T_{inlet}}{T_{sat} - T_{inlet}} = \frac{1}{1 + \eta \frac{D_h}{L_h}} \tag{4.1}$$

where $T_{allowed}$ is the bulk coolant exit temperature at which flow instability is predicted to be initiated, T_{sat} is the coolant saturation temperature at the exit, T_{inlet} is the coolant inlet temperature, and D_h and L_h are the heated diameter and heated length of the channel, respectively. Because D_h by definition is 4 times the flow area of the channel divided by the heat perimeter of the channel, it is easy to show that D_h/L_h is 4 times the ratio of the channel flow area to the channel heat transfer area.

The numerator on the left side of equation 4.1 predicts the bulk coolant temperature rise at which flow instability occurs. Thermal-hydraulic analysis of the reactor core allows the bulk coolant temperature rise from the inlet to the exit of each channel to be predicted. This steady-state thermal-hydraulic analysis can be repeated several times at successively higher power levels until flow instability is predicted to occur in the most limiting channel. The margin to flow instability is determined by comparing the power at which flow instability is predicted to first occur with the allowed reactor power of 10.0 MW for an HEU core and the proposed 12.0 MW for an LEU core.

Since the quantity on the right side of equation 4.1 is always less than 1.0, the Whittle and Forgan relationship predicts flow instability to occur before bulk boiling occurs at the exit. Although this is contrary to the original HEU safety analysis, which in some instances allows temperatures up to, but below, bulk boiling at the exit, there are no safety consequences. The reason is that, as indicated in Appendix B-1, of the 150 combinations of pressurizer pressure, inlet temperature, and flow rate that were considered in the original safety analysis, only a very few at very low flow rates were constrained by the no bulk boiling at the exit criterion. All of the others were constrained by the 50% of Bernath critical heat flux criterion.

In addition to avoiding flow instability, it is also important to avoid critical heat flux. The Croft and the Waters experiments using electrically heated channels demonstrated that flow instability occurs at powers that are about 60% of those that produce critical heat flux. Thus, one could argue that the prediction of critical heat flux in the current safety analysis is unnecessary because flow instability occurs first. However, safety analysis should also include the predicted margin to critical heat flux, even if flow instability occurs at a lower power level. Moreover, equation 4.1 indicates that the margin to flow instability is unchanged if both the power and the flow are increased so as to keep the bulk coolant exit temperature unchanged. However, if the power were increased along with the flow, at some point the heat flux would reach the critical heat flux. Thus, under extreme circumstances, critical heat flux could occur before flow instability. Hence, although the margin to critical heat flux will not be assessed as part of the current feasibility study since it is not needed to demonstrate feasibility, it will be included in the final safety analysis.

4.4 Hot Channel Factors

Because flow instability is the only thermal criterion under current consideration, only the hot channel factors that affect flow instability, as predicted by equation 4.1, need be considered at this time. The tolerances in D_h and L_h on the right side of equation 4.1 can have only a very minor impact on the allowed bulk coolant temperature rise indicate in the numerator on the left side of equation 4.1. The bulk coolant saturation temperature at the exit in the denominator of the left side of equation 4.1 is assumed to be accurately known. The uncertainty in measured inlet temperature is taken into account in the treatment of the limiting safety settings. If this uncertainty is 5°, for example, then the inlet temperature trip setting will be set no higher than 150° F, since the limiting safety system settings (LSSS) allow a maximum inlet temperature of 155° F. Therefore, all of the uncertainty of any consequence in the flow instability analysis is associated with the numerator of equation 4.1, which represents the bulk coolant temperature rise for the limiting channel in the reactor. This temperature rise is essentially proportional to the channel power (heat flux into that channel) divided by the channel flow rate. Thus, the hot channel factor analysis will focus on the potential manufacturing or calculation uncertainties that affect either the channel power

or the channel flow rate. There are two uncertainties that affect the channel power and two that affect the channel flow rate, as described in the following four subsections.

4.4.1 Hot Channel Factors – Power Distribution Uncertainty

In spite of the considerable geometric and analytical detail that goes into determining the three-dimensional distribution of power throughout the core with the aid of the MCNP5 code,[4-8] there is some uncertainty in these calculations. Based solely on judgment, it is assumed due to calculational uncertainties that the power in any one HEU or LEU fuel plate can be as much as 10% greater than is predicted in the analysis. For channels that are formed by two fuel plates, it is assumed that this 10% factor applies to only one of them. Thus, the uncertainty in power distribution contributes a 1.05 uncertainty factor to all channels that have two-sided heating and a 1.10 factor to all outer channels, which are each heated by only one fuel plate.

One specific aspect of power distribution uncertainty is the uncertainty in the location of the fuel meat. For the fresh, clean LEU core this effect was studied in considerable detail. First the MCNP5 code was used to determine the power distribution in the core when all fuel plates of all eight elements are at their nominal positions. Thermal-hydraulic analysis of this core indicated that the most limiting location was at channel 3 of element 5. (Channel 3 is near the inner radius of the core.)

For element 5, the effect of plate position tolerances on thermal safety margin was studied. Potential worst cases considered included those in which the power of plate 3 was maximized, or in which the thickness of channel 3, located between fuel plates 2 and 3, was minimized. Also, minimizing the thickness of channel 1 potentially could cause channel 1 to be limiting and could adversely influence channels 2 and 3. Channel 25 was sufficiently far from limiting in the nominal case that the extremes of channel thickness tolerances could not cause it to become limiting.

The table in the inset of Figure 4.3 shows the element 5 channel thickness configurations considered in the study. All plates in all elements are at their nominal positions except in element 5. The changes in thickness of the internal channels were confined to channels 2 through 5 of element 5, as indicated by the light blue shading in the table. The "Perturbed 1" case was designed so that the channels on either side of the limiting plate, plate 3 (indicated in the table by a thick dark vertical line between channels 3 and 4),

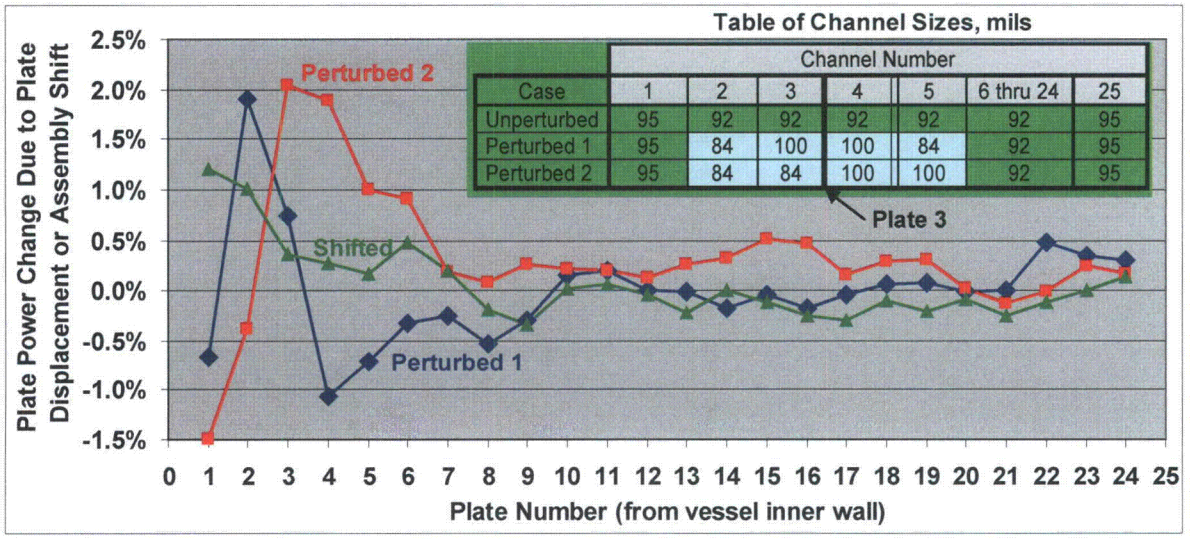


Figure 4.3 – Change in Radial Power Distribution of Element 5

would have the maximum thickness of water moderator on either side of it. This was intended to maximize the power in the plate 3.

All neutronics studies with the MCNP5 code modeled all eight elements simultaneously. The blue curve of Figure 4.3 shows the plate-by-plate effect on power distribution for element 5 due to the Perturbed 1 plate distribution. The increase in water surrounding plate 3 caused its power to increase by only 0.75%. The significantly greater increase in the power of plate 2, 1.90%, is due to moving plate 2 inward 8 mils into a region of higher neutron flux. These small power increases due to neutronic effects, however, are overshadowed by the greatly increased cooling caused by the 8-mil increase in the thickness of the limiting channel, channel 3. Therefore, further study of Perturbed 1 plate distribution was abandoned in favor of the Perturbed 2 case, which minimized the thicknesses of channels 2 and 3. The red curve of Figure 4.3 shows the plate-by-plate change in the power distribution between the Perturbed 2 and the Unperturbed cases.

A 15-mil inward shift of element 5 was also studied, which would occur if the element was positioned with the rollers touching the inner pressure vessel wall (see Figure 4.2). All of the element 5 fuel plates were shifted inward 15 mils, but nominal spacing between plates was maintained. Likewise, the elements on either side of element 5, elements 4 and 6, were assumed to be shifted outward 15 mils, Figure 4.4. The purpose of this was to maximize the power increase in element 5. If all of the elements were shifted inward by 15 mils, for example, then the effect would be shared by all of the elements -- and since total core power is fixed, the effect on element 5 would be minimal. The green curve of Figure 4.3 shows the plate-by-plate relative differences in power in the limiting element, element 5, due the shifting elements 4, 5, and 6.

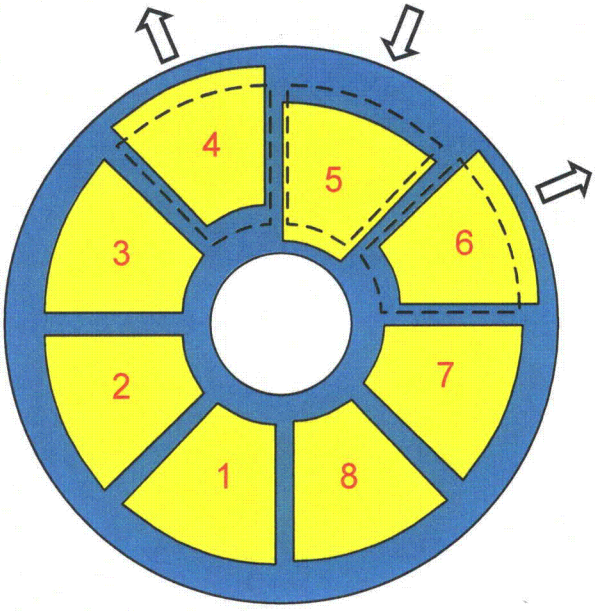


Figure 4.4 – Element Arrangement with Element 5 Shifted Inward 15 mils and Elements 4 & 6 Shifted Outward 15 mils (Shifted Case)

The three plate-by-plate distributions shown in Figure 4.3 indicated a variation in plate power that is no more than about ±2%, which is well within the ±10% assumed in the uncertainty analysis. Therefore, it was concluded that it is appropriate to assume that in studies with MCNP5 it is appropriate to assume that all of the fuel plates and fuel elements are at their nominal locations and to rely on hot channel factors to account for the possible small perturbations in fuel location.

4.4.2 Hot Channel Factors – Fuel Plate Loading Uncertainty

For a fixed environment, the power produced by a fuel plate is essentially proportional to the loading of U^{235} in the plate. The tolerance for this quantity typically is prescribed in the design documents and must be met by the fuel plate vendor. For the HEU fuel, Table 14-4 of Reference [4-2] indicates a 1.03 hot channel factor on bulk coolant enthalpy rise (essentially temperature rise). Reference [4-2] used an average channel and a series of nuclear peaking factors to represent the hottest channel. Based on this approach and the 1.03 hot channel factor, it is assumed that the fuel plate loading tolerance is 6% and that

only one of the two plates that formed the hot channel was overloaded. Therefore, in the current HEU analysis, a 1.03 hot channel factor due to U^{235} loading uncertainty will be applied to each of the internal channels and a 1.06 factor will be applied to each of the outer channels.

The monolithic LEU fuel meat is made from a thin foil that is rolled to the desired thickness. The nominal fuel meat thickness is 9 mils for plate 1 (nearest the smallest core radius), 12 mils for plate 2, 18 mils for plates 3 through 23, and 17 mils for plate 24. The tolerance on the fuel meat thickness is assumed to be ±1 mil. Thus, the tolerance loading factor for plate 1 is 10/9 (= 1.111), for plate 2 is 13/12 (= 1.083), for plates 3 through 23 is 19/18 (= 1.055), and for plate 24 is 18/17 (= 1.059). In the analysis it is assumed that only one plate of each channel can be overloaded. For the outer channels, the plate factor of 10/9 or 18/17, as appropriate, is used. For the internal channels where the two applicable nominal fuel meats are of unequal thickness, then the thinner one is assumed to apply. In channel 2, for example, which is formed by plates 1 and 2, the applicable factor is 1 + (10/9 − 1)/2, or 1.056.

4.4.3 Hot Channel Factors – Flow Distribution Uncertainty

For a series of parallel channels all of equal thickness, slight variations in manufacturing that are not captured by the tolerances and other effects that are not captured by the analytical methods can lead to variations in flow. For example, it is well-known that slight variations in inlet conditions from channel to channel can have significant effects on flow distribution. Therefore, based solely on judgment, a 1.20 uncertainty factor on flow distribution is assumed for the HEU and LEU cores. A flow distribution uncertainty factor was not included in the original MURR HEU safety analysis.

4.4.4 Hot Channel Factors – Channel Thickness Uncertainty

Variations in channel thickness can be due to tolerance in the as-built fuel plate thickness, fuel swelling, and variations in the fuel plate spacing during fuel element manufacture. For rectangular channels where the hydraulic diameter is approximately twice the channel thickness and the flow is turbulent with friction factor, $f = Re^{-\alpha}$, where Re is Reynolds number, Reference [4-9] shows that the hot channel factor component for bulk coolant temperature rise (F_{BULK}) is:

$$F_{BULK} = \left(\frac{t_{nom_chan}}{t_{hot_chan}} \right)^{\frac{3}{2-\alpha}} \tag{4.2}$$

where t_{nom_chan} is the nominal thickness of the channel and t_{hot_chan} is the minimum thickness of the channel. The Reynolds number exponent, α, is normally between 0.20 and 0.25. The 0.25 value will be used. Equation 4.2 is based on the perturbation in the flow rate of a single channel due to a decrease in channel thickness from t_{nom_chan} to t_{hot_chan} with no change in pressure drop between the inlet and outlet of the channel.

As discussed in Section 4.1, for the HEU core the nominal channel thicknesses are 110 mils for channel 1, 80 mils for channels 2 through 24, and 90 mils for channel 25. For the LEU core the nominal channel thicknesses are 95 mils for channel 1, 92 mils for channels 2 through 24, and 95 mils for channel 25. For both cores, the tolerance is ±28 mils for channel 1, ±8 mils for channels 2 through 24, and ±28 mils for channel 25.

A related concern is that swelling of the fuel meat can make the thickness of the plate greater and thereby reduce the thickness of the adjacent channels on either side. An estimate for an earlier proposed LEU

core with a maximum element lifetime of 250 MWd, which is considerably greater than the current proposed LEU element lifetime of 210 MWd, is that the highest burnups are in the innermost fuel plate, plate 1, which has a 9-mil thick fuel foil and the outermost plate, plate 24, which has a 17-mil thick fuel foil. The corresponding values of peak burnup were 40.6×10^{20} and 18.5×10^{20} fissions/cm^3, respectively. These values of maximum burnup are low relative to fuel swelling experiments, because burnup is limited by reactivity considerations. The thinnest fuel foils are the 9 mils of plate 1 and the 12 mils of plate 2. The thickest fuel foil is the 18 mils of plates 3 though 23. Figure 6.4 on page 36 of Reference [4-10] provides fractional change in volume due to swelling as a function of burnup for parametric values of temperature and molybdenum content. This figure is based on equation 6.2 of page 32 of the reference. Swelling increases with fuel temperature. The peak fuel temperature will be less than 200° C. For a U10Mo fuel foil at 200° C with a burnup of 40.6×10^{20} fissions/cm^3, this equation indicates that the fuel volume increase will be 14.4%. The corresponding value for 18.5×10^{20} fissions/cm^3 is 4.7%. A 14.4% increase in a 9 mil foil is 1.3 mils. A 4.7% increase in an 18 mil foil is 0.8 mils. Thus, the maximum fuel swelling is expected to cause about a 1 mil increase in plate thickness and a similar decrease in channel thickness.

Because the burnup that produces swelling depletes the fuel where the swelling occurs, it is very likely that the reduction in allowed flow instability power due to channel thinning caused by fuel swelling will be more than offset by the corresponding reduction in power peaking factor. Thus, it is expected that the limiting core locations will not be locations that have accrued high swelling due to burnup. Furthermore, the potential swelling on the order of 1 mil is well bounded by the overall channel thickness tolerance of 8 mils. Therefore, no further explicit consideration of fuel swelling is provided in the current feasibility study.

4.4.5 Hot Channel Factors – Uncertainties (i.e., Measurement Error) in Reactor Measured Quantities

In the operation of the MURR reactor the uncertainties in the measurement of reactor power, reactor flow, reactor inlet temperature, and pressure at the pressurizer are taken into account in the trip settings. For example, as also described above, if the uncertainty in the measurement of reactor inlet temperature is 5° F, then the LSSS setting for the reactor inlet temperature will be no higher than 150° F so that the 155° F limiting inlet temperature will not be violated. In the PLTEMP/ANL analysis the worst conditions allowed by the limiting safety conditions were assumed. Therefore, no further allowance for measurement errors is needed the analysis.

4.5 PLTEMP/ANL Computer Code

The PLTEMP/ANL code[4-4] is capable of modeling all of the MURR fuel elements at one time and considering all of the fuel plates and coolant channels of each element simultaneously. In the PLTEMP/ANL code the only coupling between parallel elements is hydraulic. The code divides the axial length of the core into a series of parallel axial slices and predicts the temperature and heat fluxes of each slice. The code considers the thermal conditions in the channel on each side of a fuel plate in determining the fraction of the power emanating from each face. This can be particularly important when the channel on one side of a fuel plate is much cooler than the channel on the other side, such as channels 1 and 25.

The code includes a hot channel factor on bulk coolant temperature rise. However, the same factor is applied to the coolant temperature rise of all channels in the core. Therefore, the channel by channel variations will be treated separately, as explained in the section 4.6.

The code explicitly includes the power produced by each plate. However, the code does not include the azimuthal variation of power along the width, or arc length, of each plate. Since the MURR cores have

thin rectangular channels with large aspect ratios, these variations in power can be extremely significant to the thermal-hydraulic performance of the core. In the PLTEMP/ANL models of the HEU and LEU cores these potentially significant variations in relative power along the arc lengths of the plate are ignored. However, they are included in the post processing of the PLTEMP/ANL results, as explained in section 4.6.

The PLTEMP/ANL code includes the axial distribution of power. Based on equation 4.1, flow instability is only a function of channel bulk coolant exit temperature rise; the relative axial power distribution has virtually no effect on flow instability. So currently, one axial power distribution is assumed to apply to the entire core. Perhaps there could be a second order effect due to the redistribution of power from channel to channel, but even that would be extremely small if it exists at all. In all of the analyses, the relative axial power distribution of channel 3 of element 1 was used. This channel is expected to be the limiting channel or close to being the limiting one. The channel specific axial distribution of power will be used in the CHF analysis for final safety analysis.

The code has a search capability which allows the assumed pressure drop across the reactor to be adjusted until the total flow rate through the reactor is predicted.

The current version of the PLTEMP/ANL code calculates the ratio of the bulk coolant temperature rise to the allowed bulk coolant temperature rise based on equation 4.1 for each heated coolant channel in the core. (The value of η is a code input quantity.) Code edits refer to this ratio as the flow instability ratio (FIR). The code output indicates the minimum value of this ratio and the channel where the minimum occurs. A small improvement was made to the current version of the code to enable it to provide the FIR for each channel in the core rather than for only the limiting channel.

The code has search capability which enables the code to automatically adjust the reactor power level until a minimum value of FIR, which is specified by code input, is achieved.

4.6 Analysis

4.6.1 Core Configurations and Operating Conditions

In the MURR HEU and LEU fuel cycles, fuel elements with varying burn up histories ranging from fresh to end of life are mixed together in the weekly operating cycle. The banked critical control blade height varies depending on the excess reactivity of core state. Therefore, the MCNP5 analysis was performed for eight reference cores for each fuel type that were considered potentially limiting. As addressed in section 3, careful consideration of these 16 configurations indicated that configurations 3B and 4B of the HEU core and configurations 7B and 8B of the LEU core were the most limiting states. Therefore, these four configurations were analyzed with the aid to the PLTEMP/ANL code in order to determine the predicted allowed flow instability power for each core type.

For this feasibility analysis, the PLTEMP analysis was performed for the MURR 10 MW HEU core technical specification Limiting Safety System Settings (LSSS) (T.S. 2.2). The LSSS conditions are 75 psia at the pressurizer, 155° F at the core inlet, and 3200 gpm through the core. The guidance in reference [4-1] was used to predict the pressure drop from the pressurizer to the core inlet. References [4-1] and [4-2] provide a series of values for the pressure drop components between the pressurizer and the core inlet for one reactor volumetric flow rate and coolant inlet temperature. In addition, Reference [4-1] provides relationships that enable these conditions to be scaled to provide the pressure drop components for other reactor flow rates and inlet temperatures. These scaling relationships can also be deduced from basic hydraulic principles. This information enabled the pressure at the core inlet, 68.0 psia, to be calculated for the LSSS conditions.

4.6.2 Core Pressure Drops

Since the MURR fuel cycle loads the set of fuel elements with the least burn up history in core positions 1 and 5 (summarized in Appendix A-1) the limiting channel is always found in either core position 1 or 5. Therefore, the analysis focused on these two elements rather than all eight elements. First all eight elements were considered simultaneously to obtain the core pressure drop. Then the core pressure drop was applied to the two elements of interest to obtain the allowed flow instability power.

For the HEU core and the LEU core, a PLTEMP/ANL case was set up that explicitly represented all eight elements with all 200 (i.e., 8 × 25) coolant channels at their respective nominal thicknesses. The LSSS core inlet temperature and flow rate were assumed. For the HEU core, the power distribution of the 3B configuration was used with an assumed reactor power of 17.0 MW. For the LEU core the 7B configuration was used with an assumed reactor power of 20.0 MW. These cases enabled the core pressure drop to be predicted for a representative HEU core and for a representative LEU core operating at or near the power that causes flow instability.

The power levels were deliberately chosen considerably above the 10.0 MW and 12.0 MW full power operating levels for the two fuels because the core pressure drop decreases with increasing power. This is due to the decrease in liquid viscosity with increasing coolant temperature. Because the hydraulic models in PLTEMP/ANL are based on single phase flow and do not include the effects of bulk, an increase in pressure drop is not predicted as flow instability is approached. Had the lower power levels been used, higher pressure drops would have been predicted. In a subsequent step, these pressure drops are applied to elements 1 and 5 and the power level at which flow instability first occurs in either element is sought. A core pressure drop based on the lower operating power level and then applied at the high flow instability power level would predict about 0.5% too much flow through each channel and would therefore predict about 0.5% higher power margin to flow instability.

4.6.3 Hot Channel Factor Application

The hot channel uncertainty components, as described in sections 4.4-1 through 4.4-4 are shown for each channel and both core types in Table 4-1. Translating the fractional tolerance into an uncertainty factor component is intuitive for the first three components since the fractional increase in power or decrease in flow to a particular channel results in the same fractional increase in bulk coolant temperature rise for that channel. For example, a 20% uncertainty on flow distribution results in a 1.20 uncertainty factor component. For the fourth hot channel factor component, equation 4.2 is used for the internal channels, i.e., channels 2 through 24, for both the HEU and LEU cores. The ratio of t_{nom_chan} to t_{hot_chan} is 80/72 (= 1.111) for the HEU core and 92/84 (= 1.095) for the LEU core. The corresponding values of F_{bulk} are 1.198 for the HEU core and 1.169 for the LEU core.

In the subsequent step of the PLTEMP/ANL flow instability analysis, where only elements 1 and 5 are considered, the outer channel thicknesses are reduced in the code input so as to include the worst-case outer channel thicknesses. One approach would be to set each outer channel size to the minimum channel thickness that it could possibly have, which is its nominal channel thickness reduced by the 28-mil thickness tolerance. This approach would unduly penalize the outer channels because with regard to hot channel factors PLTEMP/ANL treats internal and outer channels alike and the hot channel factor includes the tolerance on internal channel thickness. A better approach is to make the outer channels thicker than their minimum thicknesses so that after the hot channel factors are applied the behavior of each outer channel at its minimum thickness in predicted. This is accomplished by setting outer channel thickness so that the ratio of the assumed outer channel thickness to the minimum outer channel thickness is the same as that used in the internal channel hot channel factor analysis. In the LEU core, where both outer channels are 95±28 mils thick, the minimum channel thickness is 67 mils for both channel 1 and 25. In

Table 4-1 Hot Channel Factor Components for Enthalpy Rise

Hot Channel Factor Component	Channel					
	1	2	3	4 - 23	24	25
HEU						
Power Distribution	1.10	1.05	1.05	1.05	1.05	1.10
Fuel Plate Loading	1.06	1.03	1.03	1.03	1.03	1.06
Flow Distribution	1.20	1.20	1.20	1.20	1.20	1.20
Channel Thickness	1.198	1.198	1.198	1.198	1.198	1.198
Multiplicative Total	**1.676**	**1.555**	**1.555**	**1.555**	**1.555**	**1.676**
Total Relative to Channel 3	1.078	1.000	1.000	1.000	1.000	1.078
LEU						
Power Distribution	1.10	1.05	1.05	1.05	1.05	1.10
Fuel Plate Loading	1.111	1.056	1.042	1.028	1.029	1.059
Flow Distribution	1.20	1.20	1.20	1.20	1.20	1.20
Channel Thickness	1.169	1.169	1.169	1.169	1.169	1.169
Multiplicative Total	**1.714**	**1.554**	**1.534**	**1.514**	**1.516**	**1.634**
Total Relative to Channel 3	1.117	1.013	1.000	0.987	0.988	1.065

the PLTEMP/ANL analysis both channels are each 73.4 mils because 73.4/67 = 92/84 = 1.095. Similarly, in the HEU core, where the channel thickness is 110±28 mils for channel 1 and 90±28 mils for channel 25, in the PLTEMP/ANL code input channel 1 is 91.1 mils thick and 25 is 68.9 mils thick. This was done because the minimum HEU channel 1 and 25 thicknesses are 82.0 and 62.0 mils, respectively, and 91.1/82.0 = 68.9/62.0 = 80/72 = 1.111. Since the ratio of PLTEMP/ANL channel input thickness to minimum thickness allowed by the tolerances is made the same for internal and outer channels alike, the same hot channel factor component, as obtained from equation 4.2, applies to all channels, i.e., 1.198 for the HEU core and 1.169 for the LEU core.

A third approach would be to use the nominal outer channel thicknesses in the PLTEMP/ANL code input and to make analytical corrections in the post processing of the results. However, the approach chosen has three benefits relative to the third approach. First, the post processing of the PLEMP/ANL results is easier, since the outer channel results need no additional adjustments to account for differences in outer channel thickness and tolerances relative to the internal channels. Second, as can be demonstrated with the aid of equation 4.1, thinner channels allow higher bulk coolant outlet temperatures. Third, thinner outer channels cause the PLTEMP/ANL solution to predict higher coolant temperatures in the outer channels. Higher coolant temperatures in the PLTEMP/ANL solutions cause less of the power produced by the adjacent fuel plate to flow to the outer channel. The second and third items are legitimate mitigating effects for the outer channels which would not be captured if nominal outer channel thickness were used in the PLTEMP/ANL model. Moreover, if a smaller fraction of outer fuel plate power goes to the outer channel, then a greater fraction must go to the next channel. This is also correct and appropriate and also more limiting for the adjacent channel that gets the increased fraction of the outer fuel plate power. Thus, the approach chosen is the best among the three choices.

The four the hot channel factor components described in sections 4.4.1 through 4.4.4 are a result of essentially random uncertainties in power distribution, fuel plate loading, flow distribution, and channel thickness. In the original HEU safety analysis[4-1],[4-2] all of the uncertainty factor components that affected bulk coolant temperature rise were multiplied together. This approach in effect assumes a highly unlikely situation where all of the uncertainties simultaneously affect the most limiting channels in the most adverse way. Although a statistical treatment of these uncertainties would be more appropriate

and less limiting, the original multiplicative approach was used in order to make the current safety analysis more readily comparable to the original safety analysis for the HEU core.

Table 4-1 lists the four hot channel factor components for each channel for both fuel types. The product of the four components produces the total hot channel factor for the channel. Because the PLTEMP/ANL code input allows one value of hot channel factor for bulk coolant temperature rise, which is applied equally to all channels, the value of channel 3 was used in the code input. In the post processing the ratio of the channel value to the value for channel 3, as indicated in Table 4-1, was used to correct the flow instability power values predicted by PLTEMP/ANL for the other channels. For example, the LEU ratio for channel 1 is 1.117. Therefore, the flow instability power predicted by PLTEMP/ANL for channel 1 was divided by 1.117.

4.6.4 Power Distribution Along the Arc Length (or Width) of the Fuel Plates

In the MCNP5 analysis of the core, the fuel region of each plate of each element is divided into nine vertical stripes (azimuthal stripes) of equal width and each stripe is divided into 24 horizontal (axial) layers of equal thickness. Thus, the fuel meat of each plate is divided into $9 \times 24 = 216$ identical rectangular pieces. The power produced by each piece is predicted. The PLTEMP/ANL code uses the power of each plate, i.e, all 216 pieces are summed together. Since there are 24 fuel plates in each element, 24 values corresponding to relative volumetric power generation rate are provided in the code input for each element. The code input also includes one relative axial power shape that is applied to all plates of all elements. Thus, the detail in the MCNP5 results cannot be fully captured by the PLTEMP/ANL code.

Since the channels in the MURR reactor are thin rectangular channels with large aspect ratios, variations in power among the nine or 18 vertical fuel plate stripes that heat the channel could be important. In the PLTEMP/ANL code input, the average power of the nine vertical stripes of each plate is used to represent the plate power. However, in the post processing of the PLTEMP/ANL results, the highest power stripe of each plate is considered. The MCNP5 results are post processed so that for each fuel plate the ratio of the power of hottest vertical stripe to the average power of the nine vertical stripes is determined (see Figure 3.21). In the post processing of the PLTEMP/ANL results, these ratios are used to produce an adjustment factor for each channel. For the outer channels, the adjustment factor is the peak-to-average power ratio for the adjacent fuel plate. For the internal channels, the adjustment factor is the average of the peak-to-average power ratios of the two adjacent plates. In the post processing of the PLTEMP/ANL results the allowed flow instability power of each channel is divided by its adjustment factor.

This approach does not take into account the mitigating effect of heat transfer along the width of the fuel plate (i.e., transverse to coolant flow), which would reduce the effects of power peaking. Since the hottest stripe tends to be on the azimuthal edges of the fuel meats where they border non-fueled aluminum which is swaged into the thick aluminum side plates, this mitigation could be considerable. The current approach also assumes that the hottest parts of both plates that form an internal channel are directly across from each other. This is a worst case assumption, but probably close to being true. Thus, the predicted allowed flow instability power would be greater if these mitigating effects were included in the analysis.

4.6.5 Fraction of Power Produced in the Reactor Core

Measurements based on the current operation of the MURR reactor indicate that about 93% of the reactor power is deposited inside of the pressurized primary loop and that the remainder in deposited outside of the primary loop. This implies that when the reactor is producing 10.0 MW, about 9.3 MW are produced in the core and the rest is produced outside of the reactor pressure vessel. Since a similar situation is expected for the LEU core, for purposes of this feasibility study, a 93% factor will be assumed to apply to

both cores. Therefore, in the post processing of the PLTEMP/ANL results, the 93% factor will be included by dividing all of the PLTEMP/ANL predicted flow instability powers by 0.93.

4.7 Results

Figure 4.5 shows the reactor power at which flow instability is predicted to occur in each channel of elements 1 and 5 of the HEU core for the reference cores evaluated. Figure 4.6 shows the analogous results for the LEU core. Table 4.2 summarizes the minimum value of power in each of the eight plots of Figures 4.5 and 4.6. Thus, the minimum HEU power is 16.5 MW. The minimum occurs in channel 2 of element 1 of case 3B. For this case, channel 2 of element 5 is nearly equally limiting. Similarly, the minimum LEU power is 18.7 MW. It occurs in channel 3 of element 1 of case 7B. For this case, channel 3 of element 5 is nearly equally limiting as is channel 24 of element 1 in case 8B.

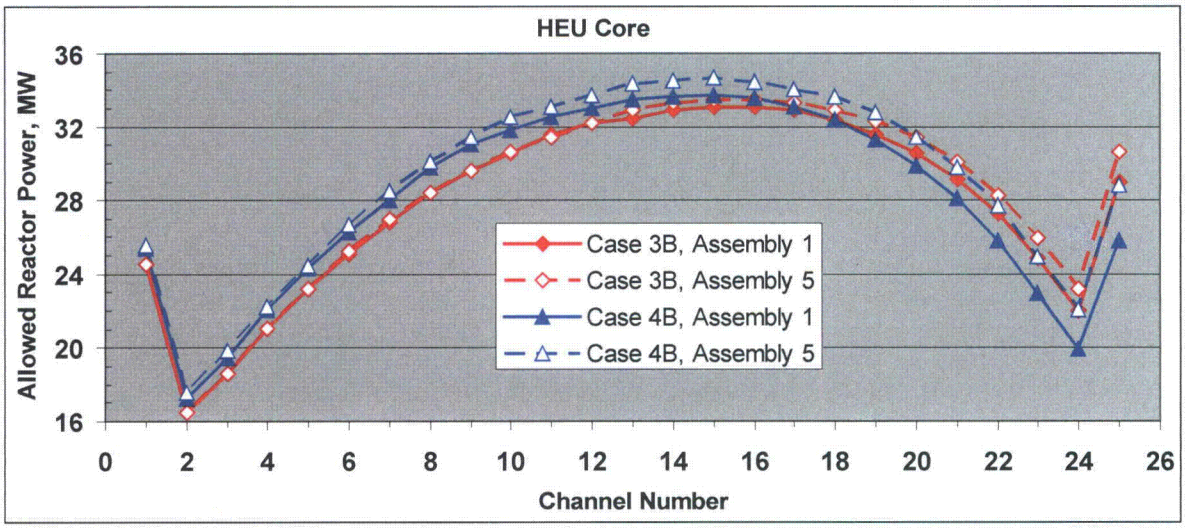


Figure 4.5 – Reactor Power Predicted to Initiate Channel Flow Instability in the HEU Core

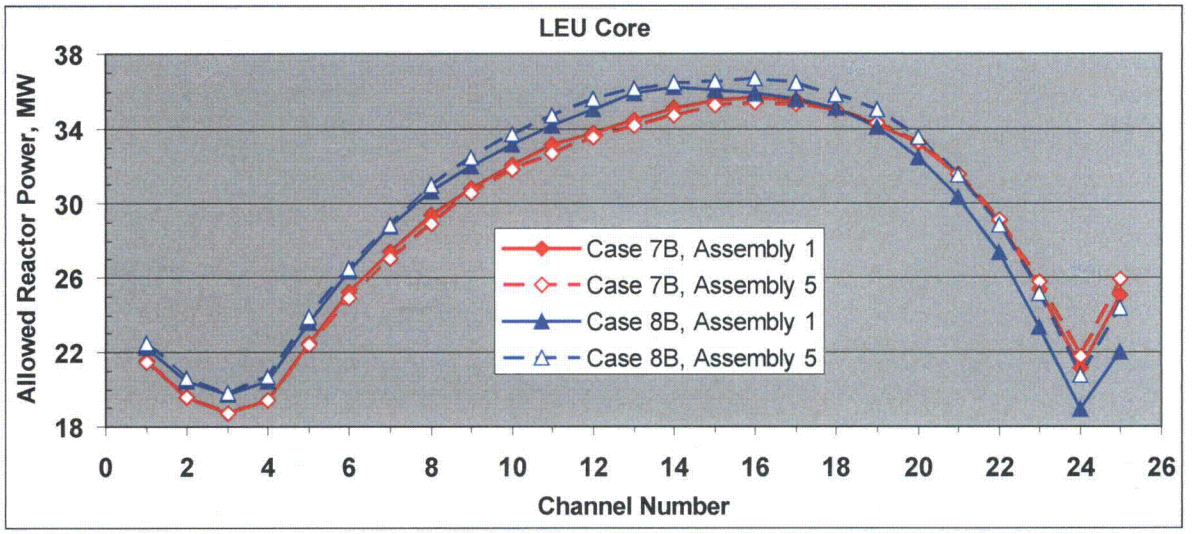


Figure 4.6 – Reactor Power Predicted to Initiate Channel Flow Instability in the LEU Core

4.8 Thermal-Hydraulic Discussion and Conclusions

The distributions of channel flow instability power shown in Figures 4.5 and 4.6 with the lowest allowed powers near the inner and outer plates of the elements and the highest allowed powers towards the middle are consistent with the curves of axial average heat flux per fuel plate that are provided in Appendix A-1. As is expected, the values of allowed power tend to be at their lowest values where the heat fluxes are at their highest.

Table 4-2 Flow Instability Power

Case	Element	Power, MW	Channel
HEU			
3B	1	**16.48**	2
	5	16.51	2
4B	1	17.30	2
	5	17.58	2
LEU			
7B	1	**18.73**	3
	5	18.74	3
8B	1	18.98	24
	5	19.79	3

Table 4.2 compares the flow instability power level at the LSSS values for pressure, temperature and flow for the four limiting cases. From this the allowed power margins in the current HEU and LEU analyses can be compared. For the HEU core, the 10.0 MW nominal value versus the predicted allowed power of 16.5 MW, implies a 6.5 MW margin. This is to be compared with the 6.7 MW margin predicted for the LEU core.

References [4-1] and [4-2] predict values for the onset of flow instability based on the original HEU analysis. This analysis used power peaking factors for the HEU core that are more conservative than the three dimensional values derived from the MCNP modeling of core power peaking factors. This is due to the power peaking factors that were obtained in 1973 from combining two different sets of peaking factors from two different two dimensional EXTERIMANATOR Code models. The radial and axial peaking factors from a R/Z model of all fresh fuel elements were combined with the azimuthal peaking factor from a theta/R model of fresh and highly burned up fuel elements combined. This produces an overall peaking factor that exceeds the actual overall three dimensional peaking factor for a worst case core. These references provide digital values for 75 psia at the pressurizer and 3200 gpm for reactor inlet temperatures of 140 and 160° F. Linear interpolation of these two flow instability values yields 14.9 MW for a reactor coolant inlet temperature of 155° F. Since the nominal reactor power for the HEU core is 10.0 MW, in the original analysis a 4.9 MW margin (14.9 MW versus 10.0 MW) was deemed acceptable. Since the nominal reactor power for the LEU core is 12.0 MW and the flow instability power in the current analysis of the LEU core is 18.7 MW, the margin is even larger, 6.7 MW.

In conclusion, based on the sole thermal-hydraulic requirement established in the original HEU safety analysis[4-1],[4-2] that flow instability be avoided, the performance of the proposed LEU core is acceptable.

4.9 Thermal-Hydraulic References

[4-1] F. R. Vaughan, *Safety Limit Analysis for the MURR Facility*, NUS-TM-EC-9, prepared for the University of Missouri by the NUS Corporation, 4 Research Place, Rockville, Maryland, 20850, May 1973.

[4-2] University of Missouri Research Reactor Safety Analysis Report, Chapter 4, Reactor Description, submitted to the U.S. Nuclear Regulatory Commission in 2006.

[4-3] R. H. Whittle and R. Forgan, "A Correlation for the Minima in the Pressure Drop Versus Flow-Rate Curves for Sub-Cooled Water Flowing in Narrow Heated Channels," *Nuclear Engineering and Design*, 1967.

[4-4] Arne P. Olson and Kalimullah, "A Users Guide to the PLTEMP/ANL V3.8 Code," Reduced Enrichment for Research and Test Reactors (RERTR) Program, Argonne National Laboratory, June 20, 2009.

[4-5] Louis Bernath, "A Theory of Local-Boiling Burnout and Its Application to Existing Data," Chemical Engineering Progress Symposium, Series No. 30, Volume 56, pp. 95-116 (1960).

[4-6] M. W. Croft, Advanced Test Reactor Burnout Heat Transfer Tests, USAEC Report IDO-24465, ATR-FE-102, Ca-2, Babcock & Wilcox Company, January 1964.

[4-7] E. D. Waters, Heat Transfer Experiments for the Advanced Test Reactor, USAEC Report BNWL-216, UC-80, Reactor Technology (TID-4500) Pacific Northwest Laboratory, Richland, Washington, May 1966.

[4-8] X-5 Monte Carlo Team, "MCNP-A General Monte Carlo N-Particle Transport Code, Version 5 Volume I, II and III," LA-UR-03-1987/LA-CP-03-0245/LA-CP-03-0284, Los Alamos National Laboratory (2003).

[4-9] W. L. Woodruff, Evaluation and Selection of Hot Channel (Peaking) Factors for Research Reactor Applications, ANL/RERTR/TM-28, RERTR Program, Argonne National Laboratory, Argonne, Illinois, February 1997 [http://www.rertr.anl.gov/METHODS/TM28.pdf].

[4-10] J. Rest, et al., U-Mo Fuels Handbook, Version 1.0, RERTR Program, Argonne National Laboratory, June 2006.

5. FEASIBILITY STUDY CONCLUSIONS AND RECOMMENDATIONS

The analyses performed in this report show that the MURR reactor can be operated safely with the new LEU fuel elements, if the U10Mo monolithic fuel can be qualified and manufactured.

As has always been true for reactor conversion projects, full safety analyses need to be performed and regulatory approvals received before the reactor will be able to convert

It is important to note that the U10Mo Monolithic Fuel is not yet qualified or commercially available. The Fuel Development (FD) and Fuel Fabrication Capability (FFC) efforts within the GTRI Reactor Conversion Program are both working to clarify the fuel specifications that will be supported for the new LEU fuel. The positive feasibility results reported at this time are predicated on the best information available to date, as communicated through the US High Performance Research Reactor Working Group (USHPWG).

Reactivity to maintain operating lifetime with LEU has been obtained by increasing the water to metal ratio in the core by thinning the fuel plates and increasing the coolant channel widths. Plates 2 through 23 were decrease from 50 mil thick to 38 mil by designing for 18 mil U10Mo foil with 10 mil clad (including any interlayer to control fuel swelling behavior). Reduced foil thicknesses have been designed in three of the fuel plates in order to control power peaking and assure safety margins. It is not yet clear whether the 10 mil clad thickness will prove too difficult or expensive to fabricate. Furthermore, experiments and analyses to prove the hydrodynamic stability of the thin 38 mil fuel plates must still be performed. Should a thicker clad and/or a stiffer plate be required, then the inherent penalty of displacing moderating water will need to be addressed to prove technical feasibility of an alternate fuel design. A contingency design for thicker fuel plates will be explored in the year ahead, in parallel with safety analyses of the current LEU design.

Furthermore, acceptable experimental fluxes will only be maintained if the reactor power can be increased from 10 MW in order to offset the inherent penalty of introducing U238 into the core. Feasibility studies to date have indicated that safety margins will be maintained with LEU fuel operated at 12 MW. The power uprate will be modeled in safety analyses. Regulatory issues of the uprate must be addressed in the near term to assure successful conversion on the aggressive GTRI schedule.

Finally, we must also note that the economic feasibility of conversion cannot be declared until commercial availability of the fuel has been developed, including credible fuel costs projections. MURR understands that GTRI is committed to addressing fuel cost differentials associated with conversion from HEU to LEU. MURR will continue to work within the USHPWG to assist the FFC in development of cost models and/or to pursue redesigns (as possible) once key cost factors are better understood.

APPENDIX A-1: HEAT FLUX DISTRIBUTIONS FOR MURR CORES

As described in Section 3.4.4, power distributions were calculated with MCNP by tallying the fission power (f7 tally) within 24 radial (i.e., plate-by-plate), 24 axial, and 9 azimuthal segments of the fuel plate meat in the entire core of eight elements (i.e., 216 equal volume segments within each plate; 5,184 segments per element). Power distributions were calculated for a variety of critical banked control blade configurations of various cores in order to identify the highest peaking factors that might limit margin to flow instability. The MCNP tallies were normalized by a post-processor to facilitate studies of different core power levels and different levels of tally detail. It should be noted that credit for power deposition outside the fuel is not modeled here, but is taken into account in the thermal-hydraulic safety margin calculation.

After considering the various contributors to power peaking discussed in Section 3.4.4, power distributions were calculated for the 16 cases that enveloped the distinct combinations of effects. All fresh cores were compared to cores in which fresh elements were combined with elements to be discharged at the end of that weekly cycle (week 58 for the HEU simulation, week 79 for the LEU simulation). Initial startup of the weekly cycle with no xenon was compared to the equilibrium xenon state at 2 days of operation. A typical flux trap loading was compared to an empty flux trap. Thus 8 cases were considered for both HEU and the proposed LEU design. The atom densities of the fuel compositions for each core state were read from REBUS-DIF3D depletion results to automatically update an MCNP input file. An automated search was then performed with MCNP to find the critical banked blade position for the core (i.e., blades moved until MCNP predicted a k-effective of 1.0). The detailed power distributions were then tallied by an MCNP run. Finally, a post-processor was applied to read the mctal file and produce normalized edits suitable for analysis (and to facilitate an automated linkage to the PLTEMP/ANL thermal hydraulics code discussed in Section 4.5).

The 16 cases are summarized in Table A-1.1. The associated Hot Stripe Heat Fluxes are listed in Table A-1.2.

The figures in this appendix illustrate several plots for each case:

- Axial Average Heat Flux in Each Plate of Each Element
- Azimuthal Peaking Factor for Each Plate of Each Element
- Hot Stripe Heat Flux for Each Plate of Each Element

Table A-1.1 – Summary of Power Distribution Evaluations

Core State that may bound power peaking					Element Burnup (MWd) at Beginning of Week				Inches withdrawn		
Fuel	Case	Burnup State	Time (Days)	Flux Trap	X1 X5	X2 X6	X3 X7	X4 X8	Blades A-D	Reg Blade	MCNP k-eff
HEU	1A	Fresh	0	Samples	0	0	0	0	12.911	10	0.99983
	2A	Fresh	2	Samples	0	0	0	0	16.782	15	1.00017
	3A	Week 58	0	Samples	0	81	65	142	17.809	10	1.00044
	4A	Week 58	2	Samples	0	81	65	142	24.031	15	1.0002
	1B	Fresh	0	Empty	0	0	0	0	13.295	10	0.99974
	2B	Fresh	2	Empty	0	0	0	0	17.367	15	0.99985
	3B	Week 58	0	Empty	0	81	65	142	18.380	10	0.99969
	4B	Week 58	2	Empty	0	81	65	142	26.000	15	1.00029
LEU	5A	Fresh	0	Samples	0	0	0	0	12.267	10	1.00037
	6A	Fresh	2	Samples	0	0	0	0	16.165	15	0.99998
	7A	Week 79	0	Samples	0	116	97	199	17.020	10	1.00011
	8A	Week 79	2	Samples	0	116	97	199	23.481	15	1.00027
	5B	Fresh	0	Empty	0	0	0	0	12.647	10	0.99995
	6B	Fresh	2	Empty	0	0	0	0	16.826	15	1.00021
	7B	**Week 79**	**0**	**Empty**	**0**	**116**	**97**	**199**	**17.632**	**10**	**1.00015**
	8B	Week 79	2	Empty	0	116	97	199	25.116	15	1.00049

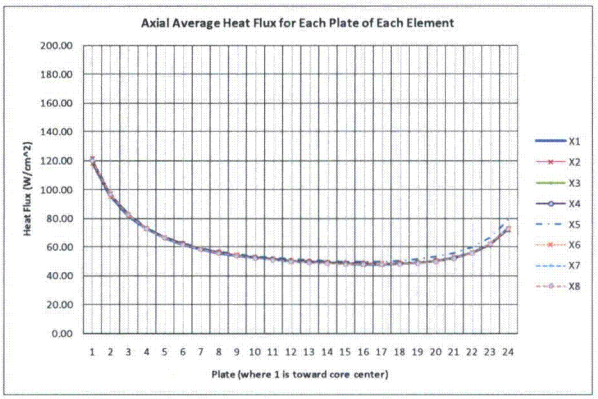
Samples indicates a typical loading of samples in all three flux trap tubes
Empty indicates neither samples nor tubes in the flux trap (i.e., "empty island" configuration)
HEU elements discharged at 150 MWd (at 10 MW operation)
LEU elements discharged at 208 MWd (at 12 MW operation)
Full blade withdrawal is 26 inches
MCNP power tally runs were made with 60M histories for σ on k-effective of ~ 12 pcm
Criticality searches were perfomed with 15M histories, σ ~ 22 pcm. Searches to 1.00000 ± 15 pcm

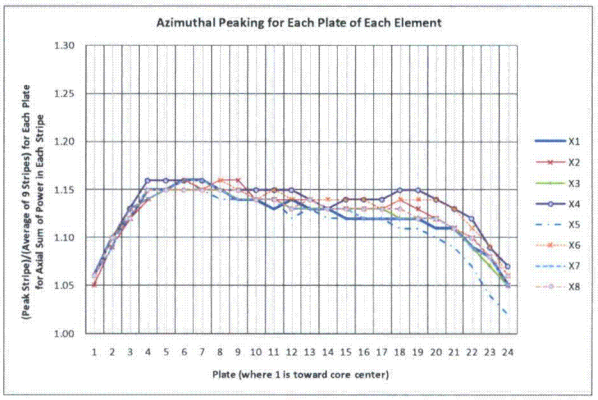
Table A-1.2 – Summary of Key Hot Stripe Heat Fluxes Evaluated

Core State that may bound power peaking					Hot Stripe Heat Flux (W/cm^2) Fresh Element in Position X1				Hot Stripe Heat Flux (W/cm^2) Fresh Element in Position X5			
Fuel	Case	Burnup State	Day	Flux Trap	Plate 1	Plate 3	Plate 23	Plate 24	Plate 1	Plate 3	Plate 23	Plate 24
HEU	1A	Fresh	0	Samples	126.7	91.4	67.3	76.8	128.8	94.0	69.4	80.4
	2A	Fresh	2	Samples	121.6	89.3	74.4	87.3	123.4	89.4	74.8	86.6
10MW	3A	Week 58	0	Samples	131.7	96.6	82.6	96.6	132.3	97.6	79.3	91.8
	4A	Week 58	2	Samples	126.3	92.6	90.4	107.4	125.6	92.6	82.8	97.8
	1B	Fresh	0	Empty	133.2	94.5	66.7	77.2	133.8	96.2	70.0	80.2
	2B	Fresh	2	Empty	127.0	91.3	74.5	87.9	129.3	92.1	74.3	87.1
	3B	**Week 58**	**0**	**Empty**	**138.6**	**99.3**	**83.0**	**97.6**	**138.9**	**99.7**	**78.9**	**92.2**
	4B	**Week 58**	**2**	**Empty**	**132.9**	**94.8**	**90.8**	**109.6**	**132.1**	**93.2**	**82.8**	**97.9**
LEU	5A	Fresh	0	Samples	116.3	134.4	84.9	100.0	119.4	136.6	90.1	107.0
12MW	6A	Fresh	2	Samples	112.2	129.5	94.6	116.0	113.4	130.4	95.8	117.2
	7A	Week 79	0	Samples	119.0	137.6	103.3	126.6	118.4	137.7	101.3	122.3
	8A	Week 79	2	Samples	114.1	130.4	113.8	142.6	113.3	130.1	105.5	131.1
	5B	Fresh	0	Empty	124.0	139.0	85.0	100.8	125.3	140.9	90.8	108.0
	6B	Fresh	2	Empty	119.1	132.4	95.8	118.0	119.6	133.1	96.4	118.2
	7B	**Week 79**	**0**	**Empty**	**124.9**	**141.0**	**104.7**	**127.6**	**125.1**	**140.8**	**102.0**	**123.2**
	8B	**Week 79**	**2**	**Empty**	**120.3**	**133.9**	**114.3**	**145.4**	**119.4**	**132.8**	**105.7**	**131.3**

Samples indicates a typical loading of samples in all three flux trap tubes
Empty indicates neither samples nor tubes in the flux trap (i.e., "empty island" configuration)

Note that HEU operates at 10 MW, while 12 MW is proposed for LEU operation. Thus a 20% increase in LEU heat flux would be expected if the element was not altered (in design and underlying physics).





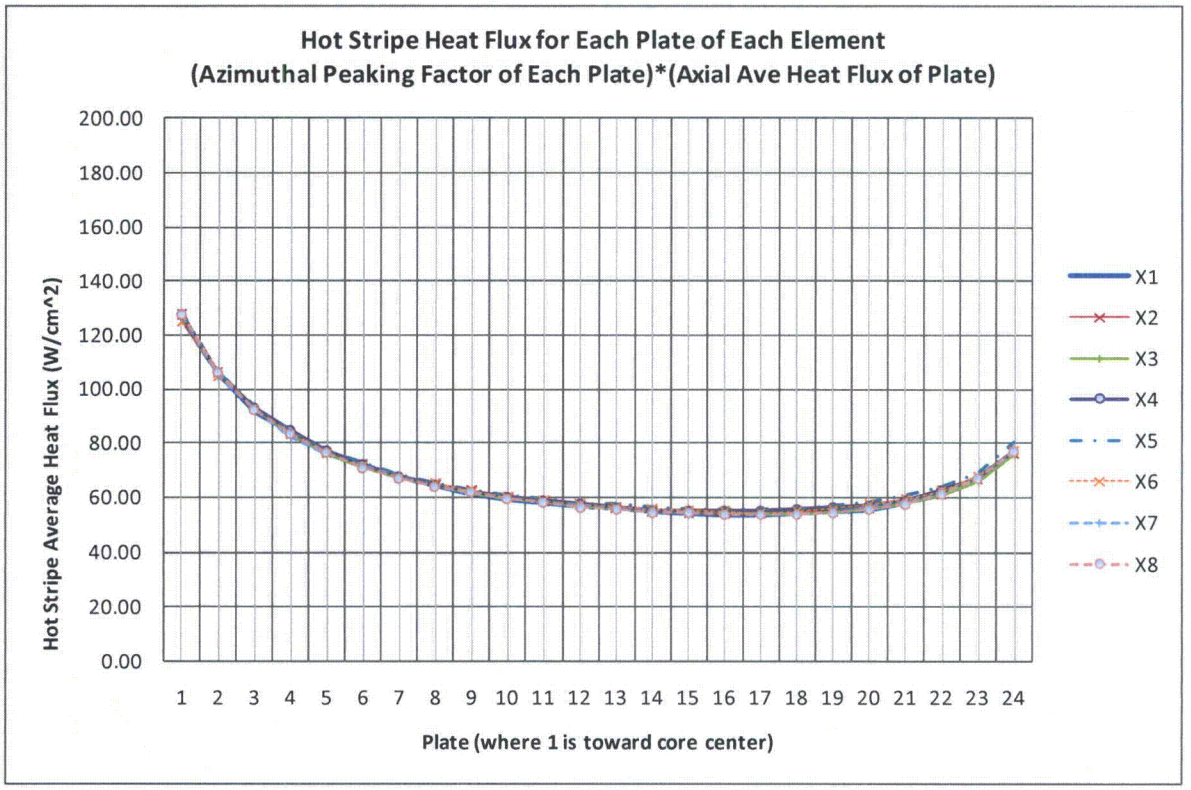
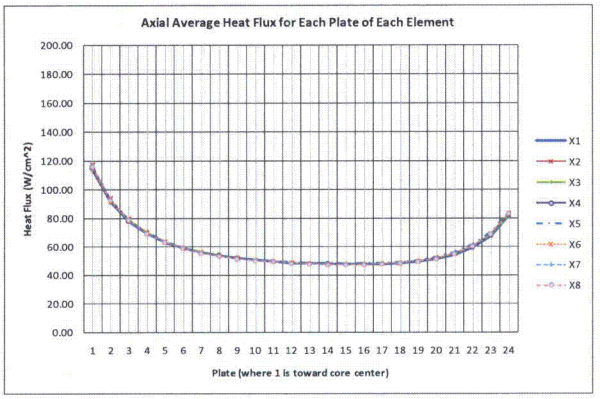
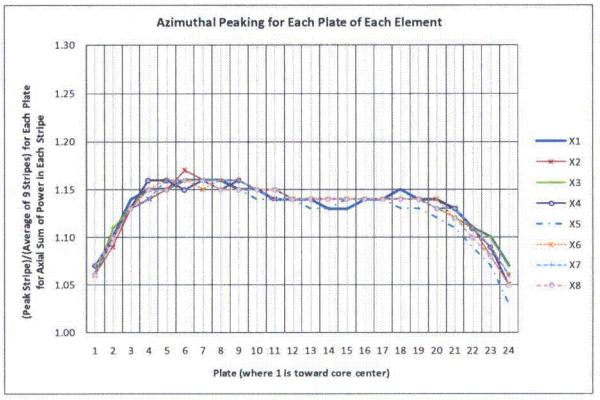


Figure A-1.1 - Case 1A: 10 MW HEU Fresh Day 0 with Flux Trap Samples





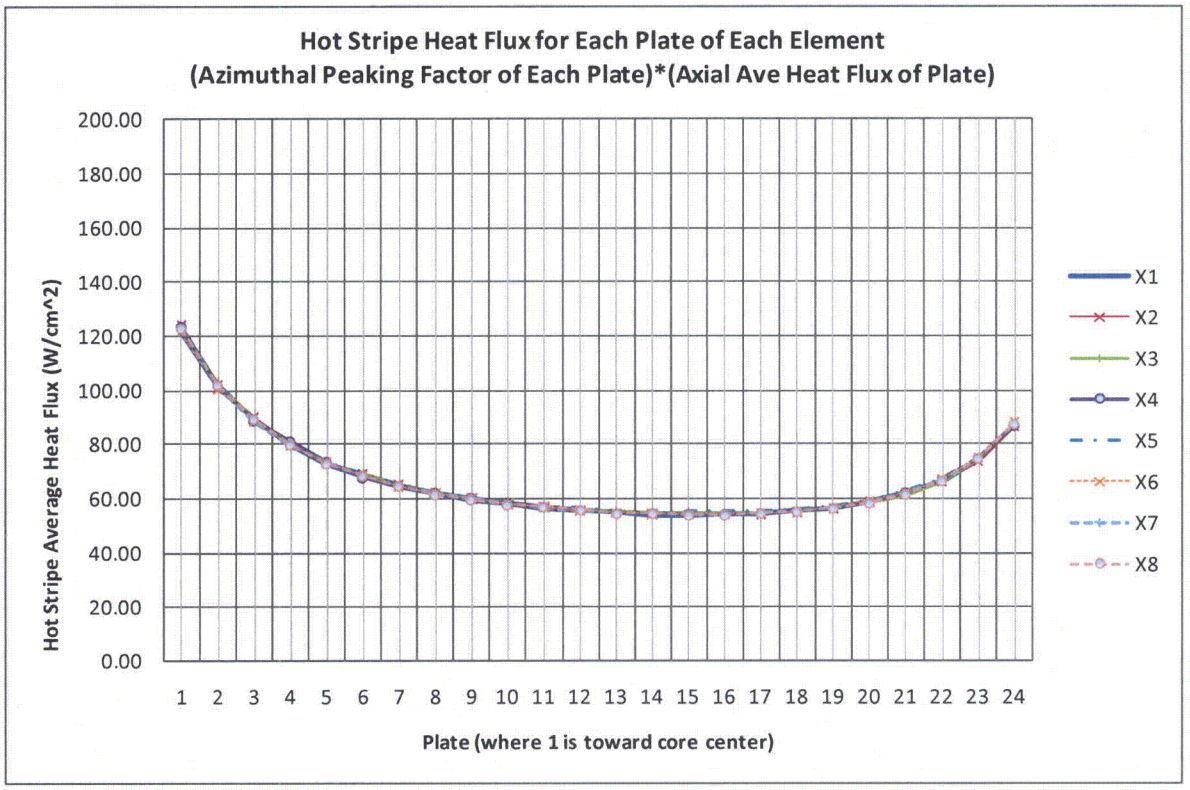
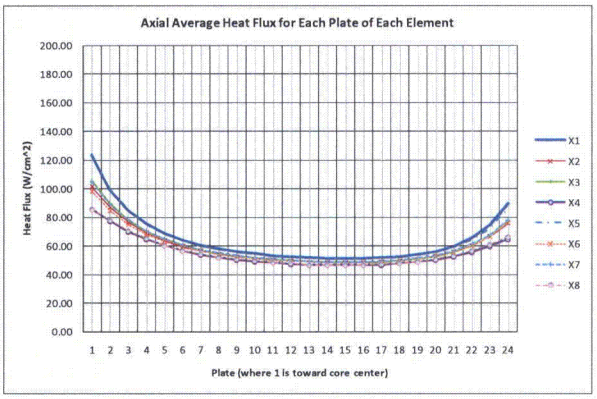
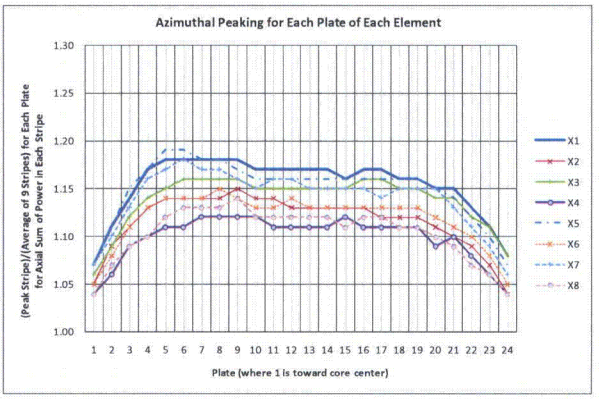


Figure A-1.2 – Case 2A: 10 MW HEU Fresh Day 2 with Flux Trap Samples





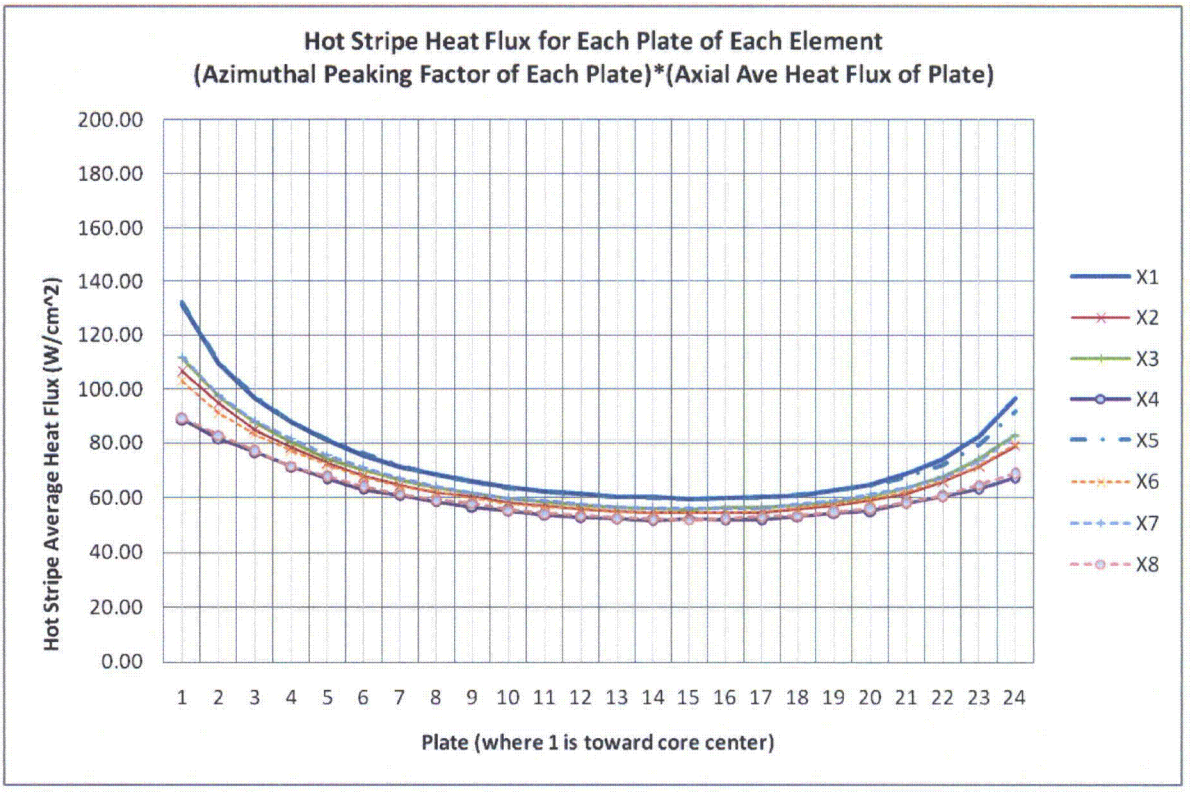
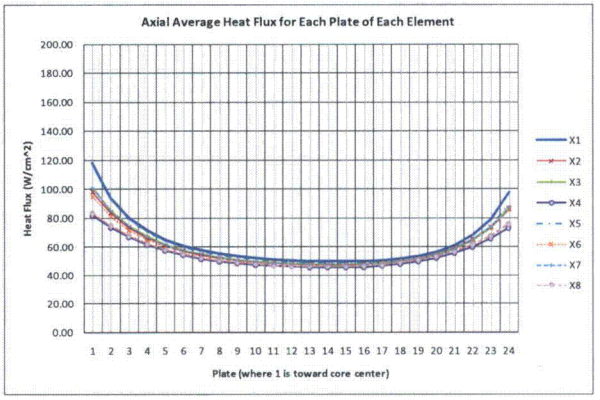
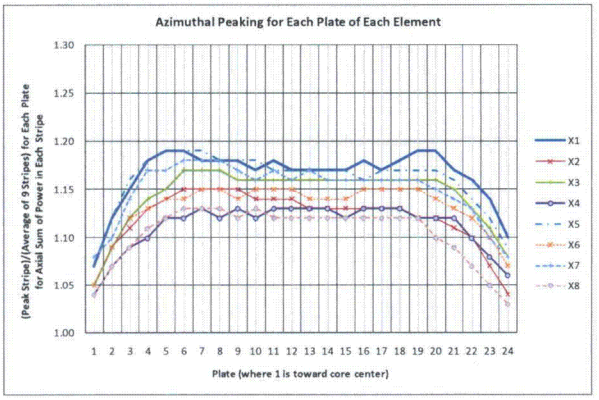


Figure A-1.3 - Case 3A: 10 MW HEU Week 58 Day 0 with Flux Trap Samples





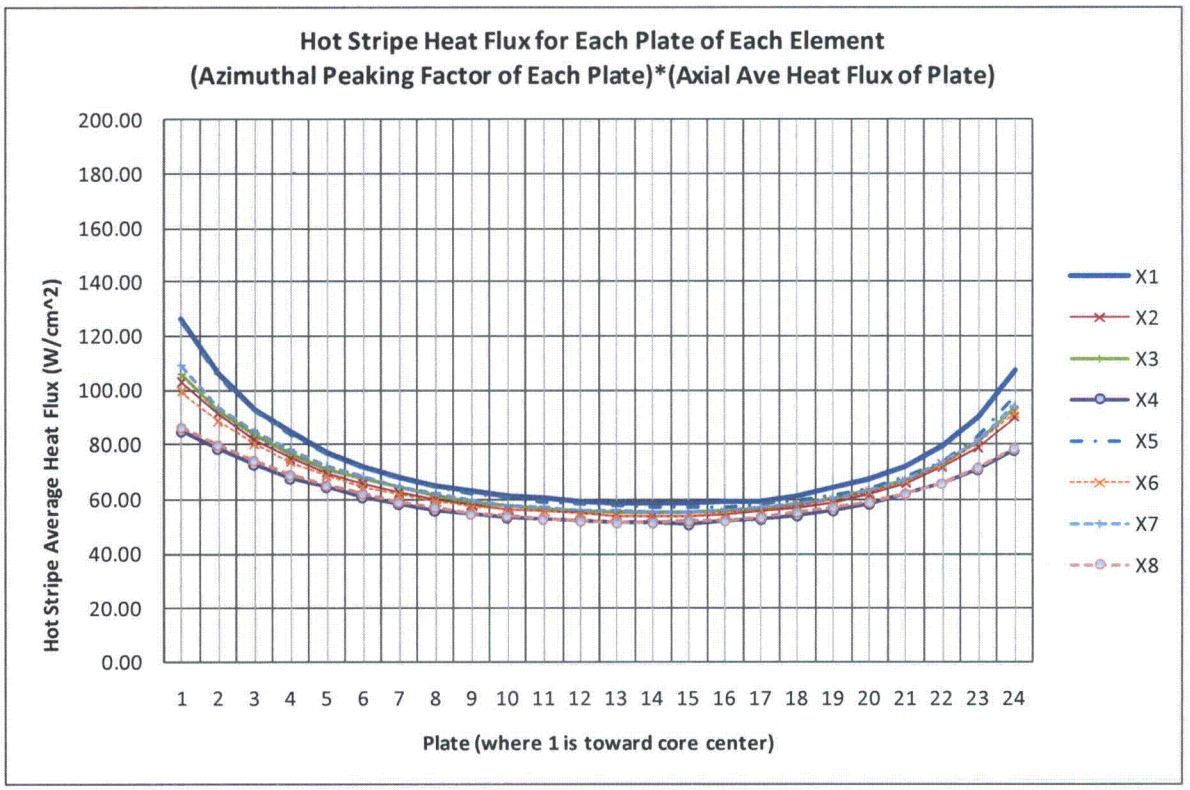
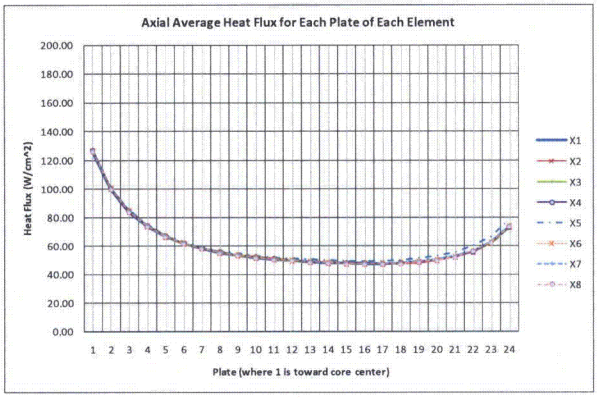
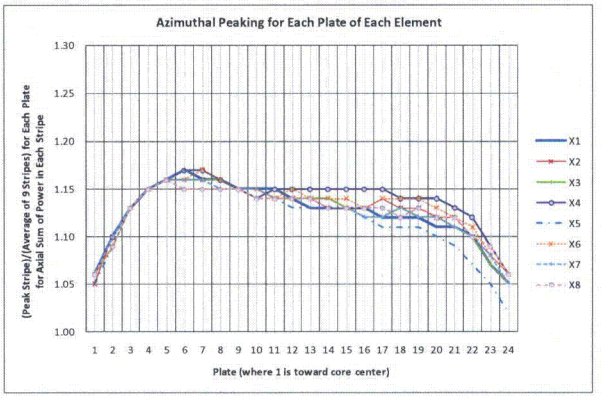


Figure A-1.4 – Case 4A: 10 MW HEU Week 58 Day 2 with Flux Trap Samples





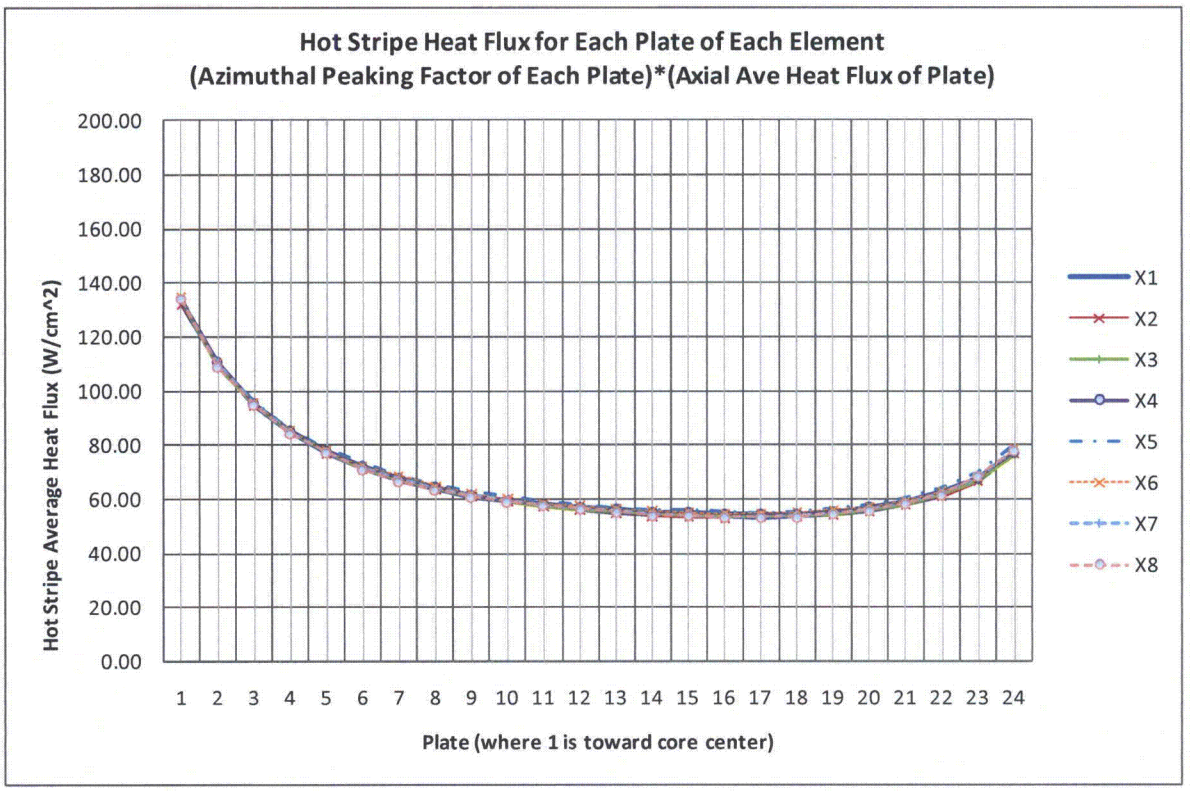
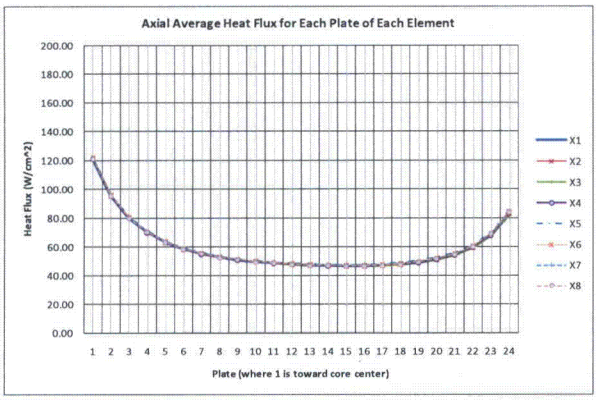
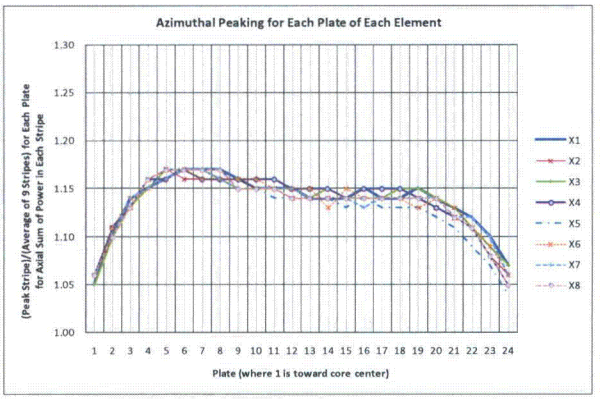


Figure A-1.5 - Case 1B: 10 MW HEU Fresh Day 0 with Empty Flux Trap





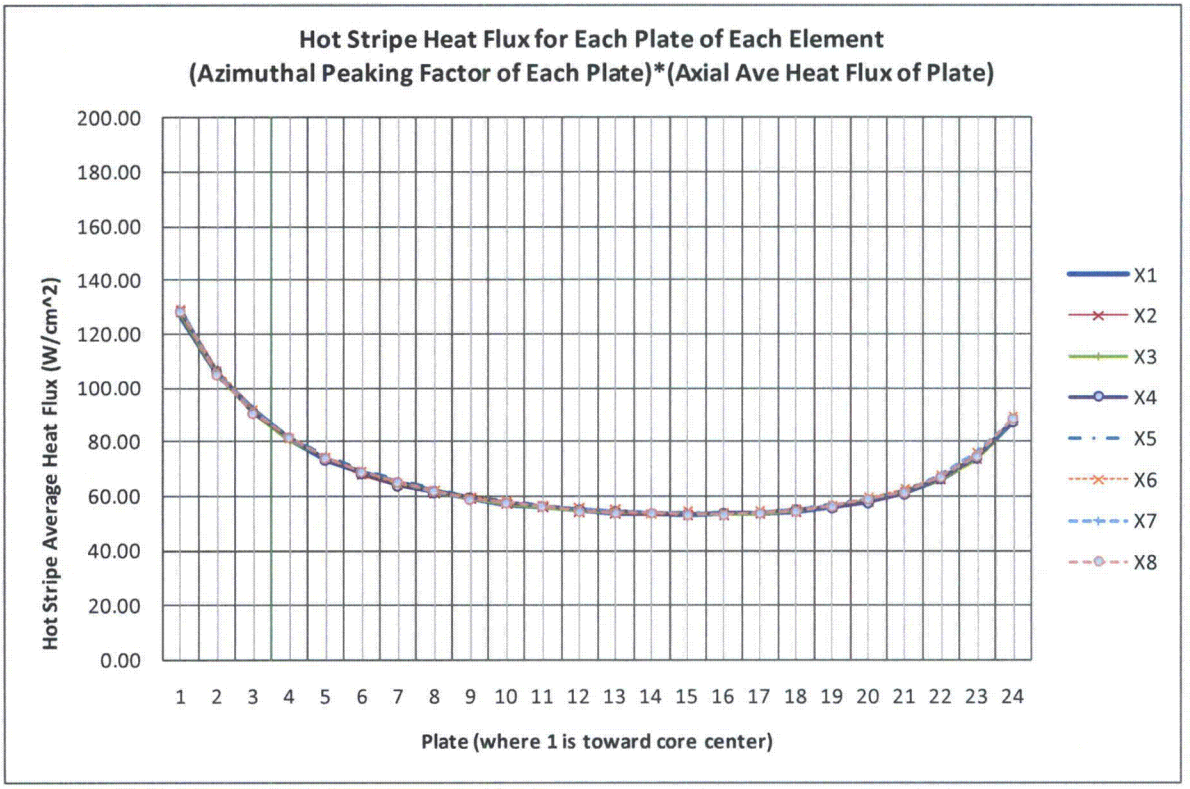
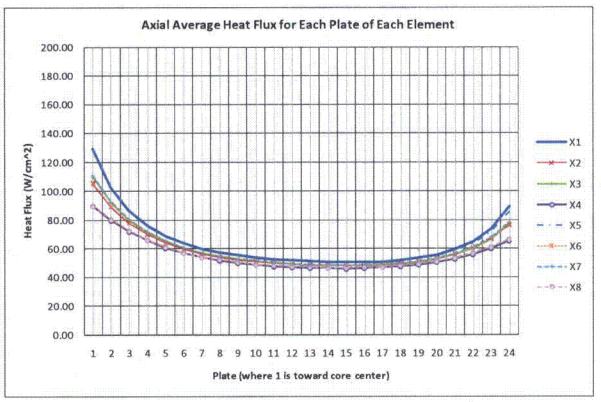
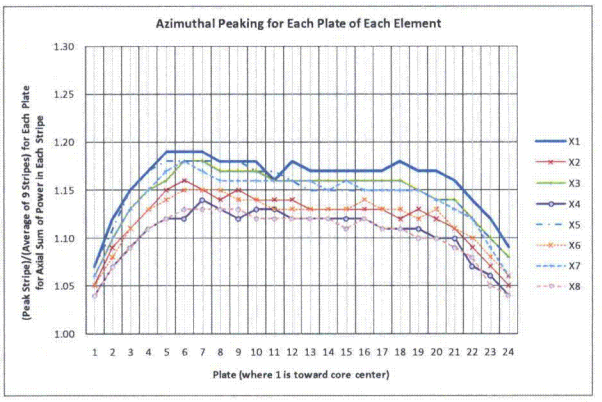


Figure A-1.6 – Case 2B: 10 MW HEU Fresh Day 2 with Empty Flux Trap





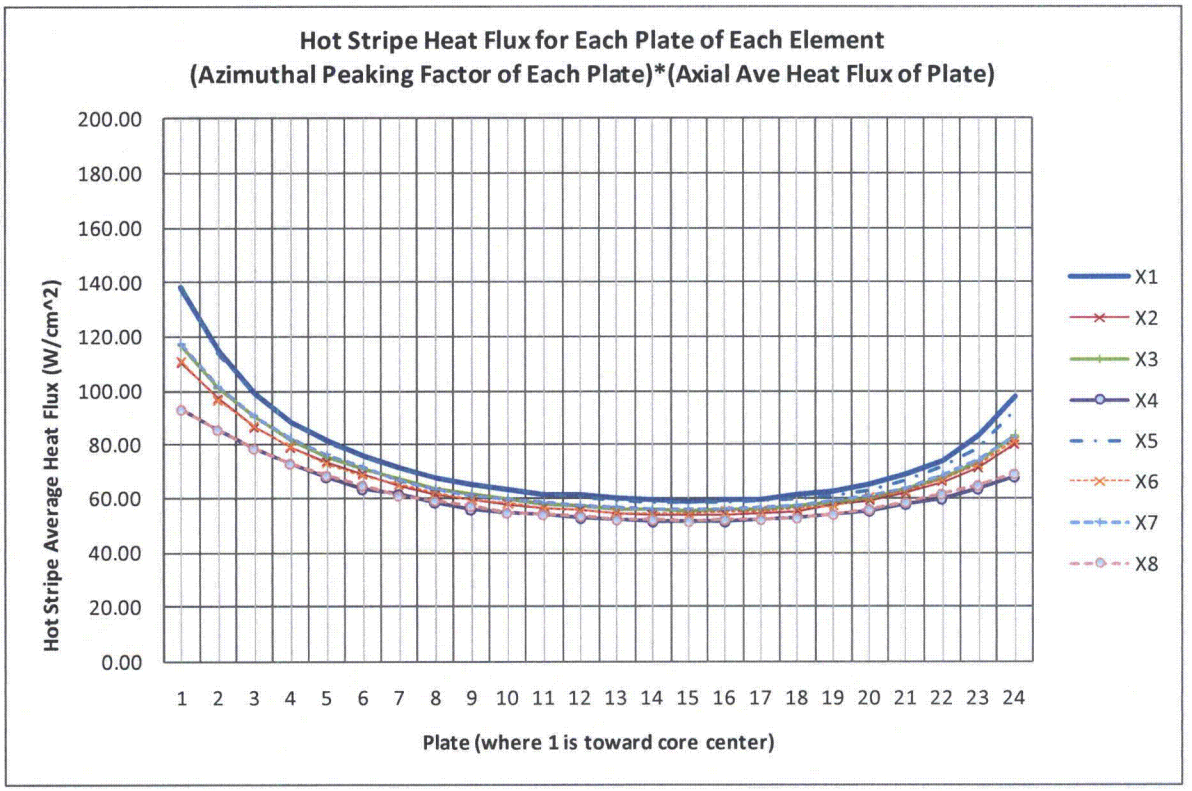
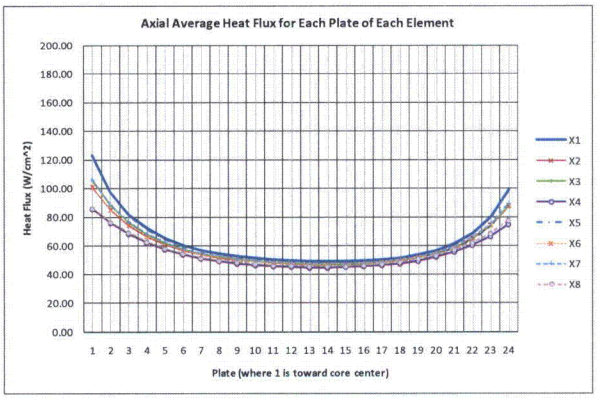
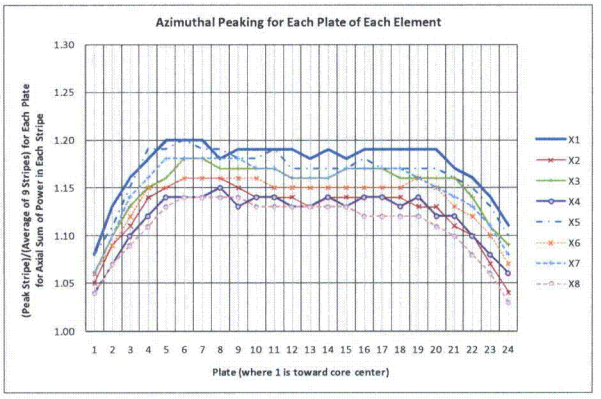


Figure A-1.7 - Case 3B: 10 MW HEU Week 58 Day 0 with Empty Flux Trap





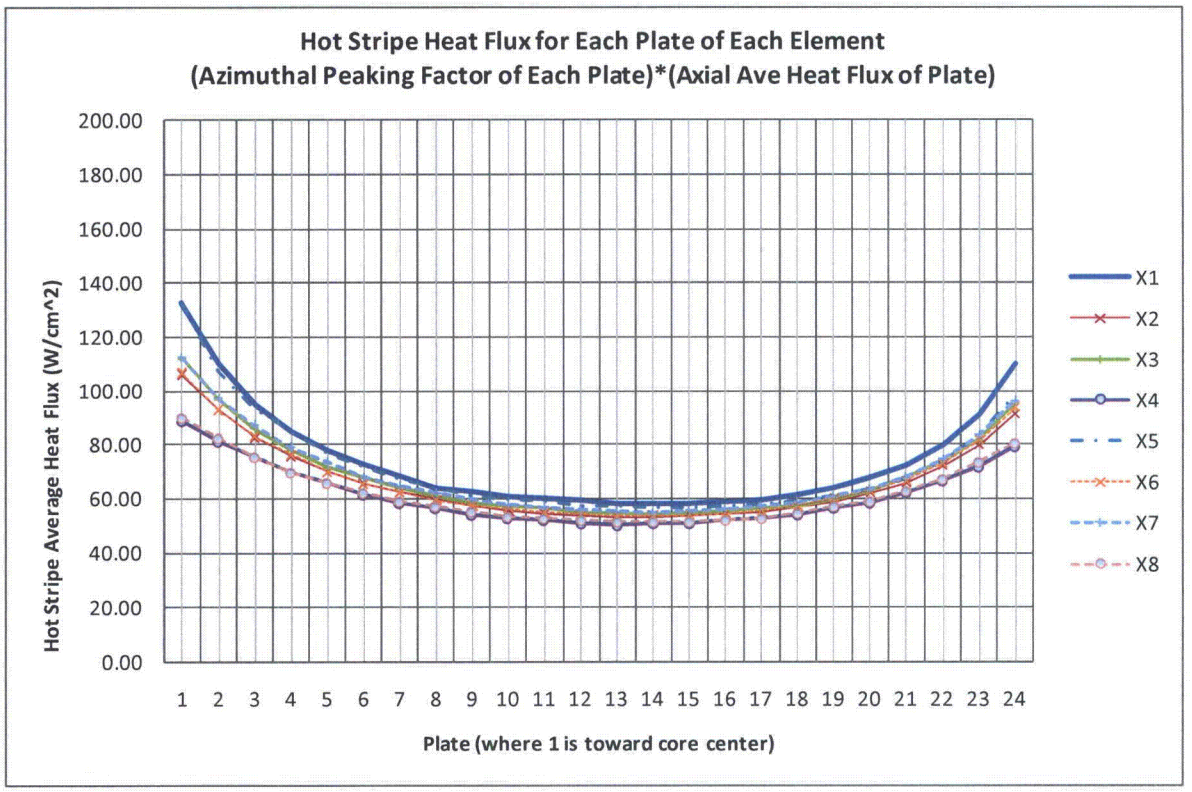
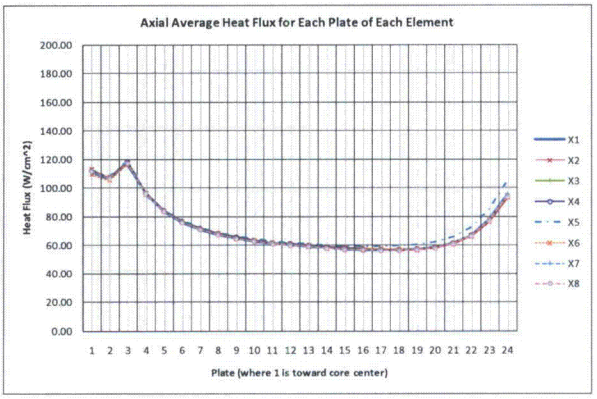
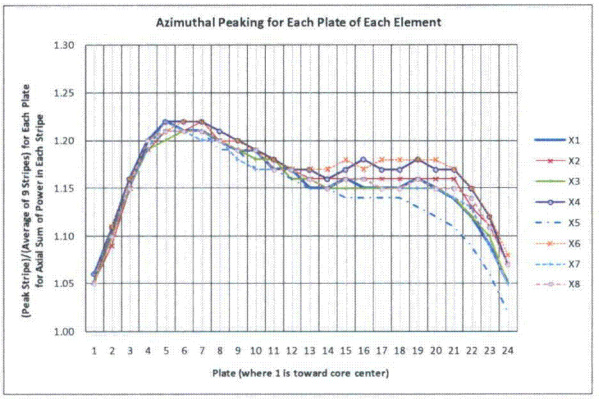


Figure A-1.8 – Case 4B: 10 MW HEU Week 58 Day 2 with Empty Flux Trap





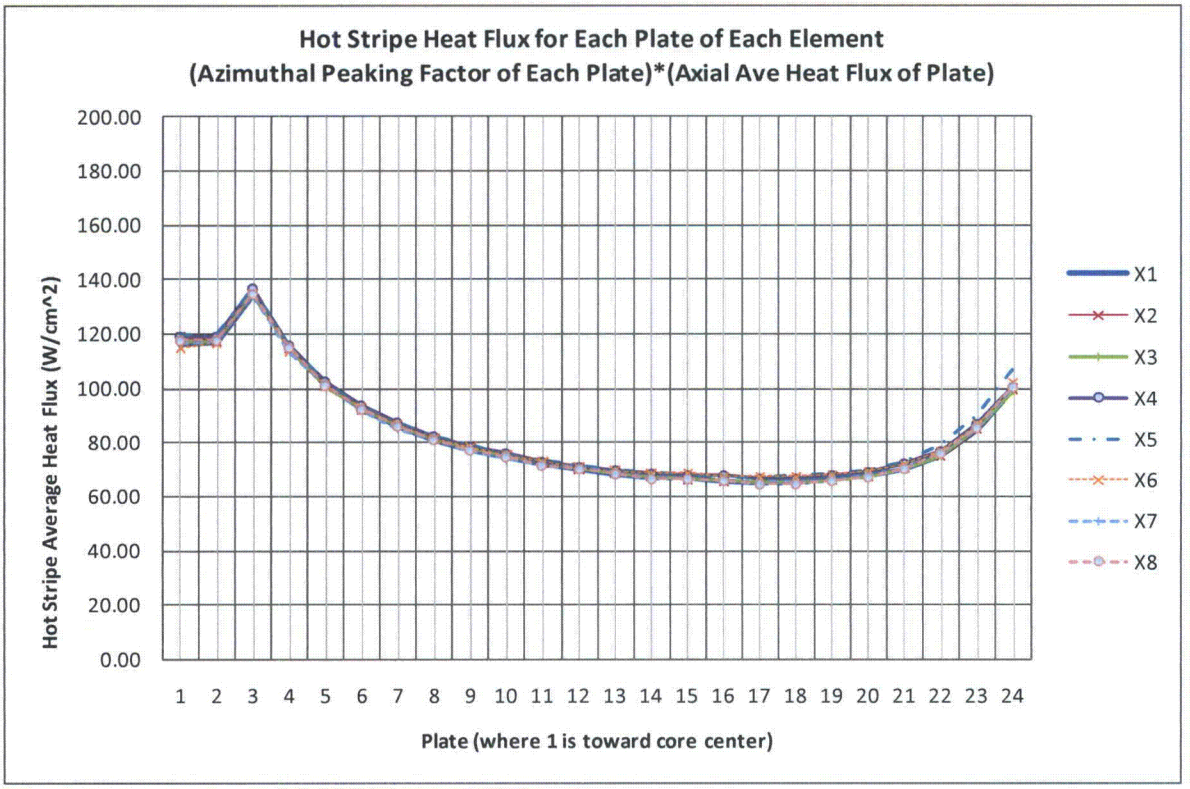
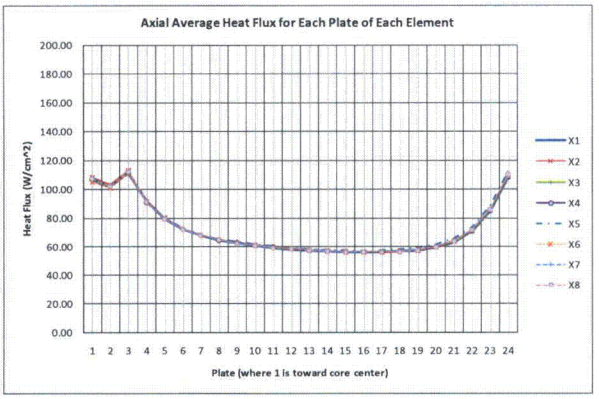
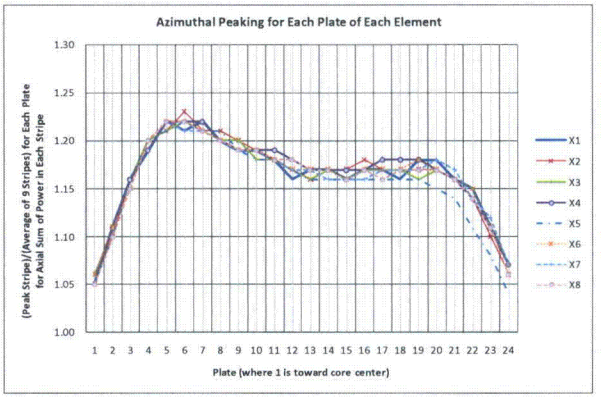


Figure A-1.9 - Case 5A: 12 MW LEU Fresh Day 0 with Flux Trap Samples





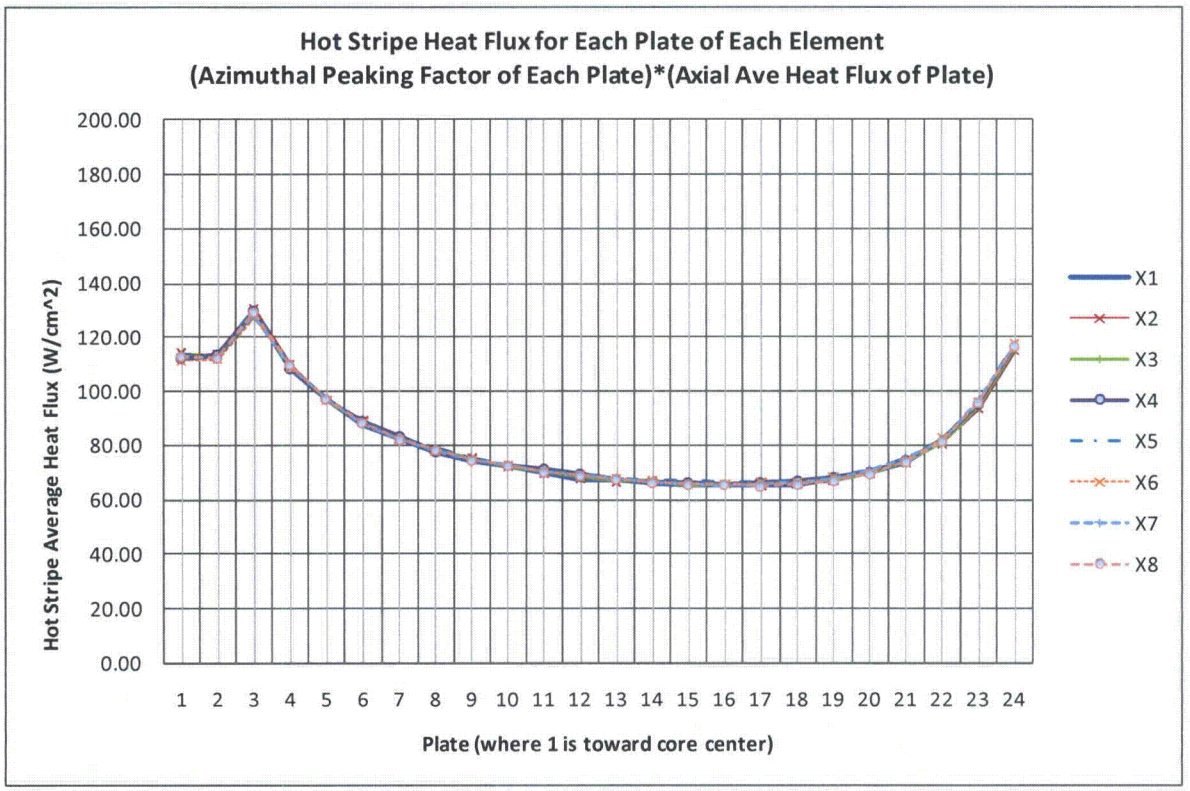
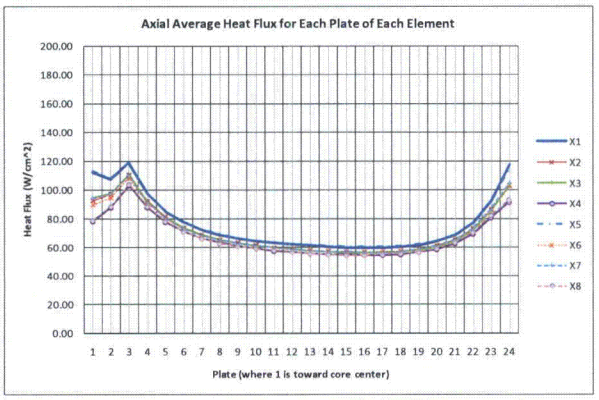
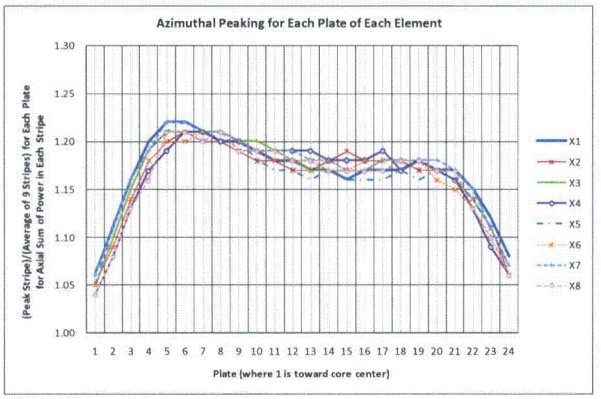


Figure A-1.10 – Case 6A: 12 MW LEU Fresh Day 2 with Flux Trap Samples





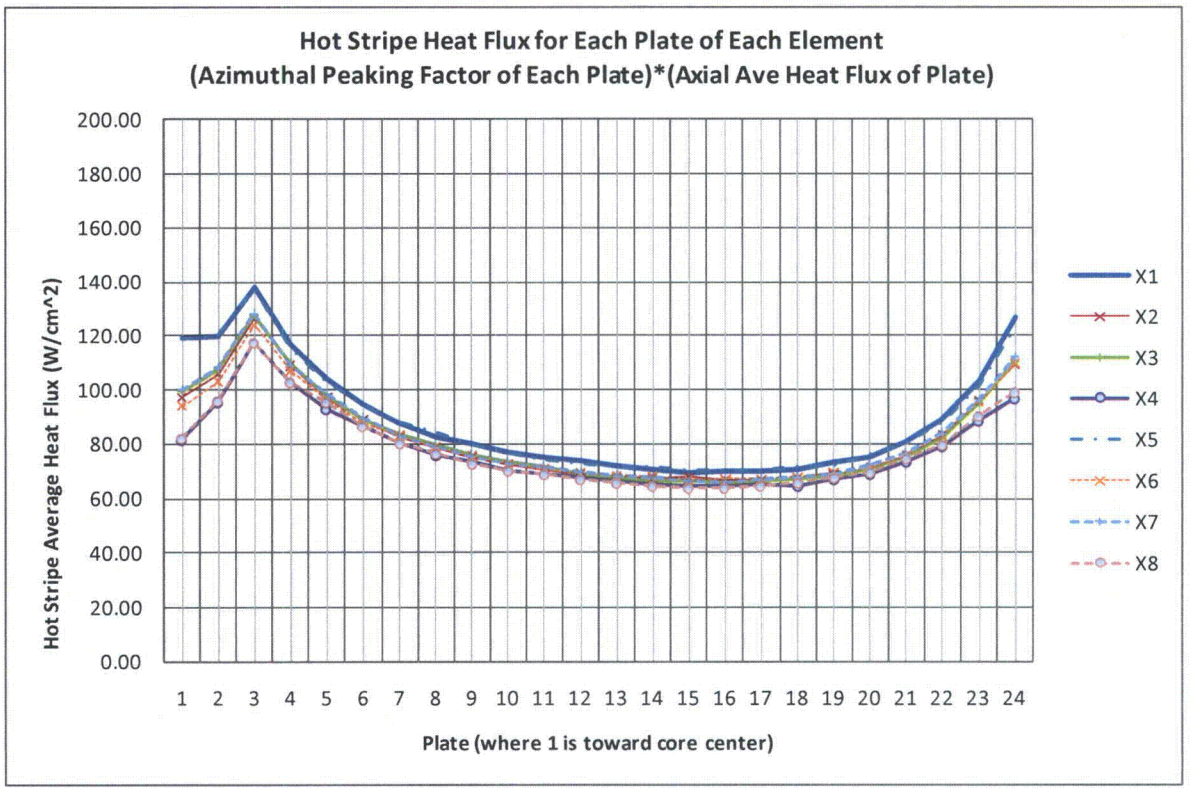
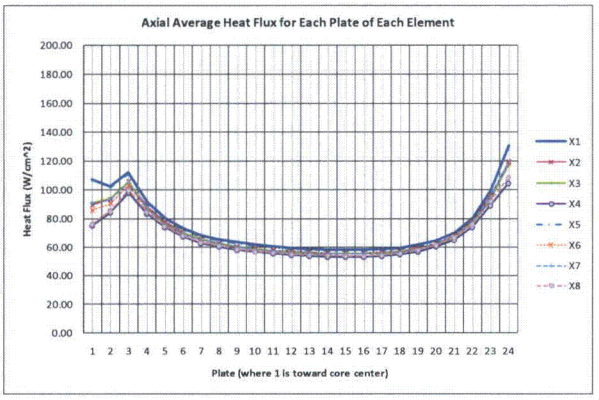
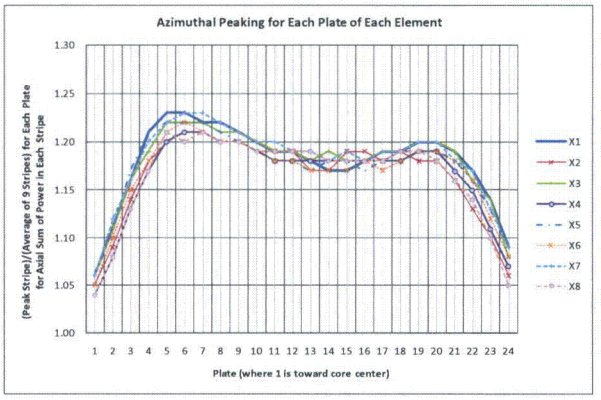


Figure A-1.11 - Case 7A: 12 MW LEU Week 79 Day 0 with Flux Trap Samples





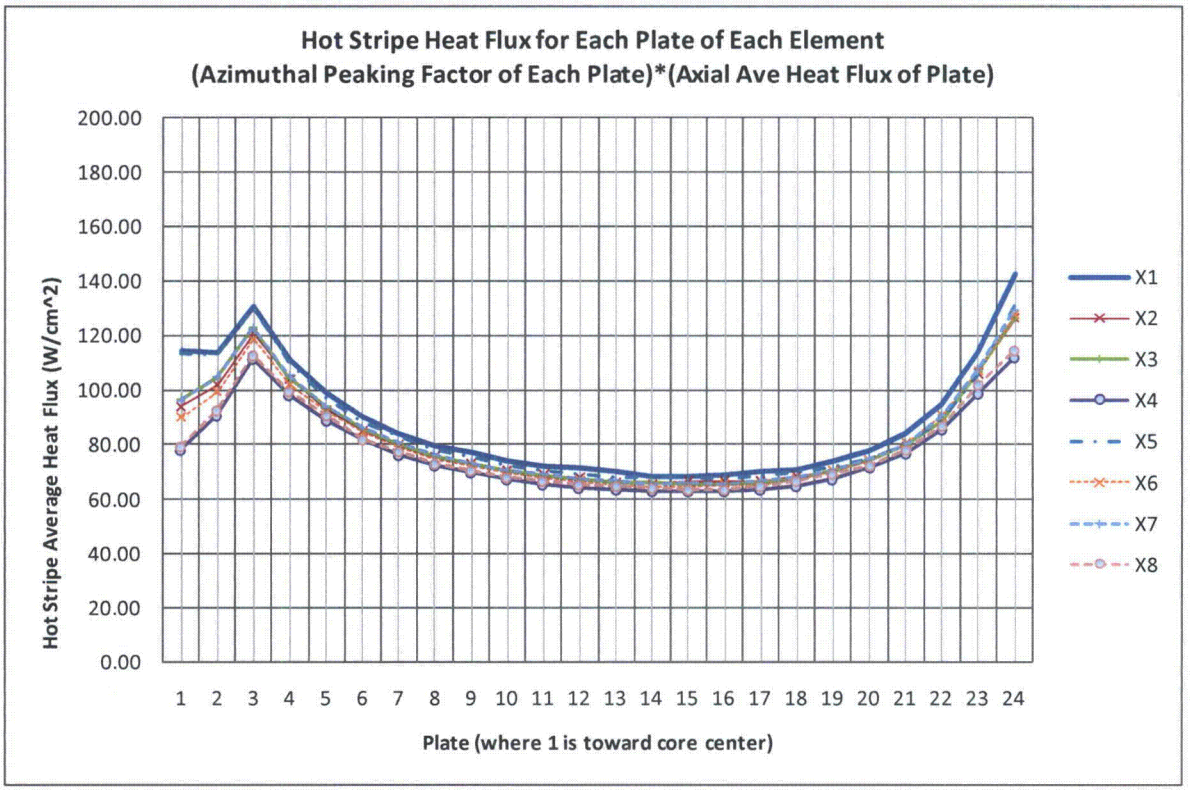
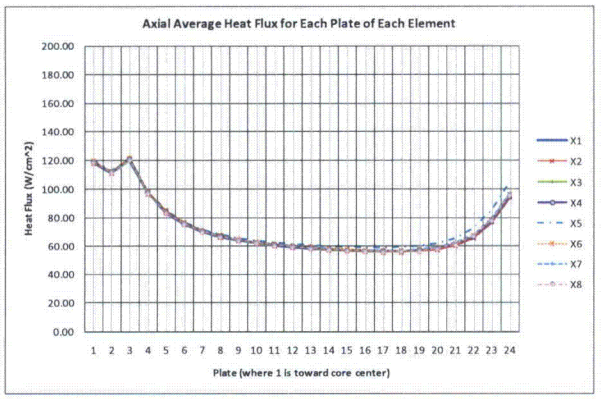
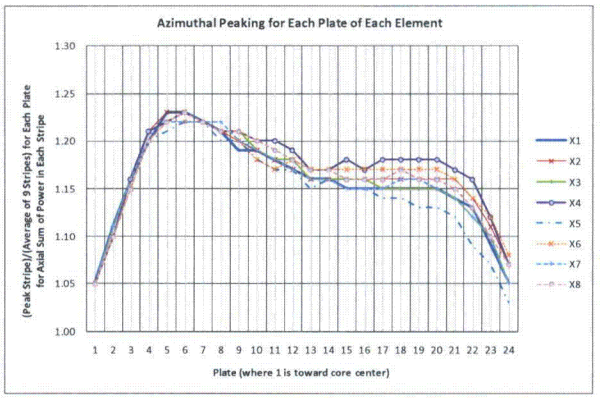


Figure A-1.12 – Case 8A: 12 MW LEU Week 79 Day 2 with Flux Trap Samples





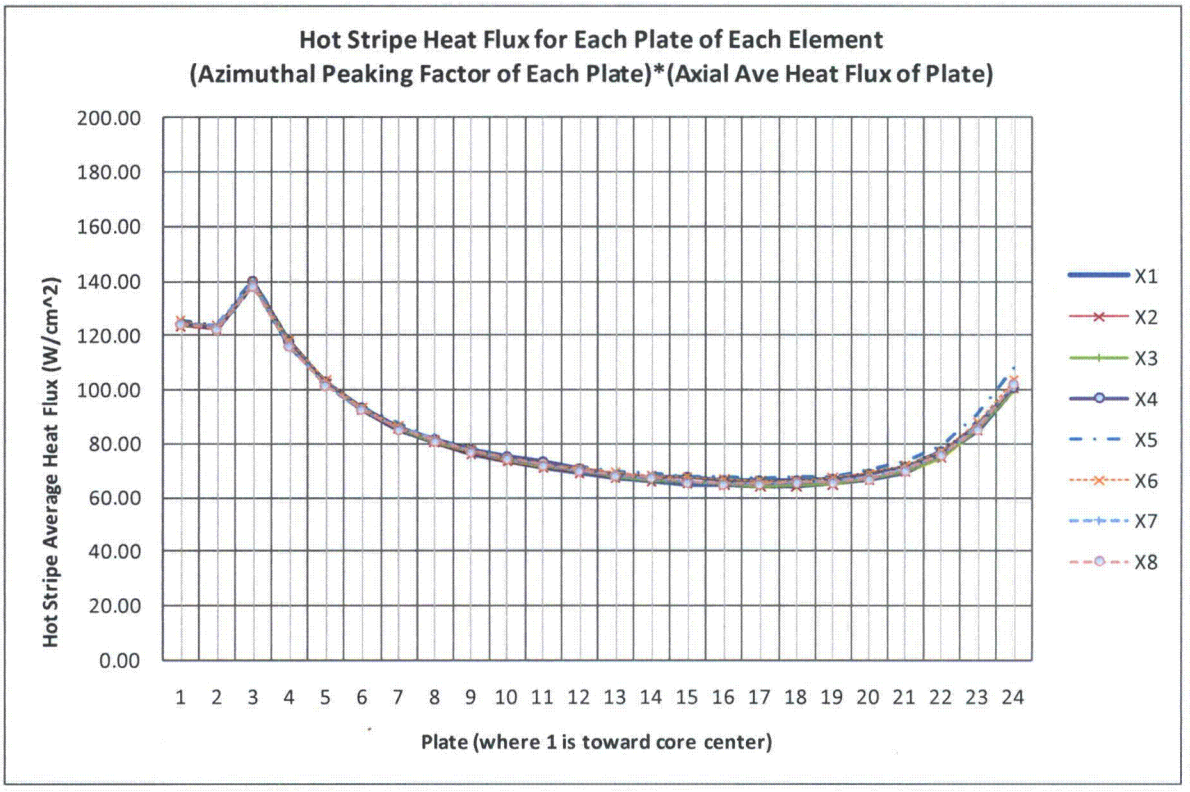
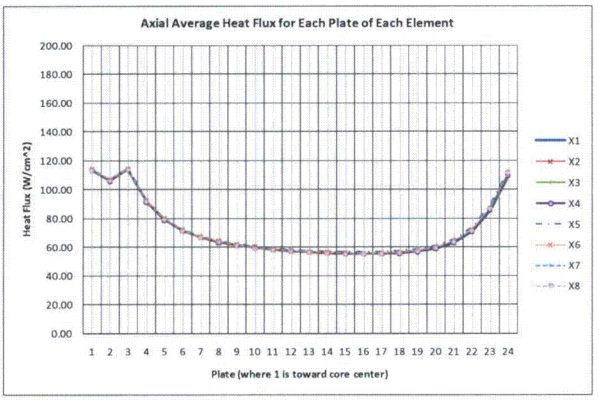
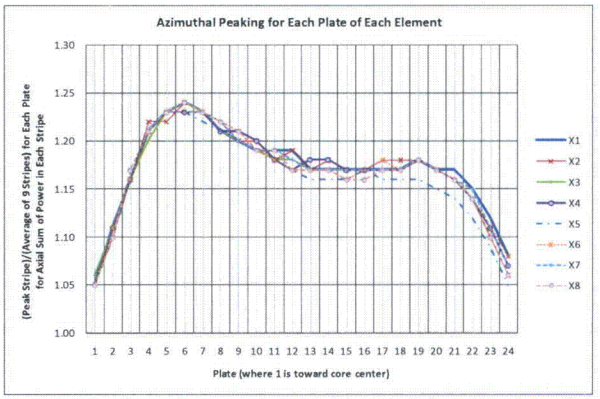


Figure A-1.13 - Case 5B: 12 MW LEU Fresh Day 0 with Empty Flux Trap





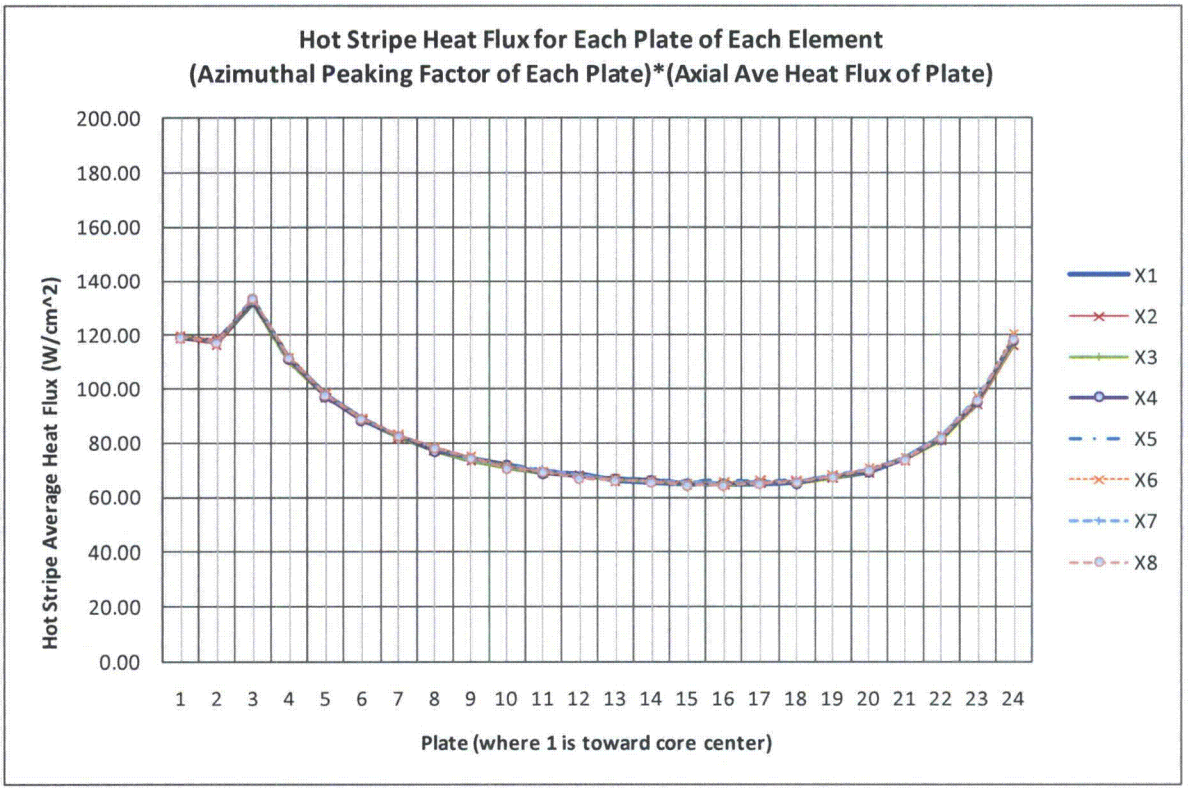
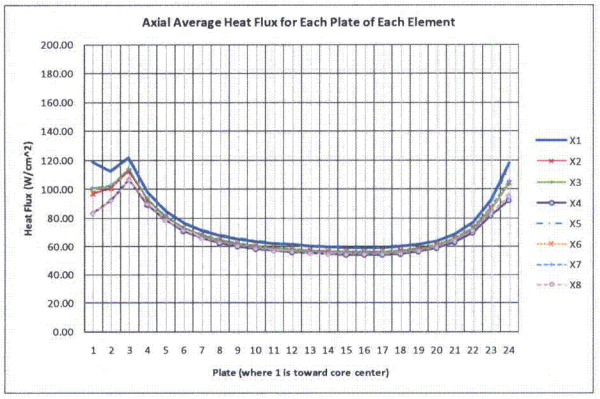
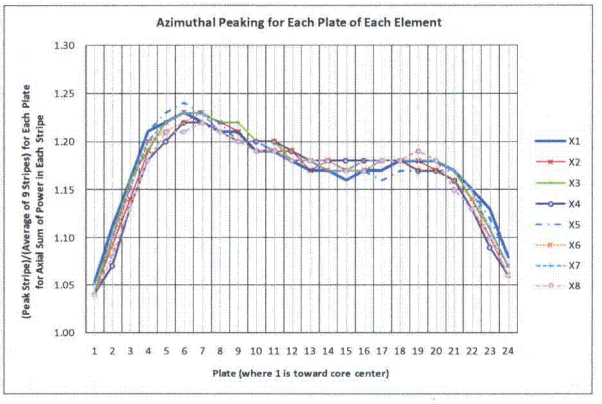


Figure A-1.14 – Case 6B: 12 MW LEU Fresh Day 2 with Empty Flux Trap





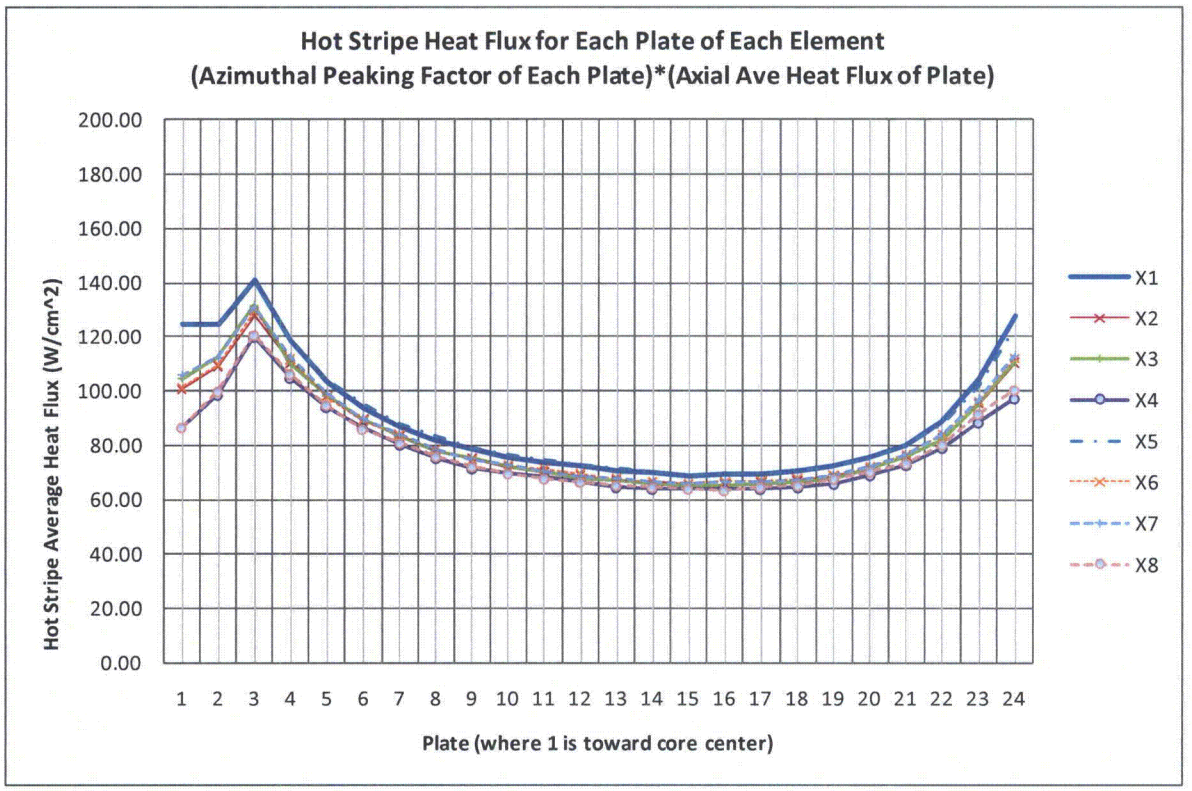
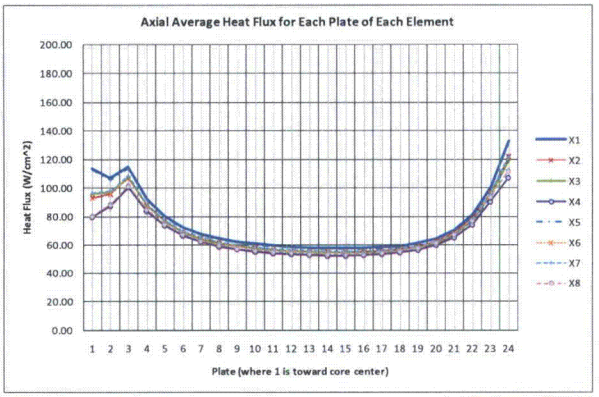
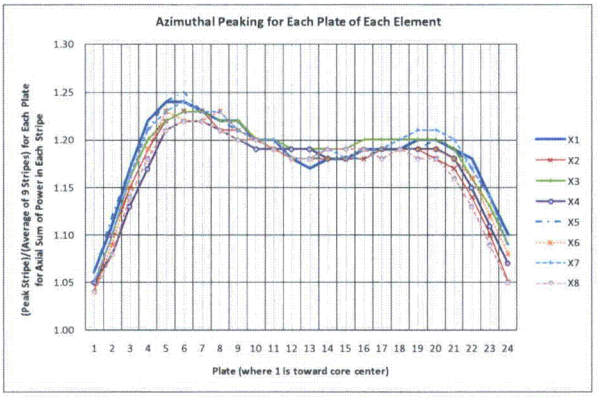


Figure A-1.15 - Case 7B: 12 MW LEU Week 79 Day 0 with Empty Flux Trap





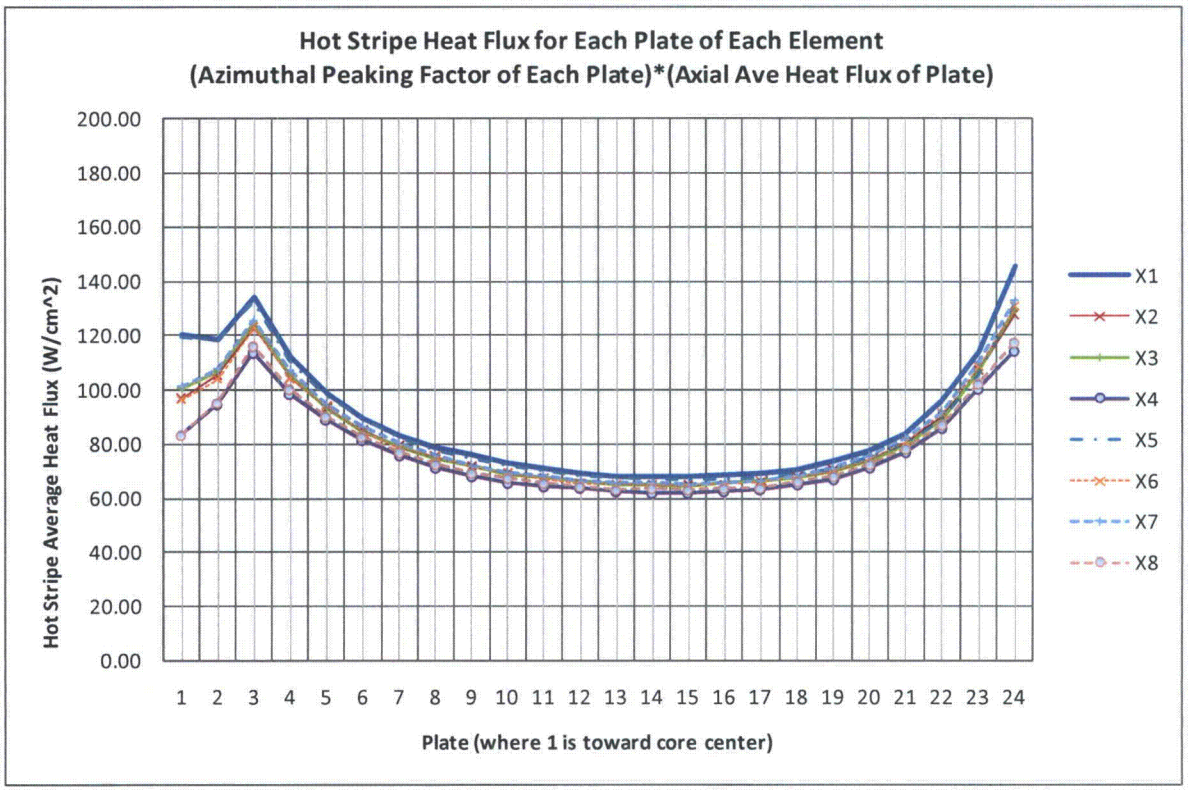


Figure A-1.16 – Case 8B: 12 MW LEU Week 79 Day 2 with Empty Flux Trap

APPENDIX B-1: REPLICATION OF MURR 1974 10 MW UPGRADE SAFETY ANALYSIS

SUMMARY

The methods used in the original HEU safety analysis[B-1.1],[B-1.2] to predict the margin to flow instability in the MURR reactor are closely replicated. For 40 combinations of pressure, inlet temperature, and flow rate the original values of allowed power are essentially duplicated, as indicated in Figure B-1.1.

1. BACKGROUND AND INTRODUCTION

An important first step in developing analytical models to predict the thermal performance of an LEU replacement core for the MURR reactor is to demonstrate an understanding of the analytical basis for the safety limits prescribed for the existing HEU core. In Reference [B-1.1] the maximum allowed reactor power is prescribe as a function of reactor inlet temperature and flow rate for pressures of 60 and 75 psia. Reference [B-1.2] repeats and extends these results to include 85 psia. For each of the three values of pressure, allowed powers are provided in a table for the 50 combination of five inlet temperatures from 120 to 200° F in steps of 20° F and ten flow rates from 400 to 4000 gpm in steps of 400 gpm. These data are also represented in graphs of power as a function of flow rate for the 15 combinations of pressure and inlet temperature. The MURR Technical Specifications limit reactor operation to a minimum pressure at the pressurizer of 75 psia, a maximum inlet temperature of 155° C, and minimum flow rate through the core of 3200 gpm. The normal operating conditions for the reactor are 78 psia at the pressurizer, an inlet temperature of 120° F, about 3800 gpm through the fuel region, and 10 MW.[B-1.3]

The criterion that was used in establishing the allowed power is the avoidance of flow instability. In the thermal analysis that was performed for the HEU core in 1973[B-1.1],[B-1.2] it was assumed that flow instability would not occur in a coolant channel if bulk boiling at the channel exit was avoided and each local value of heat flux was less than half of the corresponding value of critical heat flux as predicted by Bernath correlation[B-1.4]. This two-part criterion is based on measured data reported by Croft in 1964 for electrically-heated channels that were designed to simulate Advance Test Reactor (ATR) channels.[B-1.5] Reference [B-1.5] proposed the same criterion, except that they recommended using 60% of the Bernath critical heat flux rather than the more restrictive 50% value. Reference [B-1.5] postulated that burnout occurred by a process referred to as "hydraulic instability or autocatalytic vapor binding" which was seen as a form of critical heat flux (CHF) that occurred prematurely. Croft found that a model based on 60% of the Bernath CHF prediction fitted some of the experimental data and that burnout occurred in other cases when the exit bulk coolant temperature reached the saturation temperature.

Two years after Croft[B-1.5] reported his experiments, Waters[B-1.6] reported his measurements of flow instability in electrically-heated channels designed to be directly applicable to the Advanced Test Reactor (ATR). Appendix B-2 demonstrates that a relationship based on the work of Whittle and Forgan[B-1.7] accurately predicts the measured powers at which flow instability occurred in both the Croft and the Waters experiments. This helps to demonstrate that these two sets of experiments are consistent with each other, although the Whittle and Forgan relationship was not used in the original analysis.

2. REPLICATION OF MURR PREDICTIONS OF ALLOWED POWER

Reference [B-1.1] indicates that the allowed power was deduced with the aid of the BOLERO computer code,[B-1.8] which appears to have been written in FORTRAN. A sample input, along with a description of the input, is provided in Appendix B of Reference [B-1.1]. The reference explains what the code does, including some of the details, and provides sufficient information to enable the allowed values of power to be replicated with enough accuracy to demonstrate an understanding of the code.

The three pressures identified above (60, 75 and 85 psia) correspond to the pressure at the pressurizer. The pressure at the exit of the core is needed for the BOLERO code analysis. References [B-1.1] and [B-1.2] provide a series of values for the pressure drop components between the pressurizer and the core exit for one reactor volumetric flow rate and coolant inlet temperature. In addition, Reference [B-1.1] provides relationships that enable these conditions to be scaled to provide the pressure drop components for other reactor flow rates and inlet temperatures. These scaling relationships can also be deduced from basic hydraulic principles. This information enables the pressures at the core inlet and exit to be deduced for all reactor operating conditions.

The BOLERO code, which apparently employs a single-channel model, makes extensive use of the numbers in Table 4-14 of Reference [B-1.2], which is replicated in Table 1. The code sample input includes an axial power shape that is represented by 48 values that have an average value of 1.00. This axial power shape, the reactor coolant inlet temperature, and the total reactor power and flow rate are used in determining the bulk mixed-mean temperature for the hot channel as a function of axial position. The 2.72 factor on power and the 0.81 factor on flow rate, which are provided in the table, are used in the model in the determination of the hot channel bulk mixed-mean temperature of the coolant at each axial level.

The heat flux for the hot channel is also needed as a function of axial position. The core average heat flux is the reactor power divided by the core heat transfer area. Reference [B-1.1] indicates that the heat transfer area for the core is 184.28 ft^2. This is in close agreement with the 185.4 ft^2 area calculated independently. The hot channel average heat flux is the core average heat flux times both the 2.72 factor on power and the 0.93 factor at the bottom of the table. It appears that although 100% of the power is assumed to heat the coolant, only 93% of it is deposited in the fuel plates. The other 7% is deposited directly into the flowing coolant and, hence, does not contribute to the heat flux. The hot channel heat flux at each axial location is obtained from the hot channel average heat flux and the axial power shape. The Bernath CHF correlation requires the local value of pressure at each axial level. The BOLERO code uses the pressure at the exit of the core to represent the pressure at all axial levels. This is a slightly more limiting, but simpler, approach.

Apparently, the BOLERO code guesses a power level, calculates the local heat flux, the Bernath critical heat flux, and the ratio of the local heat flux to the Bernath critical heat flux at each axial position. Then it adjusts the power and repeats the process until the power level is found at which the maximum of the heat flux ratios among all axial positions is 0.50 or, if at a lower power level, bulk boiling first occurs at the exit. For the replication of the BOLERO code a simpler approximate approach was used. It is obvious that the limiting axial location must be between the peak of the axial power shape and the channel exit because both the bulk coolant temperature and the local heat flux are increasing between the inlet and the location of the peak heat flux. The bottom of Table 4-13 on page 4-47 of Reference [B-1.2] indicates that for normal operating conditions at 10 MW of reactor power the limiting axial location is where 0.701 of the total bulk coolant temperature rise occurs. The axial power shape in the sample BOLERO input had a peak value 1.450. However, Table 1 shows an axial peaking factor of 1.432. From this it is theorized that the limiting condition occurs a short distance past the peak of the axial power shape where the peak-to-average heat flux is 1.432 and 70.1% of the bulk coolant temperature rise has occurred. Numerical integration of the axial power shape shows that the 1.432 factor and 70.1% are approximately consistent and consistent with this theory. Therefore, in the replication of the BOLERO code results it was assumed that these correspond to the limiting CHF location.

There is another interpretation of the meaning of 50% of the Bernath CHF power. In the calculation one could adjust the reactor power level until 100% of the Bernath CHF is reached and then take 50% of that power. This approach will produce a much more limiting result because the Bernath correlation would be

evaluated at a much higher power level where the bulk coolant temperatures are considerably higher than in the method assumed for the BOLERO code replication. The appropriate approach is the one that was used by Reference [B-1.5] in establishing the 60% of Bernath formulation. Since a definitive answer was not found among the words in Reference [B-1.5], calculations were made to test the BOLERO replication approach on Figure 4-9 on page 4-21 of Reference [B-1.5]. The results, which showed a maximum ratio of local heat flux to Bernath critical heat flux of about 57%, seem to confirm that the above BOLERO replication approach is the correct interpretation.

The four solid curves in Figure 1 are plots of the tabular data provided and plotted in Reference [B-1.2]. These curves include the pressure and inlet temperature combinations that provide the highest and lowest power curves of the 15. The colored circles indicate the current replication of the earlier results and demonstrate good agreement with the original BOLERO predictions.

The tables of allowed power in References [B-1.1] and [B-1.2] underline the values that correspond to bulk boiling at the channel exit. Thus, the powers for flow rates 400 through 2400 gpm of the lowest curve and flow rates 400 and 800 gpm of the other three curves of Figure 1 were underlined as a result of the original BOLERO predictions. In the current replication, all of these would be underlined and 2800 gpm on the bottom curve and 1200 gpm on the curve immediately above the bottom curve would also be underlined. The extremely good agreement between the original BOLERO predictions and the current replication of it for the points that are in both calculations and are limited by exit temperature show that in the replication the appropriate factors have been applied to the average power and to the average flow rate to obtain the appropriate value of bulk coolant temperature at the exit. If, for example, the 0.93 were inappropriately included in the current prediction of the exit coolant temperature, the new results would differ from the original ones by about 7%. Also, for the highest flow rate in some cases the pressure drop from the pressurizer to the core inlet is more than 10 psi and to the core outlet is more than 25 psi. Since the results are sensitive to pressure, the good agreement between the MURR and current results is a form of verification of the current pressure drop predictions.

3. DISCUSSION AND CONCLUSIONS

Forty of the 150 the original 1973 predictions of allowable reactor power were replicated with reasonably good accuracy, Figure 1. These 40 span the entire range of operating conditions represented by the original 150. This replication demonstrates that the basis and the key assumptions and models that were used to make the 1973 predictions are reasonably well understood.

REFERENCES:

[B-1.1] F. R. Vaughan, *Safety Limit Analysis for the MURR Facility*, NUS-TM-EC-9, prepared for the University of Missouri by the NUS Corporation, 4 Research Place, Rockville, Maryland, 20850, May 1973.

[B-1.2] University of Missouri Research Reactor Safety Analysis Report, Chapter 4, Reactor Description, submitted to the U.S. Nuclear Regulatory Commission in 2006.

[B-1.3] Private communication with Charles McKibben, University of Missouri Research Reactor Facility, January 20, 2009.

[B-1.4] Louis Bernath, "A Theory of Local-Boiling Burnout and Its Application to Existing Data," Chemical Engineering Progress Symposium, Series No. 30, Volume 56, pp. 95-116 (1960).

[B-1.5] M. W. Croft, Advanced Test Reactor Burnout Heat Transfer Tests, USAEC Report IDO-24465, ATR-FE-102, Ca-2, Babcock & Wilcox Company, January 1964.

[B-1.6] E. D. Waters, *Heat Transfer Experiments for the Advanced Test Reactor*, USAEC Report BNWL-216, UC-80, Reactor Technology (TID-4500) Pacific Northwest Laboratory, Richland, Washington, May 1966.

[B-1.7] R. H. Whittle and R. Forgan, "A Correlation for the Minima in the Pressure Drop Versus Flow-Rate Curves for Sub-Cooled Water Flowing in Narrow Heated Channels," *Nuclear Engineering and Design*, 1967.

[B-1.8] E. R. Schmidt, M. L Couchman, D. R. Edwards, *BOLERO-II, Burnout Limit Evaluation Routine-II*, NUS-TM-ENG-119 (Rev. 3, modified).

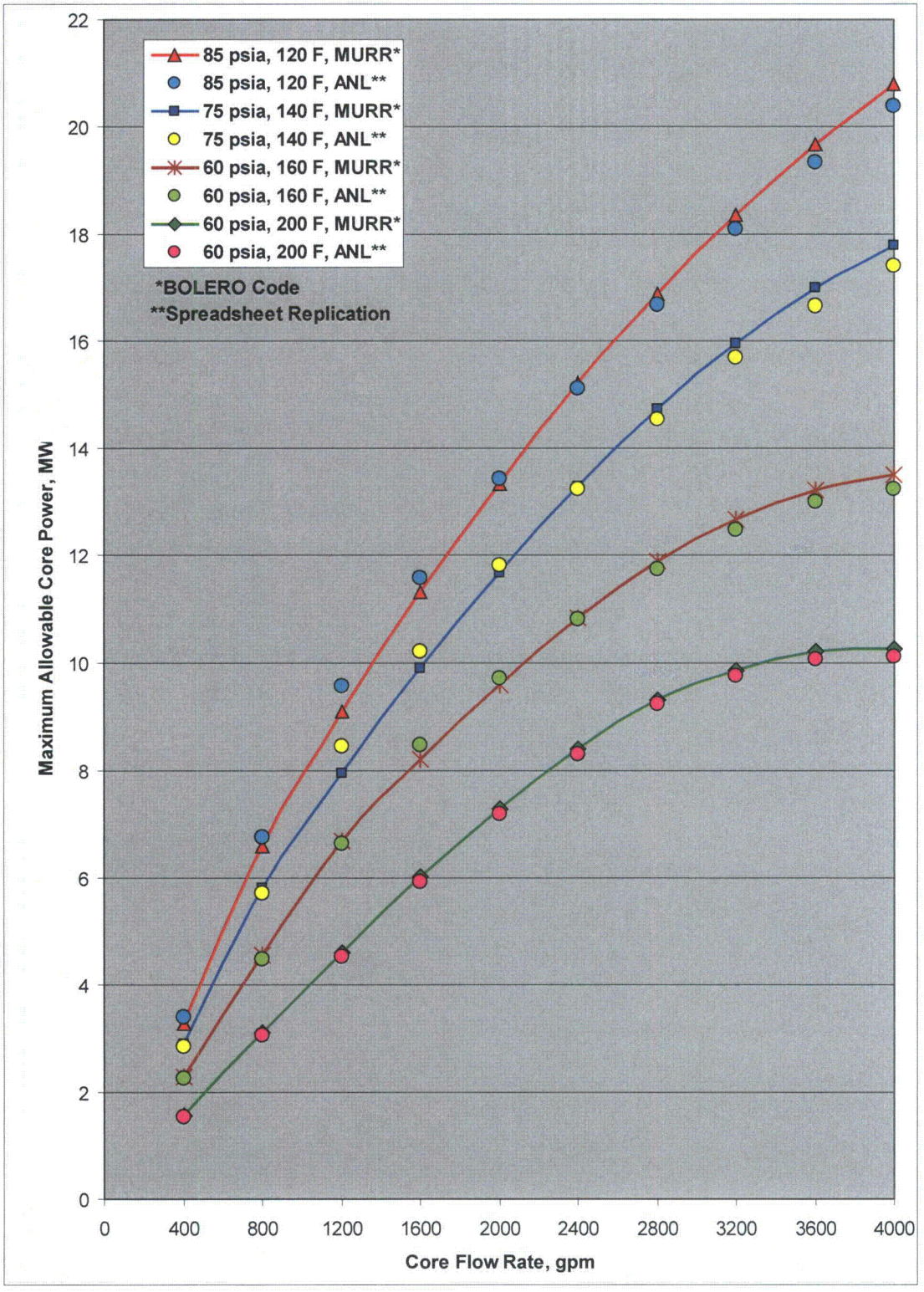


Figure B-1.1 – Maximum Allowed Core Power Based on Original Analysis Methods

Table B-1.1 – Replication of Table 4-14 of Reference [4-2]

TABLE 4-14
SUMMARY OF MURR HOT CHANNEL FACTORS

	Safety Limits Basis
On Enthalpy Rise	
Power-related Factors	
Nuclear Peaking Factors	
Radial	2.220
Non-uniform Burnup	1.112
Local (Circumferential)	1.040
Axial	1.000
Engineering Hot Channel Factors	
Fuel Content Variation	1.030
Fuel Thickness/Width Variation	1.030
Overall Product	2.72
Flow-related Factors	
Core/Loop Flow Fraction	1.000
Assembly Minimum/Average Flow Fraction	1.000
Channel Minimum/Average Flow Fraction	
Inlet Variation	1.000
Width Variation	1.000
Thickness Variation	1./1.080
Within Channel Minimum/Average Flow Fraction	
Thickness Variation	1./1.050
Effective Flow Area	0.3231/0.3505
Overall Product	0.81
On Heat Flux	
Power-related Factors	
Nuclear Peaking Factors	
Radial	2.220
Non-uniform Burnup	1.112
Local (Circumferential)	1.040
Axial	1.432
Engineering Hot Channel Factors on Flux	
Fuel Content Variation	1.030
Fuel Thickness/Width Variation	1.150
Overall Product	4.35
Energy Fraction Generated in Fuel Plate	0.930

APPENDIX B-2: PREDICTIONS OF THE FLOW INSTABILITY MEASURMENTS MADE WITH ELECTICALLY HEATED CHANNELS FOR THE ADVANCED TEST REACTOR

SUMMARY

Croft[B-2.1] and Waters[B-2.2] used tests in electrically heated channels to measure the onset of fuel burnout, caused by flow instability, in the Advance Test Reactor. The PLTEMP/ANL code[B-2.4] is used to predict the onset of flow instability in 42 of these tests. The ability of the code to predict flow instability in these tests reasonably accurately, as well as the ability of the code to predict the onset of flow instability as measured in other electrically heated tests[B-2.3],[B-2.6],[B-2.7], as reported by Olson,[B-2.5] lead to the conclusion that the code should be able to predict the onset of flow instability reasonably well for the University of Missouri Research Reactor (MURR) after it is converted from HEU to LEU fuel.

1. INTRODUCTION

When the University of Missouri Research Reactor (MURR) was designed in the 1960s the potential for fuel element* burnout by a phenomenon referred to at that time as "autocatalytic vapor binding" was of serious concern. This type of burnout was observed to occur at power levels considerably lower than those that were known to cause critical heat flux. The conversion of the MURR from HEU fuel to LEU fuel will probably require significant design changes, such as changes in coolant channel thicknesses, that could affect the thermal-hydraulic behavior of the reactor core. Therefore, the redesign of the MURR to accommodate an LEU core must address the same issues of fuel element burnout that were of concern in the 1960s.

The Advanced Test Reactor (ATR) was designed at about the same time as the MURR and had similar concerns with regard to fuel element burnout. These concerns were addressed in the ATR by two groups of thermal-hydraulic tests that employed electrically heated simulated fuel channels.[B-2.1],[B-2.2] The Croft (1964), Reference [B-2.1], tests were performed at ANL. The Waters (1966), Reference [B-2.2], tests were performed at Hanford Laboratories in Richland Washington. Since fuel element surface temperatures rise rapidly as burnout conditions are approached, channel surface temperatures were carefully monitored in these experiments. For self-protection, the experimental facilities were designed to cut off the electric power when rapidly increasing surface temperatures were detected. In both the ATR reactor and in the tests with electrically heated channels, the heated length of the fuel plate was 48 inches, which is about twice that of the MURR.

Whittle and Forgan (1967)[B-2.3] independently conducted tests with electrically heated rectangular channels that were similar to the tests by Croft and by Walters. In the Whittle and Forgan tests the heated length of the channel varied among the tests and was between 16 and 24 inches. Both Waters and Whittle and Forgan show that the cause of the fuel element burnout is due to a form of flow instability. Whittle and Forgan provide a formula that predicts when this flow instability will occur. This formula is included in the PLTEMP/ANL code.[B-2.4] Olson[B-2.5] has shown that the PLTEMP/ANL code accurately predicts the powers at which flow instability occurs in the Whittle and Forgan experiments. He also considered the electrically heated tests performed in the ANS Thermal-Hydraulic Test Loop at ORNL and report by M. Siman-Tov et al.[B-2.6],[B-2.7]

The purpose of this memorandum is to demonstrate that the PLTEMP/ANL code accurately predicts the Croft and the Waters tests. This demonstration should provide sufficient confidence that the PLTEMP/ANL code can

* For research reactors it is common to refer to "fuel assemblies" as "fuel elements". This can be confusing because in other applications a fuel element is only a single fuel rod or plate.

adequately predict the onset of flow instability for the converted MURR. The MURR core uses light water as a coolant, has a 24-inch active fuel length, downward flow in the core, and an average core velocity of about 7 m/s. The inlet temperature is about 50° C and the peak outlet is about 20° C higher than the inlet for reactor operation at 10 MW. The core pressures range from about 4 to about 5 bar. The peak heat flux is about 110 W/cm^2.

Section 2 describes the mechanism that causes flow instability. Section 3 describes the Whittle and Forgan formula for flow instability. Section 4 briefly describes both the Croft and the Waters experiments. Section 5 describes the PLTEMP/ANL models. Section 6 compares the PLTEMP/ANL predictions based on the Whittle and Forgan formula with the Croft measurements. Section 7 does the same for the Waters measurements. Section 8 provides the range of parameters for the Whittle and Forgan tests. Section 9 discusses the results and provides conclusions.

2. MECHANISM FOR FLOW INSTABILITY

Figure B-2.1, which is patterned after Reference [B-2.3], shows the mechanism for flow instability. The flow demand curve, which is the thick black curve that is labeled "Zero Power System Resistance Curve," exhibits the classic isothermal situation where liquid water flows through an unheated channel and the pressure drop increases monotonically with the flow rate. The black dashed "Pressure Drop Supply (Pump Head) Curve" curve represents the pressure differential at each flow rate that is available to drive the flow through the channel. For the zero power case the operating point must be at the intersection of these two curves and is noted by the word "Stable" on the abscissa. If the channel is heated, then at some sufficiently low flow rate subcooled nucleate boiling will begin to occur in the channel and vapor formation will be increase as the flow is reduced further. This boiling causes the hydraulic resistance and the pressure drop in the channel to increase with decreasing flow. Thus, the lower part of the "Zero Power System Resistance Curve," is replaced by the red (upper), blue (middle), or green (lower) extensions, depending on the channel power level. The green extension represents a stable flow condition because boiling begins when the flow rate is considerably below the labeled "Stable" operating flow. The blue curve is the highest stable power. For power levels above this power, the red extension, for example, the resistance and the pressure drop supply curves do not intersect. In this instance much of the channel length can be in an all-steam condition. The "All-Steam System Resistance Curve" curve, where the pressure drop is much greater for a given flow than it is for the zero-power curve, is representative of this condition. For this condition the channel flow tends to be determined by the intersection of the all-steam curve and the dashed pressure drop supply curve. The intersection is indicated by the word "Unstable" on the abscissa. Thus, when the power is increased to slightly above that represented by the blue curve, there can be rapid reduction in channel flow rate, which can lead to a channel burn-out condition.

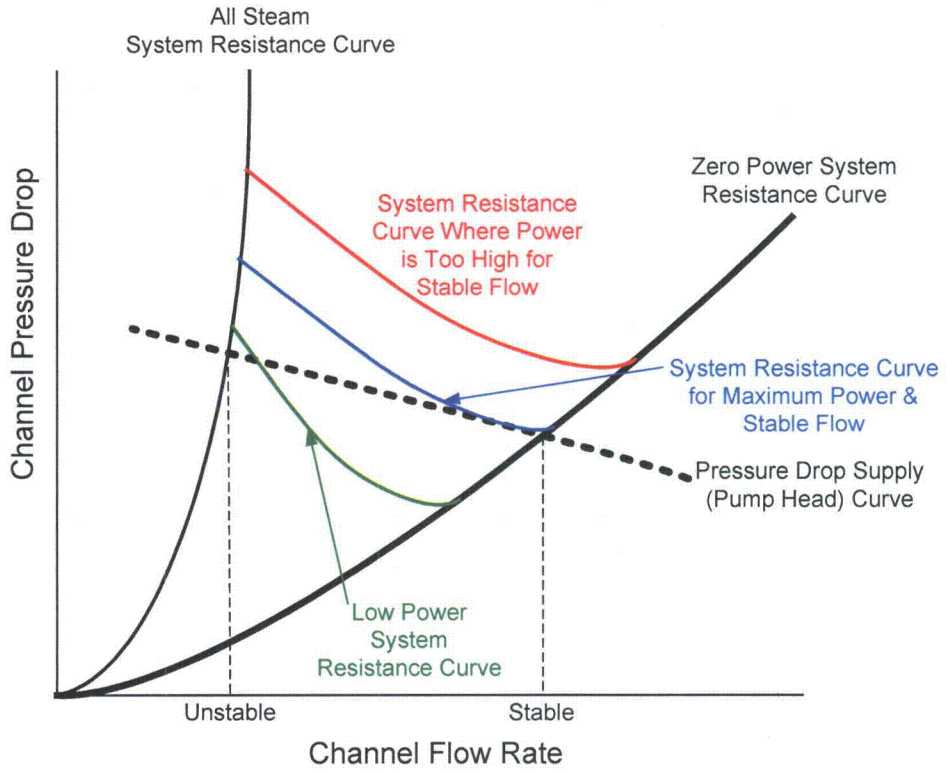


Figure B-2.1. Illustration of Excursion-Flow (Ledinegg) Instability

In a system with multiple parallel channels, such as a research reactor, the reduction in flow in one channel may not appreciably affect the total reactor flow rate. However, the large reduction in flow and the resultant excessive temperatures in one unstable channel can cause higher temperatures and flow instability in its immediate neighbors. Thus, a flow instability in one channel can propagate to other channels.

3. WHITTLE AND FORGAN FORMULA FOR PREDICTING FLOW INSTABILITY

Based on Whittle and Forgan,[B-2.3] flow instability is predicted to occur when $\Delta Tc / \Delta Tsat = R$, where ΔTc is the bulk water temperature rise from the channel inlet to the exit, $\Delta Tsat$ is the difference between coolant inlet temperature and the local coolant saturation temperature at the exit, and R is given by:

$$R = \frac{1}{1 + \eta/(L_H/D_H)} \tag{1}$$

where η is a positive constant, L_H is the heated length of the channel, and D_H is the heated diameter. The heated length is the length of the fuel meat. The heated diameter is four times the channel flow area divided by the heated perimeter, which is the perimeter of fuel meat in the channel cross section (i.e., twice the width of the fuel meat when there are two fuel plates of equal width).

A key issue is the selection of the constant η, which determines the value of R. As η is increased R goes toward zero and the allowed exit bulk coolant temperature approaches the inlet temperature. As η is decreased toward zero, R goes toward 1 and the allowed exit bulk coolant temperature approaches the saturation temperature. Reference [B-2.5] performed a statistical analysis of the 74 applicable experiments in Reference [B-2.3] and found that there is

a 95% confidence interval that 95% of the rectangular channel data measured by future Reference [B-2.3] type of measurements will not exceed an η value of 31.09. Reference [B-2.5] recommends that for consistency with INTERATOM[B-2.8] that a value of 32.5 be used for η, even though it is more conservative than the 31.09 value. Therefore, the recommended 32.5 value was used in the current analysis.

In the Whittle and Forgan experiments with rectangular channel of R was found to be between 0.78 and 0.88. This implies that flow instability is expected to occur when the coolant temperature rise from the channel inlet to the exit is between 78 and 88% of the temperature difference between the coolant inlet temperature and the coolant saturation temperature.

In the PLTEMP/ANL code the flow instability ratio (FIR) is provided in the output and is defined to be the ratio of R to (ΔTc / ΔTsat), where R is obtained from equation 1. Typically, multiple runs of the code would be made at various steady-state power levels until an FIR of 1 is obtained. The margin to flow instability is then taken to be the ratio of the channel power that produced an FIR of 1 to the channel power when the reactor is operating at its nominal full power.

4. CROFT AND WATERS EXPERIMENTS

In the ATR the fuel elements are longitudinally straight with fuel plates that are laterally curved so the element forms a 45° wedge of a concentric annulus. Croft simulated a curved fuel channel of the ATR with a single flat duct that was electrically heated from the two opposing longer sides. The duct was 1.20 inches wide with electrical heating along the middle 1.00 inches, but not along the thickness. The electric heaters produced a uniform heat flux along the width of the heated 1.00 inches. The axial heat flux shape was a chopped cosine with a peak to average of 1.4 so that the peak heat flux occurred at the middle of the 48-inch heated length and the heat flux was symmetric about the middle. Separate experiments were made with duct thicknesses of 0.054, 0.072, and 0.094 inches. The Waters tests used the same axial heat flux shape and heated length as the Croft tests. The Waters duct was 2.10 inches wide and was heated along the middle 2.00 inches of the two longer sides, but not along the thickness. The Waters tests included only a 0.070-inch thick duct size. The Waters tests used two test sections, one in which the electrical heat generation rate along the heated surface did not vary along the width of the duct and a second one in which it did vary. In both test sections one of the two heated plates was deliberately designed to produce several percent more power than the other.

Waters provides a graph which shows the lateral distribution of heat flux of each the two heated plates of the second test section. For purposes of analysis, we divided the heated width of each plate in the second test section into ten strips of equal width. From the graph for each plate we estimated the relative heat flux per strip, where the average heat flux for the entire width corresponds to 1.0, and found that the both plates have nearly the same relative heat flux distribution. Figure B-2.2, shows that average of the two relative lateral heat flux distributions.

From both the Croft and the Waters reports one is provided or can deduce for each experiment the measured inlet and outlet pressures and temperatures, the power, and the flow rate where flow instability was measured to occur. In all of the tests the water flowed from the top of the section to the bottom. Waters was aware of the Figure B-2.1 flow instability phenomenon and provided plots of system resistance curves. Croft, on the other hand, seemed to merely search for the point where a sudden temperature excursion was detected.

5. PLTEMP/ANL MODELS

For the modeling with the PLTEMP/ANL code the 48-inch heated length was represented and the duct cross-sectional dimensions were made to match those of the experiments. The 48-inch heated axial length was divided into 24 two-inch axial layers. The chopped cosine axial power shape was represented. Both fuel plates were assumed to be identical and to have the same heat flux distribution. The lateral heat flux distribution was assumed to be uniform in all cases. The coolant inlet temperature and inlet and outlet pressures, the flow rate, and the total power were treated as known input quantities and were made to agree with those of the experiments. The code outputs were the outlet coolant temperature and the flow instability ratio, R/(ΔTc / ΔTsat).

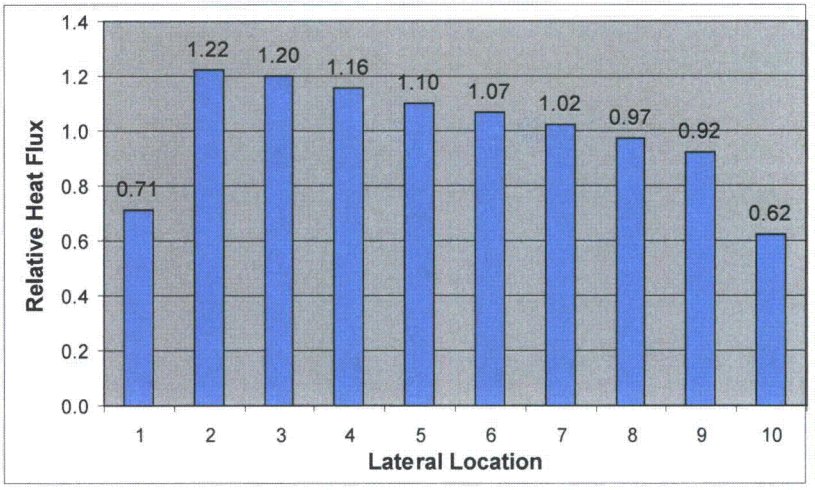


Figure B-2.2. Lateral Heat Flux Distribution in Non-Uniform Waters Test Section

The code uses SI units. Both experiments report all quantities in British unit except for power which was in kW. In order to be consistent with current scientific practice, in the comparisons of measured versus PLTEMP/ANL results we converted all units to SI.

Every unique set of onset of flow instability conditions in either the Croft or the Waters report was simulated with PLTEMP/ANL. Where duplicate tests were run or where more than one test lead to essentially the same set of conditions corresponding to the onset of flow instability, only one set of conditions was simulated with PLTEMP/ANL.

6. COMPARISON OF PLTEMP PREDICTIONS WITH CROFT MEASUREMENTS

Tables B-2.1, B-2.2, and B-2.3 provide the measured data and the corresponding PLTEMP/ANL predictions of coolant outlet temperature and flow instability ratio for the Croft tests with channel thicknesses of 0.054, 0.072, and 0.94 inches, respectively. The good agreement between the measured and the predicted coolant outlet temperature values is to be expected since the outlet temperature can be predicted from a simple energy balance. A small difference between a measure and a predicted outlet temperatures may be the result of a measured outlet temperatures not being precisely in agreement with that that would be predicted based on the other measured quantities. As can be seen, PLTEMP/ANL predicts flow instability ratios that are close to 1.0. The smallest three values are 0.912, 0.941, and 0.983. The largest four are 1.045, 1.062, 1.072, and 1.088. Thus, most of the values are within about 4% of 1.0, which corresponds to the onset of flow instability. The value of 0.912, for example, implies that PLTEMP/ANL is predicting that if the power input to the code is multiplied by 0.912, then the code would predict an FIR of 1, i.e., the onset of flow instability. To be precise the code should have been rerun at the implied reduced power and if this produced an FIR that is other than 1, then additional runs would be required until an FIR of 1 was obtained. Then the resultant PLTEMP/ANL power could be compared to the measured power. However, given the large number of tests to be analyzed and the potential for only small gain in precision that could be of little value in the current assessment, it was decided to run the code only once for each experiment and to record the FIR provided in the output.

Table B-2.1 – PLTEMP/ANL Predictions for Croft Tests with 0.054-inch Channel Thickness

Test	Power, kW	Flow, kg/s	Pressure, bar		Temperature, C			Flow Instability Ratio
					Measured		PLTEMP	
			Inlet	Outlet	Inlet	Outlet	Outlet	
1BO-5S	246 (397)*	0.424	19.37	15.58	54.4	189.4	190.3	0.985
3BO-5S	179 (289)	0.462	9.58	5.86	55.0	148.3	146.6	1.033
5BO-5S	181 (292)	0.312	17.37	15.65	55.0	189.7	190.9	0.983
6BO-5S	390 (630)	0.704	24.89	16.06	55.0	189.7	185.0	1.036
7BO-5S	132 (213)	0.393	18.20	15.65	115.0	195.6	193.0	1.006
8BO-5S	224 (362)	0.402	18.41	15.65	55.6	191.7	186.3	1.018

*The numbers in parentheses are the average heat flux over the heated areas, W/cm^2.

Table B-2.2 – PLTEMP/ANL Predictions for Croft Tests with 0.072-inch Channel Thickness

Test	Power, kW	Flow, kg/s	Pressure, bar		Temperature, C			Flow Instability Ratio
					Measured		PLTEMP	
			Inlet	Outlet	Inlet	Outlet	Outlet	
1BO-2S	396.0 (639)*	0.723	21.03	15.65	53.3	180.6	182.0	1.023
3BO-5S	287.0 (463)	0.747	11.10	5.93	56.1	147.2	146.9	1.009
5BO-3S	286 (462)	0.548	18.48	15.65	57.8	181.1	180.3	1.042
6BO-3S	286 (462)	0.517	18.55	15.65	51.7	181.1	181.7	1.023
7BO-2S	509 (822)	0.965	24.82	15.65	55.6	181.7	179.6	1.045
9BO-2S	392.0 (633)	0.713	22.41	17.37	55.6	185.0	184.6	1.039
11BO-2S	437 (706)	0.722	20.68	15.65	38.3	180.0	180.8	1.018
12BO-3S	251 (405)	0.716	20.55	15.65	110.0	190.6	191.5	0.993

*The numbers in parentheses are the average heat flux over the heated areas, W/cm^2.

Table B-2.3 – PLTEMP/ANL Predictions for Croft Tests with 0.094-inch Channel Thickness

Test	Power, kW	Flow, kg/s	Pressure, bar		Temperature, C			Flow Instability Ratio
					Measured		PLTEMP	
			Inlet	Outlet	Inlet	Outlet	Outlet	
1BO-2S	541 (873)*	1.033	22.27	15.65	54.4	177.8	177.5	1.028
2BO-5S	388 (626)	0.955	12.82	5.65	55.6	150.6	151.6	0.912
3BO-1S	387 (625)	0.973	13.03	6.55	53.9	148.9	147.9	1.000
4BO-1S	387 (625)	0.973	13.03	5.72	55.0	148.3	149.1	0.941
5BO-1S	388 (626)	0.738	20.27	15.65	54.4	180.0	177.9	1.025
6BO-5S	388 (626)	0.699	19.24	15.65	51.1	176.1	181.5	0.992
7BO-5S	387 (625)	0.748	19.99	15.86	50.6	171.7	172.3	1.071
8BO-1S	388 (626)	0.786	20.13	15.65	58.3	173.3	174.3	1.062
9BO-1S	388 (626)	1.023	15.17	7.58	55.6	145.6	145.3	1.088
10BO-4S	388 (626)	1.023	14.13	6.69	57.8	147.2	147.5	1.019

*The numbers in parentheses are the average heat flux over the heated areas, W/cm^2.

7. COMPARISON OF PLTEMP PREDICTIONS WITH WATERS MEASUREMENTS

Tables B-2.4 and B-2.5 provide the measured data and the corresponding PLTEMP/ANL predictions of coolant outlet temperature and flow instability ratio for the Waters tests. Tables B-2.4 and B-2.5 respectively are for the tests with uniform and non-uniform power generation rate distribution along the width of the channel. In Table B-2.4 the values of FIR range from 0.938 to 1.002. Thus, for the channel with the uniform power distribution across the width, PLTEMP/ANL is predicting flow instability to occur at powers levels that are between 6.2% below and 0.2% above those that were measured by Waters.

Table B-2.4 – PLTEMP/ANL Predictions for Waters Tests with Uniform Lateral Heat Flux

Test	Power, kW	Flow, kg/s	Pressure, bar		Temperature, C			Flow Instability Ratio
					Measured		PLTEMP	
			Inlet	Outlet	Inlet	Outlet	Outlet	
U141	14.4 (12)*	0.048	2.77	2.72	54.4	130.6	125.6	0.968
U149	20.5 (17)	0.071	2.78	2.69	54.4	132.2	122.9	1.002
U156	27.0 (22)	0.092	2.80	2.69	54.4	130.6	123.9	0.988
U166	36.2 (29)	0.070	11.39	11.34	54.4	176.1	175.3	0.985
U173	51.4 (41)	0.100	11.42	11.34	54.4	176.1	174.9	0.989
U180	37.5 (30)	0.054	25.16	25.13	54.4	217.8	215.0	0.962
U191	68.3 (55)	0.100	25.23	25.13	54.4	221.7	212.6	0.976
U204	472 (381)	0.760	19.99	17.55	54.4	201.7	199.6	0.949
U215	702 (567)	1.115	22.72	17.62	54.4	201.7	201.5	0.938
U222g	725 (585)	1.164	23.06	17.55	54.4	197.2	199.9	0.947

*The numbers in parentheses are the average heat flux over the heated areas, W/cm^2.

The PLTEMP/ANL results of Table B-2.5 show very high flow instability ratios ranging from 1.067 to 1.212

Table B-2.5 – PLTEMP/ANL Predictions for Waters Tests with Non-Uniform Lateral Heat Flux

Test	Power, kW	Flow, kg/s	Pressure, bar		Temperature, C			Flow Instability Ratio
					Measured		PLTEMP	
			Inlet	Outlet	Inlet	Outlet	Outlet	
N261	68.0 (55)*	0.125	25.30	25.20	54.4	181.7	181.9	1.212 (0.993)**
N271	27.4 (22)	0.108	2.88	2.79	54.4	116.1	114.8	1.154 (0.946)
N306	702 (567)	1.351	24.37	17.48	54.4	178.3	176.6	1.126 (0.923)
N314	470 (379)	0.909	20.58	17.55	54.4	177.8	176.0	1.133 (0.929)
N324	850 (686)	1.613	27.03	17.55	54.4	177.8	178.4	1.111 (0.911)
N335	720 (581)	1.401	24.37	17.41	54.4	176.1	175.3	1.136 (0.931)
N342	770 (622)	1.401	24.44	17.55	54.4	172.2	183.5	1.067 (0.875)
N346	660 (533)	1.264	23.13	17.55	54.4	174.4	177.2	1.122 (0.920)

*The numbers in parentheses are the average heat flux over the heated areas, W/cm^2.
**The value in parentheses is the flow instability ratio divided by 1.22.

because the analysis ignored the non-uniform power distribution along the width and used the average power along the width. For safety analysis we would take a conservative approach. Typically, in the neutronics calculations the fueled width is divided into about five or 10 strips of equal width and the power of each strip is provided. In the PLTEMP/ANL analysis the power of the strip with the highest power is assume to apply to each of the strips. For example, if the heated width were divided into 10 equal strips as is assumed in Figure B-2.2, then in the PLTEMP/ANL analysis the power of the heated width would be increased by a factor of 1.22 (as is shown above the second purple bar in the figure) to correspond to the relative heat flux of the hottest strip. A factor of 1.22 increase

in power would cause the bulk coolant temperature rise, ΔTc, to increase by essentially a factor of 1.22. Since the flow instability ratio is R/(ΔTc / ΔTsat), a 1.22 factor increase in ΔTc will divide the flow instability ratios shown in Table B-2.5 by a factor of 1.22. This results in the values shown in parentheses, which range from 0.875 to 0.99. Thus, for safety analysis values reasonably close to but less than 1.0 would be predicted in each case. The bias toward values less than 1 is to be expected since heat transfer and mixing with adjacent strips will reduce the coolant temperatures in the hottest strip of the experiment.

8. RANGE OF PARAMETERS IN THE WHITTLE AND FORGAN TESTS

Table B-2.6 shows the range of parameters in the Whittle and Forgan tests. Most of the Whittle and Forgan tests were performed on a rectangular duct, with a uniform heat flux both axially and width-wise over the heated regions of the plates, and with upward flow.

9. DISCUSSION AND CONCLUSIONS

Tables B-2.1 through B-2.5 and Reference [B-2.5] together show that the PLTEMP/ANL code can reasonably accurately predict the onset of flow instability for a wide range of channel pressures, temperatures, powers, and channel thicknesses for water cooled research reactors with closed rectangular channels. What was once called "autocatalytic vapor binding" is actually a form of flow instability that results from a minimum in the demand (or system resistance) curve, as shown in Figure B-2.1, which, in turn, is brought about by sufficient subcooled nucleate boiling.

Table B-2.6 – Range of Parameters of Whittle and Forgan Tests

Parameter	Minimum	Maximum
Velocity, m/s	0.61	9.1
Inlet Temp., C	35	75
Heat Flux, W/cm^2	42	340
Exit Pressure, bar	1.17	1.72
Channel Thickness, in.	0.055	0.127
Heated length, in.	16	24
Geometry	wide slot & round tube	

The three sets of independent tests with electrically heated channels have covered a wide range of conditions. Pressures have varied from 1.17 to 27.03 bar. The heated tests sections have had lengths from 16 to 48 inches. The channel thicknesses had values from 0.054 to 0.127 inches. Uniform heat fluxes have been used, as well as axially varying ones, and ones that varied both axially and across the width. The average heat flux varied from 12 to 873 W/cm^2.[†] The coolant inlet temperature varied from 35 to 115° C.

Olson[B-2.5] shows that the Whittle and Forgan relationship, as implemented in PLTEMP/ANL and with $\eta = 32.5$, predicts flow instability reasonably well for the tests conducted at ORNL and reported by M. Siman-Tov et al.[B-2.6],[B-2.7] Olson indicates that these tests were conducted with geometries relevant to research reactor conversion studies with coolant exit pressures of 1.75 to 28.8 bar, and with heat flux from 70 to 1800 W/cm^2.

Since all, or virtually all, of the tests in heated channels are for two-sided heating, the instance of one sided may be a potential source of concern. This may be of particular concern for the MURR because one of the two end fuel plates in each assembly tends to have the highest heat flux of all of the fuel plates in the assembly. Reference [B-2.9] provided an interesting perspective with regard to channels with one-side heating. He suggested that a channel that is heated from two sides could be compared to a pseudo channel heat from two sides that is formed by putting together two identical channels that are each heated from one side and are half as thick as the corresponding channel with two-sided heating. Here it is assumed that the two-sided channel and the pseudo two-sided heated channel both have the same flow rate. The major difference between these two channels is the shape of the velocity profile from one heated side to the other. The pseudo one has a zero-velocity condition at the middle of the span between the two heated walls and a hydraulic diameter that his about half as big, due to the no-slip condition at the middle of the span. The bubbles that cause flow instability tend to originate on the heat surfaces where the thermal and hydrodynamic boundary layers for the pseudo channel should be very similar to those for the channel that is heated from two sides. Moreover, the effect of the smaller hydraulic diameter for the channel heat from one side is

[†] For the Croft and Waters experiments the heat transfer area was taken to be twice the heated width of the plate (1.00 inches for Croft and 2.00 inches for Waters) times the heated length (48 inches).

included in equation (1), above, where it tends to reduce the allowed bulk coolant outlet temperature and channel power. Furthermore, Reference [B-2.3] included tubular channels heated from the outer perimeter in their flow stability experiments and showed that the equation (3) is applicable to this geometry as well. Thus, flow stability may not be strongly dependent on the shape or the configuration of the heated perimeter.

In conclusion, although there is no single test that by itself closely matches the limiting conditions in the MURR, the preponderance of measured data and the ability of the Whittle and Forgan correlation, as implemented in PLTEMP/ANL, to predict the onset of flow instability for these tests leads one to the conclusion that the same method should be able to predict the onset of flow instability in the MURR reasonably well.

REFERENCES:

[B-2.1] M. W. Croft, *Advanced Test Reactor Burnout Heat Transfer Tests*, USAEC Report IDO-24465, ATR-FE-102, Ca-2, Babcock & Wilcox Company, January 1964.

[B-2.2] E. D. Waters, *Heat Transfer Experiments for the Advanced Test Reactor*, USAEC Report BNWL-216, UC-80, Reactor Technology (TID-4500) Pacific Northwest Laboratory, Richland, Washington, May 1966.

[B-2.3] R. H. Whittle and R. Forgan, "A Correlation for the Minima in the Pressure Drop Versus Flow-Rate Curves for Sub-Cooled Water Flowing in Narrow Heated Channels," Nuclear Engineering and Design, 1967.

[B-2.4] Arne P. Olson and Kalimullah, "A Users Guide to the PLTEMP/ANL V3.0 Code," Reduced Enrichment for Research and Test Reactors (RERTR) Program, Argonne National Laboratory, May 16, 2006.

[B-2.5] A. P. Olson, "Analysis of Flow Excursion Experiments Relevant to Research Reactors," The 2006 International Meeting on Reduced Enrichment for Research and Test Reactors, October 29-November 3, 2006, Cape Town, South Africa, http://www.rertr.anl.gov/RERTR28/PDF/S7-2_Olson.pdf.

[B-2.6] M. Siman-Tov, D. K. Felde, G. Farquharson, J. L. McDuffee, M. T. McFee, A. E. Ruggles, M. W. Wendel, and G. L. Yoder, FY 1995 Progress Report on the ANS Thermal-Hydraulic Test Loop Operation and Results, ORNL/TM-12972, Oak Ridge National Laboratory (July 1997).

[B-2.7] M. Siman-Tov, D. K. Felde, J. L. McDuffee, and G. L. Yoder, Experimental Study of Static Flow Instability in Sub-cooled Flow Boiling in Parallel Channels, 4th ASME/JSME Thermal Engineers Joint Conference, Maui, Hawaii, CONF-950113--1,Oak Ridge National Laboratory (January 1995).

[B-2.8] INTERATOM, on behalf of the Minister of Research and Technology of the Federal Republic of Germany, Appendix A-1 of IAEA-TECDOC-643, "Research Reactor Core Conversion Guidebook," Vol. 2: Analysis (Appendices A-F), International Atomic Energy Agency, Vienna, (April 1992).

[B-2.9] Private communication with Arne Olson of Argonne National Laboratory, RERTR, December 10, 2008.

APPENDIX F

SAFETY LIMIT ANALYSIS FOR THE MURR

F. SAFETY LIMIT ANALYSIS FOR THE MURR

F.1 Introduction

The University of Missouri Research Reactor (MURR) Safety Limits (SLs) establish the maximum allowable reactor power limits, the dependent variable, for safe operation under different combinations of three (3) measureable independent operating parameters – primary coolant flow, reactor inlet water temperature and primary coolant pressurizer pressure. The limits provide the basis for determining the Limiting Safety System Settings (LSSSs) and operating limits for 5 and 10 MW operation (also known as Mode II and Mode I operation, respectively).

The previous Mode I and II SL curves were developed in 1973 by the NUS Corporation for the 1974 uprate in power from 5 to 10 MW. Appendix F of Addendum 4 to the MURR Hazards Summary Report (HSR) (Ref. 1) provided the SL Analysis for Mode I and II operation. This analysis generated two (2) SL curves corresponding to primary coolant pressurizer pressures of 60 and 75 psia. Section 6.0 of Addendum 5 to the MURR HSR (Ref. 2) extended the original analysis to include a third SL curve for a pressurizer pressure of 85 psia, i.e. the nominal operating pressure. The safety analysis for natural convective cooling of the core, or Mode III operation, is provided in Section 5.5.3 of the MURR HSR (Ref. 3). The power peaking factors used in the determination of the MURR SLs for Mode I and II operation are provided in Section 3.3 of Addendum 3 to the MURR HSR (Ref. 4). Appendix H of Addendum 4 to the MURR HSR (Ref. 5) provided the bases for determining the LSSSs for Mode I and Mode II operation.

While answering a relicensing Request for Additional Information (RAI) question, an error was discovered in the following document: *Safety Limit Analysis for the MURR Facility*, NUS Corporation, NUS-TM-EC-9, May 1973 (Ref. 6). NUS-TM-EC-9 was the base document that was used in preparing the original Appendix F of Addendum 4 to the MURR HSR. The error was a discrepancy between the "diameter of heated surface," known as the variable D_i, as it is defined by Bernath (Ref. 7) and a more commonly used "heat diameter" definition that was inadvertently used by the NUS Corporation when developing the SLs.

A reanalysis of the MURR SLs resulted in the generation of new reactor power limits as shown in Tables F.1, F.2, and F.3, and three new sets of SL curves corresponding to primary coolant pressurizer pressures of 60, 75, and 85 psia. The SL curves are shown in Figures F.1, F.2, and F.3, respectively. This new analysis is a replacement for the original analysis performed by the NUS Corporation. The results are the bases for the changes to the SLs for Mode I and II operation; however no changes to the LSSSs for Mode I, II, and III operation are required. This revised Appendix F of Addendum 4 to the MURR HSR combines and replaces the current versions of the following three documents:

1. Section 3.3 of Addendum 3 to the MURR HSR;
2. Appendix F of Addendum 4 to the MURR HSR; and
3. Section 6.0 of Addendum 5 to the MURR HSR.

Section 5.5.3, "Analysis of Natural Convective Cooling of the Core," of the MURR HSR assumed a combination of power peaking factors that exceed the combined power peaking factors for the current 6.2 Kg ^{235}U aluminide fuel core. The 1965 natural convective cooling analysis was based on the original 5.2

Kg ^{235}U alloy fuel core and assumed an overall power peaking factor of 4.653 for the hot spot heat flux. Mode III operation would only be used to perform reactor physics measurements on a 0 MWD core (eight fresh fuel assemblies). The 0 MWD 6.2 Kg ^{235}U aluminide fuel core has an overall power peaking factor of 3.315 for the hot spot heat flux. Including the engineering peaking factors, the overall hot spot heat flux peaking factor is 3.927. As provided later in Table F.4, the worst-case overall hot spot heat flux peaking factor for a mixed burnup 6.2 Kg ^{235}U aluminide fuel core is 4.116. Therefore, the analysis in Section 5.5.3 still conservatively envelopes Mode III operation of the MURR.

F.2 Safety Limit Criteria

The study objective was to determine core power limits for safe operation at specified combinations of possible core operating conditions. Safe operation is defined as avoiding excessive fuel or clad temperature that could cause clad failure and thereby release fission products into the primary coolant. To accomplish this, the power level that insures safe margins to both flow instability and critical heat flux are determined for the designated combination of primary coolant parameters of primary coolant flow, reactor inlet water temperature and pressurizer pressure. The following discussion presents the basis for specifying criteria that defines the safe operating margin.

In subcooled flowing water, nucleate boiling at a heated surface can substantially enhance heat transfer. However, when the heat flux is sufficiently high, a layer of vapor, which is a poor conductor of heat, can form on the heated surface and impede heat transfer to the flowing liquid from the core. This is called "critical heat flux" (CHF) or "departure from nucleate boiling" (DNB). Heat flux above CHF can cause dramatic increases in the surface temperature and severely damage the heated surface. For this reason CHF is sometimes referred to as "burnout."

When coolant is flowing in a series of parallel heated channels, such as in the MURR fuel assemblies, flow instability is possible. If the power of the reactor is sufficiently increased beyond the onset of nucleate boiling, boiling in the limiting channel(s) can increase the resistance to flow in that location. This added resistance reduces the flow in the limiting channel(s) by diverting flow to the other cooler channels. The loss of flow in the limiting channel(s), in turn, makes the boiling even more severe and further reduces the flow, resulting in a sudden flow excursion in the limiting channel(s). This is called "Ledinegg flow instability." The abnormally low flow can cause CHF to occur in that location. When flow instability leads to CHF, the cause of the failure is attributed to flow instability rather than to CHF. Correlations that predict CHF typically assume that the flow rate is maintained and that flow instability is not present.

Since 1974, the MURR SLs have been based on two groups of flow instability tests performed for the Advanced Test Reactor (ATR). The Croft (Ref. 8) tests were performed at Argonne National Laboratory (ANL) in 1963 on three channel thicknesses (0.054, 0.072, and 0.094 inches). The Waters (Ref. 9) tests were performed at Pacific Northwest Laboratory (PNL) in Richland, Washington on a channel thickness of 0.070 inches.

The conceptual design for the MURR was performed by the Internuclear Company of Clayton, Missouri, while they were designing the ATR. A literature review demonstrates that the ATR closely compares to the MURR in fuel design, although the ATR core is twice as long as the MURR core. Based on the Croft

and Waters tests and criteria suggested by Croft for the burnout (caused by flow instability) of the 0.094-inch ATR test channel, MURR adapted the following two SL criteria (Ref. 6):

1. The local heat flux at any point in the core shall be less than 0.5 of the burnout heat flux as given by the Bernath CHF Correlation at that point; and

2. The coolant exit temperature from the hot channel shall be less than the saturation temperature at the core exit pressure.

These criteria are designed to avoid flow instability. The Croft version of the first criterion, based on measurements of the 0.094-inch wide test channel, allowed the local heat flux at any point to be as large as 0.6 of the Bernath CHF. However, the MURR conservatively reduced the allowed heat flux fraction to 0.5 of the Bernath CHF. Therefore, the MURR assumed flow instability point corresponds to a CHF ratio of 2.0 based on the Bernath Correlation because, by definition, the ratio of local heat flux to CHF is the reciprocal of the CHF ratio. When the second criterion above is the more limiting, the CHF ratio based on the Bernath Correlation is greater than 2.0.

The Bernath CHF Correlation equation (1) is given by the following:

$$
\begin{aligned}
&(Q/A)_{BO} = h_{BO}\left(T_{W_{BO}} - T_b\right) \\
&h_{BO} = 10890\left(\frac{D_e}{D_e + D_i}\right) + (\text{slope})V \\
&\text{slope} = 48/D_e^{0.6}, \text{if } D_e \leq 0.1\text{ft} \\
&\text{slope} = 90 + 10/D_e, \text{if } D_e > 0.1ft \\
&T_{W_{BO}} = 57 \ln P - 54\left(\frac{P}{P+15}\right) - \frac{V}{4}
\end{aligned}
\qquad (1)
$$

where:

$(Q/A)_{BO}$	=	CHF in p.c.u./hr-ft^2 (BO stands for "burnout") (p.c.u. is a "pound centigrade unit" and 1 p.c.u. = 1.8 btu);
h_{BO}	=	heat transfer coefficient corresponding to the CHF in p.c.u./hr-ft^2-°C;
$T_{W_{BO}}$	=	wall temperature at which CHF occurs in °C;
T_b	=	local bulk coolant temperature in °C;
D_e	=	hydraulic diameter of the coolant passage in feet, which equals 4 times the flow area divided by the *wetted* perimeter;
D_i	=	diameter of the heated surface, which equals the heated perimeter divided by π in feet;
P	=	pressure in psia; and
V	=	velocity of the coolant in ft/s.

The above two safety criteria used by the MURR for the SLs since 1974 are retained in the current safety analysis and were used in defining the current SL curves. Thus, the derived curves allow sufficient margin between the SLs and the actual predicted flow instability DNB and a significantly greater margin to CHF DNB. Additionally, the usual conservatism of worst-case power peaking and non-uniform fuel

loading and appropriate hot channel factors are included, lending greater assurance that the MURR will not approach fuel failure under the most severe operating conditions for the licensed steady-state power level of 10 MW.

The reanalysis of the MURR SLs for Mode I and Mode II resulted in the generation of new reactor power limits as shown in Tables F.1, F.2 and F.3 and three (3) new SL curves corresponding to primary coolant pressurizer pressures of 60, 75, and 85 psia (413.7, 517.1, and 586.1 kPa) as shown in Figures F.1, F.2, and F.3, respectively. This new analysis is a replacement of the original analysis performed by the NUS Corporation in 1973-1974. The results are the bases for the changes to the SLs.

Table F.1
MAXIMUM ALLOWABLE CORE POWER LEVEL (MW)
WITH PRESSURIZER PRESSURE AT 60 PSIA

REACTOR INLET WATER CONDITIONS										
Temp	Flow Rate (GPM)									
°F	400	800	1200	1600	2000	2400	2800	3200	3600	4000
120	3.116	5.352	7.444	9.406	11.216	12.837	14.220	15.299	15.972	16.078
140	2.862	4.912	6.826	8.615	10.255	11.713	12.943	13.880	14.432	14.453
155	2.670	4.582	6.362	8.020	9.533	10.868	11.980	12.809	13.266	13.216
160	2.606	4.472	6.207	7.821	9.292	10.586	11.659	12.451	12.876	12.800
180	2.289	4.032	5.588	7.027	8.327	9.456	10.371	11.015	11.309	11.128
200	1.863	3.592	4.970	6.235	7.364	8.327	9.084	9.580	9.740	9.450

Note: For 400 gpm, the lowest inlet water temperature with saturation limiting at exit: 172.7 °F, 2.445 MW
For 180 °F, the highest flow rate with saturation limiting at exit: 449.0 gpm at 291.2 °F, 2.567 MW
For 200 °F, the highest flow rate with saturation limiting at exit: 701.0 gpm at 290.4 °F, 3.235 MW

Table F.2
MAXIMUM ALLOWABLE CORE POWER LEVEL (MW)
WITH PRESSURIZER PRESSURE AT 75 PSIA

REACTOR INLET WATER CONDITIONS										
Temp	Flow Rate (GPM)									
°F	400	800	1200	1600	2000	2400	2800	3200	3600	4000
120	3.369	5.799	8.093	10.273	12.326	14.227	15.944	17.434	18.639	19.480
140	3.113	5.358	7.473	9.478	11.359	13.093	14.649	15.986	17.051	17.769
155	2.922	5.027	7.007	8.880	10.632	12.240	13.674	14.894	15.850	16.472
160	2.858	4.916	6.851	8.680	10.389	11.955	13.348	14.529	15.449	16.038
180	2.597	4.474	6.229	7.881	9.417	10.814	12.043	13.067	13.840	14.295
200	2.169	4.033	5.608	7.083	8.446	9.674	10.738	11.605	12.230	12.550

Note: For 400 gpm, the lowest inlet water temperature with saturation limiting at exit: 179.4 °F, 2.609 MW
For 180 °F, the highest flow rate with saturation limiting at exit: 403.2 gpm at 306.2 °F, 2.617 MW
For 200 °F, the highest flow rate with saturation limiting at exit: 571.0 gpm at 305.9 °F, 3.085 MW

Table F.3
MAXIMUM ALLOWABLE CORE POWER LEVEL (MW)
WITH PRESSURIZER PRESSURE AT 85 PSIA

REACTOR INLET WATER CONDITIONS										
Temp	Flow Rate (GPM)									
°F	400	800	1200	1600	2000	2400	2800	3200	3600	4000
120	3.514	6.054	8.461	10.762	12.947	14.997	16.884	18.576	20.028	21.183
140	3.257	5.612	7.839	9.965	11.977	13.858	15.582	17.116	18.420	19.439
155	3.065	5.280	7.372	9.365	11.247	13.001	14.600	16.015	17.206	18.121
160	3.001	5.169	7.217	9.165	11.004	12.714	14.273	15.647	16.800	17.680
180	2.744	4.726	6.593	8.364	10.028	11.568	12.960	14.174	15.173	15.910
200	2.349	4.284	5.970	7.563	9.053	10.422	11.647	12.700	13.545	14.138

Note: For 400 gpm, the lowest inlet water temperature with saturation limiting at exit: 184.0 °F, 2.693 MW
For 200 °F, the highest flow rate with saturation limiting at exit: 516 gpm at 314.9 °F, 3.025 MW

Note: All values in Tables F.1, F.2 and F.3 are limited by mesh interval 18 except the 5 values in red, which are limited by (1) reaching saturation temperature at the exit, and (2) the 400 gpm and 180 °F point in Table F.3 which is based on mesh interval 19.

The red values in Tables F.1, F.2 and F.3 are the power limits as established by the second criterion of approaching saturation temperature at the hot channel outlet to avoid bulk boiling of the coolant. The remaining entries reflect the thermal limits established by the first criterion which requires that the local heat flux does not exceed 50% of the Bernath predicted DNB heat flux. In the present study, the power limits for coolant flow rates greater than 701 gpm are always dictated by the first criterion (50% of Bernath), while there are only five (5) data points for 400 gpm in the tables where approaching bulk boiling at the exit criterion dictates the safe power level. The transition points for going from the second criterion to the first criterion are given at the bottom of each table for increasing coolant flow rate or decreasing reactor inlet water temperature.

The three (3) sets of curves together define a four-dimensional SL envelope that prescribes limiting values for the reactor power dependent variable for the 180 different combinations of the three (3) independent variables: primary coolant flow, reactor inlet water temperature and primary coolant pressurizer pressure. Each set of curves is for a different pressurizer pressure with the independent axis being primary coolant flow and the dependent axis being the SL power level. Each of the curves corresponds to a different reactor inlet water temperature. Operation of the MURR within this safety envelope will prohibit fuel meltdown or cladding damage as a result of either flow instability or CHF DNB. To evaluate SLs for pressurizer pressures intermediate to the three cases considered, interpolation will be used. For pressurizer pressures below 60 psia, extrapolation will be used to determine the SLs.

F.3 Discussion of Results

Figures F.1, F.2, and F.3 illustrate the effects of core operating conditions on the maximum allowed core power for safe MURR operation. The increase in allowed core power with flow is provided by the Bernath Correlation, equation (1). For all lower flow rates, the Bernath allowed DNB heat flux increases with flow but the slope slightly decreases with increasing flow. This is more pronounced for lower

primary coolant pressurizer pressures and higher reactor inlet water temperatures. For the 60 psia curves, all but the 120 and 140 °F curves have a decrease in maximum allowed power for a core flow rate increasing from 3600 to 4000 gpm. This shows that the core flow rate caused drop in core outlet pressure has more of a negative effect than the higher flow rate has a positive effect. As is expected and dictated by equation (1), the allowed power decreases with increasing inlet water temperature. Similarly, the increase in allowed power with increasing pressurizer pressure is as expected because the saturation temperature of the coolant increases with pressure.

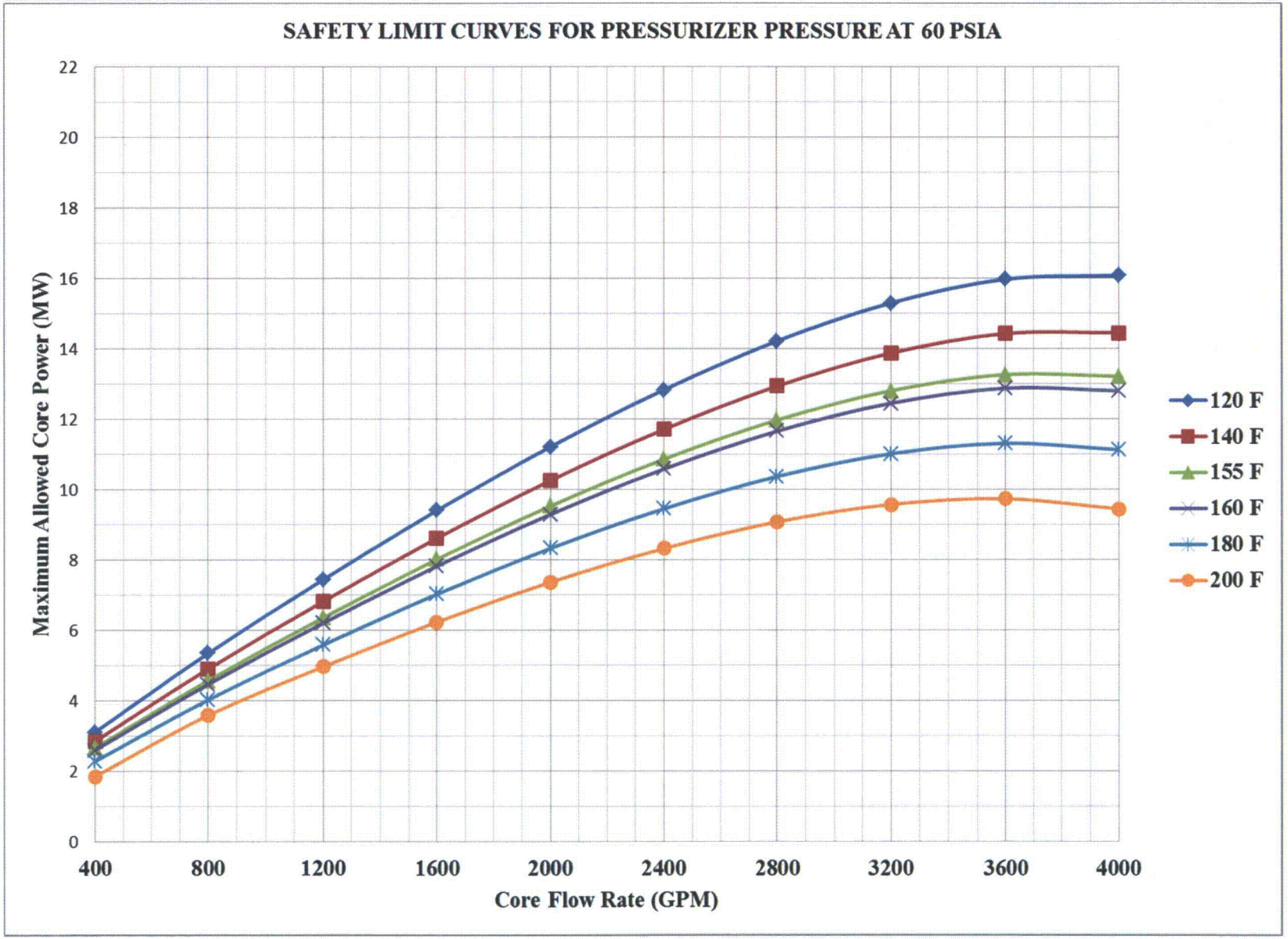


Figure F.1 – MURR Safety Limit Curves for Pressurizer Pressure at 60 PSIA

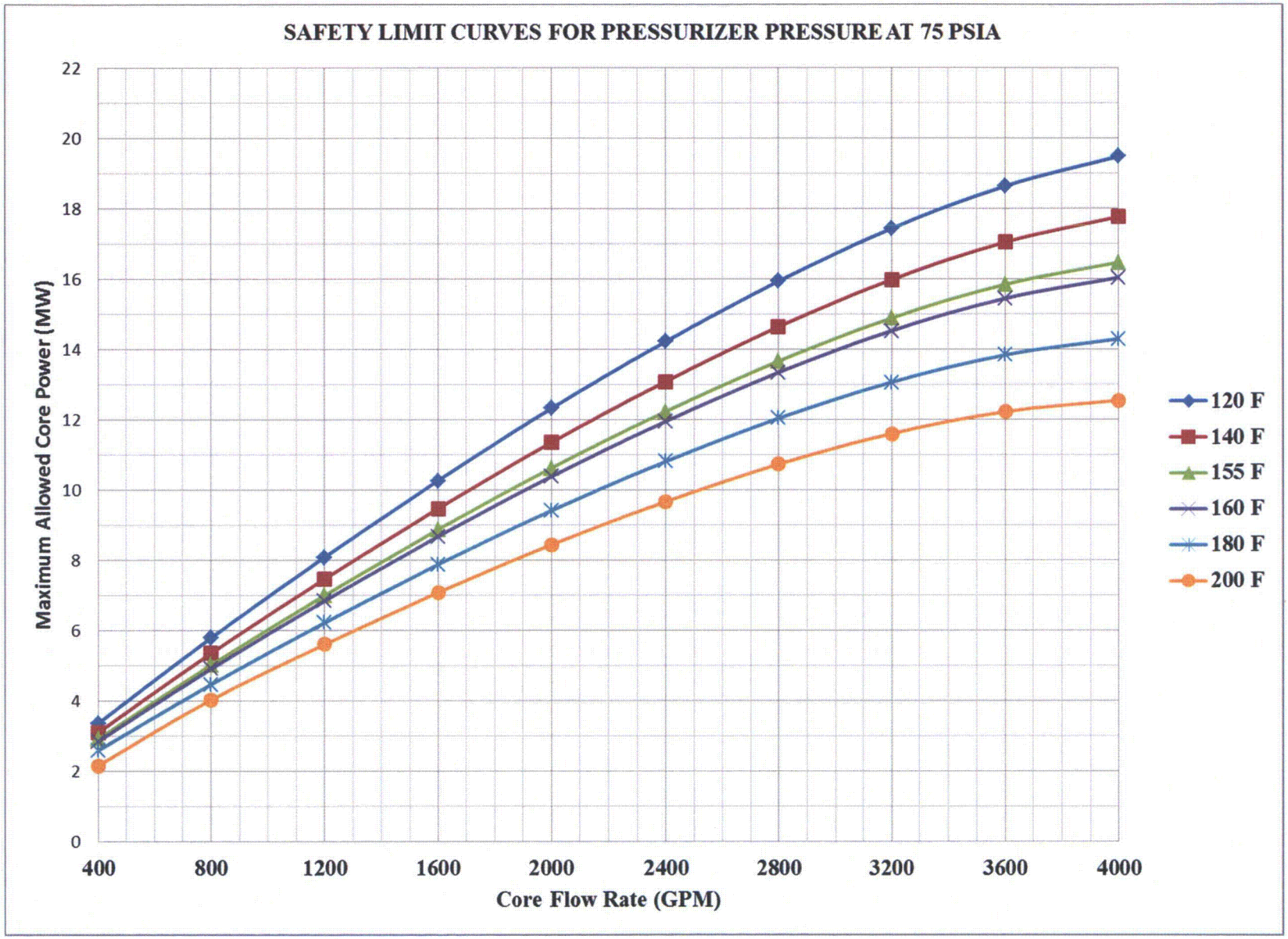


Figure F.2 – MURR Safety Limit Curves for Pressurizer Pressure at 75 PSIA

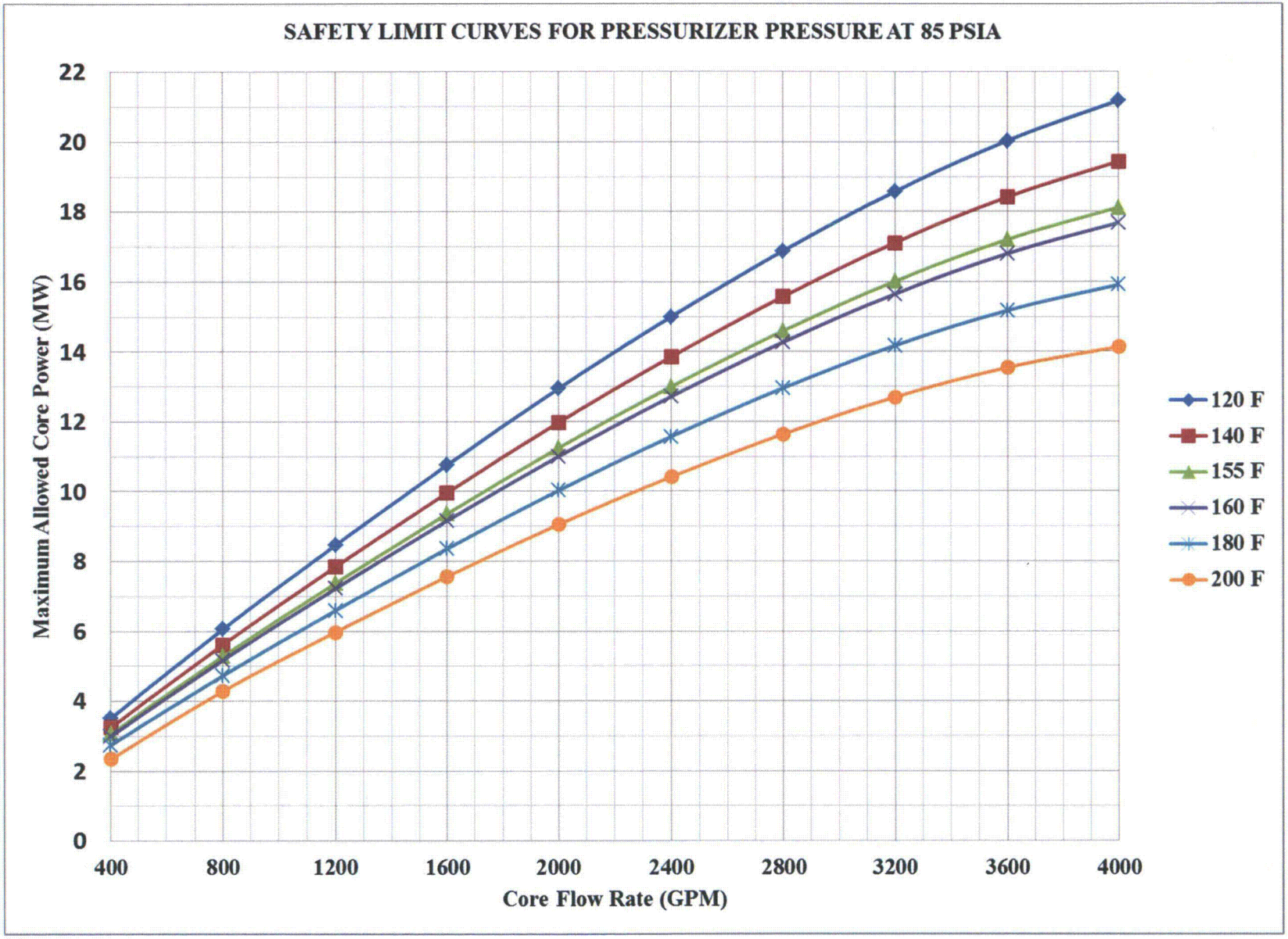


Figure F.3 – MURR Safety Limit Curves for Pressurizer Pressure at 85 PSIA

F.4 Method of Analysis

In 1974, when MURR, working with the NUS Corporation, developed the previous SLs, the peaking factors used were extremely conservative because peaking factors had to be determined utilizing three (3) different 2D diffusion code models, which was the only code method available in the early 1970's. These peaking factors were provided in the original Table F.2 of Appendix F of Addendum 4 to the MURR HSR (A detailed description is provided in Section 3.3 of Addendum 3 to the MURR HSR):

On Heat Flux
Power-Related Factors
Nuclear Peaking Factors:

Radial.....	2.220	[*from all fresh fuel R-Z model*]
Local (Circumferential).....	1.040	[*from all fresh fuel R-Θ model*]
Non-uniform Burnup.....	1.112	[*from mixed burnup fuel R-Θ model*]
Axial.....	1.432	[*from all fresh fuel R-Z model*]

The product of the above four (4) nuclear peaking factors is 3.676. With the engineering hot channel factors on flux included, the overall product is 4.35. This overall peaking factor is extremely conservative because peaking factors from two different core arrangements were combined. For a core consisting of eight (8) fresh fuel elements (0 MWD), causing a lower control rod height, higher radial and axial peaking factors are then combined with the smaller local (circumferential) peaking factor caused by no burnup. For a non-uniform burnup core with a higher control rod height, resulting in lower radial and axial peaking factors, the larger azimuthal (non-uniform burnup) factor was obtained. These four (4) factors, which cannot all occur in the same core, were then combined to provide this very conservative, overall peaking factor.

Current 3D nucleonics codes show the axial peaking factors in a mixed burnup core are lower than in an all fresh fuel core because of less excess reactivity and the corresponding higher critical control rod height position. Also, the 3D model provides an accurate average plate peaking factor, instead of the 2D approach of trying to approximate this by using the all fresh fuel radial factor (R-Z) times the non-uniform burnup azimuthal factor (R-Θ). This is a result of combining the high excess reactivity and lower critical rod height of an all fresh core with the MURR design, consisting of all the control blades external to the outer pressure vessel, which tends to push the power down and inward in the core increasing the axial and radial peaking factors for the hot fuel plate (fuel plate-1).

Since 2006, MURR has been actively collaborating with the Department of Energy's Reduced Enrichment for Research and Test Reactor (RERTR) Program on the conversion from highly-enriched uranium (HEU) to low-enriched uranium (LEU) fuel. During this time, the Argonne National Laboratory (ANL)/MURR team has benchmarked the MURR HEU fuel and reactor core design performance, which is documented in MURR Technical Data Report TDR-0125, "Feasibility Analyses for HEU to LEU Fuel Conversion of the University of Missouri Research Reactor (MURR)" (Ref. 10). The computer modeling completed in performing the feasibility analyses provides more accurate 3D peaking factors, which were used in determining the revised SLs. In addition to the feasibility analyses worst-case HEU peaking factors, an additional peaking factor of 1.062 is included to define the maximum allowable nuclear peaking factor. The maximum allowable nuclear peaking factors were combined with the engineering peaking factors, which are provided below in Table F.4, to establish the maximum allowable overall

peaking factor for enthalpy rise and heat flux used to generate the revised SLs that meet the existing criteria.

F.5 Determination of Worst-Case Safety Limit Peaking Factors

MURR Technical Data Report TDR-0125 documents the neutronic analysis steps taken to develop the code system, modeling and benchmarking for the MURR HEU fuel performance. To compare the performance of the proposed LEU design to the current HEU operation, models were developed for the current reactor reflector configuration with typical experimental loadings. To properly model the current HEU core fuel utilization, shutdown margin and experimental performance, it was necessary to develop a computational shuffling that would accurately model the actual complex fuel cycle used at MURR. This is also described in detail in TDR-0125.

Also in order to perform a comparison between HEU and LEU fuel, it was necessary to define reference cores that could be compared in order to establish feasibility of all major parameters: fuel cycle performance, shutdown margin, thermal-hydraulic steady-state safety margins, and experimental performance. It was decided that these reference cores should be close to limiting in order to provide additional confidence that the safety margin calculations treat the potentially different limiting power shapes from the HEU and LEU fuel elements. The actual limiting peaking factor for the MURR 775-gram ^{235}U aluminide fuel elements is modeled by multiplying the worst-case peaking factors by an additional 1.062 factor to determine the SLs.

Core configurations with potentially high power peaking were identified from the fuel cycle simulation in order to analyze for thermal-hydraulic behavior. The fuel cycle simulations provided a collection of more than 325 HEU Core States (4 state points per week x 82 weeks or different core combinations). Each of these State points from the REBUS-DIF3D model was examined and sorted to rank the cases with the highest peak heat flux in the core. As expected, it was found that the highest heat flux always occurs in cases where a fresh element is loaded next to an element that is near its discharge burnup limit.

Based on the selection criteria, the core conditions defined as week 58 (out of 82) of the HEU fuel cycle simulation was chosen for more detailed evaluation. Depleted fuel material compositions were extracted from the REBUS-DIF3D results for each plate and axial depletion zone in the model; this consisted of 2,304 fuel compositions (8 elements x 24 plates x 12 axial zones) for each of the HEU cores. This data was utilized as material composition data for a detailed MCNP model for calculating power distributions and estimated critical positions.

The week 58 HEU core has fuel elements with the following power history: two elements each with 0, 65, 81 and 142 MWD. Of the four different states for the week 58 core, the beginning of the week xenon-free core with no samples or sample holder loaded in the center flux trap region produces the highest power peaking factors. This is due to the highest peaking factors are always on the inner fuel plate, fuel plate-1, and initial critical rod height combined with the 100% water filled flux trap produces even higher peaking factors in fuel plate-1.

The detailed week 58 core MCNP run for the 3B Core State was used to extract the 3D power peaking factors. From these fuel plate heat flux peaking factors, the peaking factors for the hottest coolant channel (channel 2) were determined. The enthalpy rise in channel 2 is calculated based on the average

heat flux for fuel plate-1 and -2. This is conservative because both fuel plate-1 and -2 transfers a little less than half their total heat to coolant channel 2 since the coolant channels on the opposite side of each plate operates at a lower temperature than does channel 2.

The peaking factors for channel 2 are provided in Table F.4. Fuel plate-1 and -2 average and the azimuthal in the channel are calculated from the MCNP results. To establish the maximum allowable overall peaking factor, an additional 1.062 factor is included in both the enthalpy rise and the heat flux. The Engineering Hot Channel Factors are based on the MURR aluminide fuel fabrication specifications and are as used in NUS-TM-EC-9 (Ref. 6). The overall flow-related factor of 0.8197 is the product of the 0.9 (72-mils/80-mils) narrow channel thickness factor times the 0.9108 reduction of coolant velocity in the narrow channel.

Table F.4
SUMMARY OF MURR HOT CHANNEL FACTORS

On Enthalpy Rise In Channel 2			
Power-related Factors			
Nuclear Peaking Factors			
Fuel Plate-1 and -2 Average	1.9843		
Azimuthal in the Channel	1.0921		
Additional Allowable Factor	1.0620		
Engineering Hot Channel Factors			
Fuel Content Variation	1.0300		
Fuel Thickness/Width Variation	1.0300		
Overall Product	2.4416		
Flow-related Factors			
Core/Loop Flow Fraction	1.0000		
Assembly Minimum/Average Flow Fraction	1.0000		
Channel Minimum/Average Flow Fraction			
Inlet Variation	1.0000		
Width Variation	1.0000		
Thickness Variation	0.72/0.80		
Within Channel Minimum Channel Thickness effect on:			
Velocity Factor	0.9108		
Overall Factor on Flow Reduction	0.8197		
On Heat Flux From Fuel Plate-1			
Power-related Factors	For mesh interval between the following inches down the fuel plate[1]		
Mesh Interval Number	14(13-14")	18(17-18")	19(18-19")
Nuclear Peaking Factors			
Fuel Plate (Hot Plate Average)	2.215	2.215	2.215
Azimuthal Within Plate	1.070	1.070	1.070
Axial Peak	1.3805	1.2958	1.2266
Additional Allowable Factor	1.062	1.062	1.062
Engineering Hot Channel Factors			
Fuel Content Variation	1.030	1.030	1.030
Fuel Thickness/Width Variation	1.150	1.150	1.150
Overall Product	4.116	3.863	3.657
Percentage Enthalpy Rise at Hot Spot	52.3%	74.8%	79.9%
Energy Fraction Generated in Fuel Plate		93%	

Note 1: Mesh interval 14 has the highest heat flux but a lower enthalpy rise and is not the limiting point for any of the SLs. In the SL tables, out of the 180 data points, 174 are based on mesh interval 18 being the most limiting. The 85 psia, 400 gpm and 180 °F point is based on mesh interval 19 being the most limiting due to the higher enthalpy rise. The other 5 points, which are in red, are limited by saturation temperature at the channel exit due to being the lowest flow rate with the highest inlet temperature.

F.6 Method of Performing Safety Limit Calculations

A computer spreadsheet model (Ref. 11) was developed to determine the margin to flow instability for any MURR core coolant channel and the outlet saturation temperature. The spreadsheet was used to determine the MURR SLs based on whichever was the more limiting of the two previously stated criteria:

1. The local heat flux at any point in the core shall be less than 0.5 of the burnout heat flux as given by the Bernath CHF Correlation at that point; and

2. The coolant exit temperature from the hot channel shall be less than the saturation temperature at the core exit pressure.

Except for conditions of very low flow rates and high water inlet temperature, the first criterion is the more restrictive one.

The spreadsheet is arranged to calculate the reactor power level SL for any combination of the three (3) independent variables: primary coolant flow, reactor inlet water temperature and primary coolant pressurizer pressure.

The computer spreadsheet model does not consider the individual strips of each fuel plate. Instead, the power of each fuel plate is increased by its azimuthal peaking factor. This approach produces bounding values of local bulk coolant temperature because no credit is taken for azimuthal heat conduction in the fuel plates or azimuthal mixing in the coolant channels. The hottest strip of each of the two fuel plates on either side of a coolant channel is located directly across from each other. In the MURR, a fairly significant fraction, 7%, of the recoverable fission power from the fuel escapes the core as gamma or neutron radiation without creating heat in the fuel plate or in the primary coolant by depositing this 7% of the fission energy in the reflector and pool coolant system and creating the heat at those locations. Therefore, only 93% of the power contributes to the fuel plate heat fluxes heating the primary coolant.

The computer spreadsheet model determines the core power at which the SL criteria of the most limiting axial interval combination of both heat flux and enthalpy rise results in the axial heat flux for that location equal to 0.5 times the Bernath Correlation. In the SL analysis, at each axial level the Bernath CHF value must be compared with the highest heat flux of the two fuel plates that form the coolant channel. In practice this can be accomplished by using the heat fluxes of the plate with the higher plate peaking factor. The CHF is strongly affected by the margin between saturation pressure and local pressure at each mesh point. This difference decreases with increasing coolant temperature and is a significant factor in determining which mesh interval the 0.5 ratio of local heat flux to Bernath CHF occurs. The location will be after the coolant flows past the peak heat flux mesh point and reaches the worst combination of lower heat flux with a reduced margin between mesh interval coolant saturation pressure and fluid pressure. Conservatively, the spreadsheet uses the channel outlet pressure in the Bernath Correlation to calculate the CHF for each mesh point. This results in a calculated smaller margin between the mesh interval saturation pressure and the coolant pressure, which results in the SL corresponding to a mesh point closer to the peak heat flux point resulting in a lower SL power level.

The spreadsheet includes the calculations to determine the absolute pressure (psia) at the core outlet for every combination of operating conditions in this study. This uses Table F.5, which is an improved

version of the old model provided in the original Table F.3 of Appendix F of Addendum 4 to the MURR HSR. Besides the improved model for predicting pressure drops due to flow in the primary coolant system, the spreadsheet now corrects for the slightly higher elevation of the core outlet in relationship to the water level in the pressurizer, which is assumed to be at the low level SCRAM set point of 16 inches below center line for a total elevation difference of 23.25 inches (Note: Center line of the pressurizer is at an elevation of 604.5 feet). The primary coolant charging pump starts charging when pressurizer water level is 6 inches below center line. The core outlet pressure is also corrected for the velocity head loss due to the much higher coolant velocity in the core compared to primary coolant loop 'A' where the pressurizer surge line is connected.

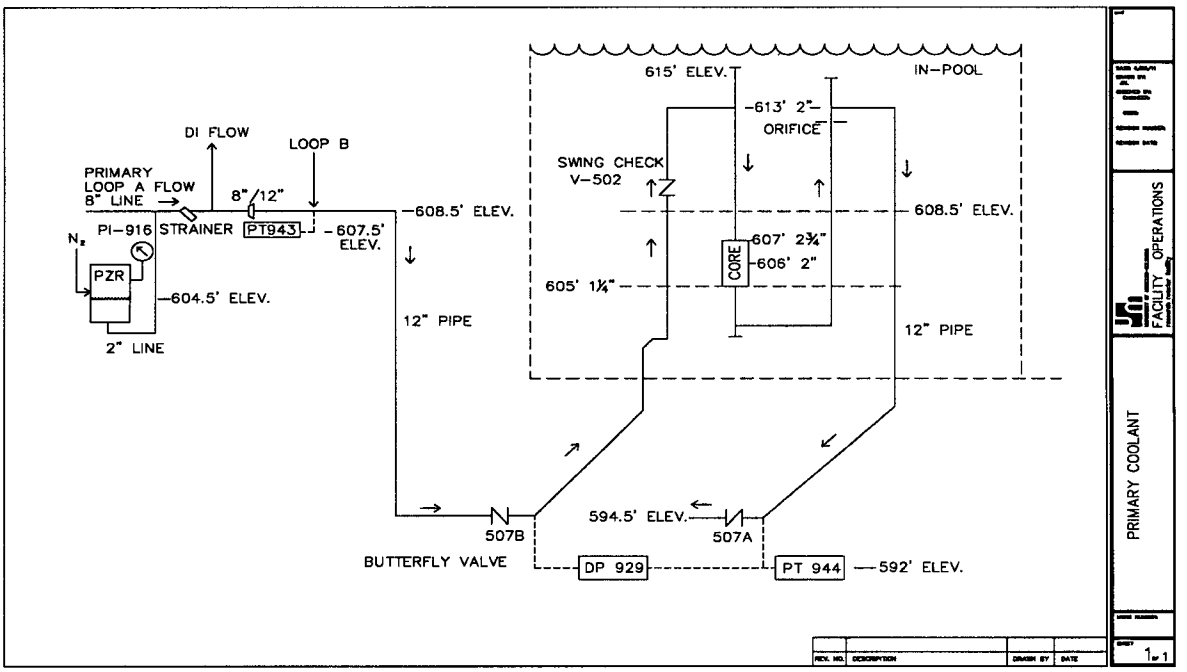


Figure F.4 – Section of Primary Coolant System for Flow Model

To improve the values listed in the original Table F.3, a flow model of the primary coolant system from the point where the pressurizer surge line connects to primary coolant loop 'A' to primary coolant isolation valve 507A (hot leg) was developed using the methodology in Crane Co. Technical Paper No. 410, "Flow of Fluids Through Valves, Fittings, and Pipe" (Ref. 12). The modeled portion of the primary coolant system is shown in Figure F.4 and includes the following pressure monitoring instrumentation:

1. PI-916 – pressure gauge for monitoring pressurizer pressure;
2. PT-943 – pressure transmitter for monitoring primary coolant heat exchanger outlet pressure (at the Tee junction point combining primary coolant loops 'A' and 'B;'
3. DPS-929 – differential pressure sensor for monitoring differential pressure across the reactor core (between primary coolant isolation valves 507A and 507B); and
4. PT-944 – pressure transmitter for monitoring reactor core outlet pressure (just before primary coolant isolation valve 507A).

There is an elevation difference of approximately 21 feet in the primary coolant system over this part of the system. The elevation differences are included in the model prediction of the calculated pressure indication. The model also includes changes in the coolant pressure due to changes in velocity as can be represented by the Bernoulli equation.

To validate the modeling and the pressure drop across the fuel elements, the model was checked and refined using the following two different operating conditions: (1) with the reactor operating at 10 MW (March 27, 2011), and (2) with the primary coolant system operating with no fuel elements installed (March 28, 2011). The modeling includes the hydraulic pressure drops and pressure head difference due to elevation in calculating what the model would have as indication at PT-943, PT-944 and DPS-929. The model calculated values agree with the recorded indication values for the condition of no fuel elements installed measurements conducted on March 28th. In the fuel elements installed model, the pressure drop across the elements was increased by a factor of 1.04 to be conservative. With this adjustment, the model calculated values for the fuel elements installed agreed with PT-943 indication and over predicted DPS-929 indication slightly by 3.2%. The PT-944 indication was predicted to be 34.9 psi compared to the actual reading of 35.0 psi.

Table F.5 groups the component pressure drops into four (4) frictional and four (4) non-frictional sets from the pressurizer to the core outlet. The path from the pressurizer to the core outlet is divided into 25 component pressure drops, ranging from 1 to 10 pressure drops per group. Primary coolant loop 'A' and loop 'B' each have the same flow rate of 1825 gpm, however 50 gpm of demineralizer flow is diverted from loop 'A' just before the 8-inch/12-inch expander. After loops 'A' and 'B' combine at the junction Tee, the combined flow is 3600 gpm in the rest of the flow path. Except for the core, the coolant temperature through all components is the inlet temperature. The core coolant temperature is taken to be the core average coolant temperature and is used to calculate the slightly higher average core flow rate as a result of the thermal expansion as indicated in the table. The pressurizer to core outlet pressure drop is the sum of the 25 component pressure drops corrected for elevation difference and coolant velocity between where the pressurizer attaches to loop 'A' and the core coolant channels.

Table F.5
REFERENCE PRESSURE DROP DATA

Component Group	ΔP_0 (PSI)	Q_0 (GPM)	T_0 (°F)	Frictional
1. 8-inch fine mesh strainer before expander (1)	4.5000	1825	120	No
2. Loop 'A' between pressurizer to expander (2-3)	0.0913	1826	120	Yes
3. Loop 'A' 8-inch/12-inch expander (4)	0.2640	1775	120	No
4. Expander through pressure vessel entrance (5-14)	3.3961	3600	120	Yes
5. In pressure vessel up to reactor core (15-19)	1.1590	3600	120	Yes
6. Step changes in pressure vessel (20-21)	0.0439	3600	120	No
7. Entrance into fuel element & channels (22-24)	0.7569	3600	120	No
8. Reactor core - 25.5 inches of fuel channel (25)	13.8049	3608.3	128.68	Yes

Description of Component Group:

1. 8-inch fine mesh strainer before the expander (1)
2. Primary coolant loop 'A' between pressurizer to expander:
   a. Pressurizer surge line to primary coolant loop 'A' centerline (2)
   b. 4.5 feet of 8-inch pipe (3)
3. Primary coolant loop 'A' 8-inch/12-inch expander (4)
4. From expander through pressure vessel entrance:
   a. 1 foot of 12-inch pipe (5)
   b. Tee combining primary coolant loop 'A' & loop 'B' (6)
   c. 65.5 feet of 12-inch pipe (7)
   d. Two 12-inch 90° elbows (8)
   e. 12-inch butterfly valve (9)
   f. 31.575 feet of 12-inch pipe (10)
   g. Two 12-inch 90° elbows (11)
   h. Three 12-inch 45° elbows (12)
   i. 12-inch swing check valve (13)
   j. Entrance Tee to pressure vessel annulus (14)
5. In pressure vessel up to reactor core:
   a. Junction of 12-inch inlet pipe through fuel element upper end fitting (15)
   b. 17.75-inch long annulus (16)
   c. 34.25-inch long annulus (17)
   d. 3.75-inch long annulus (18)
   e. Flow in fuel element upper end fitting (19)
6. Step changes in pressure vessel:
   a. Gentle reduction in annulus (20)
   b. Two step changes in annulus (21)
7. Entrance into fuel element channels:
   a. Entrance to fuel element end fitting (22)
   b. Exit from fuel element end fitting (23)
   c. Entrance into fuel element channels (24)
8. Core - 25.5 inches of fuel element channel (25)

For a known reactor inlet water temperature, T_0, of 120 °F and a known reactor core inlet flow rate (primary coolant flow), Q_0, of 3600 gpm, known component pressure drops, ΔP_0, are provided, as shown. As Table F.5 indicates, one combined value of ΔP_0 is provided for the pressure drop across each of the eight sets of components. For set number 1, Q_0 is shown in Table F.5 as 1825 gpm. This flow rate for primary coolant loop 'A' is the same for loop 'B,' however 50 gpm of demineralizer flow is diverted from loop 'A' prior to the 8-inch/12-inch expander giving the expander a flow rate of 1775 gpm. Thus, in the table for total flow rate, or effective Q_0, through the rest of the components is 3600 gpm. The method for correcting the reference ΔP components depends on the type of pressure drop involved. For non-frictional components, pressure drop is proportional to density and flow as follows:

$$\frac{\Delta P}{\Delta P_0} = \left[\frac{\rho(T)}{\rho(T_0)}\right]^{1.0} \left[\frac{Q}{Q_0}\right]^{2.0} \tag{2}$$

In this equation, the subscript 0 denotes the reference conditions as provided in Table F.5. For the frictional loss components, the pressure drop is given by:

$$\frac{\Delta P}{\Delta P_0} = \left[\frac{\rho(T)}{\rho(T_0)}\right]^{0.8} \left[\frac{Q}{Q_0}\right]^{1.8} \left[\frac{\mu(T)}{\mu(T_0)}\right]^{0.2} \tag{3}$$

where ρ is coolant density and μ is coolant dynamic viscosity. Equation (2) is for portions of the flow path that are characterized by non-frictional losses, such as changes in flow area and or direction. Equation (3) is for portions of the path that are characterized by wall friction. Component Groups 1, 3, 6 and 7 are shown in Table F.5 to be non-frictional. The rest, as indicated in the table are frictional. Both equation (2) and equation (3) can be derived from well-known hydraulic relationships for turbulent flow. In the derivation of equation (3) it is assumed that the friction factor is proportional to the Reynolds number to the −0.2 power.

F.7 Output

The core power levels limited by the criterion of ≤ 50% of the Bernath CHF were the result of iteration in the MURR SL Program. For each set of primary coolant flow, reactor inlet water temperature and primary coolant pressurizer pressure, the program iterated on core power level to determine when the most limiting 1-inch axial mesh interval with fuel plate-1 heat flux and the corresponding coolant channel 2 enthalpy rise reached this criterion. The power levels in Tables F.1, F.2 and F.3 correspond to the iteration terminating when the Bernath CHF Correlation value for the most limiting axial mesh interval in the hot channel converges to 0.499999. At all three pressurizer pressures, the very lowest flow rate of 400 gpm combined with the highest reactor inlet water temperature of 200 °F results in the power level being limited by the channel outlet temperature reaching the saturation temperature. This is also the case at 180 °F with 400 gpm flow for pressurizer pressures of 60 and 75 psia. These five points are highlighted in red with the power levels given being limited by the hot stripe exit temperature reaching the saturation temperature for the channel exit pressure.

F.9 References

1. MURR Hazards Summary Report, University of Missouri Research Reactor Facility, Addendum 4, Appendix F, *Safety Limit Analysis for the MURR*, October 1973.

2. MURR Hazards Summary Report, University of Missouri Research Reactor Facility, Addendum 5, Section 6.0, *Addendum to the Safety Limit Analysis for the MURR*, January 1974.

3. MURR Hazards Summary Report, University of Missouri Research Reactor Facility, Section 5.5.3, *Analysis of Natural Convective Cooling of the Core*, July 1965.

4. MURR Hazards Summary Report, University of Missouri Research Reactor Facility, Addendum 3, Section 3.3, *Evaluation of Power Peaking Factors in the MURR 6.2 Kg Core*, 1972.

5. MURR Hazards Summary Report, University of Missouri Research Reactor Facility, Addendum 4, Appendix H, *Bases for Limiting Safety System Settings for Modes I and II Operation*, October 1973.

6. Vaughan, F.R., "Safety Limit Analysis for the MURR Facility," NUS Corporation, NUS-TM-EC-9, Appendix A, May 1973.

7. Louis Bernath, "A Theory of Local-Boiling Burnout and Its Application to Existing Data," *Chemical Engineering Progress Symposium*, Series No. 30, Volume 56, pp. 95-116, 1960.

8. Croft, M.W., "Advanced Test Reactor Burnout Heat Transfer Tests," USAEC Report IDO-24475, Babcock & Wilcox Co., January 1964.

9. Waters, E.D., "Heat Transfer Experiments for the Advanced Test Reactor," USAEC Report BNWL-216, Battelle-Northwest, May 1966.

10. MURR Technical Data Report TDR-0125, "Feasibility Analyses for HEU to LEU Conversion of the University of Missouri Research Reactor (MURR)," University of Missouri-Columbia Research Reactor, Columbia Missouri, September 2009.

11. Feldman, E.E., "Implementation of the Flow Instability Model for the University of Missouri Reactor (MURR) that is Based on the Bernath Critical Heat Flux Correlation," Conversion Program Nuclear Engineering Division, Argonne National Laboratory, June 2011.

12. "Flow of Fluids Through Valves, Fittings, and Pipe," Technical Paper No. 410, Crane Co., 1991.

APPENDIX H

BASES FOR LIMITING SAFETY SYSTEM SETTINGS FOR MODES I AND II OPERATION

H. BASES FOR LIMITING SAFETY SYSTEM SETTINGS FOR MODES I AND II OPERATION

The Limiting Safety System Settings (LSSSs) for Modes I and II, i.e. 10 MW and 5 MW operation respectively, of the MURR are as follows. For reactor power level the LSSS is 125 % of full power for both modes thus the highest powers obtainable before a reactor scram would be 12.5 MW (1.25 x 10 MW) in Mode I and 6.25 MW (1.25 x 5 MW) in Mode II. For both modes, the LSSS on pressure is a minimum of 75 psia in the primary coolant pressurizer, and the LSSS on reactor inlet water temperature is a maximum of 155 °F. The LSSS on primary coolant flow for Mode I operation is a minimum of 1625 gpm in either of the parallel coolant loops. The same LSSS of 1625 gpm applies for the single operating loop in Mode II operation. Since 50 gpm of the primary coolant flow is diverted to the cleanup (demineralizer) system, the actual core flow rates at the LSSS are 3200 gpm in Mode I and 1575 gpm in Mode II, respectively.

The August 2011 Amendment application to the U.S. Nuclear Regulatory Commission to revise the "Safety Limit Analysis for the MURR," presented in Appendix F of Addendum 4 to the MURR Hazards Summary Report, presents parametric curves for the conditions which would lead to reaching the conservatively defined critical heat flux (CHF), corresponding to 0.5 times the Bernath CHF Correlation. From the analysis, Figure H.1 depicts the CHF conditions for the LSSS on a pressurizer pressure of 75 psia. From the curves one can predict the safety margin for several anticipated transients.

Case 1 postulates a severe power transient with primary coolant flow and pressure reduced to their LSSS values in Mode I operation. Figure H.1 predicts that the temperature LSSS of 155 °F could not be reached until the power has risen to 14.896 MW, or 2.396 MW above the reactor power scram set point, thus an ample safety margin exists for safety system reaction time required to prevent reaching the CHF threshold.

Case 2 postulates steady-state Mode I operation of the reactor with flow and pressure again reduced to their LSSS and reactor power at the LSSS of 12.5 MW. Figure H.1 predicts that CHF would not occur until a reactor inlet water temperature of 187.7 °F was obtained. The safety margin is thus 32.7 °F above the LSSS of 155 °F on reactor inlet water temperature. Primary coolant temperature increase would be slow, thus little or no margin is required for safety system reaction time. Periodic compliance checks and past operating history provide confidence that the primary coolant temperature measurement error is no greater than ± 2 °F; therefore there is excess safety margin for a temperature transient of this type.

Case 3 postulates Mode I operation with pressurizer pressure reduced to the LSSS of 75 psia, reactor power and reactor water inlet temperature raised to their LSSS of 12.5 MW and 155 °F, respectively. Figure H.1 predicts that the primary coolant flow rate could be reduced to 2469 gpm before CHF would occur, implying a safety margin of 731 gpm below the LSSS of 3200 gpm on coolant flow through the core. Operating history has shown that the true value of primary coolant flow does not vary from the measured value by more than ± 50 gpm, thus there is excess margin for safety system reaction time to scram the reactor before CHF occurs. Appendix D provides a detailed analysis of the results of the most severe loss of flow accident for the MURR.

Consideration of the same transients for Mode II (5 MW) operation yields even greater safety margins. Figure H.2 presents the results for Mode II operation of the same transients discussed for Mode I. Case

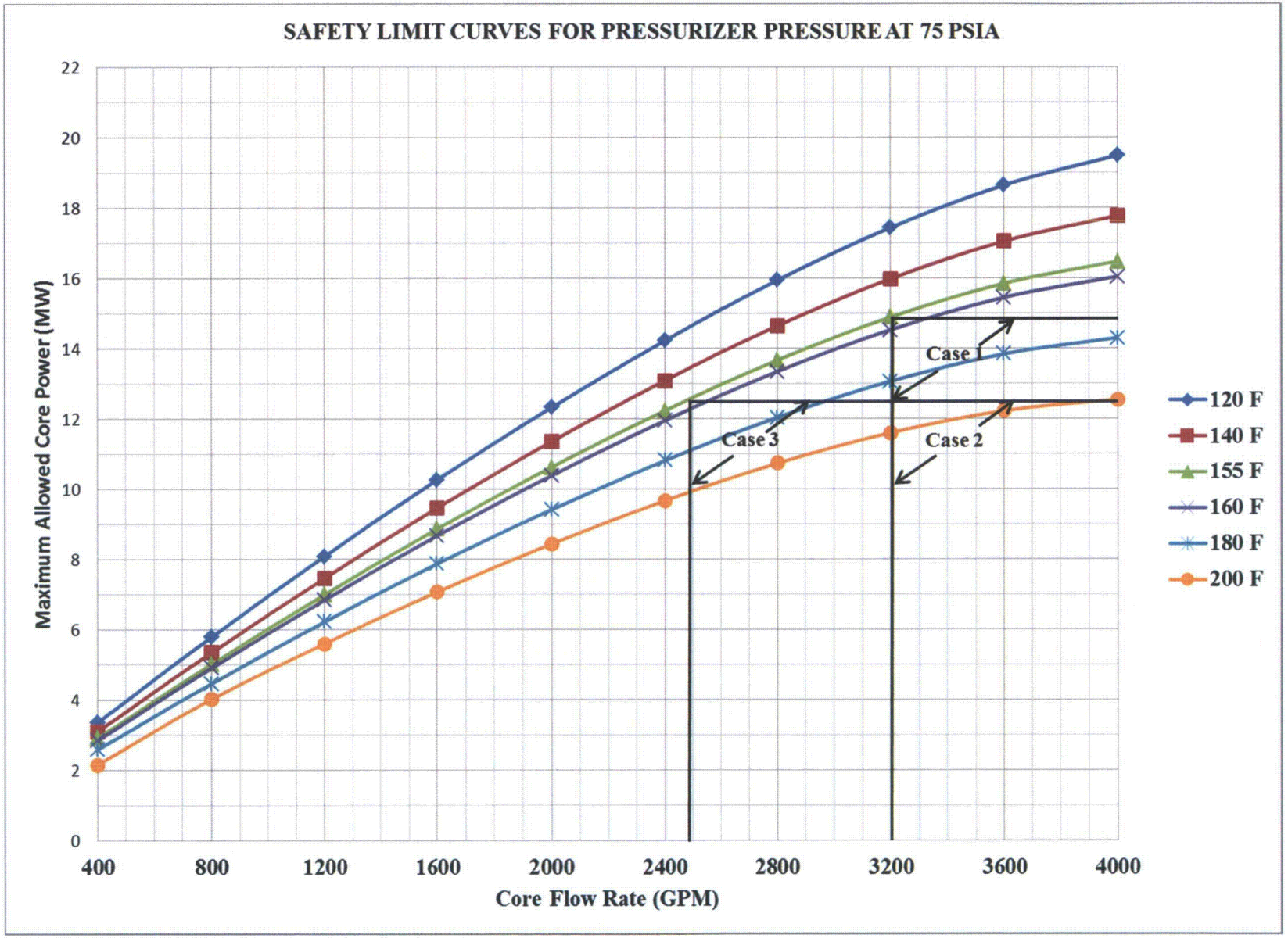


Figure H.1 – MURR CHF Curve Mode I Operation for Pressurizer Pressure at 75 PSIA

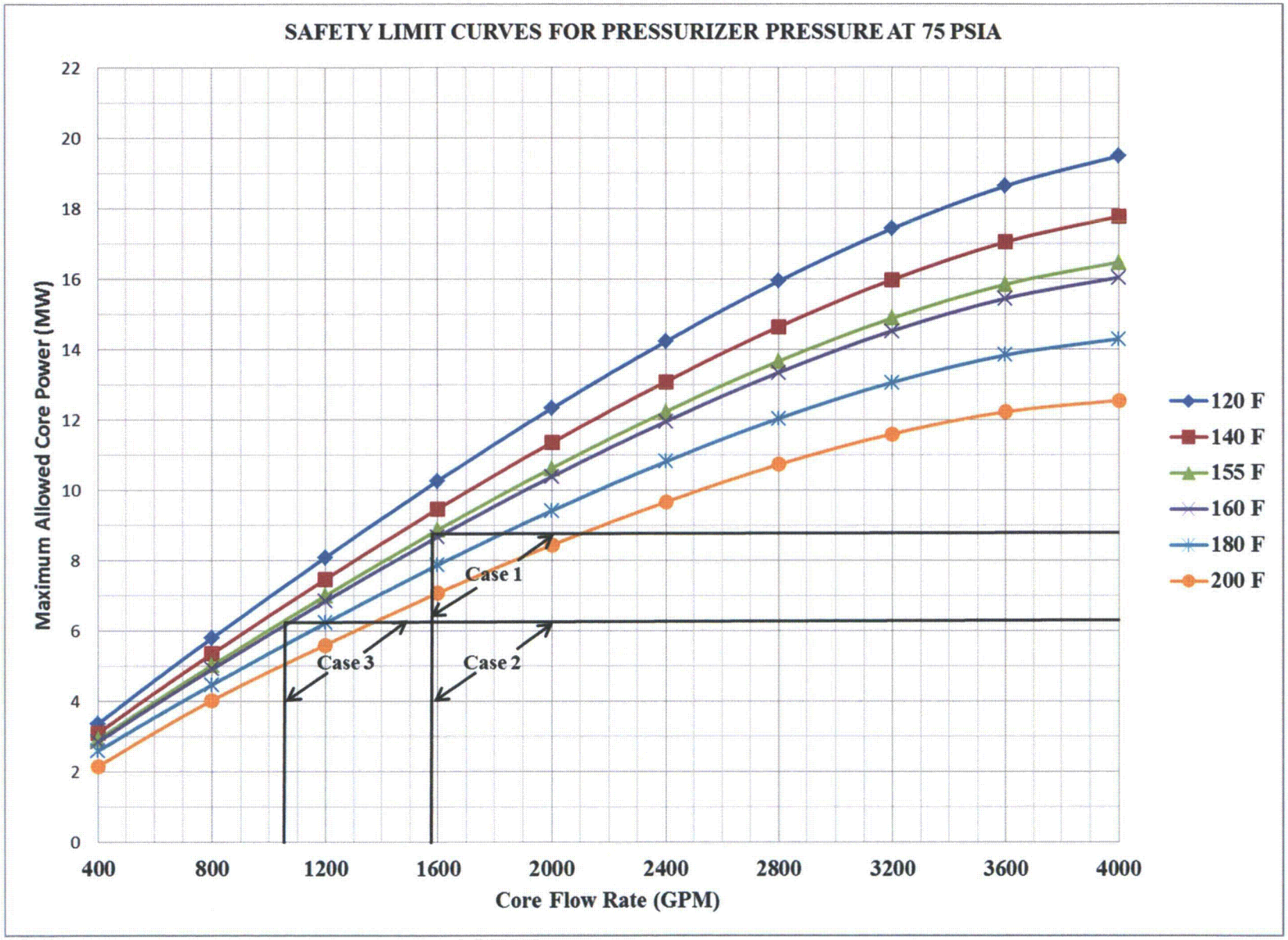


Figure H.2 – MURR CHF Curve Mode II Operation for Pressurizer Pressure at 75 PSIA

1 predicts CHF at 8.766 MW, i.e. 2.516 MW above the LSSS of 6.25 MW for Mode II. Case 2 results indicate that the reactor could be operated with a reactor inlet water temperature of 219 °F for Mode II before reaching CHF. Case 3 shows CHF occurring only with total core flow reduced to 1045 gpm or 530 gpm less than a core flow rate of 1575 gpm. Thus the safety margin is 34% of the 1575 gpm core flow rate corresponding to the LSSS flow value for Mode II operation as compared to 23% for Mode I operation.

The LSSS for pressurizer pressure is 75 psia; a margin of 17 psi above the 58 psia where CHF is predicted to occur in Mode I with reactor power raised to the LSSS and reactor inlet water temperature and flow rate reduced to their LSSS values. For Mode II, there is a 36 psi margin above the 39 psia where CHF is predicted to occur. Past operating experience has shown the pressurizer sensors to be accurate within ± 2 psi. Additionally, there are four independent sensors capable of causing a reactor scram in the event of a loss of pressure transient, thus there is sufficient margin to insure that the low pressure safety limit will not be violated.

Therefore the LSSSs on the four (4) important parameters of reactor power, primary coolant pressurizer pressure, primary coolant flow rate, and reactor inlet water temperature are easily capable of causing the reactor to scram and prevent a violation of the safety limit envelope.

TECHNICAL SPECIFICATION

UNIVERSITY OF MISSOURI
RESEARCH REACTOR FACILITY

SUBJECT: Reactor Core Safety Limit

Applicability

This specification applies to reactor power and reactor coolant system flow temperature and pressure.

Objective

The objective is to set forth parameter safety limits which shall prevent damage to the fuel element cladding.

Specification

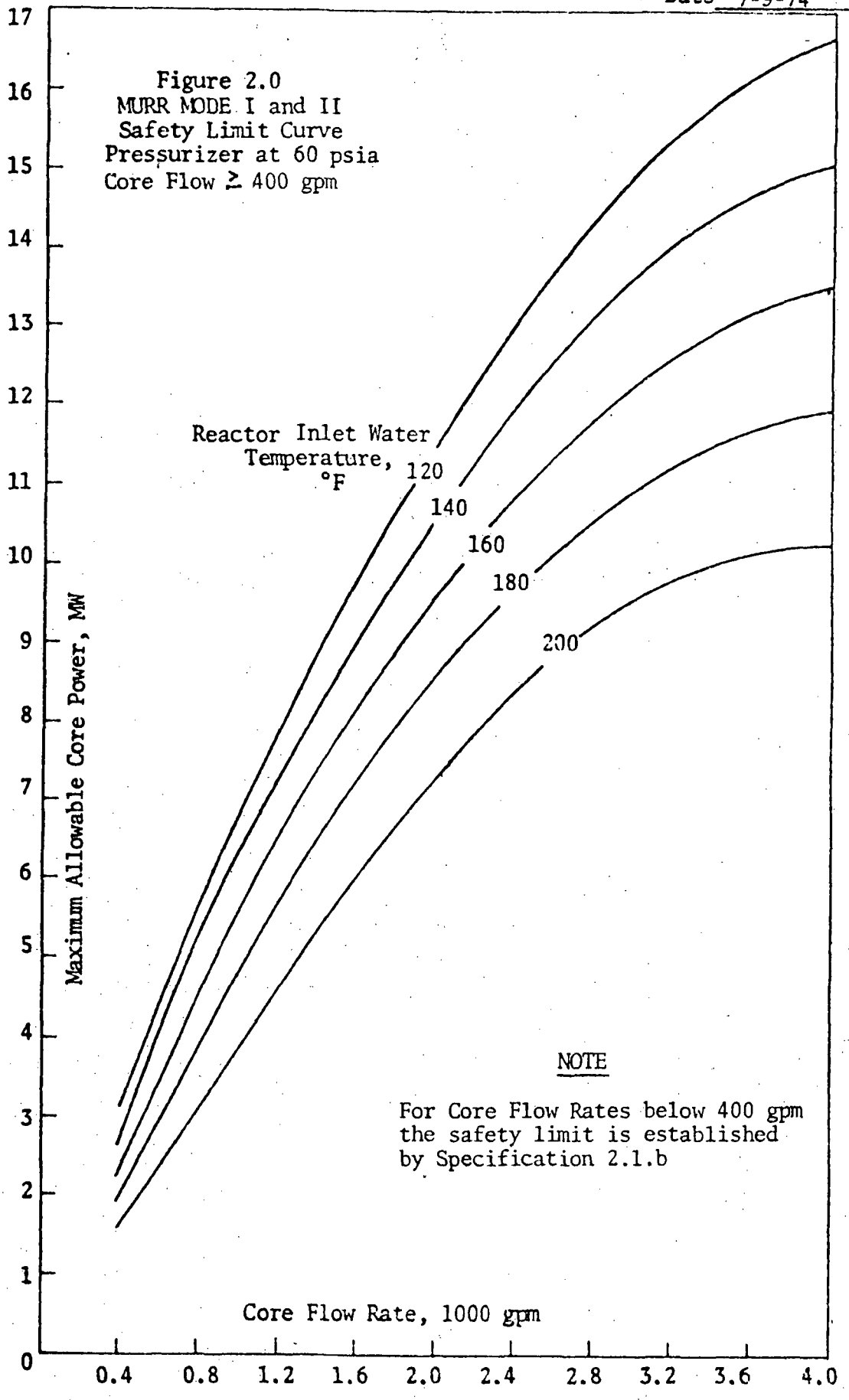
Reactor power, coolant system flow, temperature and pressure shall not exceed the following limits during reactor operation.

a. Mode I and II (Core Flow Rates $\geq$ 400 gpm)

The combination of the true values of the reactor power level, core flow rate, and reactor inlet temperature shall not exceed the limits described by Figures 2.0, 2.1, and 2.2. The limits are considered exceeded if, for flow rates greater than 400 gpm, the point defined by the reactor power level and core flow rate is at any time above the curve corresponding to the true values of the reactor inlet temperature and primary coolant system pressurizer pressure. To define values of the safety limits for

Date 7-9-74

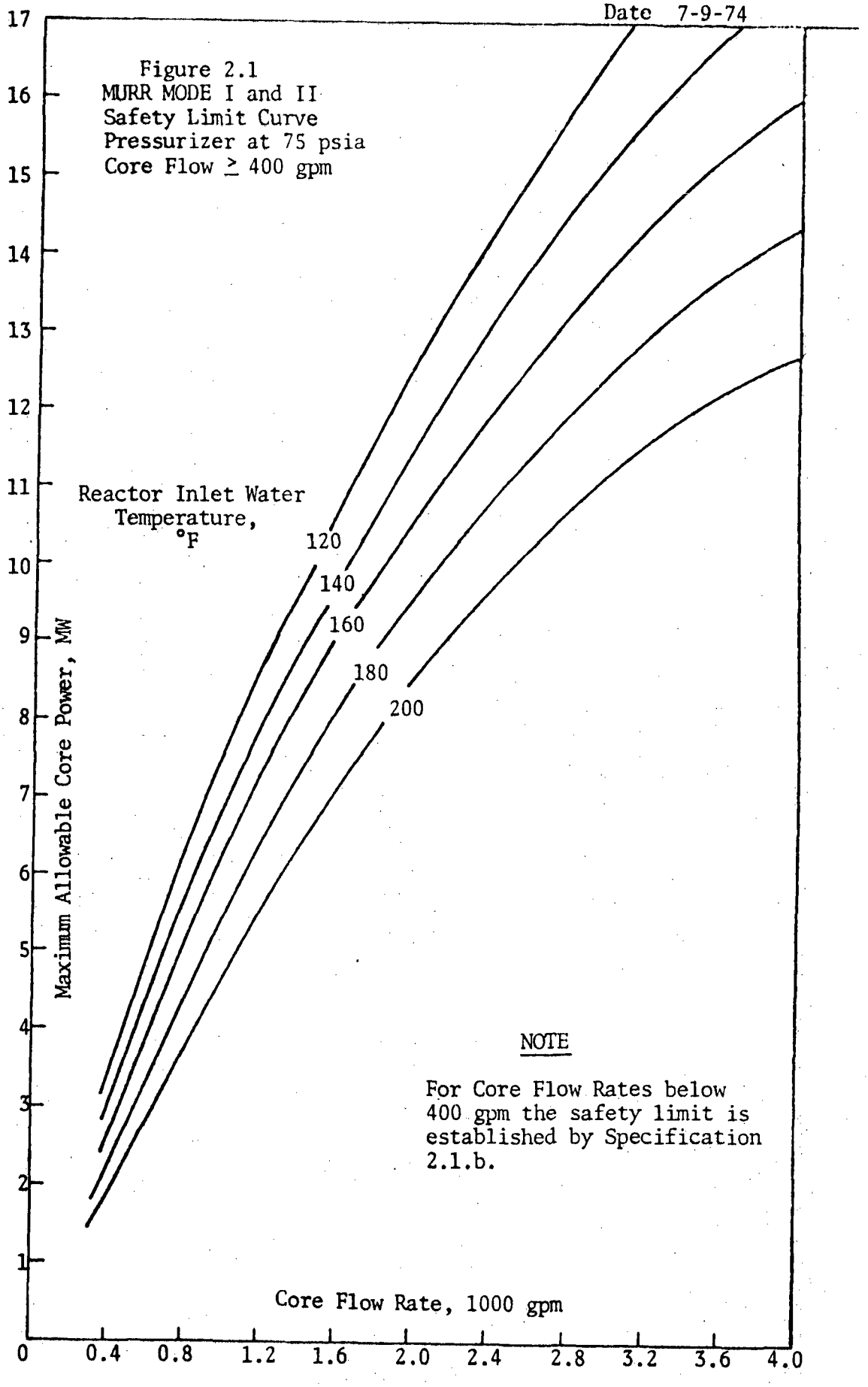
Figure 2.0
MURR MODE I and II
Safety Limit Curve
Pressurizer at 60 psia
Core Flow ≥ 400 gpm



NOTE

For Core Flow Rates below 400 gpm the safety limit is established by Specification 2.1.b

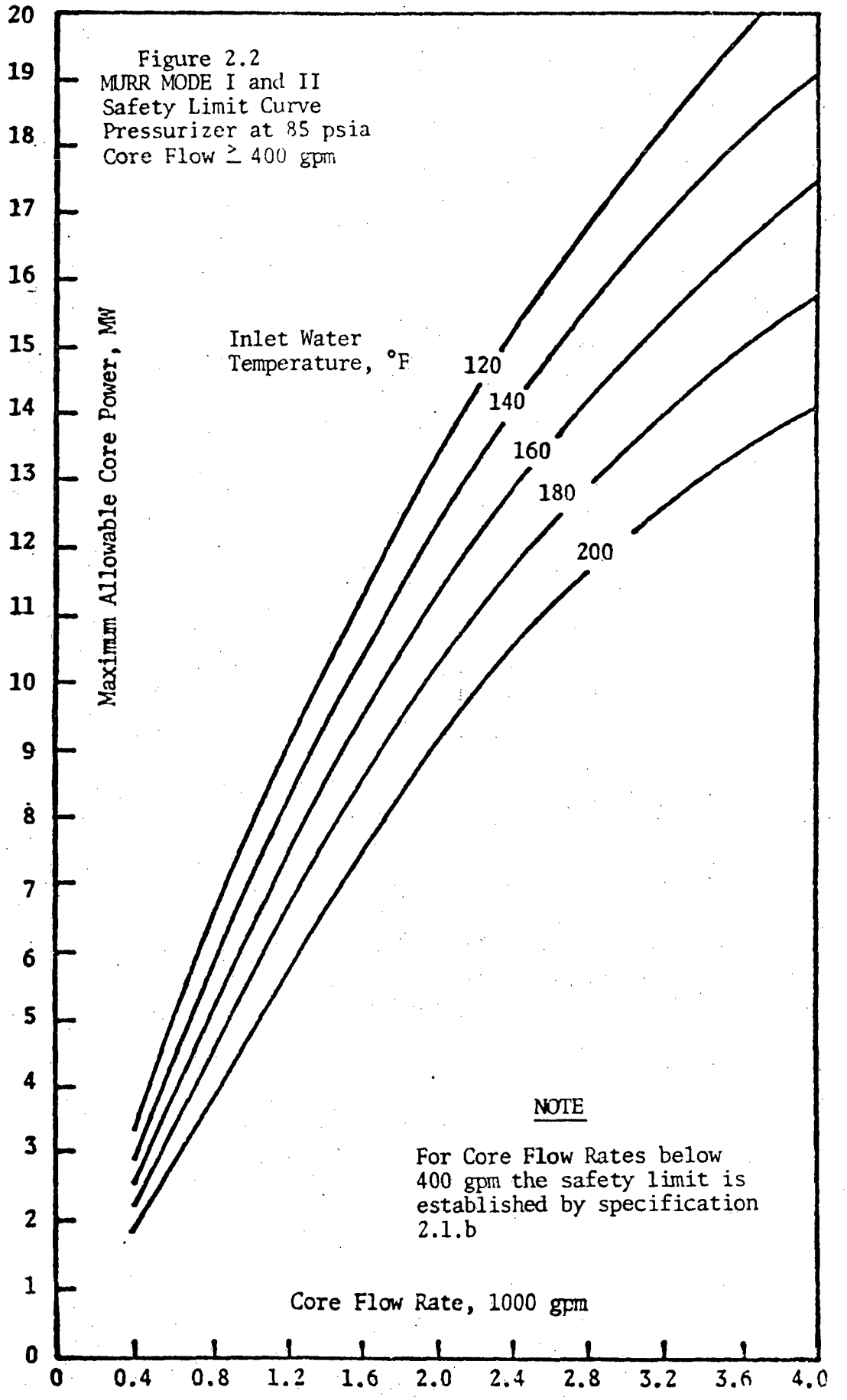
Figure 2.1
MURR MODE I and II
Safety Limit Curve
Pressurizer at 75 psia
Core Flow ≥ 400 gpm



NOTE

For Core Flow Rates below 400 gpm the safety limit is established by Specification 2.1.b.

Figure 2.2
MURR MODE I and II
Safety Limit Curve
Pressurizer at 85 psia
Core Flow ≥ 400 gpm



SUBJECT: Reactor Core Safety Limit (continued)

temperatures and/or pressures not shown in Figures 2.0, 2.1, and 2.2, interpolation or extrapolation of the data on the curves shall be used. For pressurizer pressures greater than 85 psia the 85 psia curves (Figure 2.2) shall be used and no pressure extrapolation shall be permitted.

b. Mode I and II (Core Flow Rates < 400 gpm)

Steady state power operations in Modes I and II is not authorized for a core flow rate < 400 gpm. Reactor operations with core flow below 400 gpm will occur only after a normal reactor shutdown when the primary coolant pumps are secured or following a loss of flow transient. Under the above conditions the maximum fuel cladding temperature shall not exceed 366°F.

c. Mode III

Reactor Power . . . . . 150 Kilowatts (maximum)

Bases

a. A complete safety limit analysis for the MURR is presented in Appendix F of Addendum 4 to the Hazards Summary Report (HSR). An extension of this analysis is presented in Section 6 of Addendum 5 to the HSR. A family of curves is presented which relate the reactor inlet water temperature and core flow rate to the reactor power level corresponding to a DNB ratio (DNBR) of 1.2 based on burnout heat flux data experimentally varified for ATR type fuel elements. Curves are presented for pressurizer pressures of 60, 75, and

SUBJECT: Reactor Core Safety Limit (continued)

85 psia. The safety limits were chosen from the results of this analysis for Mode I and II operation, i.e., forced convection operation above 400 gpm flow.

b. Steady state reactor operation is prohibited for core flow rates below 400 gpm by the low flow scram settings in the safety system. The region below 400 gpm will only be entered following a reactor shutdown when the primary coolant pumps are secured or during a loss of flow transient where the reactor scrams, the flow coasts down to zero, reverses, and natural convection cooling is established. Below 400 gpm core flow the criterion for the safety limit is that the fuel plate temperature must be below that temperature which would result in fuel cladding failure. The analysis of a loss of flow transient from the ultra-conservative conditions of 11 MW of power, 3000 gpm core flow and 155°F core inlet temperature indicated a maximum fuel cladding temperature of 327°F which is well below the cladding DNB temperature of 366°F.

c. Analysis of natural convection cooling of the core (Mode III operation) is presented in section 5.5.3 of the HSR.

TECHNICAL SPECIFICATION

UNIVERSITY OF MISSOURI RESEARCH REACTOR FACILITY

Number 2.1

Page 1 of 6

Date

SUBJECT: Reactor Core Safety Limit

Applicability

This specification applies to reactor power and reactor coolant system flow, temperature and pressure.

Objective

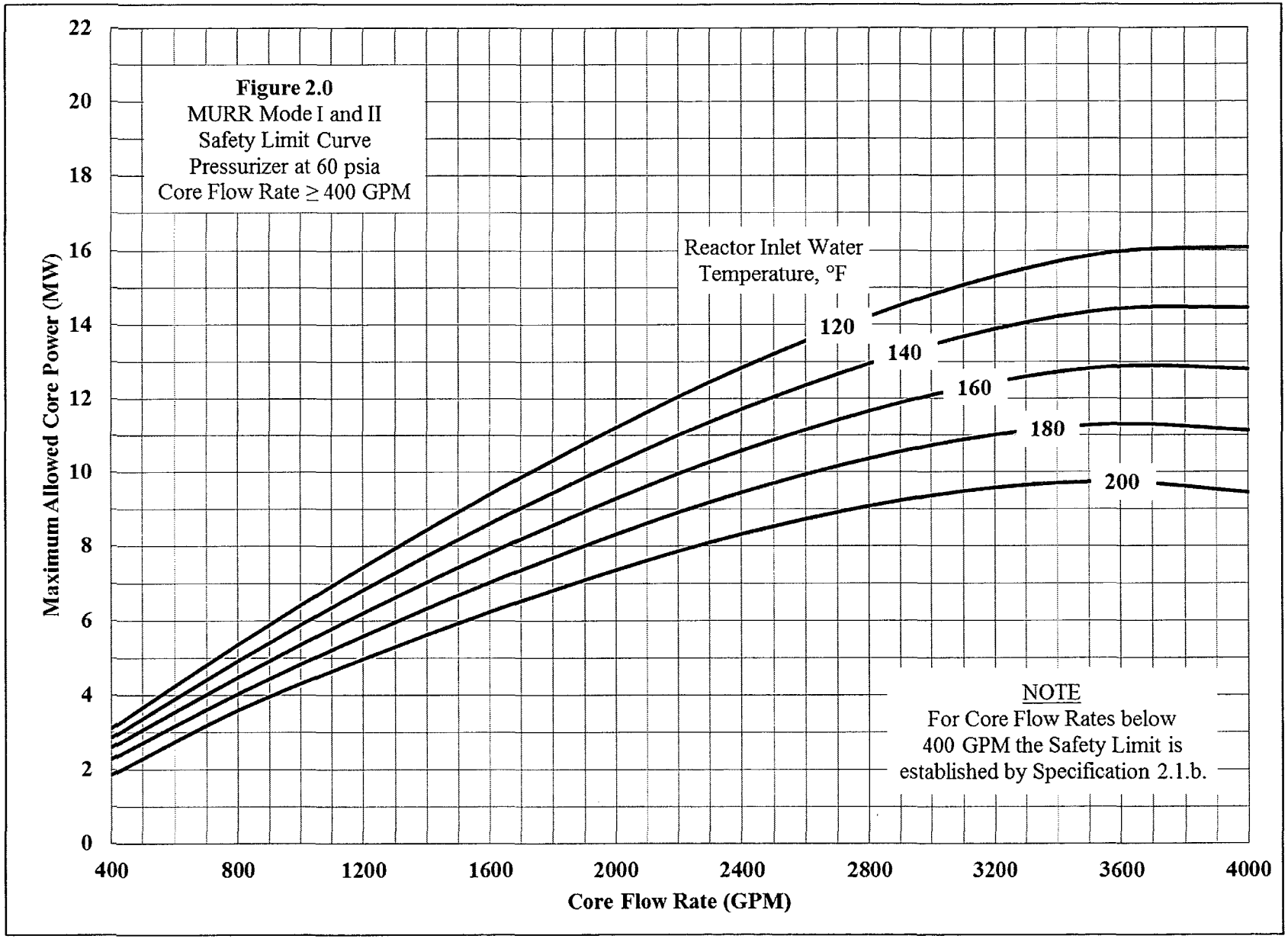
The objective is to set forth parameter safety limits which shall prevent damage to the fuel element cladding.

Specification

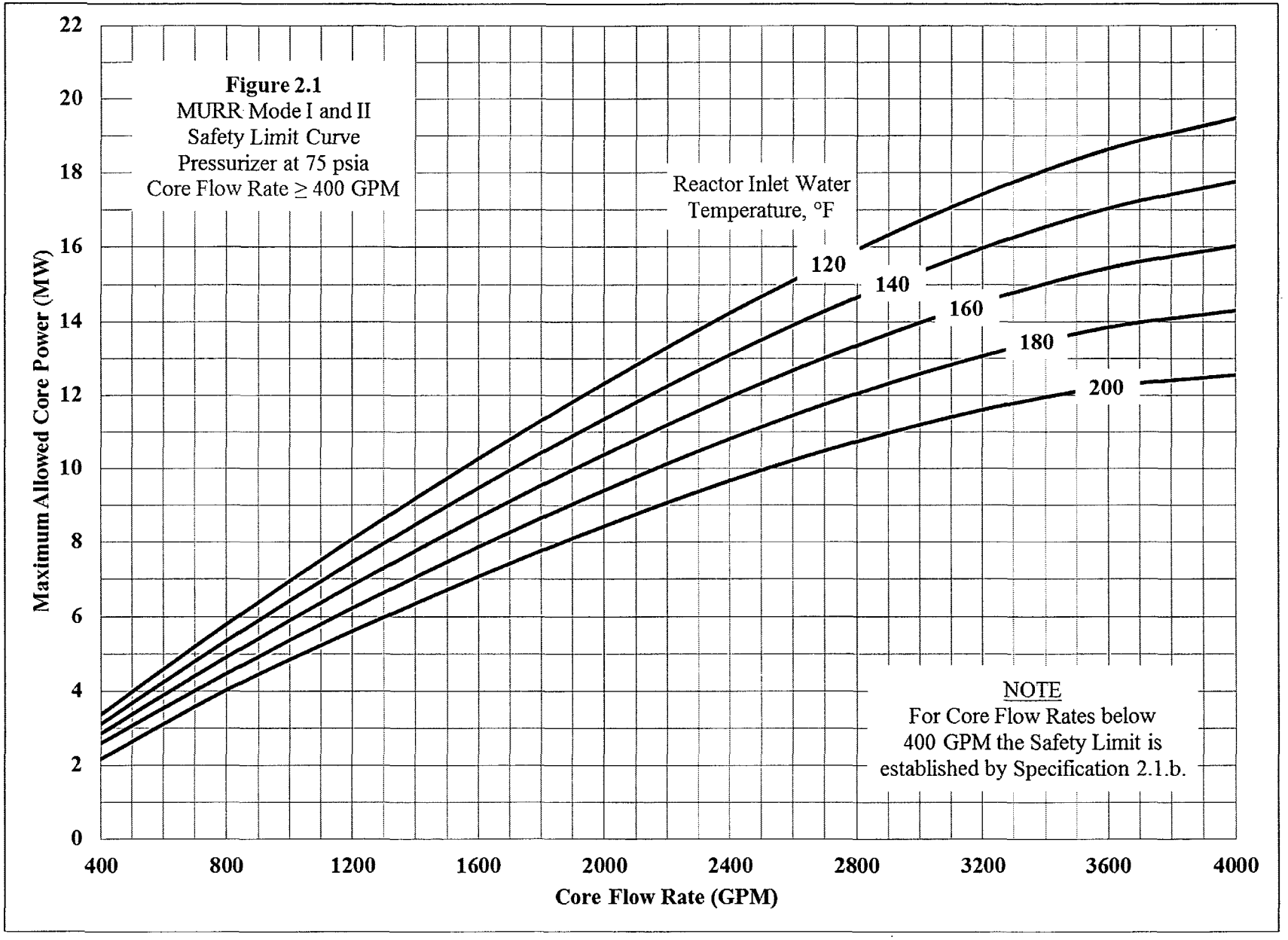
Reactor power, coolant system flow, temperature and pressure shall not exceed the following limits during reactor operation.

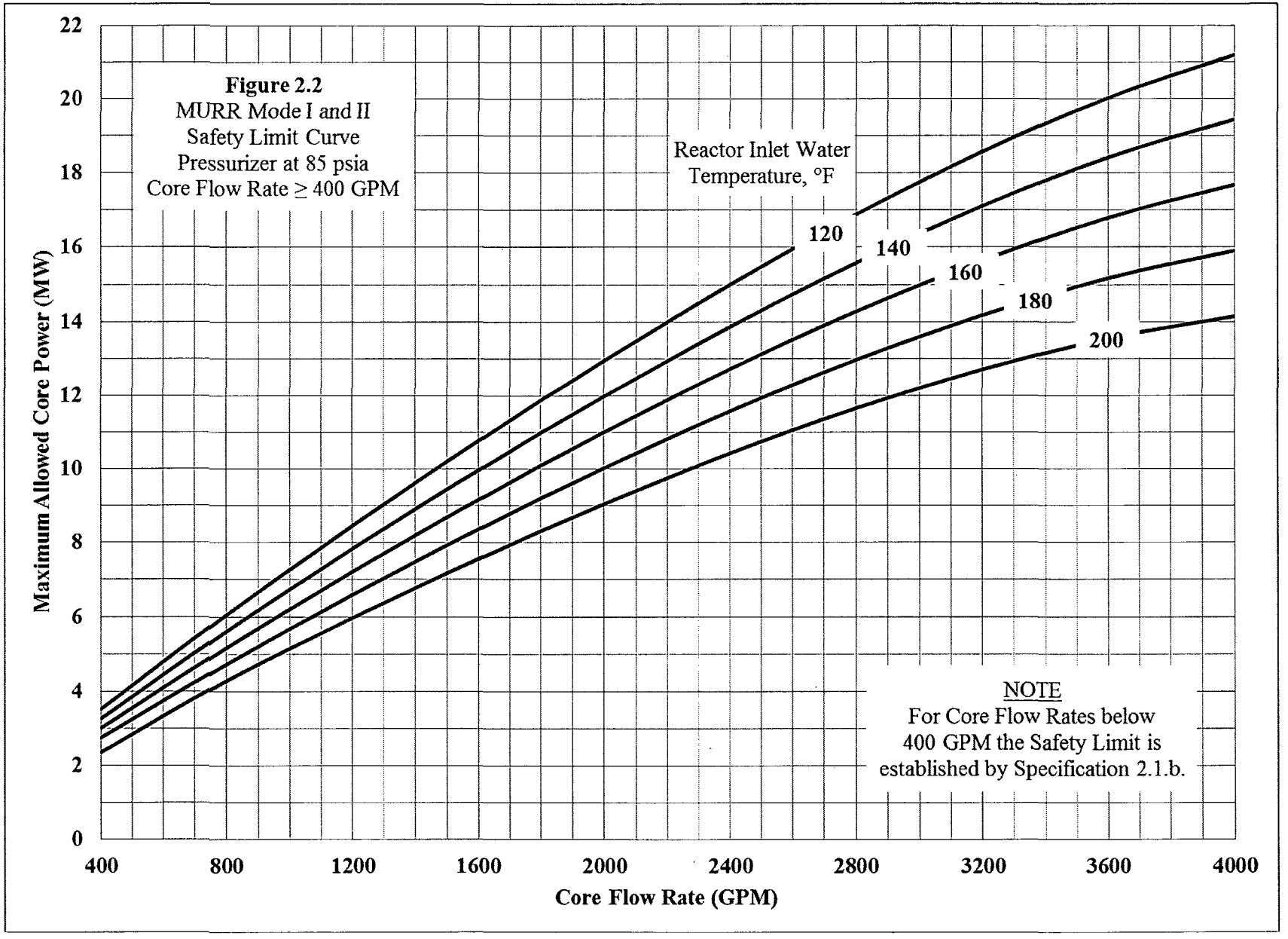
a. Mode I and II (Core Flow Rates $\geq$ 400 gpm)

The combination of the true values of the reactor power level, core flow rate, and reactor inlet water temperature shall not exceed the limits described by Figures 2.0, 2.1, and 2.2. The limits are considered exceeded if, for flow rates greater than 400 gpm, the point defined by the reactor power level and core flow rate is at any time above the curve corresponding to the true values of the reactor inlet water temperature and primary coolant system pressurizer pressure. To define values of the safety limits for



Number 2.1
Page 2 of 6
Date


Figure 2.1
MURR Mode I and II
Safety Limit Curve
Pressurizer at 75 psia
Core Flow Rate ≥ 400 GPM
Reactor Inlet Water
Temperature, °F
120
140
160
180
200
NOTE
For Core Flow Rates below
400 GPM the Safety Limit is
established by Specification 2.1.b.
Maximum Allowed Core Power (MW)
Core Flow Rate (GPM)
0
2
4
6
8
10
12
14
16
18
20
22
400
800
1200
1600
2000
2400
2800
3200
3600
4000


Figure 2.2
MURR Mode I and II
Safety Limit Curve
Pressurizer at 85 psia
Core Flow Rate ≥ 400 GPM
Reactor Inlet Water
Temperature, °F
120
140
160
180
200
NOTE
For Core Flow Rates below
400 GPM the Safety Limit is
established by Specification 2.1.b.
Maximum Allowed Core Power (MW)
0
2
4
6
8
10
12
14
16
18
20
22
400
800
1200
1600
2000
2400
2800
3200
3600
4000
Core Flow Rate (GPM)

SUBJECT: Reactor Core Safety Limit (continued)

temperatures and/or pressures not shown in Figures 2.0, 2.1, and 2.2, interpolation or extrapolation of the data on the curves shall be used. For pressurizer pressures greater than 85 psia, the 85 psia curves (Figure 2.2) shall be used and no pressure extrapolation shall be permitted.

b. Mode I and II (Core Flow Rates < 400 gpm)

Steady state power operations in Modes I and II are not authorized for a core flow rate < 400 gpm. Reactor operations with core flow below 400 gpm will occur only after a normal reactor shutdown when the primary coolant pumps are secured or following a loss of flow transient. Under the above conditions the maximum fuel cladding temperature shall not exceed 366 °F.

c. Mode III

Reactor Power.....150 Kilowatts (maximum)

Bases

a. A complete safety limit analysis for the MURR is presented in Appendix F of Addendum 4 to the Hazards Summary Report (HSR). A family of curves is presented which relate reactor inlet water temperature and core flow rate to the reactor power level corresponding to a Critical Heat Flux (CHF) ratio of 2.0 based on the Bernath CHF Correlation. This also corresponds to a flow instability Departure from Nucleate Boiling Ratio (DNBR) of 1.2 based on the burnout heat flux data experimentally verified for ATR type fuel elements. Curves are presented for pressurizer pressures of 60, 75, and 85 psia. The safety limits were

SUBJECT: Reactor Core Safety Limit (continued)

chosen from the results of this analysis for Mode I and II operation, i.e. forced convection operation above 400 gpm flow.

b. Steady state reactor operation is prohibited for core flow rates below 400 gpm by the low flow scram settings in the safety system. The region below 400 gpm will only be entered following a reactor shutdown when the primary coolant pumps are secured or during a loss of flow transient where the reactor scrams, the flow coasts down to zero, reverses, and natural convection cooling is established. Below 400 gpm core flow the criterion for the safety limit is that fuel plate temperature must be less than 900 °F; the temperature at which fuel cladding failure could occur. The analysis of a loss of flow transient from the ultra-conservative conditions of 11 MW of power, 3000 gpm core flow and 155 °F core inlet temperature indicated a maximum fuel cladding temperature of 327 °F which is well below the cladding DNB temperature of 366 °F.

c. Analysis of natural convection cooling of the core (Mode III operation) is presented in section 5.5.3 of the HSR.

ATTACHMENT 15

Argonne NATIONAL LABORATORY

Intra-Laboratory Memo

June 7, 2011

TO: John G. Stevens

FROM: Earl E. Feldman

SUBJECT: Implementation of the Flow Instability Model for the University of Missouri Reactor (MURR) That is Based on the Bernath Critical Heat Flux Correlation

IMPLEMENTATION OF THE FLOW INSTABILITY MODEL FOR THE UNIVERSITY OF MISSOURI REACTOR (MURR) THAT IS BASED ON THE BERNATH CRITICAL HEAT FLUX CORRELATION

Earl E. Feldman

Global Threat Reduction Initiative (GTRI) – Conversion Program
Nuclear Engineering Division
Argonne National Laboratory
9700 S. Cass Avenue
Argonne, Illinois 60439

ABSTRACT

A model that is based on the Bernath critical heat flux correlation and used to predict flow instability during steady-state operation of the University of Missouri Reactor (MURR) is described in detail. The model is evaluated via a computer spreadsheet, Table 8. The determination of key input data for the Table 8 model is demonstrated by a series of sample calculations shown in Tables 1 through 4. This model supersedes the model used in both References 2 and 3.

1 BACKGROUND

A key safety requirement of the University of Missouri Research Reactor (MURR) is that flow instability in the reactor core be avoided during steady-state operation. The MURR safety analysis uses the Bernath critical heat flux (CHF) correlation[1] to assess margin to flow instability.[2,3] A sufficient margin to flow instability is deemed demonstrated if the following two criteria are met: 1) the local heat flux at every location within the reactor core is no greater than half of the local value of critical heat flux based on the Bernath correlation and 2) there is no bulk boiling at the exit of any coolant channel. Except for conditions of very low flow rates and high coolant inlet temperatures, the first criterion is the more restrictive one.

A computer spreadsheet model based on the above criteria has been developed to determine the margin to flow instability for any MURR reactor core coolant channel. The purpose of this report is to describe the model and its implementation.

Another safety requirement of the MURR reactor is that an adequate margin to CHF is always maintained. The power at which the Bernath correlation predicts CHF to occur is always at least double the maximum reactor power allowed by the MURR flow instability criteria.

2 USE OF THE BERNATH CHF CORRELATION FOR THE MURR APPLICATION

The Bernath Correlation is given by:

$$
\begin{aligned}
&(Q/A)_{BO} = h_{BO}\left(T_{w_{BO}} - T_b\right) \\
&h_{BO} = 10890\left(\frac{D_e}{D_e + D_i}\right) + (\text{slope})\ V \\
&\text{slope} = 48/D_e^{\,0.6} \quad \text{if } D_e \le 0.1\ \text{ft} \\
&\text{slope} = 90 + 10/D_e \quad \text{if } D_e > 0.1\ \text{ft} \\
&T_{w_{BO}} = 57 \ln P - 54\left(\frac{P}{P+15}\right) - \frac{V}{4}
\end{aligned}
\tag{1}
$$

where $(Q/A)_{BO}$ is the critical heat flux in p.c.u.* /hr-ft^2 (BO stands for "burnout"), h_{BO} is the heat transfer coefficient corresponding to the CHF in p.c.u./hr-ft^2-C, $T_{w_{BO}}$ is the wall temperature at which CHF occurs in °C, T_b is the local bulk coolant temperature in °C, D_e is the hydraulic diameter of the coolant passage in feet, defined as four times the channel flow area divided by the total wetted perimeter of the channel, D_i is the diameter of the heater surface in feet, defined by Bernath as the heated perimeter divided by π, P is the pressure in psia, and V is the velocity of the coolant in ft/s.

Equation (1) is a function that has five independent variables, T_b, D_e, D_i, V, and P and one dependent, or output variable, $(Q/A)_{BO}$, which is the local value of Bernath critical heat flux. In the case of the MURR reactor, D_i is the sum of the heated clad surface arc lengths of the one or two fuel plates that bound the channel divided by π. The other three quantities, T_b, V, and P vary along the length of the channel.

For normal operating conditions the pressure decreases from channel inlet to exit and is about 12 or 13 psia lower at the exit than at the inlet for a 3600 gpm flow rate. As was assumed in the 1974 analysis of the MURR reactor, [2,3] the pressure, P, at the exit will be conservatively assumed to apply to all axial levels. Using the exit pressure for all axial levels is a bounding assumption because critical heat flux increases with pressure in equation (1). Thus, only T_b and V are needed as functions of axial level. The axial distribution of T_b depends on the axial distribution of heat flux from the plates that bound the channel. Since the channel flow area does not vary with axial position, V is inversely proportional to coolant density. Because bulk boiling at the channel exit it not permitted, the bulk coolant temperature over the entire channel length is always subcooled, i.e., single-phase liquid. The relatively small variation of bulk coolant density with axial location is included in the model. A Visual Basic for Applications (VBA) program (or macro) was written to automatically execute the spreadsheet model for 60 combinations of input parameter values and record the 60 sets of results in spreadsheet tables for each pressurizer pressure.

* A p.c.u. is a "pound centigrade unit". 1 p.c.u. is equal to 1.8 Btu's.

In concept, at each axial level of each channel in the reactor core, for each heated surface the ratio of local heat flux to the Bernath CHF as defined by equation (1) would be determined for an assumed reactor power level and a specified set of the three independent variables, i.e., pressurizer pressure, core coolant flow rate, and coolant inlet temperature. Then by iteration, the assumed power level would be adjusted until the largest ratio of local heat flux to local Bernath CHF throughout the core is 0.5 or a coolant channel exit temperature reaches the saturation temperature. This would provide the maximum reactor power corresponding to the MURR Safety Limit Criteria for the three specified independent variables. In practice, a computer spreadsheet model was developed which considers only one reactor coolant channel at a time. Only the potentially limiting channels in the reactor were specifically analyzed with this model. The iteration on power level was performed automatically by the computer spreadsheet so that the desired maximum heat flux ratio of 0.499999 is achieved. Hot channel factors due to manufacturing tolerances and modeling uncertainties were included in the analysis. The safety envelope for MURR was obtained by determining the value of allowed reactor power for a range of values of pressurizer pressure, core coolant flow rate, and coolant inlet temperature.

The peaking factors for heat flux at each axial level of each fuel plate are obtained from separate detailed neutronics analysis. The Bernath CHF correlation, as is obvious from inspection of equation (1), is independent of the values of reactor heat flux. The succeeding sections describe the determination of the values of the local heat flux and the various inputs to equation (1).

3 LOCAL HEAT FLUX DISTRIBUTION

The MURR reactor core is shaped like a concentric annulus that has been formed by eight geometrically identical approximately 45° annular wedge-shaped elements. In the HEU core, each element has 24 parallel equally-spaced concentric curved fuel plates. Thus, in each element there are 23 coolant channels that have two curved fuel plates as boundaries and two end coolant channels that have only one fuel plate each as a boundary. Each end channel, which is heated by only one fuel plate, has lower bulk coolant temperatures than does its immediate neighbor, which is heated by the same fuel plate plus an additional one. Therefore, the analysis need only consider the 23 channels of each assembly that are each heated by two fuel plates. Because these 23 channels are of equal thickness, the coolant velocities are essentially the same in all 23 channels. Hence, the candidate limiting channel is selected largely by comparing nuclear power peaking factors, which characterize local and average heat fluxes and coolant channel enthalpy rise.

Identifying the most limiting channel may require assessing the margin to flow instability in several candidate channels. Of course, channels with relatively large local heat fluxes must be considered. However, channels with lesser local heat fluxes could also be limiting if their bulk coolant temperatures are relatively large and thereby lead to lower values of Bernath CHF. These would be channels where the average heat flux for each fuel plate is relatively large.

In the neutronics analysis, the heated length of the core was divided into 24 equal segments. For each fuel plate in the core, 24 values of heat flux (W/cm^2) were provided for a reactor operating power of 10 MW, one value for each of the 24 equal axial segments of the

heated length of the fuel plate. The average of these 24 values provides the average heat flux for the fuel plate. The axial heat flux distribution of each fuel plate is treated as a curve consisting of 24 uniform steps.

Table 1 provides a sample calculation which is used to demonstrate the analytical procedure for representing heat flux distribution. Columns A, B, and C of the table show the axial heat flux distribution of two consecutive plates (P01 and P02) in an element (X1). The heat fluxes shown in columns B and C were taken from the MCNP output for the week 58 HEU fuel cycle from TDR-0125[4] (the feasibility report for the conversion of the MURR core to use LEU fuel instead of HEU) with no xenon and the flux trap region only containing pool water. Since all 24 steps are of equal length, their heat fluxes can be summed and divided by 24 to obtain the average, as indicated near the bottom of the table. Obviously, plate X1P01 (column B) has the higher average and, as is obvious from the values in bold at levels 14 and 15, plate X1P01 has a higher peak heat flux than does plate X1P02. Thus, the heat flux distribution of plate X1P01 would be compared with the Bernath CHF in determining the margin to flow instability.

The axial power peaking factors for the fuel plate are obtained by dividing each of the 24 local heat flux values by the plate average heat flux value. Hence, the sum of these 24 peaking factors of the fuel plate is 24.0 and the average is 1.0. The peak of these 24 numbers is the axial peak-to-average heat flux peaking factor for the fuel plate. In Table 1, for example, the plate axial peaking factors in column D was obtained by dividing each of the corresponding 24 values in column B by the average heat flux, 129.5 W/cm^2. Column E was obtained from column C in a similar manner. The axial peak-to-average values, as shown in bold at levels 14 and 15 of columns D and E, are 1.381 and 1.378 for plates X1P01 and X1P02, respectively.

The core-average heat flux is obtained by dividing the total core power by the total core heat transfer area. The heat flux values provided by the neutronics analysis are based on the assumption that all of the reactor power, which is assumed to be 10 MW in the neutronics analysis, is deposited in the fuel plates. Since the total core heat transfer area is 17.108 m^2, the core average heat flux is 10 MW / 17.108 m^2, or 58.452 W/cm^2. The ratio of the plate average heat flux to the core average heat flux is called the "plate peaking factor". Thus, the plate peaking factor for plate X1P01 is 129.5/58.46, or 2.215. Candidate limiting channels must include those channels with the higher associated plate peaking factors.

The variation of heat flux along the azimuthal direction of each fuel plate is also taken into account. In the neutronics analysis the heated arc length along the azimuthal direction of each fuel plate is divided into a series of nine equal-radian arc length vertical strips. The average heat flux of each strip is calculated. The ratio of the highest of these nine averages to the plate-average heat flux is called the "azimuthal peaking factor". The heat fluxes provided for each level in columns B and C of Table 1 are level-averaged values rather than level azimuthal maxima.

The computer spreadsheet model does not consider the individual strips of each fuel plate. Instead, in the model, the power of each fuel plate is increased by its azimuthal peaking factor. This approach produces bounding values of local bulk coolant temperature because no credit is taken for azimuthal heat conduction in the fuel plates or azimuthal mixing in the coolant

channels. The hottest strip of each of the two fuel plates on either side of a coolant channel is located directly across from each other. As shown in the Table 1 sample calculations, the azimuthal peaking factors for plates X1P01 and X1P02 are 1.07 and 1.12, respectively.

In the MURR, a significant fraction, 7%, of the fission power from the fuel escapes the core as gamma or neutron radiation without creating heat in the fuel plates or in the primary coolant. Therefore, only 93% of the power contributes to the fuel plate heat fluxes and heats the primary coolant. Because all of the values of heat flux provided in columns B and C of Table 1 are based on 100% of the 10-MW core power, as is the average core heat flux of 58.452 W/cm^2, a 0.93 factor is included in the determinations of channel heat fluxes and power.

In the safety limit analysis, at each axial level of the channel, the Bernath CHF value is determined and compared with the higher of the two corresponding plate heat fluxes. In practice, this can be accomplished by using the heat fluxes of the plate with the higher product of plate and azimuthal peaking factors. Table 2 provides a sample calculation of local heat flux, including hot channel factors, which are described in Section 6. In this particular calculation, the safety limit was found to be at 14.894 MW and the limiting axial location was level 18 of the 24 axial levels. This location had the highest ratio of local heat flux to Bernath CHF based on the corresponding axial bulk coolant temperature. This heat flux ratio was 0.499999 because in the computer spreadsheet analysis the target value was set 0.499999 in order to always guarantee that the calculated maximum value would never exceed or even reach 0.5. If a different axial level were chosen for the sample calculation, the plate axial peaking factor for that other level would have been used in place of the 1.296 values shown in bold in Table 2.

4 RELATIVE DISTRIBUTION OF CHANNEL BULK COOLANT TEMPERATURE RISE

The relative distribution of bulk coolant temperature rise from the inlet to the channel to its exit is dependent on the heat flux distributions of the two fuel plates that bound the channel. In the determination of the channel bulk coolant temperature, it is assumed that the power of each fuel plate is equally divided between the two coolant channels on each side of the fuel plate. Each of the two plates that bound a coolant channel is assumed to contribute half of its power to heat the bulk coolant of the channel. This is conservative since the other channel heated by each of the two fuel plates that bound the hot channel is cooler than the hot channel and would remove slightly more than half of the heat from the common fuel plate. Thus, for each axial level the heat flux used in determining the rise in bulk coolant temperature is the average – for the two fuel plates that bound the channel – of the product of the plate axial peaking factor at the axial level, the plate peaking factor, and the azimuthal peaking factor.

For example, column F of Table 1 is a weighted average of columns D and E. For each level, half of the column D value times its plate peaking and azimuthal peaking factors (2.215 and 1.07, respectively) was added to half of the column E value times its plate peaking and azimuthal peaking factors (1.754 and 1.12, respectively) to obtain the value in column F. The sum of the values for the 24 levels in column F, 52.01, is shown at the bottom of column F. Column G is the fraction of the channel bulk coolant temperature (or enthalpy) rise that occurs

over each level and was obtained by dividing each of the 24 level values in column F by this sum. Column G sums to 1.000, or 100%.

It is worth noting that in column F of Table 1 the slight difference in fuel meat centerline arc lengths between the two fuel plates bounding the channel is ignored, thereby avoiding additional complexity. When this arc length difference is included, for the two innermost (smallest radius) plates, which are the two being considered here that bound channel 2, 48.5 % of the smaller radius plate and 51.5% of the larger radius plate would be used instead of 50.0% of each. Combining the plate peaking and azimuthal peaking factors for the two plates with a 50/50 split produces $0.500 \times 2.215 \times 1.07 + 0.500 \times 1.754 \times 1.12 = 2.1673$. Combining the plate peaking and azimuthal peaking factors for the two plates with a 48.5/51.5 split produces $0.485 \times 2.215 \times 1.07 + 0.515 \times 1.754 \times 1.12 = 2.1612$. The latter result is 0.3% smaller than the former. Thus, the difference in results is extremely small. The use of a 50/50 split is more limiting when the product of plate peaking and azimuthal peaking factors for the smaller radius plate is greater, as it is here. The effect of the difference in plate arc lengths gets smaller with increasing plate radius. For the two plates with the largest radii the weighting is 49.4/50.6.

In the analysis, the bulk coolant temperature at the exit of each of the 24 axial levels is needed. Therefore, for each axial level, the sum of all of the column G power fractions from level 1 through the level of interest must be determined. This sum of power fractions is shown in column H. For example, the value at level 5 in column H is the sum of the column G values for levels 1 through 5. When the channel bulk coolant inlet and outlet temperatures are known, then the fractions in column H can be used to obtain the channel bulk coolant temperatures at the exits of the other 23 axial levels. Thus, the temperature at each axial level is the inlet temperature plus the product of the column H value for that level and the hot channel bulk temperature rise. The determination of the increase in bulk coolant temperature between the channel inlet and the channel exit is described in the next section.

5 CHANNEL BULK COOLANT TEMPERATURES

The channel bulk coolant inlet temperature is the same as that for the core. As in the 1973 analysis of the core[2], the channel bulk coolant temperature rise is obtained from the core average value. The core average value is the core power divided by the product of core flow rate and coolant specific heat capacity at constant pressure, which in the analysis is taken to be 4.19 kJ/kg-C. Table 3 provides a sample calculation of channel bulk coolant temperature at the exit of axial level 18 for the channel bounded by plates X1P01 and X1P02. The same methodology is applicable to all other locations in the core where a channel is bounded by two fuel plates. The sample calculation includes the hot channel factors that are described in the next section.

6 HOT CHANNEL FACTORS DUE TO MANUFACTURING TOLERANCES AND OTHER UNCERTAINTIES

Manufacturing tolerances and modeling and other uncertainties can impact heat fluxes and flow rates. Past practice in MURR safety analysis[2] has been to take a bounding approach in the analysis by assuming that the most adverse extreme of each tolerance or modeling uncertainty that is considered simultaneously impacts the most limiting locations in the core.

This approach to error propagation leads to a multiplication of hot channel factors rather than a statistical combination of these factors.

Manufacturing tolerances can cause the as-built channel to be thinner than the nominal channel. A thinner channel will have a lower velocity than its nominal counterpart and its flow rate will be smaller due to both the lower velocity and smaller flow area. This is taken into account in the analysis by assuming that the limiting channel is the thinnest that is allowed by the channel thickness tolerance. For the MURR HEU core, the spacing between fuel plates is 0.080±0.008 inches. Thus, the nominal channel thickness is taken to be 0.080 inches and the hot channel thickness is taken to be 0.072 inches.

Glasstone and Sesonske[5] provide a derivation for the relationship between the hot channel velocity, V_H, and the nominal channel velocity, V_N. In this derivation, they use the Blasius formula for friction factor for turbulent flow for which friction factor is inversely proportional to Reynolds number raised to the 0.25 power, i.e., $f \propto 1/Re^{0.25}$. If one uses their derivation and substitutes α for 0.25, one obtains the following relationship:

$$\frac{V_H}{V_N} = \left(\frac{D_H}{D_N}\right)^{\frac{1+\alpha}{2-\alpha}} \tag{2}$$

where D_H and D_N are the hydraulic diameters of the hot and nominal channels, respectively. The same relationship is also provided by Woodruff[6]. Since the ratio of the thickness to the arc length of the coolant channel is very small, the hydraulic diameter can be approximated as twice the thickness. Thus, the ratio D_H / D_N = 0.072/0.080 = 0.90. For α = 0.25, the exponent in equation (2) is 1.25/1.75 = 5/7 and the V_H/V_N, which is the hot channel factor for velocity is 0.928. In the analysis, however, a smaller values, 0.9108, is used. This was obtained by using the calculated hydraulic diameter of the narrowed limiting channel, channel 2, for D_H and the core average hydraulic diameter, which is 4 times the total core flow area divided by the total core wetted perimeter, for D_N. Hence, in the calculation D_H is 0.13876 inches, D_N is 0.15828 inches. As in Reference 5, the $5/7^{th}$ exponent is rounded off to 0.71. There, V_H/V_N is $(0.13876 / 0.15828)^{0.71} = 0.9108$.

Channel flow rate, W, is the product of channel density, velocity, and flow area. Differences in average coolant density between the hot and the nominal channels are relatively small. If these differences are ignored then:

$$\frac{W_H}{W_N} = \frac{V_H \times A_H}{V_N \times A_N} = \frac{V_H}{V_N} \times \frac{A_H}{A_N} \tag{3}$$

where W_H and W_N are the flow rates of the hot and nominal channels, respectively, and A_H and A_N are the flow areas of the hot and nominal channels, respectively. The area ratio, A_H/A_N is equal to the ratio of the channel thickness, or 0.072/0.080 = 0.90. Since V_H/V_N is 0.9108, W_H/W_N, which is the hot channel factor for flow, is $0.9108 \times 0.90 = 0.8197$.

The average density of U^{235} in the fuel matrix of the plate has a tolerance that affects plate power and heat flux. The power produced by the plate is proportional to its U^{235} density. If both plates that bound a channel are at their upper limits of U^{235} density in the fuel matrix, then the channel power increase due to this effect will be at its maximum. For example, if both plates have average fuel densities that are 3% above their nominal values, as is assumed in the current analysis, then the channel power, bulk coolant temperature rise, and average heat flux will be 3% higher. The assumption that both plates are at the upper limits of this tolerance is a bounding one.

Another manufacturing tolerance that applies to power is the fuel meat thickness. Sometimes there can be relatively large local variations in thickness in a fuel meat whose average thickness is close to its nominal value. The local variations in thickness directly impact the local heat flux, but have little impact on the bulk coolant temperature. Therefore, two hot channel factors can be used to represent the variations in fuel meat thickness – a relatively large factor, such as 1.15, which is applied to the local heat flux calculation, and a relatively small hot channel factor, such as 1.03, which would be applied to bulk coolant temperature rise. These are the values that are used in the current analysis and are consistent with Vaughan[2].

The sample calculations in Tables 2 and 3 include an "additional allowable peaking factor" of 1.062 in the overall power peaking factors for heat flux and enthalpy rise. This calculates the total overall peaking factor with which a MURR core can safely operate.

7 CHANNEL BULK COOLANT VELOCITY

The velocity at the inlet to the limiting channel is calculated as V_H of equation (2) in section 6, where V_N is the average inlet velocity for the entire reactor core and D_H, D_N, and the exponent $(1+\alpha)/(2-\alpha)$ are 0.13876, 0.15828, and 0.71, respectively, as explained in section 6. The channel velocity gradually increases from the inlet to the outlet of the channel due to the small reduction in coolant density with increasing coolant temperature. Flow rate is the product of local coolant density, flow area, and local coolant velocity. Since the flow area is assumed uniform over the entire channel length, local velocity is inversely proportional to local coolant density. Table 4 provides a sample calculation of local coolant velocity in a limiting channel at level 18.

8 CHANNEL EXIT COOLANT PRESSURE

For the analysis the pressure between the fuel plates at the exit of the limiting fueled channel is needed. The MURR technical specifications specify the minimum allowed pressure at the reactor pressurizer. Thus, a model is needed to determine the pressure drop from the pressurizer to the exit of the limiting channel. This pressure drop depends on flow rate and coolant temperature. Coolant temperatures in the core are a function of core inlet temperature, flow rate, and power.

The model provided by Reference 2 for the pressure drop from the pressurizer to the core exit was investigated by J. C. McKibben of MURR. Through measurements and analysis during March through May of 2011 he made substantial improvements to the determination of this

pressure drop. Since a formal document describing his work is not available at this time, an overview, based on discussions with him, will be presented here and will be contrasted with the Reference 2 model, which has been used for MURR safety analysis in the past.

In the Reference 2 model the path from the pressurizer to the core exit is divided into 13 parts. Each part is called a component. Each component has a single flow path or consists of two identical parallel paths. Each component has the same total flow rate. The coolant temperature through the first 12 components, which lead up to the core inlet, is the inlet temperature. The 13th component is the reactor core. Its coolant temperature is taken to be the mean of the core inlet and mixed-mean coolant outlet temperatures. The required pressure drop to the core outlet is the sum of the 13 component pressure drops.

For a known coolant temperature, T_0, of 155° F at the reactor inlet (or 165° F average through the core) and a known reactor flow rate, Q_0, of 3600 gpm, assumed known component pressure drops, ΔP_0, are provided, as shown in Table 5. As the table indicates, one combined value of ΔP_0 is provided for the pressure drop across components 1, 2, and 3 taken together and another is provide for components 5 through 10. For components 1 through 4, Q_0 is shown in the table as 1800 gpm. However, as indicated in the table, for each of these components, this value is for each of two parallel paths. Thus, in the table the total flow rate, or effective Q_0, through each component is 3600 gpm. Reference 2 provides two scaling relationships that enable pressure drops, ΔP's, to be determined for other values of flow rate, Q, and coolant temperature, T. These two relationships are:

$$\frac{\Delta P}{\Delta P_0} = \left[\frac{\rho(T)}{\rho(T_0)}\right]^{1.0}\left[\frac{Q}{Q_0}\right]^{2.0} \tag{4}$$

$$\frac{\Delta P}{\Delta P_0} = \left[\frac{\rho(T)}{\rho(T_0)}\right]^{0.8}\left[\frac{Q}{Q_0}\right]^{1.8}\left[\frac{\mu(T)}{\mu(T_0)}\right]^{0.2} \tag{5}$$

where ρ is coolant density, μ is coolant dynamic viscosity. Equation (4) is for the portions of the flow path that are characterized by non-frictional losses, such as changes in flow area and/or flow direction, as opposed to being due to wall friction in a duct. Equation (5) is for portions of the path that are characterized by wall friction (frictional) losses. Components 4 and 12 are shown in Table 5 to be non-frictional. The rest, as indicated in Table 5, are frictional.

Both equation (4) and equation (5) can be derived from well-known hydraulic relationships for turbulent flow. In the derivation of equation (5) it is assumed that the friction factor is proportional to the Reynolds number raised to the −0.2 power.

For pair values of core flow rate, Q, and inlet temperature, T, equation (4) can be evaluated once for the two non-frictional components, 4 and 12, and equation (5) can be evaluated once for the all of the other components in Table 5, except for the core. For example, for a flow rate of 3200 gpm and an inlet temperature of 155° F, $\Delta P/\Delta P_0$ from equations (4) and (5) are 0.7901 and 0.8090, respectively. The corresponding pressure drop from the pressurizer to the core inlet is: 0.7901 × [0.2689 + 0.8980] psi + 0.8090 × [3.259 + 4.08 + 0.1977] psi =

0.7901 × [1.1669] psi + 0.8090 × [7.5367] psi = 7.02 psi. The value of T for the core depends on the core temperature rise, which is a function of core power, which is initially unknown.

Figure 1, which is the basis for the new model, shows a schematic representation of the piping that carries coolant flow to the reactor core. In the figure the total core flow rate is 3600 gpm. 1825 gpm enters from the left through Loop A and another 1825 gpm enters through Loop B. At point 2 50 gpm is extract from the Loop A flow and goes to the deionizer. At point 3 the remaining 1775 gpm of the Loop A flow merges with the 1825 gpm of the Loop B flow to form the combined flow of 3600 gpm that goes through the core.

The deionizer flow remains constant regardless of core flow. Thus, for a 3200 gpm core flow rate, which is the minimum allowed by the Limiting Safety System Settings (LSSS) conditions as defined by the Technical Specifications for the MURR HEU core, the 1825 gpm values in Figure 1 would be replace by 1625 gpm, 50 gpm would go to the deionizer, as before, 1575 gpm would flow from point 2 to point 3, and the core flow would be 1575 gpm + 1625 gpm, which is 3200 gpm.

For the new model J. C. McKibben used hydraulic handbook data to predict the irrecoverable pressure drops between point 1 and 5 of Figure 1. He also employed measured data taken on March 27, 2011 on the MURR plant with the eight core fuel elements in the reactor vessel with the reactor operating at 10 MW. Also, measurements were taken on March 28, 2011 with the eight core fuel elements out of the reactor vessel, but with the primary coolant system operating. The locations where pressure measurements were made are indicated in Figure 1 by the letter "P" inside a circle. The pressure difference, which is indicated in Figure 1 by "ΔP" inside a circle, was also measured. Coolant flow rate and temperatures were also measured.

J. C. McKibben used the two sets of measurements to calibrate and adjust his analytical/handbook predictions of irrecoverable pressure drop and better determine the pressure drop across the core. Then he used his benchmarked hydraulics model to produced Table 6, which is the new model equivalent of Table 5 in the Reference 2 model. In Table 6 the core reference flow rate is 3608.3 gpm instead of 3600 gpm. This is because J. C. McKibben intended that in the application of equation (5) to the core, each volumetric flow rate be evaluated at its core average density, which is taken to be the density corresponding to the average of the core inlet and outlet temperatures. Thus, for a reference inlet flow rate of 3600 gpm, the Q_0 is the 3600 gpm × ρ_{inlet} / $\rho_{average}$, where ρ_{inlet} and $\rho_{average}$ are the inlet and average density of the coolant, respectively. Hence, the reference flow rate for the core, Q_0, is 3608.3 gpm instead of 3600 gpm. Similarly, if the actual core inlet flow rate is 3200 gpm, then Q for the core in equation (5) is 3200 gpm increase by a factor of the ratio of inlet and average core coolant densities.

Since there was no measurement at point 5 of Figure 1, J. C. McKibben deliberately overestimated the pressure drop up to point 5 so that the pressure predicted at point 5 would tend to be lower and more limiting than it would otherwise be. Thus, his approach was to deliberately err on the safe side where there is uncertainty. In the new model equations (4) and (5) are used in the same manner that they are used in the Reference 2 model, except that in the new model Q for the core corresponds to the core average density rather than the inlet density.

The nitrogen gas pressure inside the pressurizer is the measured pressurizer pressure used in the operation of the reactor. A 2-inch diameter pipe connects the bottom of the pressurizer to the 8-inch diameter Loop A pipe at point 1. Point 1 is 608 feet and 6 inches above sea level. The nominal level of the water in the pressurizer is 48 inches below point 1. The primary charging pump starts adding water to the pressurizer when the level gets down to 6 inches below the nominal value. If the pressurizer level falls so that it is 16 inches below its nominal value, a scram is initiated. The beginning of the reactor fuel plates at the core inlet is 15.25 inches below point 1. The exit of the core fuel plates, which is taken to be the core exit, is 25.5 inches below the core fuel plate inlet. These dimensions are important in the new model because it includes pressure differences due to gravity heads. The temperature in the pressurizer and in the 2-inch diameter pipe between the pressurizer and point 1 is taken to be 85° F in the analysis. For the analysis, the most limiting pressurizer level allowed was used. This level is the scram level, which is 64 inches below point 1. For the reactor at the LSSS limiting condition of flow rate, pressure, and inlet temperature (3200 gpm, 75 psia at the pressurizer, and 155° F) and a core power of 14.894 MW, which is the core power at which the new model predicts flow instability to occur, the inclusion of the gravity heads in the model causes a 0.867 psi reduction in core exit pressure. This effect was not included in the Reference 2 model.

For a core flow of 3200 gpm, the flow velocity in Loop A in the 8-inch pipe at point 1 is 10.4 ft/s and the core average velocity between the fuel plates at the core exit, point 5 in Figure 1, is 21.1 ft/s. The new model uses Bernoulli's equation to determine the decrease in pressure caused by increasing the fluid velocity from 10.4 ft/s second to 21.1 ft/s. This effect is included in the new model, but not in the Reference 2 model. For the reactor at the LSSS limiting condition of flow rate, pressure, and inlet temperature and a core power of 14.894 MW, this effect causes a 2.18 psi reduction in pressure at the core exit.

For the reactor at the LSSS limiting condition of flow rate, pressure, and inlet temperature and a core power of 14.894 MW, the irrecoverable pressure drop[†] from point 1 of Figure 1 to the point 4 is 7.02 psi in the Reference 2 model and 7.87 psi in the new model and the core (frictional) pressure drop is 9.90 psi in the Reference 2 model and 10.39 in the new model. These four pressure drop values are obtained by using equations (4) and (5) to scale the pressure drops of Table 5 or 6. Thus, the irrecoverable pressure drop from point 1 to the core exit, point 5, is 7.87 + 10.39, or 18.26 psi, in the new model, which is to be compared to 7.02 + 9.90, or 16.92 psi, in the Reference 2 model. Hence, the irrecoverable pressure drop from point 1 to point 5 is 1.34 psi greater in the new model. When this greater pressure drop is combined with the two pressure drops not included in the Reference 2 model, which are the 0.87 psi pressure drop due to gravity heads and the 2.18 psi pressure drop due to velocity increase, the new model predicts a core exit pressure of 75 − 18.26 − 0.87 − 2.18, or 53.7 psia, which is 4.4 psi lower than the 75 − 16.92, or 58.1 psia, of the Reference 2 model. If the pressure at the core exit were to be increased by 4.4 psi to 58.1 psia, the allowed reactor power for the LSSS limiting condition of flow rate, pressure, and inlet temperature would be increased by 0.51 MW to 15.4 MW.

[†] Irrecoverable pressure drops include the non-frictional pressures drops that employ the scaling equation (4) and the frictional pressure drops that employ the scaling equation (5). They do not include the recoverable pressure changes due to changes in elevation or velocity.

9 AN ALTERNATIVE APPROACH TO CORE PRESSURE DROP DETERMINATION

The Bernoulli equation is $P_1 + \rho V_1^2 / 2 + \rho g Z_1 = P_2 + \rho V_2^2 / 2 + \rho g Z_2$, where P is pressure, ρ is density, V is velocity, g is acceleration due to gravity, Z is elevation and is increasing in the upward direction, and the two subscripts 1 and 2 refer to two different locations in the fluid, where 2 is downstream of 1. This equation can be modified to include the irrecoverable pressure drop between points 1 and 2 by adding a term to the right side of the equation, such as $(K + f L/D) \rho V^2 / 2$, where K is a form loss, f is the Moody friction factor, L is path length, D is path hydraulic diameter, V, is a velocity associated with K and f. In both the Bernoulli and the modified Bernoulli equations the density ρ is a constant. When differences in density are small, such as in the reactor core, some analysts still use the modified Bernoulli equation and get around the constant-density limitation by using an average density between points 1 and 2 when evaluating irrecoverable losses due to friction and when evaluating differences in pressure due to changes in elevation. This is a reasonable approach and is used in the new model.

An alternative approach for the MURR application is to apply the modified Bernoulli equation between the points 1 and 4 of Figure 1, where density is constant, and apply the integral form of the momentum equation from points 4 to 5. In this case, points 4 and 5 are located between the two fuel plates that form the limiting, or hot, channel, which is channel 2 in the analysis. These fuel plates are the two of the smallest arc length and closest to the flux trap in MURR element 1.

The limiting channel between inlet level a and outlet level b (or points 4 and 5 in Figure 1) is modeled with the integral form of the momentum equation. The control volume used in the model is the volume contained inside the wetted perimeter of the channel between levels a and b. For a steady-state process the general form of this equation is:

$$\vec{F}_S + \int_{C.V.} \vec{B}\, du = \int_{C.S.} \vec{V}\, \rho \left(\vec{V} \bullet d\vec{A}\right) \qquad (6)$$

where, the first integral is an integral over the control volume, C.V. and the second integral is an integral over the control surface, C.S. This vector force-balance equation, which can be obtained from a fluid dynamics textbook,[7] is applied here only in the vertical, or z, direction. The positive direction is chosen to be downward and in the direction of flow from point a to point b. The first term, $\vec{F}_S$, represents the sum of the forces on the control volume surface, such as those due to pressure and shear stress. The second term is an integral of all of the body forces, $\vec{B}$, such as those due to gravity, acting within the control volume. The third term is the momentum flux term and is integrated over the control surface. This term arises because equation (6) is focused on a fixed volume in space in which mass enters and leaves, rather than on a fixed mass. The z-component of the above vector equation yields:

$$A_c (P_a - P_b) - p_{wetted} \int_a^b \tau(z)\, dz + g A_c \int_a^b \rho(z)\, dz = \frac{W_c^2}{A_c} \left(\frac{1}{\rho_b} - \frac{1}{\rho_a} \right) \qquad (7)$$

where P_a and P_b are the pressure at the inlet and the outlet of channel, respectively, p_{wetted} is the wetted perimeter of the channel, $\rho(z)$ is the coolant density of the channel, which varies along the length of the channel, $\tau(z)$ is the shear stress along the perimeter of the channel, which also varies along the length of the channel, ρ_b is the coolant density at the exit of the channel, and ρ_a is the coolant density at the inlet to the channel. Both integrals in equation (7) are always positive. The negative sign ahead of the shear force term is needed because the shear forces are always in the direction opposite of the flow direction, which is the positive direction.

The first term of equation (7) is due to the pressure difference between the inlet and the outlet of the channel. The second term is due to the friction, or shear force, at the channel surfaces. These first two terms correspond to the first term of equation (6). The third term of equation (7), which is due to gravity, corresponds to the second term of equation (6). The last term of equation (7) corresponds to the last term of equation (6). This term is equal to the channel flow rate, W_c, times the exit velocity at b minus the inlet velocity at a.

The shear stress is related to the Darcy (Moody) friction factor, f, by the following relationship:

$$\tau(z) = \frac{f(z)}{8} \frac{W_c^{\,2}}{\rho(z)\, A_c^{\,2}} \tag{8}$$

The wetted perimeter and the flow area are related by the definition of hydraulic diameter. Hence:

$$p_{wetted} \equiv \frac{4\, A_c}{D_h} \tag{9}$$

where D_h is the hydraulic diameter of the channel.

Equations (7), (8), and (9) can be combined to yield:

$$P_b = P_a - \frac{W_c^{\,2}}{2\, D_h\, A_c^{\,2}} \int_a^b \frac{f(z)}{\rho(z)}\, dz + g \int_a^b \rho(z)\, dz - \frac{W_c^{\,2}}{A_c^{\,2}} \left(\frac{1}{\rho_b} - \frac{1}{\rho_a} \right) \tag{10}$$

The last three terms on the right side of equation (10) are the friction pressure drop, the gravity term, and the momentum flux term, respectively. In equation (10) W_c/A_c is the channel mass flux, G_c, which is constant along the length of the channel and is the product of the local density and local velocity. The integrals in the friction pressure drop and gravity terms can be estimated by numerical means that divide the length from a to b into smaller regions. A simpler, and reasonably accurate, approach for the MURR application is to assume that all of the fluid in the region between a and b is at a constant temperature that is the mean of the hot channel coolant inlet and the outlet temperatures.

The new model (developed by J. C. McKibben) has analogous friction pressure drop and gravity terms to those in equation (10) that are based on the average core channel rather than the hot channel. The new model uses the mean of the core inlet and outlet temperatures in

evaluating the corresponding two integrals in its model. It does not have a momentum flux term, which, as shown below, is extremely small.

In order to demonstrate that the new model produces a pressure for use with the Bernath equation, equation (1), that is at least as low as that produced by equation (10), the pressure drops over the core region that is produced by each of the two approaches will be compared for the LSSS values of flow, inlet temperature, and pressurizer pressure (3200 gpm, 155° F, and 75 psia) and a reactor power of 14.894 MW. The hot channel inlet velocity and hydraulic diameter are used in evaluating equation (10). The hot channel inlet velocity of 18.99 ft/s is the product of the core average velocity (3200 gpm divided by the 0.3419 ft^2 core flow area), 20.85 ft/s, and the hot channel factor on velocity, 0.9108. As explained in section 6 with reference to equation (2), the hot channel hydraulic diameter is 0.13876 inches.

In the new model the application of the modified Bernoulli equation to the MURR, assumes that location 1 is at point 1 in Figure 1 and location 2 is between the fuel plates and at point 5 of Figure 1. In the new model ρ and V_2 are the core-averaged exit values. The equation (10) hot channel approach assumes that in the modified Bernoulli equation location 1 is also at point 1 in Figure 1, but location 2 is between the fuel plates and at the hot channel inlet. Table 7 compares the Bernoulli velocity pressure drop term, $\rho V_2^2 / 2$, and the friction, gravity, and momentum flux, pressure drops from point 4 to point 5 of Figure 1 for the new model with those associated with the use of equation (10) to model the pressure drop across the hot channel for LSSS values of flow, inlet temperature, and pressurizer pressure (3200 gpm, 155° F, and 75 psia) and a reactor power of 14.894 MW. The hot channel modeling causes $\rho V_2^2 / 2$ to be 2.378 psi, which is lower than the new model value, 2.897 psi, by a factor of the product of the square of the hot channel factor on velocity and the ratio of the core outlet to inlet densities, or $0.9108^2 \times 968.2 / 978.4$, or 0.821.

In Table 7 the new model core friction pressure drop, 10.394 psi, is the product of 13.8049 psi, which is the component 8 reference pressure drop of Table 6, and 0.7529, which is the scale factor provided by equation (5) to correlate a the pressure drop at reference conditions of core flow of 3608.3 gpm at a core average reference temperature of 128.68° F to the pressure drop at core conditions of 3200 gpm based on the inlet temperature and the core average temperature is 170.06° F. Before equation (5) can be evaluate, the 3200 gpm flow rate must be increased by a factor of the ratio of the inlet and outlet densities, 978.4/973.5, or 1.0050, so that it corresponds the volumetric flow at the average core density. Hence, 3200 gpm × 1.0050, or 3216 gpm, is the value of Q used in equation (5).

The equation (10) friction pressure drop used the mean of the inlet and outlet temperatures of the hot channel, 68.33° C (155° F) and 118.2° C (244.8° F), respectively. This mean temperature is 93.28° C (199.90° F). The viscosity was evaluated at this temperature and, along with the hot channel mass flux and the hydraulic diameter, produced a Reynolds number of 65681. The mass flux, or flow rate divided by the flow area, G_c, 5664 kg/m^2-s, was obtained as the product of the hot channel inlet velocity and inlet density.

The hot channel relative roughness is needed to obtain the hot channel friction factor. Based on the 1989 MURR Drawing 13005, Rev. 6, Note 5, the maximum absolute roughness of

the MURR HEU fuel plate is 63 micro inches. The relative roughness, 0.0004540, is the ratio of the absolute roughness to the hydraulic diameter. This relative roughness and the 65681 Reynolds number were used in the Colebrook equation, which is the basis for the turbulent portion of the Moody diagram, to obtain a friction factor of 0.02143.

The Colebrook equation is:

$$\frac{1}{\sqrt{f}} = 2\log_{10}\left(\frac{\varepsilon/D}{3.7} + \frac{2.51}{Re\sqrt{f}}\right) \qquad (11)$$

where f is the friction factor, ε/D is the relative roughness, and Re is the Reynolds number. A solver built into the Excel computer spreadsheet program was used to evaluate the above transcendental equation for f. With the approximation of constant density and friction factor, the friction pressure drop integral of equation (10) becomes $f\,L/D\,G_c^2/(2\,\rho)$, where L is hot channel length, 25.5 inches. The hot channel friction pressure drop was found to be 9.515 psi.

As an interesting aside, the above friction pressure drop analysis for the hot channel that employed equation (11) was repeated to predict the core pressure drop at the Table 6 reference conditions of core average temperature of 128.68° F and the volumetric flow rate for this temperature of 3608.3 gpm. This temperature and flow rate, and the core hydraulic diameter, as provided above in section 6, of 0.15828 inches were used in the calculation. Since the average core pressure is close to 4 bar, the NIST steam tables were used to determine the density and the viscosity of the coolant at this pressure and 128.68° F. The Reynolds number was found to 55276. A core pressure drop, $f\,L/D\,G_c^2/(2\,\rho)$, of 12.937 psi was obtained. Equation (5) can be used to scale this pressure drop to correspond to the Table 7 conditions of 3200 gpm at 170.06° F. The equation (5) scaling factor is 0.7529 and the resultant core pressure drop is 9.740 psi. This value is very close to the hot channel pressure drop of 9.515 psi for the same Table 7 reactor conditions. This is to be expected because both pressure drops were calculated by the same method that employed the friction factor provide by equation (11) and because both the hot channel and all other core channels share common inlet and outlet plena.

The Table 6 value of core pressure drop was deduced by J. C. McKibben based on analysis of measured data taken on the MURR plant with the core in place and with the core removed. He deliberately chose a core pressure drop on the high side of the tolerance band that resulted from uncertainty in measurement and calculation. The 12.937 psi value calculated above with the aid of equation (11) is based on the common practice for turbulent flow of using the friction factor for a round duct of the same hydraulic diameter as the one being investigated. The ratio of the measure to the calculated core pressure drops is 13.8049/12.937, or 1.067. However, reference 8 provides that turbulent flow friction factors in smooth-walled rectangular ducts within ±5% of experimentally measure values can be obtained as the product of the friction factor for circular duct and the factor $(1.0875 - 0.1125 \times \alpha^*)$, where α^* is the aspect ratio of the rectangular duct. The MURR coolant channels can be approximated as rectangular ducts with aspect ratios between about 0.02 and 0.04, causing $(1.0875 - 0.1125 \times \alpha^*)$ to be between 1.085 and 1.083, respectively. When 1.083 is combined with the 12.937 psi core pressure drop calculated above, the result, 14.01 psi, is only 1.5 % greater than the 13.8049 psi deduced by J. C. McKibben and listed in Table 6. Hence, 13.8049 psi is a very reasonable value.

The gravity head term is calculated the same way in the hot channel approach as in the new model except that in the hot channel approach the density is evaluated at the mean of the hot channel inlet and outlet temperatures rather than at the mean of the core inlet and outlet temperatures. Both approaches use the same core length of 25.5 inches. The gravity head is the product of density, acceleration due to gravity, and length. The new model predicts a gravity head pressure increase of 973.5 kg/m^3 × 9.80665 m/s^2 × (25.5 in × 0.0254 m/in) / (6894.757 Pa / psi), or 0.897 psi and the hot channel approach yields 962.7 kg/m^3 × 9.80665 m/s^2 × (25.5 in × 0.0254 m/in) / (6894.757 Pa / psi), or 0.887 psi.

The momentum flux term of equation (10) is evaluated as the product of the square of the hot channel mass flux and the difference of the reciprocal of the hot channel exit density and the reciprocal of hot channel inlet density, (5664 $kg/m^2/s)^2$ × (1/(943.5 kg/m^3) − 1/(978.4 kg/m^3)) = 1213 Pa = 0.176 psi. This very small term, which reduces the exit pressure, is not present in the new model.

The totals at the bottom of Table 7 show that for the representative limiting test case that the pressure at point 5 of Figure 1 will be 1.2 psi lower for the new model than when the equation (10) approach is used to predict the overall pressure drop for the hot channel. Since a lower exit pressure produces a lower allowed core power, the new method tends to err on the safe side.

10 HYDRAULIC DIAMETER (D_e) AND HEATED DIAMETER (D_i)

The channel hydraulic diameter (D_e), which is four times the flow area divided by the wetted perimeter, and the channel heated diameter (D_i), defined as the heated perimeter divided by π, can easily be determined for each channel in the MURR core. Since in the analysis the limiting channel flow rate and velocity are based on the hot channel thickness of 0.072 inches rather the nominal channel thickness of 0.080 inches, the value of D_e for use in equation (1) is also based on the hot channel thickness. Similarly, D_i is based on the minimum arc lengths allowed by the manufacturing tolerances.

The two fuel plates represented in Table 1 are the innermost two fuel plates and bound the second channel, where the first channel is the one adjacent to the cylindrical inner vessel wall. For the corresponding hot channel, channel 2, the value of hot channel D_e is 0.13876 inches, or 0.011563 feet, and D_i is 1.0784 inches, or 0.089867 feet.

11 COMPUTER SPREADSHEET IMPLEMENTATION

Table 8, which spans five pages, shows the computer spreadsheet that was used to predict the allowed reactor power for the LSSS combination of reactor inlet temperature of 155° F, pressure at the pressurizer of 75 psia, and total core flow rate of 3200 gpm. This table also includes the heat flux peaking factors and the hot channel factors described above. This example is also consistent with the sample calculations provided in Tables 1 through 4.

The rows of Table 8 are numbered 1 through 100. The columns are identified by letters A through O. The inputs to the spreadsheet have a color shading of yellow. These can be found

on pages 2 through 5 of the table and are describe further below. The cell with allowed reactor power output, cell B53, can be found page 2 and has a color shading of light turquoise.

The spreadsheet has two steps. Step 1 starts near the top of Table 8 on line 2. Step 2 starts on line 59 at the top on page 3. In step 1 the pressure at the reactor outlet (cell B51) is determined for use in step 2. In step 2 on line 95 the ratio of channel heat flux to Bernath CHF is determined for each level from levels 12 through 24 of the channel. This ratio is not calculated for levels 1 through 11 because the limiting location cannot occur before level 12. This is because the peak heat flux does not occur before level 12 and the coolant temperature is rising monotonically from the inlet to the outlet. The ratios at levels 12 through 24 are compared and the largest ratio is repeated in cell O95. Cell O96, which has light turquoise shading, provides the level at which the maximum occurred. As explained above, the maximum desired heat flux ratio (cell B71) is 0.499999 instead of 0.5. The value in cell B96 is the desired maximum value (cell B71) minus the maximum heat flux ratio (cell O95). Adjusting the power in cell B53 until the value in cell B96 is zero would provide a maximum heat flux ratio of 0.499999. Cell B98, which has a light turquoise shading, is the degrees Celius of subcooling at the hot channel exit. This value, which is the saturation temperature (cell B75) minus the hot channel exit temperature (cell B74), must not be allowed to become negative. Cell B100 is the minimum of cell B96 and B98. In concept, the reactor power in cell B53 would be gradually increased from a low value until either the subcooling at the channel exit, cell B98 reaches zero or cell B96 equal zero, which implies that the maximum heat flux ratio is 0.499999. A solver in the spreadsheet is used to automatically do this adjustment and determine the maximum allowed reactor power in cell B53. Since step 1 also uses the value of reactor power in cell B53 to determine the pressure at the exit of the core, the reactor exit pressure obtained in step 1 is consistent with the reactor power level that is obtained in step 2.

There are five contiguous sets of boxes on page 1 of Table 8 that have a colored rectangular boundary. The values in the light-blue bounded box, cell B4 through cell F13, were taken from Table 6 and are used in conjunction with equations (4) and (5) to obtain the pressure drop from the pressurizer to the core exit. The five pressures in the first set of green bounded box, lines 15 through 19, are the sum of the frictional and non-frictional pressures at 120° F. The five P/P_0 values in the second green bounded box, lines 21 through 25, correspond to the first set of green bounded boxes. Thus, the frictional pressure drop for the 1825 gpm leg of the Figure 1 flow schematic (from point 1 to point 2) is the product of cells B15 and B21. Similarly, cells B16 and B22 correspond to frictional pressure drop from point 3 to point 4, cells B17 and B23 correspond to non-frictional pressures drop from point 1 to point 2, cells B18 and B24 correspond to the non-frictional pressure drop from point 2 to point 3, and B19 and B25 correspond to the non-frictional pressure drop from point 3 to point 4. The sum of the products of these five pairs is the irrecoverable pressure drop from the pressurizer to the core inlet (point 1 to point 4), 7.875 psi in cell B47.

The values in the medium-blue bounded box are polynomial curve fits to steam table value of density and viscosity at 5 bar for temperatures between 40 and 100° C in increments of 1° C. These functions are of the form $y = a0 + a1 \times T + a2 \times T^2 + a3 \times T^3$, where y is density in kg/m^3 or viscosity in micro Pa s and T is temperature in °C. The values in the brown-bounded boxes use the curve fits in the medium-blue bounded box to obtain values of density and

viscosity for six temperatures. The first two temperatures in the brown-bounded boxes are the two reference temperatures in the light-blue bounded boxes, the next three are the core inlet, average of inlet and outlet, and outlet temperatures, and the last temperature is that of the pressurizer pipe and water.

The input values in cells B54 through B56 are self evident. The input value in cell B61 is the fraction of reactor power that contributes to the fuel plate heat fluxes and primary coolant temperature rise, 0.93. The input values in cells B62, B65, and B68 are hot channel factors, which are provided in section 6, above.

The power factor for enthalpy rise without additional factor, cell B63, 2.299, is Item C of Table 3. It is the product of a 1.03 hot channel factor on fuel content (maximum overload for a plate), a 1.03 hot channel factor on fuel meat thickness (tolerance factor on average fuel meat thickness) and a 2.167 factor that results from combining plate average and azimuthal peaking factors for plates X1P01 and X1P02 of Table 1. The 2.167 factor is calculated in the middle of Table 3. The product of 1.03, 1.03 and 2.167 is 2.299 (cell B63).

Cell B66, the power factor for heat flux without axial factor or additional factor, is Item C of Table 2. It is the product of a 1.03 hot channel factor on fuel content, a 1.15 hot channel factor on (local) fuel meat thickness, a 2.215 plate average peaking factor, and 1.07 plate azimuthal peaking factor, which is 2.807.

The heat transfer area needed for cell B69 is the product of the nominal fuel meat length (24 inches) and twice the sum of the nominal arc lengths of the fuel meats of all of the fuel plates in the core. This was found to be 184.15 ft^2. The flow area in cell B70 is the sum of the nominal flow areas of all 200 channels in the entire core, 0.3419 ft^2. These values are to be compared with those in Reference 2, 184.28 ft^2 for core heat transfer area and 0.3505 ft^2 for the core flow area. The input value for levels 12 through 24 that are needed for lines 78 and 79 can be found in columns D and H, respectively, of Table 1. The input D_e and D_i value in cells D86 and D87, respectively, can be found in section 10, above.

The "overall power factor for heat flux" on line 80 is the product of 2.9814 in cell B67, which is labeled "power factor for heat flux without axial factor & with add'l factor", and the plate axial peaking factor, which is on line 78. The saturation temperature at the core exit in cell B75 is based on a polynomial curve fit to steam table values over a range of pressures from 30 to 85 psia in steps of 5 psi. Lines 80 through 93 are used to evaluate the Bernath CHF. The values on line 92 are 1.8 times those on line 91. The values on line 93 are 3.152481×10^{-6} times those on line 92.

12 DISCUSSION – MOTIVIATION FOR CURRENT ANALYTICAL MODEL DEVELOPMENT

The preceding sections have described the implementation of a methodology in considerable detail. The motivation for undertaking this effort at this time is that an error was found in the manner in which D_i is defined in Reference 2. In the Bernath paper,[1] D_i is defined in the nomenclature section to be "diameter of heated surface (heated perimeter divided by π), ft.

(in.)". In the paper D_i is referred to as the "heated diameter", as can be see in the caption of Figure 1 of the paper. Other authors define "heat diameter", D_{heated}, to be 4 times the flow area divided by the *heated* perimeter. This definition is analogous to hydraulic diameter, D_e, which is defined as 4 times the flow area divided by the *wetted* perimeter. For a test section consisting of liquid flowing inside a round heated-wall tube, the two definitions of heated diameter lead to the same value. However, when the flow cross section is a thin annulus formed by a round heating element inside a round enclosure or in the case of a thin rectangular duct heated along the two longer sides, the second (D_{heated}) definition can produce a value of heated diameter that is an order of magnitude smaller than the one in the Bernath paper.

While comparing his correlation to experimental data, Bernath[1] provided values of D_i and D_e for specific experiments. One of these experiments, the W.A.P.D. data,[9] is for flow in a thin rectangular duct. The abstract of Reference 9, which is available online from OSTI, indicates that the duct dimensions are 0.097 inches by 1 inch by 27 inches long. Thus, $D_e = 4 \times (0.097 \times 1)/(2 \times (0.097 + 1))$ inches = 0.177 inches. If we assume that the two 1-inch sides of the rectangular duct are heated and the two 0.097-inch ones are not heated, then $D_i = 2 \times 1 / \pi$ inches = 0.637 inches. These values of D_e and D_i are the ones cited by Bernath. Using 4 times the flow area divided by the heat perimeter (D_{heated}) for D_i would produce 0.194 inches for a 2-inch heated perimeter. Thus, this example shows that for rectangular ducts Bernath intended that D_i be the heated perimeter divided by π.

In both References 2 and 3, D_i is referred to as the "heated hydraulic diameter". On page 14 of Reference 2 the "heated-to-wetted perimeter ratio" is given as 0.924. This ratio, which is D_e/ D_{heated}, was used in the Reference 2 safety analysis of the MURR reactor to incorrectly obtain D_i. Separate calculations of the heated and wetted perimeters of all MURR channels that are heated by two fuel plates show that this ratio ranges from about 0.88 for the first channel heated by two fuel plates (smallest radius) to 0.94 for the last. The Reference 2 analysis was closely replicated in Appendix B-1, "Replication of MURR 1974 10 MW Upgrade Safety Analysis," of TDR-0125[4] (the feasibility report for the conversion of the MURR core to use LEU fuel instead of HEU). In the replication D_i was taken to be $D_e/0.924$. D_e was taken to be 0.15573, as provided in Reference 2. Thus, Appendix B-1 of Reference 3 repeated the error in D_i in its replication of the Reference 2 results.

13 CONCLUSION

The model that was used to perform flow instability analysis for the MURR HEU core has been described in sufficient detail to enable one to independently reproduce the results of the analysis. Table 8 shows the computer spreadsheet model that was used to implement the model. Tables 1 through 4 provide sample calculations of key input parameters that are used in the Table 8 model. Key aspects of the new model developed by J. C. McKibben to determine the pressure drop from the pressurizer to the core exit are explored and explained.

REFERENCES

1. Louis Bernath, "A Theory of Local-Boiling Burnout and Its Application to Existing Data," *Chemical Engineering Progress Symposium*, Series No. 30, Volume 56, pp. 95-116 (1960).

2. F. R. Vaughan, *Safety Limit Analysis for the MURR Facility*, NUS-TM-EC-9, prepared for the University of Missouri by the NUS Corporation, 4 Research Place, Rockville, Maryland, 20850, May 1973.

3. University of Missouri Research Reactor Safety Analysis Report, Chapter 4, Reactor Description, submitted to the U.S. Nuclear Regulatory Commission in 2006.

4. Feasibility Analysis for HEU to LEU Fuel Conversion of the University of Missouri Research Reactor (MURR), TDR-0125, University of Missouri-Columbia Research Reactor, Columbia Missouri, September 30, 2009.

5. Samuel Glasstone and Alexander Sesonske, *Nuclear Reactor Engineering*, Third Edition, Van Nostrand Reinhold Company, New York, 1981, pp.407-408.

6. W. L. Woodruff, *Evaluation and Selection of Hot Channel (Peaking) Factors for Research Reactor Applications*, ANL/RERTR/TM-28, RERTR Program, Argonne National Laboratory, Argonne, Illinois, February 1997, p. 4. [http://www.rertr.anl.gov/METHODS/TM28.pdf].

7. W. F. Hughes and J. A. Brighton, *Shaum's Outline of Theory and Problems of Fluid Dynamics*, McGraw-Hill Book Company, New York, 1967, p. 29.

8. Sadik Kakac, Ramesh K. Shah, and Win Aung (Editors), *Handbook of Single-Phase Convective Heat Transfer*, John Wiley & Sons, New York, 1987, p. 4-146.

9. M. Troy, *WAPD-TH-340* (July 1957).

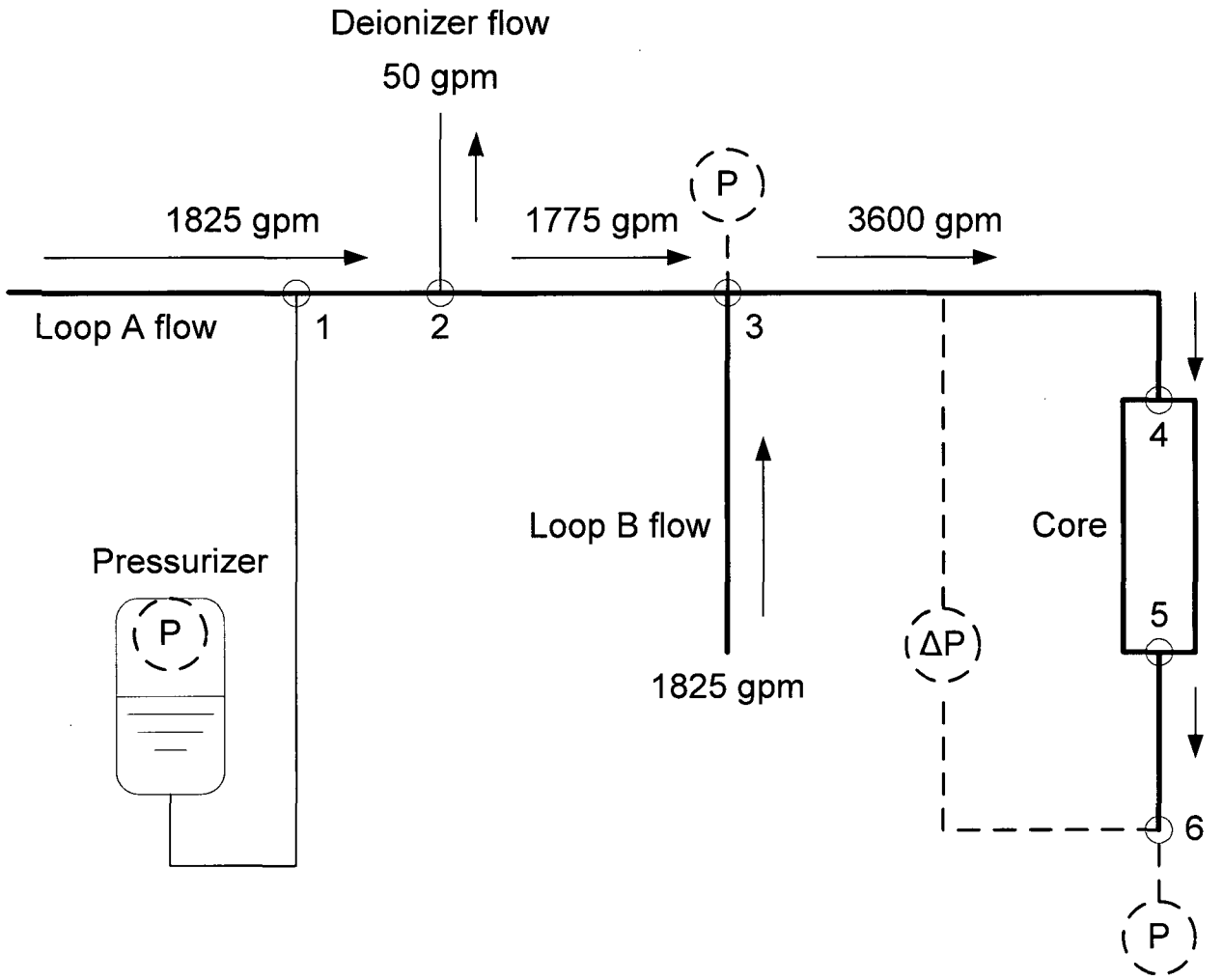


Figure 1 – Schematic Representation of the Reactor Core Inlet Piping

Table 1 – Power and Heat Flux Distribution Calculations for the Channel between Plates X1P01 and X1P02 (Core Power = 10 MW.)

A	B	C	D	E	F	G	H
	Heat Flux, W/cm^{2*}		Plate Axial Peaking Factors		Weighted Average of Cols. D & E**	Col. F / ΣCol. F	Sum of Col. G from Level 1 to Current Level
Level	X1P01	X1P02	X1P01	X1P02			
1	50.9	41.5	0.393	0.405	0.863	0.0166	0.0166
2	54.0	41.6	0.417	0.406	0.893	0.0172	0.0338
3	61.6	49.2	0.476	0.480	1.036	0.0199	0.0537
4	73.6	57.3	0.568	0.559	1.222	0.0235	0.0772
5	86.6	67.6	0.669	0.659	1.440	0.0277	0.1049
6	99.4	78.3	0.768	0.764	1.660	0.0319	0.1368
7	112.8	87.3	0.871	0.852	1.868	0.0359	0.1727
8	124.1	98.1	0.959	0.957	2.076	0.0399	0.2126
9	137.8	108.3	1.064	1.056	2.298	0.0442	0.2568
10	148.7	118.6	1.149	1.157	2.498	0.0480	0.3048
11	158.9	124.9	1.227	1.219	2.651	0.0510	0.3558
12	167.9	133.5	1.296	1.302	2.814	0.0541	0.4099
13	173.7	137.5	1.342	1.341	2.907	0.0559	0.4658
14	**178.8**	140.8	**1.381**	1.373	2.984	0.0574	0.5232
15	178.7	**141.3**	1.380	**1.378**	2.989	0.0575	0.5806
16	178.7	141.0	1.380	1.375	2.986	0.0574	0.6380
17	172.5	138.2	1.332	1.348	2.902	0.0558	0.6938
18	167.8	133.0	1.296	1.298	2.810	0.0540	0.7478
19	158.8	126.4	1.227	1.233	2.664	0.0512	0.7991
20	147.8	116.9	1.141	1.141	2.472	0.0475	0.8466
21	135.5	107.1	1.046	1.045	2.266	0.0436	0.8902
22	121.4	95.2	0.938	0.929	2.023	0.0389	0.9291
23	107.6	86.3	0.831	0.842	1.811	0.0348	0.9639
24	110.5	90.5	0.853	0.883	1.878	0.0361	1.0000
Sum	3107.9	2460.5	24.0	24.0	52.01	1.0000	
Avg.	129.5	102.5	1.000	1.000			
Max.	178.8	141.3	1.381	1.378			
Plate Peaking Factor	2.215	1.754					
Azimuthal Peaking Factor	1.07	1.12					

*The heat fluxes in this Table are based on a core heat transfer area of 17.105 m^2, which is slightly smaller than the 17.108 m^2 value provided in section 3. Therefore, in this table the core average heat flux is 10 MW / 17.105 m^2 = 58.4621 W/cm^2. The extremely small discrepancy in core heat transfer area has absolutely no effect on the allowed values of reactor power because only the heat flux ratios in this table are used in the analysis.

**0.5 × (column D × product of its plate peaking and azimuthal peaking factors + column E × product of its plate peaking and azimuthal peaking factors)

Table 2 – Sample Calculations of Local Heat Flux at Axial Level 18 for Limiting Reactor Power with All Factors Included (To Be Compared with Bernath CHF)

Reactor Power at Limiting Condition: 14.894 MW

Core Heat Transfer Area: 17.108 m^2

Fraction of Reactor Power Deposited in the Primary Loop: 0.93

Average Core Heat Flux: $0.93 \times \frac{14.894\ \text{MW}}{17.108\ \text{m}^2} =$ **0.8096 MW/m^2 = 80.96 W/cm^2**

Plate Axial Peaking Factor at Level 18
(Table 1, Column D, higher power plate of the two bounding the channel): **1.296**

Plate Average Peaking Factor (higher power plate of the two): 2.215
Plate Azimuthal Peaking Factor (higher power plate of the two): 1.07
Product of Plate Average and Azimuthal Peaking Factors (**Item A**): 2.215 × 1.07 = 2.3701

Engineering and Modeling Hot Channel Factors that Affect Local Heat Flux (**Item B**)
Fuel Content (maximum overload for a plate): 1.03
Maximum Fuel Meat Thickness / Average Thickness: 1.15
Item B = 1.03 × 1.15

Product of Items A and B (**Item C**): 2.3701 × 1.03 × 1.15 = **2.807**

Additional Allowable Peaking Factor (**Item D**): 1.062

Overall Factor on Heat Flux without Axial Power Factor (Product of Items C and D = Product of Items A, B and D): 2.807 × 1.062 = **2.981**

Local Heat Flux at Axial Level 18: 0.8096 MW/m^2 × 1.296 × 2.981 = 3.13 MW/m^2 = 313 W/cm^2

Table 3 – Sample Calculations of Local Bulk Coolant Temperature at Axial Level 18 for Limiting Reactor Power with All Factors Included

Reactor Power at Limiting Condition: 14.894 MW
Reactor Volumetric Flow Rate: 3200 gpm = 0.2019 m^3/s
Reactor and Channel Inlet Temperature: 155° F = **68.33° C**
Reactor Inlet Coolant Density: 978.4 kg/m^3
Reactor Mass Flow Rate: 0.2019 m^3/s × 978.4 kg/m^3 = 197.5 kg/s
Coolant Specific Heat Capacity: 4.19 kJ/kg-C
Fraction of Reactor Power Deposited in the Primary Loop: 0.93

Core Temperature Rise: $0.93 \times \frac{14.894\ \text{MW}}{197.5\ \text{kg/s} \times 4.19\ \text{kJ/kg}-\text{C}} =$ **16.74° C**

Fraction of Channel Bulk Coolant Temperature Rise to the Exit of Level 18 (Table 1, Column H): **0.7478**

Plate Average Peaking Factors: 2.215 (Plate 1); 1.754 (Plate 2)
Plate Azimuthal Peaking Factors: 1.07 (Plate 1); 1.12 (Plate 2)
Combination of Plate Average and Azimuthal Peaking Factors (**Item A**):
(2.215 × 1.07 + 1.754 × 1.12) / 2 = 2.167

Engineering and Modeling Hot Channel Factors That Affect Power (**Item B**)
Fuel Content (maximum overload for a plate): 1.03
Fuel Meat Thickness (tolerance factor on average fuel meat thickness): 1.03
Item B = 1.03 × 1.03

Product of Items A and B (**Item C**): 2.167 × 1.03 × 1.03 = **2.299**

Additional Allowable Peaking Factor (**Item D**): 1.062

Overall Peaking Factor for Hot Channel (Product of Items C and D = Product of Items A, B and D): 2.299 × 1.062 = **2.442**

Engineering Hot Channel Factors That Affects Flow (Due to Channel Spacing Tolerance):
Hot Channel Flow Area Factor: 0.90
Hot Channel Factor for Velocity: 0.9108

Both of the Above Combined: 0.90 × 0.9108 = **0.8197**

Maximum Bulk Coolant Temperature Rise to Channel Exit with All Hot Channel Factors Included: **16.74° C × 2.442 / 0.8197 = 49.87° C**

Bulk Coolant Temperature Rise to the Exit of Level 18: **0.7478 × 49.87° C = 37.29° C**

Bulk Coolant Temperature at the Exit of Level 18: 68.33° C + 37.29° C = 105.6° C

Table 4 – Sample Calculations of Local Bulk Coolant Velocity at Axial Level 18 for Limiting Reactor Power with All Factors Included

Reactor Volumetric Flow Rate (at Inlet Coolant Density): 3200 gpm = 0.2019 m^3/s

Reactor Core Total Coolant Flow Area: 0.3419 ft^2 = 0.03176 m^2

Average Coolant Velocity at Reactor Inlet (at Inlet Coolant Density):
0.2019 m^3/s / 0.03176 m^2 = **6.357 m/s**

Engineering Hot Channel Factor for Velocity (This is due to the hot channel having a thickness of 0.072 inches rather than the nominal value of 0.080 inches.): **0.9108**

Hot Channel Velocity at Channel Inlet: 6.357 m/s × 0.9108 = **5.790 m/s**

Reactor and Channel Inlet Temperature: 155° F = 68.3° C

Reactor Inlet Coolant Density: **978.4 kg/m^3**

Bulk Coolant Temperature at the Exit of Level 18 (See Table 3): 105.6° C

Reactor Coolant Density at the Exit of Level 18: **953.6 kg/m^3**

Hot Channel Velocity at the Exit of Level 18: 5.790 m/s × 978.4 kg/m^3 / 953.6 kg/m^3 = 5.941 m/s = 19.49 ft/s

Table 5 – Reference Hydraulic Conditions between the Pressurizer and the Core Exit Used in the Reference 2 Model

Component	ΔP_0, psi	Q_0, gpm*	T_0, °F	Frictional	Parallel Paths
1,2,3	3.259	1800	155	Yes	2
4	0.2689	1800	155	No	2
5 thru 10	4.08	3600	155	Yes	1
11	0.1977	3600	155	Yes	1
12	0.8980	3600	155	No	1
13	12.35	3600	165	Yes	in core

*Per Parallel Path

Table 6 – Reference Hydraulic Conditions between the Pressurizer and the Core Exit Used in the New Model

Component	ΔP_0, psi	Q_0, gpm	T_0, °F	Frictional
1	4.500	1825	120	No
2	0.0913	1825	120	Yes
3	0.2640	1775	120	No
4	3.3961	3600	120	Yes
5	1.1590	3600	120	Yes
6	0.0439	3600	120	No
7	0.7569	3600	120	No
8 (core)	13.8049	3608.3	128.68	Yes

Table 7 – New Model and Hot Channel Pressure Drops for 3200 gpm Core Flow, 155° F at the Core Inlet, 75 psia at the Pressurizer, and 14.894 MW Reactor Power (A negative value decreases the exit pressure.)

Item	New Model (Based on Core Avg.)	Hot Channel (Uses Eq. (10).)
Bernoulli Velocity	−2.897	−2.378
Friction	−10.394	−9.515
Gravity	+0.897	+0.887
Momentum Flux	0.	−0.176
Total	−12.394	−11.182

Table 8 – Computer Spreadsheet for Determining Allowed Power (page 1 of 5)

	A	B	C	D	E	F	G
1	Latest version as of June 6, 2011						
2	Step 1: Calculate reactor outlet pressure for specified power, flow rate, and inlet temperature.						
3							
4	New values based on benchmarked modeling.	Component	ΔP_0	Q_0	T_0	Frictional	
5	JCM 5/16/11	Group	psi	gpm	F		
6		1	4.500	1825	120	No	
7		2	0.0913	1825	120	Yes	
8		3	0.2640	1775	120	No	
9		4	3.3961	3600	120	Yes	
10		5	1.1590	3600	120	Yes	
11		6	0.0439	3600	120	No	
12		7	0.7569	3600	120	No	
13		8	13.8049	3608.3	128.68	Yes	
14							
15	1825 gpm $\Sigma \Delta P_0$ frictional at 120 F, psi	0.0913					
16	3600 gpm $\Sigma \Delta P_0$ frictional at 120 F, psi	4.5551					
17	1825 gpm $\Sigma \Delta P_0$ non-frictional at 120 F, psi	4.5000					
18	1775 gpm $\Sigma \Delta P_0$ non-frictional at 120 F, psi	0.2640					
19	3600 gpm $\Sigma \Delta P_0$ non-frictional at 120 F, psi	0.8008		Curve fit	Density	Viscosity	
20				a0	1004	1383	
21	1825 gpm frictional constant (ΔP / ΔP_0) before inlet	0.7579		a1	-0.1868	-26.04	
22	3600 gpm frictional constant (ΔP / ΔP_0) before inlet	0.7556		a2	-2.751E-03	0.2234	
23	1825 gpm non-frictional constant (ΔP / $\Delta P0$) before inlet	0.7849		a3	0	-7.318E-04	
24	1775 gpm non-frictional constant (ΔP / ΔP_0) before inlet	0.7795					
25	3600 gpm non-frictional constant (ΔP / ΔP_0) before inlet	0.7822					
26							
27		reference conditions		core conditions			pressurizer
28		inlet	core avg.	inlet	average	outlet	pipe
29	Temp, F	120	128.68	155	170.06	185.13	85.00
30	Temp, C	48.9	53.7	68.3	76.7	85.1	29.4
31	density, kg/m^3	988.3	986.0	978.4	973.5	968.2	996.1
32	viscosity, micro Pa-s	558.4	515.5	413.3	369.8	334.0	791.3

Table 8 – Computer Spreadsheet for Determining Allowed Power (page 2 of 5)

	A	B	C	D
33				
34				
35	MPa per psi	6.894757E-03		
36	Cp, kJ/kg-k	4.19		
37				
38	Core Coolant Temp Rise, C, F	16.74	30.13	
39	Core Tavg, C, F	76.7	170.06	
40				
41	pressurizer low level SCRAM, inches	-16	MPa	Bar
42	static head: pressurizer to core exit (exit has lower press.), psi	-0.8673	-0.00598	-0.05980
43	1/2 * density * velocity^2 at fuel plate exit, psi, MPa, bar	2.897	0.01997	0.19971
44	flow area of 8" pipe at pressurizer attachment, ft^2	0.34741		
45	1/2 * density * velocity^2 at pressurizer attachment, psi	0.716	0.00494	0.04936
46	net pressure drop due to increase in velocity, psi, MPa, bar	2.181	0.01503	0.15035
47	Irrecoverable ΔP from Pressurizer to Core Inlet, psi, MPa, bar	7.875	0.05430	0.54297
48	frictional constant ($\Delta P / \Delta P_0$) for core	0.7529		
49	Irrecoverable ΔP across reactor core, psi, MPa, bar	10.394	0.0717	0.7166
50	Total ΔP from Pressurizer to Core Exit, psi, MPa, bar	21.32	0.1470	1.4698
51	Reactor Outlet Presssure, psia, MPa, bar	53.68	0.3701	3.7013
52				
53	total power, MW	14.894		
54	Inlet Temp, F, C	155	68.3	
55	Flow, gpm, m^3/s, ft^3/s	3200	0.2019	7.130
56	Pressurizer Press., psia, MPa, bar	75	0.5171	5.1711
57	Flow, kg/s	197.53		
58				

Table 8 – Computer Spreadsheet for Determining Allowed Power (page 3 of 5)

	A	B	C	D	E	F	G
59	Step 2: Adjust reactor power above until maximum ratio of local heat flux to local Bernath CHF is the desire value.						
60							
61	energy fraction generated in primary loop	0.93					
62	additional (allowable peaking) factor	1.062	greater than the week 58 peaking factors				
63	power factor for enthalpy rise without additional factor	2.299					
64	power factor for enthalpy rise with additional factor	2.442					
65	hot channel flow area factor	0.90	0.900 = 72 mils/80 mils; Used in calculating hot channel				
66	power factor for heat flux without axial factor or additional factor	2.807		bulk coolant temperature to exit			
67	power factor for heat flux without axial factor & with add'l factor	2.9814					
68	engineering hot channel factor for velocity	0.9108	Used in calculating: 1. hot channel bulk temperature rise				
69	heat transfer area, ft^2, m^2	184.15	17.108		to exit & 2. hot channel velcocity		
70	flow area, ft^2, m^2	0.3419	0.03176				
71	desire ratio of (max. heat flux)/CHF	0.499999					
72							
73	hot channel bulk temperature rise to exit, C	49.9					
74	hot channel exit temperature, C	118.2					
75	saturation temperature at core exit, C	140.9					
76							

Table 8 – Computer Spreadsheet for Determining Allowed Power (page 4 of 5)
(Columns I thru O are on page 5.)

	A	B	C	D	E	F	G	H
77	Axial Level	12	13	14	15	16	17	18
78	Plate Axial Peaking Factor	1.296	1.342	1.381	1.380	1.380	1.332	1.296
79	Fractional Bulk Temperature Rise	0.4099	0.4658	0.5232	0.5806	0.6380	0.6938	0.7478
80	overall power factor for heat flux	3.864	4.000	4.116	4.114	4.114	3.970	3.863094
81	hot channel heat flux, MW/m^2	3.129	3.239	3.332	3.331	3.331	3.215	3.128
82	Tbulk at allowed power, C	88.8	91.6	94.4	97.3	100.1	102.9	105.6
83	local density, kg/m^3	965.7	963.8	961.8	959.8	957.7	955.6	953.6
84	hot channel local V, ft/s	19.24	19.28	19.32	19.36	19.40	19.45	19.49
85								
86	De, m, ft, in	3.525E-03	0.011563	0.13876				
87	Di, m, ft, in	2.739E-02	0.089867	1.0784				
88	slope	697.3						
89	T_WBO, C	180.0	180.0	180.0	180.0	180.0	180.0	180.0
90	h_BO, pcu/hr-ft^2-C	14658	14684	14712	14741	14770	14800	14829
91	(Q/A)_BO [CHF], pcu/hr-ft^2	1337541	1298906	1259143	1219216	1179223	1140246	1102395
92	(Q/A)_BO [CHF], Btu/hr-ft^2	2407574	2338030	2266457	2194589	2122601	2052443	1984310
93	(Q/A)_BO [CHF], MW/m^2	7.590	7.371	7.145	6.918	6.691	6.470	6.256
94								
95	ratio of local heat flux to local CHF	0.412237	0.439389	0.466393	0.481426	0.497726	0.496832	0.499999
96	function heat flux ratio	1.161E-08						
97								
98	degrees of subcooling at core exit, C	22.66						
99								
100	minimum of (function heat flux ratio, subcooling at exit)	1.161E-08						

Table 8 – Computer Spreadsheet for Determining Allowed Power (page 5 of 5)
(Columns B thru H are on page 4.)

	A	I	J	K	L	M	N	O
77	Axial Level	19	20	21	22	23	24	
78	Plate Axial Peaking Factor	1.227	1.141	1.046	0.938	0.831	0.853	
79	Fractional Bulk Temperature Rise	0.7991	0.8466	0.8902	0.9291	0.9639	1.0000	
80	overall power factor for heat flux	3.657	3.402	3.119	2.795	2.477	2.543	
81	hot channel heat flux, MW/m^2	2.961	2.754	2.526	2.263	2.006	2.059	
82	Tbulk at allowed power, C	108.2	110.5	112.7	114.7	116.4	118.2	
83	local density, kg/m^3	951.6	949.7	948.0	946.4	945.0	943.5	
84	hot channel local V, ft/s	19.53	19.57	19.60	19.63	19.66	19.70	
85								
86	De, m, ft, in							
87	Di, m, ft, in							
88	slope							
89	T_WBO, C	179.9	179.9	179.9	179.9	179.9	179.9	
90	h_BO, pcu/hr-ft^2-C	14857	14884	14909	14932	14952	14974	
91	(Q/A)_BO [CHF], pcu/hr-ft^2	1066402	1032909	1002131	974583	949861	924174	
92	(Q/A)_BO [CHF], Btu/hr-ft^2	1919523	1859236	1803836	1754250	1709749	1663513	
93	(Q/A)_BO [CHF], MW/m^2	6.051	5.861	5.687	5.530	5.390	5.244	
94								maximum
95	ratio of local heat flux to local CHF	0.489302	0.469895	0.444123	0.409218	0.372150	0.392653	0.499999
96	function heat flux ratio					level of maximum		18
97								
98	degrees of subcooling at core exit, C							
99								
100	minimum of (function heat flux ratio, subcooling at exit)							